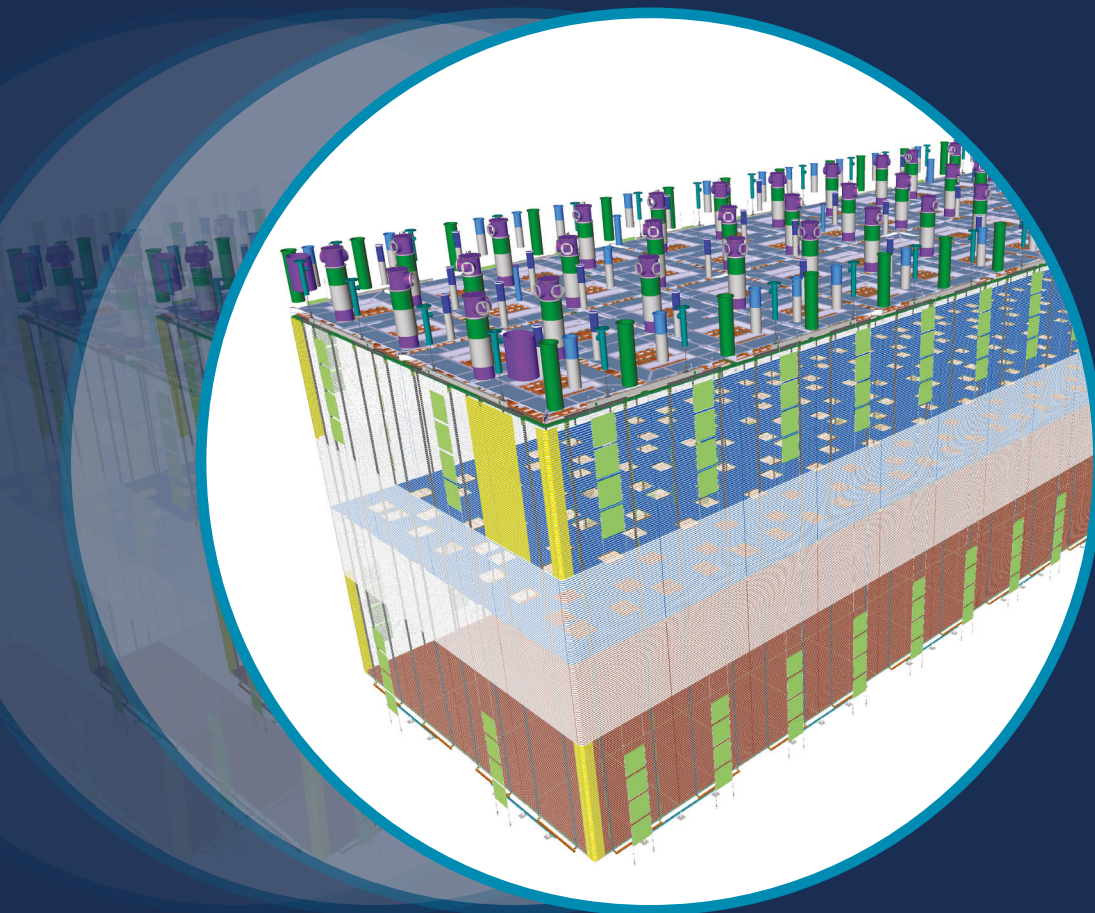


# The DUNE Far Detector Vertical Drift Technology Technical Design Report

arXiv:2312.03130v1 [hep-ex] 5 Dec 2023



June 2023  
The DUNE Collaboration

This document was prepared by the DUNE collaboration using the resources of the Fermi National Accelerator Laboratory (Fermilab), a U.S. Department of Energy, Office of Science, HEP User Facility. Fermilab is managed by Fermi Research Alliance, LLC (FRA), acting under Contract No. DE-AC02-07CH11359.

The DUNE collaboration also acknowledges the international, national, and regional funding agencies supporting the institutions who have contributed to completing this design report.

## Authors

A. Abed Abud,<sup>35</sup> B. Abi,<sup>158</sup> R. Acciarri,<sup>67</sup> M. A. Acero,<sup>12</sup> M. R. Adames,<sup>196</sup> G. Adamov,<sup>73</sup> M. Adamowski,<sup>67</sup> D. Adams,<sup>20</sup> M. Adinolfi,<sup>19</sup> C. Adriano,<sup>30</sup> A. Aduszkiewicz,<sup>82</sup> J. Aguilar,<sup>129</sup> B. Aimard,<sup>51</sup> F. Akbar,<sup>177</sup> K. Allison,<sup>43</sup> S. Alonso Monsalve,<sup>35,60</sup> M. Alrashed,<sup>122</sup> A. Alton,<sup>13</sup> R. Alvarez,<sup>39</sup> H. Amar,<sup>85</sup> P. Amedo,<sup>86,85</sup> J. Anderson,<sup>8</sup> D. A. Andrade,<sup>88</sup> C. Andreopoulos,<sup>131</sup> M. Andreotti,<sup>95,68</sup> M. P. Andrews,<sup>67</sup> F. Andrianala,<sup>5</sup> S. Andringa,<sup>130</sup> N. Anfimov,<sup>120</sup> A. Ankowski,<sup>186</sup> M. Antoniazzi,<sup>196</sup> M. Antonova,<sup>85</sup> A. Antoshkin,<sup>120</sup> A. Aranda-Fernandez,<sup>42</sup> L. Arellano,<sup>137</sup> E. Arrieta Diaz,<sup>182</sup> M. A. Arroyave,<sup>67</sup> J. Asaadi,<sup>200</sup> A. Ashkenazi,<sup>197</sup> L. Asquith,<sup>194</sup> E. Atkin,<sup>89</sup> D. Auguste,<sup>162</sup> A. Aurisano,<sup>40</sup> V. Aushev,<sup>127</sup> D. Autiero,<sup>112</sup> F. Azfar,<sup>158</sup> A. Back,<sup>92</sup> H. Back,<sup>159</sup> J. J. Back,<sup>211</sup> I. Bagaturia,<sup>73</sup> L. Bagby,<sup>67</sup> N. Balashov,<sup>120</sup> S. Balasubramanian,<sup>67</sup> P. Baldi,<sup>24</sup> W. Baldini,<sup>95</sup> B. Baller,<sup>67</sup> B. Bambah,<sup>83</sup> R. Banerjee,<sup>218</sup> F. Barao,<sup>130,114</sup> G. Barenboim,<sup>85</sup> P. Barham Alzás,<sup>35</sup> G. J. Barker,<sup>211</sup> W. Barkhouse,<sup>150</sup> G. Barr,<sup>158</sup> J. Barranco Monarca,<sup>78</sup> A. Barros,<sup>196</sup> N. Barros,<sup>130,62</sup> D. Barrow,<sup>158</sup> J. L. Barrow,<sup>138</sup> A. Basharina-Freshville,<sup>206</sup> A. Bashyal,<sup>8</sup> V. Basque,<sup>67</sup> C. Batchelor,<sup>57</sup> L. Bathe-Peters,<sup>158</sup> J.B.R. Battat,<sup>212</sup> F. Battisti,<sup>158</sup> F. Bay,<sup>4</sup> M. C. Q. Bazetto,<sup>30</sup> J. L. L. Bazo Alba,<sup>171</sup> J. F. Beacom,<sup>156</sup> E. Bechetoille,<sup>112</sup> B. Behera,<sup>69</sup> E. Belchior,<sup>133</sup> G. Bell,<sup>52</sup> L. Bellantoni,<sup>67</sup> G. Bellettini,<sup>104,169</sup> V. Bellini,<sup>94,31</sup> O. Beltramello,<sup>35</sup> N. Benekos,<sup>35</sup> C. Benitez Montiel,<sup>85,10</sup> D. Benjamin,<sup>20</sup> F. Bento Neves,<sup>130</sup> J. Berger,<sup>44</sup> S. Berkman,<sup>141</sup> P. Bernardini,<sup>98,181</sup> A. Bersani,<sup>97</sup> S. Bertolucci,<sup>93,17</sup> M. Betancourt,<sup>67</sup> A. Betancur Rodríguez,<sup>58</sup> A. Bevan,<sup>174</sup> Y. Bezawada,<sup>23</sup> A. T. Bezerra,<sup>63</sup> T. J. Bezerra,<sup>194</sup> A. Bhat,<sup>37</sup> V. Bhatnagar,<sup>161</sup> J. Bhatt,<sup>206</sup> M. Bhattacharjee,<sup>90</sup> M. Bhattacharya,<sup>67</sup> S. Bhuller,<sup>19</sup> B. Bhuyan,<sup>90</sup> S. Biagi,<sup>106</sup> J. Bian,<sup>24</sup> K. Biery,<sup>67</sup> B. Bilki,<sup>15,110</sup> M. Bishai,<sup>20</sup> A. Bitadze,<sup>137</sup> A. Blake,<sup>128</sup> F. D. Blaszczyk,<sup>67</sup> G. C. Blazey,<sup>151</sup> E. Blucher,<sup>37</sup> J. Boissevain,<sup>132</sup> S. Bolognesi,<sup>34</sup> T. Bolton,<sup>122</sup> L. Bomben,<sup>99,109</sup> M. Bonesini,<sup>99,142</sup> C. Bonilla-Diaz,<sup>32</sup> F. Bonini,<sup>20</sup> A. Booth,<sup>174</sup> F. Boran,<sup>92</sup> S. Bordoni,<sup>35</sup> R. Borges Merlo,<sup>30</sup> A. Borkum,<sup>194</sup> N. Bostan,<sup>110</sup> J. Bracinik,<sup>16</sup> D. Braga,<sup>67</sup> B. Brahma,<sup>91</sup> D. Brailsford,<sup>128</sup> F. Bramati,<sup>99</sup> A. Branca,<sup>99</sup> A. Brandt,<sup>200</sup> J. Bremer,<sup>35</sup> C. Brew,<sup>180</sup> S. J. Brice,<sup>67</sup> V. Brio,<sup>94</sup> C. Brizzolari,<sup>99,142</sup> C. Bromberg,<sup>141</sup> J. Brooke,<sup>19</sup> A. Bross,<sup>67</sup> G. Brunetti,<sup>99,142</sup> M. Brunetti,<sup>211</sup> N. Buchanan,<sup>44</sup> H. Budd,<sup>177</sup> J. Buergi,<sup>14</sup> D. Burgardt,<sup>213</sup> S. Butchart,<sup>194</sup> G. Caceres V.,<sup>23</sup> I. Cagnoli,<sup>93,17</sup> T. Cai,<sup>218</sup> R. Calabrese,<sup>95,68</sup> J. Calcutt,<sup>157</sup> M. Calin,<sup>21</sup> L. Calivers,<sup>14</sup> E. Calvo,<sup>39</sup> A. Caminata,<sup>97</sup> W. Campanelli,<sup>130</sup> A. Campos Benitez,<sup>209</sup> N. Canci,<sup>101</sup> J. Capó,<sup>85</sup> I. Caracas,<sup>136</sup> D. Caratelli,<sup>27</sup> D. Carber,<sup>44</sup> J. M. Carceller,<sup>35</sup> G. Carini,<sup>20</sup> B. Carlus,<sup>112</sup> M. F. Carneiro,<sup>20</sup> P. Carniti,<sup>99</sup> I. Caro Terrazas,<sup>44</sup> H. Carranza,<sup>200</sup> N. Carrara,<sup>23</sup> L. Carroll,<sup>122</sup> T. Carroll,<sup>215</sup> A. Carter,<sup>178</sup> D. Casazza,<sup>95</sup> J. F. Castaño Forero,<sup>7</sup> F. A. Castaño,<sup>6</sup> A. Castillo,<sup>184</sup> C. Castromonte,<sup>107</sup> E. Catano-Mur,<sup>214</sup> C. Cattadori,<sup>99</sup> F. Cavalier,<sup>162</sup> F. Cavanna,<sup>67</sup> S. Centro,<sup>160</sup> G. Cerati,<sup>67</sup> A. Cervelli,<sup>93</sup> A. Cervera Villanueva,<sup>85</sup> K. Chakraborty,<sup>168</sup> M. Chalifour,<sup>35</sup> A. Chappell,<sup>211</sup> N. Charitonidis,<sup>35</sup> A. Chatterjee,<sup>168</sup> H. Chen,<sup>20</sup> M. Chen,<sup>24</sup> W. C. Chen,<sup>202</sup> Y. Chen,<sup>186</sup> Z. Chen-Wishart,<sup>178</sup> D. Cherdack,<sup>82</sup> C. Chi,<sup>45</sup> R. Chirco,<sup>88</sup> N. Chitirasreemadam,<sup>104,169</sup> K. Cho,<sup>125</sup> S. Choate,<sup>151</sup> D. Chokheli,<sup>73</sup> P. S. Chong,<sup>166</sup> B. Chowdhury,<sup>8</sup> D. Christian,<sup>67</sup> A. Chukanov,<sup>120</sup> M. Chung,<sup>205</sup> E. Church,<sup>159</sup> M. F. Cicala,<sup>206</sup> M. Cicerchia,<sup>160</sup> V. Cicero,<sup>93,17</sup> R. Ciolini,<sup>104</sup> J. Clair,<sup>45</sup> P. Clarke,<sup>57</sup> G. Cline,<sup>129</sup> T. E. Coan,<sup>190</sup> A. G. Cocco,<sup>101</sup> J. A. B. Coelho,<sup>163</sup> A. Cohen,<sup>163</sup> J. Collot,<sup>77</sup> E. Conley,<sup>55</sup> J. M. Conrad,<sup>138</sup> M. Convery,<sup>186</sup> P. Cooke,<sup>131</sup> S. Copello,<sup>97</sup> P. Cova,<sup>100,164</sup> C. Cox,<sup>178</sup> L. Cremaldi,<sup>146</sup> L. Cremonesi,<sup>174</sup> J. I. Crespo-Anadón,<sup>39</sup> M. Crisler,<sup>67</sup> E. Cristaldo,<sup>99,10</sup> J. Crnkovic,<sup>67</sup> G. Crone,<sup>206</sup> R. Cross,<sup>211</sup> A. Cudd,<sup>43</sup> C. Cuesta,<sup>39</sup> Y. Cui,<sup>26</sup> D. Cussans,<sup>19</sup> J. Dai,<sup>77</sup> O. Dalager,<sup>24</sup> R. Dallavalle,<sup>163</sup> H. da Motta,<sup>33</sup> Z. A. Dar,<sup>214</sup> R. Darby,<sup>194</sup> L. Da Silva Peres,<sup>66</sup> Q. David,<sup>112</sup> G. S. Davies,<sup>146</sup> S. Davini,<sup>97</sup> J. Dawson,<sup>163</sup> R. De Aguiar,<sup>30</sup> P. De Almeida,<sup>30</sup> P. Debbins,<sup>110</sup> I. De Bonis,<sup>51</sup> M. P. Decowski,<sup>148,3</sup> A. de Gouvêa,<sup>152</sup> P. C. De Holanda,<sup>30</sup> I. L. De Icaza Astiz,<sup>194</sup> P. De Jong,<sup>148,3</sup> A. De la Torre,<sup>39</sup> A. Delbart,<sup>34</sup> D. Delepine,<sup>78</sup> M. Delgado,<sup>99,142</sup> A. Dell'Acqua,<sup>35</sup> G. Delle Monache,<sup>96</sup> N. Delmonte,<sup>100,164</sup> P. De Lurgio,<sup>8</sup> R. Demario,<sup>141</sup> J. R. T. de Mello Neto,<sup>66</sup> D. M. DeMuth,<sup>208</sup> S. Dennis,<sup>29</sup> C. Densham,<sup>180</sup> P. Denton,<sup>20</sup> G. W. Deptuch,<sup>20</sup> A. De Roeck,<sup>35</sup> V. De Romeri,<sup>85</sup> J. P. Detje,<sup>29</sup> J. Devine,<sup>35</sup> R. Dharmapalan,<sup>80</sup> M. Dias,<sup>204</sup> J. S. Díaz,<sup>92</sup> F. Díaz,<sup>171</sup> F. Di Capua,<sup>101,147</sup> A. Di Domenico,<sup>183,105</sup> S. Di Domizio,<sup>97,72</sup> S. Di Falco,<sup>104</sup> L. Di Giulio,<sup>35</sup> P. Ding,<sup>67</sup> L. Di Noto,<sup>97,72</sup> E. Diociaiuti,<sup>96</sup> C. Distefano,<sup>106</sup> R. Diurba,<sup>14</sup> M. Diwan,<sup>20</sup> Z. Djurcic,<sup>8</sup> D. Doering,<sup>186</sup> S. Dolan,<sup>35</sup> F. Dolek,<sup>209</sup> M. J. Dolinski,<sup>54</sup> D. Domenici,<sup>96</sup> L. Domine,<sup>186</sup> S. Donati,<sup>104,169</sup> Y. Donon,<sup>35</sup> S. Doran,<sup>111</sup> D. Douglas,<sup>186</sup> T.A. Doyle,<sup>191</sup> A. Dragone,<sup>186</sup> F. Drielsma,<sup>186</sup> L. Duarte,<sup>204</sup> D. Duchesneau,<sup>51</sup> K. Duffy,<sup>158,67</sup> K. Dugas,<sup>24</sup> P. Dunne,<sup>89</sup> B. Dutta,<sup>198</sup> H. Duyang,<sup>187</sup> O. Dvornikov,<sup>80</sup> D. A. Dwyer,<sup>129</sup> A. S. Dyshkant,<sup>151</sup> S. Dytman,<sup>170</sup> M. Eads,<sup>151</sup> A. Earle,<sup>194</sup> S. Edayath,<sup>111</sup> D. Edmunds,<sup>141</sup> J. Eisch,<sup>67</sup> P. Englezos,<sup>179</sup> A. Ereditato,<sup>37</sup> T. Erjavec,<sup>23</sup> C. O. Escobar,<sup>67</sup> J. J. Evans,<sup>137</sup> E. Ewart,<sup>92</sup> A. C. Ezeribe,<sup>185</sup> K. Fahey,<sup>67</sup> L. Fajt,<sup>35</sup> A. Falcone,<sup>99,142</sup> M. Fani',<sup>132</sup> C. Farnese,<sup>102</sup> Y. Farzan,<sup>113</sup> D. Fedoseev,<sup>120</sup> J. Felix,<sup>78</sup> Y. Feng,<sup>111</sup> E. Fernandez-Martinez,<sup>135</sup> F. Ferraro,<sup>97</sup> G. Ferry,<sup>162</sup> L. Fields,<sup>153</sup> P. Filip,<sup>49</sup> A. Filkins,<sup>195</sup> F. Filthaut,<sup>148,175</sup> R. Fine,<sup>132</sup> G. Fiorillo,<sup>101,147</sup> M. Fiorini,<sup>95,68</sup> S. Fogarty,<sup>44</sup> W. Foreman,<sup>88</sup> J. Fowler,<sup>55</sup> J. Franc,<sup>50</sup> K. Francis,<sup>151</sup> D. Franco,<sup>37</sup> J. Franklin,<sup>56</sup> J. Freeman,<sup>67</sup>

J. Fried,<sup>20</sup> A. Friedland,<sup>186</sup> S. Fuess,<sup>67</sup> I. K. Furic,<sup>69</sup> K. Furman,<sup>174</sup> A. P. Furmanski,<sup>145</sup> A. Gabrielli,<sup>93, 17</sup>  
 A. M. Gago,<sup>171</sup> F. Galizzi,<sup>99</sup> H. Gallagher,<sup>203</sup> A. Gallas,<sup>162</sup> N. Gallice,<sup>20</sup> V. Galymov,<sup>112</sup> E. Gamberini,<sup>35</sup>  
 T. Gamble,<sup>185</sup> F. Ganacim,<sup>196</sup> R. Gandhi,<sup>79</sup> S. Ganguly,<sup>67</sup> F. Gao,<sup>27</sup> S. Gao,<sup>20</sup> D. Garcia-Gamez,<sup>74</sup>  
 M. Á. García-Peris,<sup>85</sup> F. Gardim,<sup>63</sup> S. Gardiner,<sup>67</sup> D. Gastler,<sup>18</sup> A. Gauch,<sup>14</sup> J. Gauvreau,<sup>155</sup> P. Gauzzi,<sup>183, 105</sup>  
 G. Ge,<sup>45</sup> N. Geffroy,<sup>51</sup> B. Gelli,<sup>30</sup> S. Gent,<sup>189</sup> L. Gerlach,<sup>20</sup> Z. Ghorbani-Moghaddam,<sup>97</sup> P. Giammaria,<sup>30</sup>  
 T. Giammaria,<sup>95, 68</sup> D. Gibin,<sup>160, 102</sup> I. Gil-Botella,<sup>39</sup> S. Gilligan,<sup>157</sup> A. Gioiosa,<sup>104</sup> S. Giovannella,<sup>96</sup> C. Girerd,<sup>112</sup>  
 A. K. Giri,<sup>91</sup> C. Giugliano,<sup>95</sup> V. Giusti,<sup>104</sup> D. Gnani,<sup>129</sup> O. Gogota,<sup>127</sup> S. Gollapinni,<sup>132</sup> K. Gollwitzer,<sup>67</sup>  
 R. A. Gomes,<sup>64</sup> L. V. Gomez Bermeo,<sup>184</sup> L. S. Gomez Fajardo,<sup>184</sup> F. Gonnella,<sup>16</sup> D. Gonzalez-Diaz,<sup>86</sup>  
 M. Gonzalez-Lopez,<sup>135</sup> M. C. Goodman,<sup>8</sup> S. Goswami,<sup>168</sup> C. Gotti,<sup>99</sup> J. Goudeau,<sup>133</sup> E. Goudzovski,<sup>16</sup> C. Grace,<sup>129</sup>  
 E. Gramellini,<sup>137</sup> R. Gran,<sup>144</sup> E. Granados,<sup>78</sup> P. Granger,<sup>163</sup> C. Grant,<sup>18</sup> D. R. Gratieri,<sup>71, 30</sup> G. Grauso,<sup>101</sup>  
 P. Green,<sup>158</sup> S. Greenberg,<sup>22, 129</sup> J. Greer,<sup>19</sup> W. C. Griffith,<sup>194</sup> F. T. Groetschla,<sup>35</sup> K. Grzelak,<sup>210</sup> W. Gu,<sup>20</sup>  
 V. Guarino,<sup>8</sup> M. Guarise,<sup>95, 68</sup> R. Guenette,<sup>137</sup> E. Guerard,<sup>162</sup> M. Guerzoni,<sup>93</sup> D. Guffanti,<sup>99, 142</sup> A. Guglielmi,<sup>102</sup>  
 B. Guo,<sup>187</sup> Y. Guo,<sup>191</sup> A. Gupta,<sup>186</sup> V. Gupta,<sup>148, 3</sup> G. Gurung,<sup>200</sup> D. Gutierrez,<sup>172</sup> P. Guzowski,<sup>137</sup> M. M. Guzzo,<sup>30</sup>  
 S. Gwon,<sup>38</sup> K. Haaf,<sup>67</sup> A. Habig,<sup>144</sup> H. Hadavand,<sup>200</sup> R. Haenni,<sup>14</sup> L. Hagaman,<sup>216</sup> A. Hahn,<sup>67</sup> J. Haiston,<sup>188</sup>  
 J. Hakenmueller,<sup>55</sup> T. Hamernik,<sup>67</sup> P. Hamilton,<sup>89</sup> J. Hancock,<sup>16</sup> F. Happacher,<sup>96</sup> D. A. Harris,<sup>218, 67</sup> J. Hartnell,<sup>194</sup>  
 T. Hartnett,<sup>180</sup> J. Harton,<sup>44</sup> T. Hasegawa,<sup>124</sup> C. Hasnip,<sup>158</sup> R. Hatcher,<sup>67</sup> K. Hayrapetyan,<sup>174</sup> J. Hays,<sup>174</sup>  
 E. Hazen,<sup>18</sup> M. He,<sup>82</sup> A. Heavey,<sup>67</sup> K. M. Heeger,<sup>216</sup> J. Heise,<sup>193</sup> S. Henry,<sup>177</sup> M. A. Hernandez Morquecho,<sup>88</sup>  
 K. Herner,<sup>67</sup> V. Hewes,<sup>40</sup> A. Higuera,<sup>176</sup> C. Hilgenberg,<sup>145</sup> S. J. Hillier,<sup>16</sup> A. Himmel,<sup>67</sup> E. Hinkle,<sup>37</sup> L.R. Hirsch,<sup>196</sup>  
 J. Ho,<sup>53</sup> J. Hoff,<sup>67</sup> A. Holin,<sup>180</sup> T. Holvey,<sup>158</sup> E. Hoppe,<sup>159</sup> G. A. Horton-Smith,<sup>122</sup> M. Hostert,<sup>145</sup> T. Houdy,<sup>162</sup>  
 B. Howard,<sup>67</sup> R. Howell,<sup>177</sup> I. Hristova,<sup>180</sup> M. S. Hronek,<sup>67</sup> J. Huang,<sup>23</sup> R.G. Huang,<sup>129</sup> Z. Hulcher,<sup>186</sup> M. Ibrahim,<sup>61</sup>  
 G. Iles,<sup>89</sup> N. Ilic,<sup>202</sup> A. M. Iliescu,<sup>96</sup> R. Illingworth,<sup>67</sup> G. Ingratta,<sup>93, 17</sup> A. Ioannisian,<sup>217</sup> B. Irwin,<sup>145</sup> L. Isenhower,<sup>1</sup>  
 M. Ismerio Oliveira,<sup>66</sup> R. Itay,<sup>186</sup> C.M. Jackson,<sup>159</sup> V. Jain,<sup>2</sup> E. James,<sup>67</sup> W. Jang,<sup>200</sup> B. Jargowsky,<sup>24</sup> D. Jena,<sup>67</sup>  
 X. Ji,<sup>20</sup> C. Jiang,<sup>117</sup> J. Jiang,<sup>191</sup> L. Jiang,<sup>209</sup> A. Jipa,<sup>21</sup> F. R. Joaquim,<sup>130, 114</sup> W. Johnson,<sup>188</sup> B. Jones,<sup>200</sup>  
 R. Jones,<sup>185</sup> D. José Fernández,<sup>86</sup> N. Jovancevic,<sup>154</sup> M. Judah,<sup>170</sup> C. K. Jung,<sup>191</sup> T. Junk,<sup>67</sup> Y. Jwa,<sup>186, 45</sup>  
 M. Kabirnezhad,<sup>89</sup> A. C. Kaboth,<sup>178, 180</sup> I. Kadenko,<sup>127</sup> I. Kakorin,<sup>120</sup> A. Kalitkina,<sup>120</sup> D. Kalra,<sup>45</sup> F. Kamiya,<sup>65</sup>  
 M. Kandemir,<sup>59</sup> D. M. Kaplan,<sup>88</sup> G. Karagiorgi,<sup>45</sup> G. Karaman,<sup>110</sup> A. Karcher,<sup>129</sup> Y. Karyotakis,<sup>51</sup> S. Kasai,<sup>126</sup>  
 S. P. Kasetti,<sup>133</sup> L. Kashur,<sup>44</sup> I. Katsioulas,<sup>16</sup> A. Kauther,<sup>151</sup> N. Kazaryan,<sup>217</sup> L. Ke,<sup>20</sup> E. Kearns,<sup>18</sup> P.T. Keener,<sup>166</sup>  
 K.J. Kelly,<sup>35</sup> E. Kemp,<sup>30</sup> O. Kemularia,<sup>73</sup> Y. Kermaidic,<sup>162</sup> W. Ketchum,<sup>67</sup> S. H. Kettell,<sup>20</sup> M. Khabibullin,<sup>108</sup>  
 N. Khan,<sup>89</sup> A. Khotjantsev,<sup>108</sup> A. Khvedelidze,<sup>73</sup> D. Kim,<sup>198</sup> J. Kim,<sup>177</sup> B. King,<sup>67</sup> B. Kirby,<sup>45</sup> M. Kirby,<sup>20</sup>  
 A. Kish,<sup>67</sup> J. Klein,<sup>166</sup> J. Kleykamp,<sup>146</sup> A. Klustova,<sup>89</sup> T. Kobilarcik,<sup>67</sup> L. Koch,<sup>136</sup> K. Koehler,<sup>215</sup> L. W. Koerner,<sup>82</sup>  
 D. H. Koh,<sup>186</sup> L. Kolupaeva,<sup>120</sup> D. Korablev,<sup>120</sup> M. Kordosky,<sup>214</sup> T. Kosc,<sup>77</sup> U. Kose,<sup>35</sup> V. A. Kostelecký,<sup>92</sup>  
 K. Kothekar,<sup>19</sup> I. Kotler,<sup>54</sup> M. Kovalcuk,<sup>49</sup> V. Kozhukalov,<sup>120</sup> W. Krah,<sup>148</sup> R. Kralik,<sup>194</sup> M. Kramer,<sup>129</sup>  
 L. Kreczko,<sup>19</sup> F. Krennrich,<sup>111</sup> I. Kreslo,<sup>14</sup> T. Kroupova,<sup>166</sup> S. Kubota,<sup>137</sup> M. Kubu,<sup>35</sup> Y. Kudenko,<sup>108</sup>  
 V. A. Kudryavtsev,<sup>185</sup> S. Kuhlmann,<sup>8</sup> S. Kulagin,<sup>108</sup> J. Kumar,<sup>80</sup> P. Kumar,<sup>185</sup> S. Kumaran,<sup>24</sup> P. Kunze,<sup>51</sup>  
 J. Kunzmann,<sup>14</sup> R. Kuravi,<sup>129</sup> N. Kurita,<sup>186</sup> C. Kuruppu,<sup>187</sup> V. Kus,<sup>50</sup> T. Kutter,<sup>133</sup> J. Kvasnicka,<sup>49</sup> T. Labree,<sup>151</sup>  
 T. Lackey,<sup>67</sup> A. Lambert,<sup>129</sup> B. J. Land,<sup>166</sup> C. E. Lane,<sup>54</sup> N. Lane,<sup>137</sup> K. Lang,<sup>201</sup> T. Langford,<sup>216</sup> M. Langstaff,<sup>137</sup>  
 F. Lanni,<sup>35</sup> O. Lantwin,<sup>51</sup> J. Larkin,<sup>20</sup> P. Lasorak,<sup>89</sup> D. Last,<sup>166</sup> A. Laudrain,<sup>136</sup> A. Laundrie,<sup>215</sup> G. Laurenti,<sup>93</sup>  
 E. Lavaut,<sup>162</sup> A. Lawrence,<sup>129</sup> P. Laycock,<sup>20</sup> I. Lazanu,<sup>21</sup> M. Lazzaroni,<sup>100, 143</sup> T. Le,<sup>203</sup> S. Leardini,<sup>86</sup> J. Learned,<sup>80</sup>  
 T. LeCompte,<sup>186</sup> C. Lee,<sup>67</sup> V. Legin,<sup>127</sup> G. Lehmann Miotto,<sup>35</sup> R. Lehnert,<sup>92</sup> M. A. Leigui de Oliveira,<sup>65</sup>  
 M. Leitner,<sup>129</sup> D. Leon Silverio,<sup>188</sup> L. M. Lepin,<sup>137</sup> J.-Y Li,<sup>57</sup> S. W. Li,<sup>186</sup> Y. Li,<sup>20</sup> H. Liao,<sup>122</sup> C. S. Lin,<sup>129</sup>  
 D. Lindebaum,<sup>19</sup> R. A. Lineros,<sup>32</sup> J. Ling,<sup>192</sup> A. Lister,<sup>215</sup> B. R. Littlejohn,<sup>88</sup> H. Liu,<sup>20</sup> J. Liu,<sup>24</sup> Y. Liu,<sup>37</sup>  
 S. Lockwitz,<sup>67</sup> M. Lokajicek,<sup>49</sup> I. Lomidze,<sup>73</sup> K. Long,<sup>89</sup> T. V. Lopes,<sup>63</sup> J. Lopez,<sup>6</sup> I. López de Rego,<sup>39</sup>  
 N. López-March,<sup>85</sup> T. Lord,<sup>211</sup> J. M. LoSecco,<sup>153</sup> W. C. Louis,<sup>132</sup> A. Lozano Sanchez,<sup>54</sup> X.-G. Lu,<sup>211</sup> K.B. Luk,<sup>81, 22</sup>  
 B. Lunday,<sup>166</sup> X. Luo,<sup>27</sup> E. Luppi,<sup>95, 68</sup> J. Maalmi,<sup>162</sup> D. MacFarlane,<sup>186</sup> A. A. Machado,<sup>30</sup> P. Machado,<sup>67</sup>  
 C. T. Macias,<sup>92</sup> J. R. Macier,<sup>67</sup> M. MacMahon,<sup>206</sup> A. Maddalena,<sup>76</sup> A. Madera,<sup>35</sup> P. Madigan,<sup>22, 129</sup> S. Magill,<sup>8</sup>  
 C. Magueur,<sup>162</sup> K. Mahn,<sup>141</sup> A. Maio,<sup>130, 62</sup> A. Major,<sup>55</sup> K. Majumdar,<sup>131</sup> M. Man,<sup>202</sup> R. C. Mandujano,<sup>24</sup>  
 J. Maneira,<sup>130, 62</sup> S. Manly,<sup>177</sup> A. Mann,<sup>203</sup> K. Manolopoulos,<sup>180</sup> M. Manrique Plata,<sup>92</sup> S. Manthey Corchado,<sup>39</sup>  
 V. N. Manyam,<sup>20</sup> M. Marchan,<sup>67</sup> A. Marchionni,<sup>67</sup> W. Marciano,<sup>20</sup> D. Marfatia,<sup>80</sup> C. Mariani,<sup>209</sup> J. Maricic,<sup>80</sup>  
 F. Marinho,<sup>115</sup> A. D. Marino,<sup>43</sup> T. Markiewicz,<sup>186</sup> F. Das Chagas Marques,<sup>30</sup> D. Marsden,<sup>137</sup> M. Marshak,<sup>145</sup>  
 C. M. Marshall,<sup>177</sup> J. Marshall,<sup>211</sup> J. Martín-Albo,<sup>85</sup> N. Martinez,<sup>122</sup> D.A. Martinez Caicedo,<sup>188</sup> F. Martínez  
 López,<sup>174</sup> P. Martínez Miravés,<sup>85</sup> S. Martynenko,<sup>20</sup> V. Mascagna,<sup>99</sup> C. Massari,<sup>99</sup> A. Mastbaum,<sup>179</sup> F. Matichard,<sup>129</sup>  
 S. Matsuno,<sup>80</sup> G. Matteucci,<sup>101, 147</sup> J. Matthews,<sup>133</sup> C. Mauer,<sup>166</sup> N. Mauri,<sup>93, 17</sup> K. Mavrokoridis,<sup>131</sup> I. Mawby,<sup>128</sup>  
 R. Mazza,<sup>99</sup> A. Mazzacane,<sup>67</sup> T. McAskil,<sup>212</sup> N. McConkey,<sup>206</sup> K. S. McFarland,<sup>177</sup> C. McGrew,<sup>191</sup> A. McNab,<sup>137</sup>

- L. Meazza,<sup>99</sup> V. C. N. Meddage,<sup>69</sup> A. Mefodiev,<sup>108</sup> B. Mehta,<sup>161</sup> P. Mehta,<sup>118</sup> P. Melas,<sup>11</sup> O. Mena,<sup>85</sup> H. Mendez,<sup>172</sup> P. Mendez,<sup>35</sup> D. P. Méndez,<sup>20</sup> A. Menegolli,<sup>103,165</sup> G. Meng,<sup>102</sup> M. D. Messier,<sup>92</sup> S. Metallo,<sup>145</sup> J. Metcalf,<sup>203,138</sup> W. Metcalf,<sup>133</sup> M. Mewes,<sup>92</sup> H. Meyer,<sup>213</sup> T. Miao,<sup>67</sup> A. Miccoli,<sup>98</sup> G. Michna,<sup>189</sup> V. Mikola,<sup>206</sup> R. Milincic,<sup>80</sup> G. Miller,<sup>137</sup> W. Miller,<sup>145</sup> O. Mineev,<sup>108</sup> A. Minotti,<sup>99,142</sup> L. Miralles,<sup>35</sup> O. G. Miranda,<sup>41</sup> C. Mironov,<sup>163</sup> S. Miryala,<sup>20</sup> S. Miscetti,<sup>96</sup> C. S. Mishra,<sup>67</sup> S. R. Mishra,<sup>187</sup> A. Mislivec,<sup>145</sup> M. Mitchell,<sup>133</sup> D. Mladenov,<sup>35</sup> I. Mocioiu,<sup>167</sup> A. Mogan,<sup>44</sup> N. Moggi,<sup>93,17</sup> R. Mohanta,<sup>83</sup> T. A. Mohayai,<sup>92</sup> N. Mokhov,<sup>67</sup> J. Molina,<sup>10</sup> L. Molina Bueno,<sup>85</sup> E. Montagna,<sup>93,17</sup> A. Montanari,<sup>93</sup> C. Montanari,<sup>103,67,165</sup> D. Montanari,<sup>67</sup> D. Montanino,<sup>98,181</sup> L. M. Montaña Zetina,<sup>41</sup> M. Mooney,<sup>44</sup> A. F. Moor,<sup>29</sup> Z. Moore,<sup>195</sup> D. Moreno,<sup>7</sup> O. Moreno-Palacios,<sup>214</sup> L. Morescalchi,<sup>104</sup> D. Moretti,<sup>99</sup> R. Moretti,<sup>99</sup> C. Morris,<sup>82</sup> C. Mossey,<sup>67</sup> M. Mote,<sup>133</sup> C. A. Moura,<sup>65</sup> G. Moustier,<sup>128</sup> W. Mu,<sup>67</sup> L. Mualem,<sup>28</sup> J. Mueller,<sup>44</sup> M. Muether,<sup>213</sup> F. Muheim,<sup>57</sup> A. Muir,<sup>52</sup> M. Mulhearn,<sup>23</sup> D. Munford,<sup>82</sup> L. J. Munteanu,<sup>35</sup> H. Muramatsu,<sup>145</sup> J. Muraz,<sup>77</sup> M. Murphy,<sup>209</sup> T. Murphy,<sup>195</sup> J. Muse,<sup>145</sup> A. Mytilinaki,<sup>180</sup> J. Nachtman,<sup>110</sup> Y. Nagai,<sup>61</sup> S. Nagu,<sup>134</sup> M. Nalbandyan,<sup>217</sup> R. Nandakumar,<sup>180</sup> D. Naples,<sup>170</sup> S. Narita,<sup>116</sup> A. Nath,<sup>90</sup> A. Navrer-Agasson,<sup>137</sup> N. Nayak,<sup>20</sup> M. Nebot-Guinot,<sup>57</sup> A. Nehm,<sup>136</sup> J. K. Nelson,<sup>214</sup> O. Neogi,<sup>110</sup> J. Nesbit,<sup>215</sup> M. Nessi,<sup>67,35</sup> D. Newbold,<sup>180</sup> M. Newcomer,<sup>166</sup> R. Nichol,<sup>206</sup> F. Nicolas-Arnaldos,<sup>74</sup> A. Nikolica,<sup>166</sup> J. Nikolov,<sup>154</sup> E. Niner,<sup>67</sup> K. Nishimura,<sup>80</sup> A. Norman,<sup>67</sup> A. Norrick,<sup>67</sup> P. Novella,<sup>85</sup> J. A. Nowak,<sup>128</sup> M. Oberling,<sup>8</sup> J. P. Ochoa-Ricoux,<sup>24</sup> S. Oh,<sup>55</sup> S.B. Oh,<sup>67</sup> A. Olivier,<sup>153</sup> A. Olshevskiy,<sup>120</sup> T. Olson,<sup>82</sup> Y. Onel,<sup>110</sup> Y. Onishchuk,<sup>127</sup> A. Oranday,<sup>92</sup> M. Osbiston,<sup>211</sup> J. A. Osorio Vélez,<sup>6</sup> L. Otiniano Ormachea,<sup>46,107</sup> J. Ott,<sup>24</sup> L. Pagani,<sup>23</sup> G. Palacio,<sup>58</sup> O. Palamara,<sup>67</sup> S. Palestini,<sup>35</sup> J. M. Paley,<sup>67</sup> M. Pallavicini,<sup>97,72</sup> C. Palomares,<sup>39</sup> S. Pan,<sup>168</sup> P. Panda,<sup>83</sup> W. Panduro Vazquez,<sup>178</sup> E. Pantic,<sup>23</sup> V. Paolone,<sup>170</sup> V. Papadimitriou,<sup>67</sup> R. Papaleo,<sup>106</sup> A. Papanestis,<sup>180</sup> D. Papoulias,<sup>11</sup> S. Paramesvaran,<sup>19</sup> A. Paris,<sup>172</sup> S. Parke,<sup>67</sup> E. Parozzi,<sup>99,142</sup> S. Parsa,<sup>14</sup> Z. Parsa,<sup>20</sup> S. Parveen,<sup>118</sup> M. Parvu,<sup>21</sup> D. Pasciuto,<sup>104</sup> S. Pascoli,<sup>93,17</sup> L. Pasqualini,<sup>93,17</sup> J. Pasternak,<sup>89</sup> C. Patrick,<sup>57,206</sup> L. Patrizii,<sup>93</sup> R. B. Patterson,<sup>28</sup> T. Patzak,<sup>163</sup> A. Paudel,<sup>67</sup> L. Paulucci,<sup>65</sup> Z. Pavlovic,<sup>67</sup> G. Pawloski,<sup>145</sup> D. Payne,<sup>131</sup> V. Pec,<sup>49</sup> E. Pedreschi,<sup>104</sup> S. J. M. Peeters,<sup>194</sup> W. Pellico,<sup>67</sup> A. Pena Perez,<sup>186</sup> E. Pennacchio,<sup>112</sup> A. Penzo,<sup>110</sup> O. L. G. Peres,<sup>30</sup> Y. F. Perez Gonzalez,<sup>56</sup> L. Pérez-Molina,<sup>39</sup> C. Pernas,<sup>214</sup> J. Perry,<sup>57</sup> D. Pershey,<sup>55</sup> G. Pessina,<sup>99</sup> G. Petrillo,<sup>186</sup> C. Petta,<sup>94,31</sup> R. Petti,<sup>187</sup> V. Pia,<sup>93,17</sup> L. Pickering,<sup>180,178</sup> F. Pietropaolo,<sup>35,102</sup> V.L.Pimentel,<sup>47,30</sup> G. Pinaroli,<sup>20</sup> J. Pinchault,<sup>51</sup> K. Plows,<sup>158</sup> R. Plunkett,<sup>67</sup> C. Pollack,<sup>172</sup> T. Pollman,<sup>148,3</sup> F. Pompa,<sup>85</sup> X. Pons,<sup>35</sup> N. Poonthottathil,<sup>87,111</sup> F. Poppi,<sup>93,17</sup> J. Porter,<sup>194</sup> M. Potekhin,<sup>20</sup> R. Potenza,<sup>94,31</sup> J. Pozimski,<sup>89</sup> M. Pozzato,<sup>93,17</sup> S. Prakash,<sup>30</sup> T. Prakash,<sup>129</sup> C. Pratt,<sup>23</sup> M. Prest,<sup>99</sup> A. Prosser,<sup>67</sup> F. Psihas,<sup>67</sup> D. Pugnere,<sup>112</sup> X. Qian,<sup>20</sup> J. L. Raaf,<sup>67</sup> V. Radeka,<sup>20</sup> J. Rademacker,<sup>19</sup> B. Radics,<sup>218</sup> A. Rafique,<sup>8</sup> E. Raguzin,<sup>20</sup> M. Rai,<sup>211</sup> M. Rajaoalisoa,<sup>40</sup> S. Rajagopalan,<sup>20</sup> I. Rakhno,<sup>67</sup> L. Rakotondravohitra,<sup>5</sup> L. Ralte,<sup>91</sup> M. A. Ramirez Delgado,<sup>166</sup> B. Ramson,<sup>67</sup> A. Rappoldi,<sup>103,165</sup> G. Raselli,<sup>103,165</sup> P. Ratoff,<sup>128</sup> R. Ray,<sup>67</sup> H. Razafinime,<sup>40</sup> E. M. Rea,<sup>145</sup> J. S. Real,<sup>77</sup> B. Rebel,<sup>215,67</sup> R. Rechenmacher,<sup>67</sup> M. Reggiani-Guzzo,<sup>137</sup> J. Reichenbacher,<sup>188</sup> S. D. Reitzner,<sup>67</sup> H. Rejeb Sfar,<sup>35</sup> E. Renner,<sup>132</sup> A. Renshaw,<sup>82</sup> S. Rescia,<sup>20</sup> F. Resnati,<sup>35</sup> Diego Restrepo,<sup>6</sup> C. Reynolds,<sup>174</sup> M. Ribas,<sup>196</sup> S. Riboldi,<sup>100</sup> C. Riccio,<sup>191</sup> G. Riccobene,<sup>106</sup> J. S. Ricol,<sup>77</sup> M. Rigan,<sup>194</sup> E. V. Rincón,<sup>58</sup> A. Ritchie-Yates,<sup>178</sup> S. Ritter,<sup>136</sup> D. Rivera,<sup>132</sup> R. Rivera,<sup>67</sup> A. Robert,<sup>77</sup> J. L. Rocabado Rocha,<sup>85</sup> L. Rochester,<sup>186</sup> M. Roda,<sup>131</sup> P. Rodrigues,<sup>158</sup> M. J. Rodriguez Alonso,<sup>35</sup> J. Rodriguez Rondon,<sup>188</sup> S. Rosauero-Alcaraz,<sup>162</sup> P. Rosier,<sup>162</sup> D. Ross,<sup>141</sup> M. Rossella,<sup>103,165</sup> M. Rossi,<sup>35</sup> M. Ross-Lonergan,<sup>132</sup> N. Roy,<sup>218</sup> P. Roy,<sup>213</sup> C. Rubbia,<sup>75</sup> A. Ruggeri,<sup>93</sup> G. Ruiz Ferreira,<sup>137</sup> B. Russell,<sup>129</sup> D. Ruterbories,<sup>177</sup> A. Rybnikov,<sup>120</sup> A. Saa-Hernandez,<sup>86</sup> R. Saakyan,<sup>206</sup> S. Sacerdoti,<sup>163</sup> S. K. Sahoo,<sup>91</sup> N. Sahu,<sup>91</sup> K. Sakashita,<sup>124</sup> P. Sala,<sup>100,35</sup> N. Samios,<sup>20</sup> O. Samoylov,<sup>120</sup> M. C. Sanchez,<sup>70</sup> A. Sánchez Bravo,<sup>85</sup> P. Sanchez-Lucas,<sup>74</sup> V. Sandberg,<sup>132</sup> D. A. Sanders,<sup>146</sup> D. Sankey,<sup>180</sup> D. Santoro,<sup>100</sup> N. Saoulidou,<sup>11</sup> P. Sapienza,<sup>106</sup> C. Sarasty,<sup>40</sup> I. Sarcevic,<sup>9</sup> I. Sarra,<sup>96</sup> G. Savage,<sup>67</sup> V. Savinov,<sup>170</sup> G. Scanavini,<sup>216</sup> A. Scaramelli,<sup>103</sup> A. Scarff,<sup>185</sup> T. Schefke,<sup>133</sup> H. Schellman,<sup>157,67</sup> S. Schifano,<sup>95,68</sup> P. Schlabach,<sup>67</sup> D. Schmitz,<sup>37</sup> A. W. Schneider,<sup>138</sup> K. Scholberg,<sup>55</sup> A. Schukraft,<sup>67</sup> B. Schuld,<sup>43</sup> E. Segreto,<sup>30</sup> A. Selyunin,<sup>120</sup> C. R. Senise,<sup>204</sup> J. Sensenig,<sup>166</sup> M. H. Shaevitz,<sup>45</sup> P. Shanahan,<sup>67</sup> P. Sharma,<sup>161</sup> R. Kumar,<sup>173</sup> K. Shaw,<sup>194</sup> T. Shaw,<sup>67</sup> K. Shchablo,<sup>112</sup> C. Shepherd-Themistocleous,<sup>180</sup> A. Sheshukov,<sup>120</sup> W. Shi,<sup>191</sup> S. Shin,<sup>119</sup> S. Shivakoti,<sup>213</sup> I. Shoemaker,<sup>209</sup> D. Shooltz,<sup>141</sup> R. Shrock,<sup>191</sup> B. Siddi,<sup>95</sup> J. Silber,<sup>129</sup> L. Simard,<sup>162</sup> J. Sinclair,<sup>186</sup> G. Sinev,<sup>188</sup> Jaydip Singh,<sup>134</sup> J. Singh,<sup>134</sup> L. Singh,<sup>48</sup> P. Singh,<sup>174</sup> V. Singh,<sup>48</sup> S. Singh Chauhan,<sup>161</sup> R. Sipos,<sup>35</sup> C. Sironneau,<sup>163</sup> G. Sirri,<sup>93</sup> K. Siyeon,<sup>38</sup> K. Skarpaas,<sup>186</sup> J. Smedley,<sup>177</sup> E. Smith,<sup>92</sup> J. Smith,<sup>191</sup> P. Smith,<sup>92</sup> J. Smolik,<sup>50,49</sup> M. Smy,<sup>24</sup> M. Snape,<sup>211</sup> E.L. Snider,<sup>67</sup> P. Snopok,<sup>88</sup> D. Snowden-Ifft,<sup>155</sup> M. Soares Nunes,<sup>67</sup> H. Sobel,<sup>24</sup> M. Soderberg,<sup>195</sup> S. Sokolov,<sup>120</sup> C. J. Solano Salinas,<sup>207,107</sup> S. Söldner-Rembold,<sup>137</sup> S.R. Soleti,<sup>129</sup> N. Solomey,<sup>213</sup> V. Solovov,<sup>130</sup> W. E. Sondheim,<sup>132</sup> M. Sorel,<sup>85</sup> A. Sotnikov,<sup>120</sup> J. Soto-Oton,<sup>85</sup> A. Sousa,<sup>40</sup> K. Soustruznik,<sup>36</sup> F. Spinella,<sup>104</sup> J. Spitz,<sup>140</sup> N. J. C. Spooner,<sup>185</sup> K. Spurgeon,<sup>195</sup> D. Stalder,<sup>10</sup> M. Stancari,<sup>67</sup> L. Stanco,<sup>102,160</sup> J. Steenis,<sup>23</sup> R. Stein,<sup>19</sup> H. M. Steiner,<sup>129</sup> A. F. Steklain Lisbôa,<sup>196</sup>

A. Stepanova,<sup>120</sup> J. Stewart,<sup>20</sup> B. Stillwell,<sup>37</sup> J. Stock,<sup>188</sup> F. Stocker,<sup>35</sup> T. Stokes,<sup>133</sup> M. Strait,<sup>145</sup> T. Strauss,<sup>67</sup> L. Strigari,<sup>198</sup> A. Stuart,<sup>42</sup> J. G. Suarez,<sup>58</sup> J. Subash,<sup>16</sup> A. Surdo,<sup>98</sup> L. Suter,<sup>67</sup> C. M. Suter,<sup>94,31</sup> K. Sutton,<sup>28</sup> Y. Suvorov,<sup>101,147</sup> R. Svoboda,<sup>23</sup> S. K. Swain,<sup>149</sup> B. Szczerbinska,<sup>199</sup> A. M. Szec,<sup>57</sup> A. Sztuc,<sup>206</sup> A. Taffara,<sup>104</sup> N. Talukdar,<sup>187</sup> J. Tamara,<sup>7</sup> H. A. Tanaka,<sup>186</sup> S. Tang,<sup>20</sup> N. Taniuchi,<sup>29</sup> A. M. Tapia Casanova,<sup>139</sup> B. Tapia Oregui,<sup>201</sup> A. Tapper,<sup>89</sup> S. Tariq,<sup>67</sup> E. Tarpara,<sup>20</sup> E. Tatar,<sup>84</sup> R. Tayloe,<sup>92</sup> D. Tedeschi,<sup>187</sup> A. M. Teklu,<sup>191</sup> J. Tena Vidal,<sup>197</sup> P. Tennessen,<sup>129,4</sup> M. Tenti,<sup>93</sup> K. Terao,<sup>186</sup> F. Terranova,<sup>99,142</sup> G. Testera,<sup>97</sup> T. Thakore,<sup>40</sup> A. Thea,<sup>180</sup> A. Thiebault,<sup>162</sup> A. Thompson,<sup>198</sup> C. Thorn,<sup>20</sup> S. C. Timm,<sup>67</sup> E. Tiras,<sup>59,110</sup> V. Tishchenko,<sup>20</sup> N. Todorović,<sup>154</sup> L. Tomassetti,<sup>95,68</sup> A. Tonazzo,<sup>163</sup> D. Torbunov,<sup>20</sup> M. Torti,<sup>99</sup> M. Tortola,<sup>85</sup> F. Tortorici,<sup>94,31</sup> N. Tosi,<sup>93</sup> D. Totani,<sup>27</sup> M. Touns,<sup>67</sup> C. Touramanis,<sup>131</sup> R. Travaglini,<sup>93</sup> J. Trevor,<sup>28</sup> E. Triller,<sup>141</sup> S. Trilov,<sup>19</sup> D. Truncali,<sup>183,105</sup> W. H. Trzaska,<sup>121</sup> Y. Tsai,<sup>24</sup> Y.-T. Tsai,<sup>186</sup> Z. Tsamalaidze,<sup>73</sup> K. V. Tsang,<sup>186</sup> N. Tsverava,<sup>73</sup> S. Z. Tu,<sup>117</sup> S. Tufanli,<sup>35</sup> J. Turner,<sup>56</sup> M. Tuzi,<sup>85</sup> J. Tyler,<sup>122</sup> E. Tyley,<sup>185</sup> M. Tzanov,<sup>133</sup> M. A. Uchida,<sup>29</sup> J. Ureña González,<sup>85</sup> J. Urheim,<sup>92</sup> T. Usher,<sup>186</sup> H. Utaegbulam,<sup>177</sup> S. Uzunyan,<sup>151</sup> M. R. Vagins,<sup>123,24</sup> P. Vahle,<sup>214</sup> S. Valder,<sup>194</sup> G. A. Valdivieso,<sup>63</sup> E. Valencia,<sup>78</sup> R. Valentim,<sup>204</sup> Z. Vallari,<sup>28</sup> E. Vallazza,<sup>99</sup> J. W. F. Valle,<sup>85</sup> R. Van Berg,<sup>166</sup> R. G. Van de Water,<sup>132</sup> D. V. Forero,<sup>139</sup> M. Van Nuland-Troost,<sup>148</sup> F. Varanini,<sup>102</sup> D. Vargas Oliva,<sup>202</sup> G. Varner,<sup>80</sup> S. Vasina,<sup>120</sup> N. Vaughan,<sup>157</sup> K. Vaziri,<sup>67</sup> J. Vega,<sup>46</sup> S. Ventura,<sup>102</sup> A. Verdugo,<sup>39</sup> S. Vergani,<sup>206</sup> M. Verzocchi,<sup>67</sup> K. Vetter,<sup>67</sup> M. Vicenzi,<sup>20</sup> H. Vieira de Souza,<sup>163</sup> C. Vignoli,<sup>76</sup> C. Vilela,<sup>130</sup> E. Villa,<sup>35</sup> B. Viren,<sup>20</sup> A. Vizcaya-Hernandez,<sup>44</sup> T. Vrba,<sup>50</sup> Q. Vuong,<sup>177</sup> A. V. Waldron,<sup>174</sup> M. Wallbank,<sup>40</sup> J. Walsh,<sup>141</sup> T. Walton,<sup>67</sup> H. Wang,<sup>25</sup> J. Wang,<sup>188</sup> L. Wang,<sup>129</sup> M.H.L.S. Wang,<sup>67</sup> X. Wang,<sup>67</sup> Y. Wang,<sup>25</sup> K. Warburton,<sup>111</sup> D. Warner,<sup>44</sup> L. Warsame,<sup>89</sup> M.O. Wascko,<sup>89</sup> D. Waters,<sup>206</sup> A. Watson,<sup>16</sup> K. Wawrowska,<sup>180,194</sup> A. Weber,<sup>136,67</sup> M. Weber,<sup>14</sup> H. Wei,<sup>133</sup> A. Weinstein,<sup>111</sup> H. Wenzel,<sup>67</sup> S. Westerdale,<sup>26</sup> M. Wetstein,<sup>111</sup> K. Whalen,<sup>180</sup> J. Whilhelmi,<sup>216</sup> A. White,<sup>200</sup> A. White,<sup>216</sup> L. H. Whitehead,<sup>29</sup> D. Whittington,<sup>195</sup> M. J. Wilking,<sup>145</sup> A. Wilkinson,<sup>206</sup> C. Wilkinson,<sup>129</sup> F. Wilson,<sup>180</sup> R. J. Wilson,<sup>44</sup> P. Winter,<sup>8</sup> W. Wisniewski,<sup>186</sup> J. Wolcott,<sup>203</sup> J. Wolfs,<sup>177</sup> T. Wongjirad,<sup>203</sup> A. Wood,<sup>82</sup> K. Wood,<sup>129</sup> E. Worcester,<sup>20</sup> M. Worcester,<sup>20</sup> M. Wospakrik,<sup>67</sup> K. Wresilo,<sup>29</sup> C. Wret,<sup>177</sup> S. Wu,<sup>145</sup> W. Wu,<sup>67</sup> W. Wu,<sup>24</sup> M. Wurm,<sup>136</sup> J. Wyenberg,<sup>53</sup> Y. Xiao,<sup>24</sup> I. Xioidis,<sup>89</sup> B. Yaeggy,<sup>40</sup> N. Yahlali,<sup>85</sup> E. Yandel,<sup>27</sup> K. Yang,<sup>158</sup> T. Yang,<sup>67</sup> A. Yankelevich,<sup>24</sup> N. Yershov,<sup>108</sup> K. Yonehara,<sup>67</sup> T. Young,<sup>150</sup> B. Yu,<sup>20</sup> H. Yu,<sup>20</sup> J. Yu,<sup>200</sup> Y. Yu,<sup>88</sup> W. Yuan,<sup>57</sup> R. Zaki,<sup>218</sup> J. Zalesak,<sup>49</sup> L. Zambelli,<sup>51</sup> B. Zamorano,<sup>74</sup> A. Zani,<sup>100</sup> O. Zapata,<sup>6</sup> L. Zazueta,<sup>195</sup> G. P. Zeller,<sup>67</sup> J. Zennamo,<sup>67</sup> K. Zeug,<sup>215</sup> C. Zhang,<sup>20</sup> S. Zhang,<sup>92</sup> M. Zhao,<sup>20</sup> E. Zhivun,<sup>20</sup> E. D. Zimmerman,<sup>43</sup> S. Zucchelli,<sup>93,17</sup> J. Zuklin,<sup>49</sup> V. Zutshi,<sup>151</sup> and R. Zwaska<sup>67</sup>

(The DUNE Collaboration)

<sup>1</sup>Abilene Christian University, Abilene, TX 79601, USA

<sup>2</sup>University of Albany, SUNY, Albany, NY 12222, USA

<sup>3</sup>University of Amsterdam, NL-1098 XG Amsterdam, The Netherlands

<sup>4</sup>Antalya Bilim University, 07190 Döşemealtı/Antalya, Turkey

<sup>5</sup>University of Antananarivo, Antananarivo 101, Madagascar

<sup>6</sup>University of Antioquia, Medellín, Colombia

<sup>7</sup>Universidad Antonio Nariño, Bogotá, Colombia

<sup>8</sup>Argonne National Laboratory, Argonne, IL 60439, USA

<sup>9</sup>University of Arizona, Tucson, AZ 85721, USA

<sup>10</sup>Universidad Nacional de Asunción, San Lorenzo, Paraguay

<sup>11</sup>University of Athens, Zografou GR 157 84, Greece

<sup>12</sup>Universidad del Atlántico, Barranquilla, Atlántico, Colombia

<sup>13</sup>Augustana University, Sioux Falls, SD 57197, USA

<sup>14</sup>University of Bern, CH-3012 Bern, Switzerland

<sup>15</sup>Beykent University, Istanbul, Turkey

<sup>16</sup>University of Birmingham, Birmingham B15 2TT, United Kingdom

<sup>17</sup>Università di Bologna, 40127 Bologna, Italy

<sup>18</sup>Boston University, Boston, MA 02215, USA

<sup>19</sup>University of Bristol, Bristol BS8 1TL, United Kingdom

<sup>20</sup>Brookhaven National Laboratory, Upton, NY 11973, USA

<sup>21</sup>University of Bucharest, Bucharest, Romania

<sup>22</sup>University of California Berkeley, Berkeley, CA 94720, USA

<sup>23</sup>University of California Davis, Davis, CA 95616, USA

<sup>24</sup>University of California Irvine, Irvine, CA 92697, USA

<sup>25</sup>University of California Los Angeles, Los Angeles, CA 90095, USA

<sup>26</sup>University of California Riverside, Riverside CA 92521, USA

<sup>27</sup>University of California Santa Barbara, Santa Barbara, California 93106 USA

<sup>28</sup>California Institute of Technology, Pasadena, CA 91125, USA

<sup>29</sup>University of Cambridge, Cambridge CB3 0HE, United Kingdom

- <sup>30</sup>Universidade Estadual de Campinas, Campinas - SP, 13083-970, Brazil
- <sup>31</sup>Università di Catania, 2 - 95131 Catania, Italy
- <sup>32</sup>Universidad Católica del Norte, Antofagasta, Chile
- <sup>33</sup>Centro Brasileiro de Pesquisas Físicas, Rio de Janeiro, RJ 22290-180, Brazil
- <sup>34</sup>IRFU, CEA, Université Paris-Saclay, F-91191 Gif-sur-Yvette, France
- <sup>35</sup>CERN, The European Organization for Nuclear Research, 1211 Meyrin, Switzerland
- <sup>36</sup>Institute of Particle and Nuclear Physics of the Faculty of Mathematics and Physics of the Charles University, 180 00 Prague 8, Czech Republic
- <sup>37</sup>University of Chicago, Chicago, IL 60637, USA
- <sup>38</sup>Chung-Ang University, Seoul 06974, South Korea
- <sup>39</sup>CIEMAT, Centro de Investigaciones Energéticas, Medioambientales y Tecnológicas, E-28040 Madrid, Spain
- <sup>40</sup>University of Cincinnati, Cincinnati, OH 45221, USA
- <sup>41</sup>Centro de Investigación y de Estudios Avanzados del Instituto Politécnico Nacional (Cinvestav), Mexico City, Mexico
- <sup>42</sup>Universidad de Colima, Colima, Mexico
- <sup>43</sup>University of Colorado Boulder, Boulder, CO 80309, USA
- <sup>44</sup>Colorado State University, Fort Collins, CO 80523, USA
- <sup>45</sup>Columbia University, New York, NY 10027, USA
- <sup>46</sup>Comisión Nacional de Investigación y Desarrollo Aeroespacial, Lima, Peru
- <sup>47</sup>Centro de Tecnologia da Informacao Renato Archer, Amarais - Campinas, SP - CEP 13069-901
- <sup>48</sup>Central University of South Bihar, Gaya, 824236, India
- <sup>49</sup>Institute of Physics, Czech Academy of Sciences, 182 00 Prague 8, Czech Republic
- <sup>50</sup>Czech Technical University, 115 19 Prague 1, Czech Republic
- <sup>51</sup>Laboratoire d'Annecy de Physique des Particules, Université Savoie Mont Blanc, CNRS, LAPP-IN2P3, 74000 Annecy, France
- <sup>52</sup>Daresbury Laboratory, Cheshire WA4 4AD, United Kingdom
- <sup>53</sup>Dordt University, Sioux Center, IA 51250, USA
- <sup>54</sup>Drexel University, Philadelphia, PA 19104, USA
- <sup>55</sup>Duke University, Durham, NC 27708, USA
- <sup>56</sup>Durham University, Durham DH1 3LE, United Kingdom
- <sup>57</sup>University of Edinburgh, Edinburgh EH8 9YL, United Kingdom
- <sup>58</sup>Universidad EIA, Envigado, Antioquia, Colombia
- <sup>59</sup>Erciyes University, Kayseri, Turkey
- <sup>60</sup>ETH Zurich, Zurich, Switzerland
- <sup>61</sup>Eötvös Loránd University, 1053 Budapest, Hungary
- <sup>62</sup>Faculdade de Ciências da Universidade de Lisboa - FCUL, 1749-016 Lisboa, Portugal
- <sup>63</sup>Universidade Federal de Alfenas, Poços de Caldas - MG, 37715-400, Brazil
- <sup>64</sup>Universidade Federal de Goiás, Goiania, GO 74690-900, Brazil
- <sup>65</sup>Universidade Federal do ABC, Santo André - SP, 09210-580, Brazil
- <sup>66</sup>Universidade Federal do Rio de Janeiro, Rio de Janeiro - RJ, 21941-901, Brazil
- <sup>67</sup>Fermi National Accelerator Laboratory, Batavia, IL 60510, USA
- <sup>68</sup>University of Ferrara, Ferrara, Italy
- <sup>69</sup>University of Florida, Gainesville, FL 32611-8440, USA
- <sup>70</sup>Florida State University, Tallahassee, FL, 32306 USA
- <sup>71</sup>Fluminense Federal University, 9 Icaraí Niterói - RJ, 24220-900, Brazil
- <sup>72</sup>Università degli Studi di Genova, Genova, Italy
- <sup>73</sup>Georgian Technical University, Tbilisi, Georgia
- <sup>74</sup>University of Granada & CAFPE, 18002 Granada, Spain
- <sup>75</sup>Gran Sasso Science Institute, L'Aquila, Italy
- <sup>76</sup>Laboratori Nazionali del Gran Sasso, L'Aquila AQ, Italy
- <sup>77</sup>University Grenoble Alpes, CNRS, Grenoble INP, LPSC-IN2P3, 38000 Grenoble, France
- <sup>78</sup>Universidad de Guanajuato, Guanajuato, C.P. 37000, Mexico
- <sup>79</sup>Harish-Chandra Research Institute, Jhansi, Allahabad 211 019, India
- <sup>80</sup>University of Hawaii, Honolulu, HI 96822, USA
- <sup>81</sup>Hong Kong University of Science and Technology, Kowloon, Hong Kong, China
- <sup>82</sup>University of Houston, Houston, TX 77204, USA
- <sup>83</sup>University of Hyderabad, Gachibowli, Hyderabad - 500 046, India
- <sup>84</sup>Idaho State University, Pocatello, ID 83209, USA
- <sup>85</sup>Instituto de Física Corpuscular, CSIC and Universitat de València, 46980 Paterna, Valencia, Spain
- <sup>86</sup>Instituto Galego de Física de Altas Enerxías, University of Santiago de Compostela, Santiago de Compostela, 15782, Spain
- <sup>87</sup>Indian Institute of Technology Kanpur, Uttar Pradesh 208016, India
- <sup>88</sup>Illinois Institute of Technology, Chicago, IL 60616, USA
- <sup>89</sup>Imperial College of Science Technology and Medicine, London SW7 2BZ, United Kingdom
- <sup>90</sup>Indian Institute of Technology Guwahati, Guwahati, 781 039, India
- <sup>91</sup>Indian Institute of Technology Hyderabad, Hyderabad, 502285, India
- <sup>92</sup>Indiana University, Bloomington, IN 47405, USA

- <sup>93</sup>Istituto Nazionale di Fisica Nucleare Sezione di Bologna, 40127 Bologna BO, Italy
- <sup>94</sup>Istituto Nazionale di Fisica Nucleare Sezione di Catania, I-95123 Catania, Italy
- <sup>95</sup>Istituto Nazionale di Fisica Nucleare Sezione di Ferrara, I-44122 Ferrara, Italy
- <sup>96</sup>Istituto Nazionale di Fisica Nucleare Laboratori Nazionali di Frascati, Frascati, Roma, Italy
- <sup>97</sup>Istituto Nazionale di Fisica Nucleare Sezione di Genova, 16146 Genova GE, Italy
- <sup>98</sup>Istituto Nazionale di Fisica Nucleare Sezione di Lecce, 73100 - Lecce, Italy
- <sup>99</sup>Istituto Nazionale di Fisica Nucleare Sezione di Milano Bicocca, 3 - I-20126 Milano, Italy
- <sup>100</sup>Istituto Nazionale di Fisica Nucleare Sezione di Milano, 20133 Milano, Italy
- <sup>101</sup>Istituto Nazionale di Fisica Nucleare Sezione di Napoli, I-80126 Napoli, Italy
- <sup>102</sup>Istituto Nazionale di Fisica Nucleare Sezione di Padova, 35131 Padova, Italy
- <sup>103</sup>Istituto Nazionale di Fisica Nucleare Sezione di Pavia, I-27100 Pavia, Italy
- <sup>104</sup>Istituto Nazionale di Fisica Nucleare Laboratori Nazionali di Pisa, Pisa PI, Italy
- <sup>105</sup>Istituto Nazionale di Fisica Nucleare Sezione di Roma, 00185 Roma RM, Italy
- <sup>106</sup>Istituto Nazionale di Fisica Nucleare Laboratori Nazionali del Sud, 95123 Catania, Italy
- <sup>107</sup>Universidad Nacional de Ingeniería, Lima 25, Perú
- <sup>108</sup>Institute for Nuclear Research of the Russian Academy of Sciences, Moscow 117312, Russia
- <sup>109</sup>University of Insubria, Via Ravasi, 2, 21100 Varese VA, Italy
- <sup>110</sup>University of Iowa, Iowa City, IA 52242, USA
- <sup>111</sup>Iowa State University, Ames, Iowa 50011, USA
- <sup>112</sup>Institut de Physique des 2 Infinis de Lyon, 69622 Villeurbanne, France
- <sup>113</sup>Institute for Research in Fundamental Sciences, Tehran, Iran
- <sup>114</sup>Instituto Superior Técnico - IST, Universidade de Lisboa, Portugal
- <sup>115</sup>Instituto Tecnológico de Aeronáutica, Sao Jose dos Campos, Brazil
- <sup>116</sup>Iwate University, Morioka, Iwate 020-8551, Japan
- <sup>117</sup>Jackson State University, Jackson, MS 39217, USA
- <sup>118</sup>Jawaharlal Nehru University, New Delhi 110067, India
- <sup>119</sup>Jeonbuk National University, Jeonrabuk-do 54896, South Korea
- <sup>120</sup>Joint Institute for Nuclear Research, Dzhelapov Laboratory of Nuclear Problems 6 Joliot-Curie, Dubna, Moscow Region, 141980 RU
- <sup>121</sup>Jyväskylä University, FI-40014 Jyväskylä, Finland
- <sup>122</sup>Kansas State University, Manhattan, KS 66506, USA
- <sup>123</sup>Kavli Institute for the Physics and Mathematics of the Universe, Kashiwa, Chiba 277-8583, Japan
- <sup>124</sup>High Energy Accelerator Research Organization (KEK), Ibaraki, 305-0801, Japan
- <sup>125</sup>Korea Institute of Science and Technology Information, Daejeon, 34141, South Korea
- <sup>126</sup>National Institute of Technology, Kure College, Hiroshima, 737-8506, Japan
- <sup>127</sup>Taras Shevchenko National University of Kyiv, 01601 Kyiv, Ukraine
- <sup>128</sup>Lancaster University, Lancaster LA1 4YB, United Kingdom
- <sup>129</sup>Lawrence Berkeley National Laboratory, Berkeley, CA 94720, USA
- <sup>130</sup>Laboratório de Instrumentação e Física Experimental de Partículas, 1649-003 Lisboa and 3004-516 Coimbra, Portugal
- <sup>131</sup>University of Liverpool, L69 7ZE, Liverpool, United Kingdom
- <sup>132</sup>Los Alamos National Laboratory, Los Alamos, NM 87545, USA
- <sup>133</sup>Louisiana State University, Baton Rouge, LA 70803, USA
- <sup>134</sup>University of Lucknow, Uttar Pradesh 226007, India
- <sup>135</sup>Madrid Autonoma University and IFT UAM/CSIC, 28049 Madrid, Spain
- <sup>136</sup>Johannes Gutenberg-Universität Mainz, 55122 Mainz, Germany
- <sup>137</sup>University of Manchester, Manchester M13 9PL, United Kingdom
- <sup>138</sup>Massachusetts Institute of Technology, Cambridge, MA 02139, USA
- <sup>139</sup>University of Medellín, Medellín, 050026 Colombia
- <sup>140</sup>University of Michigan, Ann Arbor, MI 48109, USA
- <sup>141</sup>Michigan State University, East Lansing, MI 48824, USA
- <sup>142</sup>Università di Milano Bicocca, 20126 Milano, Italy
- <sup>143</sup>Università degli Studi di Milano, I-20133 Milano, Italy
- <sup>144</sup>University of Minnesota Duluth, Duluth, MN 55812, USA
- <sup>145</sup>University of Minnesota Twin Cities, Minneapolis, MN 55455, USA
- <sup>146</sup>University of Mississippi, University, MS 38677 USA
- <sup>147</sup>Università degli Studi di Napoli Federico II, 80138 Napoli NA, Italy
- <sup>148</sup>Nikhef National Institute of Subatomic Physics, 1098 XG Amsterdam, Netherlands
- <sup>149</sup>National Institute of Science Education and Research (NISER), Odisha 752050, India
- <sup>150</sup>University of North Dakota, Grand Forks, ND 58202-8357, USA
- <sup>151</sup>Northern Illinois University, DeKalb, IL 60115, USA
- <sup>152</sup>Northwestern University, Evanston, IL 60208, USA
- <sup>153</sup>University of Notre Dame, Notre Dame, IN 46556, USA
- <sup>154</sup>University of Novi Sad, 21102 Novi Sad, Serbia
- <sup>155</sup>Occidental College, Los Angeles, CA 90041



- <sup>156</sup> Ohio State University, Columbus, OH 43210, USA  
<sup>157</sup> Oregon State University, Corvallis, OR 97331, USA  
<sup>158</sup> University of Oxford, Oxford, OX1 3RH, United Kingdom  
<sup>159</sup> Pacific Northwest National Laboratory, Richland, WA 99352, USA  
<sup>160</sup> Università degli Studi di Padova, I-35131 Padova, Italy  
<sup>161</sup> Panjab University, Chandigarh, 160014, India  
<sup>162</sup> Université Paris-Saclay, CNRS/IN2P3, IJCLab, 91405 Orsay, France  
<sup>163</sup> Université Paris Cité, CNRS, Astroparticule et Cosmologie, Paris, France  
<sup>164</sup> University of Parma, 43121 Parma PR, Italy  
<sup>165</sup> Università degli Studi di Pavia, 27100 Pavia PV, Italy  
<sup>166</sup> University of Pennsylvania, Philadelphia, PA 19104, USA  
<sup>167</sup> Pennsylvania State University, University Park, PA 16802, USA  
<sup>168</sup> Physical Research Laboratory, Ahmedabad 380 009, India  
<sup>169</sup> Università di Pisa, I-56127 Pisa, Italy  
<sup>170</sup> University of Pittsburgh, Pittsburgh, PA 15260, USA  
<sup>171</sup> Pontificia Universidad Católica del Perú, Lima, Perú  
<sup>172</sup> University of Puerto Rico, Mayaguez 00681, Puerto Rico, USA  
<sup>173</sup> Punjab Agricultural University, Ludhiana 141004, India  
<sup>174</sup> Queen Mary University of London, London E1 4NS, United Kingdom  
<sup>175</sup> Radboud University, NL-6525 AJ Nijmegen, Netherlands  
<sup>176</sup> Rice University, Houston, TX 77005  
<sup>177</sup> University of Rochester, Rochester, NY 14627, USA  
<sup>178</sup> Royal Holloway College London, London, TW20 0EX, United Kingdom  
<sup>179</sup> Rutgers University, Piscataway, NJ, 08854, USA  
<sup>180</sup> STFC Rutherford Appleton Laboratory, Didcot OX11 0QX, United Kingdom  
<sup>181</sup> Università del Salento, 73100 Lecce, Italy  
<sup>182</sup> Universidad del Magdalena, Santa Marta - Colombia  
<sup>183</sup> Sapienza University of Rome, 00185 Roma RM, Italy  
<sup>184</sup> Universidad Sergio Arboleda, 11022 Bogotá, Colombia  
<sup>185</sup> University of Sheffield, Sheffield S3 7RH, United Kingdom  
<sup>186</sup> SLAC National Accelerator Laboratory, Menlo Park, CA 94025, USA  
<sup>187</sup> University of South Carolina, Columbia, SC 29208, USA  
<sup>188</sup> South Dakota School of Mines and Technology, Rapid City, SD 57701, USA  
<sup>189</sup> South Dakota State University, Brookings, SD 57007, USA  
<sup>190</sup> Southern Methodist University, Dallas, TX 75275, USA  
<sup>191</sup> Stony Brook University, SUNY, Stony Brook, NY 11794, USA  
<sup>192</sup> Sun Yat-Sen University, Guangzhou, 510275, China  
<sup>193</sup> Sanford Underground Research Facility, Lead, SD, 57754, USA  
<sup>194</sup> University of Sussex, Brighton, BN1 9RH, United Kingdom  
<sup>195</sup> Syracuse University, Syracuse, NY 13244, USA  
<sup>196</sup> Universidade Tecnológica Federal do Paraná, Curitiba, Brazil  
<sup>197</sup> Tel Aviv University, Tel Aviv-Yafo, Israel  
<sup>198</sup> Texas A&M University, College Station, Texas 77840  
<sup>199</sup> Texas A&M University - Corpus Christi, Corpus Christi, TX 78412, USA  
<sup>200</sup> University of Texas at Arlington, Arlington, TX 76019, USA  
<sup>201</sup> University of Texas at Austin, Austin, TX 78712, USA  
<sup>202</sup> University of Toronto, Toronto, Ontario M5S 1A1, Canada  
<sup>203</sup> Tufts University, Medford, MA 02155, USA  
<sup>204</sup> Universidade Federal de São Paulo, 09913-030, São Paulo, Brazil  
<sup>205</sup> Ulsan National Institute of Science and Technology, Ulsan 689-798, South Korea  
<sup>206</sup> University College London, London, WC1E 6BT, United Kingdom  
<sup>207</sup> Universidad Nacional Mayor de San Marcos, Lima, Peru  
<sup>208</sup> Valley City State University, Valley City, ND 58072, USA  
<sup>209</sup> Virginia Tech, Blacksburg, VA 24060, USA  
<sup>210</sup> University of Warsaw, 02-093 Warsaw, Poland  
<sup>211</sup> University of Warwick, Coventry CV4 7AL, United Kingdom  
<sup>212</sup> Wellesley College, Wellesley, MA 02481, USA  
<sup>213</sup> Wichita State University, Wichita, KS 67260, USA  
<sup>214</sup> William and Mary, Williamsburg, VA 23187, USA  
<sup>215</sup> University of Wisconsin Madison, Madison, WI 53706, USA  
<sup>216</sup> Yale University, New Haven, CT 06520, USA  
<sup>217</sup> Yerevan Institute for Theoretical Physics and Modeling, Yerevan 0036, Armenia  
<sup>218</sup> York University, Toronto M3J 1P3, Canada



# Contents

<b>Contents</b>	<b>i</b>
<b>List of Figures</b>	<b>viii</b>
<b>List of Tables</b>	<b>xvi</b>
<b>1 Executive Summary</b>	<b>1</b>
1.1 The DUNE Physics Program . . . . .	3
1.2 Far Detector Requirements and Specifications . . . . .	4
1.3 Vertical Drift Design . . . . .	7
1.3.1 Charge Readout Planes (Anodes) . . . . .	10
1.3.2 Charge Readout Electronics . . . . .	11
1.3.3 High Voltage System and Drift Field . . . . .	12
1.3.4 Photon Detection System . . . . .	15
1.3.5 Trigger and DAQ . . . . .	15
1.3.6 Prototypes and Demonstrators . . . . .	16
1.3.7 Integrated Engineering and Installation . . . . .	17
1.4 Project Organization . . . . .	21
1.5 Status of Project . . . . .	21
1.5.1 Simulation and Physics Studies . . . . .	21
1.5.2 Prototyping . . . . .	21
1.5.3 Path to Completion: Validation, Production and Installation . . . . .	23
<b>2 Physics</b>	<b>24</b>
2.1 Introduction . . . . .	24
2.2 The DUNE Physics Program . . . . .	24
2.2.1 Long-baseline Neutrino Oscillation Physics . . . . .	25
2.2.2 Supernova Neutrino Bursts and Physics with Low-energy Neutrinos . . . . .	25
2.2.3 Physics Beyond the Standard Model . . . . .	30
2.3 Simulations of FD2-VD . . . . .	31
2.3.1 Photon Detector Simulation . . . . .	31
2.3.2 Charge Readout Simulation . . . . .	34
2.3.3 Signal Processing with Wire-Cell Toolkit . . . . .	35
2.4 Low-energy Physics Performance . . . . .	35
2.4.1 SNB Trigger Efficiency . . . . .	36

2.4.1.1	SNB Trigger Efficiency with the TPC . . . . .	36
2.4.1.2	SNB Trigger Efficiency with the PDS . . . . .	38
2.4.2	Energy Resolution with TPC and PDS . . . . .	40
2.5	Long-baseline Oscillation Physics Performance . . . . .	42
2.5.1	3D Event Reconstruction with Pandora . . . . .	42
2.5.2	Neutrino Event Selection with the Convolutional Visual Network . . . . .	43
2.5.3	Neutrino Energy Reconstruction . . . . .	45
2.5.4	PDS Channel Saturation for High Energy Beam Events . . . . .	47
2.5.5	Conclusions . . . . .	48
<b>3</b>	<b>Charge Readout Planes</b>	<b>50</b>
3.1	Introduction . . . . .	50
3.2	Specifications . . . . .	54
3.3	Anode Plane Design . . . . .	55
3.4	CRP Mechanical Support Structure . . . . .	60
3.5	Top CRP Superstructures and Suspension . . . . .	65
3.6	Bottom CRP Support System . . . . .	70
3.7	Installation Procedures and Tooling . . . . .	73
3.7.1	Top Anode Plane . . . . .	73
3.7.2	Bottom Anode Plane . . . . .	75
3.8	Prototyping and Validation . . . . .	77
3.8.1	First Full-scale CRP Prototype (2021) . . . . .	78
3.8.2	CRP Production and Testing (2022) . . . . .	80
3.8.2.1	CRP-2 . . . . .	82
3.8.2.2	CRP-3 . . . . .	86
3.8.2.3	CRP-5 . . . . .	87
3.8.2.4	CRP-4 . . . . .	87
3.9	Interfaces . . . . .	89
3.10	Production and Schedule . . . . .	91
3.11	Consortium Scope and Organization . . . . .	92
3.11.1	Scope . . . . .	92
3.11.2	Institutional Responsibilities . . . . .	94
<b>4</b>	<b>Charge Readout Electronics</b>	<b>95</b>
4.1	Introduction . . . . .	95
4.2	Requirements . . . . .	96
4.3	Top Drift Readout . . . . .	98
4.3.1	System Overview . . . . .	98
4.3.2	Analog Cryogenic Electronics . . . . .	101
4.3.2.1	Cryogenic ASIC amplifier . . . . .	102
4.3.2.2	Cryogenic FE cards . . . . .	105
4.3.2.3	AMC Analog Stage . . . . .	107
4.3.2.4	Response Uniformity . . . . .	107
4.3.2.5	TDE Readout Chain Optimizations for Vertical Drift . . . . .	109
4.3.3	Signal Feedthrough Chimneys . . . . .	110
4.3.4	Digital Front-end . . . . .	114
4.3.4.1	AMC Digitization Boards . . . . .	114

4.3.4.2	$\mu$ TCA crates . . . . .	116
4.3.4.3	Front-end Timing Distribution System . . . . .	117
4.3.5	Performance in ProtoDUNE-DP . . . . .	119
4.3.6	Cold box Tests of the TDE . . . . .	121
4.3.7	TDE Services on the Cryostat Roof . . . . .	131
4.3.8	Grounding . . . . .	133
4.3.9	Production . . . . .	137
4.3.10	Quality Assurance and Control . . . . .	138
4.3.11	Installation, Integration, and Commissioning . . . . .	143
4.3.12	Interfaces . . . . .	144
4.3.13	Safety . . . . .	146
4.3.14	Management and Organization . . . . .	146
4.3.14.1	Institutions . . . . .	146
4.3.14.2	Milestones . . . . .	147
4.4	Bottom Drift Readout . . . . .	149
4.4.1	System Overview . . . . .	149
4.4.2	Specifications . . . . .	149
4.4.3	System Design . . . . .	151
4.4.3.1	Grounding and Shielding . . . . .	151
4.4.3.2	Distribution of Bias Voltages . . . . .	153
4.4.3.3	Front-End Motherboard . . . . .	154
4.4.3.4	LArASIC Front-end ASIC . . . . .	156
4.4.3.5	ColdADC ASIC . . . . .	157
4.4.3.6	COLDATA ASIC . . . . .	163
4.4.3.7	Infrastructure Inside the Cryostat . . . . .	164
4.4.3.8	Warm Interface Electronics . . . . .	168
4.4.3.9	Services on Top of the Cryostat . . . . .	170
4.4.3.10	Summary of Differences between BDE and FD1-HD TPC Electronics . . . . .	171
4.4.4	Performance with CRP . . . . .	171
4.4.5	Quality Assurance . . . . .	172
4.4.5.1	Initial Design Validation . . . . .	173
4.4.5.2	Cryogenic Tests . . . . .	173
4.4.6	Reliability Studies . . . . .	173
4.4.7	Production and Quality Control . . . . .	175
4.4.7.1	Spares Plan . . . . .	175
4.4.7.2	Procurement of Parts . . . . .	176
4.4.7.3	Assembly . . . . .	176
4.4.7.4	Quality Control . . . . .	176
4.4.8	Installation, Integration, and Commissioning . . . . .	178
4.4.9	Interfaces . . . . .	179
4.4.10	Safety . . . . .	180
4.4.11	Management and Organization . . . . .	181
4.4.11.1	Institutions . . . . .	181
4.4.11.2	Milestones . . . . .	182

<b>5</b>	<b>High Voltage System and Drift Field</b>	<b>184</b>
5.1	Introduction . . . . .	184

5.2	Requirements and Specifications . . . . .	187
5.3	HV Delivery System . . . . .	187
5.3.1	HV Power Supply and Cable . . . . .	188
5.3.2	HV Feedthrough . . . . .	189
5.3.3	HV Extender and its Coupling to HVFT . . . . .	192
5.4	HV Distribution System . . . . .	194
5.4.1	Cathode . . . . .	194
5.4.2	Field Cage . . . . .	204
5.4.2.1	Geometry, Mounting and Support . . . . .	206
5.4.2.2	Shrinkage during Cool-down . . . . .	207
5.4.2.3	E field Uniformity and Field Cage Transparency . . . . .	209
5.4.3	High Voltage Divider Boards (HVDB) . . . . .	215
5.4.4	Field Cage Support Feedthroughs . . . . .	216
5.4.5	Field Cage Assembly and Installation Procedure and Tools . . . . .	218
5.5	Design Validation . . . . .	218
5.6	Production, Handling and Quality Control . . . . .	221
5.7	Interfaces . . . . .	222
5.8	Production Timetable . . . . .	223
5.9	Organization and Management . . . . .	223
5.9.1	Institutional Responsibilities . . . . .	223
5.9.2	High-level Schedule . . . . .	224

**6 Photon Detection System 226**

6.1	Introduction . . . . .	226
6.2	Design Specifications, Performance and Scope . . . . .	229
6.2.1	Specifications and Performance . . . . .	229
6.2.2	PD Consortium Scope . . . . .	234
6.3	Photon Detector System Overview . . . . .	235
6.4	Light Collectors . . . . .	238
6.4.1	Cathode Modules HV Discharge Protection . . . . .	242
6.4.2	Membrane Modules Suspension System . . . . .	242
6.5	PDS Module Signal . . . . .	243
6.5.1	Silicon Photosensors . . . . .	243
6.5.2	Signal Ganging . . . . .	244
6.6	Sensor Biasing and Signal Readout . . . . .	246
6.6.1	Membrane Mount Modules . . . . .	246
6.6.2	Cathode Mount Modules . . . . .	246
6.6.2.1	Power-over-Fiber for Active Devices on the Cathode . . . . .	246
6.6.2.2	Signal Transmission . . . . .	250
6.6.2.3	Power and Signal Fiber Routing . . . . .	253
6.7	Light Response Monitoring and SiPM Calibration . . . . .	255
6.8	Design Validation . . . . .	257
6.8.1	Xenon doping in ProtoDUNE-SP . . . . .	257
6.8.2	X-ARAPUCA Module Optical and Mechanical Development . . . . .	259
6.8.3	Cryogenic PD Testing Facility for FD2-VD Module 0 . . . . .	261
6.8.4	PD Module Validation . . . . .	262
6.8.5	Cathode-Mount Module Cold Electronics Validation . . . . .	262

6.9	Production and Assembly	268
6.10	Interfaces	269
6.10.1	Charge Readout Plane (CRP)	269
6.10.2	Bottom Drift Electronics (BDE)	270
6.10.3	Cathode Plane Assembly and High Voltage System (HVS)	270
6.10.4	Data Acquisition (DAQ)	271
6.10.5	Cryogenics Instrumentation and Slow Control (SC)	271
6.10.6	Facility, Integration and Installation Interfaces (I&I)	271
6.10.7	Calibration and Monitoring	272
6.10.8	Physics, Software and Computing	272
6.11	Transport and Handling	272
6.12	Quality Assurance and Quality Control	273
6.12.1	Design Quality Assurance	273
6.12.2	Production and Assembly Quality Assurance	274
6.12.3	Production and Assembly Quality Control	275
6.12.4	Installation Quality Control	276
6.13	Safety	276
6.14	Organization and Management	277
6.14.1	Consortium Organization	277
6.14.2	High-Level Schedule	281
<b>7</b>	<b>Trigger and DAQ</b>	<b>284</b>
7.1	Introduction	284
7.2	Requirements and Specifications	286
7.3	Interfaces	291
7.4	Trigger and DAQ (TDAQ) System Design	292
7.4.1	Timing and Clock Distribution	294
7.4.2	Readout	295
7.4.3	Trigger and Data Filter	297
7.4.3.1	Strategies for Data Retention	297
7.4.3.2	Trigger Performance Studies	300
7.4.4	Data Collection	301
7.4.5	Run Control, Configuration and Monitoring	304
7.4.6	Data Quality Monitoring	308
7.5	Design Validation and Development	309
7.5.1	CERN Cold box	309
7.5.2	Module 0	309
7.6	Hardware Procurement and QA/QC	309
7.6.1	Timing System	309
7.6.1.1	Custom Components	309
7.6.1.2	COTS Items	310
7.6.1.3	Timing System QA/QC	310
7.6.2	TDAQ COTS Items	310
7.6.3	Procurement Process	311
7.6.4	Quality Assurance and Control	312
7.7	Assembly, Installation, and Integration	313
7.7.1	DAQ Facilities and Infrastructure	313

7.7.2	Ross Dry Basement . . . . .	313
7.7.3	The MCR in the CUC . . . . .	313
7.7.4	The DAQ Barracks . . . . .	313
7.7.5	Installation Schedule . . . . .	315
7.7.6	Installation Scheme . . . . .	315
7.7.7	Networking . . . . .	316
7.7.8	Rack Layout . . . . .	316
7.8	Organization and Schedule . . . . .	318
7.8.1	TDAQ Consortium . . . . .	318
7.8.2	Schedule . . . . .	320
	7.8.2.1 Scheduling Approach . . . . .	320
	7.8.2.2 Milestones . . . . .	322
<b>8</b>	<b>FD2-VD Module 0</b>	<b>324</b>
8.1	Introduction . . . . .	324
8.2	Cold box Test Facility . . . . .	326
8.3	FD2-VD Module 0 . . . . .	328
8.3.1	Charge-readout Planes (CRPs) . . . . .	330
	8.3.1.1 Top CRPs . . . . .	330
	8.3.1.2 Bottom CRPs . . . . .	330
8.3.2	HV System . . . . .	333
	8.3.2.1 HV Delivery . . . . .	333
	8.3.2.2 Cathode . . . . .	333
	8.3.2.3 Field Cage . . . . .	335
8.3.3	Photon Detectors . . . . .	337
8.3.4	Data Acquisition (DAQ) . . . . .	337
8.3.5	Beam Plug . . . . .	337
8.3.6	Installation . . . . .	338
8.3.7	Infrastructure . . . . .	340
8.3.8	Timeline and Strategy for Fill and Operation . . . . .	340
<b>9</b>	<b>Integrated Engineering and Installation</b>	<b>341</b>
9.1	Introduction . . . . .	341
9.2	Requirements and Specifications . . . . .	341
9.3	Detector Integration . . . . .	342
9.3.1	Responsibilities and Activities . . . . .	342
9.3.2	Cryostat and Cryogenics Systems . . . . .	343
	9.3.2.1 Cryostat Design Overview . . . . .	343
	9.3.2.2 Detector Assembly within Cryostat . . . . .	345
	9.3.2.3 Cryostat Roof Penetrations: Parameters and Uses . . . . .	345
	9.3.2.4 Cryogenics Infrastructure in the Cryostat . . . . .	345
	9.3.2.5 Cryogenic Instrumentation . . . . .	348
9.3.3	Electrical Infrastructure . . . . .	352
	9.3.3.1 Grounding and Detector Power . . . . .	352
	9.3.3.2 Detector Readout Electronics . . . . .	352
9.4	Safety . . . . .	353
9.4.1	Documentation Approval Process . . . . .	353



9.4.2	Support and Responsibilities . . . . .	355
9.4.3	Safety Program . . . . .	355
9.5	Detector Safety . . . . .	356
9.6	CRP and Cathode Support Structures . . . . .	357
9.7	Installation Infrastructure . . . . .	357
9.8	Detector Installation . . . . .	365
9.8.1	Installations on Cryostat Roof . . . . .	365
9.8.2	Preparing the Cryostat Interior . . . . .	366
9.8.3	Detector Component Installation . . . . .	366
9.9	Interfaces . . . . .	382
9.10	Organization and Management . . . . .	384
9.10.1	Contributing Institutions . . . . .	384
9.10.2	High-level Schedule . . . . .	384
<b>10</b>	<b>Project Management</b>	<b>385</b>
10.1	Project Organization . . . . .	385
10.1.1	DUNE Collaboration and Consortia . . . . .	385
10.1.2	LBNF/DUNE Project . . . . .	386
10.1.3	Far Detector and Cryogenics (FDC) Subproject . . . . .	388
10.1.4	Technical Boards . . . . .	389
10.1.5	Joint Project Office . . . . .	390
10.2	Risks . . . . .	391
10.3	Schedule . . . . .	394
10.3.1	Prototyping Schedule . . . . .	395
10.3.2	Production and Installation Schedule . . . . .	395
	<b>Glossary</b>	<b>398</b>
	<b>References</b>	<b>417</b>

# List of Figures

1.1	Placement of detector modules in the north and south caverns . . . . .	2
1.2	Conceptual vertical drift design with PCB-based charge readout . . . . .	8
1.3	Vertical drift detector . . . . .	9
1.4	Exploded view of a top superstructure and CRPs . . . . .	11
1.5	System architecture of the top drift readout electronics . . . . .	12
1.6	System architecture of the bottom drift readout electronics . . . . .	13
1.7	HV system components inside the cryostat . . . . .	14
1.8	Cosmic ray track from the prototype CRP-4 (BDE) . . . . .	17
1.9	Installation of a CRP in a cold box . . . . .	18
1.10	FD2-VD installation gray room . . . . .	19
1.11	Space allocation in the cryostat and gray room during CRP installation . . . . .	20
1.12	Model of the Module 0 detector . . . . .	22
2.1	Long-baseline (LBL) 2D resolutions . . . . .	26
2.2	LBL MH and CPV . . . . .	26
2.3	Supernova (SN) time-dependent flux parameters . . . . .	28
2.4	Low-energy cross sections . . . . .	28
2.5	Interacted $\nu_e$ -CC energy spectrum . . . . .	29
2.6	TPC SN burst (SNB) triggering . . . . .	37
2.7	PDS trigger efficiencies . . . . .	39
2.8	MARLEY tracking efficiency and energy resolution for low-energy events . . . . .	40
2.9	PDS energy resolution for the FD2-VD . . . . .	41
2.10	Pandora reco efficiencies of leading lepton (CC interactions) in FD1-HD/FD2-VD . . . . .	43
2.11	Pandora reco efficiencies of the leading $\mu^-$ (CC interactions) in FD1-HD/FD2-VD . . . . .	44
2.12	CVN score distributions for respective signal and backgrounds, FHC mode, FD2-VD . . . . .	44
2.13	CVN score distributions for respective signal and backgrounds, FHC mode, FD1-HD . . . . .	45
2.14	Neutrino selection efficiencies in FHC beam mode using the CVN . . . . .	46
2.15	Reconstructed neutrino energy residuals for different reconstruction hypotheses . . . . .	47
2.16	Peak amplitude distribution and fraction of events that saturate . . . . .	48
3.1	Exploded view of a top superstructure and CRPs . . . . .	51
3.2	Basic electrode strip configuration for the three-view top and bottom CRUs . . . . .	52
3.3	Anode PCB hole pattern and board stack . . . . .	57
3.4	Drift path in the anode plane . . . . .	57
3.5	PCB panel and PCB segment details . . . . .	59
3.6	PCBs bonded edge-to-edge to create PCB panel . . . . .	60

3.7	Top and bottom CRP adapter boards . . . . .	61
3.8	CRP edge cards . . . . .	62
3.9	CRP illustration showing its two component CRUs . . . . .	63
3.10	CRP spacer and anode attachment to the composite frame . . . . .	63
3.11	CRP glass epoxy skin . . . . .	64
3.12	CRP composite frame profiles . . . . .	64
3.13	CRP composite frame junction system . . . . .	65
3.14	CRP superstructure pattern in the cryostat . . . . .	66
3.15	Dimensions and positions of the superstructures . . . . .	66
3.16	CRP superstructure suspension cables for cathode . . . . .	67
3.17	CRP superstructure before and after assembly . . . . .	68
3.18	CRP superstructure corner extensions . . . . .	68
3.19	CRP decoupling system . . . . .	69
3.20	Views of suspension feedthrough system for a CRP superstructure . . . . .	70
3.21	Bottom CRP supported on the membrane by posts . . . . .	71
3.22	Bottom CRP support components . . . . .	72
3.23	Bottom CRP adapter plate attachment . . . . .	72
3.24	CRP signal cabling . . . . .	74
3.25	Top CRP and superstructure assembly . . . . .	74
3.26	Top CRP superstructure installation . . . . .	75
3.27	Crane lifting bottom CRP . . . . .	75
3.28	BottomCRP lifting system components . . . . .	76
3.29	CRP tine cage . . . . .	76
3.30	CRP truss system with bottom CRP . . . . .	77
3.31	3D model of the first full-scale CRP . . . . .	78
3.32	First full-scale CRP cold box insertion . . . . .	79
3.33	First cosmic track in full-scale CRP in the cold box. . . . .	80
3.34	PCB gluing details . . . . .	81
3.35	PCB silver-printing details . . . . .	81
3.36	PCB panel cold testing and drying before assembly . . . . .	82
3.37	CRP attachment to the two halves of composite frame . . . . .	83
3.38	Details of the finalized CRP assembly . . . . .	83
3.39	CRP-2 with the team involved in construction . . . . .	84
3.40	CRP-2 transport and preparations at EHN1 . . . . .	85
3.41	Examples from the tracks recorder during the CRP-2 cold box test . . . . .	85
3.42	Finalized CRP-3 assembly inside the clean room at CERN building 185 . . . . .	86
3.43	Hit map of CRP-3 for one of the runs during the cold box tests . . . . .	87
3.44	CRP-5a assembly at the Yale Wright Laboratory . . . . .	88
3.45	Silver-coated perforated PCBs for CRP-4 . . . . .	89
3.46	Key CRP milestones and activities toward FD2-VD . . . . .	92
4.1	System architecture of the top drift readout electronics . . . . .	99
4.2	System architecture of the TDE electronics . . . . .	101
4.3	Examples of differential output signals from the LARZIC ASIC . . . . .	103
4.4	LARZIC chip die with connections and single-channel layout . . . . .	104
4.5	Details of the LARZIC charge injection and channel selection systems . . . . .	105
4.6	SPI bus daisy-chaining of multiple LARZIC ASICs . . . . .	105

4.7	FE cryogenic amplifier card	106
4.8	Schematic of the analog stage on the AMC	107
4.9	Charge injection system with varicaps connected to FE	108
4.10	ProtoDUNE-DP FE card calibration results	108
4.11	TDE response to bipolar charge injection signals	110
4.12	FE cryogenic amplifier card mounted on a SFT sliding blade	111
4.13	Access to a FE cryogenic amplifier card in a SFT chimney	111
4.14	FE cards plugged into the top side of a cold flange	112
4.15	Warm flange of a SFT chimney in ProtoDUNE-DP	113
4.16	Cryostat roof layout with locations of the SFT chimneys	113
4.17	CAD models of the FD2-VD chimneys	114
4.18	A front-end $\mu$ TCA digitization card (CRO-AMC)	115
4.19	Schematic diagram of the AMC digitization board	115
4.20	$\mu$ TCA crate with a 40 Gbit/s MCH	117
4.21	Cold box fiber network infrastructure for 40 Gbit/s bandwidth	118
4.22	WR end-node slave card	119
4.23	Charge readout system on the ProtoDUNE-DP cryostat roof	120
4.24	Cosmic ray events acquired with ProtoDUNE-DP	120
4.25	Cosmic ray tracks acquired with ProtoDUNE-DP demonstrating 6 m drift	122
4.26	Timeline of the 2021-2022 TDE tests	123
4.27	TDE integration test at EHN1 (summer 2021)	124
4.28	FFT noise spectrum during the integration test	125
4.29	TDE installation on the cold box for the test of CRP-1	125
4.30	First raw data event displays acquired during cold box Run-1	126
4.31	Example of application of the Coherent Noise Removal (CNR) procedure	127
4.32	Noise performance for the three views of CRP-1 before CNR	128
4.33	Noise performance for the three views of CRP-1 after CNR	128
4.34	Calorimetric response stability for CRP-1/CRP-1b	129
4.35	TDE readout chain in the Faraday cage and the cold box for CRP-2 tests	129
4.36	Cosmic ray tracks collected during CRP-2 and CRP-3 cold box runs	130
4.37	Noise levels before and after CNR for CRP-2 and CRP-3	130
4.38	Model of cryostat roof I-beams structure and chimneys	131
4.39	Large (48-card) chimney cabling to $\mu$ TCA crates	132
4.40	Layout of the WR switch positions on the mezzanine	133
4.41	Layout of the LV power supplies and distribution boxes on mezzanine	134
4.42	Rack mountable LV power supply and distribution box	134
4.43	Layout of the calibration box positions on mezzanine	135
4.44	TDE grounding scheme	137
4.45	Duplicated test bench system at a second QC center	140
4.46	New version of the calibration card	140
4.47	Production QC test bench scheme	141
4.48	Summary of the QC tests duration	143
4.49	TPC readout electronics architecture in the bottom drift	152
4.50	FEMB for DUNE FD2-VD	154
4.51	FEMB noise	155
4.52	FE ASIC block diagram	156
4.53	FE ASIC channel schematic	157

4.54	LArASIC pulse . . . . .	158
4.55	ColdADC block diagram . . . . .	159
4.56	ColdADC raw INL and DNL . . . . .	160
4.57	ColdADC corrected INL and DNL . . . . .	161
4.58	ColdADC FFT ch4 dif 39kHz . . . . .	161
4.59	ENOB vs freq ch8 . . . . .	162
4.60	ColdADC crosstalk . . . . .	162
4.61	ColdDATA block diagram . . . . .	163
4.62	ColdDATA links with long cable . . . . .	165
4.63	Aluminum CE Box for DUNE . . . . .	165
4.64	FEMB CE boxes mounted on CRPs and cabled to patch panels . . . . .	166
4.65	TPC cold electronics feedthrough . . . . .	167
4.66	Exploded view of the cold electronics signal flange for ProtoDUNE-SP . . . . .	168
4.67	Low voltage power distribution to the WIB and FEMBs . . . . .	169
4.68	Warm interface board . . . . .	169
4.69	Warm interface board software and firmware . . . . .	170
4.70	Cosmic ray track from CRP-4 (BDE) . . . . .	172
4.71	The Cryogenic Test System . . . . .	174
4.72	Key CRO milestones and activities toward FD2-VD . . . . .	183
5.1	HVS schematic . . . . .	185
5.2	HV system components inside the cryostat . . . . .	186
5.3	Power supply photos and schematic of HV delivery system to the cryostat . . . . .	189
5.4	Components of the full-scale HV long-term stability test in the NP02 cryostat . . . . .	191
5.5	Photo and drawing of a HVFT . . . . .	192
5.6	HVFT+extender assembly connection and interface . . . . .	193
5.7	Diagram of a cathode module with integrated PD units . . . . .	195
5.8	View of the two half frames that form a cathode module frame . . . . .	195
5.9	Dimensions of the I-shape and C-shape beams used for cathode frame construction . . . . .	196
5.10	Cathode supermodule suspended from CRP superstructure . . . . .	197
5.11	Electrical fields close to the cathode surface . . . . .	199
5.12	Volume within specification vs field homogeneity specification . . . . .	199
5.13	View of a portion of a cathode module . . . . .	200
5.14	Frame opening of PD fibers and cables . . . . .	200
5.15	Cathode suspension system . . . . .	202
5.16	Cathode top adjusting device . . . . .	202
5.17	Model of test bench for rope characterization . . . . .	203
5.18	Cathode length-adjusting device (LAD) . . . . .	204
5.19	Cathode length-adjusting device tests . . . . .	205
5.20	Field cage with 70% optical transparency . . . . .	206
5.21	Field cage module with bent profiles . . . . .	207
5.22	Field cage support structure . . . . .	208
5.23	E field uniformity near the cathode-FC intersection . . . . .	210
5.24	Cathode HV bus . . . . .	211
5.25	Profiles for 70% transparent field cage . . . . .	213
5.26	FEA of E field at the transition region of the 70% transparent field cage . . . . .	214
5.27	Resistor divider board . . . . .	215

5.28	Field cage support feedthrough . . . . .	217
5.29	Field cage assembly and installation tools . . . . .	219
5.30	Key HVS milestones and activities toward FD2-VD . . . . .	225
6.1	FD2-VD PDS detector module . . . . .	227
6.2	X-ARAPUCA modules mounting positions concept . . . . .	228
6.3	Central cathode module showing the PD modules placement . . . . .	229
6.4	Reference configuration light yield map . . . . .	231
6.5	Improved spatial uniformity of response by instrumenting membrane short walls . . . . .	232
6.6	Conceptual diagram of power and signal routing . . . . .	236
6.7	Mounted X-ARAPUCA modules; view through the field cage . . . . .	237
6.8	FD2-VD PDS detector module . . . . .	239
6.9	WLS plate centered in the frame by spring-loaded dynamic mounting system . . . . .	240
6.10	SiPMs mounted to flexible PCB . . . . .	241
6.11	Module frame with discharge shield for SiPMs . . . . .	243
6.12	Fixation system for membrane-mount PD modules. . . . .	244
6.13	Equivalent circuit for the passive ganging of 20 SiPMs . . . . .	245
6.14	PDS SiPM flexible boards . . . . .	245
6.15	Block diagram of a single PoF system . . . . .	247
6.16	Photograph of a PoF transmitter module . . . . .	248
6.17	Basic block layouts for PoF power systems . . . . .	249
6.18	DUNE cold electronics motherboard for the PDS . . . . .	250
6.19	Readout electronics for cathode-mount PD modules . . . . .	251
6.20	Linearity of response for the PDS SoF laser diodes. . . . .	252
6.21	Cathode module optical fiber routing . . . . .	254
6.22	PDS flange with 8 cat6 feedthroughs . . . . .	254
6.23	Location of UV calibration light sources on the anode plane. . . . .	256
6.24	PDS diffuser and bare fiber . . . . .	256
6.25	Xenon light sensitive X-ARAPUCA signal in ProtoDUNE-SP following xenon injections . . . . .	259
6.26	Light recovery following xenon injection in ProtoDUNE-SP . . . . .	260
6.27	PDS mini-cold box test facility at CERN . . . . .	261
6.28	CERN cold box facility with three X-ARAPUCA prototype modules . . . . .	263
6.29	Charge distribution from PD cathode module cold box test with PoF and SoF . . . . .	264
6.30	Average signal from PD cathode module cold box test with PoF and SoF . . . . .	265
6.31	Linearity of PD waveform amplitude and integral . . . . .	265
6.32	SoF dynamic range . . . . .	266
6.33	X-ARAPUCA baseline noise with PoF lasers OFF and ON . . . . .	267
6.34	Fourier transform of X-ARAPUCA baseline signal with cathode HV OFF and ON . . . . .	267
6.35	Time difference between two X-ARAPUCA module channels . . . . .	267
6.36	Key PDS milestones and activities toward FD2-VD . . . . .	283
7.1	TDAQ subsystems diagram . . . . .	285
7.2	Physical view diagram of the TDAQ system. . . . .	286
7.3	Conceptual overview of TDAQ system functionality . . . . .	291
7.4	TDAQ subsystems diagram . . . . .	296
7.5	Data selection work flow . . . . .	298
7.6	trigger primitive hits in collection channels in ProtoDUNE-SP . . . . .	300

7.7	Trigger efficiency curves . . . . .	302
7.8	Muon trigger in cold box and reconstructed angles of muons . . . . .	303
7.9	Michel events, simulation and data . . . . .	303
7.10	TDAQ subsystems diagram with data collection . . . . .	304
7.11	TDAQ subsystems diagram with data collection . . . . .	307
7.12	DQM diagram . . . . .	308
7.13	DAQ room in Ross Dry . . . . .	314
7.14	DAQ Barracks . . . . .	315
7.15	DAQ network. . . . .	317
7.16	DAQ racks for for FD2-VD . . . . .	321
7.17	TDAQ Consortium Management Structure . . . . .	322
7.18	Key DAQ milestones and activities toward FD2-VD . . . . .	323
8.1	Inner volume of NP02 during installation of the FD2-VD Module 0 detector. . . . .	325
8.2	Cold box during installation of a CRP . . . . .	326
8.3	Schematic layout of detector components inside the cold box . . . . .	327
8.4	Typical raw data event display with reconstructed image . . . . .	327
8.5	3D model of FD2-VD Module 0 . . . . .	329
8.6	CRP mechanical support structure connected to the support feedthroughs . . . . .	330
8.7	Top CRP signal feedthroughs (SFTs) . . . . .	331
8.8	Bottom CRP supports . . . . .	331
8.9	Bottom CRP cable routing in FD2-VD Module 0 . . . . .	332
8.10	Suspended two-module cathode supermodule, with HV extender . . . . .	334
8.11	Detail of the cathode hanging device and the X-ARAPUCA locations . . . . .	335
8.12	Field cage layout in FD2-VD Module 0 design . . . . .	336
8.13	Beam plug concept for FD2-VD Module 0 . . . . .	338
8.14	Photo of the FD1-HD Module 0 beam plug . . . . .	339
9.1	Cryostat and mezzanines . . . . .	343
9.2	Cryostat TCO layout and dimensions . . . . .	344
9.3	The layout of penetrations on the cryostat roof . . . . .	346
9.4	Layout of penetrations, detail . . . . .	347
9.5	Internal cryogenic piping at the top . . . . .	349
9.6	Internal cryogenic piping and floor supports . . . . .	349
9.7	Purity monitors . . . . .	351
9.8	Detector power budget . . . . .	353
9.9	Optical fiber plan . . . . .	354
9.10	Space allocation in the cryostat and gray room during CRP installation . . . . .	358
9.11	FD2-VD installation gray room . . . . .	359
9.12	TCO hoist system . . . . .	360
9.13	Cryostat temporary floor . . . . .	361
9.14	Air flow in the cryostat . . . . .	362
9.15	Air flow through the TCO . . . . .	363
9.16	TDE chimney installation gantry-cart . . . . .	364
9.17	DAQ barracks . . . . .	365
9.18	East end wall PD and HV extender installation . . . . .	367
9.19	BDE cable and wall-mounted PD installation . . . . .	368

9.20	Top CRP circular cable trays . . . . .	369
9.21	Cryostat layout during top CRP installation . . . . .	370
9.22	Top CRP and cathode installation sequence . . . . .	372
9.23	Cabling access top CRP . . . . .	373
9.24	Field cage support beams and roof positioning flange . . . . .	374
9.25	Field cage carts . . . . .	375
9.26	Field cage installation sequence . . . . .	376
9.27	Field cage roof penetration and floor support . . . . .	378
9.28	Bottom CRP tooling . . . . .	379
9.29	Bottom CRP installation . . . . .	380
9.30	Jib crane for Row 20 installation . . . . .	381
9.31	Final CRP installation . . . . .	381
10.1	DUNE consortia . . . . .	386
10.2	Global project organization . . . . .	387
10.3	FDC organization . . . . .	388
10.4	Project development plan for FD2-VD . . . . .	394
10.5	Near-term FD2-VD milestones tracked by LBNC . . . . .	396
10.6	Vertical drift production and installation schedule . . . . .	397





# List of Tables

1.1	Far Detector Specifications . . . . .	5
2.1	Simulation input parameters and physical constants . . . . .	33
2.2	Input parameters for the optical digitization stage in the simulation . . . . .	33
2.3	Backgrounds . . . . .	36
2.4	PDS trigger efficiencies . . . . .	39
2.5	Overall neutrino selection efficiencies and purities using the CVN . . . . .	45
2.6	Reconstructed neutrino energy resolutions for the three event hypotheses . . . . .	47
3.1	Anode plane component list with quantities and sizes . . . . .	53
3.2	CRP anode plane specifications . . . . .	54
3.3	Key parameters for the baseline anode design . . . . .	56
3.4	CRP interfaces . . . . .	90
3.5	CRP production timetable . . . . .	93
3.6	CRP institutions . . . . .	94
4.1	CRO electronics requirements . . . . .	97
4.2	Top drift charge readout electronics: unit counts . . . . .	101
4.3	TDE LARZIC ASIC specifications . . . . .	102
4.4	Components to be produced for the TDE . . . . .	137
4.5	TDE production timetable . . . . .	139
4.6	FD2-VD TDE electronics consortium intitutions . . . . .	147
4.7	Milestones of the TDE consortium . . . . .	148
4.8	BDE specifications . . . . .	149
4.9	ColdADC power dissipation . . . . .	163
4.10	TPC electronics system interfaces . . . . .	180
4.11	FD2-VD BDE TPC electronics consortium intitutions . . . . .	181
4.12	TPC electronics consortium schedule . . . . .	182
5.1	HV specifications . . . . .	187
5.2	Expected cathode deformation . . . . .	196
5.3	Length differences of ropes supporting the cathode . . . . .	203
5.4	HV interface links . . . . .	222
5.5	HV system production timetable . . . . .	223
5.6	HV institutions . . . . .	224
5.7	HVS consortium schedule . . . . .	225

6.1	PDS specifications . . . . .	230
6.2	PDS performance . . . . .	230
6.3	PDS reference configuration . . . . .	234
6.4	Summary of FD2-VD PDS scintillation medium and reference design technology . . . . .	237
6.5	FD2-VD photon detector system components . . . . .	238
6.6	PD basic unit: X-ARAPUCA module . . . . .	239
6.7	Power estimates for PoF cathode SiPM system . . . . .	248
6.8	PD module prototypes . . . . .	262
6.9	PDS interface links . . . . .	269
6.10	PDS consortium institutions. . . . .	277
6.11	PDS deliverables and responsible institutions . . . . .	279
6.12	PDS milestones . . . . .	282
7.1	TDAQ specifications . . . . .	287
7.2	Detector parameters of FD2-VD driving the TDAQ design. . . . .	290
7.3	TDAQ component counts for FD2-VD . . . . .	290
7.4	TDAQ components' external interfaces . . . . .	292
7.5	Custom items in DTS . . . . .	310
7.6	COTS items in DTS . . . . .	310
7.7	COTS items in TDAQ . . . . .	311
7.8	TDAQ deliverables by institution . . . . .	318
7.9	TDAQ Top-level milestones focused on FD2-VD . . . . .	323
9.1	Installation specifications . . . . .	341
9.2	Cryostat roof penetration parameters . . . . .	348
9.3	Installation interface links . . . . .	383
9.4	FSII Institutions . . . . .	384
9.5	Detector integration and installation schedule . . . . .	384
10.1	FD2-VD Risks . . . . .	392

# Chapter 1

## Executive Summary

The Deep Underground Neutrino Experiment (DUNE) is designed to conduct a broad exploration of the three-flavor model of neutrino physics with unprecedented detail [1]. Chief among DUNE's potential discoveries is an unambiguous determination of the neutrino mass hierarchy and high-precision measurements of the parameters in the Pontecorvo-Maki-Nakagawa-Sakata (PMNS) matrix, especially the charge conjugation and parity (CP) violating parameter  $\delta$ . Other goals include determining whether the 2-3 neutrino mixing is maximal and, if not, measuring the octant of  $\Theta_{23}$ ; searching for sterile neutrinos; detecting a supernova neutrino burst (SNB) in or near our galaxy should a supernova occur; and searching for proton decay.

To achieve these goals, DUNE will build on the strategies of previous and current long-baseline neutrino experiments, such as K2K [2], MINOS [3], T2K [4], and NOvA [5], for which horn-focused beamlines produce beams of almost entirely muon neutrinos. The beam's parameters are measured by a near detector (ND), located just downstream of the beamline, and a far detector (FD), some distance away. For DUNE, the project is building a beamline at Fermi National Accelerator Laboratory (Fermilab), in Batavia, Illinois, that is designed to extract a proton beam from the Fermilab Main Injector (MI) and transport it to a target area where the collisions generate a beam of charged particles. This secondary beam aimed towards the FD is followed by a decay region where the particles of the secondary beam decay to generate the neutrino beam. The beam intersects the FD, located 1300 km away and 4850 feet (1,480 m) underground at the Sanford Underground Research Facility (SURF) in Lead, South Dakota.

Liquid argon time-projection chamber (LArTPC) technology has been selected for the DUNE FD. This technology combines fine-grained tracking with total absorption calorimetry to provide a detailed view of particle interactions, making it a powerful tool for neutrino physics and underground physics such as proton decay and supernova-neutrino observation. It provides millimeter-scale resolution in 3D for all charged particles. Particle types can be identified both by their  $dE/dx$  and by track patterns, e.g., the decays of stopping particles. The modest radiation length (14 cm) is sufficiently short to identify and contain electromagnetic showers from electrons and photons, but long enough to provide good  $e/\gamma$  separation by  $dE/dx$  (one versus two minimum ionizing particles (MIPs)) at the beginning of the shower. In addition, photons can be distinguished from electrons emanating from an event vertex by any gaps between the vertex and the start of the track. These

characteristics allow the LArTPC to identify and reconstruct signal events with high efficiency, while rejecting backgrounds, to provide a high-purity data sample [6].

In addition, taking advantage of the excellent scintillation properties of liquid argon (LAr), the FD will be instrumented with photon detectors (PDs) that will provide precise time information and additional calorimetric information.

The DUNE FD will be implemented as a set of four modules using independent cryostats, each containing about 17.5 kt of LAr. The cryostats, 65.8 m long by 17.8 m wide by 18.9 m high, have interior dimensions 62.0 m by 15.1 m by 14.0 m. An 11.3 m wide, 60.5 m long mezzanine is installed 2.3 m above each cryostat to house cryogenics and the data acquisition (DAQ) equipment. A second narrower mezzanine is provided for the 78 detector electronics racks.

The first module, called the horizontal drift detector module (FD1-HD), will be located in the east end of the north cavern and the second, the vertical drift detector module (FD2-VD), will be installed in the east end of the south cavern (see Figure 1.1). This arrangement will minimize interference between installation activities on the separate modules. A central utility cavern (CUC) (190 m long by 19.3 m wide by 11 m high) will house electrical, HVAC, internet, cryogenics, and other infrastructure for all the detector modules.

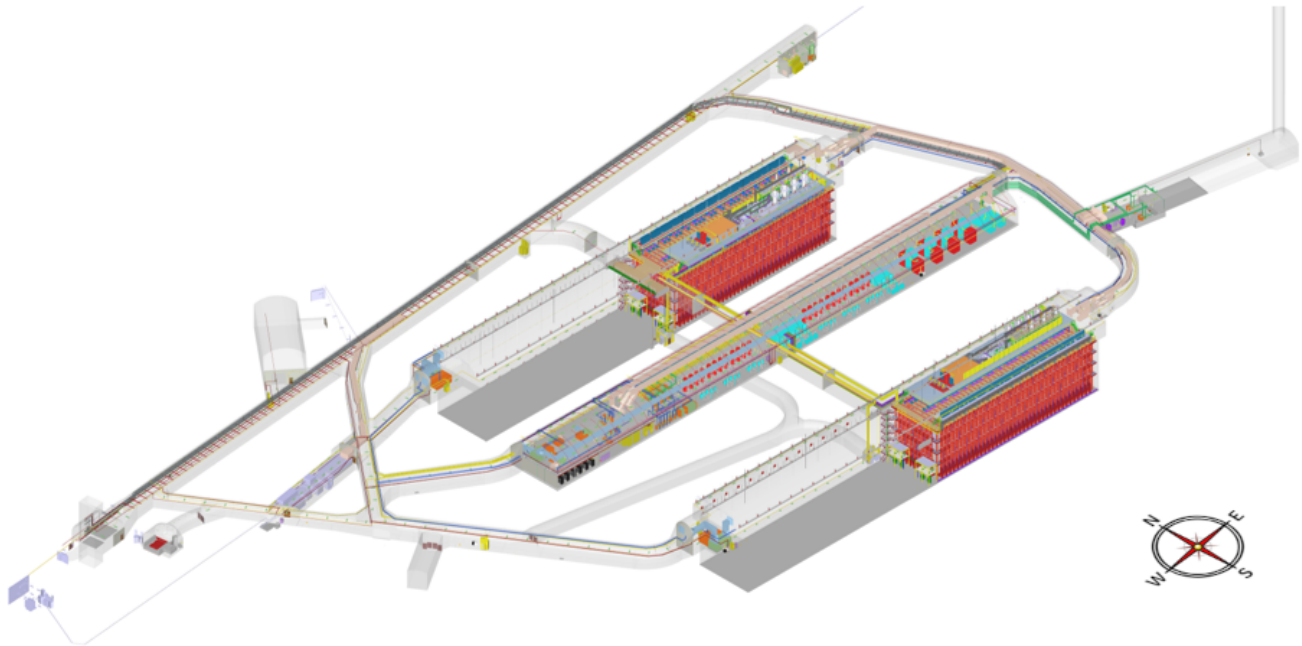


Figure 1.1: Placement of detector modules at the east end of the north and south caverns at the SURF 4850 foot level. The CUC is located between the detector caverns.

The first two far detector LArTPC modules differ in design. FD1-HD uses technology [7], based on techniques used successfully by previous LArTPC detectors, including [8], [9], and [10]. Ionization electrons from charged particles will drift horizontally under the influence of an electric field ( $E$  field) produced by vertically-oriented cathode and anode planes, with the active volume surrounded by a . The anode is formed by anode plane assemblies (APAs) that feature planes of thin wires wrapped around and soldered onto an insulating frame. Two wire planes acquire

induced signals as the ionization electrons drift past them, and the third wire plane collects the ionization electrons. A photon detection system (PDS) implements [11] technology.

This describes the design for the second far detector module, FD2-VD, which implements vertical drift technology. This design features a horizontal cathode plane placed at mid-height in the active volume of the cryostat, dividing the LArTPC into two vertically stacked equal volumes, each 6.5 m in height. The s are constructed of perforated printed circuit boards (s) with etched electrodes forming a three-view charge readout. The top anode plane is placed close to the cryostat top, just below the surface of the LAr, and the other is located as close to the bottom of the cryostat as possible. Ionization electrons will drift vertically, up or down, towards one of the anode planes.

The FD2-VD design offers a slightly larger instrumented volume ( $60.0 \times 13.5 \times 13.0 \text{ m}^3$ ) compared to the FD1-HD design and simpler, more cost-effective construction and installation due to its geometry and structure. The LAr will be doped with a small quantity of xenon, which has no impact on the time projection chamber (TPC) operation but significantly enhances the PDS performance. The FD2-VD design will implement the same X-ARAPUCA PDS technology as the FD1-HD design.

LBNF/DUNE is committed to protecting the health and safety of staff, the community, and the environment, as described in the LBNF/DUNE Integrated Environmental, Safety, and Health Management Plan [12], as well as to ensuring a safe work environment for DUNE workers at all institutions and protecting the public from hazards associated with constructing and operating DUNE. Accidents and injuries are preventable, and the ES&H team will work with the global LBNF/DUNE project and DUNE collaboration to establish an injury-free workplace. All work will be performed so as to preserve the quality of the environment and prevent property damage.

## 1.1 The DUNE Physics Program

To reach the necessary precision on its measurements, DUNE will need to collect a few thousand neutrino interactions over a period of about ten years. The number of interactions is the product of (1) the intensity of the neutrino beam, (2) the probability that a neutrino will oscillate (approximately 0.02), (3) the interaction cross section, and (4) the detector mass. Currently, the highest proton beam power that a target can safely withstand is between 1 and 2 MW, which limits the achievable neutrino beam intensity. This points to a required detector mass in the tens-of-kilotons range [13].

Central to achieving DUNE's physics program is the construction of a detector that combines the many-kiloton fiducial mass necessary for rare event searches with sub-centimeter spatial resolution. The ability to accurately image the fine details of neutrino interactions will enable data analyses to select the possibly rare, desired signals from a much larger background. As discussed in Chapter 2, the FD2-VD LArTPC will enable selection and analysis of events ranging from the MeV energy scale of solar and SNB neutrinos to the GeV energy scale of neutrinos produced from the neutrino beam at Fermilab.

A search for leptonic Charge Conjugation-Parity Symmetry Violation (CPV) requires a study of  $\nu_e$  appearance in the mostly  $\nu_\mu$  beam. This analysis requires the capability to separate electromagnetic

activity induced by charged current (CC)  $\nu_e$  interactions from similar activity arising from photons, such as photons from  $\pi^0$  decay. Two signatures allow this differentiation: (1) photon showers are typically preceded by a gap prior to conversion, characterized by the 18 cm conversion length in LAr; and (2) the initial part of a photon shower, where an electron-positron pair is produced, has twice the  $dE/dx$  of the initial part of an electron-induced shower.

A search for nucleon decay, where the primary channel of interest is  $p \rightarrow K^+\bar{\nu}$ , must identify kaon tracks as short as a few centimeters. It is also vital to accurately limit these possible nucleon-decay events to an origin within the fiducial volume, suppressing cosmic-muon-induced backgrounds. Here the detection of argon-scintillation photons is important for determining the time of the event.

Detecting a SNB poses different challenges, those of dealing with a high data rate while maintaining the high detector uptime required to ensure the capture of such a rare event. The signature of a SNB is a collection of MeV-energy electron tracks a few centimeters in length from CC  $\nu_e$  interactions, spread over the entire detector volume. To fully reconstruct a SNB, the entire detector must be read out with a data rate of up to 2 TB/s, for 30 s to 100 s, including a 4 s pre-trigger window.

## 1.2 Far Detector Requirements and Specifications

The DUNE far detector modules are required to have fiducial mass in the multi-kiloton range. This large target mass, combined with mm-scale TPC spatial resolution, will allow the separation of physics signatures of interest from the numerous backgrounds. The qualitative FD physics requirements are listed here:

- The FD shall enable identification of  $\nu_\mu$  and  $\nu_e$  charged current interactions, regardless of the final state; in particular,
  - separation of muons from other charged particles at high efficiency using energy deposition and range;
  - separation of electromagnetic showers from charged particle tracks at high efficiency using topological information;
  - identification of photon-induced showers based on observation of gaps between the start of the shower and the neutrino interaction vertex;
  - separation of electron- and photon-induced showers using ionization density at the start of the shower;
  - separation of protons from other particles using ionization density and range.
- The FD shall provide sufficient energy resolution for electromagnetic showers to allow measurement of the electron neutrino ( $\nu_e$ ) energy spectrum.
- The FD shall be modular to facilitate construction, installation and testing 1.5 km underground (the of SURF).
- The active volume shall be maximized.

The specifications listed in Table 1.1 ensure that the FD2-VD detector module will satisfy the physics requirements. These specifications, most of which are common to both FD2-VD and FD1-

HD designs, trace back to higher-level requirements on the DUNE experiment and ultimately to its science objectives [14].

Table 1.1: Specifications common to both far detector modules (labeled FD-1 through FD-30), and for FD2-VD (FD2-31 through FD2-35).

Label	Description	Specification (Goal)	Rationale	Validation
FD-1	Minimum drift field	$> 250 \text{ V/cm}$ ( $> 450 \text{ V/cm}$ )	Lessens impacts of $e^-$ -Ar recombination, $e^-$ lifetime, $e^-$ diffusion and space charge.	ProtoDUNE
FD-2	System noise	$< 1000 e^-$	Provides $>5:1$ S/N on induction planes for pattern recognition and two-track separation.	
FD-3	Light yield	$> 20 \text{ PE/MeV}$ (avg), $> 0.5 \text{ PE/MeV}$ (min)	Gives PDS energy resolution comparable to that of the TPC for 5-7 MeV SN $\nu$ s, and allows tagging of $> 99\%$ of nucleon decay backgrounds with light at all points in detector.	Supernova and nucleon decay events in the FD with full simulation and reconstruction.
FD-4	Time resolution	$< 1 \mu\text{s}$ ( $< 100 \text{ ns}$ )	Enables 1 mm position resolution for 10 MeV SNB candidate events for instantaneous rate $< 1 \text{ m}^{-3}\text{ms}^{-1}$ .	
FD-5	Liquid argon purity	$< 50 \text{ ppt}$ ( $< 30 \text{ ppt}$ )	Provides $>5:1$ S/N on induction planes for pattern recognition and two-track separation.	Purity monitors and cosmic ray tracks
FD-7	Drift field nonuniformity due to component alignment	$< 1\%$ throughout volume	Maintains APA, CPA, FC orientation and shape.	ProtoDUNE
FD-11	Drift field nonuniformity due to HVS	$< 1\%$ in 99.8% of active volume	High reconstruction efficiency.	ProtoDUNE and simulation
FD-12	Cathode HV power supply ripple contribution to system noise	$< 100 e^-$	Maximize live time; maintain high S/N.	Engineering calculation, in situ measurement, ProtoDUNE
FD-13	Front-end peaking time	$1 \mu\text{s}$	Vertex resolution; optimized for approximately 5 mm anode readout spacing.	
FD-14	Signal saturation level	$500\,000 e^-$ (Adjustable so as to see saturation in less than 10% of beam-produced events)	Maintain calorimetric performance for multi-proton final state.	
FD-15	LAr nitrogen contamination	$< 10 \text{ ppm}$	Maintain $0.5 \text{ PE/MeV}$ PDS sensitivity required for triggering proton decay near cathode.	In situ measurement
FD-17	Cathode resistivity	$> 1 \text{ M}\Omega/\text{square}$ ( $> 1 \text{ G}\Omega/\text{square}$ )	Detector damage prevention.	ProtoDUNE



FD-18	Cryogenic monitoring devices		Constrain uncertainties on detection efficiency, fiducial volume.	ProtoDUNE
FD-19	ADC sampling frequency	$\sim 2$ MHz	Match 1 $\mu$ s shaping time.	
FD-20	Number of ADC bits	$\geq 12$ bits	Makes ADC noise contribution negligible (low end); matches signal saturation specification (high end).	
FD-21	Cold electronics power consumption (in-LAr)	$< 50$ mW/channel	No bubbles in LAr to reduce HV discharge risk.	
FD-22	Data rate to tape	$< 30$ PB/year	Cost. Bandwidth.	ProtoDUNE
FD-23	Supernova trigger	Efficiency for a SNB producing at least 60 interactions with a $\nu$ energy $> 10$ MeV in 12 kt of active detector mass during the first 10 s of the burst.	$> 95\%$ efficiency for SNB within 20 kpc	Simulation and bench tests
FD-24	Local electric fields	$< 30$ kV/cm	Maximize live time; maintain high S/N.	ProtoDUNE
FD-25	Non-FE noise contributions	$\ll 1000 e^-$	High S/N for high reconstruction efficiency.	
FD-26	LAr impurity contributions from components	$\ll 30$ ppt	Maintain HV operating range for high live time fraction.	ProtoDUNE
FD-27	Introduced radioactivity	less than that from $^{39}\text{Ar}$	Maintain low radiological backgrounds for SNB searches.	ProtoDUNE and assays during construction
FD-28	Dead channels	$< 1\%$	Minimize the degradation in physics performance over the $> 20$ -year detector operation.	
FD-29	Detector uptime	$> 98\%$ ( $> 99\%$ )	Meet physics goals in timely fashion.	ProtoDUNE
FD-30	Individual detector module uptime	$> 90\%$ ( $> 95\%$ )	Meet physics goals in timely fashion.	ProtoDUNE
FD2-31	CRP anode plane global flatness	$< 20$ mm	Maintains drift field uniformity of $< 1\%$ throughout each drift region	cold box test
FD2-32	CRP minimum permeability	$> 15\%$	Allows efficient local heat dissipation and free LAr circulation	CFD simulation
FD2-33	Gaps between CRPs	5 mm for CRPs within superstructure; 10 mm between superstructures	Minimizes loss of FV and allows space for cabling	ProtoDUNE
FD2-34	CRP shield plane on cathode-facing side		Reduces impact on electronics from cathode discharge	cold box test and ProtoDUNE

---

FD2-35	CRP strip width and pitch	< 8.5 mm (ind.); < 5.5 mm (coll.); gaps 0.5 mm	S/N consistent with 100% hit reconstruction efficiency for MIPs. Spacing provides 1.5 cm vertex resolution in $y$ - $z$ plane.	ProtoDUNE and bench tests
--------	---------------------------	--	--	---------------------------

---

### 1.3 Vertical Drift Design

The FD2-VD design (Figures 1.2 and 1.3) has evolved from the DUNE dual-phase (DP) design [15], and in large measure from the experience gained with , which was installed and operated at the European Laboratory for Particle Physics (CERN) in 2019-2022. The DP design, with one anode plane at the top of the drift volume, and one cathode plane at the bottom, offered many attractive features, such as simplicity of construction and installation, homogeneity of the active volume, and the prospect of increasing the signal by developing avalanches in the gas phase to compensate for the signal losses over the long (several millisecond) drift times. It also presented challenges, namely, it required cathode operation at higher voltages, and the presence of high voltages (up to a few kV) in the gas phase. The FD2-VD design offers many of the same advantages while avoiding the challenges associated with the liquid-gas phase interface and taking advantage of the successes of the ProtoDUNE-SP design features.

Electron lifetime values well above a few milliseconds (ms) have now been measured in large LArTPCs, including both detectors, with lifetimes of many tens of ms in ProtoDUNE-SP. These results have exceeded expectations, lessening the motivation for the DP gas-phase signal gain. The experience accumulated by the DUNE collaboration in the construction, installation, and operation of ProtoDUNE-SP and ProtoDUNE-DP represents a solid basis from which to evolve the design and construction of the second detector module, optimizing the collection of electrons drifting along the vertical detector axis in the liquid phase.

The vertical drift design simplifies the detector construction and installation, and reduces the overall detector costs relative to the well-established single-phase (SP) horizontal drift design based on large wire plane assemblies. It uses most of the same structural elements as DP, e.g., the charge-readout planes (CRPs) that form the anode planes and the field cage that hangs from the cryostat roof and is constructed of modular elements that are easy to produce, transport, and install. The main difference between the FD2-VD and DP designs is the removal of the extraction of ionization electrons to the gas phase and the subsequent charge amplification stage. In the FD2-VD CRPs, a pair of perforated PCBs, etched with readout strips, now operate completely immersed in LAr. The absence of high voltage (HV) in the gas layer makes the FD2-VD design much less sensitive to environmental conditions, such as any instability of the LAr surface or floating contaminants.

The absence of gain in the FD2-VD CRPs results in a smaller, but more stable signal amplitude collected by the anodes. The signal reduction related to the unit gain in the perforated anodes is fully compensated by (1) increased strip pitch, (2) absence of extraction and collection inefficiencies present in the DP, and (3) charge collection on a single readout view rather than on two views oriented along orthogonal directions.

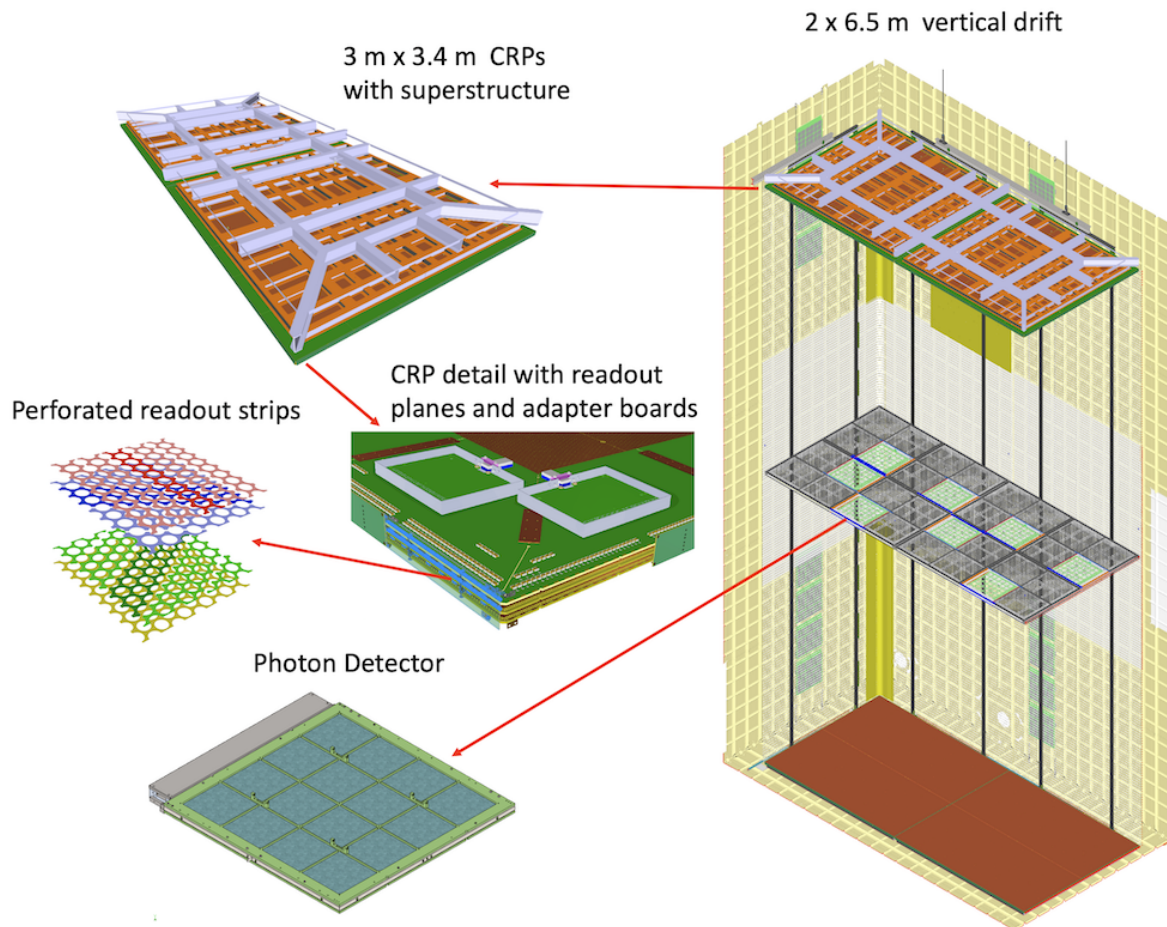


Figure 1.2: Schematic of vertical drift concept with PCB-based charge readout. Corrugations on cryostat wall shown in yellow; PCB-based CRPs (brown, at top and bottom with superstructure in gray for top CRPs); cathode (violet, at mid-height with openings for photon detectors); field cage modules (white) hung vertically around perimeter (70% transparent portion in regions near anode planes); photon detectors, placed in the openings on the cathode and on the cryostat walls, around the perimeter in the vertical regions near the anode planes.

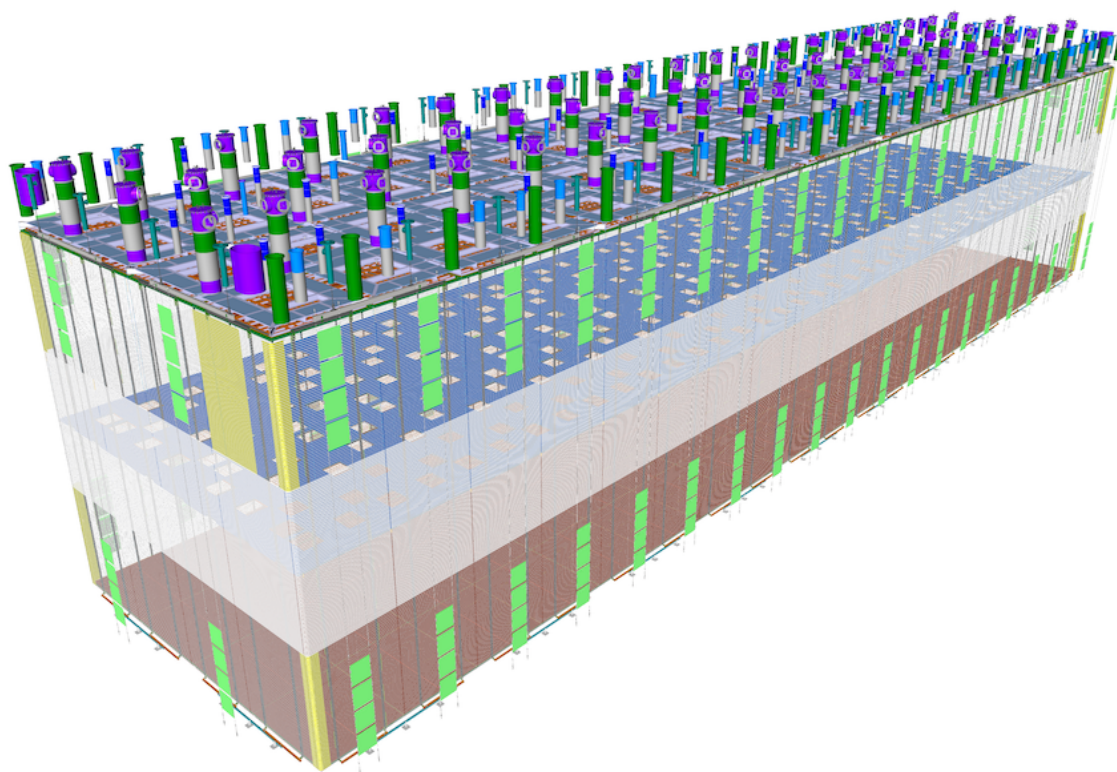


Figure 1.3: Perspective view of the FD2-VD detector.

The FD2-VD anode has a signal amplitude comparable to what a DP anode would have seen, but with much more reliability. Furthermore, considering that the drift length in FD2-VD is shorter than in the DP design, the minimal signal level will at least a factor of four larger.

Removing the cathode from the proximity of the cryostat floor maximizes the active volume by exploiting the total available vertical space of almost 13 m. The FD2-VD cathode is designed with a minimal thickness and hangs from the same top support structure of the detector that supports the top CRPs.

Having subdivided the detector into two vertically stacked drift volumes of 6.5 m height each, the same CRP geometry can be used for the top and bottom drift. The top CRPs, suspended just under the liquid surface, are aligned parallel to this surface. This anode plane preserves full accessibility to the top drift electronics ( ) via signal feedthrough chimneys (SFT chimneys), as demonstrated in ProtoDUNE-DP. The bottom CRPs are supported by feet on the cryostat floor, are mechanically independent of the rest of the detector, and are not subject to movements. The bottom drift electronics ( ) implements the same cold electronics (CE) as proven in ProtoDUNE-SP, with some adaptations to accommodate the CRP geometry and modularity.

Before providing brief descriptions of each of the major subsystems in this chapter, the important features of the FD2-VD design that make it a compelling candidate for the second far detector module are listed here:

- maximize the active volume;
- high modularity of detector components;
- simplified anode structure based on standard industrial techniques;
- simplified cold testing of instrumented anode modules, for which large cryogenic vessels are not required;
- field cage structure independent of the other detector components;
- extended drift distance;
- reduction of dead material in the active volume, maximizing fiducial mass;
- design allowing for improved light detection coverage;
- simplified and faster installation and quality assurance (QA)/quality control (QC) procedures, not requiring large in situ infrastructures; and
- cost-effectiveness.

### 1.3.1 Charge Readout Planes (Anodes)

The baseline design FD2-VD anodes, illustrated in Figure 1.4, are fabricated from two double-sided perforated PCBs, 3.2 mm thick, that are connected mechanically, with their perforations aligned, to form charge-readout units (CRUs). A pair of CRUs is attached to a composite frame to form a CRP; the frame provides mechanical support and planarity. The holes allow the electrons to pass through to reach the collection strips. Each anode plane consists of 80 CRPs in the same layout. The CRPs in the top drift volume, operating completely immersed in the LAr, are suspended from the cryostat roof using a set of superstructures, and the bottom CRPs are supported by posts positioned on the cryostat floor. The superstructures hold either two or six

CRPs, and allow adjustment, via an externally accessible suspension system, to compensate for possible deformations in the cryostat roof geometry.

The innermost face of a CRP, i.e., the PCB face directly opposite the cathode, has a copper guard plane to absorb any unexpected discharges. The reverse side of this PCB is etched with strips that form the first induction plane. The other PCB has strips on the side facing the inner PCB forming the second induction plane, and has the collection plane strips on its reverse side. The three planes of strips are segmented at about 7.5 and 5 mm pitch, for induction and conduction planes, respectively, and are set at 60° angles relative to each other to maximize information in the charge readout from different projections. A potential difference of about 1 kV must be applied across each PCB to guarantee full transmission of the electrons through the holes.

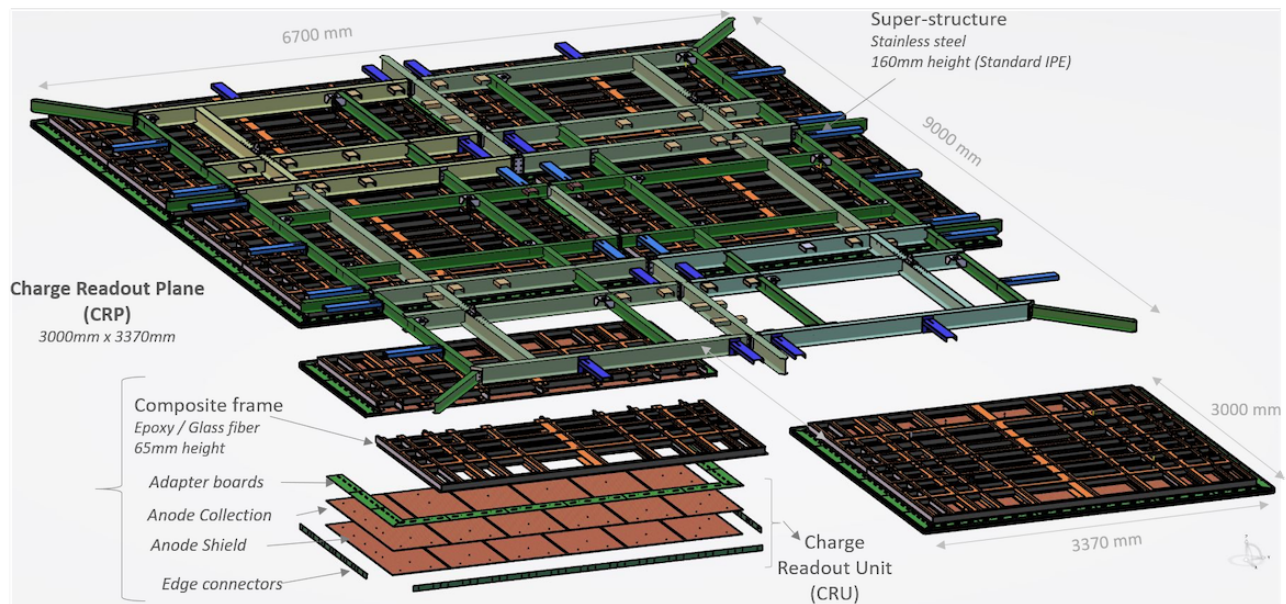


Figure 1.4: A top superstructure (green structure on top) that holds a set of six CRPs, and below it an exploded view of a CRP showing its components: the PCBs (brown), adapter boards (green) and edge connectors that together form a CRU, and composite frame (black and orange).

### 1.3.2 Charge Readout Electronics

The FD2-VD top and bottom drift volumes will implement different charge readout (CRO) electronics, top drift electronics (TDE) and bottom drift electronics (BDE), in order to take maximal advantage of placement of the top anode near the cryostat roof and to leverage the local amplification and digitization of the signal on the bottom anode to maximize the signal to noise. The TDE, based on the design used in ProtoDUNE-DP, has both cold and warm components. The BDE optimizes signal to noise with the same CE used in the FD1-HD with signal processing and digitization on the CRP in the LAr.

The TDE design preserves access to the cryogenic amplifiers via SFT chimneys, without interfering with the detector operation, and keeps the digitization electronics completely accessible on the cryostat roof. Figure 1.5 illustrates the TDE.

The CE design shown in Figure 1.6 amplifies and digitizes signals directly on the CRP to maximize

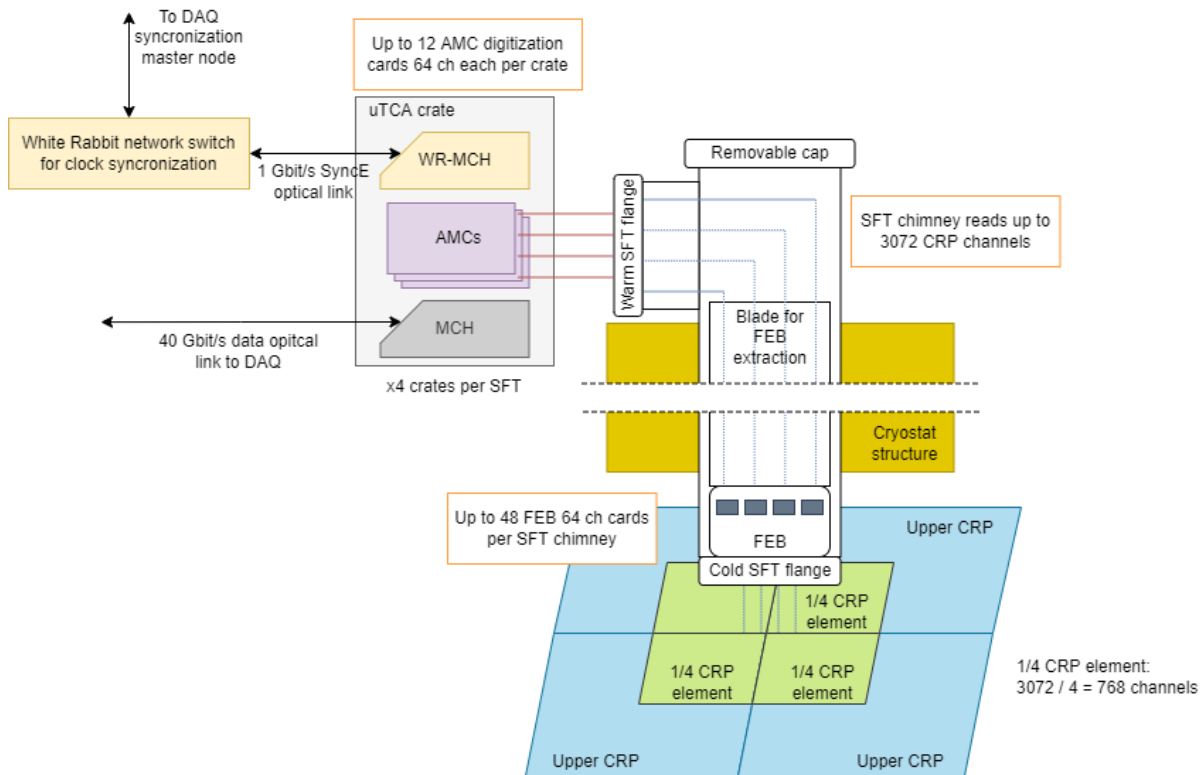


Figure 1.5: System architecture of the top drift readout electronics.

the signal to noise performance.

### 1.3.3 High Voltage System and Drift Field

The DUNE FD2-VD detector module design, which includes two drift volumes of equal drift distance 6.5 m and a nominal uniform E field of 450 V/cm, has a horizontal cathode plane placed at detector mid-height held at a negative voltage and horizontal anode planes (biased at near-ground potentials) at the top and bottom of the detector. The main high voltage system (HVS) components are illustrated in Figure 1.7.

The HVS is divided into two systems: (1) supply and delivery, and (2) distribution. The supply and delivery system consists of a negative high voltage power supply (), HV cables with integrated resistors to form a low-pass filter network, a HV feedthrough (), and a 6 m long extender inside the cryostat to deliver  $-294$  kV to the cathode. The distribution system consists of the cathode plane, the field cage, and the field cage termination supplies. The cathode plane is an array of 80 cathode modules, with the same footprint as the CRPs, formed by highly resistive top and bottom panels mounted on fiber-reinforced plastic () frames. The modular field cage consists of horizontal extruded aluminum electrode profiles stacked vertically at a 6 cm pitch. A resistive chain for voltage division between the profiles provides the voltage gradient between the cathode and the top-most and bottom-most field-shaping rings.

In addition to the primary function of providing uniform E fields in the two drift volumes, both the cathode and the field cage designs are tailored to accommodate PDS modules (Section 1.3.4) since

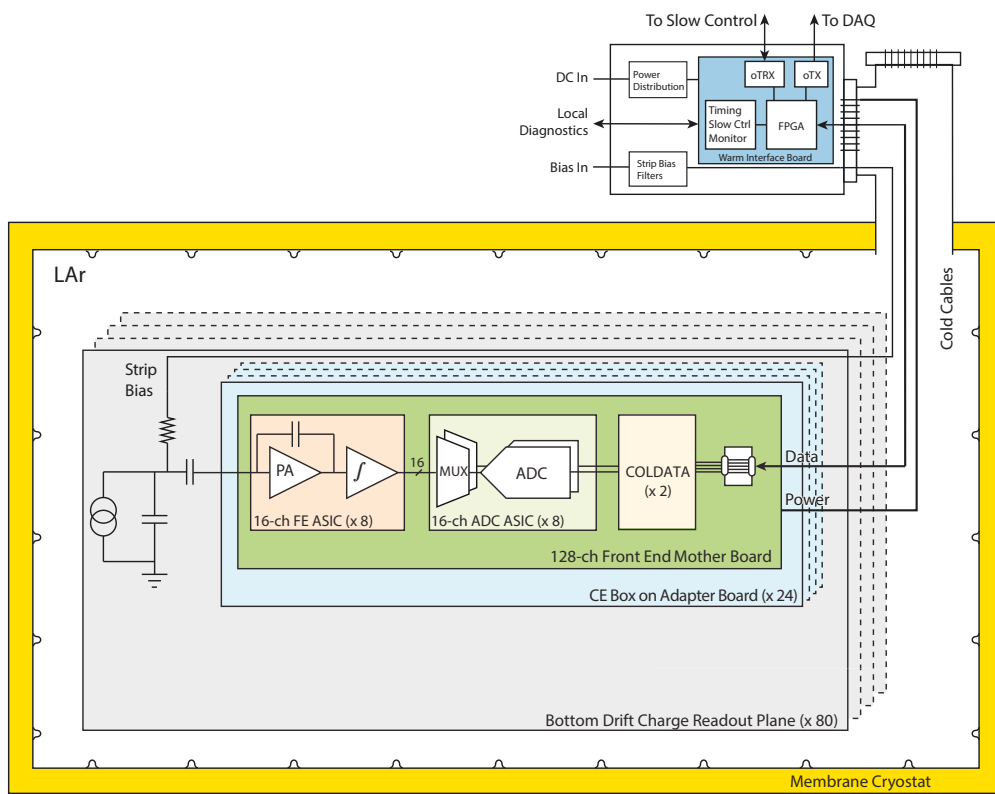


Figure 1.6: System architecture of the bottom drift readout electronics.



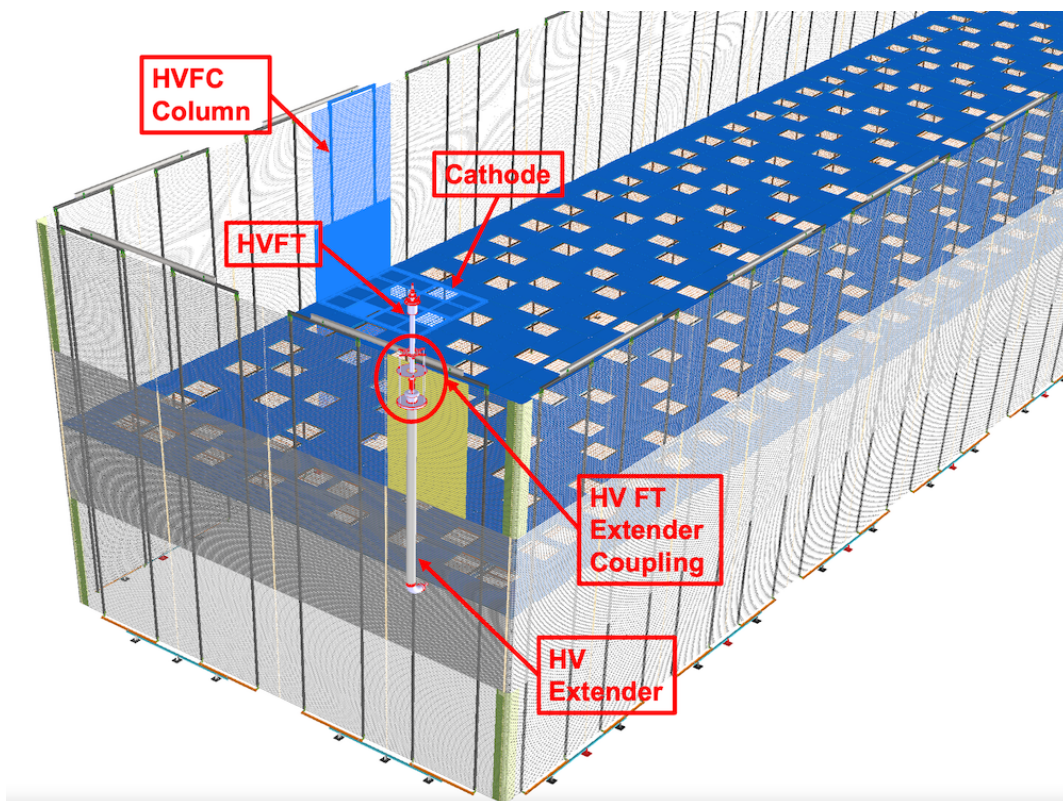


Figure 1.7: A birds-eye view of the field cage, with one full-height field cage column (highlighted in cyan) that extends the entire height, the HV feedthrough and extender (in the foreground), and the cathode (with one cathode module highlighted in cyan).

it is not possible to place them behind the anode plane, as in the FD1-HD design. Each cathode module is designed to hold four double-sided X-ARAPUCA PDS modules that are exposed to the top and bottom drift volumes through highly transparent wire mesh windows. Along the walls, the field cage is designed with narrower profiles in the region within 4 m of the anode plane to provide 70% optical transparency to single-sided PDS mounted on the cryostat membrane walls behind them, and conventional-width profiles within 2 m of the cathode plane.

### 1.3.4 Photon Detection System

The FD2-VD will implement X-ARAPUCA [11, 16] PDS. Functionally, an X-ARAPUCA module is a light trap that captures wavelength-shifted photons inside boxes with highly reflective internal surfaces until they are eventually detected by silicon photomultipliers (SiPMs). An X-ARAPUCA module has a light collecting area of approximately  $600 \times 600 \text{ mm}^2$  and a light collection window on either one face (for wall-mount modules) or on two faces (for cathode-mount modules). The wavelength-shifted photons are converted to electrical signals by 160 SiPMs distributed evenly around the perimeter of the PD module. Groups of SiPMs are electrically connected to form just two output signals, each corresponding to the sum of the response of 80 SiPMs.

Since their primary components are almost identical to those of FD1-HD, only modest R&D was required for the FD2-VD PDS modules. The primary differences were to optimize the module geometry and the proximity of the SiPMs to the wavelength-shifting (WLS) plates. Both of these are more favorable in FD2-VD, leading to more efficient light collection onto the SiPMs. As discussed in Section 1.3.3, the design has the PDs mounted on the four cryostat membrane walls and on the cathode structure, facing both top and bottom drift volumes. This configuration produces approximately uniform light measurement across the entire TPC active volume.

Cathode-mount PDs are electrically referenced to the cathode voltage, avoiding any direct path to ground. While membrane-mount PDs adopt the same copper-based sensor biasing and read-out techniques as in FD1-HD, cathode-mount PDS required new solutions to meet the challenging constraint imposed by HVS operation. The cathode-mount PDS are powered using non-conductive power-over-fiber (PoF) technology [17], and the output signals are transmitted through non-conductive optical fibers (signal-over-fiber (SoF)), thus providing voltage isolation in both signal reception and transmission. PoF is a well established technology, but extensive use in a cryogenic detector is a new application.

Converting electrical signals to optical signals in LAr has been recognized as a critical aspect of the FD2-VD PDS design, and an aggressive R&D plan to identify cold transceiver solutions operating at LAr temperature was mounted and completed.

### 1.3.5 Trigger and DAQ

The trigger and data acquisition () system is responsible for triggering on, receiving, processing, and recording data from the DUNE experiment. The main challenge for the DUNE TDAQ lies in the development of effective, resilient software and firmware that optimize the performance of the underlying hardware. The design is driven not only by data rate and throughput considerations, but also — and predominantly — by the stringent uptime requirements of the experiment.

The TDAQ for DUNE has been designed and developed coherently by a joint consortium. The TDAQ systems for the ND and the different FD modules differ only in minor details to support the electronics and the data selection criteria for each.

The TDAQ has been subdivided into a set of subsystems. All the subsystems rely on the functionality provided by the DAQ control, configuration and monitoring subsystem (CCM) and data quality monitoring (DQM), that provide the “glue” to the overall TDAQ, transforming the set of components into a coherent system.

The TDAQ is mainly composed of commercial off-the-shelf (COTS) components. A high-performance Ethernet network interconnects all the elements and allows them to operate as a single, distributed system. At the output of the TDAQ the high-bandwidth Wide Area Network (WAN) allows the transfer of data from SURF to Fermilab.

### 1.3.6 Prototypes and Demonstrators

The FD2-VD prototyping and demonstration program has followed a phased approach. Commissioning of the first full-scale prototypes was achieved by the end of 2021. Further development continued in 2022–2023 with the procurement, validation, and installation of full-scale components into for a validation test, which is expected to collect data in 2024. The timing of operation of FD2-VD Module 0 is currently uncertain due to challenges in obtaining the needed  $\sim 1$  kton of LAr needed to fill the cryostat.

This multi-phased program has been taking place at both CERN and other facilities of appropriate scale for each test. The tests and demonstrations performed throughout 2021–2022 included tests of the perforated PCB anode design, followed by optimization of the operating conditions and readout. Following stand-alone tests of the HV system components, a full-scale, extended test of the HV distribution system was completed in the NP02 cryostat at CERN in 2022, with a new feedthrough and the 6 m long HV extender, delivering 300 kV to the cathode plane 6 m under the liquid surface. This test also validated the detection of cosmic muons across the full 6 m anode-to-cathode drift length.

The first full-size CRP module for FD2-VD, equipped for both TDE and BDE readout, was successfully tested in a shallow cryostat (cold box) from fall 2021 through winter 2022. This setup included PDS modules installed on the cathode, and a membrane-mounted PDS on the wall. Figure 4.70 shows cosmic ray tracks detected with a bottom CRP module using the BDE readout system in the cold box. The plots on the top show 2D images from the readout views, and the bottom plots show corresponding signal waveforms from channels in the induction views (left and center) and in the collection view (right).

In 2022, the prototyping and validation activities included procurement of the additional four CRP modules required for the FD2-VD Module 0 program. The development of manufacturing, assembly, and QA/QC procedures for the CRPs has been a central part of this activity.

During this same period, validation activities have taken place for the PDS system, both in dedicated setups and together with charge readout components in the cryostats at CERN. Stability tests of the components in a cryogenic environment progressed in 2022 and 2023. The risk asso-

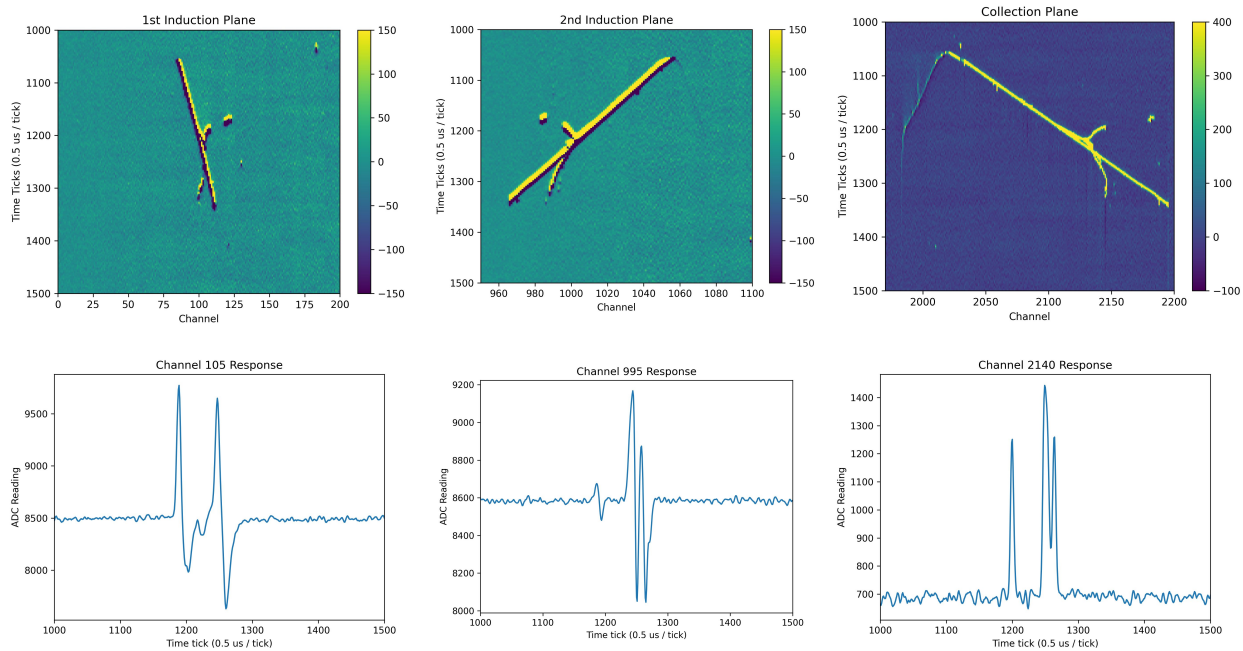


Figure 1.8: A sample cosmic ray track recorded using CRP-4 read out with BDE. The individual channel waveforms shown are for strips that recorded ionization from multiple tracks.

ciated with accidental discharges of the cathode HV has been studied with detailed simulations, and mitigated with design optimization.

### 1.3.7 Integrated Engineering and Installation

Detector integration is the responsibility of the LBNF/DUNE-US team in cooperation with the DUNE consortium technical leads. It comprises activities ranging from 3D model integration, to integration with Far Site Conventional Facilities (FSCF), to warehousing and logistics, to management and oversight of the underground installation. These activities require specialized engineering skills and involve oversight functions from groups within the project, e.g., the review office (RO), the compliance office, and safety professionals, and close coordination with the Fermilab South Dakota Services Division (SDSD) and the South Dakota Science and Technology Authority (SDSTA) at SURF.

Installation of the FD2-VD components requires neither manipulation of extremely large or delicate objects (e.g., the APAs for FD1-HD) nor significant assembly underground. This eliminates the need for a large cleanroom adjacent to the cryostat and large cold boxes for component testing, which greatly simplifies the required infrastructure. Outside the cryostat a protected area ( ) equivalent to an ISO-8 cleanroom, illustrated in Figure 1.10, is needed for preparation and cleaning of components, and to rig them for transportation into the cryostat. The largest objects to be moved into the cryostat, the CRP superstructures, are 9 m by 6 m. The gray room covers the entire temporary construction opening (TCO) opening to protect the inside of the cryostat.

Much progress has been made in 2022 on the installation plans for FD2-VD, including the design

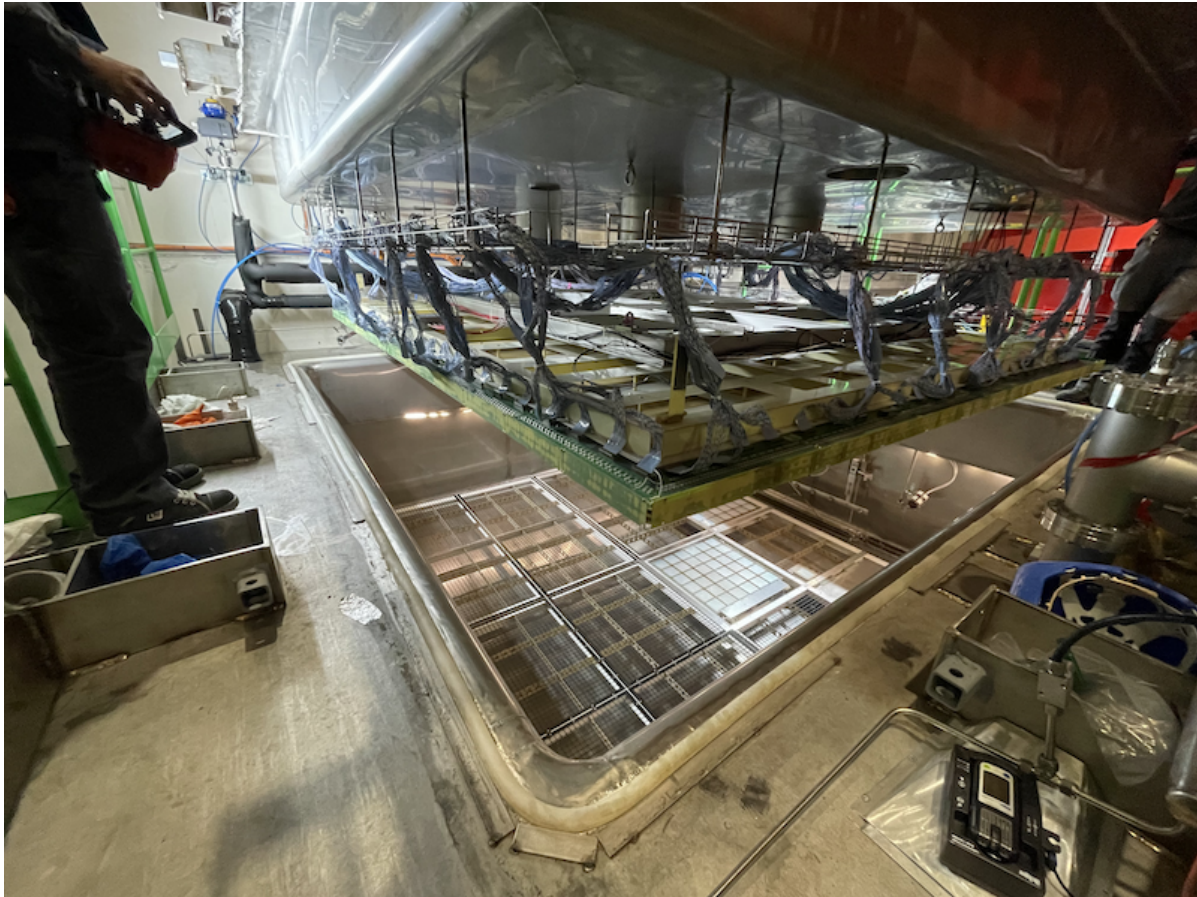


Figure 1.9: The cold box during installation of a CRP. The cathode is visible on the bottom, with an X-ARAPUCA PD installed.

of tools and procedures to enable robust QC, and safe, clean, and efficient installation. Figure 1.11 illustrates space allocation during a phase of detector installation.

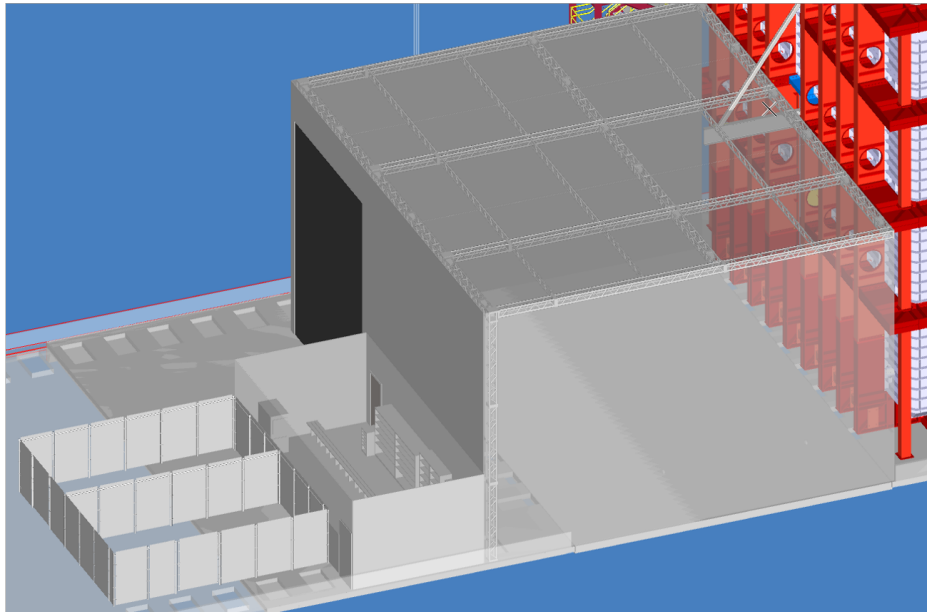


Figure 1.10: The gray room for the installation of the FD2-VD detector module. The small structures to the left of the gray room are the changing room and fenced areas for storage, and a small machine shop.

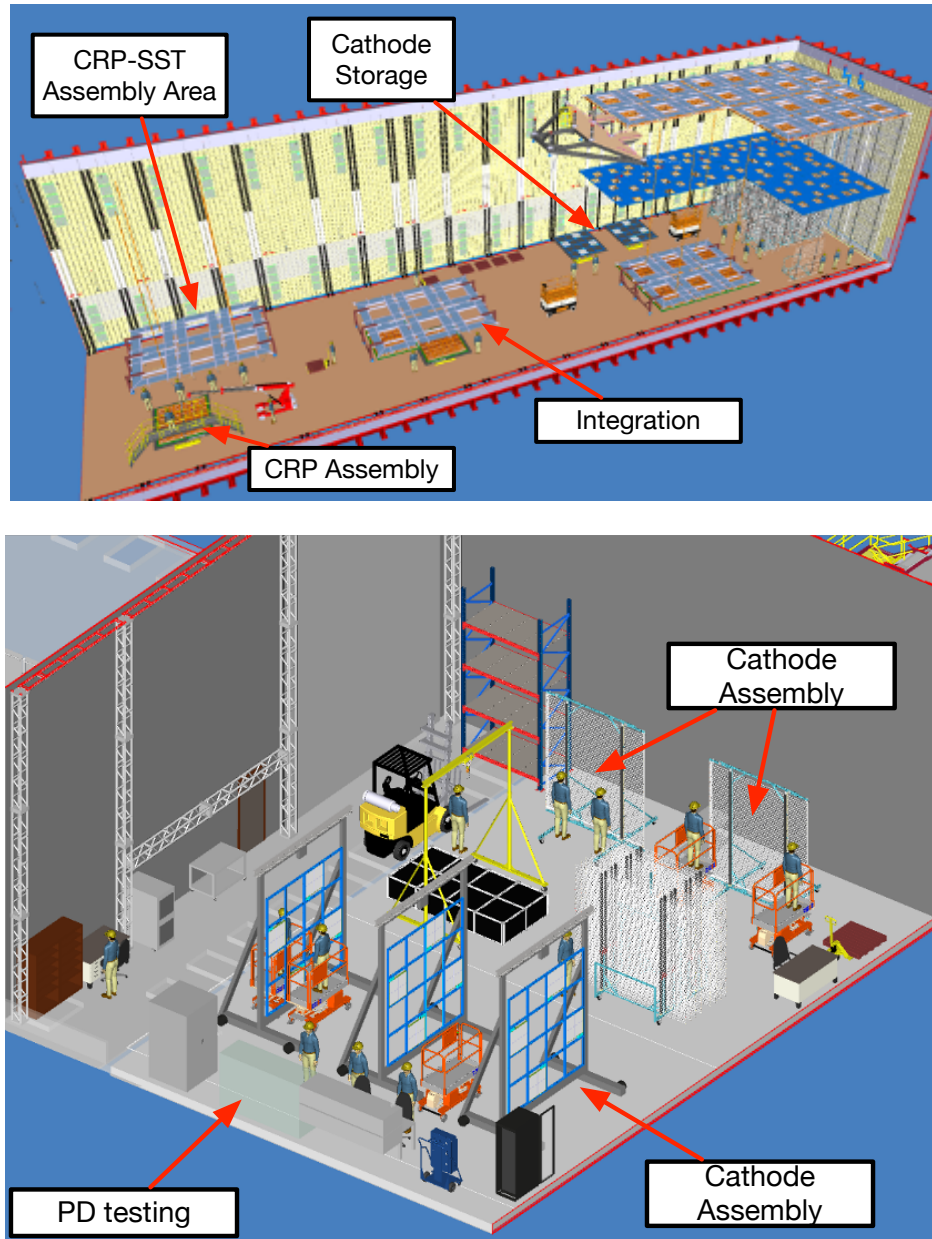


Figure 1.11: Top: Model of the main space allocations inside the cryostat during week 8 of CRP installation. Bottom: The gray room work area and space allocations.

## 1.4 Project Organization

The LBNF and DUNE enterprise (LBNF/DUNE) has been organized into five subprojects. Chapter 10 outlines the roles and responsibilities of the various subprojects and their leadership, and of the DUNE collaboration. In particular, the FD2-VD effort is part of the Far Detector and Cryogenics Subproject (), with a dedicated Deputy Project Director and a Technical Coordinator. Construction of the DUNE detector components is carried out by consortia of collaborating institutions, who assume responsibility for detector subsystems. Each consortium plans, constructs, and participates in the installation, commissioning and operation of its subsystem. A total of nine FD consortia have been formed to cover the subsystems required for FD1-HD and FD2-VD, two of which focus exclusively on FD2-VD (CRP and TDE); most of the others have responsibility for subsystems common to both far detector technologies. Centrally organized support groups for cryogenics, integration work and installation activities assist the consortia in their work on all phases of the project.

## 1.5 Status of Project

### 1.5.1 Simulation and Physics Studies

Simulation of FD2-VD was developed from the framework used for the DP concept using the tools developed for SP. A large sample of simulated data with the baseline geometry implemented for FD2-VD Module 0 and CRP-2 through CRP-5 (Section 3.8.2), with strips oriented at  $-30^\circ$ ,  $30^\circ$  and  $90^\circ$  was produced in summer 2022. As expected, due to the similarity between the FD2-VD and FD1-HD readout designs, the samples of both have shown similar performance.

Simulation of the PDS has been used to optimize the location of the PDS modules, resulting in the baseline design presented in this TDR. Placing sensors on the cathode in addition to the walls significantly improves the level and uniformity of light yield (LY), which will increase the performance of the detector for all interactions and in particular for low-energy neutrino physics, e.g., SNBs and the high-energy tail of solar neutrinos. Current software activities include the integration of light simulation into the framework of Liquid Argon Software (LArSoft).

### 1.5.2 Prototyping

As discussed in Section 1.3.6, the prototyping and validation activities that began in 2021 and 2022 will culminate in the FD2-VD Module 0 detector. The procurement and validation procedures for the detector components, which include full functionality and integration tests in the cold box setup, is well advanced. Installation in the NP02 cryostat is underway and will be completed in Q2 2023.

Figure 1.12 shows a schematic of FD2-VD Module 0, which includes two top and two bottom CRPs, and two cathode modules, separating the active volume into two drift regions, each 3.2 m long. PDS are mounted on the cathodes and on the cryostat membrane walls.



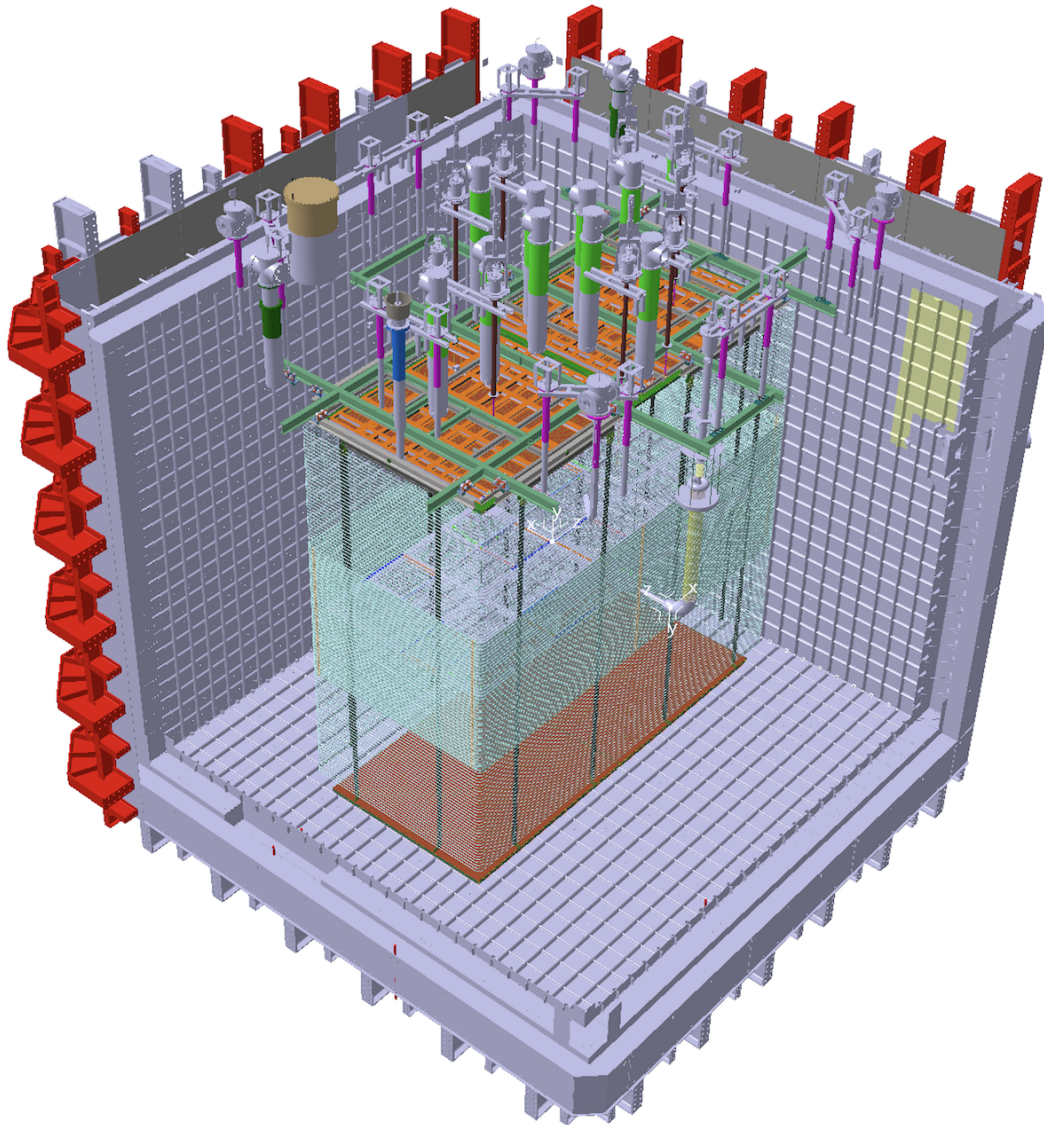


Figure 1.12: A model of the FD2-VD Module 0 layout in the NP02 cryostat.

### 1.5.3 Path to Completion: Validation, Production and Installation

The FD2-VD schedule has been added to the LBNF/DUNE project schedule. R&D and prototyping, including validation and optimization, have been completed; further validation will continue in 2023–2024, when the FD2-VD Module 0 detector is installed and operated, respectively, at the CERN Neutrino Platform, with operations dates still somewhat uncertain. The plan includes final design reviews in early 2023, based on this TDR, and assessment of the detector performance for scintillation light and charge collection and readout.

The production of detector components is scheduled to start in 2024, after the production readiness reviews (PRRs), and complete in 2027. Transport to the far detector site, SURF, will take place in 2026–2027. Installation at the far site is scheduled to start with the warm cryostat structure. The detector assembly and installation will take place in 2027–2028. Purge and fill of the cryostat is scheduled in 2029–2030.

# Chapter 2

## Physics

### 2.1 Introduction

The Deep Underground Neutrino Experiment (DUNE) physics program is described in detail in the physics volume of the DUNE Technical Design Report ( ) [1] and in a series of journal articles [18–20]. The physics sensitivities presented in the TDR assume a modular liquid argon time-projection chamber (LArTPC) far detector (FD) with an initial fiducial mass of 20 kt that is expanded to 40 kt, a broadband neutrino beam beginning at 1.2 MW beam power that gets upgraded to 2.4 MW beam power, and a capable near detector (ND) to reduce systematic uncertainties. The TDR results are derived from a simulation and reconstruction of the single-phase (SP) horizontal drift detector module (FD1-HD) module design. It is implicitly assumed that all four FD modules will have at least the same performance as the FD1-HD. In this chapter, the expected physics performance of DUNE including the SP vertical drift detector module (FD2-VD) module design is presented, based on detailed simulations of the vertical drift detector.

Section 2.2 reviews the DUNE physics program. For low-energy signals, such as solar and supernova neutrino burst (SNB) neutrinos, the FD2-VD design provides opportunities to improve the physics performance, primarily due to improved photon detection. The full simulation of the photon detection system (PDS) and charge readout system for FD2-VD are described in Section 2.3. Studies of low-energy physics performance, including photon detection information, are presented in Section 2.4. The reconstruction of high-energy signals in the vertical and horizontal drift designs is expected to be very similar. Section 2.5 describes the performance of the charge readout system for long-baseline neutrino oscillation physics.

### 2.2 The DUNE Physics Program

DUNE has three primary physics goals:

- measure the parameters governing long-baseline (LBL) neutrino oscillations, including the neutrino mass ordering, the charge conjugation and parity (CP) violating phase  $\delta_{CP}$ , and

the mixing parameters  $\theta_{23}$  and  $\theta_{13}$ , and test the three-flavor oscillation paradigm;

- make astrophysics measurements with neutrinos from a SNB, as well as other measurements with MeV-scale neutrinos;
- search for physics beyond the Standard Model ().

The motivation for this physics program is discussed extensively elsewhere [1].

### 2.2.1 Long-baseline Neutrino Oscillation Physics

DUNE measures neutrino oscillations as a function of neutrino energy over more than a full oscillatory period. The LArTPC FD provides exquisite imaging capability, allowing efficient separation of  $\nu_\mu$  and  $\nu_e$  charged current (CC) reactions which are characterized by either a long muon track or an electromagnetic shower initiated by an electron. The LArTPC is also sensitive to hadrons produced in neutrino interactions, enabling precise neutrino energy reconstruction over a broad range of energies.

Examples of the ultimate physics sensitivity of DUNE are given in Figures 2.1 and 2.2. These sensitivity projections are based on a full simulation of the FD1-HD. The exposures are quoted in kiloton-megawatt-years, the product of the FD fiducial mass in kilotons, the proton beam intensity in megawatts, and the number of years, including an accelerator up-time factor based on demonstrated Fermi National Accelerator Laboratory (Fermilab) performance. The principal characteristics of the FD that impact the physics reach of the experiment are:

- fiducial mass;
- reconstruction efficiency for  $\nu_\mu$  and  $\nu_e$  charged-currents, and rejection of backgrounds primarily from neutrino neutral current (NC) interactions with a  $\pi^0$  in the final state;
- neutrino energy reconstruction in charged-current events; and
- systematic uncertainties related to, e.g., energy scales and particle responses.

Compared to the FD1-HD, the FD2-VD is expected to have the same or possibly greater fiducial mass for the same physical module size, therefore the expected FD2-VD event sample is expected to be at least as large as that of the FD1-HD. The reconstruction efficiency based on the current FD2-VD simulation is discussed in Section 2.5.2. The efficiencies are very similar to what was achieved with FD1-HD, and they are expected to further converge as the FD2-VD simulation and reconstruction continues to mature. The energy reconstruction for FD2-VD is discussed in Section 2.5.3, and full simulations indicate that they are nearly identical for both technologies. Both detector modules are expected to have similar targeted calibration programs, which will constrain energy scales and particle responses equally well. In summary, no significant differences between the performance of the FD1-HD and FD2-VD modules are expected for long-baseline neutrino oscillations physics.

### 2.2.2 Supernova Neutrino Bursts and Physics with Low-energy Neutrinos

The DUNE FD2-VD is expected to have good sensitivity to neutrinos with energies above several MeV thanks to a PDS designed to achieve an efficient light collection and a large, unobstructed

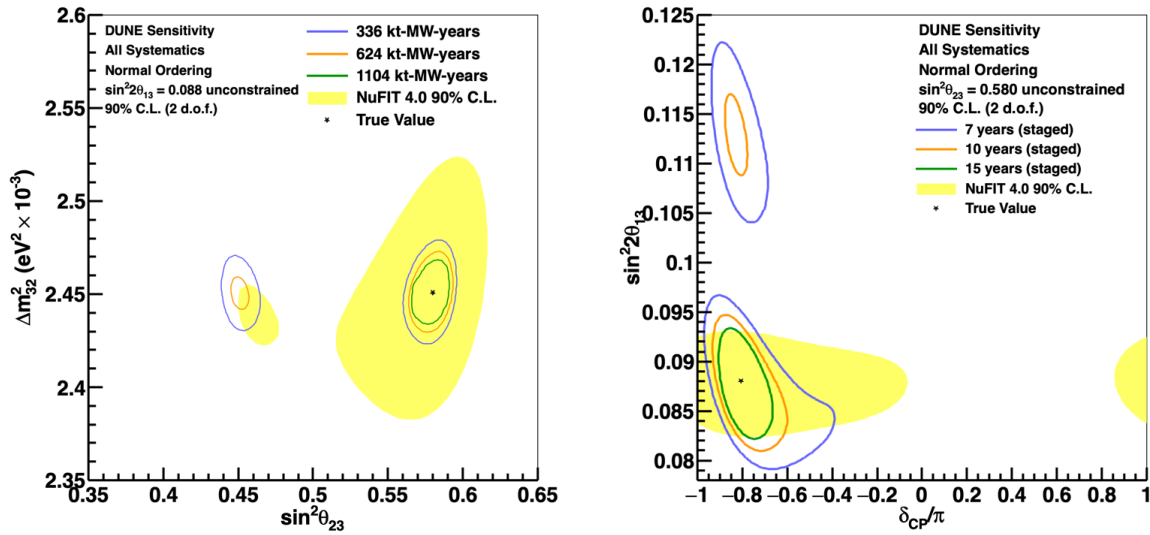


Figure 2.1: DUNE's ultimate measurement capability for  $\sin^2 \theta_{23}$  and  $\Delta m_{32}^2$  (left), and  $\sin^2 2\theta_{13}$  and  $\delta_{CP}$  (right). DUNE can significantly improve on current measurements of the atmospheric mixing parameters, and measure the CP violating phase, while achieving similar precision in  $\theta_{13}$  to the current reactor measurements. The shaded area shows the current allowed region from global fits to data by NuFit [21].

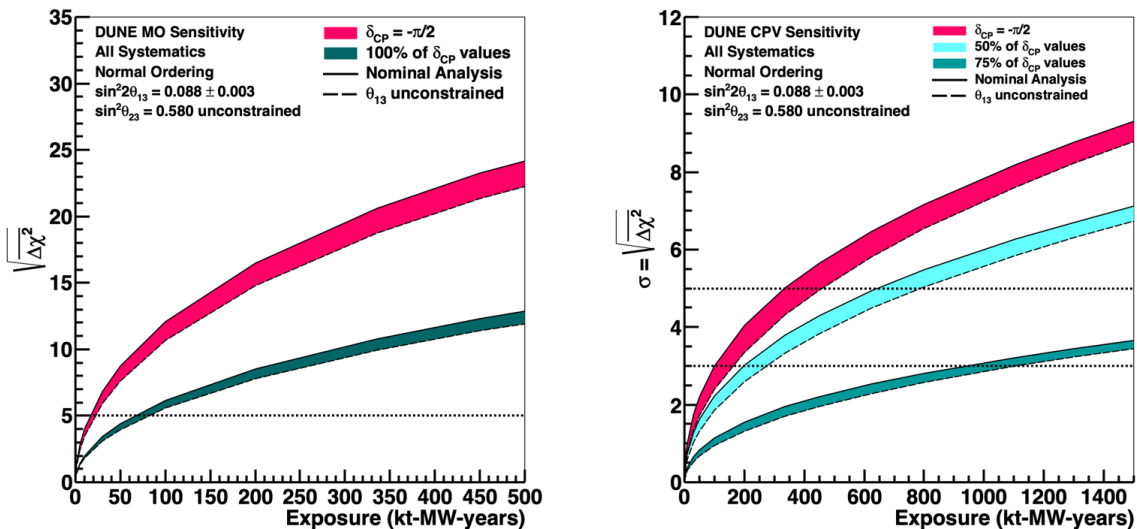


Figure 2.2: The significance with which DUNE can resolve the neutrino mass ordering (left), and Charge Conjugation-Parity Symmetry Violation (CPV) (right), assuming the true mass ordering is normal. The curves represent different assumptions about the value of  $\delta_{CP}$ , and the width of the bands correspond to the effect of using an external constraint on  $\theta_{13}$  from reactor experiments.

liquid argon (LAr) volume that enables efficient rejection of background originating in the cryostat and electronics assemblies. Charged-current interactions of  $\nu_e$  at MeV energies create short electron tracks in LAr, potentially accompanied by gamma ray and other secondary particle signatures. Of proposed detector technologies at the multi-kt scale, the LArTPC technology has optimal sensitivity to detecting  $\nu_e$  flavor low-energy neutrinos. This few-MeV regime is of particular interest for studying a galactic core-collapse supernova (SN) by measuring the associated burst of neutrinos, referred to as the SNB, released during the collapse which has been the primary focus of DUNE low-energy sensitivity studies. DUNE will also have sensitivity to neutrinos from other astrophysical sources, including solar neutrinos.

Each SN releases an intense source of neutrinos of all flavors. During a SN 99% of the gravitational binding energy of the star ( $\sim 10^{53}$  ergs) is released as neutrinos and antineutrinos of all flavors, which play the role of astrophysical messengers, escaping from the SN core. In the event of a galactic SN, DUNE data will probe the inner evolution of the core-collapse mechanism by studying the time and energy spectra of neutrinos arriving at DUNE. SN neutrinos are emitted in a burst of a few tens of seconds duration [22]. There are three qualitative stages of in a supernova collapse, as shown in Figure 2.3, which can be distinguished and studied with DUNE data. These are:

1. The neutronization burst – a large pulse of  $\nu_e$  emission takes place in the first tens of milliseconds as electrons are captured on protons in the stellar core during the formation of a proto-neutron star. A neutrino sphere forms around the proto-neutron star, inside of which the density is so large that neutrinos become trapped; at this point the neutronization burst of  $\nu_e$  emission quenches.
2. The accretion phase – during accretion, lasting from tens to hundreds of ms, neutrino emission is dominated by interactions of gas falling from the outer layers of the progenitor onto the outer extant of the proto-neutron star.
3. The cooling phase – after infall, the proto-neutron star cools over several seconds. The neutrino opacity drops, allowing neutrinos to escape the core. While trapped within the core, neutrino species thermalize resulting in near equipartition of neutrino species.

LAr uniquely offers sensitivity to the  $\nu_e$  component of a SNB via the dominant CC interaction: absorption of  $\nu_e$  on  $^{40}\text{Ar}$ ,  $\nu_e + ^{40}\text{Ar} \rightarrow e^- + ^{40}\text{K}^*$ . In CC interactions in argon, the final state  $e^-$  is observed with any additional de-excitation products as the final-state  $^{40}\text{K}^*$  decays to its ground state. Thus, DUNE will provide a distinct signature of the SN collapse in contrast to water and scintillator-based detectors, which are dominantly sensitive to  $\bar{\nu}_e$  through inverse beta decay. Additional channels in argon include  $\nu - e$  elastic scattering (ES),  $\nu - ^{40}\text{Ar}$  NC interactions, and  $\bar{\nu}_e - ^{40}\text{Ar}$  CC interactions. Cross sections for the most relevant interactions are shown in Figure 2.4.

The predicted event rate from a SNB is calculated by folding together expected neutrino differential energy spectra and cross sections for the relevant channels using SuperNova Observatories with GLOBES (SNOWGLOBES) [23]. Monte Carlo (MC) simulated events are generated using the time and energy of incident neutrinos for a particular SNB model using the Model of Argon Reaction Low Energy Yields (MARLEY) [24, 25] interaction model to simulate the dominant  $\nu_e$  CC neutrino interaction and using -based detector models to simulate the DUNE FD detector simulation. Studies of simulated ES and NC interactions are forthcoming. Standard LArTPC algorithms are applied to reconstruct electron tracks. All visible energy from the event is used to

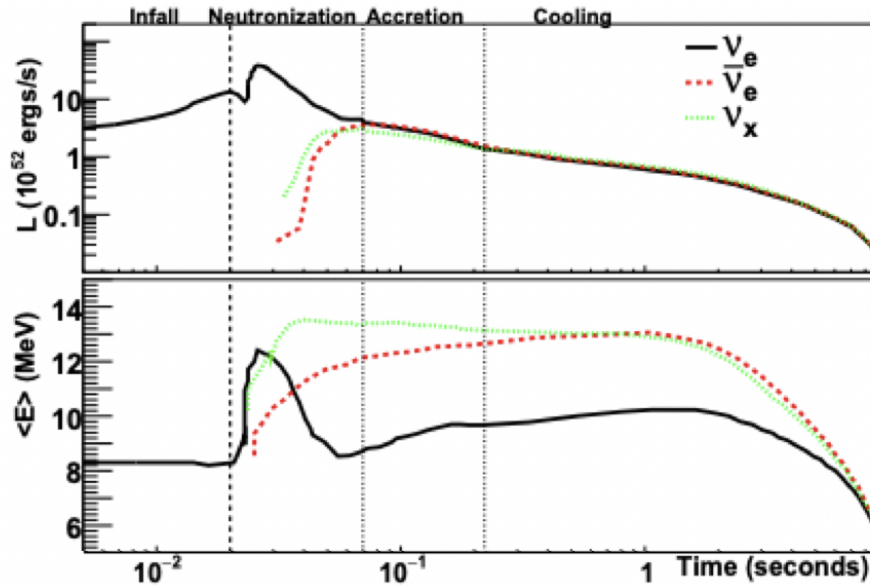


Figure 2.3: Expected time-dependent flux parameters for a specific model for an electron-capture supernova [22]. No flavor transitions are assumed. The top plot shows the luminosity as a function of time, and the bottom plot shows average neutrino energy.  $\nu_x$  stands for  $\nu_\tau$  and  $\nu_\mu$  including  $\bar{\nu}_x$ .

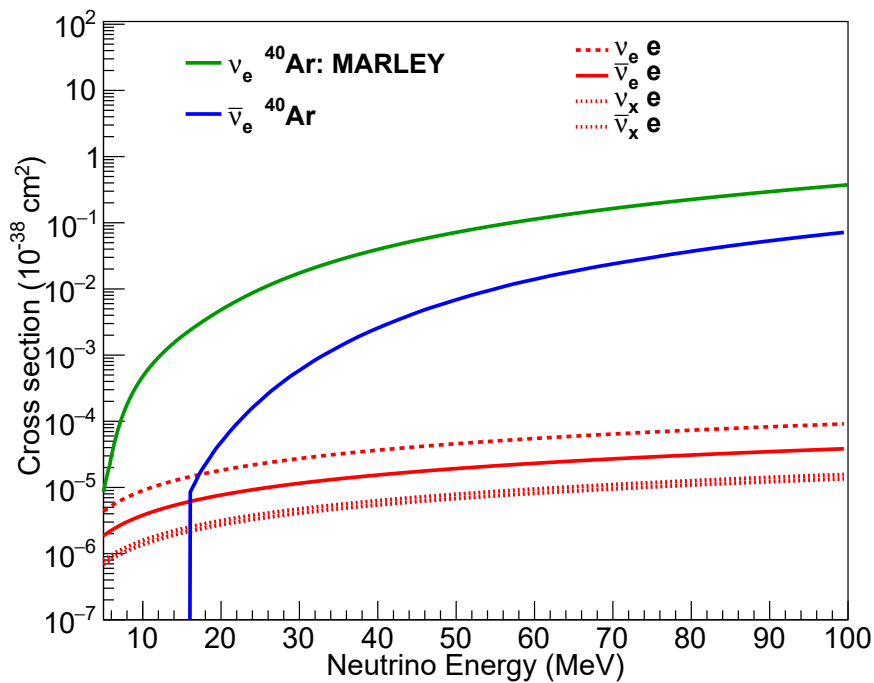


Figure 2.4: Cross sections for SN-relevant interactions in argon as a function of neutrino energy, from [20].

calculate the incident neutrino energy. PDs are used to determine the time, and thus drift distance, of events. DUNE is also exploring methods for incorporating novel photon detector reconstruction and calorimetry to expand its low-energy physics reach.

Details of the simulation and reconstruction are provided in [1, 20]. Predicted event rates vary up to an order of magnitude among different SNB models, and rates will scale as the inverse square of SN distance. As a benchmark, DUNE would observe  $\sim 3300$   $\nu_e$  CC, 210 ES and 160  $\bar{\nu}_e$  CC events for a core collapse SN at 10 kpc in the model [26], assuming 40 kt fiducial mass of argon for DUNE. The expected electron neutrino energy spectrum for three SN models is shown in Figure 2.5 for events scattering in DUNE.

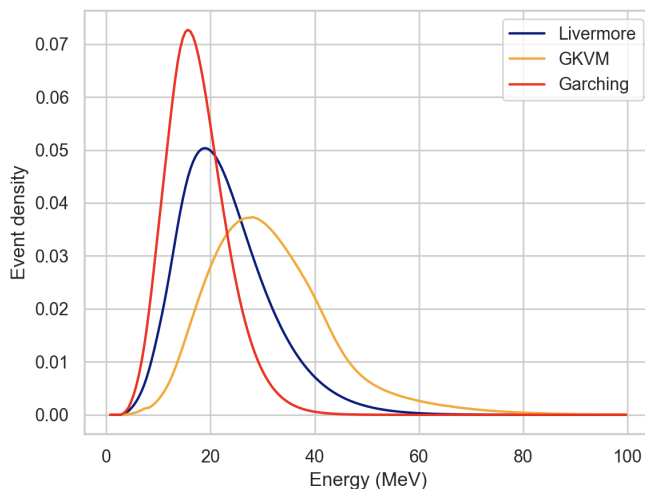


Figure 2.5: Probability density as a function of neutrino energy for  $\nu_e$  CC events interacting in DUNE for three SNB models with arbitrary normalization.

Detection of  $\nu_e$  CC interactions from solar and other low-energy neutrinos is challenging in a LArTPC because of relatively high intrinsic detection energy threshold, about 5 MeV, and because radioactive backgrounds in the same energy regime can affect triggering capability. However, compared with other technologies, a LArTPC offers a large CC event rate and unique potential to distinguish between CC, ES, and NC interactions on an event basis due to sub-cm reconstruction performance. Furthermore, observed energy from the final state  $\nu_e$  CC interaction is much more tightly correlated with the incident neutrino energy on an event-by-event basis than the electron recoil spectrum from the ES channel that has been used for past solar neutrino observations such as in Super-Kamiokande [27]. Due to this, DUNE can make more precise spectral measurements. Though background rates are large, the LArTPC FD2-VD detector allows for background reduction using fiducialization techniques. The solar neutrino event rate is also substantial in the DUNE FD,  $\sim 100$  per day, allowing samples of a few  $10^5$  events after ten years of data collection. Detailed studies of solar neutrino detection capability are underway in DUNE along with subsequent physics sensitivity studies showing promise to improve on current measurements of oscillation parameters after applying fiducial and threshold restrictions. Similarly, DUNE can search for the diffuse supernova neutrino background (DSNB) [28] at energies just above the endpoint of the solar neutrino spectrum. As DUNE is primarily sensitive to the  $\nu_e$  component, it is the only experiment with sensitivity to the neutrino component of the DSNB.

In summary, DUNE anticipates a broad low-energy physics program with sensitivity to the DSNB,



solar neutrinos, and SNB neutrinos, including sensitivity to BSM effects in these astrophysical neutrino samples, as well as participation in multi-messenger astronomy via early alert and pointing capabilities. DUNE has the capability to uncover a broad range of SN and neutrino physics phenomena, including sensitivity to neutrino mass ordering, collective effects, and potentially many other topics.

In comparison with the FD1-HD, the FD2-VD presents two main advantages to perform low-energy physics searches. First, there is a larger free LAr volume with no nearby components, so the geometric fiducial criteria, used to reject high-rate radiological backgrounds originating from detector components, encompasses a larger fraction of the total active LAr mass than in the FD1-HD design. Secondly, an effort has been made to design the PDS to achieve an efficient light collection, as presented in Section 2.3, which translates to improved reconstructed energy resolution and timing capabilities. Section 2.4 discusses the low-energy physics studies carried out to evaluate the physics reach of the FD2-VD design. The SNB triggering efficiency of the FD2-VD is presented in Section 2.4.1 and the reconstructed energy resolution in Section 2.4.2. Importantly updated sensitivity for the FD1-HD TDR studies are forthcoming to capture improvements to the background model allowing direct comparisons to studies shown in this document.

### 2.2.3 Physics Beyond the Standard Model

Thanks to its deep underground location and large fiducial mass, as well as its excellent event imaging, particle identification, and calorimetric capabilities, the DUNE FD will be a powerful instrument for the search of phenomena beyond the Standard Model (BSM), including dedicated FD-only probes of the following topics [19]:

- Boosted dark matter (BDM): The DUNE FD will be sensitive to hypothetical BDM particles originating from various astrophysical sources in the universe, such as the galactic halo, the Sun, and dwarf spheroidal galaxies.
- Baryon number violation (BNV): DUNE will search for nucleon decay and neutron-antineutron oscillations, baryon-number-violating processes whose existence is predicted by many physics theories beyond the SM. The LArTPC technology is particularly well-suited for the observation of proton and neutron decays into charged kaons.

Potential enhancements of the FD2-VD design over the FD1-HD may include a larger fiducial volume, improved energy resolution over the CP-optimized beam and atmospheric neutrino ranges, and improved timing resolution. These enhancements would further extend DUNE's sensitivity to the FD-only BSM probes mentioned above, as well as to BSM probes using a combination of the DUNE FD with the ND complex [19], specifically:

- Search for active-sterile neutrino mixing and related phenomenology: DUNE is sensitive over a broad range of potential sterile neutrino mass splittings by looking for disappearance of CC and NC interactions over the long distance separating the ND and FD, and can help distinguish between recently proposed more complex scenarios aimed at resolving the tension between long-baseline null results and short-baseline anomalies. These measurements will also probe other related phenomenology, such as neutrino propagation through large extra-dimensions.

- Searches for non-unitarity of the Pontecorvo-Maki-Nakagawa-Sakata (PMNS) matrix: Through precision measurements of neutrino mixing parameters, DUNE will help assess the unitarity of the PMNS matrix, with any deviations requiring new physics explanations. Of particular relevance are FD measurements of atmospheric tau neutrino interactions, which would probe the least constrained sector of the PMNS matrix.
- Searches for nonstandard interactions (NSIs): DUNE is uniquely sensitive to NSIs affecting neutrino propagation through the Earth by leveraging its very long baseline and wide-band beam. If the DUNE data are consistent with standard oscillations for three massive neutrinos, DUNE will improve current constraints on  $\epsilon_{\tau e}$  and  $\epsilon_{\mu e}$ , the magnitude of the NSI relative to standard weak interactions, by a factor of 2 to 5, which may be further extended with improved FD energy resolution.
- Searches for violation of Lorentz or charge, parity, and time reversal symmetry (CPT) Symmetry: CPT symmetry, the combination of charge conjugation, parity and time reversal, is a cornerstone of any local, relativistic quantum field theory, and its potential violation would have wide-range repercussions in our understanding of particle physics. Through neutrino and antineutrino measurements with the DUNE ND and FD, DUNE can improve the present limits on Lorentz and CPT violation by several orders of magnitude, contributing an essential test of these fundamental assumptions of quantum field theory.

## 2.3 Simulations of FD2-VD

### 2.3.1 Photon Detector Simulation

The FD2-VD PDS uses large s [29] distributed over five different planes (cathode and the four membrane walls) to collect scintillation light. An effort to optimize the PDs' locations taking into account the constraints present (e.g., mechanics, interface with other systems, installation) has been undertaken to provide the most uniform detection light yield (LY), i.e., how many photoelectrons will be detected by the PDS with a given energy deposited in a given position within the volume <sup>1</sup>, possible across the detector volume. Dependence on the drift direction is reduced due to the sensors placed over the walls along the  $y$ - $z$  plane, as described in Chapter 6. On the one hand, this solution aims to provide an improved energy reconstruction. On the other hand, it improves the position reconstruction and timing capabilities needed for triggering non-beam physics events, such as supernova burst or nucleon decay events, and fiducializing them along the drift direction.

A fully integrated PDS simulation was developed within the Liquid Argon Software (LArSoft) framework. In the simulation chain, after particles are generated and propagated using Geant4, energy deposits along tracks are retrieved in order to estimate the number of electrons and photons generated at each step. The ionization charge is calculated based on the modified Birks or Box model with a correction at low E field [30]. From the number of electrons and the total energy deposited, the number of photons is obtained, keeping the appropriate energy partitioning between charge and light. Since a very large number of scintillation photons (25000 ph/MeV at 500 V/cm) is produced in LAr, it is very computationally demanding to individually propagate all photons using Geant4. Instead, a fast simulation for photons is implemented, currently using a generative neural network.

<sup>1</sup>This is not the same definition as the scintillator light yield, which depends on the physical characteristics of the medium alone and is given in units of photons per energy deposited.

The fast photon simulation relies on a generative neural network to predict the fraction of photons (called visibility) reaching each photon detector (PD) from a given point in the detector [31]. This method is flexible enough to be used with any kind of boundary condition. The generative model can be trained ahead of time using a full Geant4 optical simulation, with photons emitted from random vertices within the cryostat volume with isotropic initial directions ( $\sim 10^6$  photons per point). The output is saved to a computable graph and deployed in DUNE’s LArSoft-based software stack. This procedure is followed for both 128 nm photons (Ar scintillation) and 176 nm photons (Xe scintillation) to account for the wavelength-dependent Rayleigh scattering and material reflectivity in the simulation of Xe-doped LAr (see Section 6.1). When the computable graph is loaded into LArSoft, it quickly emulates photon transport by computing the visibility of each photon detector according to the photon emission vertex along the particle’s track. This method is 20 to 50 times faster than the Geant4 simulation without introducing voxelization, which would limit the resolution of the simulation. While the computable graph is more accurate than previous ‘photon library’-based methods, it is not a perfect recreation of Geant4. The differences primarily occur in regions like corners with many reflections that typically do not contribute the majority of the observed light. The model inference also requires a relatively small amount of memory. The samples for ProtoDUNE-like and DUNE FD-like geometries show the required memory for the model inference is around 15% of the Geant4 simulation. Furthermore, the memory usage does not directly scale with detector volume.

When simulating events, the computable graph is used to assign the photons produced in the interaction to individual PDs. The time of arrival of the photons takes into account both the time profile of the scintillation process as well as the propagation time in the argon, including the effect of scattering. The emission times for Ar and Xe are treated separately. Argon emission follows a two exponential profile for fast and slow decays whereas the model used for Xe takes into account the time of the intermediate processes  $\text{Ar}_2^* + \text{Xe} \rightarrow \text{ArXe}^*$  and  $\text{ArXe}^* + \text{Xe} \rightarrow \text{Xe}_2^*$ , and finally the  $\text{Xe}_2^*$  excimer decay time, with parameters obtained from preliminary ProtoDUNE-SP analysis.

The PDS design presented in the FD2-VD CDR [32] was used for the studies discussed in this chapter. It does not include improvements implemented in this TDR such as the membrane coverage over the short walls, which increases uniformity in the LY closer to the end caps of the detector (see Section 6.2.1), nor the repositioning of the border cathode PDs farther inward, away from the field cage, to mitigate the risk of electrical discharge. These changes, which will be implemented in the simulation software in early 2023, should only affect in a significant way events simulated in the  $\sim 15\%$  of the volume closest to the cathode edges. The studies presented in this chapter did not use the full time projection chamber (TPC) volume; instead a subset of the top FD2-VD drift volume was used, i.e., the full width (13.5 m) and drift length (6.5 m), but only 21 m of the full detector length (58.2 m). Studies have shown that this volume is sufficient to characterize the light propagation anywhere in the full volume; disregarding the light that would be collected by more distant PDs has a negligible effect.

In the simulation, the aluminum field cage profiles are included individually, as described in Section 5.4.2, and they are assigned a reflectivity value of 70%. On the other hand, the anode is included as a single volume with an effective reflectivity that takes into account the metallic area of the perforated anode that could reflect light (about  $\sim 40\%$  of the total area) and the wavelength. The relevant detector parameters and photon emission/propagation constants used in the MC generation are listed in Table 2.1 (reflectivity assumed as specular for all materials listed).

Values for liquid argon doped with Xe with a 10 ppm concentration take into consideration the latest ProtoDUNE measurements [33] showing that from the totality of photons emitted, 53% will come from Xe dimmers deexcitation and of the 47% that is emitted by Ar dimmers deexcitation, 35% will be absorbed in the medium during propagation.

Table 2.1: Simulation input parameters and physical constants.

Parameter	Value	Comment
LAr Photon Yield (mip, 500 V/cm)	25,000 ph/MeV	23% Singlet (Fast) emission 77% Triplet (Slow) emission
Xe doping in Ar	10 ppm	53% of total light emitted at 176 nm 35% of light loss at 128 nm
Rayleigh Scattering Length	$\lambda_R(128 \text{ nm}) = 1 \text{ m}$ $\lambda_R(176 \text{ nm}) = 8.5 \text{ m}$	Ar light [33, 34] Xe light
Absorption Length	$\lambda_{Abs}(128 \text{ nm}) = 20 \text{ m}$ $\lambda_{Abs}(176 \text{ nm}) = 80 \text{ m}$	3 ppm of N <sub>2</sub>
X-ARAPUCA Det. Efficiency	$\epsilon_D = 3\%$	See Section 6.4
Field Cage Reflectivity [35, 36]	R=70%	Narrower profile in $\sim 60\%$ of longer walls
Cryostat Reflectivity	R(128 nm) = 30% R(176 nm) = 40%	
Anode Reflectivity	R(128 nm) = 6% R(176 nm) = 12%	Assuming solid area of perforated PCB of 40%

After the generation and propagation of photons coming from energy deposits in the detector volume, the digitization of the light signal is performed assuming that each detected photon will generate a signal, called a single photoelectron (PE), with an idealized shape of a fast rising exponential and a slower exponential decay. The waveform is built by considering the relevant electronics characteristics. Details on the digitization parameters are given in Table 2.2.

Table 2.2: Input parameters for the optical digitization stage in the simulation.

Parameter	Value
Single PE rise time	10 ns
Single PE decay time	200 ns
Single PE peak	10 ADC
Crosstalk probability	20%
Electronic channels	2
Baseline	500 ADC
Electronics noise	2 ADC
Saturation	14 bits
Sampling frequency	62.5 MHz

The reconstruction of light signal includes the identification of optical hits in the recorded photon detector's waveforms, triggered by the criteria of signal above 1.5 photoelectron. Optical hits are later combined in optical flashes by a time coincidence criteria. Optical waveforms, hits, and flashes are the basic elements used for analyzing the light signal.

### 2.3.2 Charge Readout Simulation

Despite the mechanical and electronic differences between the FD1-HD and FD2-VD detector modules, their underlying detection principles are the same. This parity has been exploited in the software, where a model of FD2-VD has been implemented in the LArSoft framework with a nearly identical simulation and reconstruction workflow to FD1-HD. Because of this similarity, many of the advanced reconstruction techniques that were developed for the FD1-HD [1] have been reused by the FD2-VD, with some retuning and reoptimization required. The simulation and reconstruction for FD1-HD has been described extensively elsewhere [1] and will only be briefly summarised here. The overall simulation and reconstruction for both detectors can be broken down into the following steps:

1. **Event generation:** Simulation of neutrino interactions within the detector volume, relying on a neutrino interaction generator such as Generates Events for Neutrino Interaction Experiments (GENIE).
2. **Particle propagation:** Simulation of the trajectories and interactions of the neutrino interaction's final state particles through the detector volume using Geant4. The number of electrons ionized from the liquid argon and the number of scintillation photons produced from recombination are calculated at the end of this step.
3. **Detector response:** The signal simulation of the raw output of the detector, as would be expected from the data acquisition (DAQ). This step involves transportation of the ionization electrons to the anode plane, and simulation of the charge readout's response to those electrons.
4. **Signal processing:** The first step of the reconstruction is to remove detector effects (such as the shaping time of the electronics) and noise from the raw waveforms, recovering the true charge waveforms observed on the readout channels.
5. **Hit reconstruction:** A search for, and fits to, peaks in the charge waveforms. These fitted peaks are called hits.
6. **Pattern recognition:** The process of clustering waveform hits, and matching those clusters across readout planes to form 3D representations of particles. This is typically handled by a dedicated package such as [37] (see section 2.5.1).
7. **High level reconstruction:** Advanced reconstruction techniques that are applied to upstream reconstruction to deduce particle and neutrino-level properties. These include neutrino flavor tagging with a convolutional visual network (CVN) (see section 2.5.2) and neutrino energy reconstruction (see section 2.5.3).

Despite the general software similarity between FD1-HD and FD2-VD, direct comparisons are, in some cases, complicated by advances made in the software since the most recent full end-to-end FD1-HD production. For the benchmark performance plots in previous design reports [1], the neutrino interaction generator was GENIE version 2.12, and a simplified model was used to simulate the detector response. Since then, the LArSoft framework has moved forward to GENIE version 3.0, and a more realistic detector response model is simulated through the Wire-Cell Toolkit (WCT), in addition to several other incremental improvements to algorithms. These recent additions are included in the FD2-VD samples that are shown in detector performance comparisons throughout this chapter, but those same additions are not included in FD1-HD benchmark being compared to.

### 2.3.3 Signal Processing with Wire-Cell Toolkit

WCT is a software suite based on the tomographic reconstruction principle. It provides algorithms for the 2D convolution-based LArTPC signal simulation and signal processing. This simulation agrees with real detector data better than the previous 1D version. It is used and validated for wire readouts in the and the experiments [38, 39]. Initial validations for the PCB readout was done using a 50L prototype. As a reverse process, the first step in the LArTPC charge reconstruction is the , which extracts original ionization electron distributions from digitized TPC waveforms. The Wire-Cell 2D deconvolution based LArTPC algorithm is a core port of FD2-VD’s simulation and reconstruction, and has been validated using real detector data. A similar detector response model is currently being deployed for FD1-HD.

## 2.4 Low-energy Physics Performance

The design and optimization of the PDS in terms of detection coverage, detection efficiency, and timing capabilities may allow for the enhancement of the DUNE physics reach. A high LY is highly appealing for low-energy physics as it entails improvements in the triggering efficiency and energy resolution.

As a window into this possibility, the TPC and PDS trigger efficiencies and energy resolutions for low-energy neutrino events are studied in Sections 2.4.1 and 2.4.2, respectively.

The MC simulation for SNB events in LArSoft employs the MARLEY generator [24, 25]. MARLEY simulates neutrino-nucleus interactions in LAr in the tens-of-MeV range by selecting an initial excited state of the final state  $^{40}\text{K}^*$  nucleus and sampling an outgoing electron direction according to the  $\nu_e\text{CC}$  differential cross section. After simulating the initial two-body  $^{40}\text{Ar}(\nu_e, e^-)^{40}\text{K}^*$  reaction for an event, MARLEY also handles the subsequent nuclear de-excitation.

Background generation follows the *BxDecay0* package<sup>2</sup>, a C++ library providing simulated nuclear decays that is integrated into LArSoft. A radiological model was developed for the FD1-HD and adapted for the FD2-VD design. It includes radioactive decays in the LAr bulk ( $^{39}\text{Ar}$ ,  $^{42}\text{Ar}$ ,  $^{85}\text{Kr}$ ,  $^{222}\text{Rn}$  and their decay chains), the cathode (drifted  $^{42}\text{K}$  from LAr’s  $^{42}\text{Ar}$  decays,  $^{40}\text{K}$  and the  $^{238}\text{U}$  decay chain), the charge-readout planes (CRPs) ( $^{60}\text{Co}$  and the  $^{238}\text{U}$  decay chain), the PDS ( $^{222}\text{Rn}$  decay chain), and external sources (gammas and neutrons from surrounding rocks). Table 2.3 summarizes the different activities considered. This background model is much more detailed than the one considered in the FD1-HD TDR, although even further improvements are planned, as for instance, a more accurate model of the cavern gammas.

After the generation stage, events pass through the Geant4 stage to estimate the number of electrons and photons reaching each detector channel, with special attention to neutron transport and electromagnetic physics (*QGSP\_BERT\_HP\_EMZ* physics list), and the digitizer stage, where the corresponding recorded signals will be generated. Finally, the reconstruction stage provides input for the physics analysis.

<sup>2</sup><https://github.com/BxCppDev/bxdecay0>

Table 2.3: Activities taken into account in the radiological model. The numbers are coming from estimations or dedicated measurements.

Component	Activity (mBq/cm <sup>3</sup> )
<sup>39</sup> Ar in LAr	1.41
<sup>42</sup> Ar and <sup>42</sup> K in LAr	$0.128 \times 10^{-3}$
<sup>85</sup> Kr in LAr	0.16
<sup>222</sup> Rn chain in LAr	$1.395 \times 10^{-3}$
<sup>40</sup> K in cathode	9.1
<sup>238</sup> U chain in cathode	0.113
<sup>60</sup> Co in anode	0.361
<sup>238</sup> U chain in anode	95
<sup>222</sup> Rn chain in PDS	0.021
External neutrons (rocks, concrete walls, etc)	$7.6 \times 10^{-3}$
Cavern gammas	64

### 2.4.1 SNB Trigger Efficiency

As a supernova (SN) is such a rare and unpredictable event, it is vital that DUNE trigger on each galactic SNB. The SNB trigger will be limited by radiological backgrounds within the LAr volume and, relying on an increase in physics activity within the active volume. The detector must be able to detect and reconstruct events in the range 5–100 MeV, and special triggering and DAQ requirements must take into account the short, intense nature of the burst, as well as the need for prompt propagation of information worldwide. The trigger is required to achieve 95% efficiency for a neutrino burst from a SN at 20 kpc. A SNB is expected to last approximately 30 seconds, but can last as long as a few hundred seconds; a large fraction of the events are expected within approximately the 1-2 seconds of the burst.

The DUNE detector systems must be configured to provide information to other observatories on possible astrophysical events (such as a galactic SN) in a short enough time to allow global coordination. This interval should be less than 30 minutes, and preferably on a few-minute timescale. Any SNB trigger observed in DUNE will be forwarded immediately to SuperNova Early Warning System (SNEWS) [40] to allow observation of the evolution of the event.

In DUNE, the trigger on a SNB can be done using either TPC or PDS information. In both cases, the trigger scheme exploits the time coincidence of multiple signals over a timescale matching the typical SN luminosity evolution. A redundant and highly efficient triggering scheme is envisaged. This section describes a trigger design study based on the TPC and another on the PDS.

#### 2.4.1.1 SNB Trigger Efficiency with the TPC

With the planned DAQ computing resources, the reconstruction available for real-time triggering of a SNB in DUNE will be limited. The SNB trigger is based on s, reconstructed TPC hits that include basic information such as start-time, time-over-threshold, channel number, and pulse-integral (a value proportional to the charge collected in that channel). Clusters are formed from

nearby trigger primitives and the detector is triggered if the number of clusters observed in a sliding 10 second time window passes above a certain threshold.

The algorithm to trigger a SNB should be robust and reliable. To determine the number of clusters in the TPC, the trigger primitives are sorted by time and channel number. SNB MC samples with low-energy neutrino interactions were generated and combined to create a stream of trigger primitives to understand DUNE’s potential to trigger on a burst. Clustering is performed to group nearby hits within 20 ticks ( $10 \mu\text{s}$ ) and two channels (in order to keep the algorithm robust against dead channels). If at least six trigger primitives are clustered together, the cluster is taken as a neutrino candidate. The mean number of trigger primitives reconstructed together in a cluster is proportional to the neutrino energy. This algorithm has  $> 50\%$  efficiency for identifying neutrinos with  $\geq 16 \text{ MeV}$  of energy with modest efficiency at lower energies (see Section 7.4.3.2). The number of clusters accumulated in a sliding 10 second window is then calculated to determine whether the detector should trigger.

An important constraint of DUNE regarding the SNB triggering is the number of fake triggers the DAQ can handle. As in previous DUNE studies [13] and required by SNEWS, the maximal tolerable rate of false triggers is assumed to be one per month. Using the radiological model previously described and summarized in Table 2.3, a rate of background events was found to be around 1 Hz, using a selection of six trigger primitives per cluster. Neutrons from the rocks are the main source of remaining backgrounds, since their capture in Ar atoms produces a gamma cascade that is similar to a SNB neutrino interaction. A requirement of 25 clusters in a ten second interval produces about one fake trigger per month.

With a requirement of 25 clusters, each with at least six trigger primitives, reconstructed within 10 seconds, the SNB triggering efficiency is depicted in the left plot of Figure 2.6, calculated with Poisson statistics. In this plot, the efficiency is given in terms of true interactions in 10 kt. Using the Garching model [22], depicted in Figure 2.3, the efficiency in terms of the SNB distance is shown on the right plot of Figure 2.6. This model gives the time dependency of the interactions, which is taken into account when setting a ten second window for triggering. Figure 2.6 shows that the trigger requirement is met with the TPC signal of the FD2-VD and the Garching model, which is the most conservative of the three considered in this document.

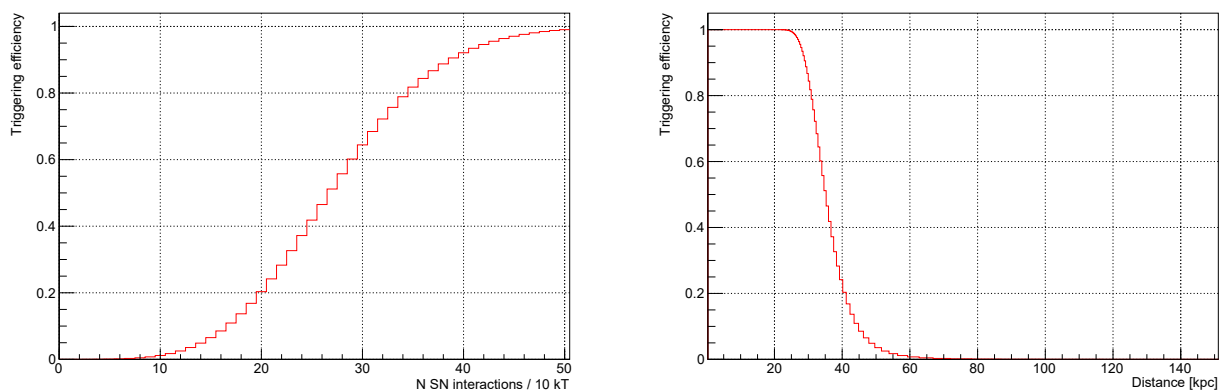


Figure 2.6: SNB triggering efficiency using the TPC signal. Left: In terms of the real number of interactions. Right: Converted to the distance from an SNB.



### 2.4.1.2 SNB Trigger Efficiency with the PDS

The PDS-based SNB trigger uses optical flashes that are clustered according to trigger primitive hits in the optical detectors reconstructed nearby in time and space. For the PDS trigger study, a real-time algorithm provides the trigger primitives by searching for optical hits and optical clusters based on time and spatial information.

MC samples were generated using a subset of the FD2-VD geometry consisting of one drift gap height, full width, and 21 m length along the detector long side. A SNB simulation was run using the FD2-VD geometry producing  $10^6$   $\nu_e$ -CC events with the MARLEY event generator. A sample of  $10^6$  simulated exposures, each using a 8.5 ms exposure time, was

produced with the radiological model, including the radioactive decays listed in Table 2.3. The PDS trigger study was carried out for three different core-collapse SN neutrino flux models: Livermore, Garching, and GKVM, as detailed in [20].

First a clustering algorithm was developed. For this, an optical hit is defined as a peak in the digitized signal arriving in one of the optical channels that is above 1.5 PE. A cluster is defined as a collection of hits that present certain correlations in time and space, such that they are believed to have all been caused by the same underlying neutrino event inside the detector. The parameters explored to optimize the clustering algorithm are:

- Maximum cluster duration – the maximum time difference between the earliest and the latest hit in the cluster.
- Maximum time difference between consecutive hits.
- Maximum spatial distance between neighboring optical channels detecting the hits.
- Minimum hit multiplicity – the minimum number of hits required to classify a collection of hits as a cluster.

As an orientation, the optimal parameters were around 300 ns for the maximum cluster duration, 200 ns for the maximum hit time differences, 250 cm for the maximum hit spatial distances, and 10 for the minimum hit multiplicity.

Second, a trigger algorithm was simulated. For a given set of parameters, the clustering algorithm is run on the whole set of SNB and background events. A classifier (boosted decision tree), trained on the clusters produced by this set of parameters, may be used to discriminate between signal neutrino and radiological background events that is trained based on the cluster parameters.

Next, for a fixed neutrino energy spectrum, the clustering algorithm is run on 1000 subsamples of SN events and corresponding backgrounds, using a burst time window of one second, which was found close to optimal for identifying a SNB. This classifier is then applied to remove  $> 50\%$  of the background while keeping most ( $> 90\%$ ) of the SNB signal.

A  $\chi^2$  test is performed on each of these subsamples, comparing the signal with the expected background. Hit multiplicity (number of hits in a cluster) is the variable used to perform the comparison, as this was found to have the highest discriminating power. The trigger is activated

successfully if the significance of the  $\chi^2$  test is above a critical value indicating a trigger frequency of one per month, a requirement for limiting data rates with DUNE and SNEWS. The trigger efficiency for this set of parameters is estimated as the number of successful s over the total number of subsamples.

The next step is to iterate through a wide set of parameters and select those that yield the higher trigger efficiency for a particular neutrino spectrum. For the three SNB flux models considered, the efficiency values are presented in Table 2.4 and Figure 2.7.

Table 2.4: PDS trigger efficiencies for three different SN models and a range of distances for a 12 kt FD2-VD module. The rightmost column indicates the distance at which efficiency falls below 95% .

	Eff. at 10 kpc	Eff. at 15 kpc	Eff. at 20 kpc	95% thresh. (kpc)
Livermore	1	0.954	0.492	16.12
Garching	0.758	0.066	0.006	9.24
GKVM	1	1	1	28.56

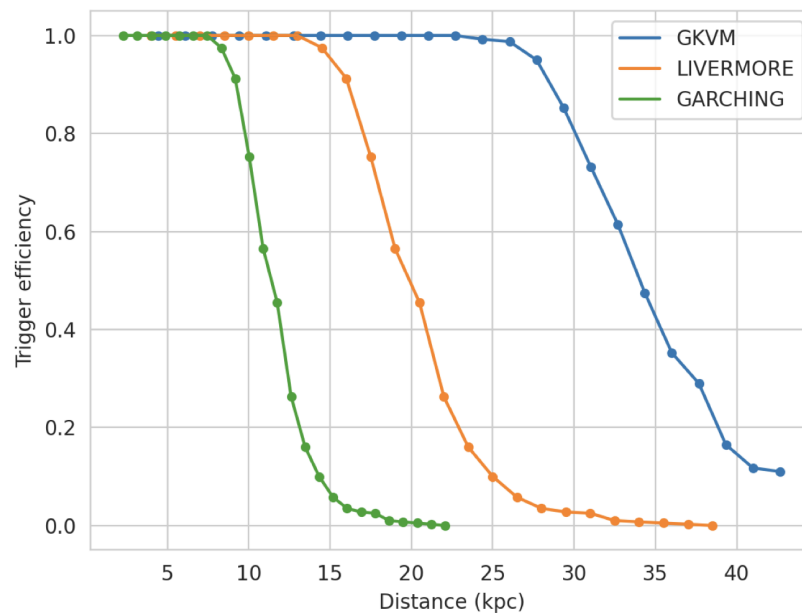


Figure 2.7: PDS trigger efficiencies for three different SN models and a range of distances for a 12 kton FD-2 VD module.

DUNE’s current PDS trigger sensitivity to a core-collapse SN is found to be in the 5-20 kpc range, the precise value being highly dependent on the SNB flux model. The FD2-VD PDS should yield a highly efficient trigger for a SN occurring anywhere in the Milky Way when combined with other subsystems, and the proposed trigger strategy meets the requirements, although it has a dependency on the model. For a direct comparison with the FD1-HD, a new study is in progress updating the simulation parameters and the radiological model.

## 2.4.2 Energy Resolution with TPC and PDS

A simulation has been performed to assess the energy resolution for neutrino interactions in the 5 to 30 MeV energy range. For this, MARLEY was used to generate monoenergetic signal samples with ( $\mathcal{O}(10^4)$ ) events in 1 MeV steps). The full DUNE simulation and reconstruction chain was also run as previously described.

From the sample without backgrounds, a calibration was performed to transform the charge read by the TPC into the energy deposited by the interacting neutrino. This was done by summing the charge of all the hits, after electron drift lifetime correction, as long as the true neutrino vertex was at least 15 cm from any surrounding wall-like structure so that the full event topology is contained.

To compute the visible energy in a given event, an algorithm that takes the local information from 2D trajectories, stitching together nearby 2D hits was used to form reconstructed clusters. Next 3D track information was produced by taking the 2D clusters and matching them in the three 2D projection strip planes to build the tracks. A calorimetric sum of the hits associated with the highest charge track and surrounding clusters was performed (after electron lifetime correction) both for signal-only and signal-and-background generation in order to evaluate the impact of radiological background on the low-energy detector performance.

Figure 2.8 shows both the tracking performance and energy resolution attained for the signal-only sample. The tracking efficiency grows with energy and presents a plateau at  $\sim 90\%$  and the energy resolution is comparable to the FD1-HD module. A closer look at track reconstruction at low energy with the PCB technology will be taken in order to evaluate possible improvements in this metric. The presence of backgrounds does not affect the signal tracking efficiency and brings only a small degradation on the energy resolution, especially on the lower energy end.

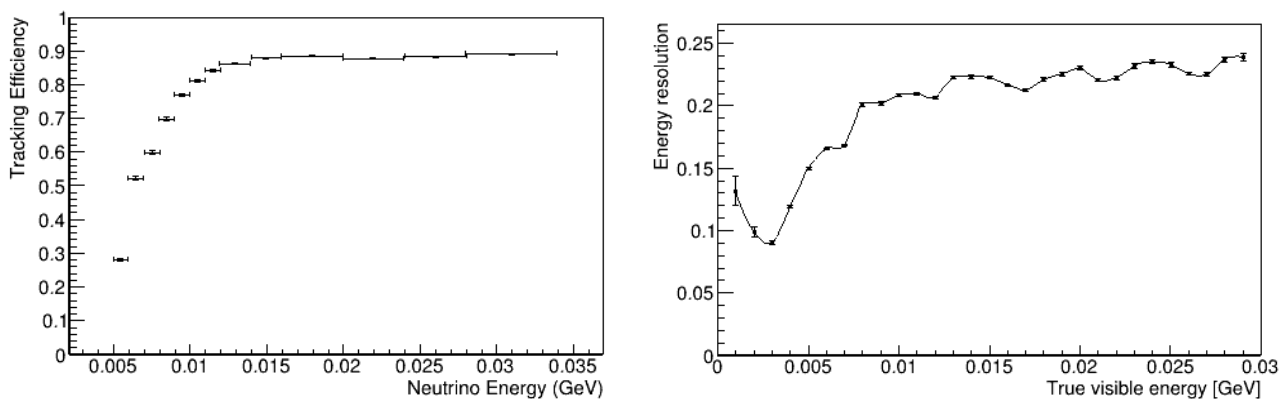


Figure 2.8: Left: Tracking efficiency for MARLEY CC  $\nu_e$  scattering on  $^{40}\text{Ar}$  events. Right: Energy resolution for low-energy events, defined as the root mean square (RMS) of the distribution of the fractional difference between the reconstructed and the visible energy with respect to visible energy, as a function of neutrino energy for reconstructed TPC tracks corrected for drift attenuation.

The PDS should be able to provide a calorimetric energy measurement for low-energy events, complementary to the TPC energy measurement. Achieving PDS energy resolution comparable to the TPC will allow taking advantage of the anti-correlation between the emission of light and

charge signals. The PDS energy performance at low energy was studied for MARLEY-generated neutrino events simulated in the FD2-VD detector geometry. Neutrino interactions with energies between 4 MeV and 100 MeV were uniformly generated within the TPC, and analysis was performed by selecting events in the central region of the detector along the beam direction to avoid border effects from the cryostat’s end caps.

A precise knowledge of the LY as a function of position e.g., from a dedicated calibration, will enable calorimetric energy reconstruction from photon counting. Since the LY of a detector is position-dependent, the energy reconstruction was carried out by correcting the total observed number of photoelectrons using the simulated neutrino’s true position in the detector. In future analyses, a reconstructed position based on PDS and TPC signals can be used. The energy resolution was obtained as the standard deviation of the Gaussian fit to the distribution of the relative difference of visible energy to the reconstructed deposited energy.

Figure 2.9 shows the energy resolution with statistical-only uncertainties when using collected light from simulated low-energy neutrinos. The fit presents the expected behavior, consisting of the “noise,” “stochastic,” and “constant” terms added in quadrature ( $\sqrt{p_0^2 + (p_1/\sqrt{E})^2 + (p_2/E)^2}$ ). The stochastic term ( $\propto p_1$ ) corresponds to the intrinsic statistical spread in the number of photons detected given by Poisson statistics, whereas the noise contribution ( $\propto p_2$ ) is due to the cumulative electronic noise of the ARAPUCA cells’ readout chain (simulated baseline and dark noises). The constant term alone ( $p_0$ ) provides an energy resolution of the PDS at higher energy of about 10%. The largest contribution to this number comes from the calibration procedure currently being used. It relies on averaging the LY over a large region ( $0.25 \times 1 \times 2 \text{ m}^3$ ) in order to obtain the total expected number of photons landing on a given PD. Further exploitation of the computable graph photon simulation, combined with rigorous calibrations should significantly reduce this term and improve the energy resolution.

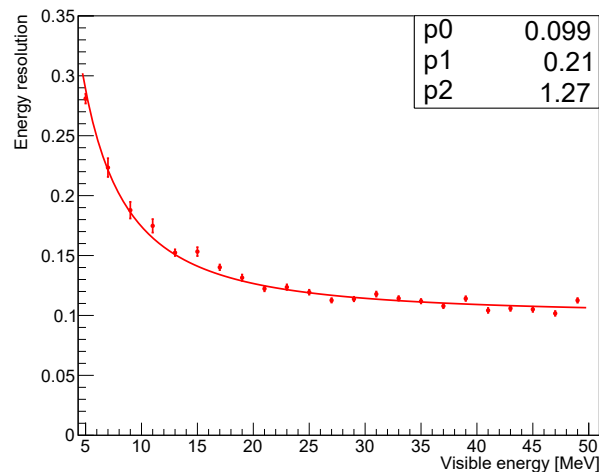


Figure 2.9: PDS energy resolution with statistical-only uncertainties for the FD2-VD. The fit shows a function of the form  $\sqrt{p_0^2 + (p_1/\sqrt{E})^2 + (p_2/E)^2}$ , with  $p_0$ ,  $p_1$ , and  $p_2$  representing the constant, stochastic and noise coefficients respectively.

## 2.5 Long-baseline Oscillation Physics Performance

The LBL neutrino oscillation physics sensitivity of DUNE is described in the FD1-HD TDR [1] and in two related journal articles [41, 42]. The analysis described in those references is based on simulations of the FD1-HD. The performance of the FD for the oscillation analysis depends on three main factors, all of which are expected to be very similar in FD1-HD and FD2-VD: the reconstruction efficiency and background rejection for CC  $\nu_\mu$  and  $\nu_e$  signals, the neutrino energy estimation for these signal events, and the residual calibration uncertainties. The two detector designs can be compared in these three areas, without completely repeating the LBL analysis, which requires tens of millions of CPU core hours, largely dominated by the processing time of the  $\sim 1,000,000$  throws for each of the  $\sim 150$  systematic uncertainties.

The inputs to the oscillation analysis are selected samples of  $\nu_\mu$  and  $\nu_e$  CC candidates, in and beam modes, with a neutrino energy estimate for each event. The reconstruction stages required to categorize the event type and estimate its energy are signal processing (using Wire-Cell, described in Section 2.3.3), hit reconstruction, 3D event reconstruction (using Pandora, described in Section 2.5.1), event selection (using a CVN, described in Section 2.5.2), and neutrino energy reconstruction (based on Pandora, described in Section 2.5.3). The hit reconstruction, which finds signal peaks on the strip waveforms, is identical to the FD1-HD and is not described here.

The performance benchmarks presented here are based on a simulation of six million neutrino interactions in FHC beam mode. FHC results are shown. Comparisons of RHC events were not possible due to a technical difficulty with the tape system at Fermilab that prohibited accessing the relevant files for FD1-HD. These FHC comparisons used a FD1-HD simulation that was based on a simplified detector response and a reconstruction that has undergone years of optimization and is substantially more mature than its FD2-VD counterpart. For FD2-VD, some areas of the simulation and reconstruction have undergone a first round of optimisation (sections 2.3.3, 2.5.2 and 2.5.3) while other areas (section 2.5.1) rely on tunings taken from FD1-HD, with FD2-VD tuning planned for the future. In all cases, the preliminary FD2-VD performance is expected to converge with that of FD1-HD once the additional realism is added to the FD1-HD simulation, and the FD2-VD reconstruction undergoes further development and optimizations.

### 2.5.1 3D Event Reconstruction with Pandora

Pandora is a multi-algorithm reconstruction suite [37], with specific design features to perform pattern recognition on plane-based LArTPCs. The overall aim of Pandora's reconstruction is to read in the reconstructed 2D hits from a LArTPC, and output fully 3D representations of the particles emanating from the neutrino vertex. Due to the similarities between the two detector modules coupled with Pandora's detector-agnostic nature, the FD2-VD instance of Pandora was able to inherit all configurations and tunings from the FD1-HD and achieve competitive performance out of the box.

Figure 2.10 shows Pandora's reconstruction efficiency of the simulated leading lepton in CC interactions, shown as a function of the lepton's true momentum. The efficiencies are shown for both the FD2-VD and FD1-HD. Performance is similar for both detector modules, with only a small relative deficit in efficiency for the FD2-VD, especially for electrons. Figure 2.11 similarly shows Pandora's reconstruction efficiency of the leading muon, but as a function of the muon's

angle in the anode plane. While the performance is again competitive between the two detectors, Figure 2.11 also shows that both detectors have consistent angular acceptance, even when the muon is aligned with the direction of the wires/strips in a given anode plane (about  $\pm 30^\circ$  and  $90^\circ$  for both detectors). This is due to the three-plane design of both detector designs: when the readout quality of one plane is compromised because of the co-linearity of the lepton with that plane’s readout, the other two complementary planes provide enough information to achieve 3D reconstruction [43].

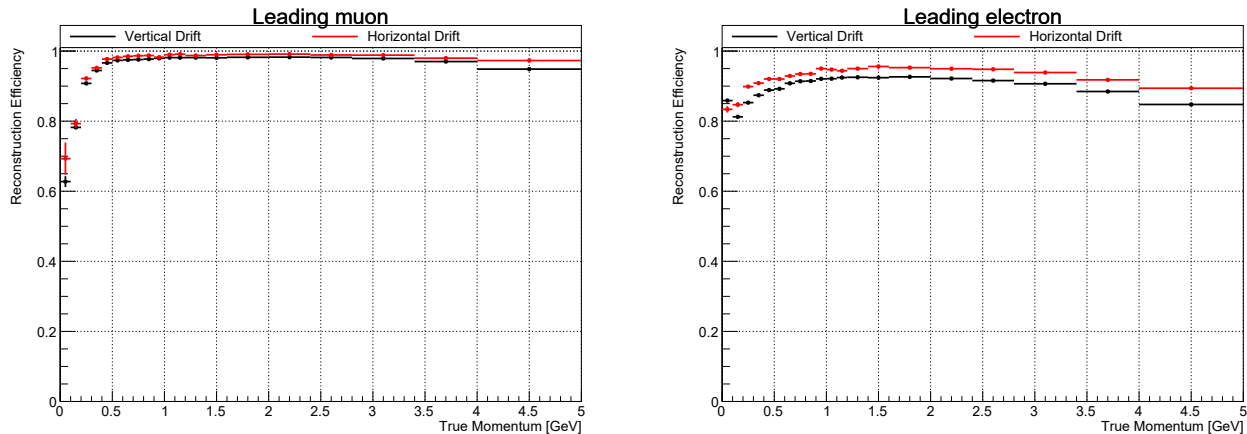


Figure 2.10: Pandora’s reconstruction efficiencies of the leading lepton from CC neutrino interactions in FD1-HD and FD2-VD. The efficiencies are shown as a function of the leading lepton’s true momentum. Left:  $\mu^-$ . Right:  $e^-$ .

## 2.5.2 Neutrino Event Selection with the Convolutional Visual Network

The CVN [44] is the primary means of flavor-tagging a neutrino interaction in the DUNE far detector, and was used extensively in the DUNE oscillation sensitivity analysis with FD1-HD [1]. The CVN is a deep learning-based image recognition technique that can exploit the fine-grained detail observed in a LArTPC to maximize selection power. The technical configuration of the CVN has been described extensively elsewhere [1, 44]. The CVN was retrained for FD2-VD using approximately three million simulated neutrino interactions. The simulated neutrinos were processed through the FD2-VD’s reconstruction chain up to the hit reconstruction, where the reconstructed hits provide the primary input to the CVN.

The primary output of the CVN is a set of scores that describe how likely the observed neutrino interaction is to be  $\nu_\mu$  CC,  $\nu_e$  CC,  $\nu_\tau$  CC, or NC. The CVN score distributions for FD2-VD are shown in Figure 2.12, displaying a good degree of separation between signal and background. For comparative purposes, the equivalent scores for FD1-HD are shown in Figure 2.13.

The trained CVN was used to develop a neutrino selection, where a tuned cut was applied to the CVN score. The cut was separately tuned to maximize the product of selection efficiency and purity for  $\nu_\mu$  CC and  $\nu_e$  CC interactions. This procedure was followed in both the FD1-HD and FD2-VD detector simulations. Figure 2.14 shows the resulting selection efficiency as a function of true neutrino energy for the  $\nu_\mu$  CC and  $\nu_e$  CC selections while Table 2.5 shows the overall selection efficiencies and purities. The overall selection performance is similar between the two detector designs, with the most notable difference being a small divergence in the  $\nu_e$  CC purity.

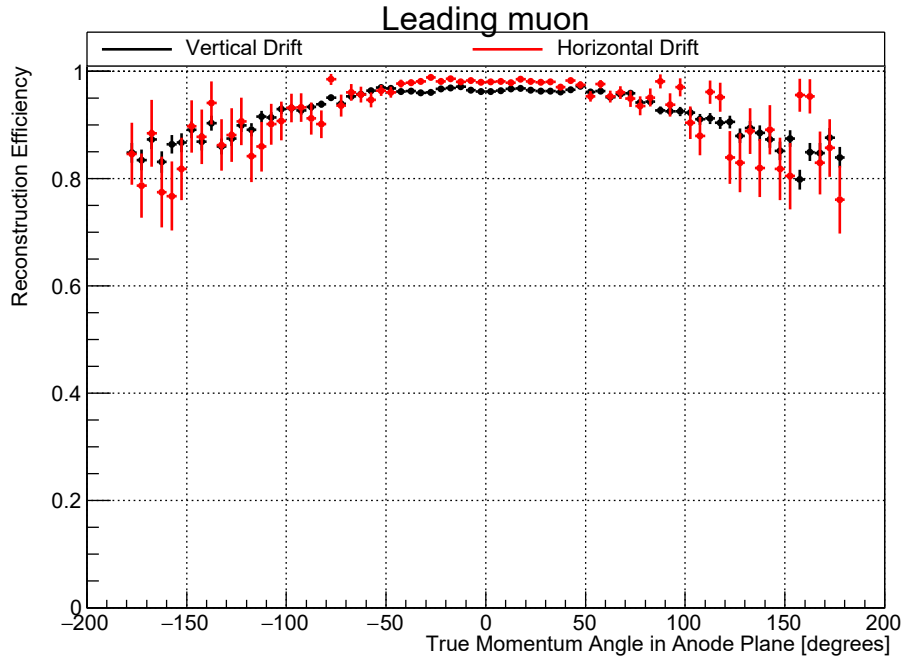


Figure 2.11: Pandora's reconstruction efficiencies of the leading  $\mu^-$  from CC neutrino interactions in FD1-HD and FD2-VD. The efficiencies are shown as a function of the muon's angle in the plane of the anode.

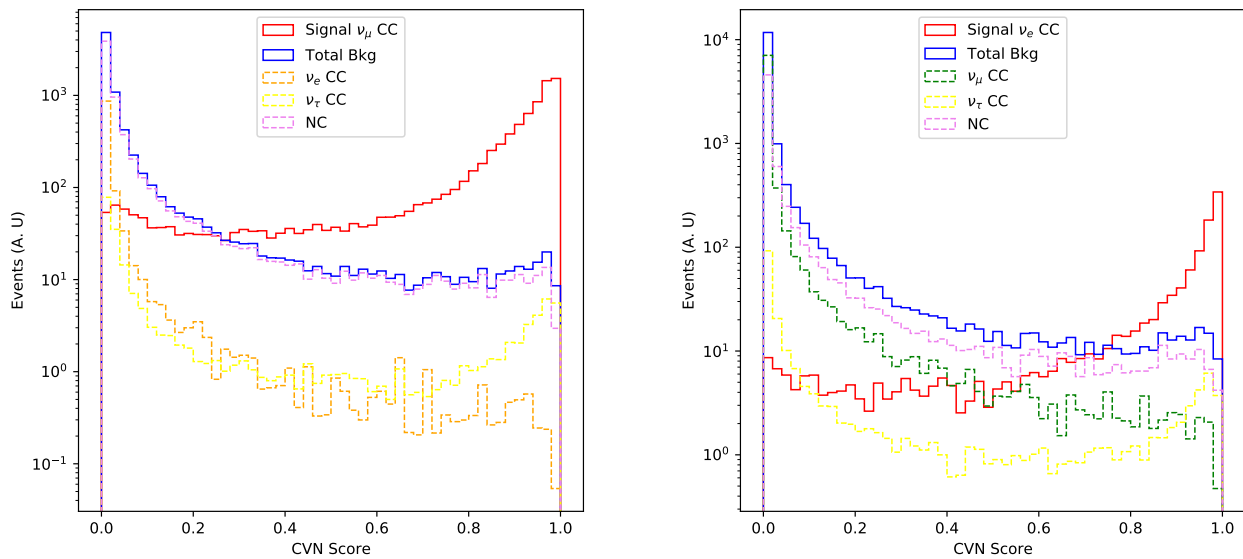


Figure 2.12: CVN score distributions for their respective signal and backgrounds in FHC beam mode for FD2-VD. Left:  $\nu_\mu$  CC score. Right:  $\nu_e$  CC score.

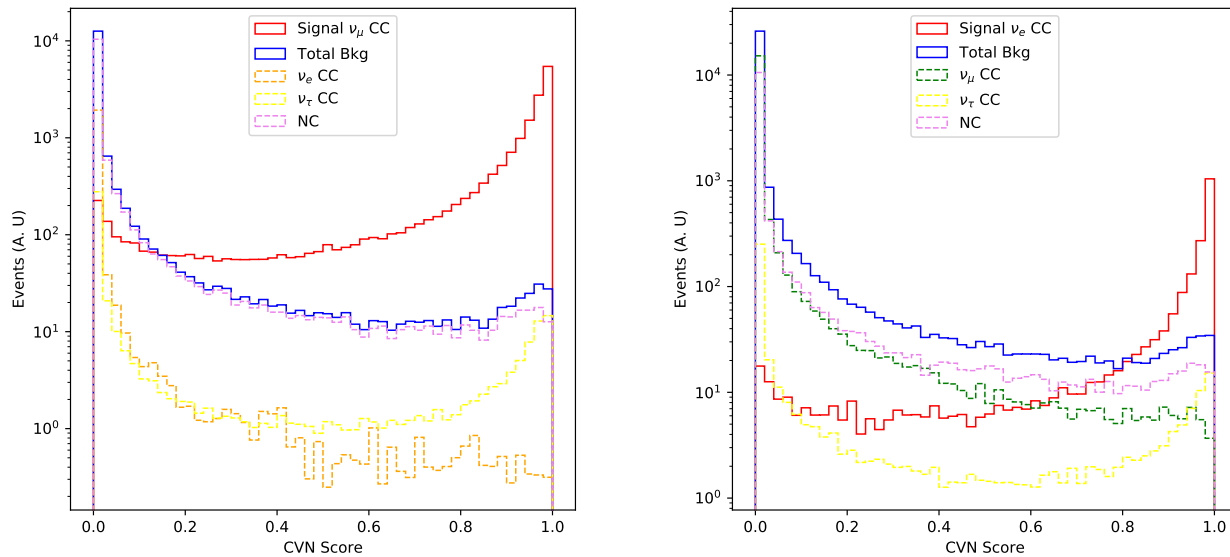


Figure 2.13: CVN score distributions for their respective signal and backgrounds in FHC beam mode for FD1-HD. Left:  $\nu_\mu$  CC score. Right:  $\nu_e$  CC score.

The FD2-VD instance of the CVN is much more recent and is still under active development and tuning, and it is expected that these small differences will converge over time.

The cut on the CVN score can also be tuned to achieve equal purities between the FD1-HD and FD2-VD versions, where the FD1-HD cut is optimized and the FD2-VD cut is forced to meet the same selection purity. With the current version of the FD2-VD CVN tuning, this gives an 8% decrease in average  $\nu_e$  CC efficiency. As the purities are identical, all of the background uncertainties would be the same in a LBL sensitivity analysis. This selection would therefore result in the same sensitivities, but with 8% additional required exposure. This does not account for the increased fiducial volume size of FD2-VD, which would reduce the required exposure. Given the relative immaturity of the FD2-VD reconstruction, this estimated increase in exposure time should be taken as a worst-case scenario.

### 2.5.3 Neutrino Energy Reconstruction

The neutrino energy reconstruction is based on the algorithm developed for FD1-HD [1]. The method uses the 3D reconstruction provided by Pandora to identify, and separate out, the leading lepton and hadronic system. The lepton is always taken to be the longest primary reconstructed

	$\nu_e$ CC efficiency	$\nu_e$ CC purity	$\nu_\mu$ CC efficiency	$\nu_\mu$ CC purity
FD2-VD	84%	83%	94%	93%
FD1-HD	86%	88%	97%	94%

Table 2.5: The overall neutrino selection efficiencies and purities using the CVN. The results for the FD2-VD and FD1-HD detectors are shown.



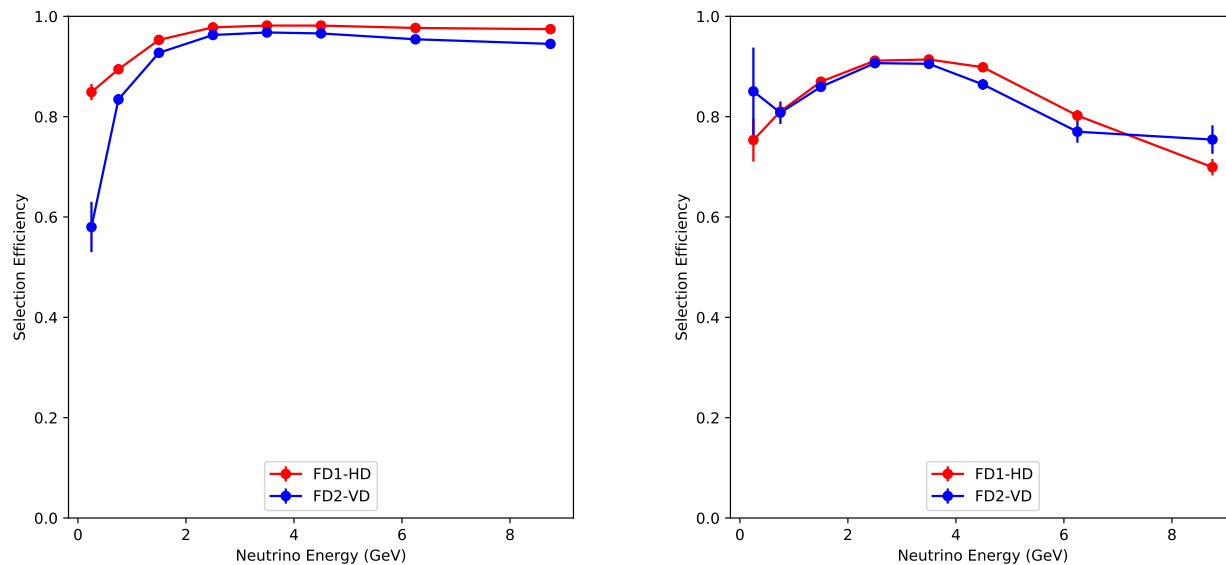


Figure 2.14: The neutrino selection efficiencies in FHC beam mode using the CVN. Left:  $\nu_\mu$ . Right:  $\nu_e$ .

track or the highest-charge primary reconstructed shower, depending on whether the neutrino interaction is being reconstructed under a  $\nu_\mu$  or  $\nu_e$  hypothesis. All of the reconstructed hits not associated with the reconstructed lepton are assigned to the hadronic system. The neutrino energy is then calculated as

$$E_\nu = E_{\text{lepton}}^{\text{cor}} + E_{\text{hadron}}^{\text{cor}}, \quad (2.1)$$

where  $E_{\text{lepton}}^{\text{cor}}$  and  $E_{\text{hadron}}^{\text{cor}}$  are the reconstructed energies of the leptonic and hadronic systems respectively. The muon energy is estimated by range or multiple Coulomb scattering, depending on whether the muon is fully contained in the detector. Both the electron and hadron energies are estimated using reconstructed hit-based calorimetry.  $E_{\text{lepton}}^{\text{cor}}$  and  $E_{\text{hadron}}^{\text{cor}}$  are independently corrected using a simulation-based calibration curve to minimize the energy reconstruction bias; this calibration curve was retuned for the FD2-VD detector.

The fractional energy residuals for the three event categories are shown in Figure 2.15, and the overall energy resolutions (the width of the Gaussian fits to the fraction energy residuals) are summarized in Table 2.6. The full reconstructed neutrino energy spectrum is used in all oscillation studies; the Gaussian fit results given are merely a convenient way to quantify the observed resolution. Reconstructed energy performance is nearly identical between FD1-HD and FD2-VD.

FD2-VD will have a targeted calibration program that is currently under development, and will be very similar to that for the FD1-HD. It is expected that detector uncertainties that are relevant for LBL oscillation sensitivities, such as energy scales and particle responses, will be at the same level in both detector modules. A dedicated hadron and electron test beam run will occur for both FD1-

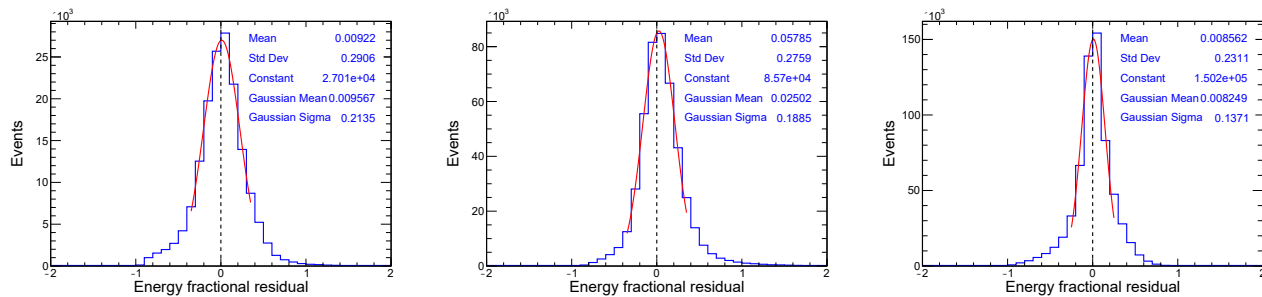


Figure 2.15: The reconstructed neutrino energy residuals for the different reconstruction hypotheses with overlaid Gaussian fits to the center region of the distributions. Left:  $\nu_\mu$  hypothesis with contained muon. Middle:  $\nu_\mu$  hypothesis with exiting muon. Right:  $\nu_e$  hypothesis.

Event hypothesis	Vertical Drift	Horizontal Drift
$\nu_\mu$ CC with contained $\mu$ track	21%	18%
$\nu_\mu$ CC with exiting $\mu$ track	19%	20%
$\nu_e$ CC	14%	13%

Table 2.6: The reconstructed neutrino energy resolutions for the three event hypotheses. The energy resolutions for both FD2-VD and FD1-HD are shown.

HD and FD2-VD, so any hadronic response uncertainties that are constrained by test beam data will be very similar. To the extent that calibration uncertainties are uncorrelated between FD1-HD and FD2-VD, it may be possible to decrease the overall systematic uncertainty because specific effects will impact only the portion of the overall FD sample from a given module. Uncertainties on particle propagation in LAr, for example, will be fully correlated between FD1-HD and FD2-VD. Any increase in sensitivity due to uncorrelated detector uncertainties is expected to be very small.

## 2.5.4 PDS Channel Saturation for High Energy Beam Events

One of the PDS requirements is the ability to retrieve information contained in the photon signal even for extreme events, e.g., when higher energy interactions ( $\mathcal{O}(10 \text{ GeV})$ ) occur near the planes instrumented with X-ARAPUCA devices. Estimates were performed for the fraction of PD electronic channels that can saturate using the LArSoft MC simulation with neutrino beam events. These are meant to ensure the 14-bit PDS readout design satisfies the needs of the experiment and to determine whether signal saturation effects are a concern for the FD2-VD module in some particular cases.

Two data sets of  $10^5$  events each of  $\nu_\mu$  and  $\nu_e$  beam neutrinos were used. The optical waveforms were obtained for all PDS readout channels in the simulation taking into account all physical effects and parameters described in Section 2.3.1. The number of channels in which the signal saturates (amplitude  $> 2^{14}$  ADC) and the total number of valid waveforms in each event were calculated. A waveform is considered valid if its amplitude exceeds a threshold of 1.5 PE. Figure 2.16 (left) shows the distribution of the registered valid waveforms' peak amplitudes where the maximum value peak indicates the number of times a channel signal was saturated over all analyzed data events.

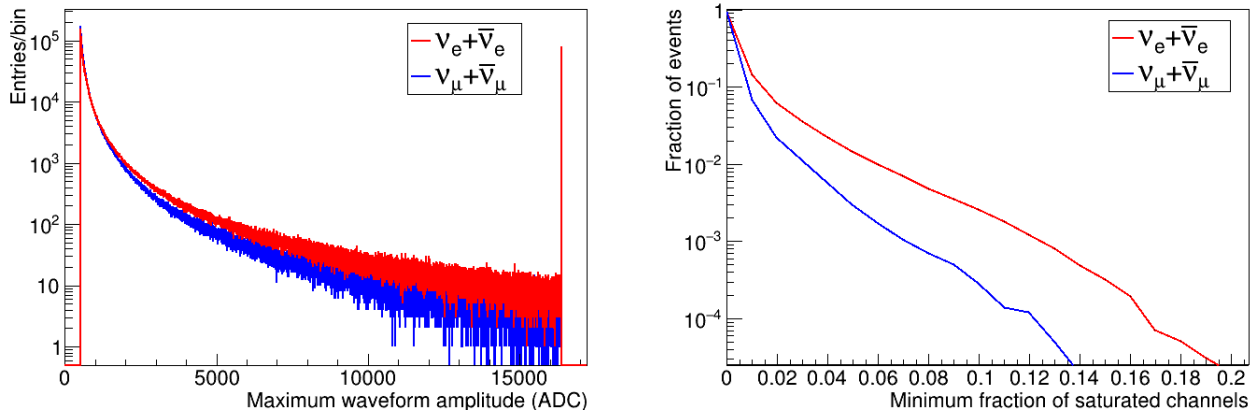


Figure 2.16: Left: Distribution of the channels peak amplitude. Maximum values corresponds to the maximum amplitude of  $2^{14}$  ADC. Right: Fraction of events as function of the fraction of its valid channels per event that saturate above a certain minimum level required.

Figure 2.16 (right) shows the fraction of beam  $\nu_\mu$  and  $\nu_e$  events in which a fraction of the valid channels saturate above a certain minimum level. The obtained fractions of events are kept at levels that satisfy the PDS requirements.

The small fraction of saturated channels per event increases with the incoming neutrino energy, with a slightly higher probability for primary interaction positions closer to the cathode. The effect on the PDS energy reconstruction capability was evaluated by calculating the decrease in the hit area caused by saturation. For  $\nu_\mu$  ( $\nu_e$ ) events the average fraction reduction of the summed signal integrals was estimated to be  $\sim 2(3)\%$  per event and an average of 15(16)% for each saturated channel. These numbers indicate PDS energy calibration and reconstruction should not be significantly affected by saturation effects and that these rare situations representing extreme events do not compromise the requirement of up to 20% of saturated PD channels in a given beam event (Table 6.1). We note that the dynamic range simulated in our studies, up to approximately  $2^{14}/10 \simeq 1600$  photoelectrons (PEs), is lower than our 1–2000 PEs specification (see Chapter 6), so an even lower fraction of saturated events is expected.

## 2.5.5 Conclusions

Despite the relative infancy of the FD2-VD simulation and reconstruction, in addition to some known differences between the FD1-HD and FD2-VD software, the performance is similar between the two detector designs for GeV neutrino interactions relevant for LBL oscillation physics. The small differences in performance will be investigated and are expected to converge over time. The FD1-HD simulation and reconstruction will be updated and a new simulation campaign will be run as part of this effort.

The LBL oscillation sensitivities, including the sensitivity to observe CPV, depend on the selection efficiency, energy reconstruction, and detector uncertainties, all of which are very similar in both detector configurations. Hence, the oscillation sensitivities obtained in the FD1-HD TDR analysis [1] are also valid for a configuration where the FD contains both FD1-HD and FD2-VD modules.

An update to the LBL oscillation sensitivity estimates in DUNE is currently underway and expected to be available in 2024. The primary improvement, relative to the previous estimates, is a more realistic treatment of the ND, as its design is now at a stage where realistic simulations are possible. However, as part of this update, it is planned to also include full simulation and reconstruction samples of the FD2-VD module in addition to those of the FD1-HD. Given the analysis and results presented in this chapter, it is not expected that this will have any significant impact on the results.

# Chapter 3

## Charge Readout Planes

### 3.1 Introduction

Since the liquid argon time-projection chamber (LArTPC) technology was first proposed [45], intense R&D and novel ideas have fueled continuous evolution. Major developments in most of the LArTPC core components have led to substantial improvements in performance and stability. These include new photon detector (PD) technologies, improvements in the high voltage (HV) and cold electronics (CE) systems, resistive cathode designs, and modular s. Charge collection has changed very little, however, and multi-layer wire planes remain the standard anode technology.

Only in the last few years have new anode ideas been proposed and partially developed to replace the conventional wire planes. A modified version of the traditional LArTPC chamber has been under development since 2010 in a dual-phase (DP) configuration [46], in which the usual wire arrays are replaced by multiple large electron multiplier (LEM) planes, which are derived from Gas Electron Multiplier (GEM) detectors [47]. Leveraging the advancements in LEM technology, this dedicated R&D program has been developing an anode technology using perforated PCB-based charge readout (CRO) with projecting electrodes immersed in liquid argon (LAr) [48].

The vertical drift detector module (FD2-VD) anode design will implement PCB-based charge readout using stacked, perforated PCBs with etched electrode strips. The PCBs are attached to a composite frame to form charge-readout planes (CRPs); the frame provides mechanical support and maintains the required planarity. Figure 3.1 provides an overview of the structure and Table 3.1 lists its components and their quantities and sizes. As discussed in Chapter 1, the FD2-VD detector module is split vertically into two drift volumes, with CRPs at the top and bottom of the cryostat forming the anode planes, both of which are immersed in LAr, and a horizontal cathode plane placed midway between them. The CRPs in the top drift volume are collected into sets of “superstructures” that are suspended from the cryostat roof and the bottom CRPs are supported by posts positioned on the cryostat floor. The top drift volume electronics components are mounted on signal feedthrough flanges on the cryostat ceiling. The CRPs at the bottom have integrated CE attached to them.

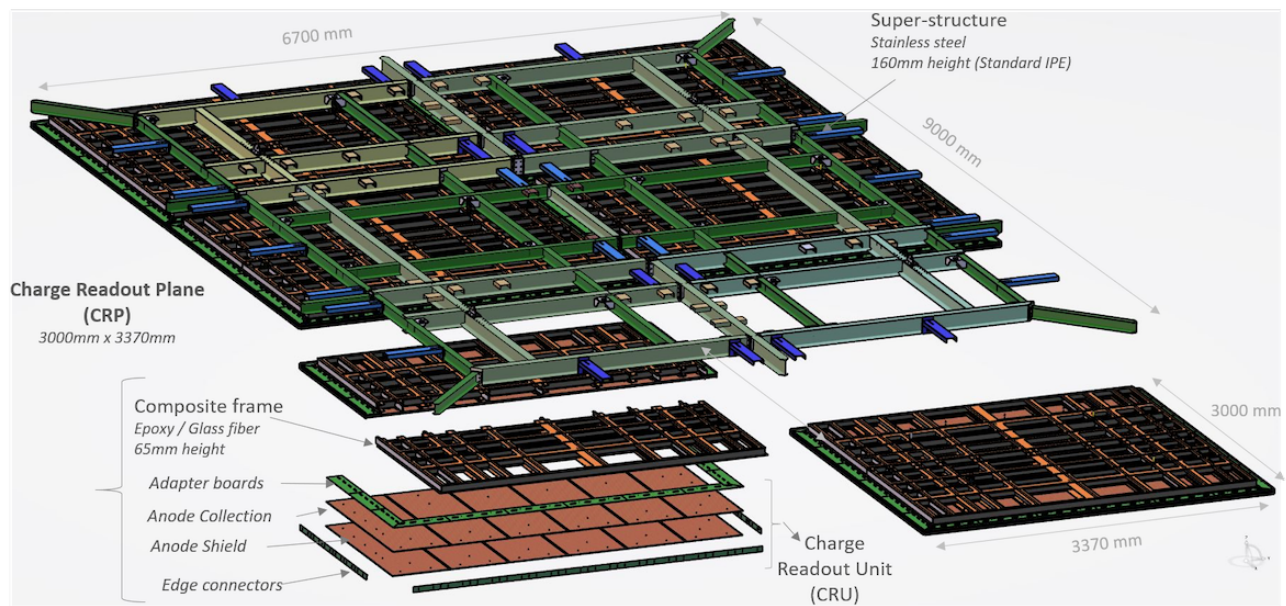


Figure 3.1: A top superstructure (green structure on top) that holds a set of six CRPs, and below it an exploded view of a CRP showing its components: the PCBs (brown), adapter boards (green) and edge connectors that together form a CRU, and composite frame (black and orange). Dimensions are given.

The anode plane design for the FD2-VD provides three-view charge readout and is constructed of two stacked, perforated PCBs with biased strip electrodes on one or both faces. The three sets of electrode strips are set at different angles relative to each other, as shown in Figure 3.2, to provide charge readout from different projections. A PCB-based anode is less expensive and less delicate than a wire-based anode plane and can be produced more rapidly using commercially available tools. It therefore offers attractive potential reductions in cost, schedule, and risk. The design of the CRPs incorporates the lessons learned from [15], intense R&D activities from 2019 to 2021, and ongoing prototyping activities. CRPs are modular structures for purposes of fabrication, assembly, and transportation; they are constructed from two half-size anode plane pieces, called CRUs, and a composite frame.

To protect against possible risk from cathode charge injection, the PCB view facing the drift volume is a shield plane with no readout. The back face of this PCB becomes the first induction plane, the front face of the second anode PCB is the second induction plane, and its back face (facing either the cryostat roof facing or the bottom membrane) is the collection plane.

Electronics adapter boards, an interface between the anode planes and readout electronics for strip biasing and charge readout, are attached to the two-PCB stack. Vertical interconnection between the anode planes and adapter boards are done via small PCBs called “edge cards.” Small connectors on the edge cards are in contact with the strips on the PCB end and with the electrical pads on the adapter boards at the other end. Anode PCBs, adapter boards, and edge cards are connected to a composite frame that serves as the mechanical support structure. Together, the perforated PCBs, adapter boards, and edge cards form a CRU, and two CRUs plus a composite frame form a CRP. Each FD2-VD anode plane is a grid of 80 (20 by 4) CRPs that spans the horizontal area of the detector.

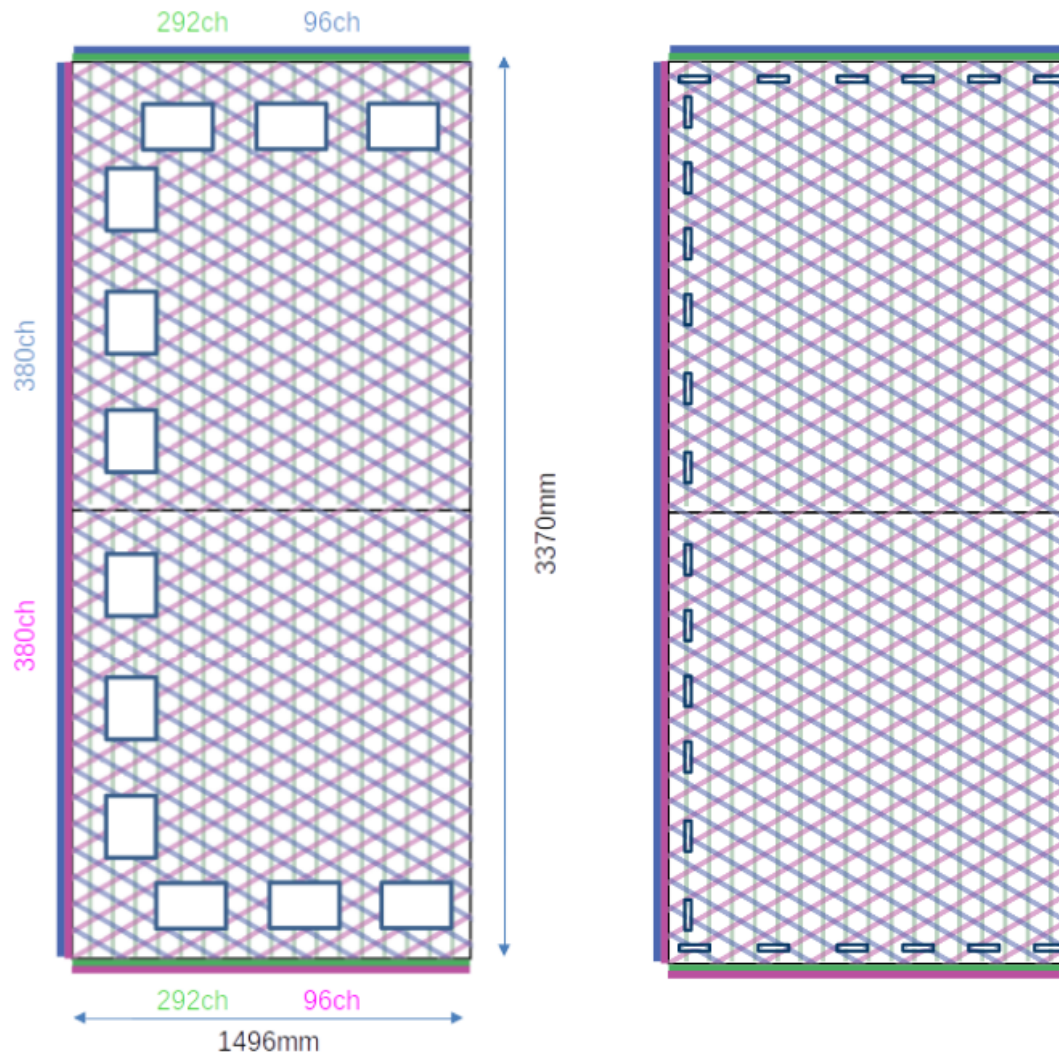


Figure 3.2: Illustration of the basic electrode strip configuration for a top (right) and bottom (left) CRUs. Each CRU is constructed from a one-view (induction-1, magenta) PCB panel, overlaid with a two-view (induction-2, blue and collection, green) PCB panel, and readout electronics adapter boards (along the edges) that host cable connectors for the top anode plane, or CE readout modules for the bottom. The lines at half-height indicate electrical discontinuity for the collection plane strips. Strip pitches and adapter boards are not drawn to scale.

Table 3.1: Reference three-view anode plane component list with quantities and sizes.

Component	Sub-components	Quantity	Size
PCB segment	(none)	12 per CRU (glued and stacked), 3840 total	in 6 different flavors and 3 sizes. See Section 3.3
PCB panel	PCB segment	2 per CRU (stacked), 640 total	$1.494 \times 3.366 \text{ m}^2$
View (also called "layer")	electrode strips on PCB	1 set of parallel strips per PCB panel side	See Table 3.3
Adapter board	4-layer PCB + bias capacitors and resistors	12 per CRU, 3840 total	in 7 different flavors and sizes for top and bottom
Edge cards	4-layer PCB + small connectors	24 per CRU, 7680 total	in 3 different flavors and sizes for top and bottom
CRU	2 PCB panels + 12 adapter boards + 24 edge cards	2 per CRP, 320 total	$1.496 \times 3.370 \text{ m}^2$
CRP	2 CRUs + composite frame	80 per anode plane, 160 total	$2.993 \times 3.370 \text{ m}^2$
Top superstructure	6 or 2 CRPs	16 (top anode plane only, twelve 6-CRP, four 2-CRP)	$9.0 \times 6.7 \text{ m}$ and $3.0 \times 6.7 \text{ m}$
Anode plane	80 CRPs	2	$60.0 \times 13.5 \text{ m}^2$



PCB-based readout in LAr has well defined induction and collection signals, and is well suited for a vertical drift, which enables a larger, unobstructed active volume with a longer drift distance than DUNE’s horizontal drift detector module (FD1-HD) offers. Bias voltages that direct electron trajectories to the holes enable uniform, fully localized and sharp signals both for collection and induction signals.

The PCB-based design is well suited to capturing the induction signal for tracks that have a large dip angle (i.e., are nearly parallel to the E field direction). Induction signals in LArTPCs are bipolar with positive and negative lobes, and the effect of signal cancellation between the lobes grows as the dip angle increases. The PCB anode design aims to enhance the asymmetry of the induction signal by pairing a short high lobe formed inside the holes with a long low lobe formed in an extended open low-field region. This asymmetry will reduce the cancellation effect, enhancing signals from tracks with large dip angles.

## 3.2 Specifications

The principal specifications for the CRPs concern the anode planarity, the transparency to liquid flow, and the geometrical structure configurations. Table 3.2 lists these and the other specifications developed for the CRP design to meet overall detector performance requirements.

Table 3.2: CRP anode plane specifications

Label	Description	Specification (Goal)	Rationale	Validation
FD-2	Active area	Maximize total active area.	Maximize area for data collection	ProtoDUNE
FD-6	Missing/unreadable channels	<1%, with a goal of <0.5%	Reconstruction efficiency	ProtoDUNE
FD-7	Drift field nonuniformity due to component alignment	< 1% throughout volume	Maintains anode, cathode, FC orientation and shape.	FD2-VD Module 0
FD2-31	CRP anode plane global flatness	< 20 mm	Maintains drift field uniformity of < 1% throughout each drift region	cold box test
FD2-32	CRP minimum permeability	> 15%	Allows efficient local heat dissipation and free LAr circulation	CFD simulation
FD2-33	Gaps between CRPs	5 mm for CRPs within superstructure; 10 mm between superstructures	Minimizes loss of FV and allows space for cabling	ProtoDUNE
FD2-34	CRP shield plane on cathode-facing side		Reduces impact on electronics from cathode discharge	cold box test and ProtoDUNE
FD2-35	CRP strip width and pitch	< 8.5 mm (ind.); < 5.5 mm (coll.); gaps 0.5 mm	S/N consistent with 100% hit reconstruction efficiency for MIPs. Spacing provides 1.5 cm vertex resolution in $y$ - $z$ plane.	ProtoDUNE and bench tests

FD2-36	Vertical gap between the PCBs	>8 mm	Allows >5 $\mu$ s drift time between the two PCBs for better separation of the signal and ensures a safe running environment at voltages lower than the component ratings.	Prototyping and bench tests
FD2-37	Anode plane bias voltages	<2 kV	Beyond this value the size and cost of capacitors shoot up and choices plummet.	Prototyping and bench tests
FD2-38	Minimum wall thickness between holes	0.5 mm	This is for mechanical properties of the perforated PCB; given the full electron transparency, the hole size does not have any effect on charge collection.	Prototyping and bench tests

Regarding FD-7, a maximum overall deformation on an individual CRP of 10 mm allows the E field amplitude to remain within 1% of the nominal value, and limits the drift line deflection to 3 mm.

In FD2-33 the horizontal gaps of 5 mm and 10 mm as listed refer to measurements at warm. These gaps allow for positioning the CRPs and accommodating the cables that support the cathode structure. Due to the different shrinkage properties of the frames and PCBs when cooled to LAr temperature, these gaps become about 4 mm and 20 mm at cold, respectively.

Regarding FD-35, vertical position tolerance of < 4 mm between two adjacent CRPs keeps the drift line distortion around the CRP borders below 6 mm.

### 3.3 Anode Plane Design

As discussed in Section 3.1, the anode plane design for FD2-VD features three layers of readout channels (two induction views and a collection view) plus a shield layer, and is constructed by stacking two double-sided anode PCBs. The configuration is illustrated in Figure 3.2. The readout strips on the three views are all at different angles relative to each other. The shield layer, which faces the cathode, provides additional safety for the readout electronics; when connected to a sufficiently large capacitor bank ( $\mathcal{O}(\mu F)$ ), it could block up to 95% of the capacitive coupling between the cathode and the first induction plane. This additional layer of electrode requires an increase in overall bias voltage differential across the entire anode stack. The back side of the cathode-facing PCB is the first induction plane (induction-1), with strips running diagonally at 30°. The front side of the second PCB is the second induction plane (induction-2), with induction strips at -30°. Its back side is the collection plane, with strips running perpendicular to the beam (90°) to offer the best charge measurement for the beam events.

Dimensional details of the PCB layout and schematics of a cross-section of the anode PCB stack are listed in Table 3.3 and illustrated in Figure 3.3. The perforation pattern on both PCBs is arranged such that the narrow gaps between two strips always bisect a row of holes. The hole

pattern on the cathode-facing PCB aligns with the pattern on the second PCB to improve electron transparency and liquid flow. The strip pitch is 5.1 mm for the collection view and 7.65 mm for the induction views. The gap between strips on the three views is set to 0.5 mm. Strip lengths are 1.68 for collection, and up to 1.72 m for the induction views. The numbers of readout channels are 476, 476 and 584 per charge-readout unit (CRU) for induction-1, induction-2 and collection, respectively, totaling 3072 channels on a CRP. The detailed design drawings for the perforated PCBs can be found at [49].

Table 3.3: Key parameters for anode design

Parameter	Three-view configuration		
	Induction 1	Induction 2	Collection
Strip length [m]	up to 1.74	up to 1.74	1.68
Strip pitch [mm]	7.65	7.65	5.1
Strip gap [mm]	0.5	0.5	0.5
Unit capacitance [pF/m]	103	103	81
Total capacitance [pF]	up to 177	up to 177	135
Number of strips per CRU	476	476	584
Number of readout channels per CRP	3072		
Strip angle w.r.t. beam	30°	-30°	90°
Bias voltage [V] for a shield plane bias at -1500 V	-500	0	1000
Hole diameter [mm]	2.4	2.4	2.4
Inter-PCB gap within CRP (at room temp.) [cm]	1		

Given the smaller separation between the strips on the PCB and higher dielectric constant of the FR-4, the anode PCB has higher capacitance per unit length relative to the wire-based charge readout. Electrostatic finite element analysis (FEA) calculations predict a capacitance per unit length of about  $\sim 100$  pF/m for the strips immersed in LAr, versus 20 pF/m for the FD1-HD anode plane assembly (APA) wires. The reference  $1.496 \times 3.370$  m<sup>2</sup> CRU segmentation keeps the detector capacitance and, as a consequence, its contribution to the electronic noise, similar to that of the APAs.

The CRP and the bias voltages, illustrated in Figure 3.3, are designed to first focus the drifting electrons into the cathode-facing PCB’s perforations, then defocus them as they travel toward the second PCB, and refocus them through its perforations, as shown in Figure 3.4. The shapes of the signals from the induction and collection planes are well adapted to the shaping and sampling frequency of the readout electronics. As mentioned in Section 3.1, the asymmetric bipolar signals on the induction planes are expected to enhance measurement of tracks having a large dip angle relative to the readout plane.

With the chosen perforation pattern and thickness of the s, and external fields of  $\sim 500$  V/cm, the voltage differential required for complete charge extraction through the holes is estimated to be about 1 kV. The minimum transfer field between the two anode PCBs should be equal to the drift

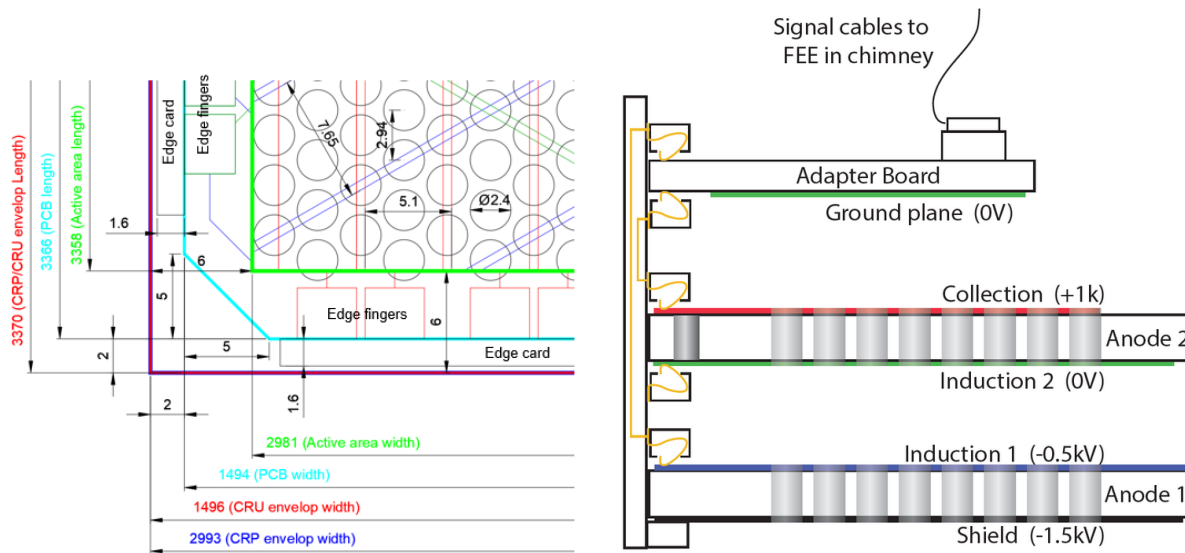


Figure 3.3: Left: details of the hole and strip pattern on the anode PCBs. The pitches and gaps between electrodes are given; the electrode widths are 7.65 mm (induction-1, blue), 7.65 mm (induction-2, green), and 5.1 mm (collection, red). Right: Illustration of the anode layers, adapter board and edge card stack. Bias voltages for each plane are shown.

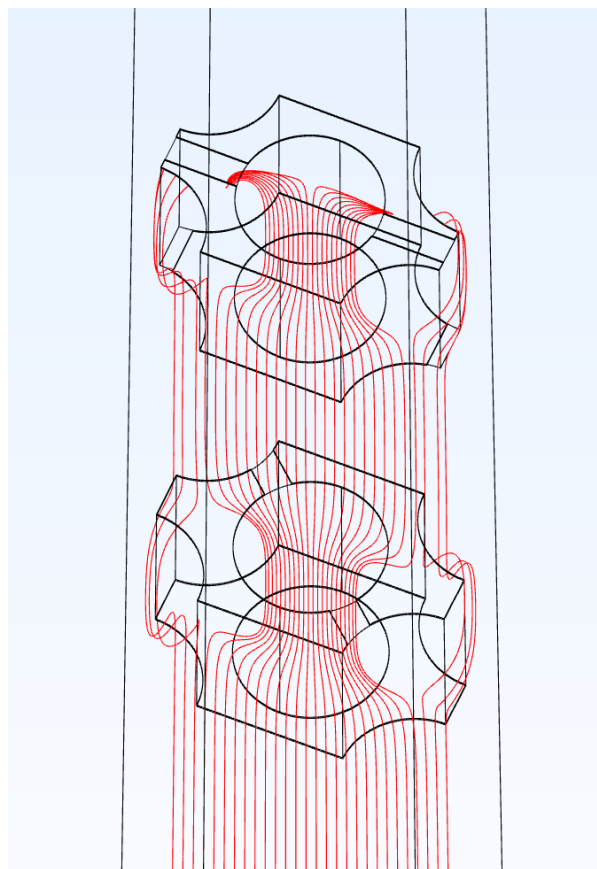


Figure 3.4: Field lines in the two-PCB design of the perforated anode plane, illustrating the path of ionization electrons from a track segment. The study used 3.2 mm PCB thickness, 2.4 mm hole size and 10 mm gap between the PCB panels.

field (450 V/cm). The separation between the stacked PCB panels in a CRU is determined by the stack height of the connectors used between them. Both the separation between the PCB panels and the gap between the inner PCB panel and the adapter board is 10 mm. Since the distance between the two PCB panels impacts the transfer field, which in turn affects the electron transfer, the voltage differential between the two induction planes is set accordingly.

Figure 3.2 shows the strip layout for both the top and bottom CRUs. Each PCB panel is constructed by joining six PCB segments (12 segments total for a CRU, 24 for a CRP). The segments are commercially produced, standard 2-layer, 3.2 mm thick perforated PCBs with dimensions given in the figure. Each PCB panel requires three different “flavors” of PCB segment, with the copper traces running at the correct angles. As shown in Figure 3.5, the middle four segments (segments 2-5) are identical, but segment 1 and segment 6 are different. Each segment has “half-lap” joint surfaces (one for segments 1 and 6, two for segments 2-5), where a half-thickness of the PCB is removed for 2-cm width along its long edge. The half-lap portions of the PCB segments are epoxied together to form a PCB panel.

Once the PCB segments are mechanically bonded to form a PCB panel, electrodes on the induction-1, induction-2, and collection views are bridged by screen-printing conductive ink patches onto them. Figure 3.6 is a concept drawing of the PCB “half-lap” edge-to-edge bonding method and the electrical bridging with conductive silver ink patches. The ink is applied at the surface over the joint using a special mask is then treated under  $\sim 120^\circ\text{C}$  for  $\sim 3$  hours for polymerization. Once polymerized, it allows electrical continuity between the patched surfaces.

The interface between the anode planes and readout electronics is implemented via adapter boards that link the readout pads along the edges of the CRUs to the readout cables (top CRPs) or to the CE modules (bottom CRPs). In addition to being an interface to the readout electronics, adapter boards also provide an interface for biasing the PCB views. Adapter boards are four-layer PCBs that host current-limiting resistors, HV AC coupling capacitors, connectors for readout electronics, noise filters on the bias line, and various bias and charge readout lines on different layers of the board. Each CRU has 12 boards installed around its periphery. Adapter boards for the top and bottom CRPs have different designs to accommodate the different readout systems. As shown in Figure 3.7, both top and bottom CRPs have 12 adapter boards, of seven distinct designs. Design models, assembly and manufacturing details, electrical specifications for all flavors of the top and bottom CRP adapter boards can be found respectively at [50, 51].

Vertical interconnection between the PCB views and adapter boards is done via edge cards. Figure 3.8 shows how edge cards are attached to the CRP. Edge cards are small four-layer PCB boards with connectors soldered on them. There are 24 edge cards plugged and secured on a CRU. Connectors on the edge cards are in physical contact with the pads on the anode strips and adapter boards. As well as biasing the readout strips, they bring the signal from strips to the readout electronics. Edge cards of identical designs are used for the top and bottom CRPs. There are three designs, each responsible for different sets of channels to be connected to the adapter boards. Details for each design and electrical schematics can be found at [52]. As shown in Figure 3.8, to secure the edge cards in place and ensure their electrical contact with pads, they are mechanically supported by 3D printed guides and brackets. The guides are glued onto specific locations on the boards to maintain a 1 cm gap between the PCB panels and adapter boards. Brackets bolt the cards to the adapter boards and to the shield plane.

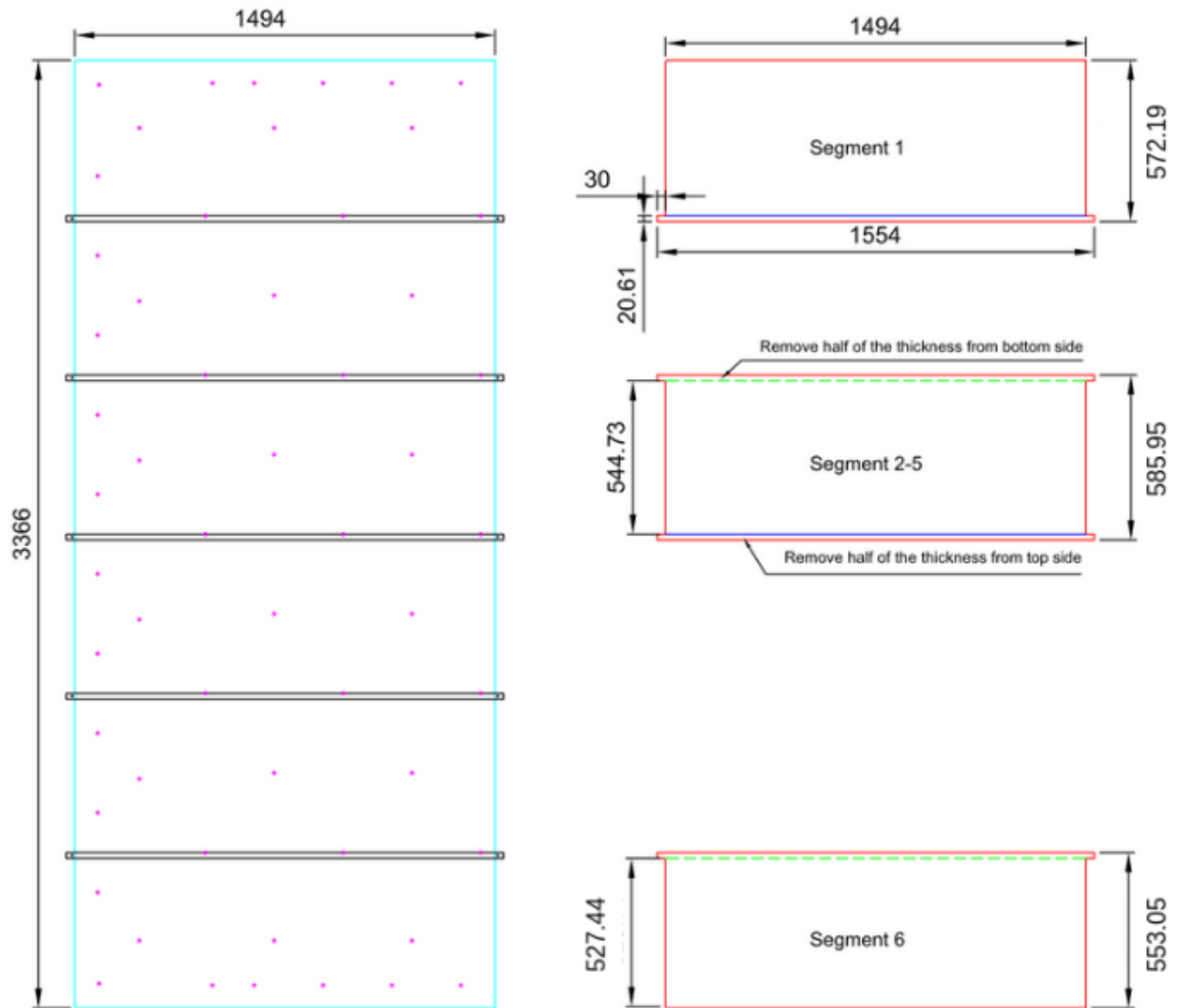


Figure 3.5: Each PCB panel is constructed by gluing six PCB segments together. There are three different flavors with different widths, half-lap joints and copper patterns: segment-1, four identical middle segments and segment-6.

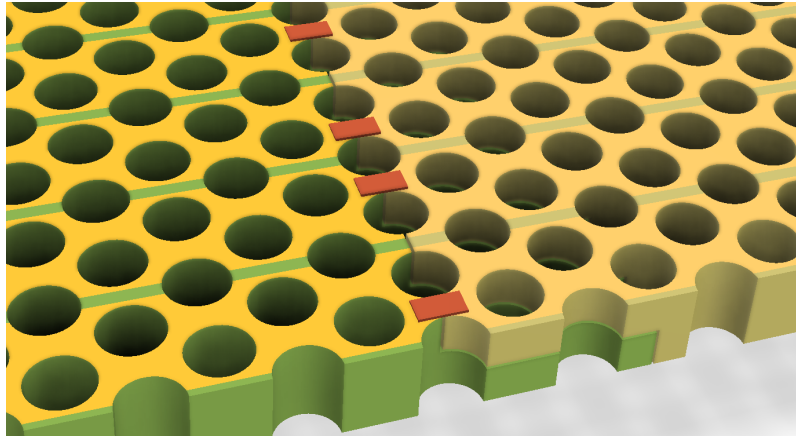


Figure 3.6: The PCB panel are constructed from smaller PCB segments using “half-lap” joint bonding technique (yellow and green overlap). Electrodes on one (induction-1) or both (induction-2 and collection) sides of a bonded PCB panel are bridged by screen printing conductive ink patches on the PCB (red).

### 3.4 CRP Mechanical Support Structure

A CRP is designed to have the thermomechanical stability and planarity to meet the E field uniformity requirement so as to ensure optimal ionization charge detection and collection.

Figure 3.9 illustrates a full CRP mechanical support, which is a composite frame made of two parts that fit together. Each part is designed to attach and support a complete CRU; the top and bottom CRPs use a similar composite structure and concept. A full CRP is built from two half composite structures holding a CRU each. The right-hand image shows a detail of the composite structure at the edge close to the two half-CRPs junction parts.

The CRP dimensions (Table 3.1) take into account the largest size PCB that the industrial manufacturers can provide and maximize the active detection area in the cryostat. The full FD2-VD module will implement 80 CRPs each on the top and bottom (160 total). The top CRPs are suspended from the cryostat roof and the bottom CRPs are supported by posts placed on the cryostat floor.

The rigid composite frame for a CRP is made of two layers (“skins”) made of perforated (water-jet-cut) glass-reinforced epoxy laminate material, each 2.4 mm thick, separated by imbricated (overlapping) U-shaped profiles made of Durostone® EPGM Epoxy (), of transverse dimensions 60 mm  $\times$  23 mm  $\times$  3 mm. The frame is composed of two identical sections (half-frames) of dimensions 3.3 m  $\times$  1.56 m for a bottom half-CRP and 3.2 m  $\times$  1.5 m for a top one. A CRU is connected via attachments to the composite half-frame for mechanical support (Figure 3.10). The advantage of having the structure split into two parts that are easily connectable, allows building, testing and transport of the smaller half-CRPs from the production sites to Sanford Underground Research Facility (SURF). Each full-size CRP is assembled from two half-CRPs only after transport into the cryostat.

At several positions in the top anode plane frames, G10 spacers are used in place of the FRP profiles,

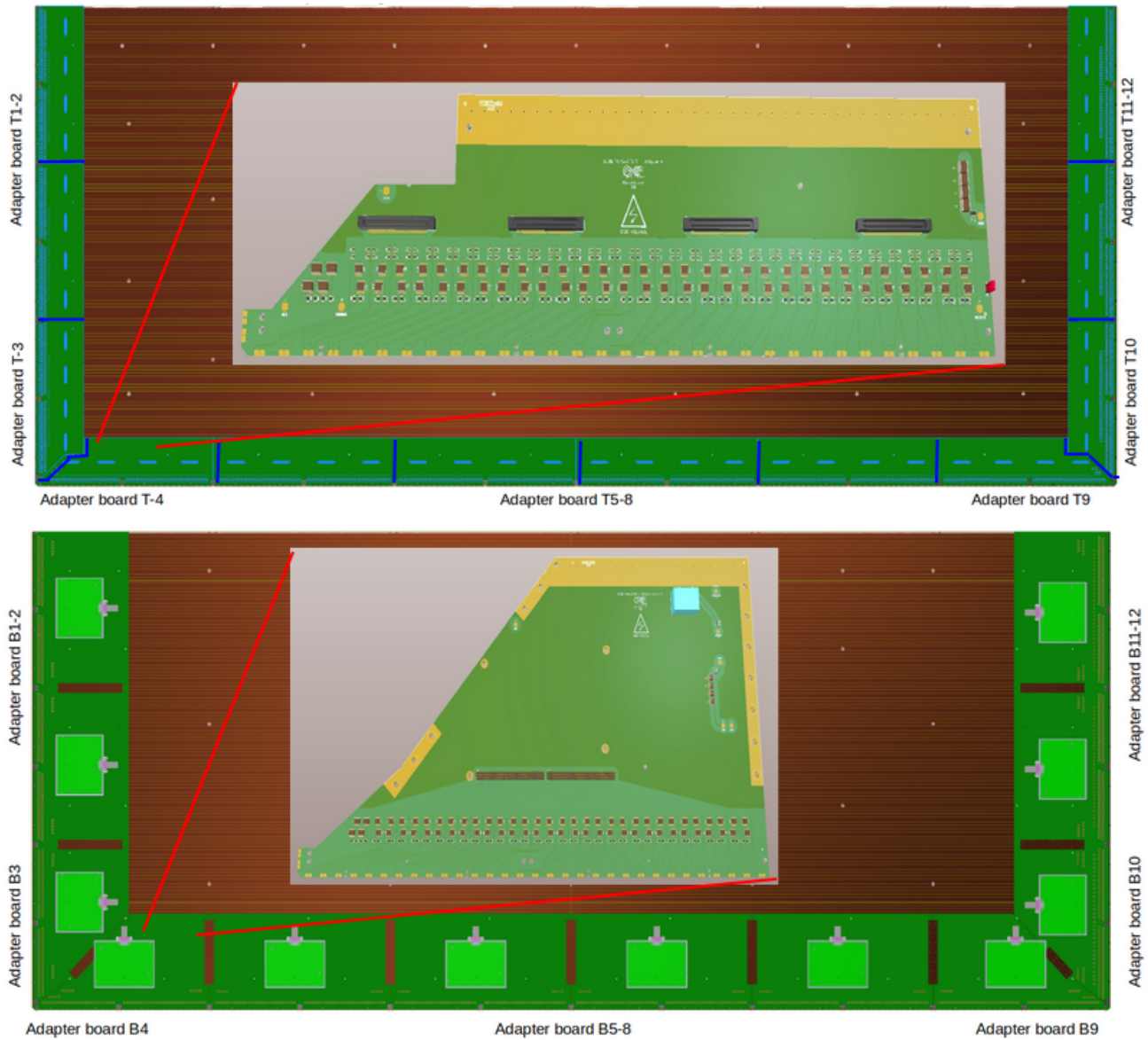


Figure 3.7: Top and bottom CRP adapter boards. The top image shows an inset with details.



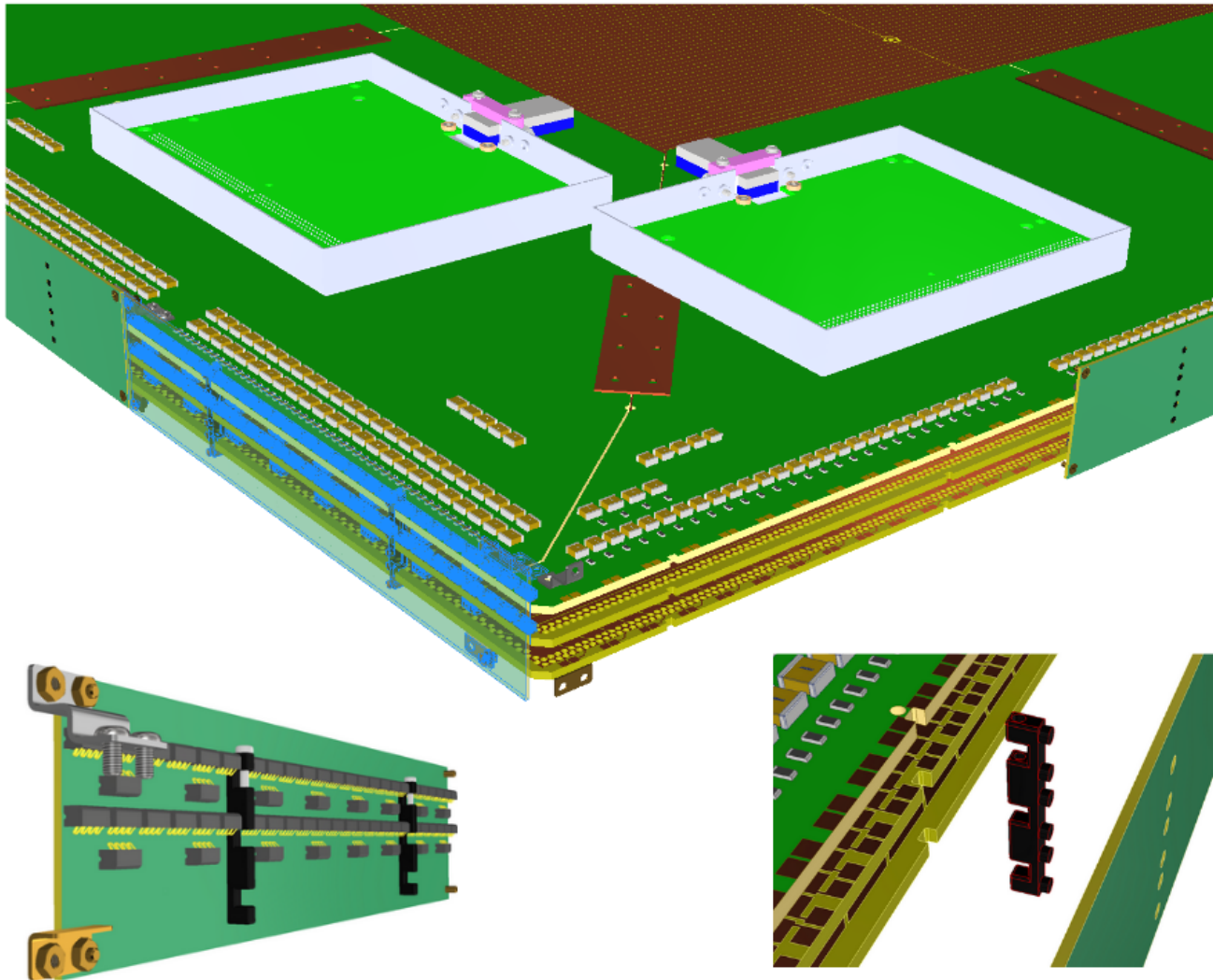


Figure 3.8: Top: Details of anode assembly and edge card installation. Two layers of PCB panel are visible with an adapter board on top of them. Edge cards are plugged into the side (blue/transparent edge card on the left shows the details of the connectors, also a green one on the right). FEMBs (bright green rectangles) and capacitors on the adapter boards are also visible. Bottom left: An edge card showing connectors with yellow pins. 3D printed guides (black) and brackets are also shown. Bottom right: 3D printed guide, its location for gluing onto the edge card, and dedicated notches on the adapter board and PCBs are shown.

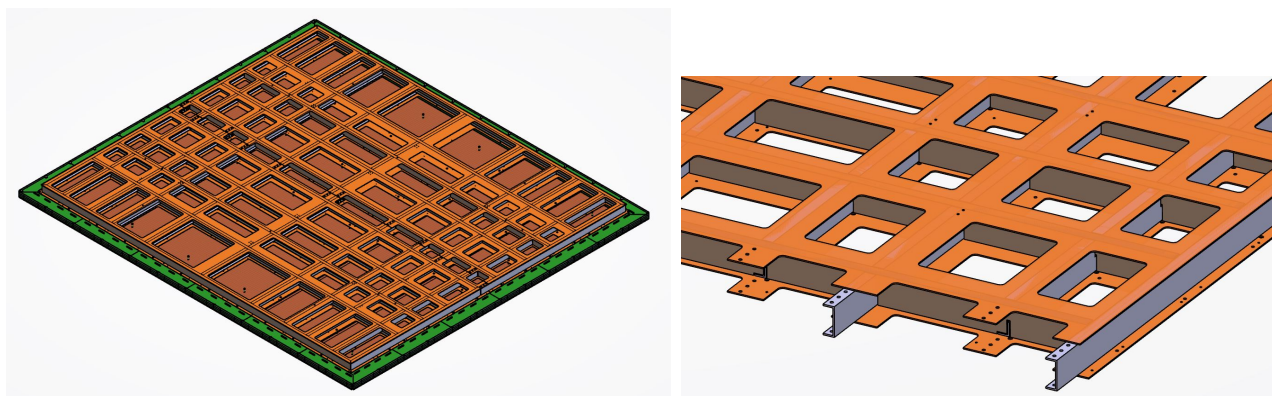


Figure 3.9: Left: Illustration of a complete top CRP with its composite frame (orange skins and gray profiles) coupled to the CRUs underneath. Right: Detail of the composite structure close to the CRP junction parts that are used to link the two CRUs.

reducing the weight. The anode PCBs and adapter boards are connected to the composite frame via a number of suspension points using machined pins and spacers made of PEEK material.

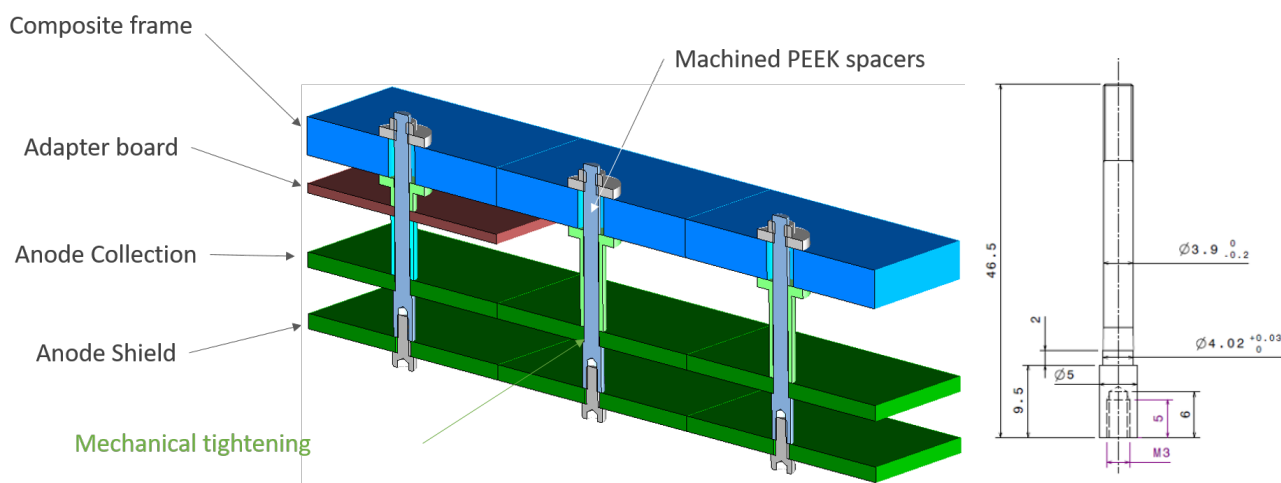


Figure 3.10: Details of the different spacers (light blue and light green) and attachment screws used to link the two anode layers and the adapter boards to the composite frame.

The two fiber glass-epoxy water-jet-cut skins are fabricated from prepreg with two  $0^\circ/90^\circ$  layers and two  $+45^\circ/-45^\circ$  layers for the glass-fiber orientation of the composite material. The skins are produced between two metallic plates before being cured in an oven under vacuum. Then they are water-jet cut to create the openings. Figure 3.11 (left) shows one skin of a top CRP after the complete process. The right-hand image shows the final composite frame.

The glass-reinforced epoxy laminate material for the skin of the frame was chosen to match the thermomechanical behavior of the CRUs to (1) avoid over-stress from differential thermal contraction, and (2) control the (horizontal) spacing between CRUs. The coefficients of thermal contraction of both the perforated anodes and the composite frame material have been measured to be the same within  $1 \times 10^{-6} \text{K}^{-1}$ . The holes in the structure serve to reduce the weight, allow for LAr flow across the anode planes, and allow access to the adapter boards and connectors in order to connect the readout electronics.

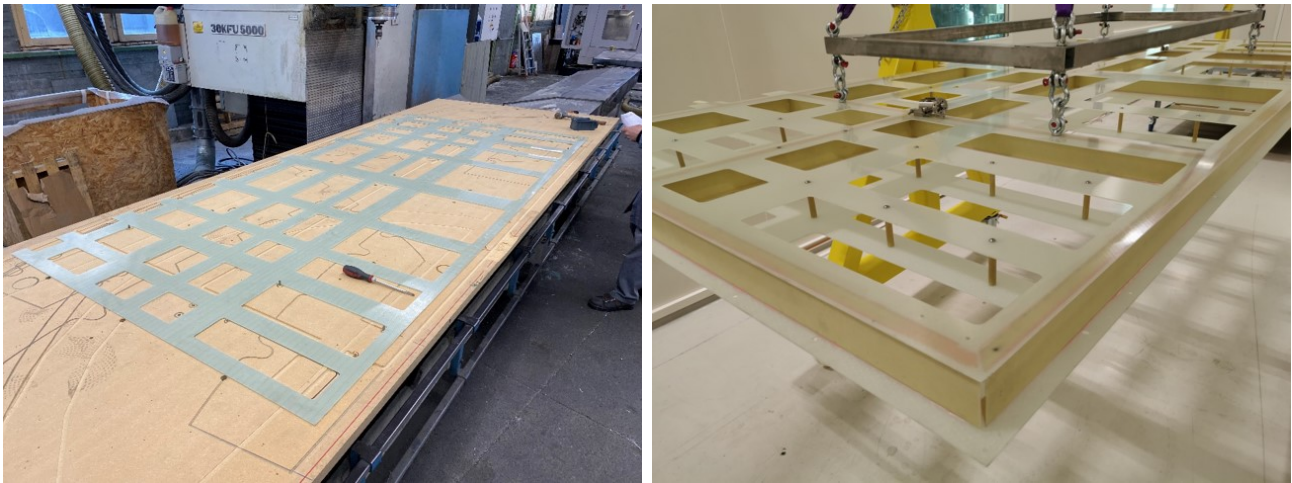


Figure 3.11: Left: One glass-epoxy skin after being machined and before being glued to FRP profiles. Right: the final composite frame after its construction, showing G10 rods used in place of profiles in several locations.

The height of the composite frame is optimized to retain the necessary stiffness while keeping its weight under 100 kg. The weight for a top CRP frame is well under that at 35 kg. A bottom frame must be stiffer to support the electronics boxes installed along the periphery; this is accomplished by using twice the number of profiles, which increases the weight to 90 kg.

Figure 3.12 shows a portion of a CRP composite frame with a detail of the U-beam profile interconnections at the crossing points. Figure 3.13 shows how the two half-frames are coupled. Twelve junctions are distributed along the long CRP side, made by imbrication of protruding U-shape profiles of one half under the fiber glass skins of the other half, and securing with six screws.

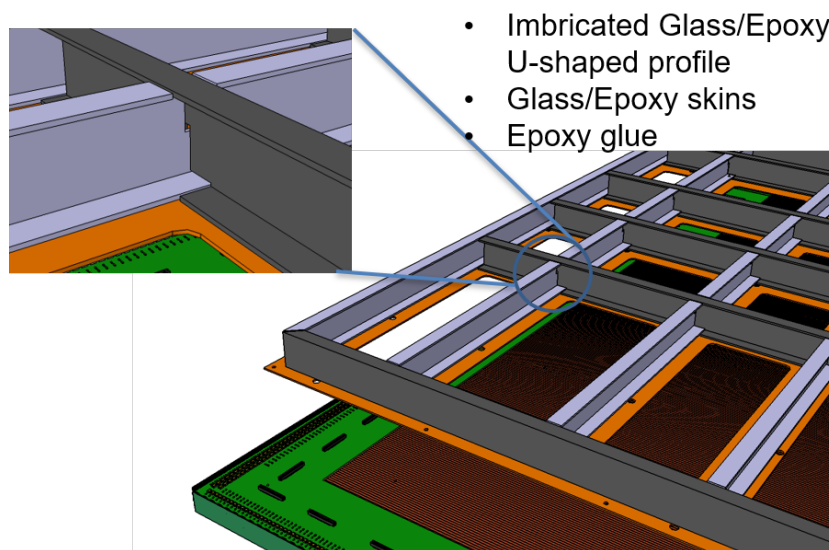


Figure 3.12: CAD rendering of CRP composite frame profiles with a fiber glass epoxy layer glued to one side.

FEA calculations of both kinds of composite frame have been performed. They included the full weight of the CRP, the adapter boards, the electronics, and the positions of the suspension for

the top or the feet for the bottom. The results showed that the maximum deformation expected under gravity (without buoyant forces) of the structure over the full CRP size at warm is less than 1.3 mm for the two composite geometries described above.

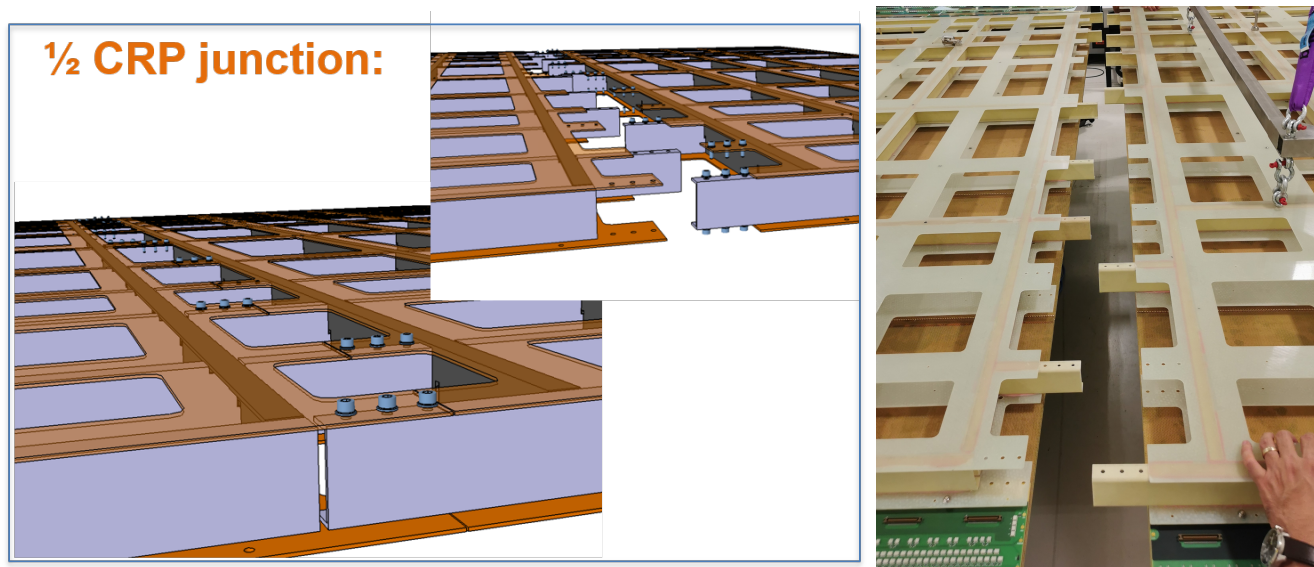


Figure 3.13: Left: CAD rendering of the CRP composite frame junction system to couple two CRUs; Right: photo of the first assembly of 2 half CRPs during the CRP-2 prototype production.

The baseline design specifies 61 suspension points per CRU between the CRU and the composite frame, based on FEA calculations, with a higher density along the borders to keep the relative deformation of the anode PCB layers under 1 mm over their length, while keeping the overall CRU planarity to about 2 mm. This requirement ensures that the connections between the anode strips and the adapter boards can be made easily and with sufficient precision.

The two stacked anode PCBs are vertically separated by 10 mm and the adapter boards are 11 mm from the nearest anode layer. The CRUs are attached to the composite frame at the 61 suspension points using machined pins and spacers made of PEEK material. Figure 3.10 shows the design for attaching the different PCB layers to the composite frame using the spacers and screws. The spacers will be inserted (cryo-fitted) into the supporting holes made in the PCB (4 mm diameter) with a force appropriate to prevent them from turning when the screws are tightened. This mechanical tightening allows a quick, accurate, and clean assembly with no gluing.

### 3.5 Top CRP Superstructures and Suspension

The CRPs that compose the top anode plane are suspended from the cryostat roof via a set of 16 “superstructures” (SST), 12 large (holding six CRPs) and four small (two CRPs), that serve to minimize the number of suspension penetrations required (Figure 3.14). The superstructures also support the cathode modules 6.5 m below, using the same suspension pattern. Each superstructure is suspended from four points through dedicated feedthroughs in the cryostat roof, represented by white dots in the figure. This will allow finely spaced vertical adjustments to compensate for possible deformations of the cryostat roof geometry after cooling and filling with LAr, and will maintain the planarity and horizontality of the entire anode plane within the required 20 mm.

The superstructure will be fully immersed in the LAr with a nominal position corresponding to a few cm below the liquid surface. The position of the top of the superstructure with respect to the liquid level will be monitored by capacitive level meters located at its corners, to an absolute position precision of the order of a mm.

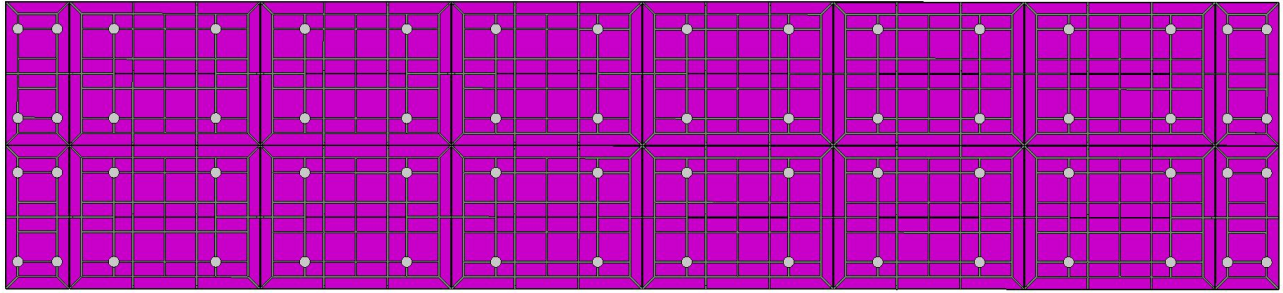


Figure 3.14: Layout of the 16 superstructures for the top CRPs. The four superstructures at the ends each hold two CRPs, the other twelve each hold six, for a total of 80. The white dots indicate the positions of the suspension feedthroughs.

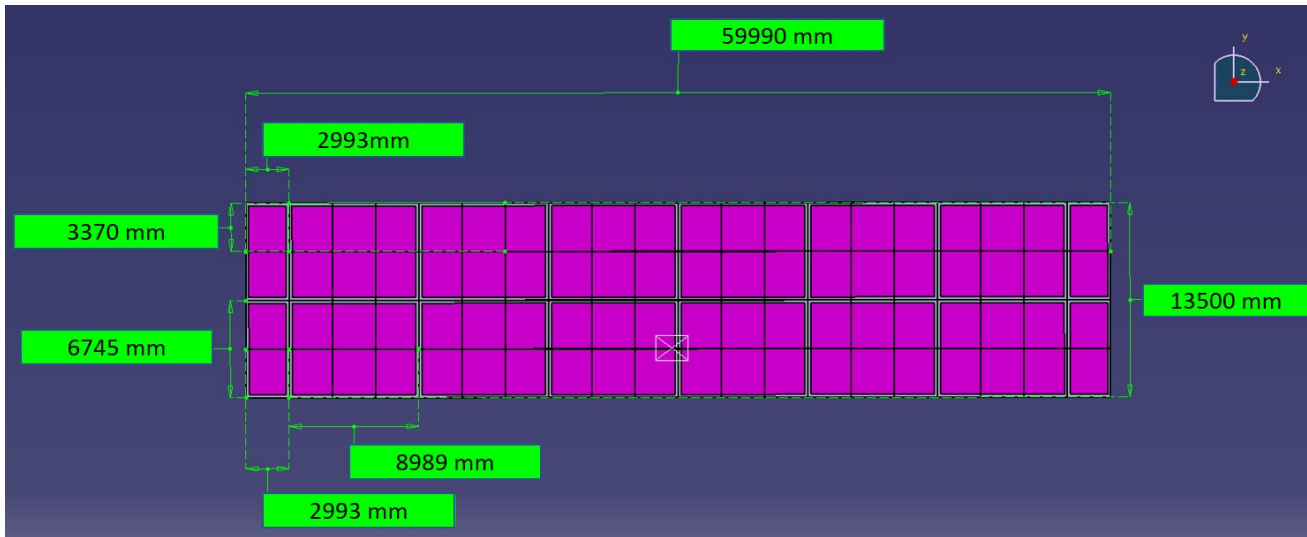


Figure 3.15: Dimensions and positions of the 16 superstructures and the CRPs for the top anode plane. The gap between CRPs within the same superstructure is 5 mm in both horizontal dimensions, and 10 mm between CRPs in adjacent superstructures.

The gap between CRPs within the same superstructure is 5 mm in both horizontal dimensions, and 10 mm between CRPs in adjacent superstructures. Given the CRP dimensions of  $3.370 \times 2.993$  m, the large superstructure dimensions are  $8.989 \times 6.745$  m and the small are  $2.993 \times 6.745$  m as illustrated in Figure 3.15. The slope of the vertical deformation of the roof is expected to be smaller near the cryostat ends than closer to the center, therefore the smaller, two-CRP superstructures in this location are designed to take into account the potential need to perform differential height adjustments along the first and last three meters along the beam direction. During the filling of the cryostat, parts of the roof will deform (downwards) up to 10 mm in the vertical direction, mostly near the center.

During operation the vertical position of the roof is expected to change up to  $\pm 1$  mm due to variations between the internal and external pressures (again, mostly near the center). The CRP super-

structures also support the cathode supermodules, which have similar dimensions (Section 5.4.1). For the large superstructure ( $9 \times 6.7$  m), the cathode modules are attached by means of twelve suspension cables, ten attached at the CRP superstructure extremities and two near the center. For the small superstructures ( $3 \times 6.7$  m), the cathode modules are attached by six cables, four at the extremities and two near the center, as shown in Figure 3.16. The cables are made of Dyneema fibers<sup>1</sup>, a high-strength composite material.

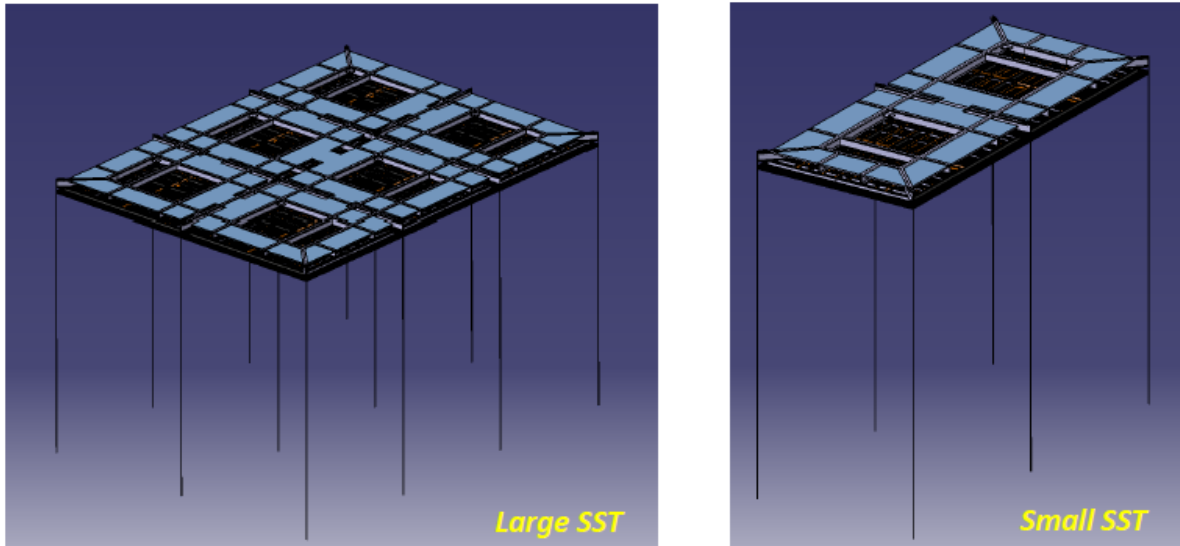


Figure 3.16: Model of the cable locations on the superstructures (SST) used to suspend the cathode supermodules, after attachment of the CRPs to the superstructure.

The baseline design for the CRP-supporting superstructure consists of a stainless steel frame composed of S6 $\times$ 12.5, S4 $\times$ 7.7 and C4 $\times$ 4.5 standard US profiles. The superstructure will also be used to support people to allow cabling of the top CRPs at the cold flanges below the chimneys (after the superstructures are raised close to the cryostat roof). Catwalks and safety systems are added to the stainless steel frame for this purpose. Figure 3.17 shows a superstructure frame designed for a group of six CRPs ( $9 \times 6.7$  m) where the catwalks (dark areas) and the beam profiles are visible.

Each superstructure is assembled underground at SURF from either six or two stainless steel modules. The modular design allows use of standard transport to the site and down the Ross shaft in the cage. Assembly, during which the modules are bolted together, will take place inside the cryostat. The four extensions at the superstructure corners are used to connect to the cathode suspension cables. Several configurations have been studied and FEA calculations have been performed with the appropriate constraints applied on the superstructure as it is suspended by four points. The calculations have yielded maximal deformations of the order of 5 mm given the full charge loading from the six CRPs (assuming 200 kg each), an attached cathode supermodule (600 kg), and the catwalks at warm. Figure 3.18 shows a closeup view of a large superstructure corner with CRPs attached, catwalk grids and the beam extensions to attach the cathode modules.

In the optimized superstructure design, the change in deformation when the suspension anchoring

<sup>1</sup>In LAr, the ropes are expected to stretch by  $\sim 14$  mm due to thermal expansion at low temperature (Dyneema has a negative of about  $-10^{-5}/K$ ). Dyneema®, [https://www.dsm.com/dyneema/en\\_GB/home.html](https://www.dsm.com/dyneema/en_GB/home.html)

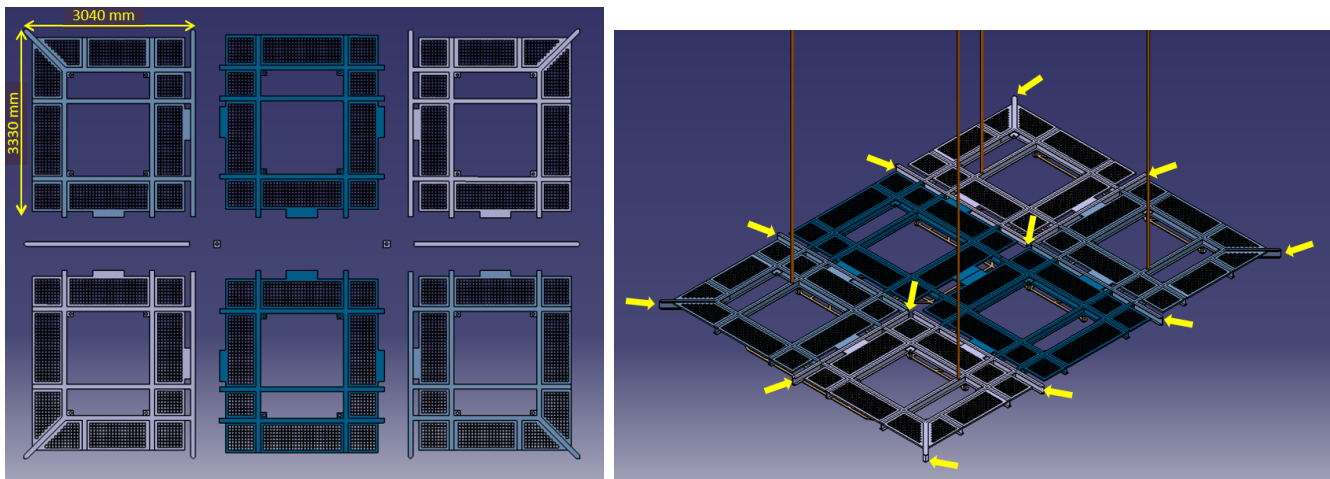


Figure 3.17: (Left) CRP superstructure modules (metallic frames) before assembly and (right) after assembly with the four cables used to suspend it. The six CRPs to which it will attach are not shown. The yellow arrows indicate the 12 points of attachment of the cathode suspension ropes.

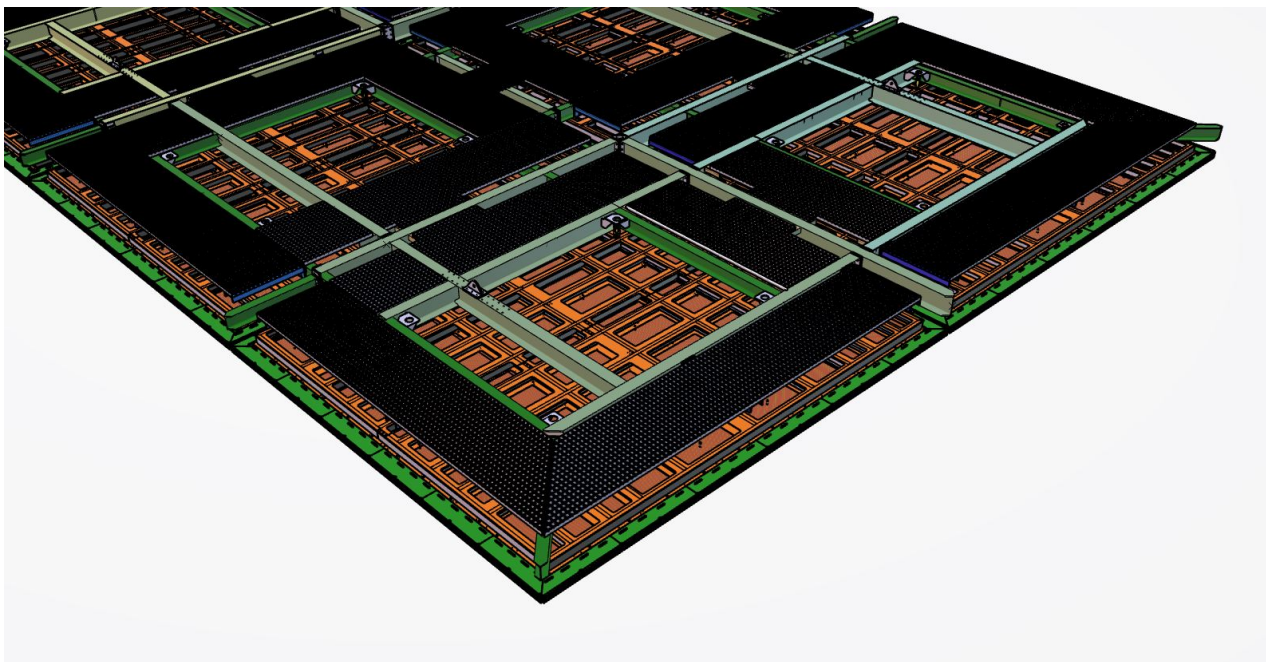


Figure 3.18: Details of the corner extensions of a top superstructure (foreground and at right, green) with CRPs attached below. The catwalk and the stainless steel beams are visible.

points are shifted by up to 250 mm is very low. This amount of shifting is expected on some of the suspension cables taking into account the cryostat roof's main structure beam positions. This deformation is negligible compared to the centered suspension positions. Additional calculations have been done assuming the cathode suspension points and the CRP attachment points are shifted by a few cm. These shifts add no more than a mm to the global deformation.

Each CRP is attached at four points to a superstructure via decoupling devices that allow transverse displacement of the two structures relative to each other during cool-down without impacting the planarity or the mechanical behavior of the CRP assembly. The decoupling system defines a central fixed point on the CRP towards which all its components shrink.

The decoupling system implements three different types of mechanical links between the metallic and composite frames. One is a solid vertical bar attachment that defines the fixed position of the CRP with respect to the superstructure. The other links are made with double-ball joints, which allow free displacement in any direction during differential thermal shrinkage while keeping the vertical positions of both structures fixed. To prevent the CRP from rotating around the fixed point, a guiding rail constrains one of the double-ball joints to move in a chosen direction. Complete sets of junction components between the CRP composite and metallic frame have been built for the three recent prototype CRPs and successfully tested in the cold box. Figure 3.19 illustrates the three types of mechanical links and the principle for a single CRP attached to a metallic superstructure, and shows the final components built and used to couple the CRP composite prototypes to the metallic frame for the cold box tests in 2022. The height of each connecting decoupling system is 92 mm with a diameter of the support of 37 mm. All pieces are made of stainless steel.

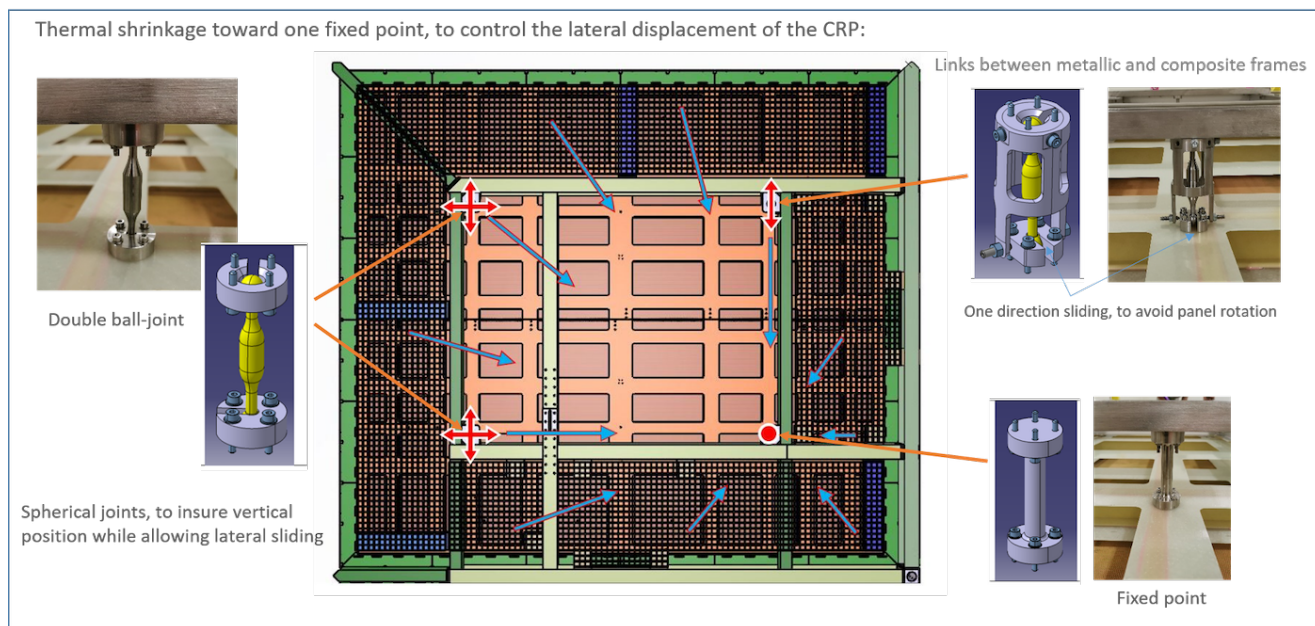


Figure 3.19: Illustration of the decoupling system and the three types of links designed to compensate for differential thermal contraction of the top CRP superstructures made of fiber glass composite and stainless steel. The photos show the final components built and validated with the CRP prototyping.

Each CRP superstructure is hung by four cables from the top of the cryostat and attached to



a motorized system that allows vertical adjustment after the cryostat is filled. The principle of the suspension system is similar to that used to control the ProtoDUNE-DP CRPs in which the suspension feedthroughs are arranged geometrically such that their barycenter coincides with that of the CRP superstructure, and an automated system is used to suspend the structures at the required position and adjust them precisely in the cryostat.

Figure 3.20 shows the design planned for the suspension feedthroughs, including the bellows and the motors to be installed on top of the cryostat. The blue part on left image linking the two pieces of cables acts as a mechanical end-of-stroke to limit the movement downwards and to provide a mechanical safety stop. The photograph on the right shows one of the twelve similar suspension systems built and installed on the ProtoDUNE-DP cryostat roof.

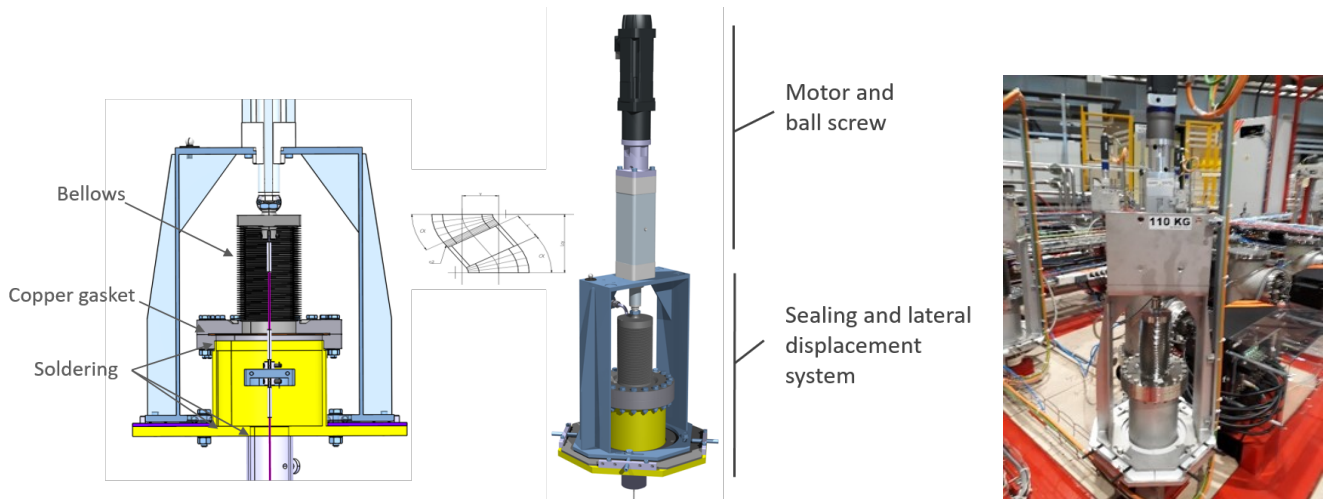


Figure 3.20: Diagrams and photo of suspension feedthrough system for a CRP superstructure.

Using long pushing screws at the level of the adjusting table on the cryostat roof, the transverse position of the suspension cable can be translated by a few cm, allowing correction (using metrology) of the superstructure before raising it.

The size of the bellows in the suspension feedthrough determines the maximum vertical displacement, and the baseline design bellows enables a range of about  $\pm 40$  mm. To allow for maintenance or replacement of the bellows, the system incorporates a mechanical stop and a simple device to obstruct the chimney, closing it off. To allow for precise surveying of the feedthrough position during installation, a special slot is available at the top of the suspension feedthrough for mounting a laser tracker target.

### 3.6 Bottom CRP Support System

The bottom CRPs are identical to the top ones, each composed of two CRUs plus a composite frame. On the bottom anode plane, each CRP is supported about 160 mm above the membrane surface by four dead-weight load bearing supports, as shown on Figure 3.21, positioned inside flat portions of the cryostat inner membrane. There is no intermediate metallic structure, as for the top. The number of posts and density have been optimized to take into account the weight

distribution of the CE cards and boxes, as well as the need to use the composite structure as a stress relief for the cabling of the bottom electronics. The height of the supports can be finely adjusted during installation to set the horizontality and planarity of each CRP.

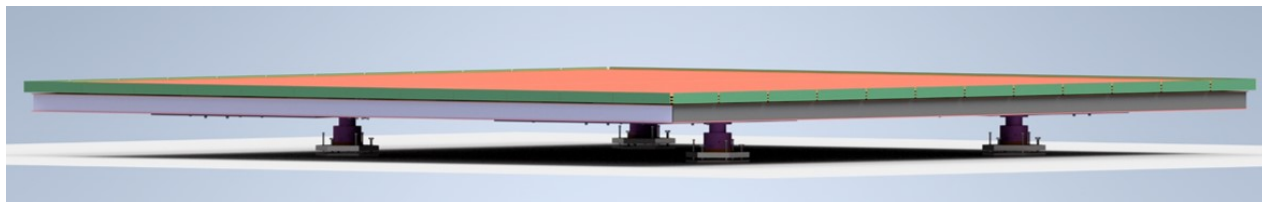


Figure 3.21: Illustration of a bottom CRP supported about 160 mm above the membrane flat surface by four posts.

Each support is attached to the CRP composite frame using an adapter plate made out of FR-4 (Figure 3.22). The support component consists of an aluminum post, a sliding plastic connection, and a stainless steel foot, which together span the 15.9 cm gap between the CRP and cryostat floor. A low-friction sliding plastic connection allows the support to displace in-plane with the CRP as thermal contraction occurs. The stainless steel foot matches the thermal contraction properties of the cryostat membrane, ensuring a slip-free interface. The support feet and sliding connections are mounted to the aluminum post using a custom designed centering mechanism. The purpose of the mechanism is to keep the foot and sliding connection locked and centered during installation. One connection among the four is fixed in order for the CRP to contract towards this point, and one connection is guided along one direction to prevent any possible rotation of the CRP during thermal contraction. The two other connections are free to slide in any direction. The centering system allows for travel within a 7 mm radius of the center. This is sufficient for the maximum anticipated thermal contraction displacement of 6.3 mm. A completely fixed version of the centering mechanism is used for the fixed support configurations.

Adapter plates are used for mounting the bottom support to the underside of the CRPs, two per CRU. Made out of FR-4 glass composite, these plates match the thermal contraction of the CRP structure and provide the needed rigidity. The adapter plate is 3/8 inch thick, although that value may change based on material availability and analysis of the plate deflection under load.

Twelve M4 bolts are used to attach each adapter plate to the composite frame just inside of the CRP corners, as seen in Figure 3.23. The plates span the U-shaped profiles of the composite structure at three horizontal and vertical positions. Two adapter plates will be bolted to each CRU at the production site

The support design features height adjustment for leveling of the CRP and a centering mechanism that fixes the free-sliding feet during installation.

The adapter plates are perforated with a field of 5.5 mm holes, which provide a universal plane for mounting all required bottom support positions and allow flow of both LAr and vapor/bubbles during the filling process. Six stainless steel M6 bolts are arranged in a ring pattern at the desired support mount location to attach the aluminum support post to the adapter plate. The six chosen holes have threaded inserts for the bolts. Since the mount positions are different for each CRU, care must be taken to ensure the correct positioning of inserts and labeling of CRU. The inserts

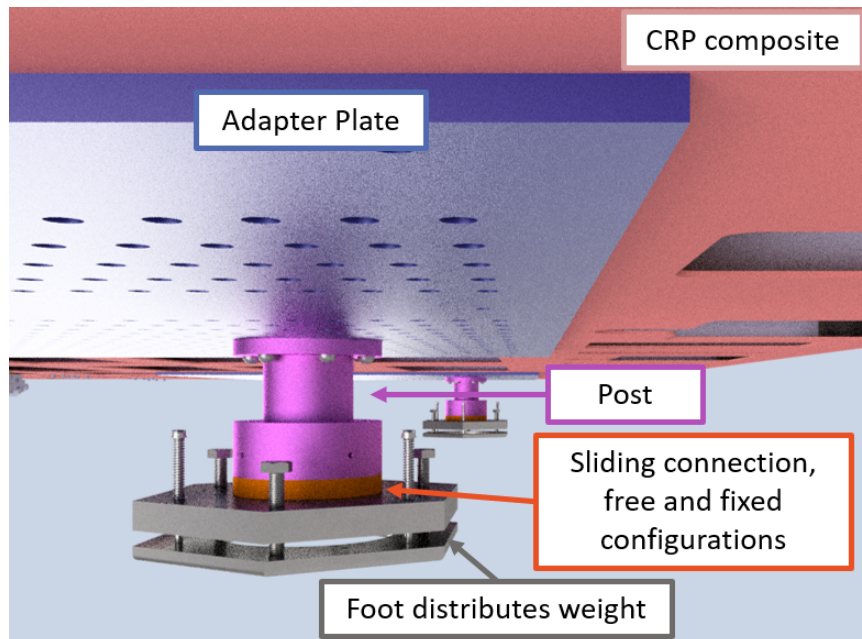


Figure 3.22: The bottom support design consists of four components: the adapter plate out of G10/FR-4, and aluminum post, a low-friction plastic sliding connection, and a type 316 stainless steel foot.

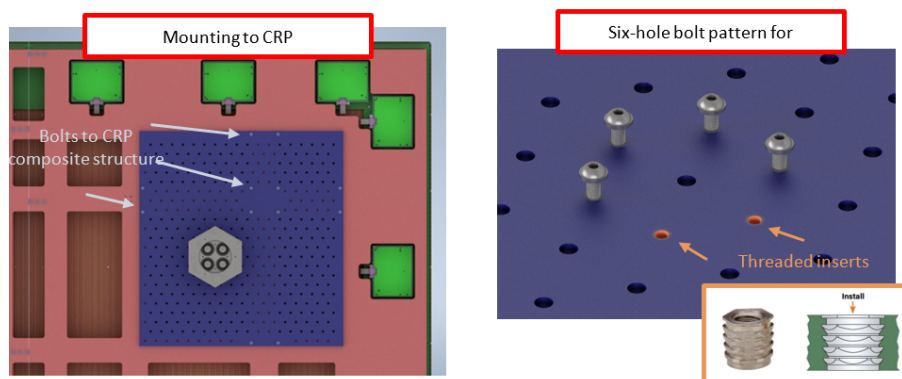


Figure 3.23: Adapter plates are attached to the CRUs at the CRP factory. Bottom supports are attached to the adapter plate using a six-holed bolt pattern

are press fit into the adapter plate holes from the reverse side so that when supports are bolted on, the inserts can be further tightened. Belleville washers are used with the six bolts, maintaining bolt tension during the thermal contraction of the aluminum post's bolting flange. Contraction of the support post's bolt ring relative to the adapter plate is accounted for and aids in the tightening of the bolted connection.

The foot of the support is made out of two type 316 stainless steel plates. The thicker 3/4 inch plate provides contact for the sliding mechanism and material for mounting the centering mechanism hardware as well as hardware for height adjustment of the foot. A thinner 3/8 inch plate is attached to the thicker plate using retaining bolts and pre-tensioned springs. This thinner plate has filleted bottom edges so as not to mar the membrane floor with which it will be in contact. The distance between the two plates can be adjusted  $\pm 10$  mm using three adjustment screws. The adjustment screws use hex heads so that they can be easily accessed and adjusted from the side, since when installed on a CRP they can't be accessed from above. Independent height adjustment of each bottom support allows for the in-place leveling of CRP during installation within the cryostat.

The horizontality of each bottom CRP and the overall planarity will be adjusted using the adjustable supporting feet during the installation and verified with metrology measurements.

## 3.7 Installation Procedures and Tooling

The CRP installation procedures have been developed and presented at the in May 2022. This section summarizes these procedures.

### 3.7.1 Top Anode Plane

All top CRP installation work will take place inside the cryostat except the suspension and lifting systems, which are installed on top of the cryostat. The steps are detailed in Section 9.8.3.

The installation process includes the top CRP signal cabling to the chimneys after the cathode module attachment and the raising of the complete system to a height called "cabling position," which allows access for people doing the cabling on top of the superstructure. This intermediate position is defined by a distance of 800 mm between the top of the superstructure and the cryostat membrane. When the cabling is completed and tested on a SST, it is raised to the final operating position defined by a distance of 490 mm between the top of the superstructure and the cryostat membrane. At that moment the long cables used with the electrical winches to raise the whole SST are replaced by the final suspension cables on the suspension feedthroughs.

There are 96 signal cables per CRP for a total of 7680 cables connected to 105 TDE chimneys. The cabling process also includes the connection of the bias cables (three per CRP) for a total of 240 cables to the cold HV filter boxes sitting on the composite frame. The cables are routed on top of the superstructures to field cage support feedthroughs.

The main steps of the top CRP installation also shown in Figures 3.24 to 3.26 are:

- Install circular cable trays with pre-routed cables on a temporary jig (Figure 3.24 left, center)

- Assemble superstructures;
- Assemble CRPs from half-CRPs extracted from a transport cradle (Figure 3.25 left);
- Install CRPs under superstructures and perform metrology measurements (Figure 3.25 center, right);
- Install the suspension system and lifting winches;
- Install the elevated workstation;
- Raise the superstructure together with the cathode supermodule (Figure 3.26 left);
- Cable the CRPs when superstructures are at cabling positions under the roof (Figure 3.24 right, Figure 3.26 right); and
- Raise the superstructures to their nominal positions.

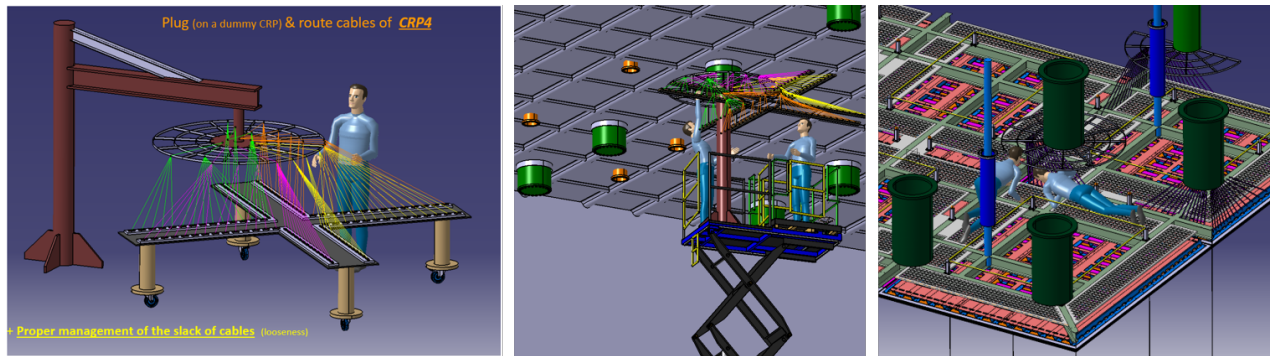


Figure 3.24: CRP signal cabling steps: Left: pre-route the cables on a jig with the circular cable tray to be attached (middle) to the bottom part of the chimney. The cables on their cable trays are installed before the CRPs are raised to the cabling position. Right: when the superstructures are at 800 mm from the cryostat membrane, a team of trained people transfer the pre-routed cable connectors from the jig to the CRP adapter board connectors.

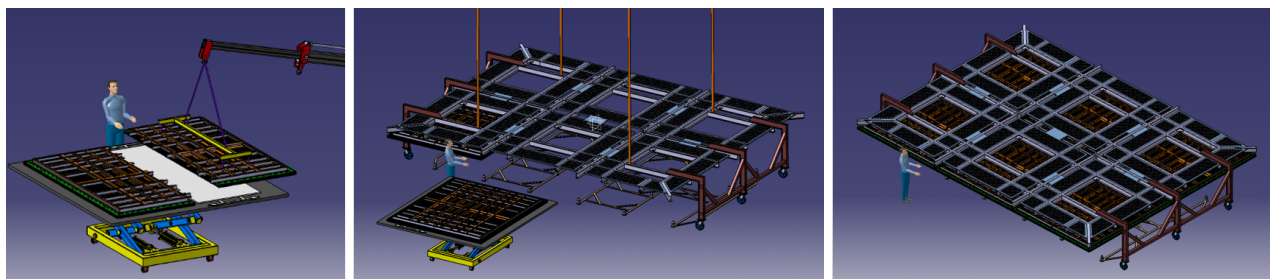


Figure 3.25: Assembly of a top CRP from two half-CRPs on a dedicated table that rolls under the superstructure for attachment to the decoupling systems. The last picture on the right shows a complete superstructure with six CRPs installed ready to be raised.

The quality control (QC) processes to perform during CRP installation are:

- Visually inspect CRP;
- Power the CRP anode bias circuit to control the complete electrical chain with low voltage;
- Verify metrology of superstructure assembly;
- Check the electrical connectivity of the CRP connections to the signal feedthroughs after cabling together with TDE consortium; and

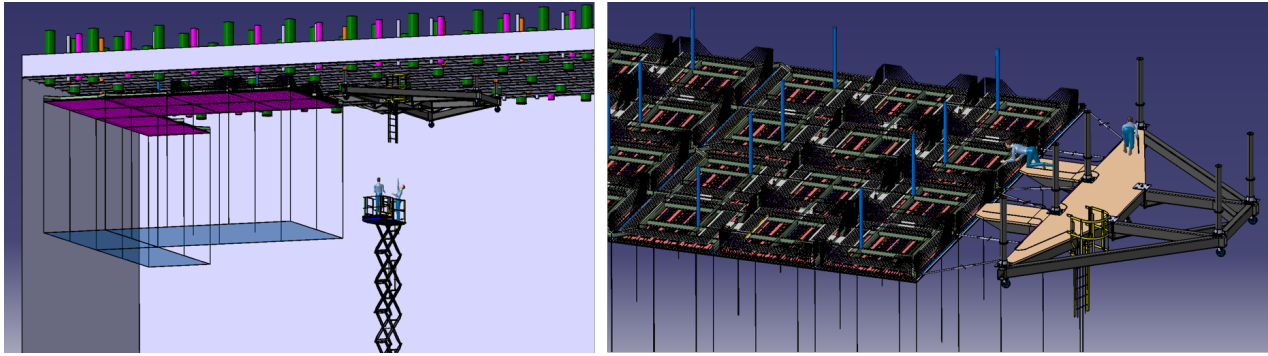


Figure 3.26: Left: Illustration of CRP superstructure installation with the elevated workstation for cabling and three installed superstructures (two small and one large) with the cathodes suspended. Right: View from above of two large SSTs connected to the elevated workstation to perform the CRP cabling .

- Check the electrical connectivity of the anode bias cables to the biasing system on the cryostat roof together with HV consortium.

### 3.7.2 Bottom Anode Plane

Bottom CRPs will be installed anode-side up using a system that lifts them from below using tines attached to a lifting carriage that is hoisted by a crane (Figure 3.27). The combined weight of the CRP and lifting system is restricted to 510 kg, and the center of mass of the system is at least 2.3 m in front of the crane. This distance is needed when lifting the CRP from the short edge and when rotating a CRP below the crane. Lightweight construction of the tines and carriage system is therefore necessary to keep the total lift weight down.

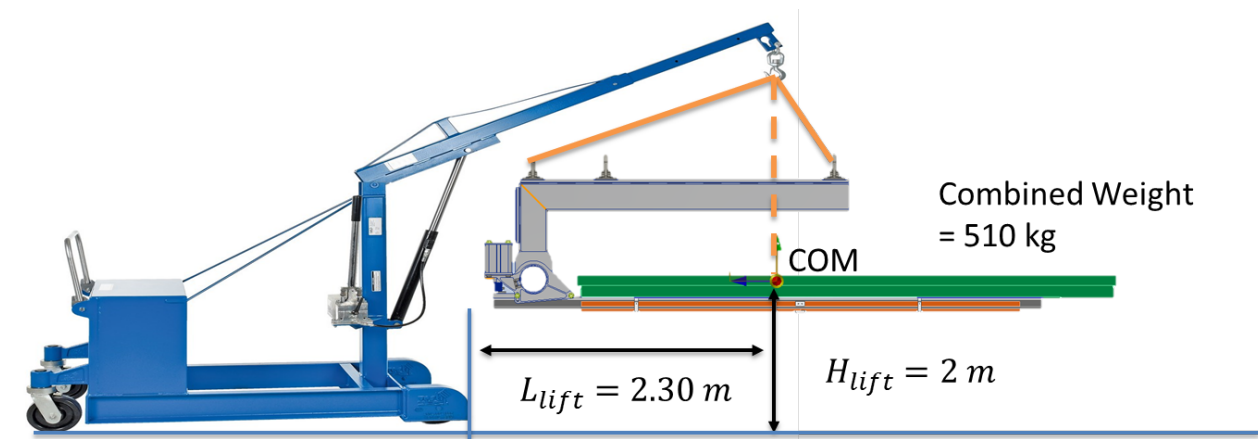


Figure 3.27: Counterbalanced crane lifting a bottom CRP using the tine and carriage system to pick up the CRP from below the adapter plates.

The system consists of three components: the CRP and its attachments, the tines, and the carriage as shown in Figure 3.28

Tines are inserted and extracted from under the CRP as individual units. Detachable from the lifting carriage, the tines can be maneuvered manually underneath the CRP, guided and slung

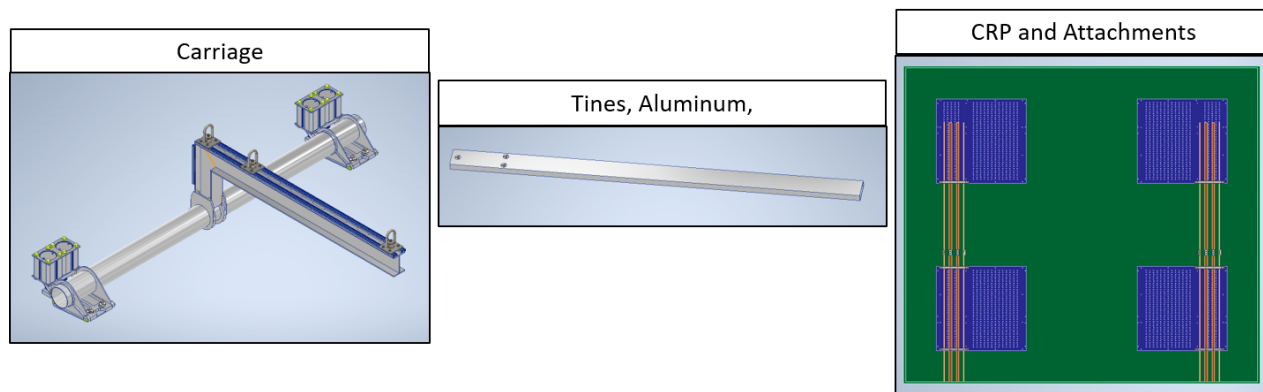


Figure 3.28: Components of the bottom CRP lifting system. The tine guiding system, called “tine cage,” located below the CRP is shown as the orange bars on the right figure. They are attached to the adapter plates in blue.

into place by a tine cage shown in Figure 3.29. The cage ensures that the tines pick up from the adapter plates and don’t collide with under-CRP wiring harnesses. The tines feature a stop bar that contacts the side of the CRP structure, avoiding contact with the grounding plane and edge boards. This prevents the tines from being over-inserted.

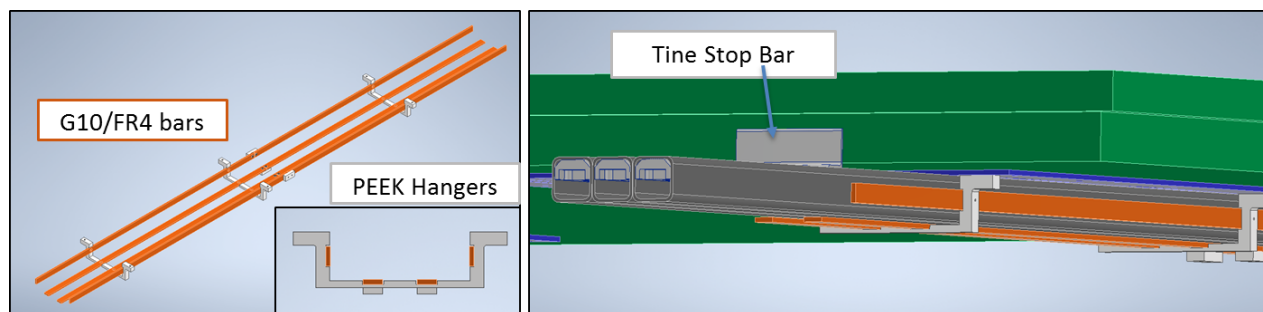


Figure 3.29: Details of the tine cage in orange. The tines are placed and guided underneath the CRP using the tine cage.

The tine cage consists of PEEK hangers and G10/FR-4 bars that run the length of the tine insertion. The cages will be installed within the cryostat as the CRP is being worked on on the assembly table, the hangers will be attached to the adapter plates in areas where the bottom supports are not attached. The tine cages will remain underneath the CRP after installation. They will shrink at the same rate as the CRP structure during filling.

The main steps of the bottom CRP installation inside the cryostat are:

- Assemble CRPs from half-CRPs;
- Outfit each CRP with four support feet and two patch panels;
- Assemble installation truss on membrane floor at location of CRP installation;
- Lift CRP onto installation truss;
- Attach cables to patch panels and test electronics;
- Survey and adjust position of CRP;

- Level screws on bottom support feet;
- Raise CRP from the installation truss;
- Break down and remove the installation truss from below;
- Lower CRP to floor (anode side up); and
- Align to neighboring CRP and/or reference bar using edge bump blocks.

The CE cables are connected to the patch panels located under the CRP before being lowered down to the floor. To allow this cabling, the CRP is positioned with the lifting system on the installation truss as shown in Figure 3.30. The installation truss will be used also to survey and level the CRP.

The truss is assembled on the membrane floor out of bolt-together components and uses fixed support feet for CRP-like load transfer to floor. The CRP is placed on top of installation 1.22 m above the membrane floor.

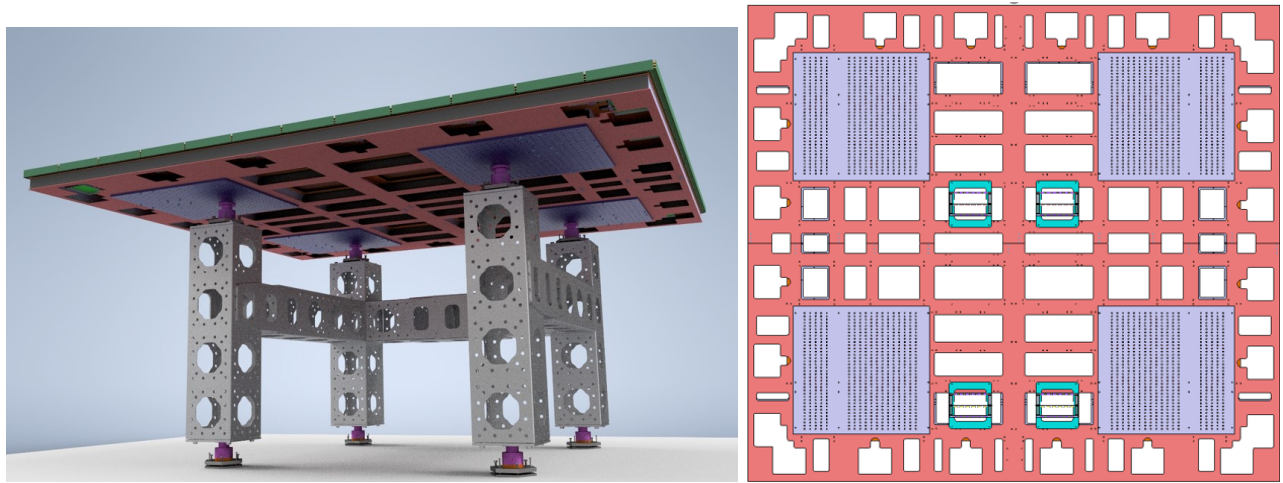


Figure 3.30: Left: Truss system with a bottom CRP sitting on it for cabling of the CE to the CRP patch panels. Right: Bottom view of the CRP showing the position of the four patch panels in blue.

### 3.8 Prototyping and Validation

The first step in prototyping was a proof-of-principle of the perforated PCB-based charge readout. It was successfully demonstrated at small scale at the 50L time projection chamber (TPC) setup at European Laboratory for Particle Physics (CERN) for both two-view anode and later three-view anode readout. As described in detail in [32], further tests at the 50L TPC led to improvements in the three-view geometry and detector components, and optimization of the anode operation.

Next, CRP prototyping moved to the first full-scale CRP in 2021, which was built and tested at CERN to validate the design and construction procedures. It was of the design described in the FD2-VD [32] and details are given in Section 3.8.1.

While the first full scale CRP was undergoing testing, the CRP design was still evolving to better address the physics needs, to facilitate production and assembly, and to reduce the cost of various



sub-components. This document describes the evolved design. With the new CRP design in place, four new full-scale CRPs (CRP-2 through CRP-5) were constructed in 2022. CRP-2 and CRP-3 were built as top CRPs while CRP-4 and CRP-5 as bottom CRPs. These four CRPs will be installed into the in 2023. Production details for these CRPs, as well as warm and cold box tests, are described in Section 3.8.2.

### 3.8.1 First Full-scale CRP Prototype (2021)

As shown in Figure 3.31, the first full-scale CRP had a hybrid setup where one half of the CRP was equipped for and the other half for TDE.

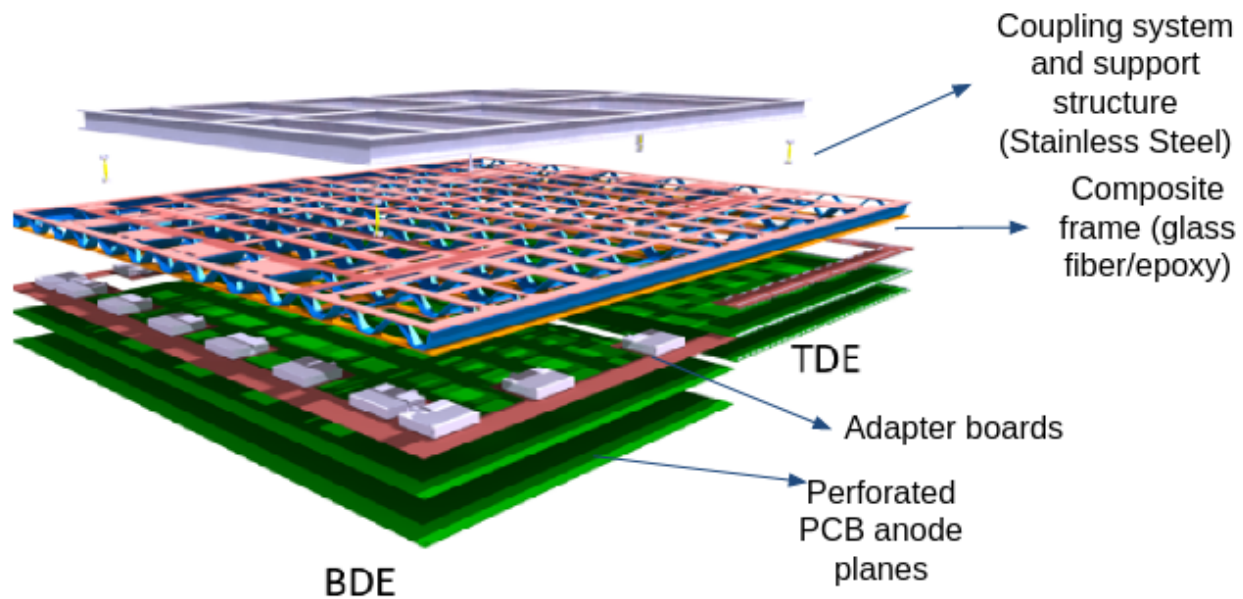


Figure 3.31: 3D model of the first full-scale CRP that was tested in the cold box. Perforated PCB anodes, adapter boards, composite frame and support structures are shown in exploded view. This CRP had a hybrid setup in which both readout electronics designs (BDE and TDE) were integrated.

The perforated PCB had a three-view layout with a shielding layer and the induction-1 view on the first PCB panel, and the induction-2 and collection views on the second PCB panel. Strip orientations were  $(48^\circ, 0^\circ, 90^\circ)$  for the induction-1, induction-2 and collection views, respectively. Two sets of adapter boards were produced to accommodate the needs of BDE and TDE. Interconnection between the anode planes and adapter boards was done using surface-mounted connectors and pins.

The CRP support structure, composed of a composite frame, coupling system and metallic structure, was designed specifically for this CRP to be compatible with both types of readout electronics. The CRP design was finalized in April 2021 and it was fully assembled over the following six months.

This CRP was assembled in the clean room at building 185 at CERN. Following the reception of the PCB segment from the manufacturer, QC and cleaning was performed and the components were prepared for gluing. Six segments were glued together to form a PCB panel with dimensions of  $1.7\text{ m} \times 3\text{ m}$ . Silver printing and QC tests both at room and cryogenic temperatures followed the gluing. Once the PCB panels were ready, surface-mount connectors and pins were soldered onto them. Then the panels were stacked together and the adapter boards installed. The anode and adapter board assembly were then connected to the composite frame and metallic structure.

Once assembled, BDE was installed on one of the CRUs and all channels were tested. The CRP was then moved to Experiment Hall North One (EHN1) and attached to the cold box lid. Before warm and cold testing, the TDE, CRP bias filter and cables, as well as the cabling of the BDE and TDE were installed. The CRP was then put into the dedicated testing area prepared inside the clean room for warm tests, during which noise levels of each readout electronics were measured. Different grounding configurations and bias line filtering options were also tested. Once the characterization of the CRP was finalized at the room temperature, it went into the cold box for cryogenic testing. Figure 3.32 shows the CRP being moved to the cold box before it was closed.



Figure 3.32: Left: CRP moved from warm testing area to be inserted into the cold box. Right: The cold box just before it is closed.

There were two test runs with this CRP in the cold box; the second run included improved grounding for the BDE. During the two runs, millions of triggers were collected by the two readout chains. Figure 3.33 shows an example of a cosmic track recorded by the BDE. Details from the cold box runs and TDE analysis of the collected data is presented in Section 4.3.6.

The CRP was very stable during the cold box runs. Problematic channels, defined as those with with no signal, or partial signal due to lost connectivity in one of the silver print junctions, or higher noise, were quantified as 1.3% of the channels. They were monitored during the cold box runs and no additional degradation was observed. Results from the cold box runs demonstrated that the full-scale CRP behaved well and in line with expectations from the 50L TPC tests.

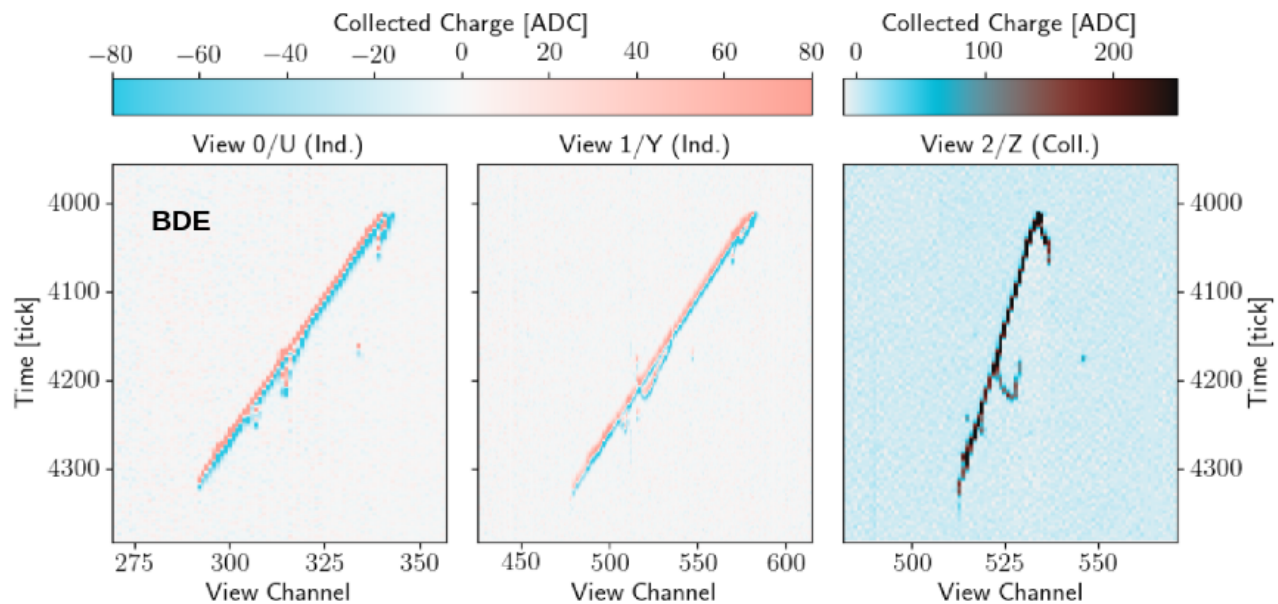


Figure 3.33: Cosmic ray track recorded by the first CRP. Induction and collection views are shown.

### 3.8.2 CRP Production and Testing (2022)

The anode PCBs were produced using 3.2 mm thick FR-4 as the base material and are perforated with 2.4 mm holes.

A bare PCB board has a  $35\ \mu\text{m}$  thick copper image applied on both sides. In order to evaluate the finishing options, CRP-4 used a silver coating over the copper. Given that six PCB segments are glued together to form a CRP panel, milling on the “half-lap” joint is one of the important steps in the PCB production. A gap or an uneven surface between two glued PCBs could create difficulties for the silver printing.

The thickness of the board was measured before milling, and half of the measured thickness plus  $50\ \mu\text{m}$  was removed on the half-lap joint. The tolerances on this process are  $+0/-50\ \mu\text{m}$ .

At the prototyping stage, production of perforated PCBs for a CRP has been taking 4-6 weeks. Upon receiving the PCB segments they have been visually inspected for any possible production problems, then the segments have been cleaned, washed and dried prior to gluing. Preparation for gluing starts with covering the half-lap regions with a special tape to prevent the epoxy from spreading to unwanted regions. Then epoxy was applied to the half-lap surface using a roller.

Adjacent PCB segments were aligned by using two sets of alignment holes with metallic pins inserted into them. Once all six panels were aligned and glued, they were covered with a vacuum cloth and sealed under vacuum for drying. Drying takes approximately one day. Once dry, the assembly was inspected. Figure 3.34 shows the gluing process.

Next, the electrical connections between them were made by applying silver ink, a mixture of silver

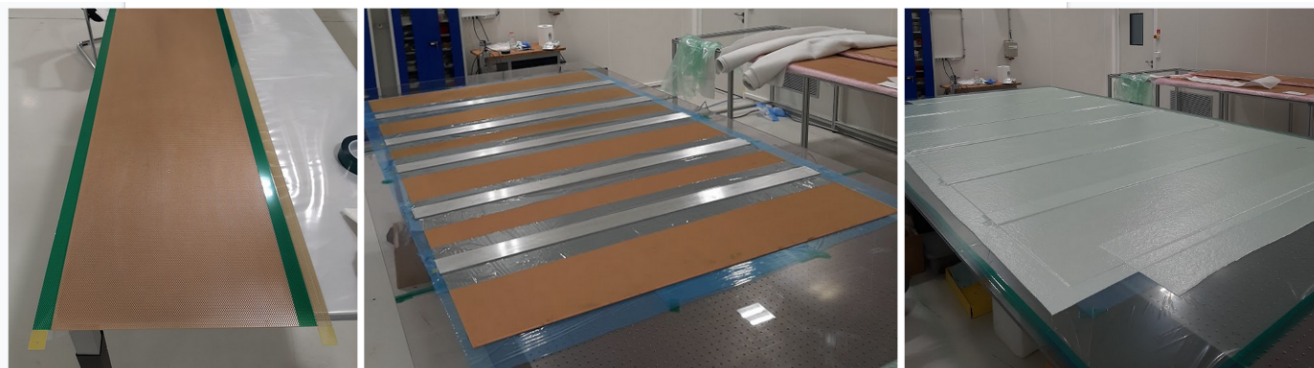


Figure 3.34: Left: Preparation of PCB segment for epoxy application. Middle: Six PCB segments are glued, aligned and ready to be sealed. Right: Glued assembly is under vacuum for drying.

and epoxy, to the joint points using a special screen. Then it was treated under  $\sim 120^{\circ}\text{C}$  for  $\sim 3$  hours for its polymerization. Figure 3.35 shows the silver ink application using the screen, epoxy treatment with heat, and the result.

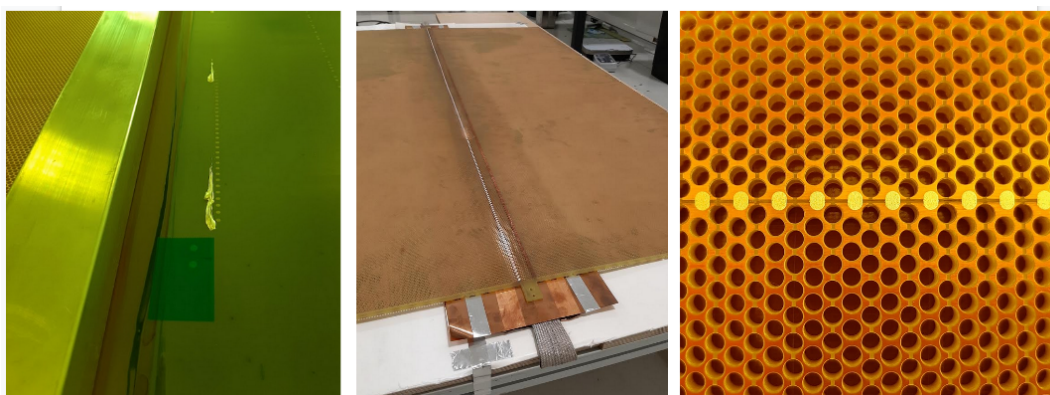


Figure 3.35: Left: Screen for the silver ink. Silver ink is visible (gray) next to the dot pattern, ready to be applied. Middle: Treatment of the silver print at high temperature for polymerization. Right: Result of silver printing.

The initial electrical continuity and isolation tests were performed at room temperature, followed by cold tests in a large cryogenic bath, then drying and cleaning before assembly. It is ready for CRU assembly. Figure 3.36 shows a picture from testing PCB panels in LAr and drying cleaned panels for the assembly.

The CRP assembly started by inserting PEEK support screws to the induction-2/collection plane. Each pin was kept at cold before being cryo-fit to the special holes on the PCB. Once the support pins were installed, the induction-2/collection plane was placed on top of the shield/induction-1. The two planes were aligned using the corners and support screws, then the shield/induction-1 board was connected to the pins using nylon screws.

At this point the PCB assembly was ready for the adapter board installation. The adapter boards sit on the spacers that are installed on the PEEK pins, located at the periphery of the PCB assembly. Once the PCB panels were stacked and the adapter boards installed, the assembly was



Figure 3.36: Left: Cryogenic test of the glued and silver printed PCB panel. Right: Drying in the clean room after final cleaning prior to assembly.

attached to the composite frame using the PEEK support screws. Upon receipt of the composite frame from the manufacturer, the two halves were first visually inspected and cleaned. For this prototyping stage, the composite frames were tested in a large cryogenic bath to check for any mechanical issues or flatness deviations. Figure 3.37 shows the composite frame received from the manufacturer, its attachment to the CRU and connecting the two halves into the CRP.

As the final step of the CRP assembly, the vertical interconnection between the anode layers and adapter boards was done by installing the edge cards, which are plugged into the three sides of the anode assembly. Figure 3.38 shows the final CRP assembly. The process of constructing a CRP takes roughly a month for a group of three people: three weeks for PCB panel preparations and a week for the final assembly.

### 3.8.2.1 CRP-2

CRP-2 was constructed in July 2022. Despite careful preparations, the results using the silver printing mask were not satisfactory and several channels required manual corrections. Taking into account preparation time, difficulty, and unsatisfactory results, using a screen for silver printing was discarded. It was done manually for the remaining two PCB panels of the CRP-2.

Adapter boards for CRP-2 and CRP-3 were produced both by the CERN PCB workshop and a commercial company<sup>2</sup>. Edge cards for CRP-2 and CRP-3 were also produced by a commercial company<sup>3</sup>. The adapter boards and edge cards were assembled at the CERN electronics assembly lab. The composite structure of CRP-2 was delivered in early May in two parts. They were bolted together and the composite assembly was finalized by the following week.

Figure 3.39 shows the finalized CRP-2 along with some of the people involved in the construction.

<sup>2</sup>Tecnomec Srl

<sup>3</sup>PCBWay



Figure 3.37: Top Left: Two halves of the composite frame as received from the manufacturer. Top Middle: Half composites are attached to the anode assembly and they are ready to be connected. Top Right: Connecting two half units. Bottom: Composite frames are connected and assembly is ready for the edge card installation.

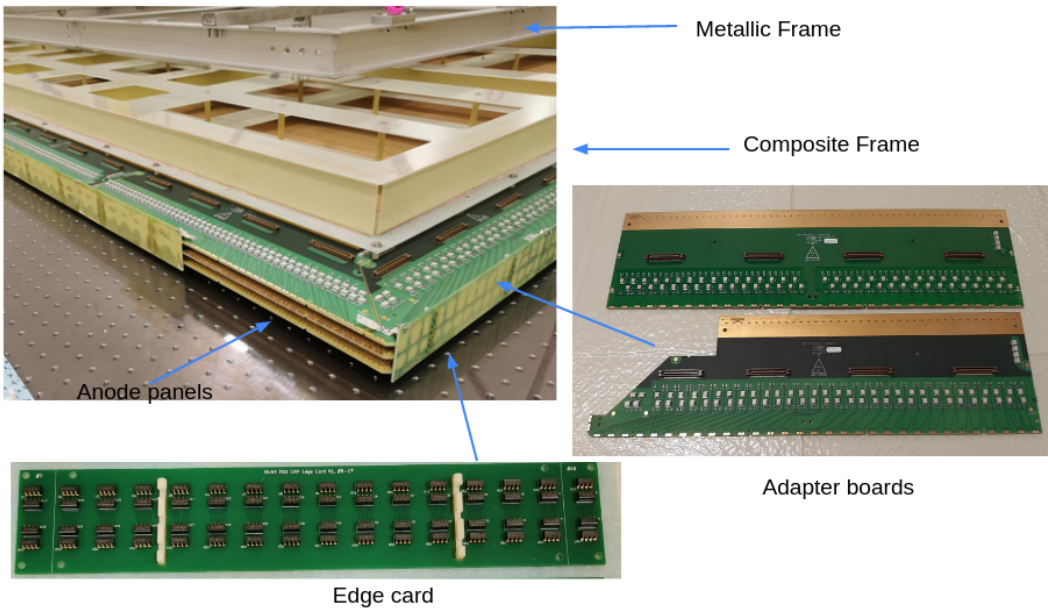


Figure 3.38: Finalized top CRP assembly where the different components are shown. One edge card at the (left) corner is removed to reveal the PCB panel adapter board stack. U-beam and skin structure of the composite frame are visible. Adapter boards and edge card are also shown.

Upon finalizing the assembly in the clean room at CERN building 185, CRP-2 was put into the transportation box and shipped to EHN1 for warm and cold testing (Figure 3.40, top left). At EHN1, CRP-2 was attached to the cold box roof and secured to the required height (Figure 3.40, top right). Then, the TDE signal cables were connected to the adapter boards on one end and to the readout chimney on the other end. After finalizing the level meter installation and necessary cabling, CRP-2, secured to the cold box roof, was moved to the Faraday cage for warm testing. Figure 3.40 shows the CRP plus cold box roof at EHN1 and their transport to the dedicated Faraday cage for warm testing.

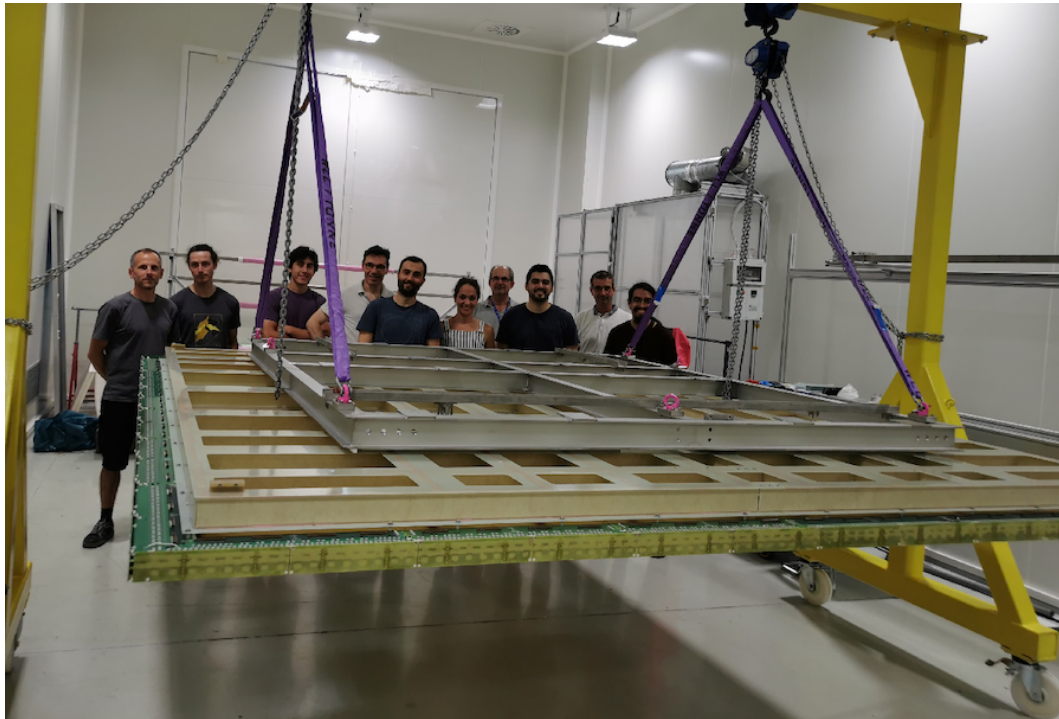


Figure 3.39: Finalized CRP-2 assembly and some of the people involved in the construction.

Once inside the Faraday cage, the biasing circuit for the CRP-2 was finalized. Cold filters were installed, and HV cables were routed and attached to the HV flange on top of the cold box roof. A voltage  $\sim 50$  V was applied to each bias line to check for any leakage current, and none was found. The TDE group then made extensive warm noise measurements and identified four channels with very low noise and 10 channels with a slightly higher noise levels.

The assembly was moved to the cold box for testing. Very soon after the filling, very clean samples of tracks at low noise conditions were collected. Figure 3.41 shows few examples from the detected cosmic ray tracks. Analysis of the collected data is presented in Section 4.3.6.

Detailed analysis confirmed, however, that the abnormal noise observed at warm was also present in the data collected in the cold box. In fact, additional channels with lower noise or partial signal appeared. Most of these newly found problematic channels were close to strips located on the induction-2 plane on one CRU only. In early September 2022, this CRU was disassembled, and visual inspection and electrical measurements revealed electrical discontinuity on the silver joints in the non-responsive regions. The silver joints were then manually fixed, remeasured, and validated.

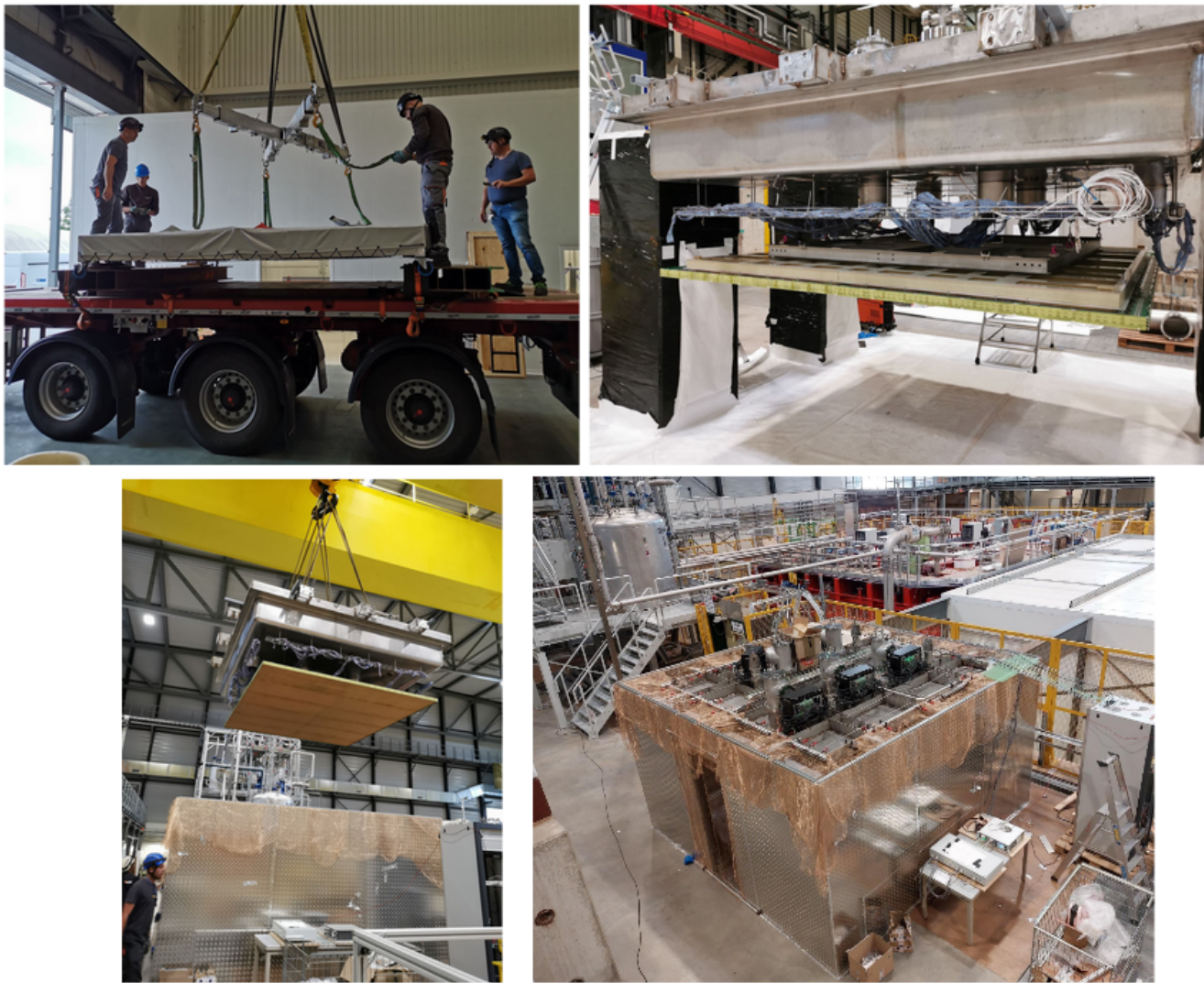


Figure 3.40: Top Left: CRP-2 inside the transport box is being loaded to a truck for the transport to EHN1. Top Right: At EHN1, CPR-2 is attached to the cold box roof and raised to the final height. Bottom Left: The cold box roof with the attached CRP-2 is on its way to the Faraday cage. Bottom Right: The cold box roof positioned at its final position on the Faraday cage room.

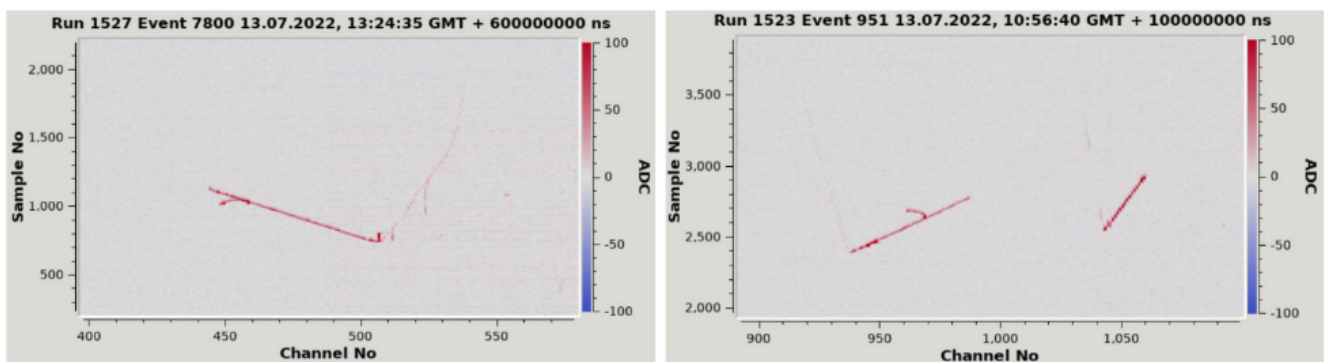


Figure 3.41: Two examples from the cosmic ray tracks recorded with CRP-2 during the cold box run.



CRP-2 was re-assembled at the end of October and capacitance measurements confirmed that the problems on induction-2 were no longer present. During the second cold box runs in early November, CRP-2 worked as designed and tests were concluded successfully. More than 1M triggers were collected during the cold box runs with CPR-2.

### 3.8.2.2 CRP-3

PCB gluing for the CRP-3 production was finalized at the end of July 2022 and silver printing was concluded at the end of August. After QA/QC tests at room and cryogenic temperatures, assembly took place at the end of September 2022. See Figure 3.42.

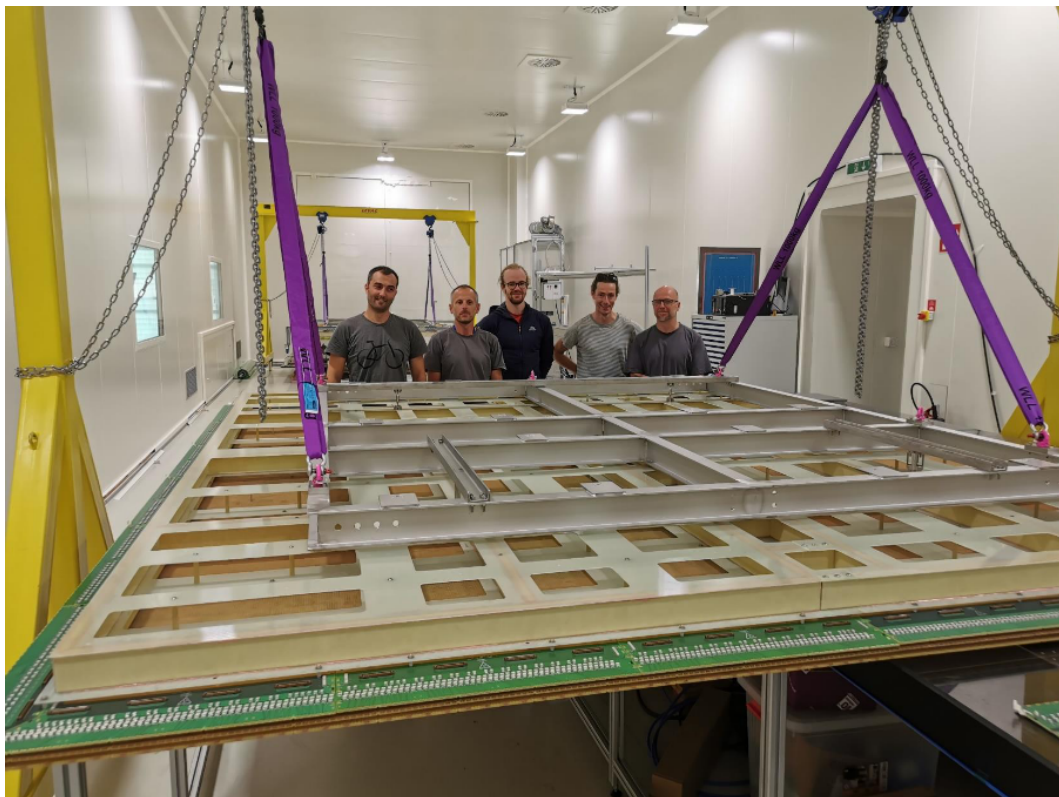


Figure 3.42: Finalized CRP-3 assembly inside the clean room at CERN building 185 and some of the CRP assembly team.

Before the cold box test, capacitance tests revealed contact problems that were then found to be due to inadequate mechanical support. The problem was quickly resolved by adding mechanical supports to the edge cards. Two other channels were found to have breaks in the silver joint, and two with shorts.

Following Faraday cage tests, the cold box test was performed in mid-October, and both CPR-3 and TDE readout responded as expected; clean cosmic tracks were visible immediately. No major issues were observed during the tests. See Figure 3.43. Analysis of the collected data with CRP-3 is presented in the Section 4.3.6.

After the cold box tests, CRP-3 was moved back to 185 to be stored in the clean room until its installation in Module-0.

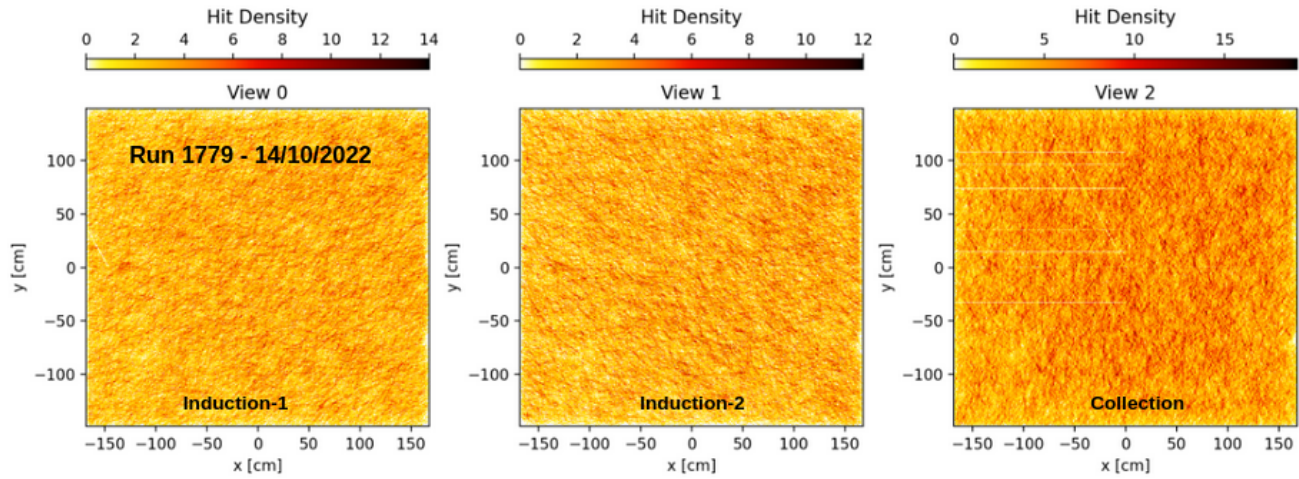


Figure 3.43: Hit map of CRP-3 during one of the runs in the cold box.

### 3.8.2.3 CRP-5

CRP-5 was split into its two halves, CRP-5a, to be assembled in the U.S., and CRP-5b, to be assembled at CERN. The PCB preparation and QC for both were finalized at CERN by the middle of July 2022. The two PCB panels for CRP-5a, half composite frame, and various small components were packed and shipped in early August to Yale University for assembly. In addition to the assembly steps followed for CRP-2 and CRP-3, a thin copper grounding layer was also attached to the CRP-5a composite frame.

Figure 3.44 shows various photos from the CRP-5a assembly at Yale. After assembly, CRP-5a was shipped to BNL for extensive testing.

At BNL, once the safety procedures were approved and reviews were passed, CRP-5a was moved out of the shipping crate, FEMBs were installed, cabling was finalized, and warm tests were conducted by late November. Cold tests were started immediately afterwards. For the cold tests at BNL, a dedicated cold box was built and certified. At the time of writing, the cold tests are ongoing.

Following the extensive cold-tests at BNL, CRP-5a will be shipped to CERN where it will be connected to CRP-5b. CRP-5b was assembled at CERN at the end of November, and FEMBs were installed and tested in December. The full CRP-5 will be tested in the cold box at CERN in early 2023.

### 3.8.2.4 CRP-4

CRP-4 is the second bottom CRP prototype. The PCB gluing and silver printing were done at CERN in 2022 and the assembly will be completed at Yale University by January 2023.

As shown in Figure 3.45, perforated PCBs for CRP-4 has a layer of silver coating over the bare copper. The silver coating is not costly and may address possible oxidation issues given the long-term storage that may be required. Figure 3.45 shows perforated PCBs with silver coating and

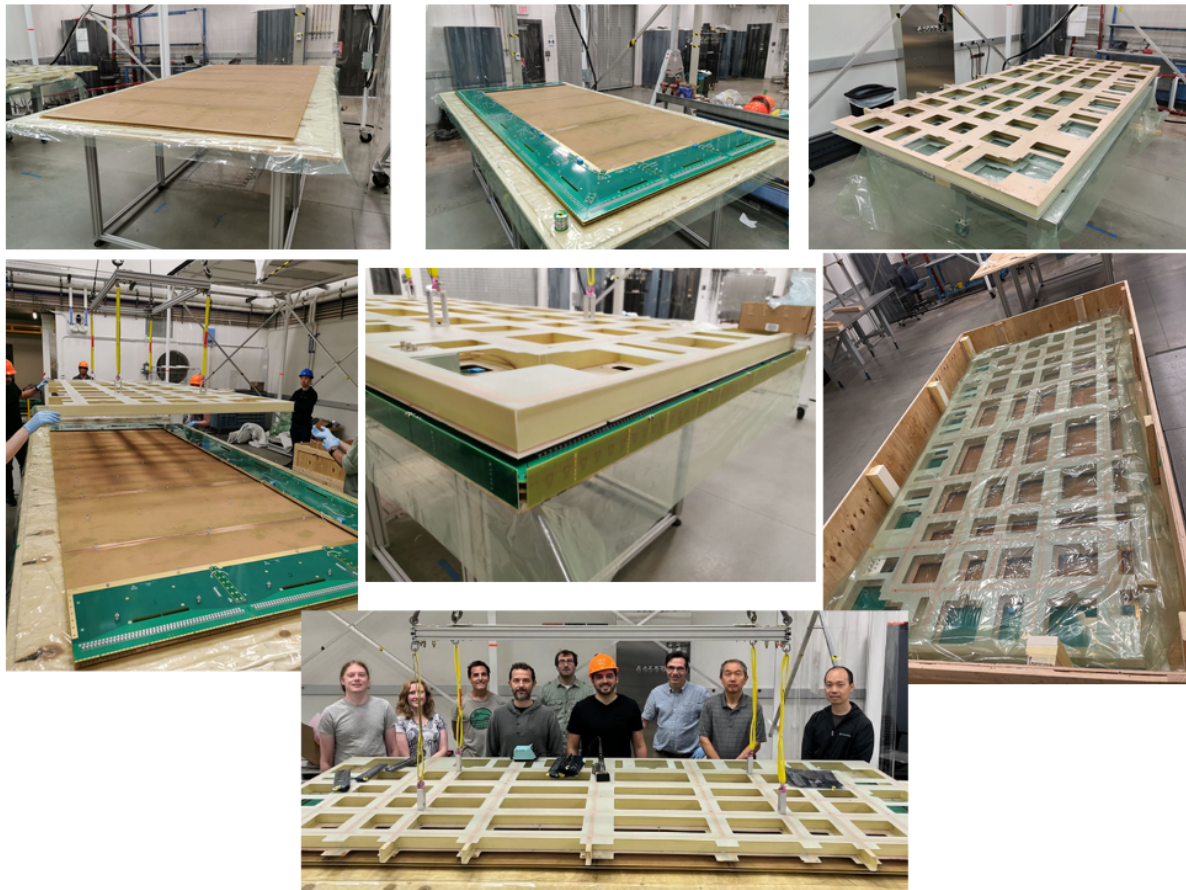


Figure 3.44: Top Left: Two PCB panels are stacked together using the PEEK spacers. Top Middle: Installed adapter boards on the PCB panel assembly. Top Right: The half composite frame with the copper grounding plane attached to it. Middle Left: Attaching composite frame to the anode assembly. Middle Center: Installation of edge cards. Middle Right: CRP-5a is ready to be moved to BNL. Bottom: Team that assembled the CRP-5a.

PCB panels built from them.

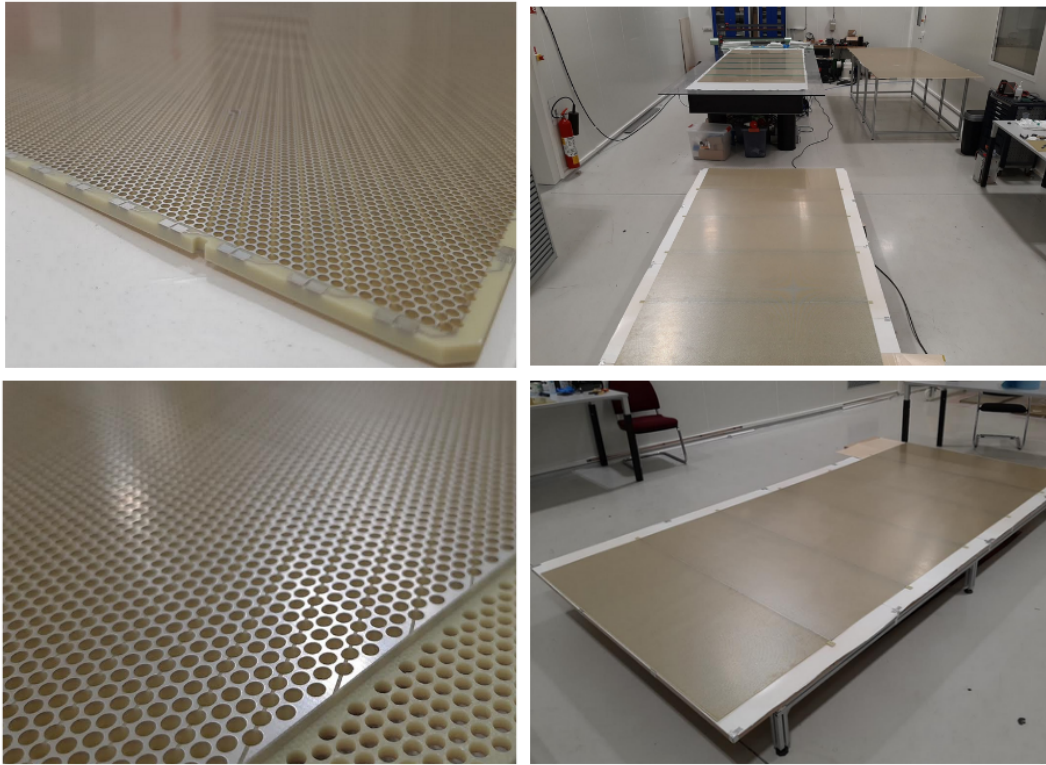


Figure 3.45: Top and Bottom Left: Close up images from the silver coated perforated PCBs. Top Right: Panels for CRP-4; One on a low table (foreground), one on the optical table (rear), and a stack of two on the workbench (right). Bottom Right: A PCB panel for CRP-4.

In early December, upon finalizing all the necessary preparations at CERN, four PCB panels, the composite structures, and various small components were shipped to Yale for assembly. After the assembly and integration of cold electronics, CRP-4 will be cold-tested at a dedicated test stand at Yale, then shipped to CERN, possibly for another cold box test, and later its integration into FD2-VD Module 0.

### 3.9 Interfaces

CRP consortium has interfaces with the BDE, TDE, and HV consortia and with the group. Table 3.4 summarizes the interfaces, with references to the current versions of the interface documents. More details follow.

The CRP and BDE consortia share mechanical and electrical interfaces. Mechanical interfaces include installation of front-end mother boards (FEMBs) to the CRP adapter boards, installation of patch panels to the composite frame and cable routing for the BDE. Electrical interfaces include biasing the CRP planes and FEMB-copper plane grounding connections. Design, production and installation of the adapter boards and composite frame, installation and testing of FEMBs, cable routing to the patch panel are CRP consortium responsibilities. BDE consortium is responsible for the design and production of bottom CRP bias connections and warm filter on the BDE flange, procurement and installation of the cold HV cables, final CE cabling inside the cryostat. In

Table 3.4: CRP interfacing systems (linked to interface documents) and interface descriptions.

Interfacing System	Description
BDE	Mechanical (connections of CE boxes, patch panel and cable routing) and electrical (bias voltages, FEMB–copper plane connection, grounding scheme)
TDE	Signal cables, cable routing, cable installation and circular cable trays
HV	Mechanical (support of cathode modules) and electrical (bias connections on the field cage flange, bias power supplies, warm cables for all CRPs, as well as the cold cables for the top CRPs)
Installation	Infrastructure: Design files, 2D drawings, safety analysis and approval, fabrication of 16 supermodule structures, rigging equipment, tooling and hardware. Installation: Engineering notes, procedures, tooling, storage space and rigging equipment. Bottom and top CRP installation.

addition, BDE is responsible for the signal and power cables for the FEMBs, and the test stand for the bottom CRP factories.

The interfaces between the CRP and TDE consortia include signal cables, cable routing, cable installation and their support via circular cable trays. The CRP consortium is responsible for the design and production of the top adapter boards, procurement of the flat signal readout cables, installation of the flat cables to the cold flanges inside the cryostat, design and production of the circular cable trays to dispatch the cables from the cold flange to the CRP adapter boards. The TDE consortium is responsible for the installation of the chimneys and providing mechanical attachment points for these cable trays to the chimneys.

The interfaces between the CRP and HV consortia include supporting the weight of the cathode under the CRP superstructure, providing bias connections for the top CRPs on the field cage flange, procuring CRP bias power supplies, providing warm bias HV cables for all the CRPs and cold HV cables for the top CRPs. The CRP consortium is responsible for the design of the support structure and the quality assurance (QA)QC testing of all its components, including the anchor points of the cathode suspension ropes. The HV consortium is responsible for the complete model of the cathode module, including detailed weight distribution, rope selection and the design of the connection between the ropes and the superstructure anchor points. In addition, HV is responsible for implementing safe high voltage (SHV) feedthroughs to allow the top CRP bias voltage channels to be brought out of the cryostat through the field cage support penetrations, and procurement of the bias power supplies and warm cables for all CRPs, and the cold cables for the top CRPs.

The CRP and FSII group share infrastructure and installation interfaces. Infrastructure interfaces include design files, 2D drawings, safety analyses and approvals, fabrication of 16 supermodule structures, rigging equipment, tooling and hardware. The CRP consortium is responsible for providing approved engineering notes and 2D drawings of the two types of CRP superstructures, safety analyses and approvals of the superstructure design, assembly procedures, testing and QC information for the superstructures. In addition, it will provide the design of the motorized suspension system and related hardware for the CRP support structure as well as the automated level adjusting system and related hardware. FSII is responsible for fabricating the 16 superstructures

(four small and 12 large), and providing any crates or boxes, tooling, hardware (nuts and bolts) needed to assemble the superstructures. FSII will also provide the rigging equipment needed to move the superstructures underground and into the cryostat, and the related drawings.

The installation interfaces between the CRP consortium and the FSII group include bottom and top CRP installation, provision of engineering notes, procedures, tooling, storage space and rigging equipment. CRP consortium is responsible for providing temporary winches, roof flanges, and cables to lift the CRP to position in the cryostat. Providing engineering notes, safety related documentation, installation procedures, cleaning procedures, parts and tooling are also CRP consortium responsibilities. FSII will provide any crates or boxes needed to move the superstructures, storage space in the cavern area for 20 half-CRPs storage/transport crates, a gantry crane that meets CRP specifications to be used to lift the half-CRP onto the assembly table. The CRP consortium provides the CRP assembly table.

For the top CRP installation, the CRP consortium is responsible for providing any required tooling including the elevated workstation. CRP personnel are responsible for cabling the CRP from the superstructure. The survey plan for CRP installation will be a joint responsibility. For the bottom CRP installation, CRP consortium will provide procedures, and design and construction of the bottom CRP support structure. FSII will provide commercial equipment to place the CRPs in position.

### 3.10 Production and Schedule

The production model for the CRPs takes into account the experience gained from the procurement of components for the cold box tests (Sections 3.8.2 and 3.8.1), which will go into FD2-VD Module 0. A timetable for procurement and assembly has been developed that feeds into the schedule outlined in Chapter 10.

The production of the 3840 PCB segments is planned between October 2024 and October 2026. Vendor/s will be selected accordance with CERN's procurement process. The delivery rate is required to be 50 PCB segments per week to allow a six month ramping-up period. The PCB segments will be delivered to CERN where the gluing, silver printing and QC will be performed. Multiple batches of PCB panel shipments from CERN to assembly sites are expected. This phase is scheduled from October 2024 to January 2027.

The production and assembly of the adapter boards and edge cards will be performed by the industrial contractors between January 2024 and June 2026.

Components for CRP assembly, namely composite frames, decoupling system, cables, and connectors for readout for the TDE will be manufactured by industry between November 2024 and July 2026.

Assembly sites will be set up at collaborating institutions, two in the EU and two in the U.S. Preparatory work (including design and manufacturing of tooling, cold test bench installation, test and site validation) will begin in 2024, with production starting at a lower rate in early 2025. Full-speed production of one CRP per week at each site is expected starting in June 2025 in the

EU for top CRPs, and from April 2026 in the U.S. for bottom CRPs. This assembly rate is based on one shift per day, five days per week, as validated in the assembly of CRP-1. A second shift per day could be added if needed. The assembly operation is expected to be completed in August 2026 for the top CRPs and July 2027 for the bottom CRPs.

Manufacturing the top superstructures and suspension feedthroughs will be done by industry contractors between November 2024 and December 2026. The automation system for the suspension of the top superstructures will be developed the collaborating institutions. The supports for the bottom CRPs will be produced industrially between September 2025 and October 2026. Installation tooling will be manufactured at the same time at collaborating institutions.

The production schedule is summarized in Table 3.5.

A more detailed schedule for production and installation of the FD2-VD is found in Figure 3.46.

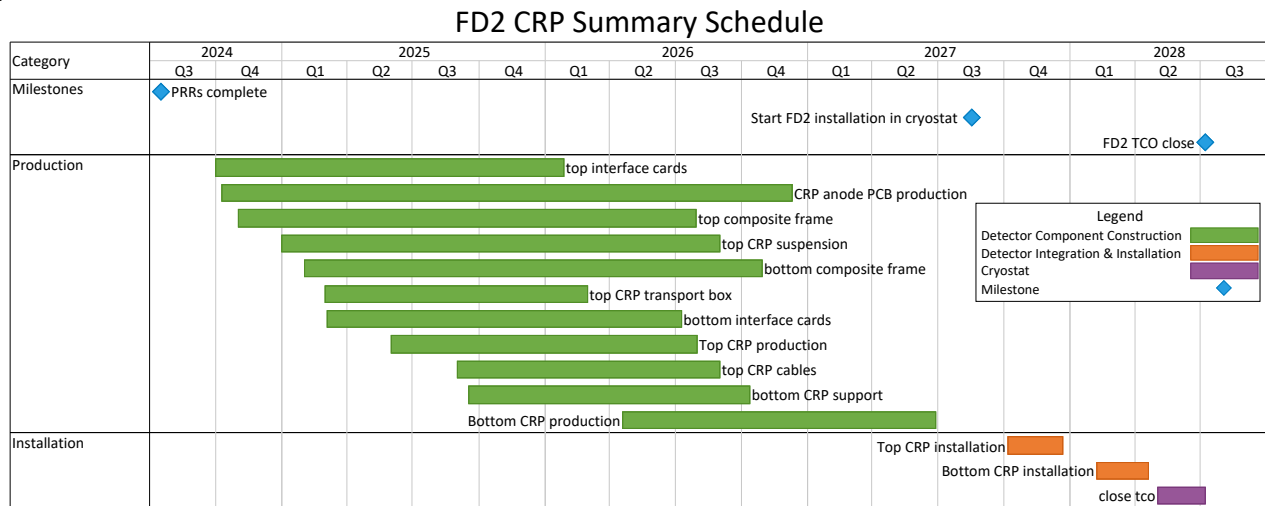


Figure 3.46: Key CRP milestones and activities toward the FD2-VD in graphical format (Data from [53]).

## 3.11 Consortium Scope and Organization

### 3.11.1 Scope

The scope of the CRP system, provided by the CRP consortium, covers the procurement of materials, fabrication, warm and cold testing, QA/QC, delivery, and installation of all components needed to complete the top and the bottom CRP anode planes.

The following subsystems and items are included:

- Production of the anodes;
- Production of the adapter boards and edge cards;
- Production of the composite frames and of the mechanical links between the anode layers, adapter boards and structures;
- Production of the superstructures for the top CRP plane;
- Production of the mechanical support systems for the bottom CRP plane;

Table 3.5: CRP Production Timetable. Items where industrial procurement/manufacture is not indicated will take place at collaborating institutions.

Item	Tasks	Dates
Perforated anode PCBs	<ul style="list-style-type: none"> <li>Construction of panels and drilling of holes</li> </ul>	Oct 2024 – Oct 2026
Interface boards (adapter boards and edge cards)	<ul style="list-style-type: none"> <li>Production of four-layer PCBs (industry)</li> <li>Procurement of capacitors, resistors and connectors</li> </ul>	Oct 2024 – Aug 2025
PCB anode plane assembly	<ul style="list-style-type: none"> <li>PCB gluing, silver printing and QC</li> </ul>	Jan 2025 – Dec 2026
Top CRP Interface board assembly	<ul style="list-style-type: none"> <li>Adapter board assembly (industry)</li> <li>Edge card assembly (industry)</li> </ul>	Oct 2024 – Jan 2026 Oct 2024 – Jan 2026
Bottom CRP Interface board assembly	<ul style="list-style-type: none"> <li>Adapter board assembly (industry)</li> <li>Edge card assembly (industry)</li> </ul>	Mar 2025 – Jun 2026 Mar 2025 – Jun 2026
Top Composite Frame production	<ul style="list-style-type: none"> <li>Fabrication</li> </ul>	Nov 2024 – Jul 2026
Bottom Composite Frame production	<ul style="list-style-type: none"> <li>Fabrication</li> </ul>	Feb 2025 – Oct 2026
Top CRP assembly	<ul style="list-style-type: none"> <li>Assemble the anode layers</li> <li>Connect adapter and interconnection boards</li> <li>Connect the mechanical frame</li> </ul>	Jun 2025 – Jul 2026
Bottom CRP assembly	Same sequence as for Top	Apr 2026 – Jun 2027
Top CRP superstructure	<ul style="list-style-type: none"> <li>Production of large superstructure components (industry)</li> </ul>	Nov 2024 – Jul 2026
Top suspension feedthroughs	<ul style="list-style-type: none"> <li>Production of the 64 FTs components (industry)</li> <li>Superstructure suspension automation system</li> </ul>	Jan 2025 – Sep 2026 May 2025 – Dec 2026
Bottom mechanical support	<ul style="list-style-type: none"> <li>Production (industry)</li> <li>Tooling for installation</li> </ul>	Sept 2025 – Oct 2026 Sept 2025 – Oct 2026



- Production of the suspension system and position control for the top CRP superstructures;
- Production of the HV distribution system associated with the top CRPs for biasing;
- Production of the level meter system associated with the top anode;
- Production of the cabling of the CRPs to the cold flange of the top electronics;
- Production of the transportation and storage boxes for the CRPs;
- Setting up of the anode plane assembly site;
- Construction and setting up of CRP production sites at collaborating institutions
- Assembly of the CRPs at the factories;
- Testing of the assembled CRPs at the factories;
- Placing the CRPs into transport boxes and delivering them to SURF;
- Design and fabrication of specific tooling for installation in the cryostat;
- Installing and cabling the CRPs in the cryostat.

The scope also includes R&D, design validation for the detector components, fabrication, integration, and testing of prototype CRPs in various cold test setups that started in 2021 and that will be pursued with FD2-VD Module 0 in 2023. (Chapter 8).

### 3.11.2 Institutional Responsibilities

Table 3.6: Institutions participating in the CRP consortium

Institution	Country	Detector & Deliverables
European Organization for Nuclear Research (CERN)	Switzerland	Anodes, anode panel assembly and test
Brookhaven National Laboratory	USA	Anodes, Interface boards, CRP assembly, installation, bottom CRP transport frames
Chicago University	USA	CRP assembly
LAPP Annecy IN2P3	France	CRP mechanical design, assembly, composite support frame design and procurement, superstructures design, automation system, installation
LPSC Grenoble IN2P3	France	CRP assembly, top CRP transport frames, installation, level meters
University of Wisconsin	USA	Bottom CRP support feet system design and procurement, installation
Yale University	USA	CRP assembly

# Chapter 4

## Charge Readout Electronics

### 4.1 Introduction

The time projection chamber (TPC) charge readout (CRO) encompasses the hardware systems necessary to amplify, digitize, and transmit the TPC ionization charge signals out of the DUNE vertical drift detector module (FD2-VD) detector module. This includes the front-end (FE) electronics (amplifiers, digitizers, digital controllers), power and data cabling, related cryostat feedthroughs, and power supplies.

The CRO as presented here does not include the electronics associated with the detection and recording of liquid argon (LAr) scintillation photons, called the light readout (LRO). The LRO is discussed in Chapter 6.

The FD2-VD top and bottom drift volumes will implement different CRO electronics in order to take maximal advantage of the different configurations of the two drift volumes. The top volume front-end (FE) electronics (“top drift electronics” or ), based on the design developed for the proposed dual-phase (DP) far detector module [15] design and used in , has both cold and warm components. Because of the long cable paths from the bottom charge-readout planes (CRPs) to the cryostat roof, the cold electronics (CE) CRO solution chosen for the bottom drift volume ( ) is the same as that used in the horizontal drift detector module (FD1-HD) design [7,34] and validated in . This CE design was developed to collect signals throughout the full depth range of the FD1-HD anode plane assemblies (APAs), and therefore to operate in the conditions and depth of the FD2-VD bottom .

The FD2-VD concept has developed out of the DP design implemented in ProtoDUNE-DP. The top drift volume is very similar to a DP detector with the CRP suspended from the cryostat roof. This scheme naturally allows using the existing DP electronics, which was designed to read anode strips and performed well in ProtoDUNE-DP. In particular, this FD2-VD design preserves straightforward access to the cryogenic amplifiers via signal feedthrough chimneys (SFT chimneys) at any time, without interfering with the detector operation, and keeps the digitization electronics completely accessible on the cryostat roof. Accessing the cryogenic electronics in the SFT chimneys

is a simple operation, which was demonstrated in ProtoDUNE-DP. This accessibility will also allow DUNE to take advantage of technological evolution and potential cost reductions, as has already been witnessed, for example regarding the Micro Telecommunications Computing Architecture ( $\mu$ TCA) digital components with the development of a 40 Gbit/s bandwidth capability since 2020.

Detector integration aspects are optimized according to the characteristics of the TDE and BDE configurations. The bottom drift CRPs lie close to the cryostat floor, supported by posts as described in Section 3.6. The top drift CRPs hang from the cryostat roof, supported by superstructures, from which the cathode modules are also suspended. The layout of the top CRPs is designed to facilitate access to the electronics via the cryostat roof. The weight of the TDE is supported by the SFT chimneys and does not affect the mechanical structure of the top drift CRPs. Since the top electronics is inside the SFT chimneys, no heat dissipates directly onto the CRP structures from the electronics components. In addition, the separation between the CRPs and the TDE will introduce fewer constraints on the installation schedule and simplify quality control (QC) procedures.

Because of the different layouts, risks are different between the top and bottom CRO electronics. In particular, the top CRPs would be exposed to any bubbles and/or dust contamination that may float towards the liquid surface during the detector filling. Either bubbling or dust could cause sparking to occur in the anode plane. Although this risk is low, the accessibility of the electronics provides definitive mitigation for for this risk and guarantees effective functioning of the TDE over a very long life span.

The bottom drift (cold) electronics (BDE) components are located below the bottom CRPs; the heat dissipation in this area was carefully studied [54], and no issues of local heat accumulation arose. The BDE is designed with a requirement of greater than 30 years of operational lifetime. The prototype BDE operated in LAr at ProtoDUNE-SP for over a year without any degradation in performance. A run with the final electronics is being planned. In addition, dedicated accelerated aging studies on the s and other key components are ongoing to ensure long-term reliability.

Adopting different solutions for the top and bottom drift volumes also takes advantage of a dedicated international R&D program started in 2006 that has provided resources and non-U.S. funding for the TDE. ProtoDUNE-DP demonstrated this technology at the level of 10k channels, a scale roughly 1/20 that of FD2-VD.

The scope of the CRP electronics CRO system includes the selection and procurement of materials for, and the fabrication, testing, delivery, and installation of the system.

## 4.2 Requirements

The TPC electronics system is designed to produce a digital record representing the waveform of the current produced by charge induction and collection on the strips.

The requirements/specifications for the top and bottom drift electronics are listed in Table 4.1, approved by the DUNE Executive Board, and are the same as commonly defined in the DUNE design reports for the FD1-HD and ProtoDUNE-DP electronics.

Table 4.1: CRO electronics requirements

Label	Description	Specification (Goal)	Rationale
FD-2	System noise	$< 1000 e^-$	Provides $>5:1$ S/N on induction planes for pattern recognition and two-track separation.
FD-13	Front-end peaking time	$1 \mu\text{s}$	Vertex resolution; optimized for approximately 5 mm anode readout spacing.
FD-14	Signal saturation level	$500\,000 e^-$ (Adjustable so as to see saturation in less than 10% of beam-produced events)	Maintain calorimetric performance for multi-proton final state.
FD-19	ADC sampling frequency	$\sim 2 \text{ MHz}$	Match $1 \mu\text{s}$ shaping time.
FD-20	Number of ADC bits	$\geq 12$ bits	Makes ADC noise contribution negligible (low end); matches signal saturation specification (high end).
FD-21	Cold electronics power consumption (in-LAr)	$< 50 \text{ mW/channel}$	No bubbles in LAr to reduce HV discharge risk.
FD-25	Non-FE noise contributions	$\ll 1000 e^-$	High S/N for high reconstruction efficiency.
FD-28	Dead channels	$< 1\%$	Minimize the degradation in physics performance over the $> 20$ -year detector operation.

Below is more information on the items (numbers correspond to Table 4.1):

- FD-2 System noise  $< 1000 e^-$ : total system noise seen by each CRP strip should be less than 1000 enc of noise. It is expected that random noise on the FE amplifier will be the dominant contribution to the total system noise.
- FD-13 Front-end peaking time of  $\sim 1 \mu\text{s}$
- FD-14 Signal saturation level  $\sim 500,000$  electrons: the largest signals correspond to events with multiple protons produced in the primary event, in particular, when the trajectories of one or more of those particles are parallel to the strips, causing the charge over a long path length to be collected within a short time period.
- FD-19 ADC sampling frequency  $\sim 2 \text{ MHz}$ : this value is chosen to match  $1 \mu\text{s}$  shaping time (the approximate Nyquist requirement).
- FD-20 Number of ADC bits  $\geq 12$ : the lower end of the ADC dynamic range is driven by the requirement that the ADC digitization not contribute to the total electronics noise. The upper end of the ADC dynamic range is defined by the signal saturation level. The two requirements with the specification for the total electronics noise results in the 12 bit ADC digitization requirement.
- FD-21 Cold electronics power consumption in LAr  $< 50 \text{ mW/channel}$ : CE power consumption must be low enough to prevent the occurrence of local heat accumulation.

- FD-25 Non-FE noise contributions  $\ll 1000 e^-$ : noise contribution from all non-FE noise sources should be much lower than the system noise requirement.
- FD-28 Dead channels  $< 1\%$ : detector components shall be sufficiently reliable so as to ensure that the number of dead channels does not exceed 1% over the lifetime of the experiment.

## 4.3 Top Drift Readout

### 4.3.1 System Overview

The top drift charge-readout system (TDE) is the outcome of a long R&D process, launched before DUNE and aimed at optimizing cost and performance. It is based on the design used in ProtoDUNE-DP [15]. Minor modifications and some optimizations were made to the design in 2021 to adapt it for the top anode plane of the FD2-VD module, which has a total of 245,760 readout channels.

The FD2-VD TDE was extensively tested in 2021 and 2022 in a series of cold box CRP tests, including tests of the two top drift CRPs that will be used in , and which match the final CRP channel layout and the final layout of the associated TDE readout system adopted for FD2-VD. Figure 4.1 illustrates the architecture of the TDE system. Each strip of the top drift CRPs is read by a system of front end (FE) cryogenic analog amplifiers that connect to external FE digital warm electronics through SFT chimneys in the cryostat roof.

The analog amplifiers are implemented in ASICs located on FE cards that are bonded to extractable blades, allowing servicing or replacement via a hot swapping procedure. Each card plugs into a cold flange at the bottom of its SFT chimney. Each FE card hosts four ASICs, each of which reads 16 channels.

The FE cards operate at the bottom of the SFT chimneys in close proximity to the CRPs. The nitrogen-filled inner volume of the SFT chimneys is separated from the cryostat and the external environment by a pair of vacuum-tight feedthrough flanges that dispatch signals and slow controls. The analog electronics is thereby completely shielded from the environment and operates at cryogenic temperatures.

The SFT chimney cold flanges define the interface to the CRPs. The adapter boards mounted on the CRPs are connected with flat cables to the connectors on the cold flange side facing the cryostat.

The FE cards, mounted on 2 m long blades, glide along the guiding rails inside SFT chimneys to plug into dedicated connectors mounted on the inner side of the cold flange (within the chimney volume). The FE card ASICs amplify the input signal and produce analog differential output signals carried by flat cables running along the blades up to warm flanges located near the top of the SFT chimneys. The warm flanges seal the chimney from the outside environment. They pass slow control and low-voltage lines to the FE cards inside and bring out the differential analog signals.

The SFT chimneys are designed explicitly to allow access to the FE cards during detector operation.

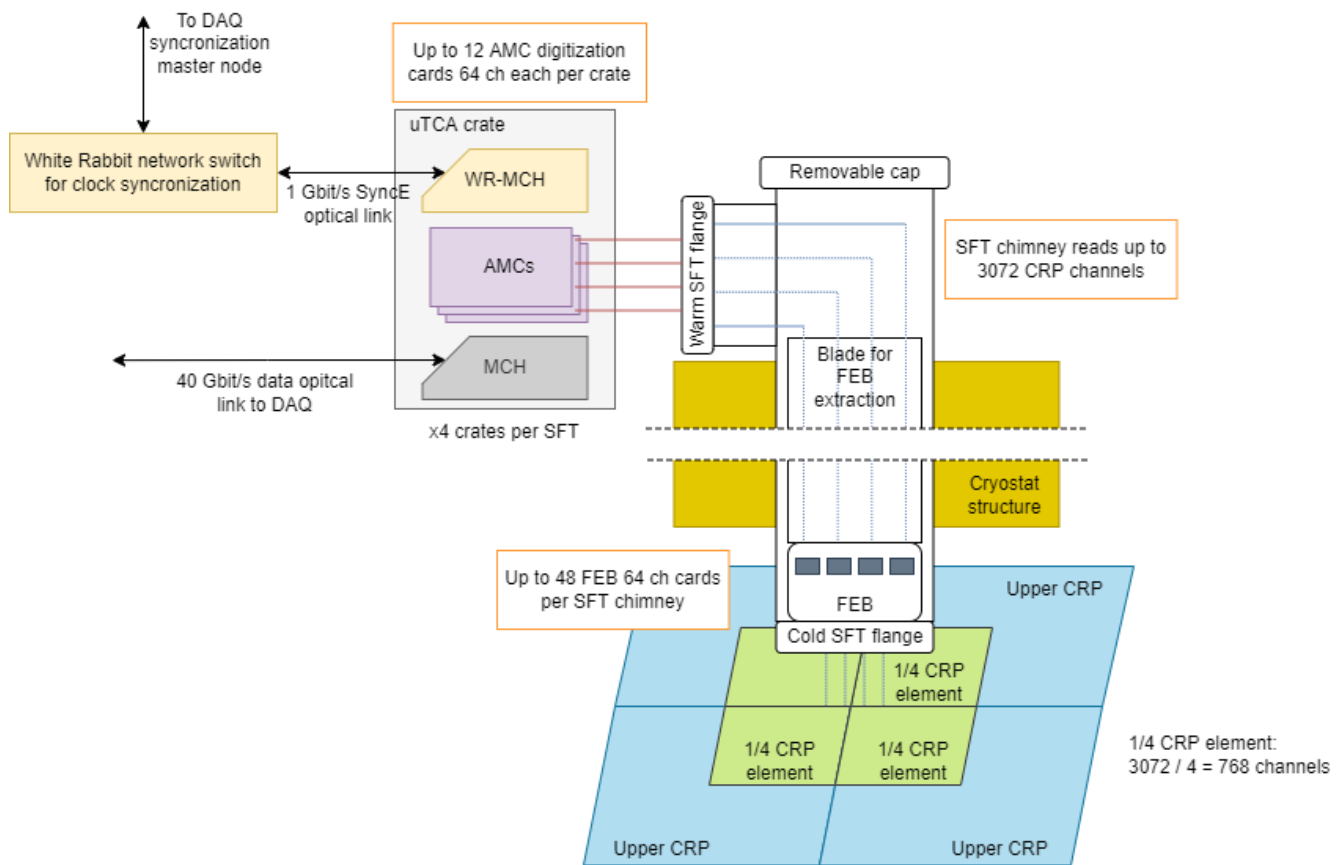


Figure 4.1: System architecture of the top drift readout electronics.

A top cap is removed to open the chimney inner volume, allowing extraction and re-insertion of the blade-FE cards assembly from the cryostat roof. During access, nitrogen flow is activated to prevent humidity from entering the signal feedthrough (SFT) inner volume. Moreover, replacement of a FE card can be executed via hot swapping without switching off the rest of the electronics, and without interfering with the detector operation.

A system of this design was successfully deployed and operated in 2019-2022 in ProtoDUNE-DP, where the FE cards were installed in groups of 10 in smaller-radius SFT chimneys.

The FD2-VD TDE system contains 105 SFT chimneys of two types. One type (positioned along the long edges of the cryostat), of which there are 21 on each side (42 total), each hosts 24 FE cards (SFT24). The other 63 (three rows of 21) each host 48 cards (SFT48). Except for the SFT48s at the ends, these larger ones are positioned above each intersection of four CRPs, and read 3072 channels from the eight CRUs. The end SFT48s read out half as many channels (1536). The SFT24s each read out four CRUs (1536 channels), except for those at the ends, which read out two (768 channels). Table 4.2 lists the counts.

The external warm flanges on a SFT chimney connect the amplified signals to the FE digitization system, located on the cryostat roof. Installing the digital electronics on the cryostat roof allows use of inexpensive  $\mu$ TCA electronics, a standard that is commonly used in the telecommunications industry.

The amplified signals from FE cards pass through the warm flange to the digitization cards (advanced mezzanine card (AMC)). The AMCs are hosted in  $\mu$ TCA crates and are connected to the warm flanges with shielded VHDCI cables. Each  $\mu$ TCA crate can host up to 12 AMC FE digitization units of 64 channels each. Therefore an SFT48 interfaces to four  $\mu$ TCA crates, except for those at the end, which interface to two.

Each  $\mu$ TCA crate also hosts a MicroTCA Carrier Hub (MCH) switch that supports 40 Gbit/s bandwidth via an Ethernet optical link connection to the back-end data acquisition (DAQ). AMCs send their data to the DAQ via the MCH by using 10 Gbit/s XAUI Ethernet lanes in the crate backplane. Given the 12 bit dynamics and 2 MHz continuous sampling of the signals, the occupancy of the link, assuming 12 AMCs operating simultaneously in each  $\mu$ TCA crate, corresponds to about 60% of the maximal MCH bandwidth. No data compression is thus required.

The design of the DAQ system on the receiving side of the Ethernet links is common to both far detector (FD) modules. The FE digitization system is coupled to a local timing distribution system based on the White Rabbit (WR) standard, which is connected to the DUNE timing system.

Each  $\mu$ TCA crate contains a WR end-node (White Rabbit  $\mu$ TCA Carrier Hub (WR-MCH)) that serves as the local synchronization source to the global reference clock for all AMCs hosted in the same crate. The  $\mu$ TCA crate contains a WR slave end-node card, a WR Lite Embedded Node (LEN) (Seven Solutions OEM WR-LEN), as a mezzanine card. The WR-LEN is a commercial off-the-shelf (COTS) component that runs on customized firmware to enable it to decode the trigger timestamp data packet received over the WR network, in addition to the WR synchronization packets. This firmware, developed for the integration of the WR-LEN in the WR-MCH, also allows for the distribution of both the timing and synchronization signals on dedicated lines of the

crate backplane to the AMC and the time-stamping data packets. The WR-MCHs are connected to the global timing via a network of dedicated switches.

Table 4.2: Top drift charge readout electronics: unit counts for final CRP and readout system configuration.

Item	Quantity
3.0 m x 1.7 m CRUs in the top drift	160
Anode channels per CRP	3072
Channels per FE card or AMC card	64
FE cards or AMC cards per CRP	48
Number of SFT	105
FE card slots per SFT	48 or 24
$\mu$ TCA crates	320
AMC cards per crate	12
WR-MCH	320
40 Gb/s data links	320
Anode channels in the top drift	245,760

### 4.3.2 Analog Cryogenic Electronics

The FD2-VD top drift cryogenic analog FE electronics and the SFT chimneys are similar to those implemented in ProtoDUNE-DP [15]. Figure 4.2 shows a synopsis of the analog chain including the ASIC and the analog stage (analog-to-digital converter (ADC) buffer ADA4940) integrated in the AMC card before the ADC. The LARZIC ASIC integrates a cryogenic Charge Sensitive Amplifier (CSA) and a differential output buffer stage acting as low-pass filter.

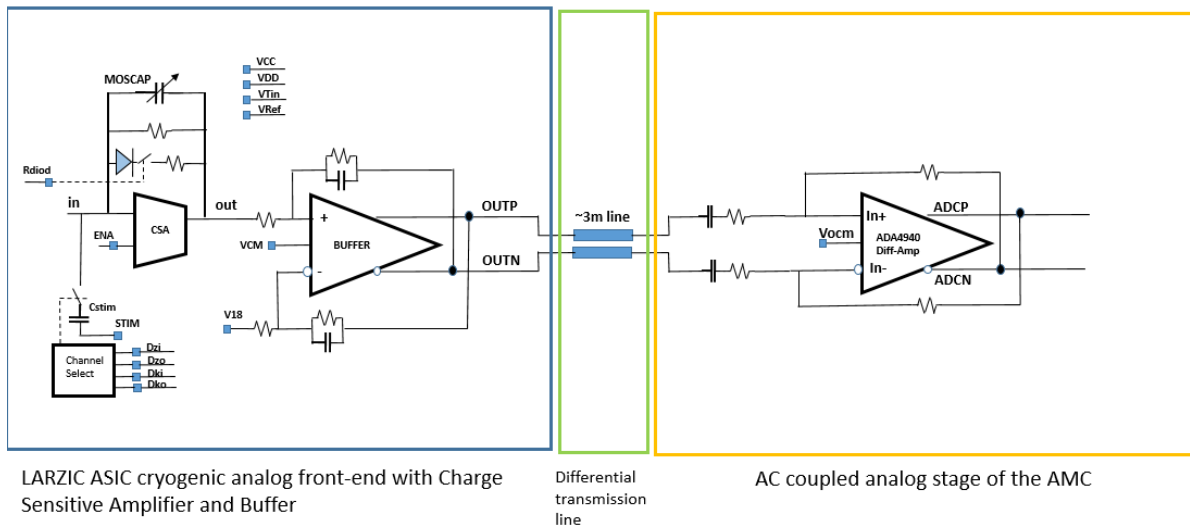


Figure 4.2: Synopsis of the TDE analog chain including the LARZIC ASIC and the analog stage (ADC buffer) present in the AMC.



### 4.3.2.1 Cryogenic ASIC amplifier

The cryogenic Charge Sensitive Amplifier (CSA) ASIC (LARZIC) is the principal component of the FE analog cards. Its design is based on 0.35  $\mu\text{m}$  technology, for which R&D began in 2006. The chips are produced at CMP<sup>1</sup> and AMS Full Service Foundry<sup>2</sup>.

This technology remains fully exploitable for production on the timescale of the DUNE far detector modules. Each ASIC contains 16 amplifier channels with differential line buffers and has a power consumption of 11 mW/channel. The main characteristics of the LARZIC ASIC are listed in Table 4.3).

Table 4.3: Top drift charge cryogenic LARZIC ASIC main characteristics and specifications

Label	Description
Technology	CMOS 0.35 $\mu\text{m}$
Channels per ASIC	16
Integrated components per channel	Charge sensitive amplifier + differential buffer
Peaking time	1 $\mu\text{s}$
Operation temperature	Typically around 110 K at the bottom of the SFT chimneys, the LARZIC/FE card can operate as well at LN2 temperature
Power consumption	11 mW/channel
ENC	<400 electrons at cold, < 600 electrons at warm
Conversion factor	14 mV/fC (including all the entire TDE analog chain ASIC + ADC buffer)
Calibration	Integrated charge injection system with embedded capacitors and the possibility of activating single channels or groups of channels
Crosstalk	<1%
Unipolar dynamics (ASIC)	Linear up to 400 fC, max signals up to 1200fC with dual-slope regime (used in dual-phase)
Bipolar dynamics (ASIC)	Linear up to +-200 fC
Bipolar dynamics (ASIC+ADC buffer)	Linear up to +-80 fC

The CSA has linear gain for input charges of up to 400 fC and a logarithmic response in the 400–1200 fC range. This double-slope behavior is obtained by using a MOSCAP capacitor in the feedback loop of the amplifier that changes its capacitance above a certain signal threshold. The MOSCAP yields a lower gain for input charges larger 400 fC. The feedback circuit includes also a selectable branch (Rdiode) with a resistor in series to a diode, acting over the discharge time. The activation of this branch in the feedback circuit guarantees similar discharge times in the

<sup>1</sup>Circuits Multi-Projets®, <https://mycmp.fr/>

<sup>2</sup>ams®, <https://ams.com/full-service-foundry>

dual-slope regime for signals smaller or exceeding the 400 fC threshold by keeping the RC of the feedback circuit at about 500 ns in both cases.

The possibility for a dynamic range larger than 400 fC was mainly developed for the DP application (with large electron multiplier (LEM) gain of at least 20) and is of much less importance for the FD2-VD, where the dynamics of the entire analog chain has been re-optimized to work in bipolar mode. In this configuration, the ASIC features a linear regime up to  $\pm 200$  fC, where the linearity is at the 1% level. The signal dynamic range is then limited to  $\pm 80$  fC by the ADC dynamics after accounting for the AMC analog stage.

The LARZIC output signals are transmitted on differential lines at  $120\ \Omega$  to the AMC analog input stage. The buffer integrated in the LARZIC produces positive and negative differential signals (Figure 4.3) separated by an adjustable positive offset (V18). These signals are then processed by the differential amplifier embedded in the AMC, which is AC coupled at the end of the transmission line.

Five independent DC supply voltages are supplied for the operation of the LARZIC ASIC: VCC (supply voltage of the differential buffer), VDD (supply voltage for the output stage of the CSA), VRef (reference voltage used by the cascode stage of the CSA), V18 (bias voltage applied to the buffer circuit to separate the signal branches), and  $V_{T_{in}}$  (supply voltage for the input transistor of the CSA). These voltages are typically 3.3, 3.3, 1.4, 1.8, and 2.2 V respectively. The ASIC can be completely disabled (switched off) with an external enable control level (ENA).

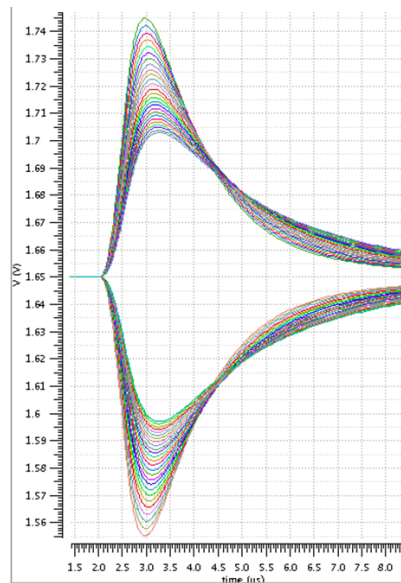


Figure 4.3: Examples of differential output signals from the LARZIC ASIC

Figure 4.4 shows the LARZIC ASIC chip die with its electrical connections together with an enlarged view of a single channel layout.

The LARZIC is equipped with a charge injection system with embedded capacitors ( $C_{stim} = 1$  pF). A slow control system allows selection of injection from an external signal injection source connected to the stimulus (STIM) line for single channels or for a desired configuration of channels (Figure 4.5). This configuration is defined with a Serial Peripheral Interface (SPI) bus including

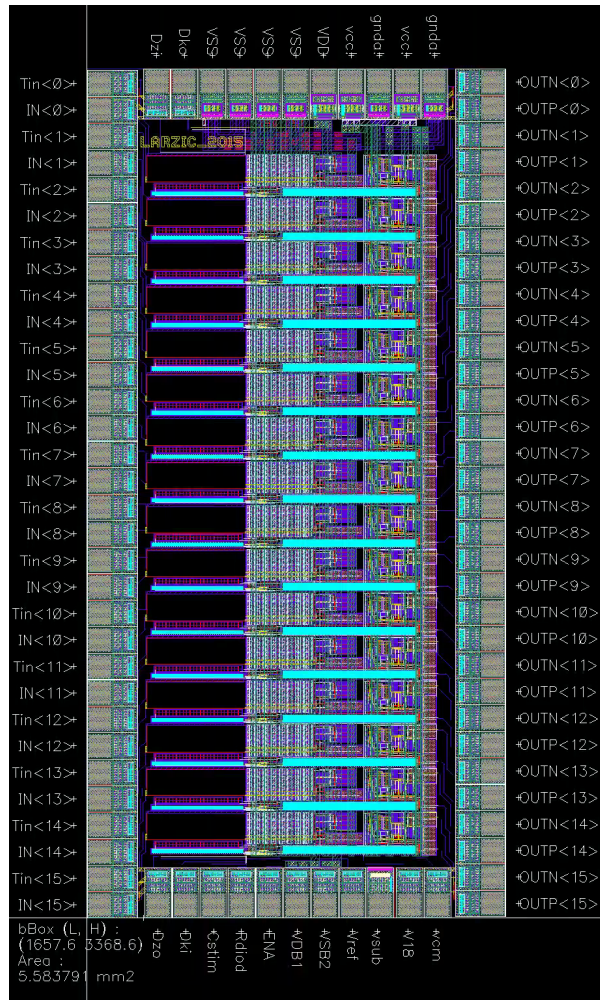


Figure 4.4: Top: LARZIC ASIC chip die with its electrical connections. Bottom: enlarged view of a single-channel layout ( $1100 \mu\text{m} \times 170 \mu\text{m}$ )

input and output data and clock lines (Dzi, Dzo, Dki, Dko). The option to activate injection single channels has also allowed measurement of the crosstalk, which was found to be negligible ( $<1\%$ ).

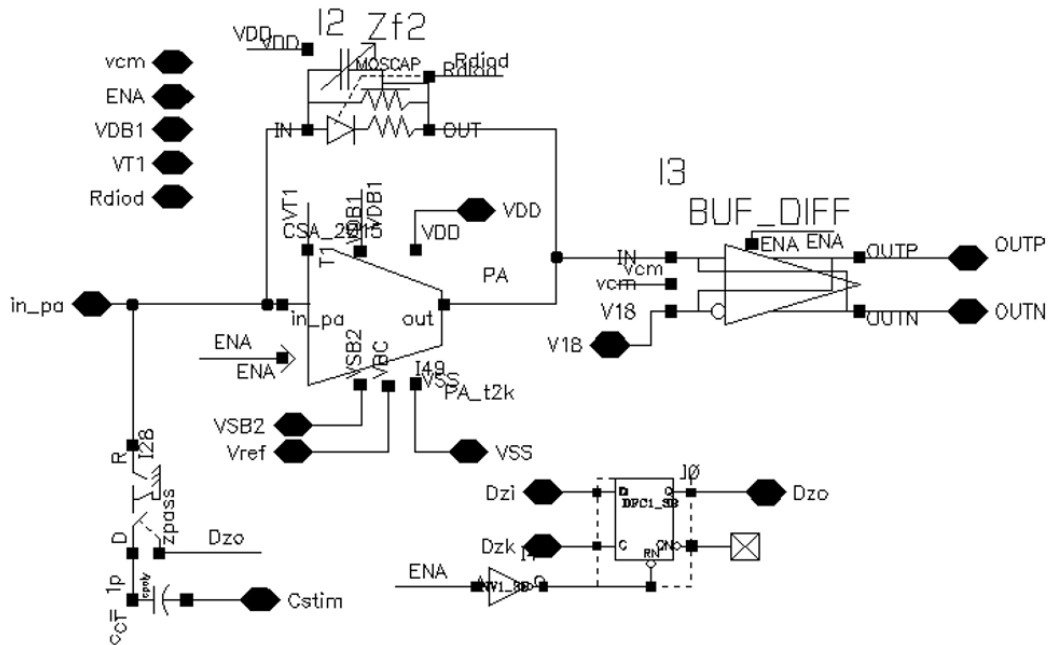


Figure 4.5: Details of the LARZIC charge injection system and channel selection system

Multiple LARZIC ASIC chips on the same FE card can be daisy-chained on the SPI bus using the input and output clock and data connections as shown in Figure 4.6.

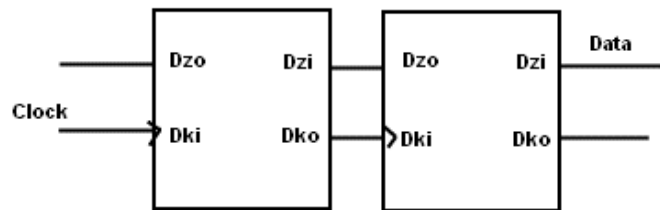


Figure 4.6: SPI bus daisy-chaining of multiple LARZIC ASICs

#### 4.3.2.2 Cryogenic FE cards

The FE cards amplify bipolar signals that are propagated with differential analog lines to the digitization system located in the  $\mu$ TCA crates on the cryostat roof.

Each cryogenic FE card holds four amplifier ASICs and a few passive discrete components for total of 64 readout channels. Common input low-voltage supply lines (VCC, VDD, VRef, V18 and  $V_{T_{in}}$ ) are distributed on the FE card to the four ASICs. Banks of blocking capacitors suited to work at cryogenic temperatures further filter the power lines, which are previously filtered by the low-voltage filtering and distribution system connected to the power supply so as to distribute the power to the chimneys.

Similarly, the configuration control signals (ENA, Rdioid) and the charge injection signal STIM are connected to the ASICs. The ASICs are daisy-chained for the clock and data SPI bus signals,

which define the global charge injection configuration of the 64 channels. Pull-up resistors mounted on the FE card define the default configuration of the FE card, in the absence of external ENA levels which otherwise have to be applied to the FE cards via the warm flange.

Two independent input connectors, each handling 32 signal channels, bring the CRP signals to the two groups of two ASICs. The output connectors include a 68-pin connector for the output of the second group of 32 channels. The output of the first group of 32 channels is on a larger output connector of 80 pins, which is also used for the connection of the low-voltage and control lines, and the external charge injection signal.

The FE card (Figure 4.7) originally included some front-end components, which in the case of the DP were high voltage (HV) rated and used to polarize the CRP anode strips (2.2 nF decoupling capacitors and 1 G $\Omega$  resistors, rated up to 3 kV).

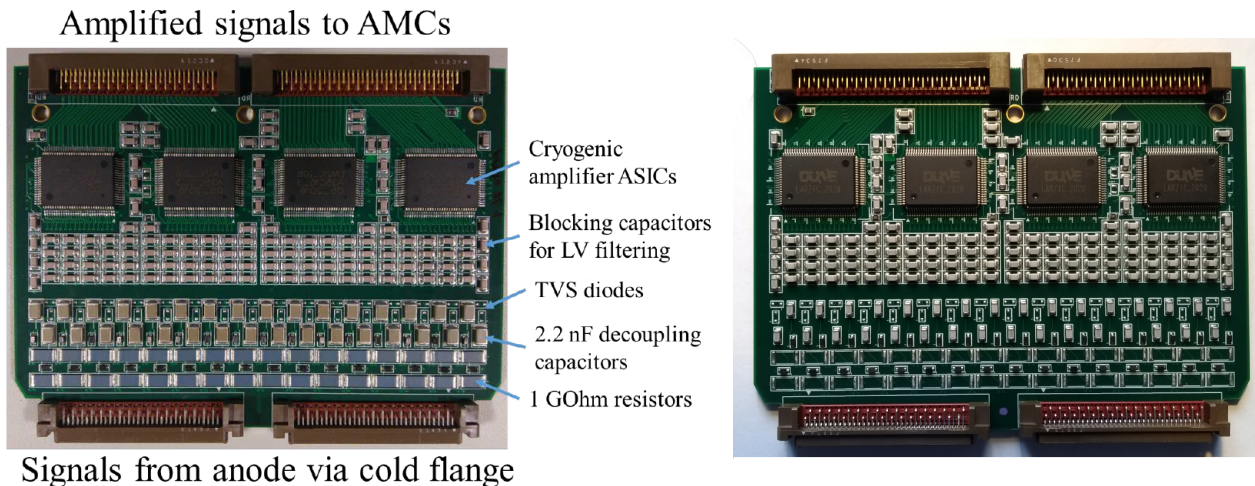


Figure 4.7: FE cryogenic amplifier card for the DP (left) and for the FD2-VD (right) configurations.

This configuration has been simplified for the FD2-VD since these polarization components are mounted on the adapter boards themselves and no longer needed on the FE cards.

An protection device (TVS diodes Bourns CDSOD323-T08LC) is also included in each input stage and is used to protect the amplifiers against discharges coming from the detector. The particular device was selected after extensively checking the performance of different ESD components, subjecting them to many discharges of a few kV and a stored energy similar to the one of the LEMs.

These components proved to be very efficient in the DP to protect against frequent LEM sparking. In general the FE card and ASIC design are very robust — for several years the FE cards have been manipulated with bare hands with no particular precautions, without causing any observable damage. Very minor modifications have been made to the configuration of the FE cards for their use in FD2-VD:

- The FD2-VD design has decoupling capacitors and biasing resistors as part of the anode system on the CRP's adapter board rather than on the input stage of each amplifier channel.

- The FD2-VD uses a simplified, customized version of the FE cards (Figure 4.7) where the decoupling and biasing components, rated for operation at several kV, have been removed.
- The FE cards still host ESD protection components with diode pairs, which are very effective since they were originally designed for the DP application to withstand LEM discharges at 3 kV.

### 4.3.2.3 AMC Analog Stage

As previously described, the AMC cards include an analog stage with a differential amplifier (ADC buffer ADA4940-2) before the ADC, see Figure 4.8.

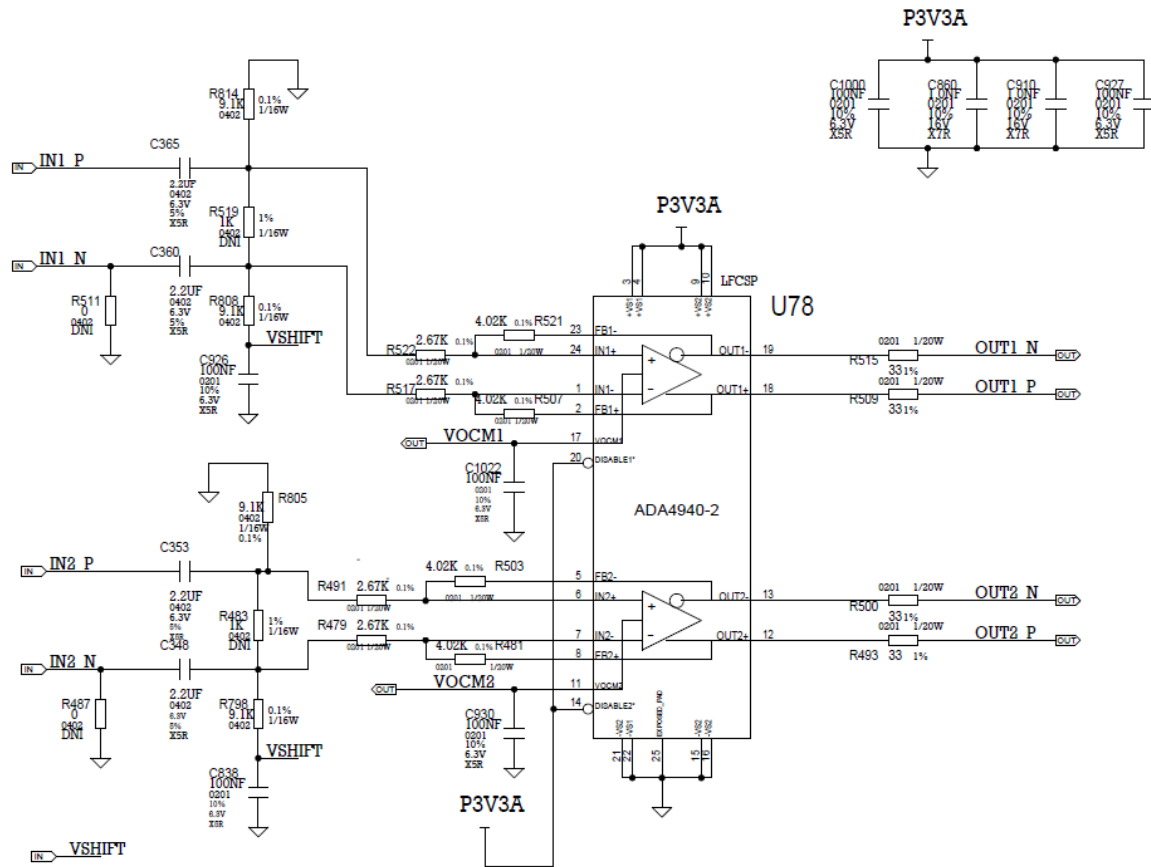


Figure 4.8: Two-channel schematic of the analog stage on the AMC with differential amplifiers connected to the signal transmission lines.

This stage is AC coupled to the signal transmission lines from the FE card. For the DP application, where the anodes had two identical collection views, the detector signals were unipolar and the analog stage was set with an external offset (VSHIFT) in order to fully exploit the ADC dynamics. For FD2-VD, VSHIFT is set at ground and the baseline is naturally placed at half of the ADC range (2048 counts) allowing for equivalent dynamics for the digitization of signals of both polarities.

### 4.3.2.4 Response Uniformity

The TDE analog chain features excellent channel response uniformity. Extensive calibration campaigns were systematically performed for the different production runs, demonstrating high uni-

formity.

A dedicated calibration card was developed for the first production run for ProtoDUNE-DP to test and calibrate the analog FE cards (see Figure 4.9). The calibration card hosts a bank of 32 (QuadTech 7600) air varicaps, mechanically trimmed and calibrated individually, that are tuned to  $<2\%$  within the nominal target value of 1.1 pF.

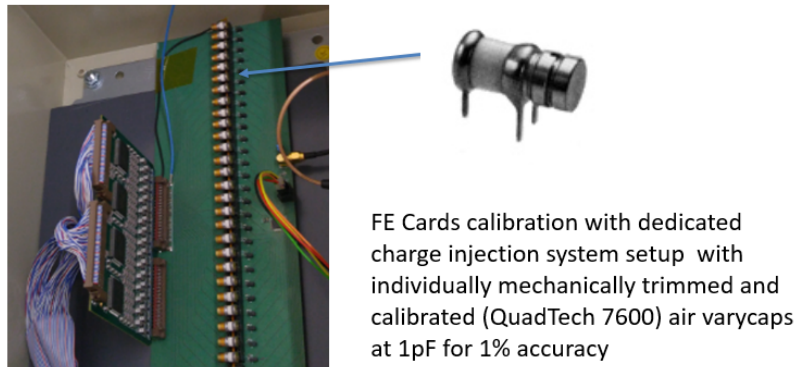


Figure 4.9: 32-channel charge injection system with calibrated varicaps, with a FE card connected to it via one of its input connectors.

A known charge can be injected into a given FE card channel by pulsing its corresponding capacitor with an external pulse generator. The channel selection is performed by a 32:1 analog MUX controllable via SPI. For this initial version of the injection card, the design featuring a single 32-channel output connector, only half of the channels could be tested at the same time, so a full test of each FE card required swapping the input connector of the card and retesting.

These tests resulted in (see Figure 4.10) a remarkable 2% uniformity across channels. A tiny systematic effect that accounts for this dispersion was found among the two blocks of 32 channels corresponding to the same injection card. The effect is related to the accuracy of the injection system itself. This result indicates that the intrinsic response uniformity at the level of the LARZIC ASIC is even better than 2%.

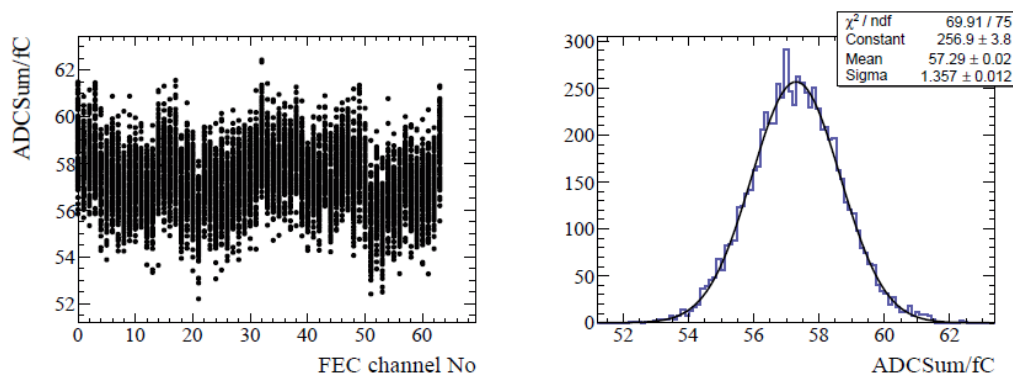


Figure 4.10: Superimposed calibration results for all FE cards produced to equip ProtoDUNE-DP as a function of the channel number on the card (1-64)

The calibration card allows for testing continuity of the entire analog chain, starting from the

input connectors of the FE card. The injected signals follow the same path as the signals coming from the CRP. A complementary technique enables ASIC calibration via charge injection through its internal calibration circuitry, as mentioned in Section 4.3.2.1.

This testing technique has been used throughout the prototyping program and will be used in FD2-VD to perform periodic calibration checks once the TDE system is installed. The ASIC calibration uses an SPI-like bus (clock and data lines) that can activate one or more channels of the FE card for injection. A calibration pulse, delivered to the warm flange and passed by a dedicated conductor on the flat cables, generates the injection charge. The protocol consists of passing 64 bit codes at 1 bit per clock cycle to enable (1) or disable (0) any combination of the 64 channels.

The direct ASIC injection tests will:

- check correct channel mapping. This can be done by addressing the channels via the SPI bus for two possible patterns (1 channel over 8 enabled and 1 channel over 64 enabled); and
- measure the linearity of the response and compare it to the reference template.

The two calibration methods, charge injection via the LARZIC ASIC or via the injection card connected to the FE card input, have yielded equivalent and excellent results, channel-by-channel, at the 1% level, enabling flexibility in the calibration policy. The ability to address single channels in different configurations has also allowed measurements of the crosstalk, which is  $< 1\%$ .

The calibration method that uses the external pulsing card has proved preferable at the level of the QC tests during production since it allows for integrity tests of the all connections in the FE card along the same signal path as for signals coming from the CRP. The calibration card was explicitly developed for this purpose.

In 2022 a new version of the calibration card that introduced several simplifications was designed and successfully tested. This design is also more compact and easier to produce. In particular, -embedded capacitors replace the trimmed varicaps, and by including two 32-channel output connectors, a full FE card can be tested in one run.

#### 4.3.2.5 TDE Readout Chain Optimizations for Vertical Drift

The TDE readout electronics, originally developed for the DP detector design, operated successfully in the (2016-2018) and in ProtoDUNE-DP (2019-2022). The configuration was optimized in 2021 for FD2-VD by adapting the signal dynamics to the bipolar signals produced by the two induction views. As discussed above, the modifications included the removal of the HV-rated decoupling and biasing components on the DP anode FE cards, with equivalent components now present on the anode adapter boards. The analog electronics was already bipolar except for the baseline shift applied at the ADC buffer, which was removed setting VSHIFT at ground. The AMC analog stage gain was increased to 4, yielding a total conversion factor of the analog chain of 14 mV/fC, which matches better expected signals ranges. New productions for all elements of the chain were carried out after these modifications.



The new configuration was extensively tested starting in summer 2021 at European Laboratory for Particle Physics (CERN), first with the tests in a dedicated integration facility, then with the first CRP in the cold box, and finally in late 2022 with the tests of the two top-drift CRPs built for FD2-VD Module 0.

Figure 4.11 shows examples of the measured response to charge injection signals in bipolar mode for the equivalent charge released by a minimum ionizing particles.

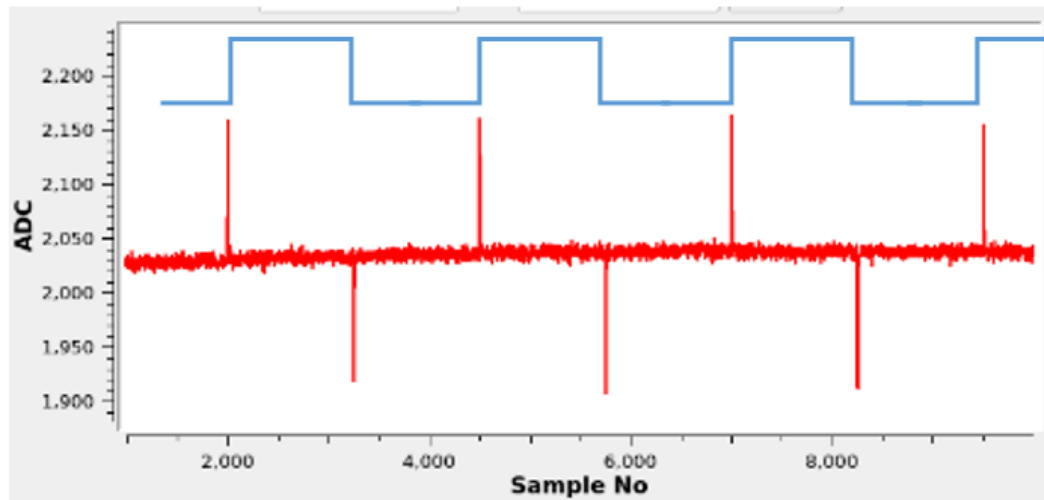


Figure 4.11: TDE response to bipolar charge injection signals. The amplitude of the square wave pattern produces injected charges equivalent to minimum ionizing particles (MIPs) for both polarities.

Additional developments centered on the digital electronics chain, with the successful conversion of the readout system to the 40 Gbit/s standard at the  $\mu$ TCA crates MCH connectivity, as described in Section 4.3.4.2.

### 4.3.3 Signal Feedthrough Chimneys

The FE cards are mounted on sliding blades that can be inserted into or extracted from the SFTs (see Figure 4.12).

The SFT chimneys, ultra-high-vacuum-sealed on the top and bottom, enable access to the FE analog electronics for repair or replacement while the detector is operational, without affecting the inner cryostat volume. This capability was well demonstrated during the operation of ProtoDUNE-DP (see Figure 4.13).

The metallic structure of the SFT chimneys acts as a Faraday cage, isolating the FE ASICs from environmental interference. The vacuum-tight feedthrough flanges at both ends of the SFT chimneys dispatch the signal and slow control lines to and from the FE electronics inside it. The bottom (cold) feedthrough flange isolates the inner volume of the detector from the chimney volume and interconnects the signals from the CRP to the analog FE cards. Figure 4.14 illustrates how the FE cards (shown dismounted from their blades) are plugged into the top side of a cold flange.

The (warm) feedthrough flange at the top seals the chimney from the outside environment, passes

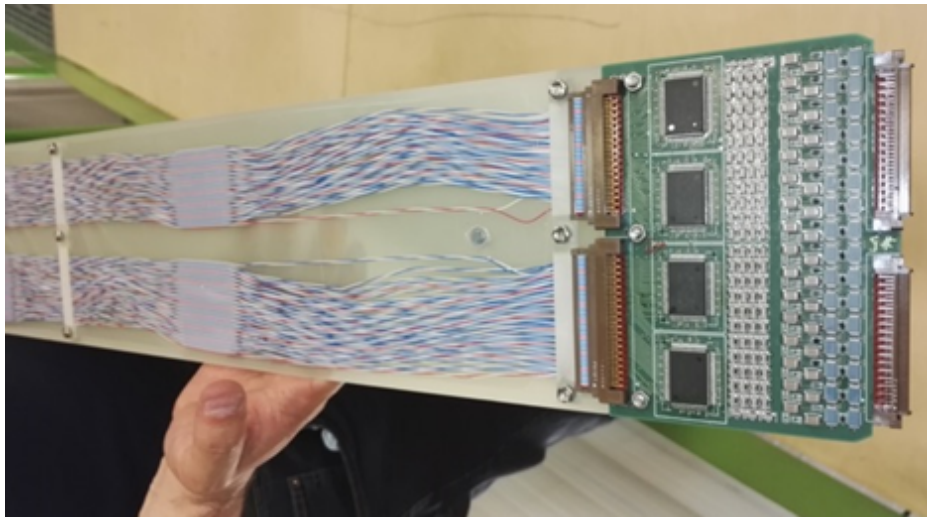


Figure 4.12: A FE cryogenic amplifier card mounted on a SFT sliding blade.



Figure 4.13: Access to a FE cryogenic amplifier card in a SFT chimney.

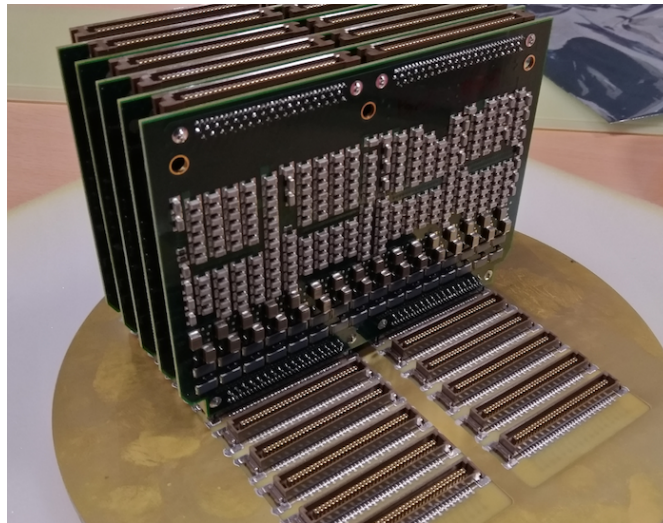


Figure 4.14: FE cards (seen from the chimney side and dismounted from the blades) plugged into the top side of a ProtoDUNE-DP cold flange.

the low-voltage and control lines to the enclosed FE electronics, and feeds out the differential analog signal lines from the FE amplifiers (see Figure 4.15).

Twenty power supply and filtering/distribution units are distributed along the cryostat on the detector electronics mezzanine to feed the SFT chimneys. A similar number of calibration/control boxes are also arranged on the mezzanine.

Based on ProtoDUNE-DP experience and optimization of the cryostat design, the 63 roof penetrations (three rows of 21) for the inner FD2-VD chimneys (those not along the sides) were increased to 526 mm diameter and the chimneys have been configured to host up to 48 FE cryogenic cards, for a maximum of 3072 readout channels per chimney. The chimneys located along the cryostat long sides (21 penetrations per side), host only 24 FE cards each and fit into smaller penetrations of 381 mm diameter. This arrangement accommodates a total of 105 chimneys (see Figure 4.16), reading 245,760 channels.

Both chimney designs use the same warm flanges, each serving a set of 24 cards. The larger chimneys have two warm flanges in a V-shape configuration. Figure 4.17 shows 3D models of the chimneys, including the warm flanges, as well as a bottom view with the cold flange removed to show the location of the FE cards.

The design of the 24/48 card chimneys was developed in 2022. Thermal simulations were done and prototypes for the two sizes are being built. These prototypes will be tested and characterized in a dedicated test-bench environment, in parallel with FD2-VD Module 0 operation. The cryostat is already equipped with 10-card chimneys from ProtoDUNE-DP and its roof structure cannot be modified to host the new larger chimneys.

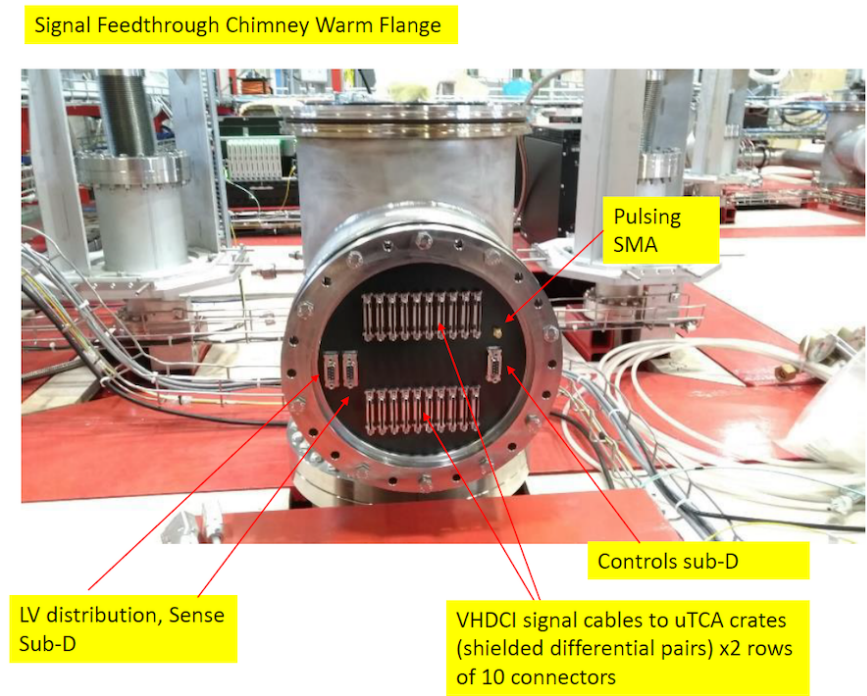


Figure 4.15: Warm flange of a SFT chimney in ProtoDUNE-DP

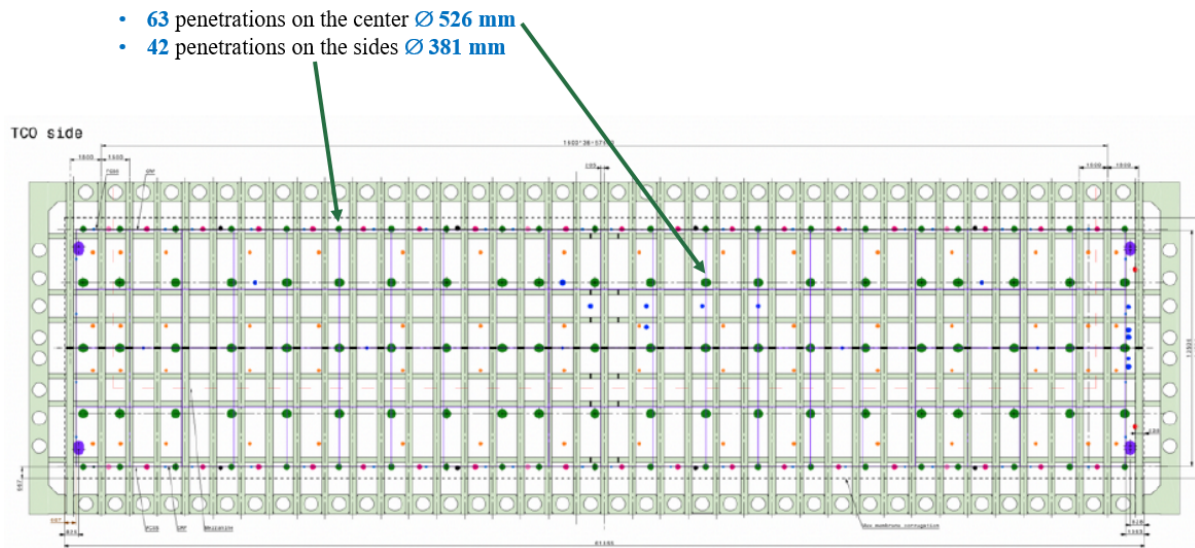


Figure 4.16: Cryostat roof layout including the location of the top drift SFT chimneys.

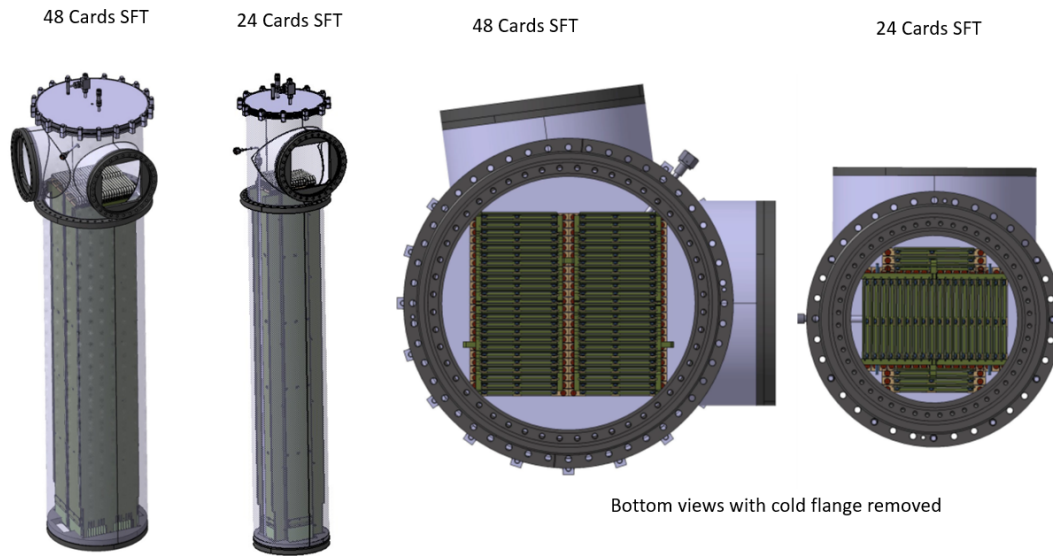


Figure 4.17: CAD models of the FD2-VD chimney designs for 24 and 48 cards. In the views at left, the chimneys are transparent to show the blades inside and the FE cards plugged into the cold flange at the bottom. The two projections at right are bottom views where the cold flange has been removed to show the position of the FE cards (in green).

### 4.3.4 Digital Front-end

The warm digital electronics, located on the cryostat roof, digitizes the analog signals coming from the SFT chimneys and transmits them to the DAQ system.

#### 4.3.4.1 AMC Digitization Boards

Each  $\mu$ TCA crate can host up to 12 CRO AMCs. The configuration planned for the TDE readout includes 12 AMCs in each crate. Each card (see Figure 4.18) has eight Analog Devices AD92574<sup>3</sup> ADC chips, two dual-port memories, and a field programmable gate array (FPGA) (Altera Cyclone V<sup>4</sup>) on board.

The components were chosen to meet functional design requirements and technical criteria such as cost, chip footprint, power consumption, and ease of use [15].

The FPGA provides a virtual processor that handles the readout and data transmission. Given the programming flexibility provided by the firmware, which can be flashed to all AMCs via the crate network connection, this digital FE stage can also analyze and compress the data before transmitting them over the network. Figure 4.19 shows a schematic diagram of the AMC digitization board.

The AMC generates a continuous stream of data for each readout channel. Each AMC has 64 channels and digitizes the signals coming from one analog FE card. The AMCs can be programmed in different operating configurations, offering quite a bit of flexibility: sampling can be performed

<sup>3</sup>Analog Devices, [www.analog.com](http://www.analog.com)

<sup>4</sup>Altera Cyclone®, <https://www.intel.com/content/www/us/en/programmable/b/cyclone-v.html>

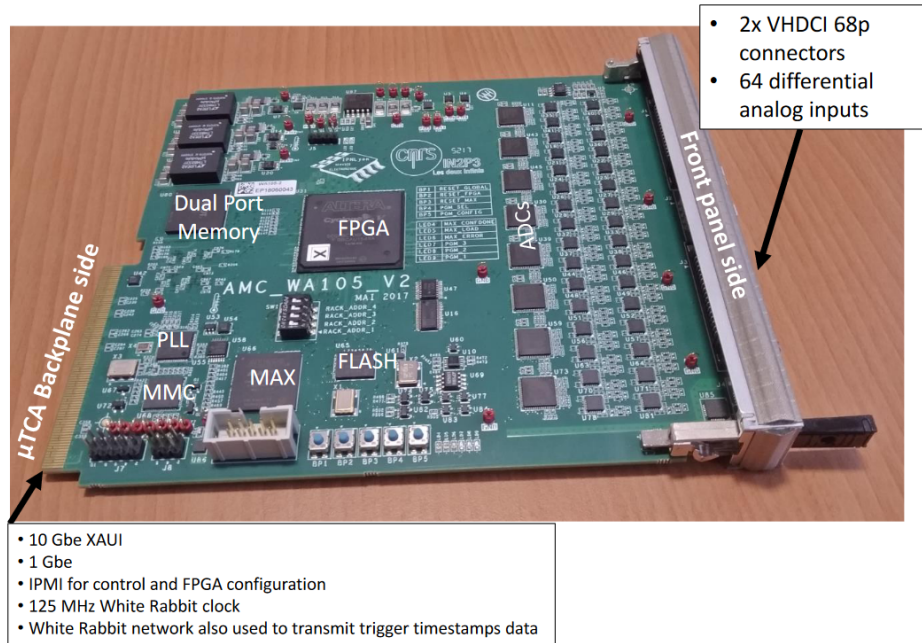


Figure 4.18: A front-end  $\mu$ TCA digitization card (CRO AMCs): the two VHDCI connectors on the right attach to the cables that bring analog signals from the warm flange to the AMC.

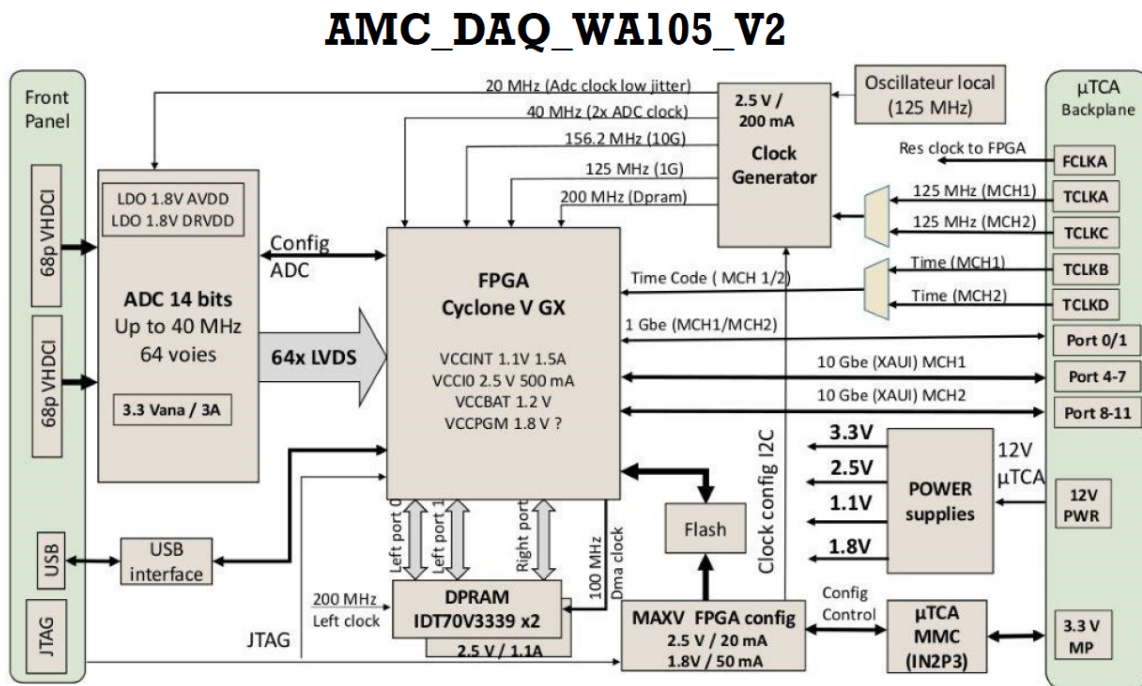


Figure 4.19: Schematic diagram of the AMC digitization board.

either at 2.5 or at 2.0 MSPS; data can have 12 bit or 14 bit dynamics; data compression may be implemented or not; the AMCs can acquire drift windows based on external triggers (external trigger mode) or can simply continuously stream all the sampled data to the DAQ system.

For the final AMCs output, data acquired at a given resolution/sampling rate are down-sampled in the FPGA. This capability provides flexibility in the operating conditions. For instance, when operating in the 2.5 MSPS sampling mode, data are acquired at a sampling rate a factor of eight higher, then down-sampled in the FPGA to 2.5 MHz. Similarly, data with 12 bit dynamics are produced by selecting only the twelve most significant bits from each digitized 14 bit sample. In the running configuration adopted for ProtoDUNE-DP, final sampling was done at 2.5 MSPS, 12 bit. These 12 bit data could then be losslessly compressed using an optimized version of the Huffman algorithm, or kept uncompressed, and in both cases buffered and organized into frames for network transmission in external trigger mode. The configuration planned for FD2-VD operation is simpler; it is based on a 2.0 MSPS final sampling rate, 12 bit dynamics, and continuous streaming with no data compression applied.

For the FD2-VD, the ADC dynamics has been optimized to deal with bipolar signals by removing the level offset used in ProtoDUNE-DP. Each AMC card has 10 Gbit/s individual connectivity to the backplane of the  $\mu$ TCA crate. Each  $\mu$ TCA crate contains a network switch, MCH, through which data collected from the hosted AMC cards are sent to the DAQ. The timing synchronization of the AMCs is achieved via a WR-MCH module (also housed in the crate) connected to a WR network, which ensures the last stage of the timing distribution at the level of the FE units. The MCH and WR-MCH require one optical fiber link each.

ProtoDUNE-DP functioned with MCHes operating at 10 Gbit/s. In this initial design, where the connectivity of each crate was limited to 10 Gbit/s, lossless Huffman data compression in the AMCs was used to ensure the necessary bandwidth for continuous streaming from ten AMC cards to the DAQ system.

Starting in 2021, the readout system for the cold box tests used the upgraded 40 Gbit/s connectivity on each  $\mu$ TCA crate. The cold box tests of the top-drift CRPs in 2021-2022 were conducted by reading the AMC in external trigger mode, without compression, similar to the operation of ProtoDUNE-DP. The new uncompressed operation mode for the cold box however profited of the final 40 Gbit/s connectivity, which does not have bandwidth limitations.

The TDE baseline design has relied since the beginning on Ethernet links and data transmission in UDP packets. Beyond its original use in the TDE, in 2022 the DAQ design evolved to adopt this readout scheme for the DUNE detectors.

Continuous streaming firmware for the AMCs was developed by the TDE in 2022, using the UDP data format agreed to by the DAQ consortium at the Preliminary Design Reviews (s).

#### 4.3.4.2 $\mu$ TCA crates

In 2020 the commercial MCH technology had evolved, without increased costs, to 40 Gbit/s connectivity. The 40 Gbit/s links provide enough bandwidth to comfortably support continuous data streaming from each crate (768 readout channels) without the need for any data compression or

zero skipping. This is the baseline operation mode for the top drift electronics.

The use of 40 Gbit/s data links for each crate was extensively tested in April-July 2021 and it has been systematically implemented since the first CRP cold box test in fall 2021. It has now been validated as the reference design for FD2-VD. Figure 4.20 shows a TDE  $\mu$ TCA crate equipped with a 40 Gbit/s MCH.



Figure 4.20:  $\mu$ TCA crate with a 40 Gbit/s MCH.

In order to fully exploit the new MCHs, the cold box also implemented a dedicated fiber network infrastructure in 2021 (see Figure 4.21) supporting a total bandwidth up to 240 Gbit/s and up to five  $\mu$ TCA crates for the full TDE tests on CRP-2 and CRP-3. Customized optical patch cables were developed to connect the crates to this infrastructure. This was the first large-scale  $\mu$ TCA 40 Gbit/s system to operate anywhere in the world.

#### 4.3.4.3 Front-end Timing Distribution System

The last stage of the TDE timing distribution at the level of the FE units uses a WR network that combines the synchronous 1 Gbit/s Ethernet (SyncE) technology with the exchange of (V2) packets to synchronize clocks of distant nodes to a common time while automatically compensating for the propagation delays. The system is fed by a high-stability Global Positioning System (GPS) disciplined oscillator (GPSDO) providing a clock reference signal to be distributed over the physical layer interface of the WR Ethernet network.

The network topology uses specially designed switches that have standard IEEE802.1x Ethernet bridge functionality with additional WR-specific extensions to preserve clock accuracy. Time and frequency information is distributed to the nodes on the WR network via optical fibers.

The WR protocol automatically performs dynamic self-calibrations to account for any propagation delays and keeps all connected nodes continuously synchronized to sub-nanosecond precision, independently of the network topology and changes in environmental conditions. The WR Ethernet network can be also used to transport data other than the PTP packets used for synchronization, which occupy a very small bandwidth, e.g., to transmit the data containing the WR timestamps of external trigger signals. The AMCs use these timestamps to select the drift-window data samples starting at the the time of the external trigger.



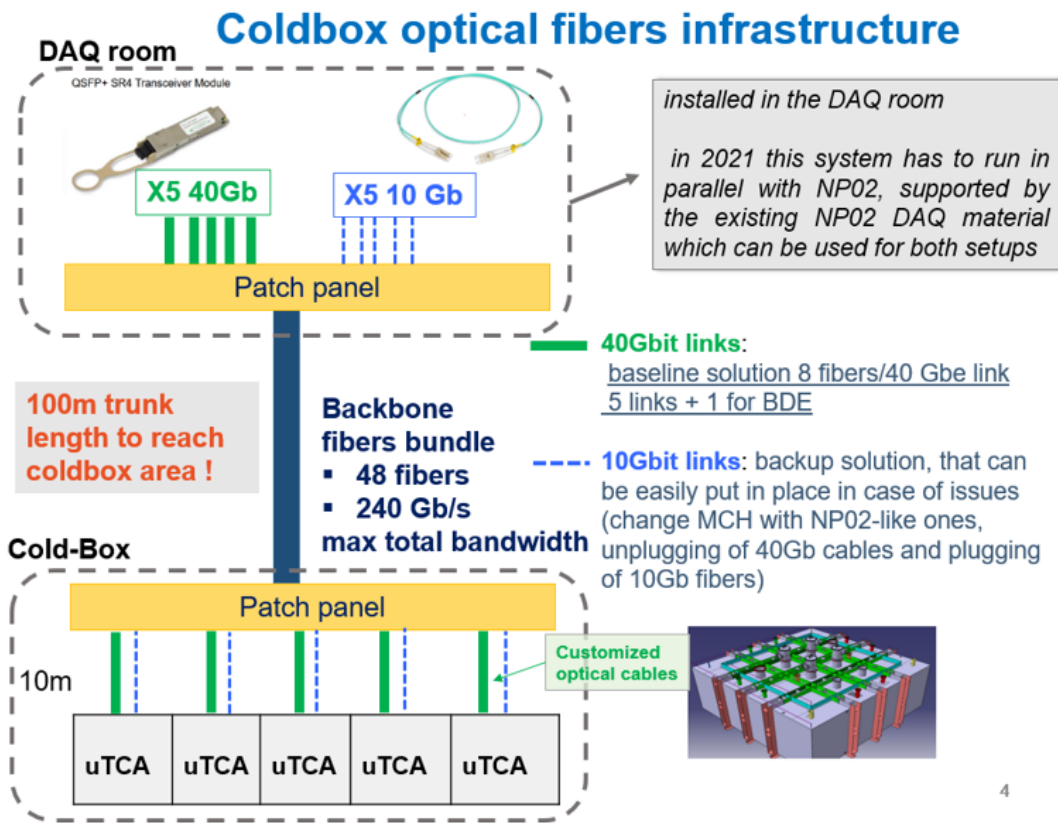


Figure 4.21: Cold box fiber network infrastructure supporting a system of five  $\mu$ TCA crates with 40 Gbit/s MCH for the tests of the full CRP TDE.

The first WR switch connected to the DUNE timing system acts as the WR network grandmaster (WR grandmaster), and it is connected via 1 Gbit/s optical links through a cascade of secondary WR switches to the WR end-node slave cards (see Figure 4.22). A WR end-node slave card is present in each  $\mu$ TCA crate (WR-MCH) and it is used to keep the AMCs synchronized to the reference time signals and to distribute timestamp data to them.

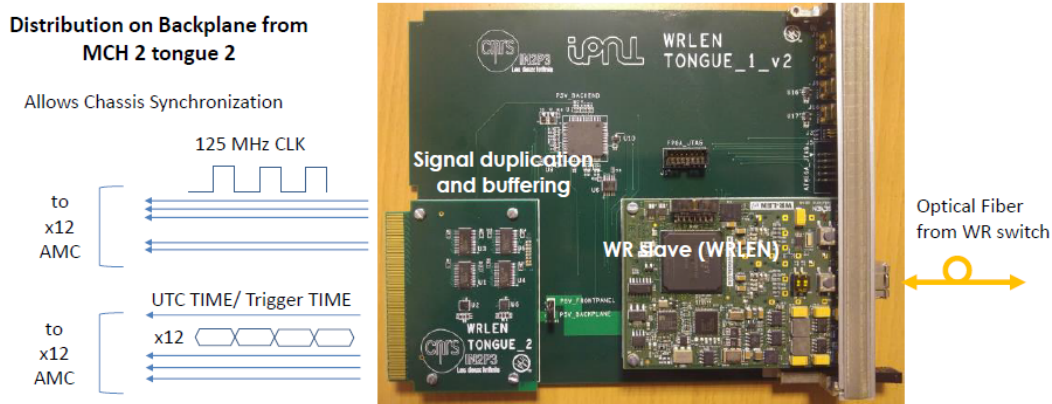


Figure 4.22: WR end-node slave card.

The WR end-node slave card is a  $\mu$ TCA board into which the WLREN (commercial WR end-node) mezzanine is plugged. This card occupies the second MCH slot and provides power to the WRLEN via standard  $\mu$ TCA facilities. It delivers the signals  $WR_{clock}$  (125 MHz) and  $WR_{DATA}$  for synchronization to each AMC via dedicated lanes on the  $\mu$ TCA crate backplane.

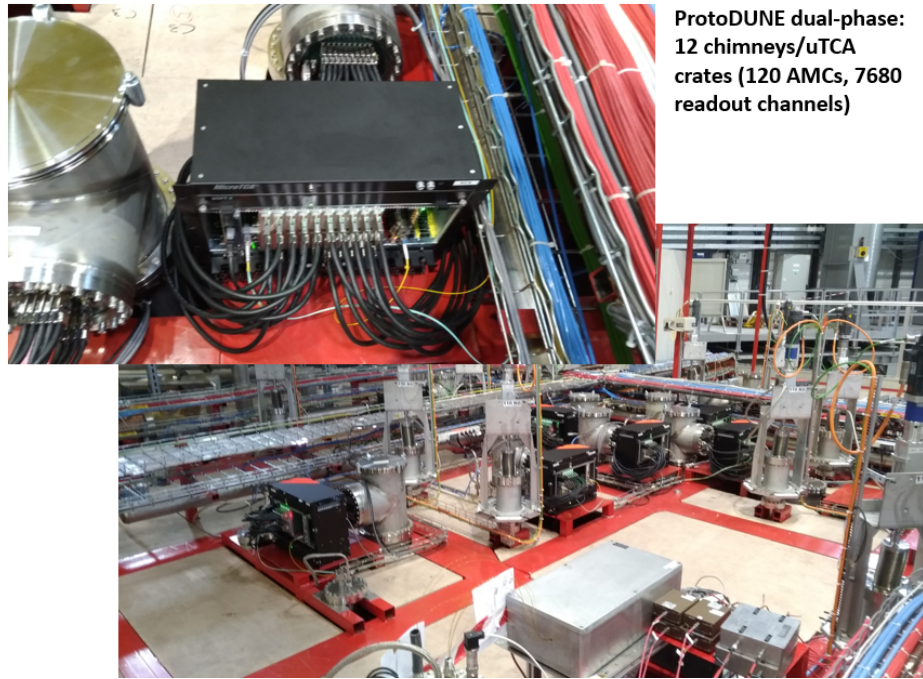
### 4.3.5 Performance in ProtoDUNE-DP

The elements of the TDE readout chain operated reliably in the WA105 DP demonstrator (2016-2017) and ProtoDUNE-DP (2019-2022). These elements are very similar to those planned for the FD2-VD TDE apart from the minor modifications previously described.

All the components had undergone very rigorous QC procedures before installation and demonstrated reliability over extended time periods with no failures. The WR time distribution chain in NP02, for instance, was in continuous operation with no interruptions from 2019 to 2022. Figure 4.23 shows the charge readout system on the ProtoDUNE-DP cryostat roof and Figure 4.24 shows some cosmic ray events that it read out. During ProtoDUNE-DP operations, 100% of the channels were active.

The ProtoDUNE-DP cards operated with a typical intrinsic noise around 600 electrons. Overall noise levels in ProtoDUNE-DP were dominated by environmental conditions inside the cryostat related to grounding imperfections of the slow-control connections at their dedicated cryostat flanges (HV, temperature probes, cameras, and CRP instrumentation). Strip capacitance for the FD2-VD application is lower than in the DP design. The electronics is well suited to reading strips in this capacitance range.

The ProtoDUNE-DP electronics, despite a higher gain (from the LEM micro-pattern detectors operating in the gas phase), received lower-amplitude input signals than those that have been produced by the CRPs developed for FD2-VD. During ProtoDUNE-DP data collection, the gain

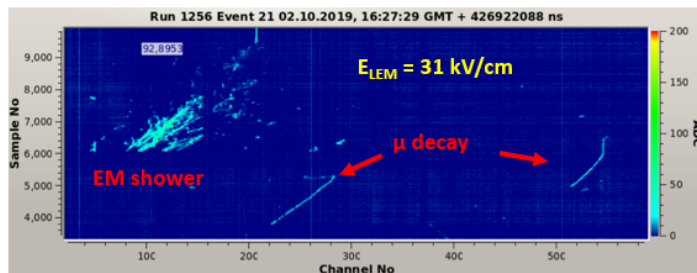


ProtoDUNE dual-phase:  
12 chimneys/uTCA  
crates (120 AMCs, 7680  
readout channels)

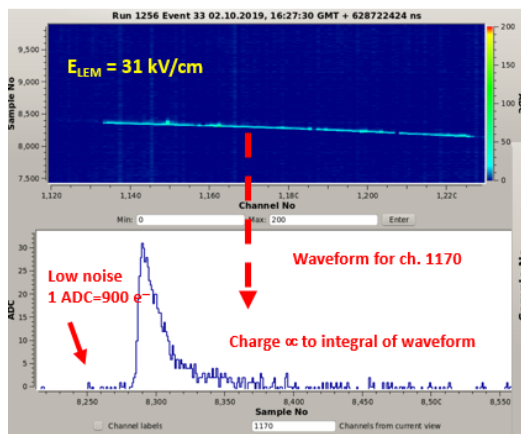
Figure 4.23: Charge readout system on the ProtoDUNE-DP cryostat roof.

Cosmic ray events  
in protoDUNE dual-phase

*Electromagnetic shower + two muon decays*



*Horizontal muon track*



*Multiple hadronic interactions in a shower*

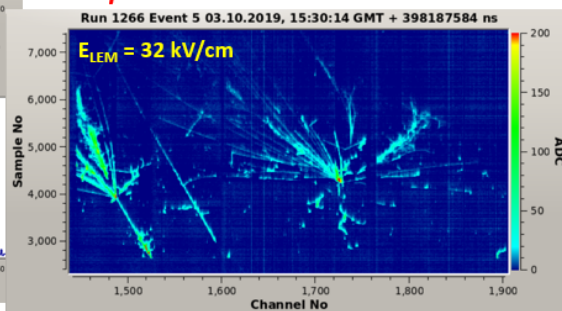


Figure 4.24: Cosmic ray events acquired with ProtoDUNE-DP

was limited to 6. Several factors conspired to erode its signal amplitude: that fact that two collection views shared the signal, a finer strip pitch, and inefficiencies related to the extraction of the electrons into the gas phase and their collection on the anodes. The performance of the TDE in the 2021 and 2022 cold box tests (Section 3.8.2) has in fact surpassed that of ProtoDUNE-SP in terms of noise and signal amplitude.

ProtoDUNE-DP operated in two runs: Run1 (July 2019 - September 2020) and Run2 (September 2021 - March 2022). Before Run2 the cryostat was emptied to replace the HV extender delivering 300 kV to the cathode, because it had developed a short circuit to the field cage at the beginning of Run1. Run2 included the stability tests of the HV distribution system designed for FD2-VD. Operating the TPC at the design voltage of 300 kV provided the opportunity to observe 6 m long tracks of cosmic ray muons crossing the entire anode-to-cathode drift length. For this demonstration, the ProtoDUNE-DP readout electronics was used with an anode of 1 m<sup>2</sup> active surface, equipped with a grid for the extraction of ionization electrons into the gas phase, but without LEMs for gas amplification. In this configuration of charge-sharing among readout views and using narrower strips, the signal amplitude was approximately four times smaller than in the FD2-VD configuration. Data for this observation were collected with an electron lifetime in LAr of about 2 to 3 ms, to be compared to a maximum drift time of 3.7 ms in ProtoDUNE-DP.

Despite these limitations, thanks to the good performance and the low noise achieved by the TDE electronics, a large sample of clean cosmic ray tracks was collected (over 1M events and 120 TB of data) and successfully reconstructed. Figure 4.25 shows examples of cosmic ray events collected in these conditions. They represent the operation of a LArTPC over the largest drift distance used so far.

### 4.3.6 Cold box Tests of the TDE

Starting in fall 2021, the TDE readout chain has undergone a very intensive campaign of qualification tests along with the CRP prototypes both at warm in a Faraday cage and in the cold box. In the first tests, CRP-1 was equipped with both TDE and BDE electronics. A modified setup, the CRP-1b, included grounding improvements and the installation of an isolation transformer.

The first CRP with the final channel layout and strip orientations (CRP-2) was built for the top drift layout and tested in the Faraday cage and in the cold box in June-July 2022 (Section 3.8.2.1). The second “final” module (CRP-3, Section 3.8.2.2) was also tested in both the Faraday cage and the cold box in September-October 2022. CRP-2 was tested for a second time in the cold box in October-November 2022 after some corrections to the anode boards. These tests concluded the qualification campaign of the CRPs and TDE for the top drift volume of FD2-VD Module 0.

During this campaign, the CRPs were mounted to the cold box roof and the assembly was used in both the warm and cold tests. The TDE readout chain was installed and dismantled about 20 times throughout this process with no deterioration. This provided an excellent opportunity to develop and validate installation procedures, and also demonstrated the robustness of the components. A graphical timeline of all these milestones and achievements is presented in Figure 4.26.

After defining the required adaptations relative to the DP design, the new components for the TDE cold box test, listed below, were procured in spring 2021 and extensively tested before

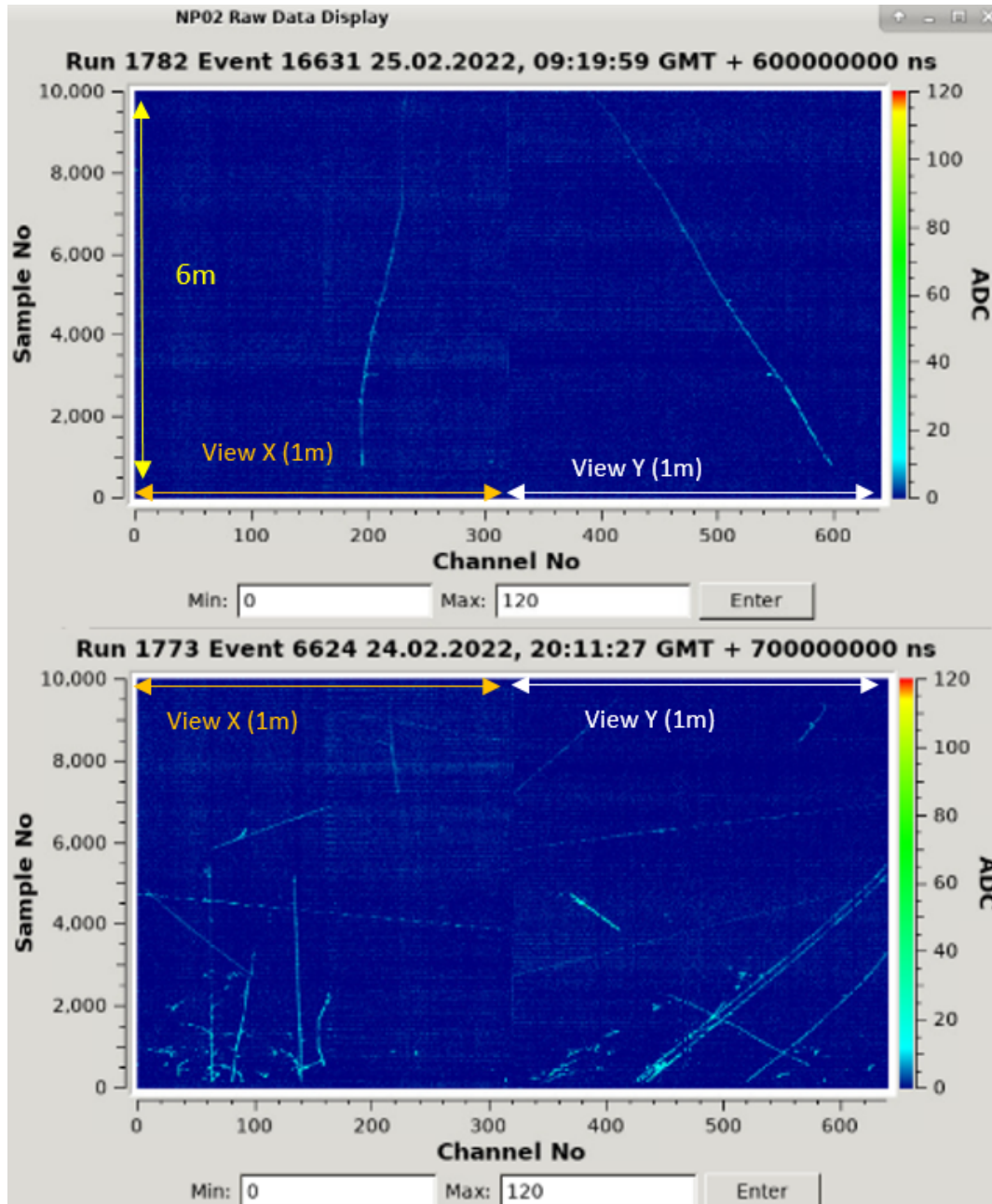


Figure 4.25: Cosmic ray tracks acquired with ProtoDUNE-DP demonstrating 6 m drift

**Timeline of Top Drift Electronics activities and achieved milestones**

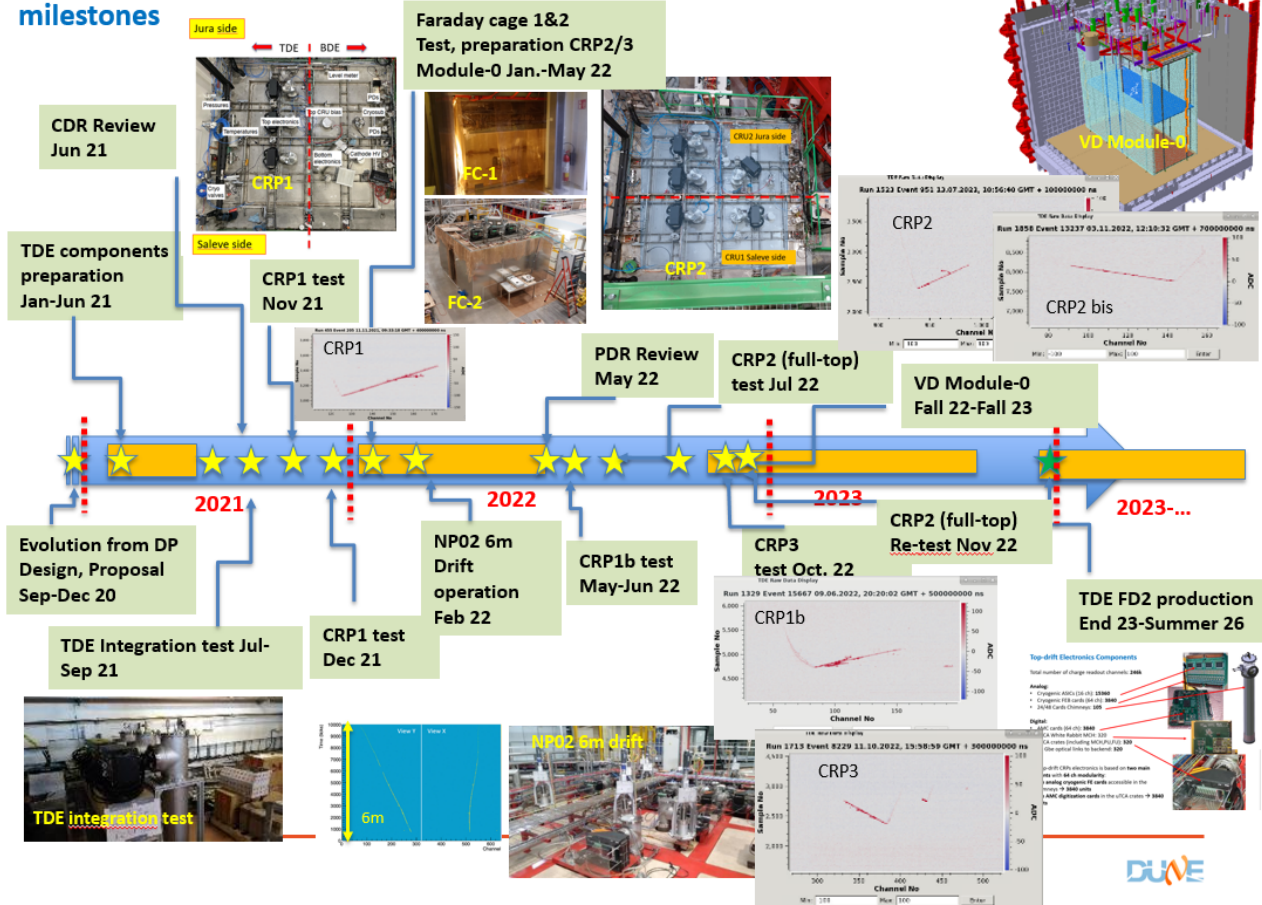


Figure 4.26: Timeline of the 2021-2022 TDE tests.

installing them in the TDE integration test at CERN a few months later. The following lists the modifications:

- New production of ASICs,
- New front-end cards,
- Modified digitization cards for bipolar signals
- New timing cards and a new cold box-dedicated timing distribution network, independent of infrastructures in the NP02 experimental area,
- New MCHs in  $\mu$ TCA crates at 40 Gbit/s and associated fiber network infrastructure,
- New low-voltage generation and distribution system, independent of NP02,
- New calibration system, also usable for FD2-VD,
- New DAQ/network system setup,
- New cold/warm flanges,
- VHDCI cabling and inner chimney cabling, and
- Five ten-card mini-chimneys, optimized for the cold box roof thickness.

A full integration test of these elements was performed at warm, without the cold box roof and without CRPs, starting in July 2021 in a dedicated area at Experiment Hall North One (EHN1) (see Figure 4.27).



Figure 4.27: TDE integration test at EHN1 in summer 2021

This integration test validated the entire readout chain and, despite the rudimentary grounding scheme of this test facility (connected to the building ground), demonstrated a low noise level of 2.5 ADC root mean square (RMS), in agreement with expectations at warm with no strips connected, and the absence of coherent noise (see Figure 4.28).

The integration test started with a single chimney. In September-October 2021 it was extended to three chimneys, and all channels were tested with the DAQ and shown to be active. The integration setup was dismantled at the end of October 2021 and the components were moved to the cold box area where they were installed on the cold box roof (see Figure 4.29).

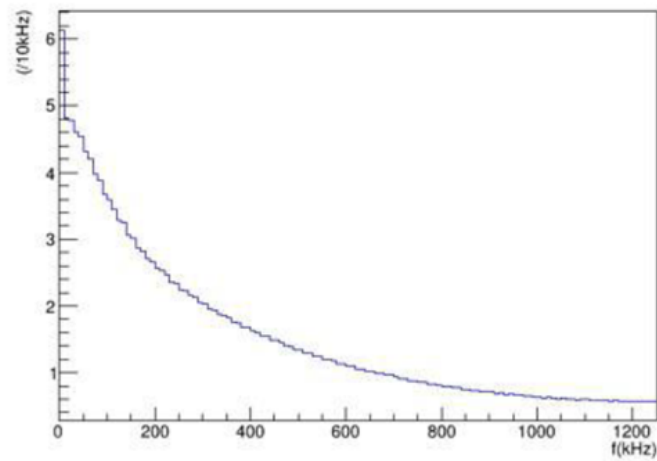


Figure 4.28: Fast Fourier Transform (FFT) noise spectrum during the integration test showing the absence of coherent noise peaks

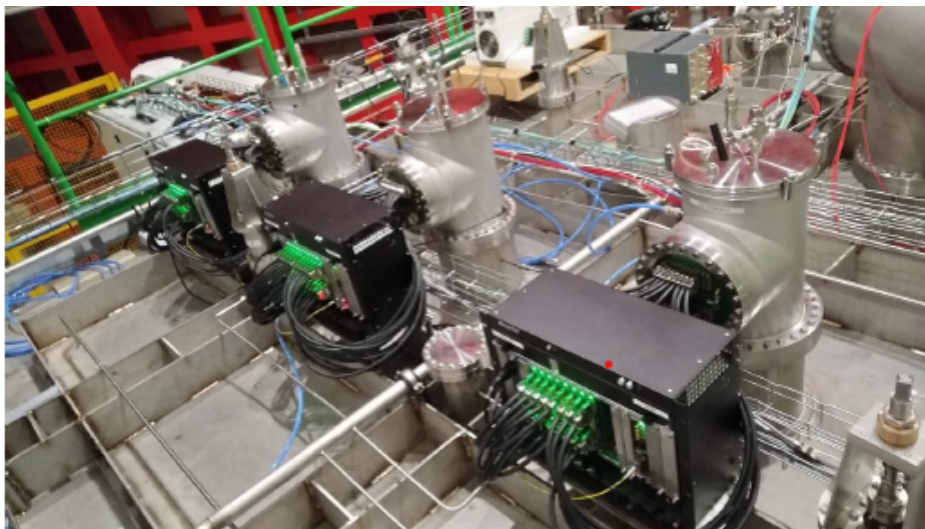


Figure 4.29: TDE installation on the cold box cryostat roof for the test of CRP-1



After validating the installation and the cryogenics system, the cold box was filled with LAr on 11 November 2021 (Run-1, covering the period 11-19 November). After filling, the anode biases and the cathode HV were activated. Clean tracks were immediately visible, indicating good performance of the TDE.

Figure 4.30 shows examples of raw cosmic ray data events acquired with the TDE, without treatment for coherent noise removal (CNR). Waveforms for the three views highlight the different signal shapes for the two induction views (bipolar) and the collection view (unipolar).

### First cosmic ray data with TDE: Raw data online event display, no noise removal

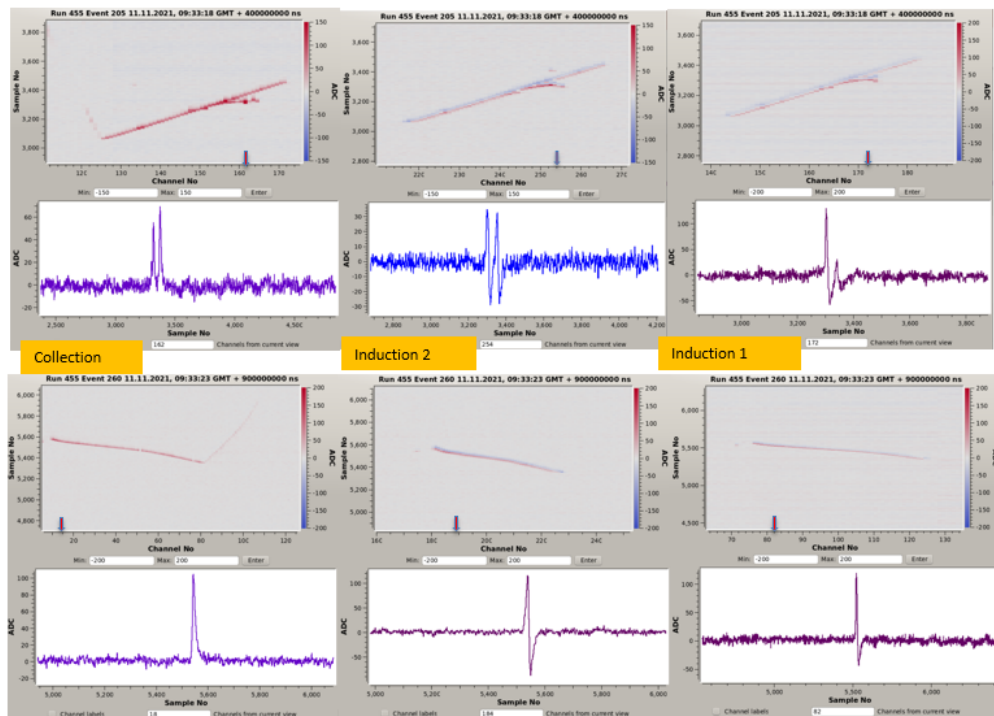


Figure 4.30: Raw cosmic ray data event displays of the first events acquired with the TDE during cold box Run-1

A large cosmic ray data sample that can be used for CRP performance studies was then acquired with the TDE. Run-1 collected 0.74M triggers, corresponding to 20 TB, and with Run-2, this statistic climbed to 1.6M triggers. Already from Run-1, results demonstrated detection performance well in line with expectations from previous tests performed in a 50 liter TPC setup.

Although the cold box grounding system during these runs left some low-level coherent noise that affected the electronics, the standard DUNE Coherent Noise Removal (CNR) procedure, shown in Figure 4.31, was able to remove it easily.

A slight worsening of the coherent noise conditions for the half-CRP readout with the TDE was observed in Run-2. This was traced back to a bad contact that had developed on the bias connection on two anode adapter boards serving half of the induction-2 view. Once CNR was applied offline, noise levels became comparable to those obtained in ProtoDUNE-SP.

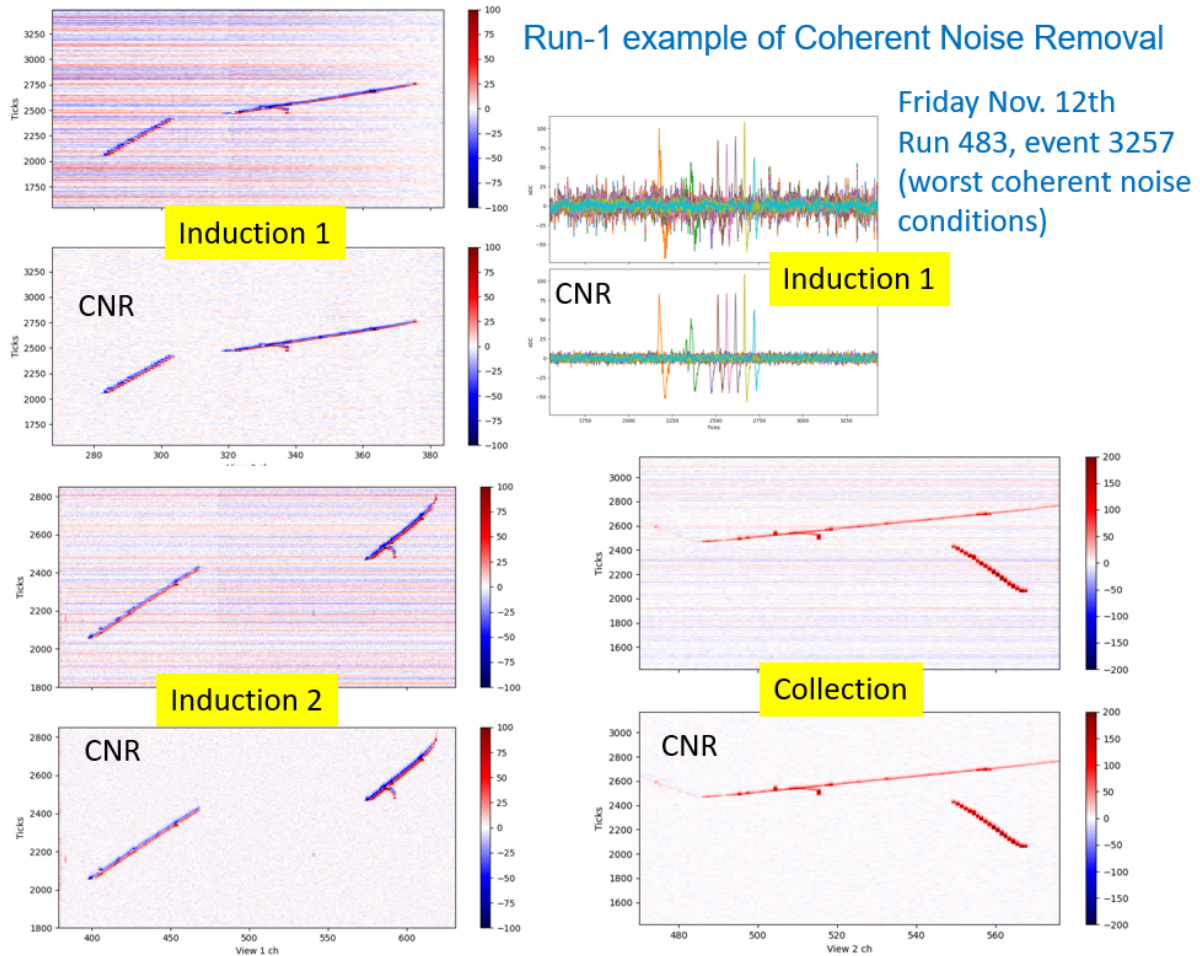


Figure 4.31: Example of application of the Coherent Noise Removal (CNR) procedure to event 3257 of Run 483. Plots with tracks in the three CRP views, produced with and without CNR, show on the horizontal axis the channel number, on the vertical axis the time ticks. The color code corresponds to the signals amplitude in ADC counts. The plot at the top right shows the wave-forms of for all channels of induction 1 for this event before and after CNR

Figures 4.32 and 4.33 show summaries of the noise performance for the three views of CRP-1 for the TDE (Run-1 and Run-2) and the BDE (Run-2) before and after the CNR procedure, respectively.

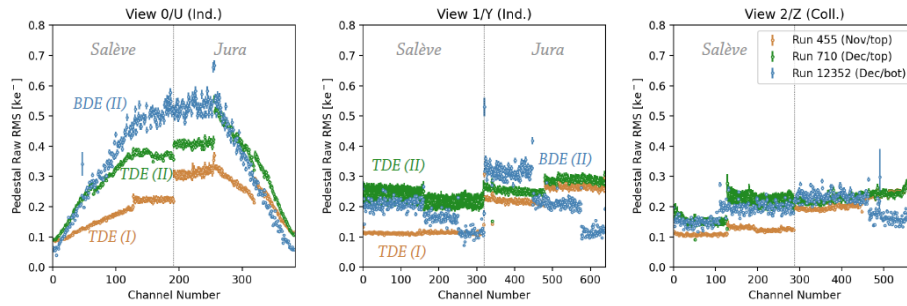


Figure 4.32: Noise performance for the three views of CRP-1 before CNR

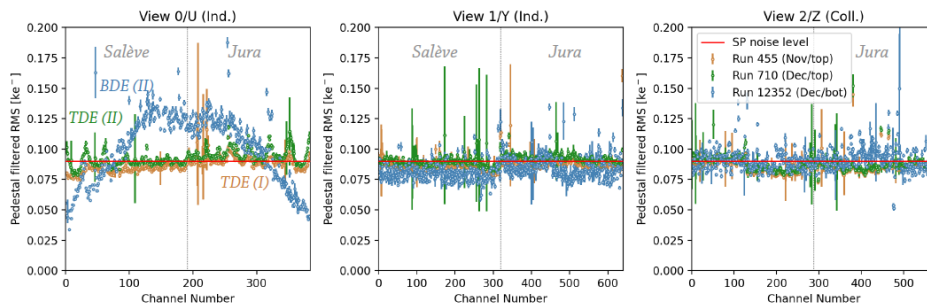


Figure 4.33: Noise performance for the three views of CRP-1 after CNR. The red line represents the noise level in ProtoDUNE-SP.

These first cold box tests showed that the noise levels were in line with expectations, with an RMS corresponding to 2.7 ADC counts (666 electrons) for a capacitance of about of 200 pF. The coherent noise contamination conditions greatly improved in spring 2022 with the installation of an isolation transformer and other minor setup improvements, and better shielding of the flanges used for the slow control services. This was demonstrated in subsequent cold box tests of CRP-1b, CRP-2 and CRP-3.

Besides reduced coherent noise, the test of CRP-1b allowed comparison of the signal to CRP-1 over several months. Figure 4.34 shows superimposed  $dQ/ds$  and  $dE/dx$  curves for the November (black) and June (red) CRP-1 runs. The Landau distributions correspond to the nominal values/shapes and show a very good detector resolution. The curves corresponding to the two different periods are practically indistinguishable, demonstrating the stability of the detector and of its readout system.

Figure 4.35 shows the Faraday cage and cold box installations for the tests performed on CRP-2 in June-July 2022. This first full vertical drift CRP used 48 FE readout cards installed on five 10-card chimneys. The chimneys were connected to five 48-AMC crates.

Given the grounding improvements already performed on the cold box in spring 2022, cosmic ray tracks were collected for the full CRP tests in very clean coherent noise conditions. Figure 4.36

## Calorimetry through time

- $dQ/ds$  corrected from impurity losses
- $E_{\text{drift}}$  June estimated at  $\sim 450$  V/cm

-> No changes with to November runs

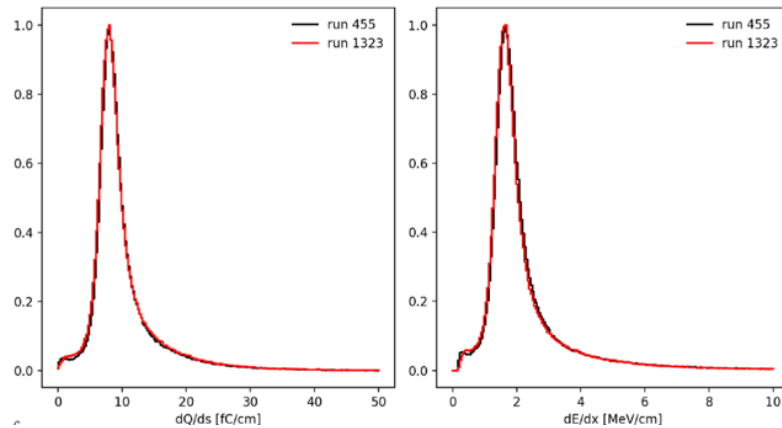


Figure 4.34: Calorimetric response stability for runs taken several months apart with CRP-1/CRP-1b.

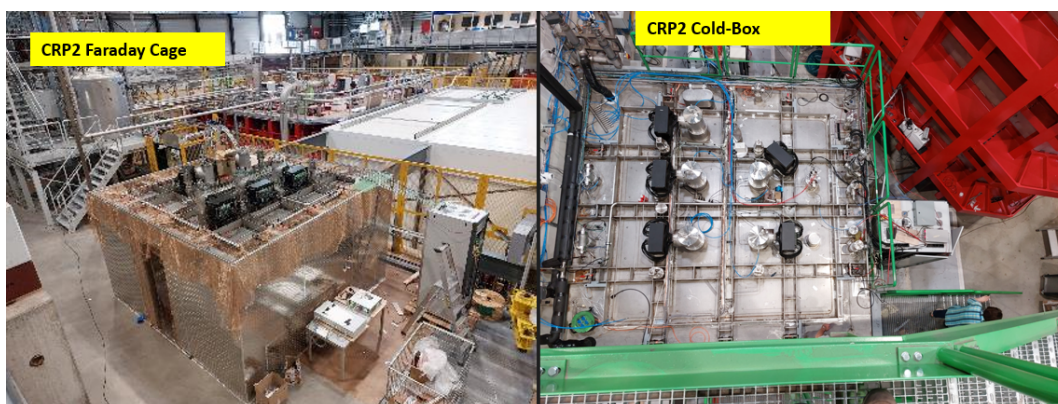


Figure 4.35: Left: TDE readout chain installed in the Faraday cage. Right: cold box setup for the CRP-2 tests in July 2022

shows two cosmic ray tracks acquired with CRP-2 in July 2022 and with CRP-3 in October 2022, respectively. The raw data from the collection view is shown with no noise treatment.

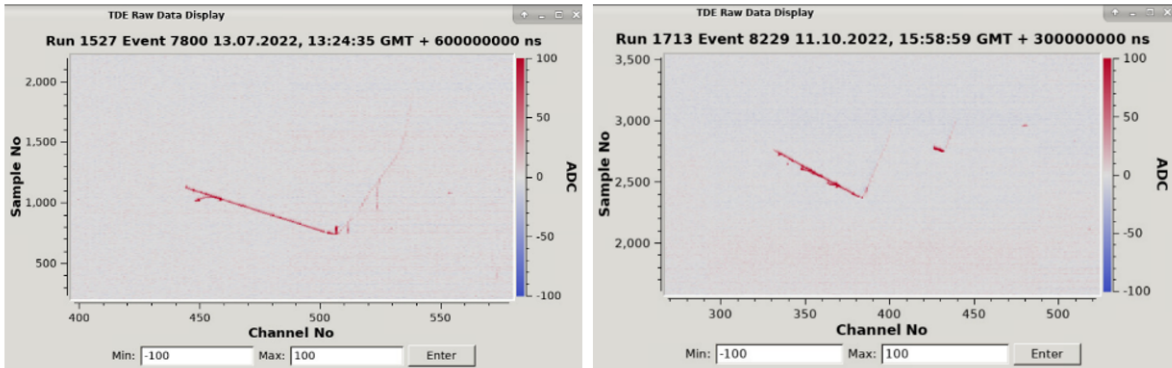


Figure 4.36: Examples of cosmic ray tracks collected during the cold box runs for CRP-2 (left) and CRP-3 (right).

The noise levels for CRP-2 and CRP-3 before and after noise reduction are summarized in Figure 4.37. Compared to the cold box runs of CRP-1 in 2021, the significant reduction of the coherent noise contamination is evident.

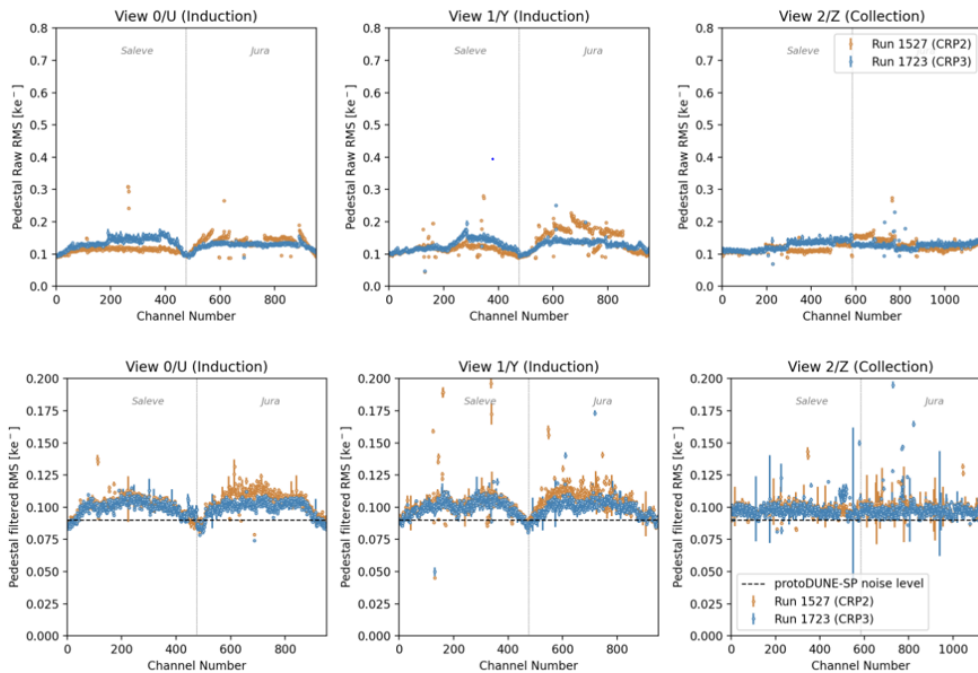


Figure 4.37: Noise levels before (top) and after (bottom) CNR for the operation of CRP-2 and CRP-3.

Due to the good performance of the TDE in the cold box runs, it was possible to collect a high statistics sample of cosmic-ray events. These were used to finely map and characterize the response of CRP-2 and CRP-3, which will be installed in FD2-VD Module 0 in early 2023.

### 4.3.7 TDE Services on the Cryostat Roof

A 3D model of the cryostat roof (Figure 4.38) shows the position of the chimneys with respect to the steel I-beam structure. The larger chimneys have two warm flanges, each connected to two  $\mu$ TCA crates via the VHDCI cables. The smaller chimneys have a single warm flange.



Figure 4.38: 3D view of the cryostat roof I-beam structure and the position of both the larger and smaller chimneys.

The positioning of the chimneys with respect to the I-beams allows positioning the crates directly on the top surface of the I-beams and to cable them to the warm flanges via the front connections of the AMC cards. Each  $\mu$ TCA crate requires connection to a 110V AC power cord, a WR fiber, and a data fiber. Each warm flange requires connection to two low-voltage cables, a cable for controls, and a pulsing cable. A single sense cable is used for two warm flanges.

Figure 4.39 illustrates the VHDCI cable connections of a large (48-card) chimney to the four  $\mu$ TCA crates, and the position of the cable trays for the service cables and the flanges.

The 24-card chimney connections are similar, but connect to only two  $\mu$ TCA crates to a single flange.

The infrastructure needed to support the TDE installation and operation on the cryostat roof includes the following items:

- 110 V AC power network to supply the power to the  $\mu$ TCA crates. Each TDE crate (hosting 12 AMC card, the MCH, the WR-MCH and the power and the cooling units) has a typical power consumption  $< 500$  W.
- $N_2$  network to purge and fill the chimneys before the cryostat cool-down and for accessing a blade. The network is made of plastic pipes with the  $N_2$  at about 10 mbar overpressure. Experience comes from NP02 and the cold box tests. After the initial chimney purging (typically equivalent to 10 volumes) the  $N_2$  circulation is closed, until an access is needed in cryogenic conditions. In that case the  $N_2$  flow must be started before opening the chimney cap to keep humidity from entering the chimney. Once the chimney is closed again, purging should continue for ten equivalent volumes ( $10 \times 0.46$  m<sup>3</sup>). The  $N_2$  flow should complete

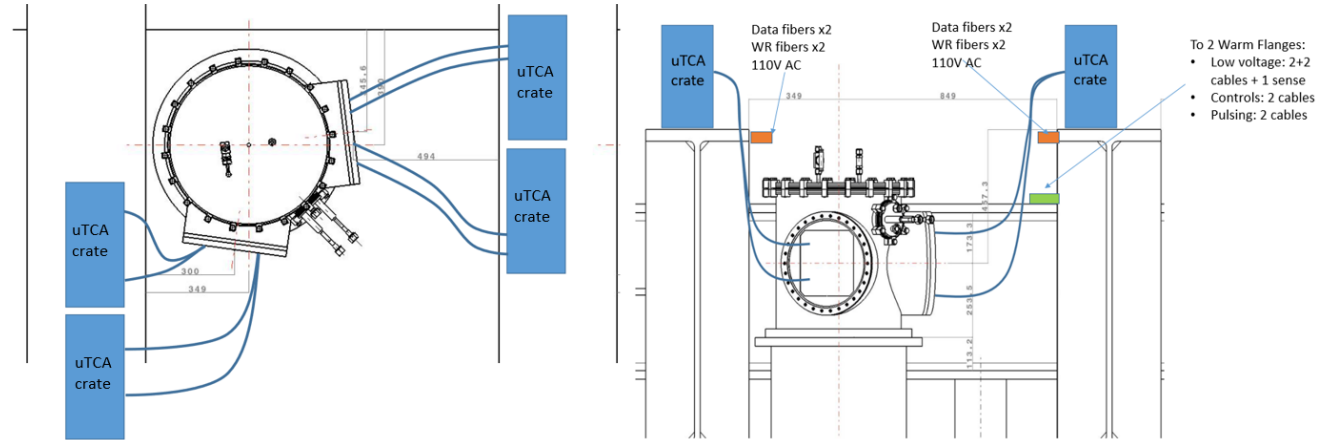


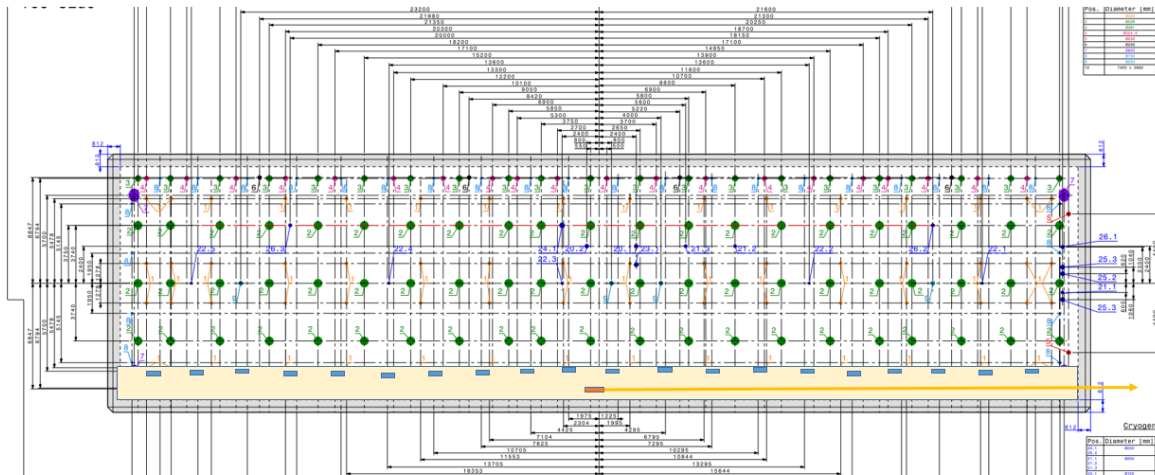
Figure 4.39: Top and side views of a larger (48-card) chimney with the VHDCI cabling to four  $\mu$ TCA crates, including the integration of the cable trays on the I-beam structure.

purging in a few hours. Each chimney has a plastic input pipe and an output valve to directly vent the  $N_2$  into the environment during purging.

- The WR network for the timing distribution. The WR-MCH in each  $\mu$ TCA crate is connected with a single fiber to a Level 1 (L1) WR switch. Given the ports' topology on the switches, 19 L1 WR switches are needed to connect the 320 crates. These switches will be installed in the detector mezzanine racks and should be evenly distributed along the 60 m length of the detector. The 19 uplinks of the L1 switches are then aggregated in a patch panel located in the middle of the mezzanine (by length) which is connected to a 24-fiber trunk cable length going to the DAQ room (see Figure 4.40). In the DAQ room the 19 links are connected to two cascaded Level 2 (L2) switches, the first one of which acts as WR grandmaster and is connected with its 1 PPS and 10 MHz inputs to the DUNE timing system. A WR time-tagging unit in the DAQ room is connected to the second switch and it ensures signal time-tagging from the DAQ. Each WR switch requires about 200 W max AC power and occupies 1U.
- The low-voltage generation and distribution system for the TDE FE includes twenty units, each capable of serving four larger chimneys (192 FE cards in total). Given that the TDE readout system includes 3840 FE cards distributed in 24- and 48-card chimneys, a total of 20 low-voltage units is needed. These should also be evenly distributed along the mezzanine racks along the detector length (see Figure 4.41). A large chimney, for instance, will have its two warm flanges connected with four nine-wire shielded cables to the low-voltage distribution unit, where a single cable serves a group of 12 FE cards. A small chimney will have its warm flange connected via only two low-voltage cables. A low voltage unit is composed of a power supply (Wiener crate MPOD Micro 2 LX 800 W with two modules MPV 4008I) and a low-voltage filtering and distribution box (see Figure 4.42). An additional nine-wire low-voltage shielded cable can be connected to a warm flange to the low-voltage unit for voltage sensing. Each small chimney warm flange has two sense connectors corresponding to the two independent low-voltage cables, but only one sense connector is connected via a low-voltage

cable to the distribution box, with the other one kept in case verifications are needed. Each low-voltage unit requires max 1 kW AC power, and occupies 3U+4U.

- Each chimney warm flange has one sub-D 9 connector for the controls and one SMA connector for charge injection. The controls connector will be connected (with the same kind of cables used for the low voltages), together with a coaxial cable for pulsing, to a calibration unit. The calibration units will also be installed in the mezzanine racks. A calibration unit could serve 16 flanges. Eleven calibration units will be then needed to connect the 105 chimneys. These calibration units should also be distributed evenly along the mezzanine racks (see Figure 4.43). They will require AC power < 100 W per unit and occupy 2U.
- Each  $\mu$ TCA crate is connected via an optical fiber data patch cable to a patch panel on the cryostat roof. The patch cable aggregates eight optical fibers to establish a 40 Gbit/s connection between the MCH and the DAQ system. The DAQ consortium is responsible for defining the positions of the patch panels on the cryostat roof and it is responsible of providing these items and the corresponding trunk cables going to the DAQ room.



White-Rabbit: 1 switch = 18 ports : 1 uplink + 17 inputs

For 320 crates needed 19 switches distributed in the mezzanine racks along 60 m, each switch connects 17 crates

19 uplinks concentrated in a patch panel at the cryostat center with a trunk (24 fibers) going to daq room

Two additional switches cascaded in DAQ room (1 Grand Master)

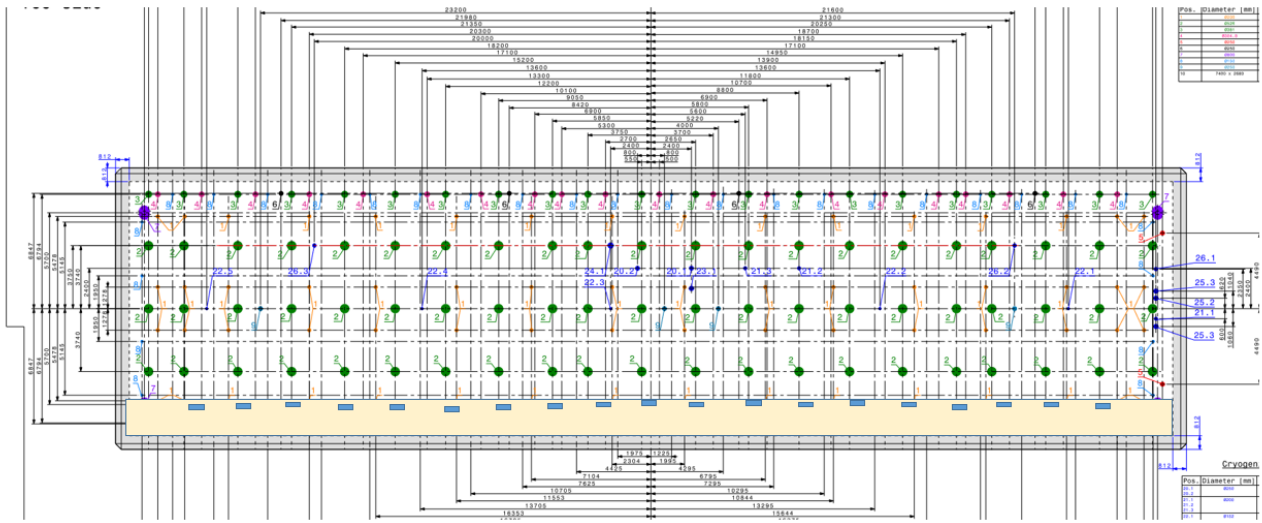
Figure 4.40: Layout of the WR switch positions (blue boxes) on the cryostat roof with the uplinks connected to the patch panel at the mezzanine center (orange box).

### 4.3.8 Grounding

An overview of the TDE grounding plan, which relies exclusively on the cryostat ground, is available in [55].

The TDE readout chain has the front-end analog electronics (FE cards) completely enclosed in a Faraday cage, the SFT chimney. Each chimney, which is at the cryostat ground potential, is made of stainless steel and is in tight mechanical contact with the flanges of the cryostat penetrations.





Low-voltage power-supply and filtering/distribution units. 20 units, each unit serving 8 warm flanges with 16 LV cables (x4 48 cards chimneys)  
 Each warm flange needs the connection of 2 LV cables + 1 sense

→ needed 20 units evenly distributed in the mezzanine racks along 60 m

a central column 3x2+2=8 warm flanges; 16 LV cables + 8 sense  
 first and last columns = 8 LV cables + 5 sense

Figure 4.41: Layout of the low-voltage power supplies and distribution boxes positions on the cryostat roof mezzanine (blue boxes).

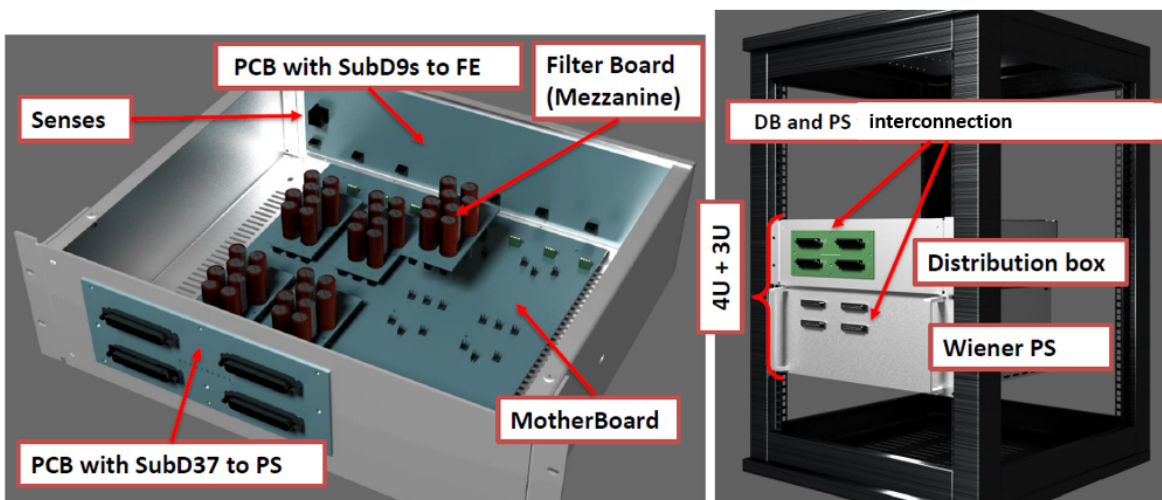
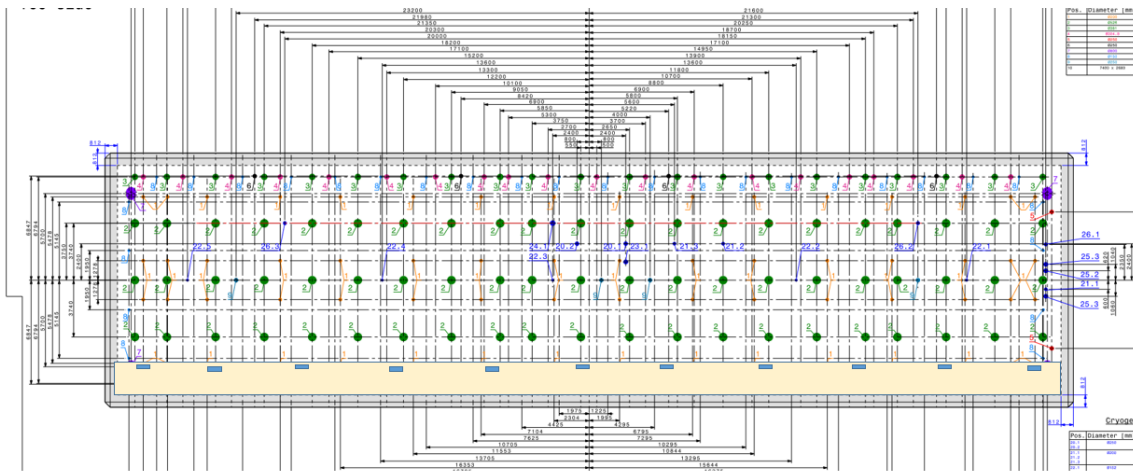


Figure 4.42: Rack mountable low-voltage power supply and distribution box to be installed on the cryostat mezzanine.



Calibration. Each unit serving 16 warm flanges  
 Each warm flange needs the connection of 1 control cable + 1 pulsing cable  
 a central column  $3 \times 2 + 2 = 8$  warm flanges: 8 control cables + 8 pulsing cables  
 first and last columns = 5 control cables + 5 pulsing cables

→ needed 11 units evenly distributed in the mezzanine racks along 60 m  
 Also possible to reduce cable lengths to install more units (20, as the LV units) with a smaller number of output connections

Figure 4.43: Layout of the calibration box positions on the cryostat roof mezzanine (blue boxes).

Contact between the cold flange PCB and the mechanical ring of the flange is required for cryostat tightness and for electrical contact to ground, which is effected by the pressure produced by multiple bolts used to close the flange ring.

The chimneys/cryostat are the grounding reference for the entire TDE readout chain.

The secure grounding at the flanges (for which the design of the warm flange PCB is an important aspect) and the exclusive use of shielded cables for all connections external to the chimneys together prevent any connections from injecting noise. Another advantage of the TDE design is that there are no components of the readout chain inside the cryostat, so it is not possible to induce noise on any other systems.

Both the cold and warm flange PCBs in the chimneys have a ground plane that is in tight contact with the flange mechanics (and hence the cryostat ground). The FE card grounds are connected to these ground planes, and therefore all possible connections are well grounded at the flanges.

On the warm flange the connectors for the VHDCI connectors, the SMA connector for pulsing and the sub-D connectors for the low-voltage supplies and the control signals are connected to the flange/cryostat ground. Only shielded cables are used: VHDCI cables to send the differential analog signals to the AMCs, shielded multi-wire cables for the connections of the low voltages and the controls, and coaxial cable for the charge injection pulsing. The shields of all cables are grounded at the cryostat warm flange.

The chimneys receive the signals from the adapter boards mounted on the CRPs via flat cables connected at cold flanges at the bottom of the chimneys.

These flat cables connect the adapter board to the ground at the cold flanges. Each flat cable has 68 wires, 32 of which are used to read the 32 channels from the adapter board. The remaining 36 wires (34 ground wires + two unused channels) are used for grounding.

To avoid grounding loops over the CRP area, the adapter board ground planes are not interconnected among different boards. Each board is only connected via its flat cables to a chimney. The anode adapter boards just ensure the routing of the strips signals to the flat cable connectors for the connection to the cold flange and the HV polarization of the strips.

The polarization voltages are applied to the anode strips via a network of biasing and decoupling passive components on the adapter boards. These are connected to a HV cable going to a filter and distribution box on the CRP frame. There are two boxes on each CRP daisy-chained and, connected via a single shielded coaxial cable to a dedicated flange on the cryostat. The cable shield is grounded only on its box end; it is not connected to the adapter board ground plane. Several adapter boards are daisy-chained for the distribution of a HV bias voltage so that only the first one of the chain is connected to the filtering board and a single HV cable is used. However the adapter boards are only daisy chained for the HV potentials but not for the ground, as explained. The CRP biasing is in the scope of the CRP consortium.

The AMCs that digitize the differential signals brought by the VHDCI cables from the warm flange are referred via the shield of the VHDCI cables to the cryostat ground and not to the  $\mu$ TCA crate chassis ground. The analog stage in the AMCs is AC coupled to the twisted pairs present in the VHDCI cables. Each  $\mu$ TCA crate is connected to the power network via an isolation transformer.

The low-voltage distribution system includes a power supply and a filtering and distribution box that suppresses the power supply ripple. The power supply (Wiener crate MPOD Micro 2 LX 800 W with two modules MPV 4008I) is connected to an isolation transformer. The grounding of the low-voltage distribution system to the cryostat ground is ensured by the shielded cables going to the warm flanges and the ground connectors (three ground wires per dub-D 9 connector, the other wires bring the five supply voltages, one voltage VCC, which is associated to higher currents, uses two wires). The low-voltage cables are routed on cable trays on the cryostat surface on top of copper foils connected to the cryostat ground.

The grounding scheme in Figure 4.44 summarizes the description of the grounding aspects in the TDE readout chain presented above.

The accessibility of the cryogenic electronics allows disconnecting the FE cards from the flat cables to check if any coherent noise has infiltrated the analog chain from the external connections due to grounding issues. This also provides a very good handle for checking the grounding of the entire chain.

This operation was performed several times in ProtoDUNE-DP and in the cold box. The results have always been consistent with the measurement of the intrinsic noise of the amplifiers; i.e., absence of any form of coherent noise coming from the readout system itself. These checks have shown that coherent noise, observed before disconnection of the FE cards, was either originating from grounding issues on the CRP or entering the cryostat from another path and being picked-up by the CRP anode strips.

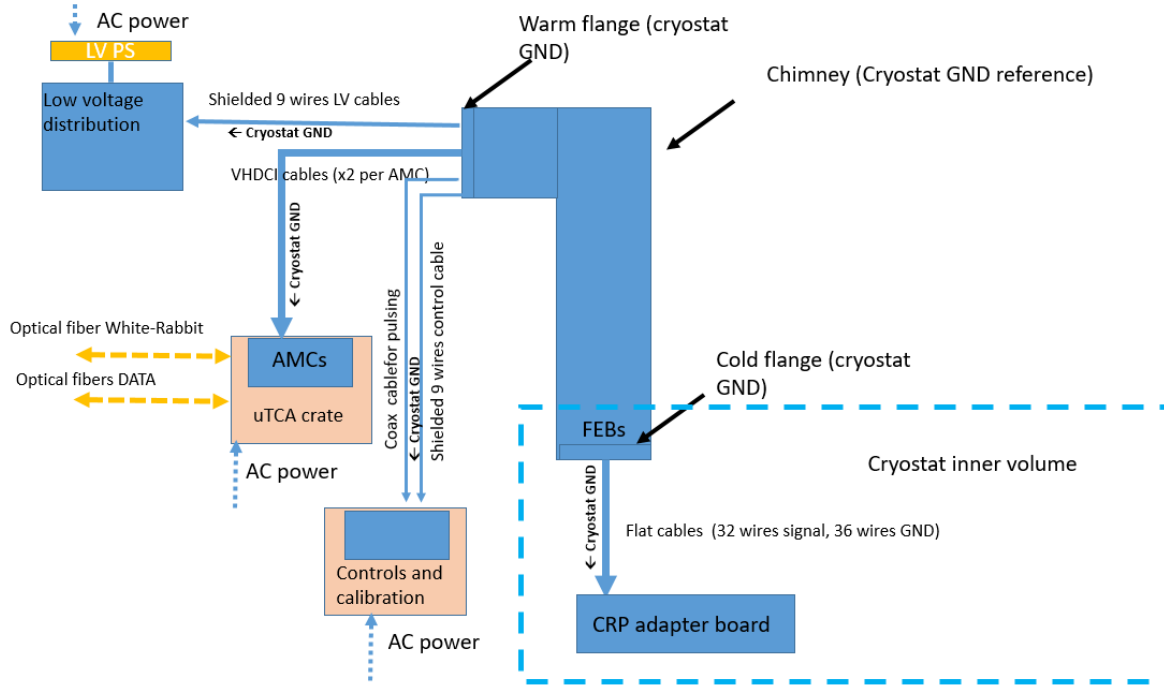


Figure 4.44: TDE grounding scheme.

### 4.3.9 Production

The TDE readout chain includes components for the analog and digital front-end stages as well as for the timing distribution system and the SFT chimneys. The main components are listed in Table 4.4, and shown in Figure 4.1.

Table 4.4: Components to be produced for the top drift charge readout electronics

Item	Unit Counts
LARZIC ASIC (16 ch.)	15360
Cryogenic FE cards (64 ch.)	3840
24-card (smaller) chimneys	42
48-card (larger) chimneys	63
AMC cards	3840
$\mu$ TCA WR MCH	320
$\mu$ TCA crates (including MCH, PU and CU)	320
40 Gbe Ethernet optical links to back end	320

The main elements of the readout system are the FE cards and the digitization AMC cards, both of which require 3840 units. The production yield, given past experience, is close to 100%; some rare welding defects, which once identified, have always been fixed.

The analog FE cards are located in the chimneys and remain accessible throughout the lifetime of the experiment. The rest of the system components ( $\mu$ TCA crates with AMC) are located in the ambient temperature of the detector cavern at the cryostat roof or in the vicinity and thus

remain accessible. Working with these components at CERN over the course of several years, no replacements have been needed under normal conditions. However, in order to ensure compliance with the requirement of maintaining fully functioning channels over the long term, a sufficient stock of spare components will be maintained on site.

It is therefore planned to order spares in appropriate quantities, according to the characteristics of the system and possible exposure to risks. The number of spares will range from 5% (e.g., for the FE cards) and 3% (for the AMCs), to at least 20% for the LARZIC ASIC. Other components, e.g., the chimneys/PS or timing system elements, will have 2% spares.

Within the time requirements dictated by the FD2-VD installation schedule, the TDE production organization aims to minimize production risks by conducting QC tests as each production batch is delivered.

The production is organized as follows:

- The production of the main components: FE cryogenic cards, AMC cards,  $\mu$ TCA crates, cables, and chimneys can take place in parallel.
- The minimal production and testing for all the components is of the order of one year, and could be done in parallel, starting a year before the items are needed for installation in South Dakota. However, given that FD2-VD installation is set to start in 2027, a three-year production time will be implemented, allowing staggered production throughout the years 2023 through 2026.

This arrangement will smooth the spending profile over three years, and provide better flexibility and risk mitigation with respect to production delays, production non-conformities and manpower involved in the QC.

- Deliveries will be planned in monthly batches, starting one to two months after the beginning of the production. The QC activities will be performed upon delivery of each batch allowing for earlier detection and correction of any problems and for regular follow-up with the production team. It will also limit any delay to a single batch or a fraction thereof, and therefore to a single month, which can be easily re-absorbed on the production schedule.

Relationships with vendors, component design, other aspects of production, and the quality assurance (QA)/QC procedures have been honed since 2016 via the development of the WA105 DP demonstrator, ProtoDUNE-DP, the vertical drift cold box tests, and finally the FD2-VD Module 0, procuring a total of about 10k channels over this time. Some components, e.g., the FE cards and the AMCs have been procured from different companies at different stages.

The milestones in Table 4.5 include periods for production and QC from 2023 to 2026. The “ready for installation” milestone is set three months before actual installation.

### 4.3.10 Quality Assurance and Control

It is crucial that the FD2-VD CRO electronics chain be fully understood and completely debugged. The QA plan must ensure that the number of functioning channels satisfies the DUNE requirement (<1% of non-functioning channels) for the lifetime of the experiment. Testing policies were defined

Table 4.5: Top drift electronics production timetable

Item	Dates
AMC digitization cards	June 2024 – July 2025
Cryogenic ASICs and FE cards	March 2024 – Dec 2025
Timing end nodes	Jul 2024 – July 2025
$\mu$ TCA crates	Jul 2024 – July 2025
SFT chimneys	October 2024 – April 2026
Cabling	February 2025 – July 2026
Ready for installation	September 2026

and optimized during the previous TDE production phases.

QC procedures applied at the production companies (e.g., optical and electrical tests) are carefully defined in the contracts. However, experience has shown that any change in the production lines, personnel, or execution of the QC procedures can lead to problems during production, and that additional QC procedures are required upon receipt of components.

The TDE QC procedures, in place since 2014, are very thorough and involve full operation tests of the components. They have reliably detected problems; for example, systematic issues in production of electronics cards have been prevented via early validation of prototype cards prior to mass production. The immediate identification and correction of production anomalies has resulted in the attainment of zero defects at installation, and the maintenance of nearly zero malfunctioning channels over several years of operation at CERN.

All components in the readout chain undergo full-functionality and operation tests at the single channel level, completely emulating the use of the components in the final detector layout. For connection components, such as the flanges, an individual channel-by-channel continuity test is also required.

The TDE QC tests are done on a test bench setup that emulates the full detector readout chain. The setup, while quite sophisticated, is minimally configured, requiring only a single readout  $\mu$ TCA crate. It can therefore be replicated in several locations at moderate cost. A new test bench, shown in Figure 4.45, was constructed in 2022 in a QC center at LP2I Bordeaux. It is a replica of the test bench used for several years at IP2I Lyon. These analog readout tests, which are conducted using a calibration system with an external pulsing card (Section 4.3.2.4), enable very high accuracy (at the  $\sim 1\%$  level).

In the absence of anomalies, the very high uniformity response of the electronics is also at the 1% level. This testing procedure enables immediate detection of small problems related to bad connections or to malfunctions at the FE cards or successive elements in the analog chain.

A new version of the calibration charge-injection board with PCB-embedded capacitors, shown in Figure 4.46, was successfully designed and tested in 2022. It is more compact and easier to produce, and will enable multiple QC tests to be done in parallel.

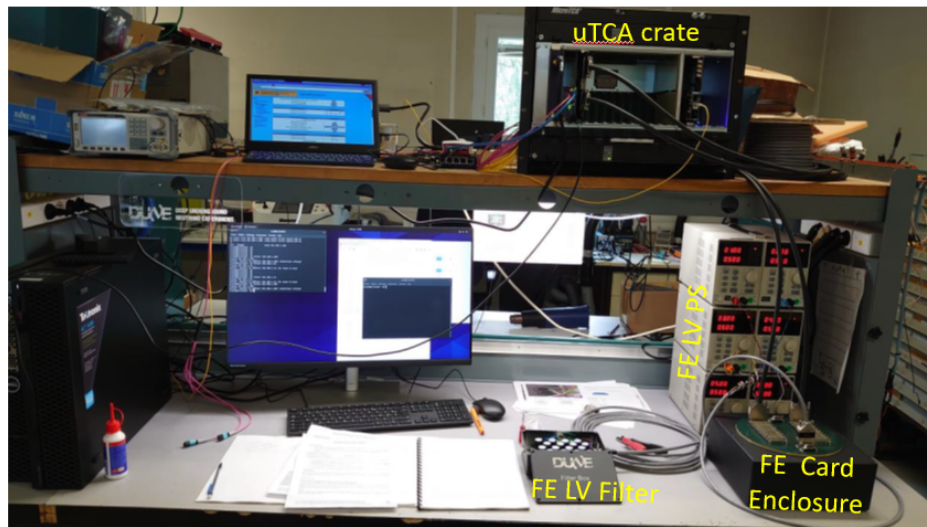


Figure 4.45: Duplicated test bench system at a second QC center

## Injection card with embedded capacitors

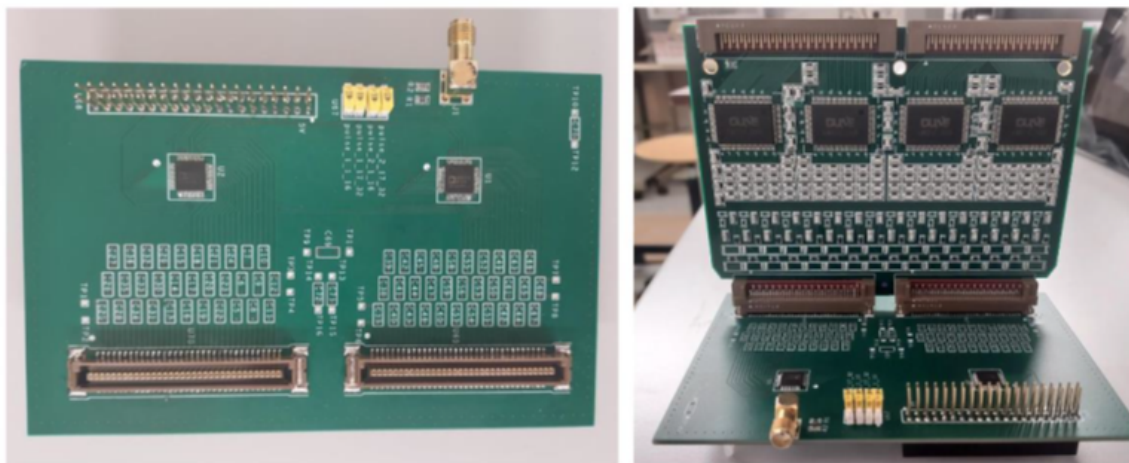


Figure 4.46: New version of the calibration card, with embedded PCB capacitors, used in the QC tests.

The QC tests will be pipelined with production in order to quickly identify and correct any potential systematic defects in the manufacturing. To the extent possible, the production will be organized in monthly batches so as to both mitigate production risks and ensure continuous checks on the production process.

The post-delivery QC procedures will be performed at test sites. The test reports for each element will be logged in a common database, following the DUNE hardware database requirements. To facilitate the execution of the tests and any follow-up, each component will be labeled with its unique identifier in the database. The test benches will be equipped with bar-code readers interfaced to the QC software for the immediate identification of components and transmission of test results to the database.

The dedicated test-bench setup is schematically illustrated in Figure 4.47. The setup is a miniature version of the FD2-VD TDE system, which will enable full functionality tests of the various elements of the both the analog and digital chains.

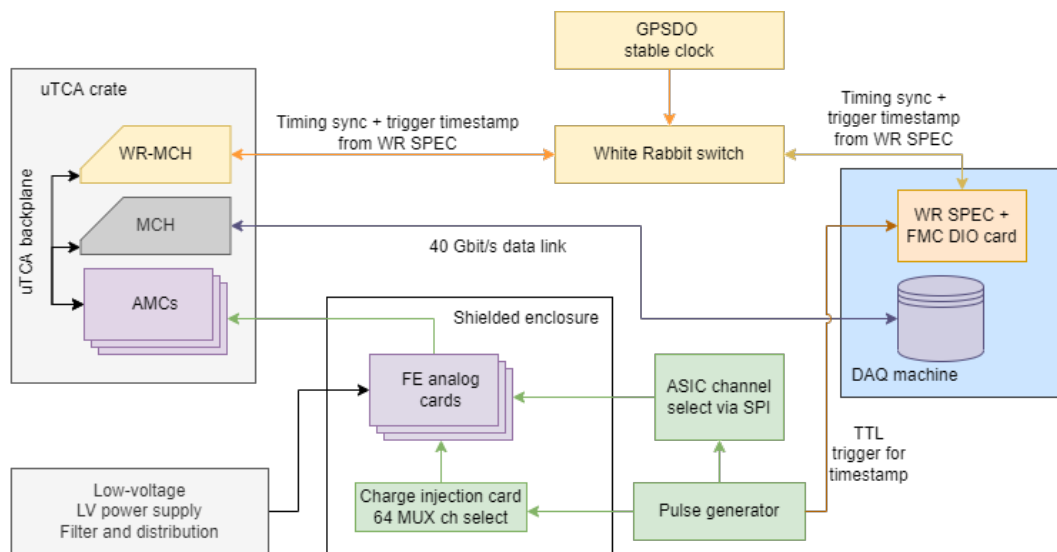


Figure 4.47: Production QC test bench scheme.

It includes:

- The hardware for WR trigger timing and synchronization;
- The low-voltage system to power the FE analog cards and the voltage/current monitoring;
- One computer for DAQ and online analysis;
- FE analog cards (to be tested or used as support to test other elements of the chain) located in a shielded enclosure with a warm flange feedthrough;
- A  $\mu$ TCA crate with AMCs (to be tested or used as support to test other elements of the chain); and
- Systems to inject calibration charge either via external injection capacitors or internal calibration circuitry on the pre-amplifier ASIC.

In triggered readout mode, the trigger time stamp information is used by the AMC to output the



data sequence that matches the trigger timing, which, for the QC tests, is related to the timing of the charge injection pulse distributed to the analog front-end cards.

The construction schedule, which is driven by the availability of the detector for installation rather than by the production and testing time of the electronics components, very conservatively assumes the following:

- The testing time is typically shorter than the production time.
- The span of the production and testing activities over several years allows the possibility of reabsorbing delays.
- The time needed to execute the tests using the two test benches is a few days per month.
- It would be easy to expand the test-bench including multiple  $\mu$ TCA crates operating in parallel; for instance going from one crate to two or four crates, depending on needs.
- Buffer time is available at the end of the production runs before installation.

The FE cards have been and are currently comfortably tested at a rate of at least five per hour per test bench, testing a single card at a time, or about 40 FE cards per day. It would be easy to test up to 10 cards in an automated way at the same time on a test bench, i.e., testing up to 400 cards a day.

By taking a conservative margin this shows that the 400 cards of a monthly batch could be tested over two days relying on a single test site equipped with a single test-bench. This time shrinks to a single day by including two sites (baseline assumption) or by operating two test benches in parallel.

AMC boards are tested in batches of 12 on a single  $\mu$ TCA crate bench. Testing a batch, including various insertion manipulations, takes at most one hour, enabling the testing of up to 96 cards per day on a single test bench, and the entire monthly production batch of 320 in less than 3.5 days (or half that if two test setups are used). This time can be shortened further by running multiple crate benches in parallel connected to the same DAQ system.

The tests of the  $\mu$ TCA crates and of the WR end nodes can be performed at the same time (and with complete DAQ operation) since these two elements are coupled. Production of WR end-nodes is faster than that of crates, but testing activities can be combined in a single test.

The WR end-node components are pretested and there have never been problems. On the basis of this coupled test scheme, one hour per site should be sufficient to test a new  $\mu$ TCA-WR system. A monthly batch of 46 units can therefore be tested in three days assuming two sites. Again, this time can be shortened by running more than one crate in parallel. Figure 4.48 summarizes these QC activities.

The chimneys will be tested at warm for vacuum tightness at the level of a few  $10^{-3}$  mbar. The chimneys should be leak-tight down to a few  $10^{-9}$  mbar l/s.

A randomly selected sub-sample of chimneys will be tested at cryogenic temperatures. After the

Item	Element	Nominal quantities	Dates	Production span (months)	Testing time (months)	Units to be tested/month	Technical testing time for a single site/TB chain (hours)	Consevatively assumed testing time on a single site/TB chain (days)	Testing time assuming two sites with a single chain or two TB chains in a single site (days)	Additional gain factors in case of parallel operation of multiple uTCA systems on a TB chain
1	AMC cards	3840	12/2023-6/2025	19	12	320	27	4	2	2 or 4
2	FE cards (including ASICs)	3840	5/2024-12/2025	20	12	320	6,4	2	1	
3	uTCA crates (with PU,MCH,CU)	320	7/2024-1/2025	12	7	46	46	6	3	2 or 4
4	White Rabbit end-nodes	320	7/2024-1/2025	7	7	46	included in (3)	included in (3)	included in (3)	included in (3)

Figure 4.48: Summary of the QC tests duration for monthly batches of components.

target temperature is reached at the cold flange ( $\sim 100\text{K}$ ) a new round of helium leak tests is performed to ascertain that it is still leak-tight to  $10^{-9}$  mbar l/s.

A full set of blades will be installed to check the behavior of the guiding system at cryogenic temperature. The continuity of the signal lines for warm and cold flanges will be verified for each channel. This procedure can be automated with 64:1 MUX and 1:64 DEMUX stages connected at the input and the output of a given signal chain (e.g., warm flange inner side / outer side). By enabling a single input channel at a time, a sweep over the output channels will verify that only the corresponding output channel is active. Presence of signals on any other channel would imply a resistive contact that would need to be fixed.

### 4.3.11 Installation, Integration, and Commissioning

The installation, integration and commissioning procedures for the TDE were repeated many times during the development and operation of ProtoDUNE-DP and the cold box tests in 2021-2022, demonstrating the absence of significant risks, for both material and personnel.

The installation in FD2-VD has been studied together with the team, and besides the installation of detector components, the related documentation includes cabling layout, power requirement, and schedule.

The predecessors to the TDE installation work are:

- Cryostat roof completed (walking surface available);
- Cryostat detector mezzanines in place;
- Cryostat penetrations welded and leak tested;
- Mezzanine racks, power to racks, and safety system in place;
- Power and fibers for the  $\mu\text{TCA}$  crates in cable trays; and
- DAQ ready to readout the  $\mu\text{TCA}$  crates (i.e., TDE commissioning, which may be accomplished using a portable system).

The TDE installation is then subdivided into three phases:

- Mezzanine Racks: Installation of all TDE electronics ancillary modules in the racks on the mezzanine (low-voltage generation and power distribution systems, level 1 switches. Cali-

bration and control units). Cabling. Powering and testing of all these units.

- Chimneys: Insertion of all 105 chimneys in the cryostat penetrations. Connection to the penetration flanges interfacing to the chimneys followed by leak testing. Positioning of the mechanical stands/mounts of the  $\mu$ TCA crates. Connections to the  $N_2$  distribution network for chimney purging.
- TDE electronic components: installation of the blades with the FE cards in chimneys. Positioning of the  $\mu$ TCA crates on their stands. Cabling of the  $\mu$ TCA crates to the warm flanges. Commissioning.

The installation and integration of TDE is to a large extent independent of CRP installation activities, although proper coordination is needed. To avoid possible damage to the electronics related to the CRPs and interfering with cabling activities inside the cryostat, the blades in already-equipped chimneys can be lifted from the cold flanges and connected back once the CRP cabling is completed. However, complete and activated chimneys are required in order to test CRP cabling. Purging and filling of the chimneys with  $LN_2$  is not required during commissioning phase, but must be done before the cryostat cool-down.

### 4.3.12 Interfaces

The TDE system has important interfaces with the CRP and DAQ consortia and with FSII, which are defined and documented as cited:

- CRP-TDE [56]
- DAQ-TDE [57]
- Installation-TDE [58]

Each document describes the interfaces between two consortia to complete the design, fabrication and installation of the far-detector.

The interface with the CRPs is defined at the chimneys' cold flanges. The cold flanges are part of the TDE system and everything below the flanges, including the flat cables used for the CRP connection is the responsibility of the CRP consortium.

The flat cable connectors on the cold flange and the matching cables are well defined. The flat cables have a length of 2.2 m apart some exceptions in particular chimney locations. A circular cable tray designed and produced by the CRP consortium for the routing of the flat cables is attached to the bottom of each chimney. The TDE consortium provides the fixation points on the cold flange for it.

At the production level: the CRP consortium fabricates the anode adapter boards and provides the flat cables; the TDE consortium provides the chimneys and cold flanges.

At the installation level: the chimneys and cold front-end electronics are installed by the TDE consortium; the flat cable connection to the cold flange and the circular cable trays installation is performed by the CRP consortium.

The TDE data readout happens via 320 fiber connections (40 Gbit/s) between the MCH on TDE side and the back-end on the DAQ side, involving the following:

- The TDE system includes 320  $\mu$ TCA crates, with 12 AMC cards/crate and 64 channels per AMC.
- In each crate data are collected by an MCH, having a 120 Gb/s maximal connectivity, when exploiting three ports operating at 40 Gb/s each (this total 120 Gb/s bandwidth corresponds to 10 Gbit/s connectivity at the level of a single AMC, supported for all the 12 cards in the crate).
- The MCH has a MPT-CXP 24 connector, supporting up to three 40 Gb/s ports.
- Assuming a sampling rate 2 MHz, 12 (16) bits, the raw data flow is 17 (23) Gb/s (with 12 AMC cards operating in continuous streaming mode).
- For the TDE application only one port of the MCH is connected, ensuring a 40 Gbit/s connectivity, with a factor of two safety margin on the needed bandwidth.
- Since just a single MCH port is used, customized MTP patch cables have been designed and produced. These accommodate a group of eight fibers corresponding to the selected port [59].
- The other optical cable patch end is terminated with a standard MTP-12F connector with only two groups of four fibers connected (standard 40 Gbit/s connectivity). It can be plugged into a QSFP+ transceiver in any commercial network card.
- The 40 Gbit/s system and these patch cables have already been tested and validated during cold box data taking in 2021. Cables needed for FD2-VD Module 0 have been procured.

The TDE consortium has responsibility for the data link aggregation into the optical cables for MCH connection and for the procurement of customized optical patch cables.

The DAQ consortium is responsible for the connection to the DAQ room via patch panels distributed on the cryostat roof close to the crates and with connected trunk cables going to the DAQ room. Optimization criteria will drive the definition of the patch panels' position.

The TDE readout is based on UDP packet in JUMBO frames. This readout was already operated with WA105 DP demonstrator, ProtoDUNE-DP, and the CRP cold box tests in external trigger mode. A firmware to work in continuous data streaming mode has been developed.

The data format from TDE to DAQ is based on an evolution of ProtoDUNE-DP data format, agreed with the DAQ consortium and detailed in [60]. The data packets structure includes: a header followed by the associated ADC samples. The header includes information on the channel identification, timestamp, global DAQ timestamp, error flags, and so on.

The timing distribution of the TDE is using WR components. There is a dedicated WR end node in each of the 320  $\mu$ TCA, connected to network including 19 WR switches. The WR grandmaster is integrated in the DUNE central timing system which provides the 1 PPS and 10 MHz signals.

The TDE and DAQ consortia are jointly responsible of the integration of the WR grandmaster switch with the DUNE timing system. A DUNE timestamp counter will be maintained by the AMCs as well as the TAI one. This counter is reset/aligned to the timestamp of the DUNE timing

and synchronization subsystem (DTS) signal.

The TDE-installation interface document includes several aspects which are also reported in the TDE installation section of this chapter.

Additional technical and engineering details (installation of dedicated cable trays close to the chimneys, racks allocation on mezzanine and cables routing, the DAQ fiber patch panels on the cryostat roof, the path of the network for the  $N_2$  distribution to the chimneys ) are in progress.

### 4.3.13 Safety

This section describes the basic requirement for materials and personnel safety during the TDE installation activities. All the work will be performed entirely on the cryostat roof.

For what concerns material safety, the TDE FE cards are very robust and can be manipulated bare hands without ESD issues. They are resistant to repeated (tens of thousands) discharges at a few kV.

In order to avoid any risks, the TDE concept allows lifting and unplugging the blades from the cold flanges should any welding activities occur inside the cryostat during installation.

The chimneys are the heaviest objects ( $\sim 200$  kg). The tooling for the rigging on the chimneys was designed by the I&I team and the TDE experts. Points where the load can be applied during rigging without damaging the chimneys have been defined. For risk mitigation, the chimney installation happens before the installation of fragile components as the  $\mu$ TCA crates.

There are no particular safety rules for the protection of people apart the standard ones for the manipulation of loads and work underground.

### 4.3.14 Management and Organization

#### 4.3.14.1 Institutions

The consortium is responsible for delivering the electronics used for the readout of the CRPs for the top-drift volume of FD2-VD.

The production of the system elements in the TDE consortium is foreseen to be funded by the France-IN2P3 DUNE project, with possible contributions from Japanese and U.S. groups for testing and installation at SURF.

The list of institutions contributing to the TDE consortium is shown in Table 4.6.

Institutional responsibilities are summarized below:

- LARZIC ASIC design and procurement: IN2P3 IP2I, IN2P3 LP2I
- FE cards design and procurement: IN2P3 IP2I, IN2P3 LP2I
- SFT chimney design and procurement: IN2P3 IJCLAB

Table 4.6: Institutions participating in the FD2-VD TDE consortium

Institution
IN2P3 IJCLAB Orsay
IN2P3 IP2I Lyon
IN2P3 LP2I Bordeaux
Iwate University
KEK
NITKC
Southern Methodist University (SMU)

- AMC cards design and procurement: IN2P3 IP2I, IN2P3 LP2I
- $\mu$ TCA crates design and procurement: IN2P3 IP2I
- timing system end-nodes design and procurement: IN2P3 IP2I, IN2P3 LP2I
- LV PS and filtering and distribution boxes design and procurement: IN2P3 IP2I, IN2P3 LP2I
- VHDCI cables design and procurement: IN2P3 IP2I, IN2P3 LP2I
- Calibration units design and procurement: IN2P3 IP2I, IN2P3 LP2I
- QC testing: all institutions
- Installation and commissioning: all institutions

#### 4.3.14.2 Milestones

The milestones of the FD2-VD TDE consortium are listed in Table 4.7.

Table 4.7: Milestones of the TDE consortium.

Milestone	Date
Test of first full top drift CRP (CRP-2)	July 2022
Test of second full top drift CRP (CRP-2)	October 2022
Start of Module-0 installation	October 2022
Completion of top drift CRP tests	November 2022
Completion of Final Design Review	March 2023
Completion of Production Readiness Review	End of 2023
Start of AMC production	June 2024
Start of FE cards production	October 2024
Start of $\mu$ TCA crates production	July 2024
Start of timing system production	July 2024
Start of cabling production	February 2025
Start of chimneys production	October 2024
End of timing system production and QC	July 2025
End of AMC production and QC	July 2025
End of $\mu$ TCA crates production and QC	July 2025
End of FE cards production and QC	December 2025
End of cabling production	July 2026
End of chimneys production and QC	April 2026
Delivery to SURF completed	September 2026
Completed TDE installation and commissioning	December 2027

## 4.4 Bottom Drift Readout

### 4.4.1 System Overview

The CRO electronics for the bottom drift volume is based on, and therefore similar to, the successfully deployed ProtoDUNE-SP CE [7], and on the ASICs developed for the FD1-HD detector module. The same ASICs will be used for both detector technologies.

The system architecture is shown in Figure 4.49. Anode signals are input to front-end mother boards (FEMBs) mounted on the edges of the CRPs. The anode signals are amplified, shaped, and input to ADCs. The digitized signals are multiplexed in groups of 32 channels, and output on serial links operating at 1.25 Gbps. Short (2.5 m) power and signal cables connect the FEMBs to patch panels near one edge of each half-CRP. Long (25 m) power and signal cables are connected to the patch panels and routed up the sides of the cryostat to penetrations distributed along the top of the cryostat near each of the long sides, where they are connected to warm interface boards (WIBs) through feedthrough flanges. The WIBs further concentrate the data and output information from groups of 256 channels over optical links at roughly 10 Gbps to the DAQ system.

### 4.4.2 Specifications

In addition to the high level requirements listed in Table 4.1, the BDE consortium has defined a number of engineering specifications, listed in Table 4.8. Some of these are derived from the requirements and others represent design choices.

Table 4.8: BDE specifications

Label	Description	Specification (Goal)	Rationale
FD-CE-1	Number of baselines in the front-end amplifier	2	Use a single type of amplifier for both induction and collection strips
FD-CE-2	Gain of the front-end amplifier	$\sim 10$ mV/fC (Adjustable in the range 5 mV/fC to 25 mV/fC)	The gain of the FE amplifier is obtained from the maximum charge to be observed without saturation and from the operating voltage of the amplifier, that depends on the technology choice.
FD-CE-3	System synchronization	50 ns (10 ns)	The dispersion of the sampling times on different strips of a CRP should be much smaller than the sampling time (500 ns) and give a negligible contribution to the hit resolution.
FD-CE-4	Number of channels per FEMB	128	Design
FD-CE-5	Number of links between the FEMB and the WIB	4 at 1.25 Gbps	Balance between reducing the number of links and reliability and power issues when increasing the data transmission speed.
FD-CE-6	Number of FEMBs per WIB	4	The total number of FEMB per WIB is a balance between the complexity of the boards, the mechanics inside the crate holding the WIBs, and the required processing power of the FPGA on the WIB.



FD-CE-7	Data transmission speed between the WIB and the DAQ backend	10 Gbps		Balance between cost of the FPGA on the WIB and reduction of the number of optical fiber links for each WIB.
FD-CE-9	Ability to resolve two tracks	Time corresponding to $\sim 5$ mm		Should be about the same as the strip pitch and the longitudinal diffusion of electrons drifting to the CRP
FD-CE-10	Recovery from a very large input pulse	Monotonic recovery without nonlinear behavior		Recovery from saturation must be predictable so that dead time is known.
FD-CE-11	Maximum allowable crosstalk	$< 1\%$ ( $< 0.1\%$ )		Some crosstalk can be mitigated in signal deconvolution. At 0.1% the effect of crosstalk can be ignored
FD-CE-12	Input capacitance to front end ASIC	120 pF to 210 pF		Cold electronics should be optimized for the specified range of capacitance.
FD-CE-17	Provision for PDS cables			Enough space must be provided in the cryostat penetration for the PDS and CALCI cables.
FD-CE-18	Differential NonLinearity (DNL)	Absolute value $< 1$ (12-bit) LSB		The minimum requirement ensures no missing (12-bit) codes; the goal is as low as is practical.
FD-CE-19	Integral NonLinearity (INL)	Absolute value $< 1$ (12-bit) LSB		Should not contribute to energy resolution
FD-CE-20	Equivalent Number of Bits (ENOB)	$> 10.3$		Pulse amplification and digitization should not contribute to energy measurement uncertainty.
FD-CE-21	Number of WIBs in each Warm Interface Crate (WIEC)	6		Design choice; one WIEC per CRP
FD-CE-22	Number of Power and Timing Cards (PTCs) in each Warm Interface Crate (WIEC)	1		Design choice; one WIEC per CRP
FD-CE-23	WIB timing and clocks			WIBs must receive clock signals from the DUNE Timing System through the Power and Timing Card and provide the 62.5 MHz clock to the FEMBs.
FD-CE-24	WIB data processing			WIB must be able to receive high-speed TPC data from FEMBs, format the data, and transmit it over optical fibers to the DAQ
FD-CE-25	WIB interface to Slow Control			WIB must be able to interface to the Slow Control system
FD-CE-26	Calibration of readout electronics			WIB must be capable of performing calibration of the FEMBs via charge injection to the front end ASICs.
FD-CE-27	PTC timing distribution			The PTC must transmit clock and control signals from the timing system to the WIBs and multiplex the return signals
FD-CE-28	PTC power distribution			The PTC must step down the 48V from the LVPS to 12V and distribute power to the WIBs.

FD-CE-29	PTC monitoring		The PTC must be able to gather WIB status and transmit relevant information to the DUNE Detector Safety System (DDSS). It must also be able to receive inhibit/enable signals from the DDSS and transmit them to the WIBs
FD-CE-30	PTC output voltage ripple	<15 mV	The ripple on the 12V provided to the WIBs must not be larger than 15 mV.
FD-CE-31	WIB clock jitter	<180 ps	The 62.5 MHz clock provided to the FEMBs by the WIBs is used to generate the ADC sampling clock. ADC sampling clock jitter adds effective noise to the digitization. Assuming ENOB of $\sim 11$ and a signal bandwidth of 350 kHz, the required signal to noise ratio is $\sim 68$ dB. This translates to a sampling clock jitter of 180 ps.
FD-CE-35	ADC overflow protection		When the input signal exceeds the upper or lower limit of the ADC range, the output should be fixed at the maximum or minimum value.

### 4.4.3 System Design

This section describes the overall system design of the BDE, starting in Section 4.4.3.1 with a description of the grounding and shielding scheme adopted to minimize the overall noise in the FD2-VD module, followed in Section 4.4.3.2 by a discussion of the bias voltage distribution system. Section 4.4.3.3 describes the FEMBs, including the design of the ASICs that will be used. Section 4.4.3.7 discusses the infrastructure for the BDE inside the cryostat, including the cold boxes that shield the FEMBs, the cold cables, and the cryostat feedthroughs. Section 4.4.3.8 describes the electronics mounted on the warm side of the feedthroughs, and section 4.4.3.9 describes the services that provide the low-voltage power and the bias voltage to the BDE.

#### 4.4.3.1 Grounding and Shielding

The overall approach to minimizing the system noise relies on enclosing the sensitive anode planes in a nearly hermetic Faraday cage, then carefully controlling currents flowing into or out of that protected volume through the unavoidable penetrations needed to build a working detector. Done carefully, this can avert all unwanted disturbances that result in detector noise. Such disturbances could be induced on the anode strips by changing currents flowing inside the cryostat or even on the cryostat walls as, for instance, a temperature-sensing circuit that acts as a receiving antenna on the outside of the cryostat and a transmitting antenna in the interior. In addition, unwanted signals might be injected into the electronics either in the cold or just outside the cryostat by direct conduction along unavoidable power or signal connections to other devices. This approach to minimizing the detector noise by using appropriate grounding and shielding procedures is discussed in detail in [61]. It results in the following set of requirements that need to be respected during the design and the construction of the FD2-VD:

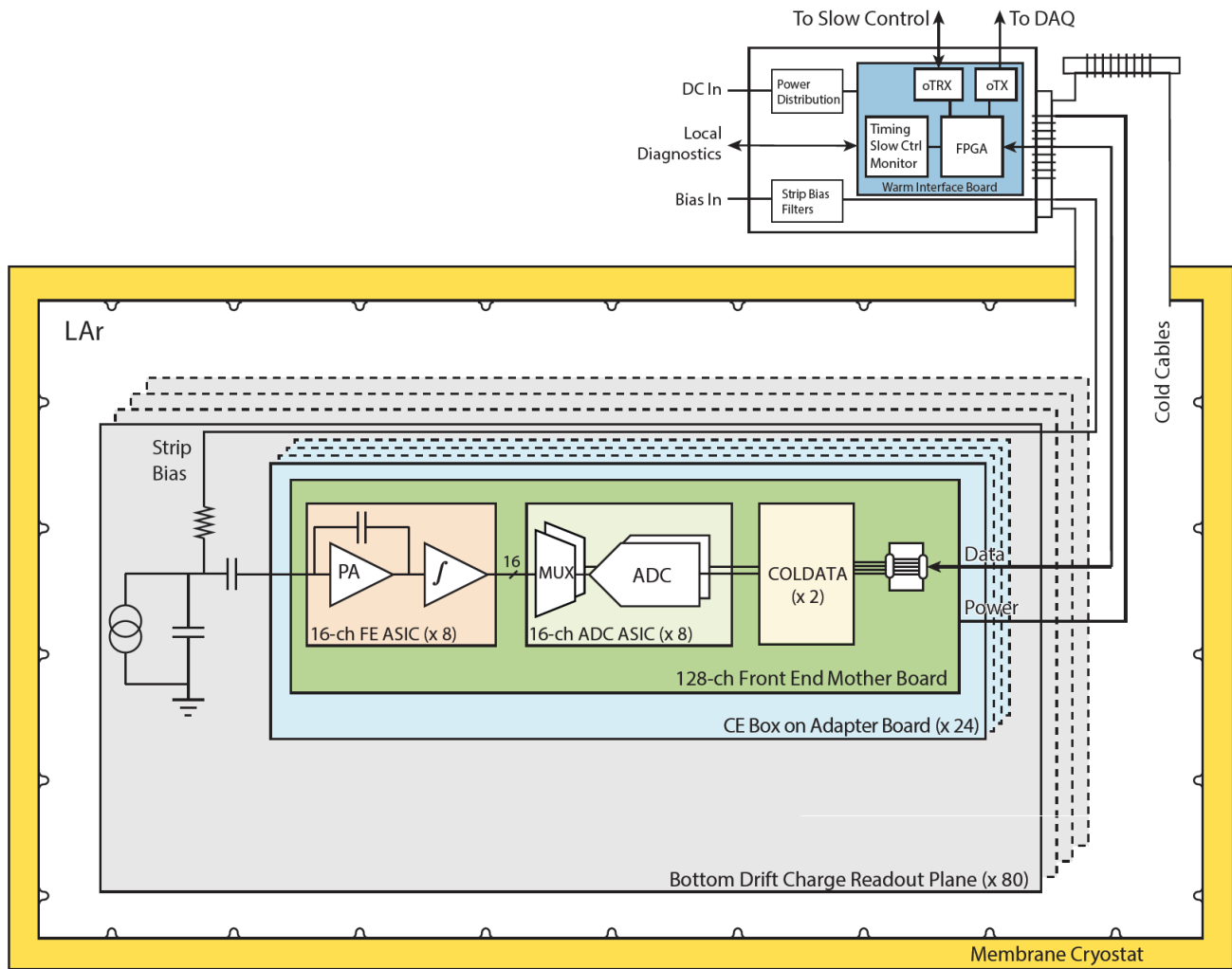


Figure 4.49: System architecture of the TPC readout electronics in the bottom drift volume.

- The CRP copper ground plane shall be connected to the common of all the FE ASICs;
- All electrical connections (low-voltage power, bias voltage, clock, control, and data readout) from one CRP shall lead to a single signal feedthrough (SFT);
- All CRPs shall be insulated from each other;
- The common of the FE ASIC and the rest of the TPC readout electronics shall be connected to the common plane of the FEMB;
- The return leads of the CRP strip bias lines and any shield for the clock, control, and data readout shall be connected to the common plane of the FEMB at one end and to the flange of the SFT at the other end; these shall be the only connections of the CRP ground plane to the cryostat;
- The mechanical supports of the CRP shall ensure that the CRP is electrically isolated from the cryostat;
- The last stage of the readout strip and shielding plane bias filters shall be connected to the common of all the FE ASICs and therefore to the CRP ground plane.

To minimize system noise, the TPC electronics cables for each CRP enter the cryostat through a single CE flange. This creates, for grounding purposes, an integrated unit consisting of a CRP ground plane, FEMB ground for all 24 CE modules, a TPC flange, and warm interface electronics. The input amplifiers on the FE ASICs have their ground terminals connected to the CRP ground plane. All power-return leads and cable shields are connected to both the ground plane of the FEMB and to the TPC signal flange.

The only location where this integrated unit makes electrical contact with the cryostat, which defines the detector ground and acts as a Faraday cage, is at a single point on the CE feedthrough board in the TPC signal flange where the cables exit the cryostat. Mechanical support of the CRPs is accomplished using insulated supports. To avoid structural ground loops, the CRPs are electrically insulated from each other.

Filtering circuits for the CRP strip bias voltages are locally referenced to the ground plane of the FEMBs through low-impedance electrical connections. This approach ensures a ground-return path in close proximity to the bias-voltage and signal paths. The close proximity of the current paths minimizes the size of potential loops to further suppress noise pickup.

#### 4.4.3.2 Distribution of Bias Voltages

The CRP includes two perforated PCBs with strips on both sides. The strips are biased such that electrons pass through the holes in the PCBs unimpeded until they are collected on the final strip layer on the back of the second board. This condition is referred to as “transparency.”

The filtering of strip bias voltages and the coupling of wire signals passing onto the charge amplifier circuits is done on adapter boards that connect to edge boards that mount on the edges of the CRPs and connect to the CRP strips (see Section 3.3). Each adapter board includes filters for the collection and first induction plane strip wire bias voltages, while the second induction plane strips have a floating voltage. In addition, each board has pairs of bias resistors and AC coupling capacitors. The coupling capacitors block levels while passing AC signals to the FEMBs. On the FEMBs, clamping diodes limit the input voltage received at the amplifier circuits to between

$1.8V + U_D$  and  $0V - U_D$ , where  $U_D$  is the threshold voltage of the diode, approximately  $0.7V$  at LAr temperature. The amplifier circuit has a  $22\text{ nF}$  coupling capacitor at the input to avoid leakage current from the protection clamping diodes. Tests of the protection mechanism have been performed by discharging  $4.7\text{ nF}$  capacitors holding a voltage of  $1\text{ kV}$  ( $2.35\text{ mJ}$  of stored energy). The diodes have survived more than 250 discharges at temperature.

#### 4.4.3.3 Front-End Motherboard

Each CRP is instrumented with 24 FEMBs. Each FEMB receives signals from 128 strips. The FEMB contains eight 16-channel chips, eight 16-channel ASICs, and two control and communication ASICs. The FEMB also contains regulators that produce the voltages required by the ASICs and filter those voltages. The LArASIC inputs are protected by two external diodes as well as internal diodes in the chip.

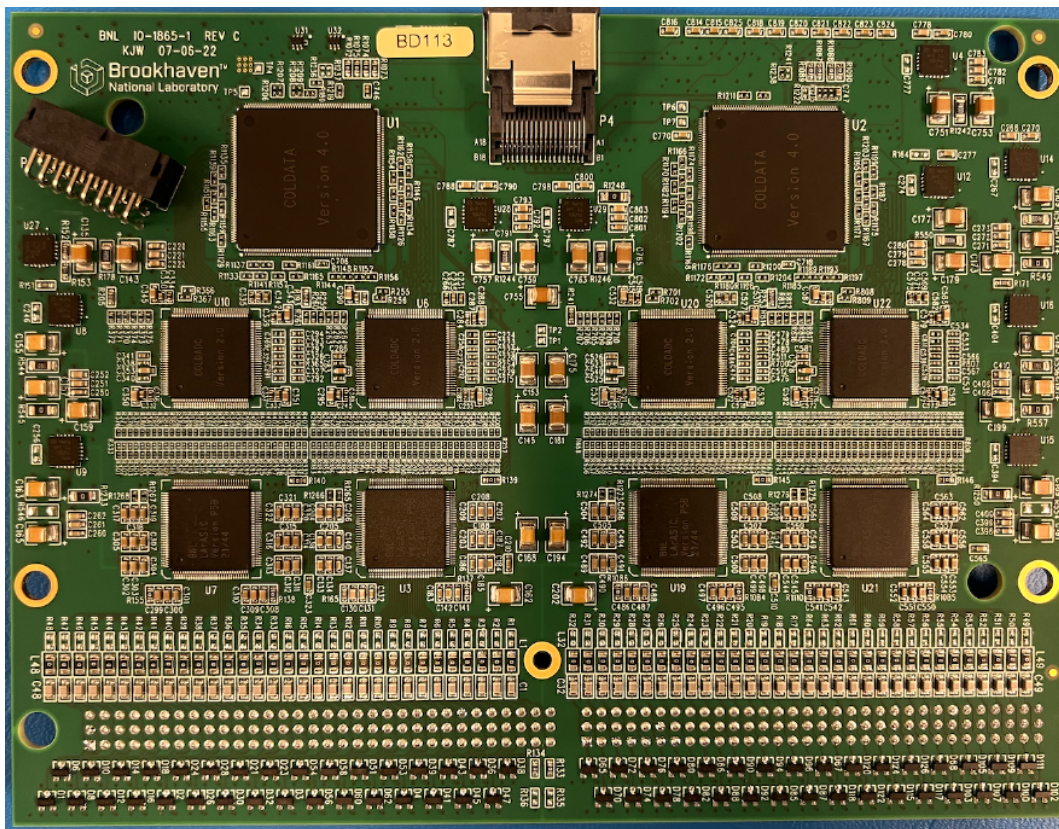


Figure 4.50: Bottom drift electronics FEMB: Four LArASIC front-end ASICs (at the bottom of the picture) and four ColdADC ASICs are mounted on the visible side of the printed circuit board. Another four LArASICs and four ColdADCs are mounted on the other side of the printed circuit board. Two COLDATA ASICs (the larger parts near the top of the picture) concentrate data from the ColdADCs and transmit data to the WIB using  $1.25\text{ Gbps}$  serial links.

The functionality of the FEMB for DUNE is very similar to that of the FEMB used in ProtoDUNE-SP. The design has changed slightly to accommodate the new ASICs (fewer voltage regulators are required) and features have been added to allow the analog values of the ColdADC reference voltages to be measured. The FEMB used in ProtoDUNE-SP consisted of an “analog motherboard” and a “digital daughterboard” which included an FPGA. The DUNE FEMB is implemented on a

single printed circuit board and is often referred to as a “monolithic FEMB.” The DUNE FEMB for FD2-VD (shown in Figure 4.50) is identical to the FEMB used in FD1-HD except that it uses a 36-pin miniSAS connector instead of a Samtec connector for data I/O. This allows the use of miniSAS cables on the CRPs. The miniSAS cables are less expensive and more flexible than the Samtec data cables, but the insertion loss is significantly greater on the miniSAS cables, so they cannot be used for the full run between the FEMBs and the WIBs.

The power consumption of the FEMB ASICs depends on whether the LArASICs are operated in single ended or differential mode. In single ended mode, the ASICs consume  $\sim 29$  mW/channel. In differential mode, this increases to  $\sim 34$  mW/channel. Including the power consumption of the voltage regulators, the power consumption in differential mode is slightly less than 45 mW/channel.

The noise measured with 150 pF at the input is shown as a function of peaking time in Figure 4.51.

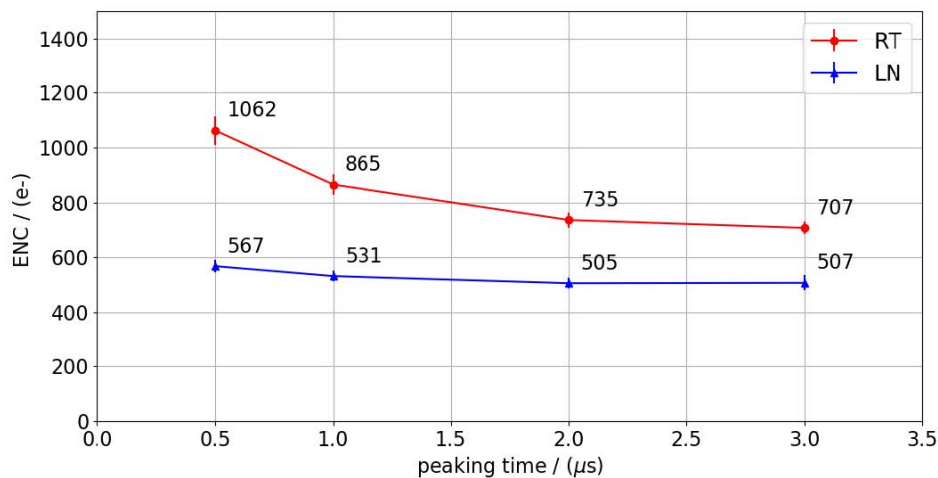


Figure 4.51: Noise as a function of peaking time for 150 pF input capacitance, measured at room temperature (red) and in liquid nitrogen (blue). For these measurements the LArASIC gain was set to 14 mV/fC and single ended output was used.

All the discrete components mounted on the FEMB have been characterized for operation in LAr. Some of the components (resistors, capacitors, diodes) used on the ProtoDUNE-SP FEMB belong to the same family of components already used for other boards operating in a cryogenic environment, namely the boards used for the accordion LAr calorimeter, providing relevant information on the lifetime of these components, which is discussed later in Section 4.4.6. That section also discusses procedures for the measurement of the lifetime of discrete components that have been adopted in recent years to demonstrate that the TPC electronics can survive in LAr. These types of measurements have been performed already for other neutrino experiments that use liquid argon time-projection chamber (LArTPC) technology.

In the case of custom ASICs, appropriate steps must be taken prior to starting the layout of the chips. Both COLDATA and ColdADC are implemented in a 65 nm CMOS process. The designs were done using cold transistor models produced by Logix Consulting<sup>5</sup>. Logix made measurements

<sup>5</sup>Logix™ Consulting, <http://www.lgx.com/>.

of 65 nm transistors (supplied by Fermi National Accelerator Laboratory (Fermilab)) at LN<sub>2</sub> temperature and extracted and provided to the design teams Simulation Program with Integrated Circuit Emphasis (SPICE) models valid at LN<sub>2</sub> temperature. These models were used in analog simulations of COLDATA and ColdADC subcircuits. In order to eliminate the risk of accelerated aging due to the hot-carrier effect [62], no transistor with a channel length less than 90 nm was used in either ASIC design. A special library of standard cells using 90 nm channel-length transistors was developed by members of the University of Pennsylvania and Fermilab groups. Timing parameters were developed for this standard cell library using the Cadence Liberate tool<sup>6</sup> and the Logix SPICE models. Most of the digital logic used in ColdADC and COLDATA was synthesized from Verilog code using this standard cell library and the Cadence Innovus tool<sup>7</sup>. Innovus was also used for the layout of the synthesized logic. The design of LArASIC is implemented in a 180 nm CMOS process. The models used during the design of LArASIC were obtained by extrapolating the parameters of the models provided by the foundry, which are generally valid in the 230 K to 400 K range. After the design was complete, simulations using cold models provided by Logix Consulting were used to verify the design.

#### 4.4.3.4 LArASIC Front-end ASIC

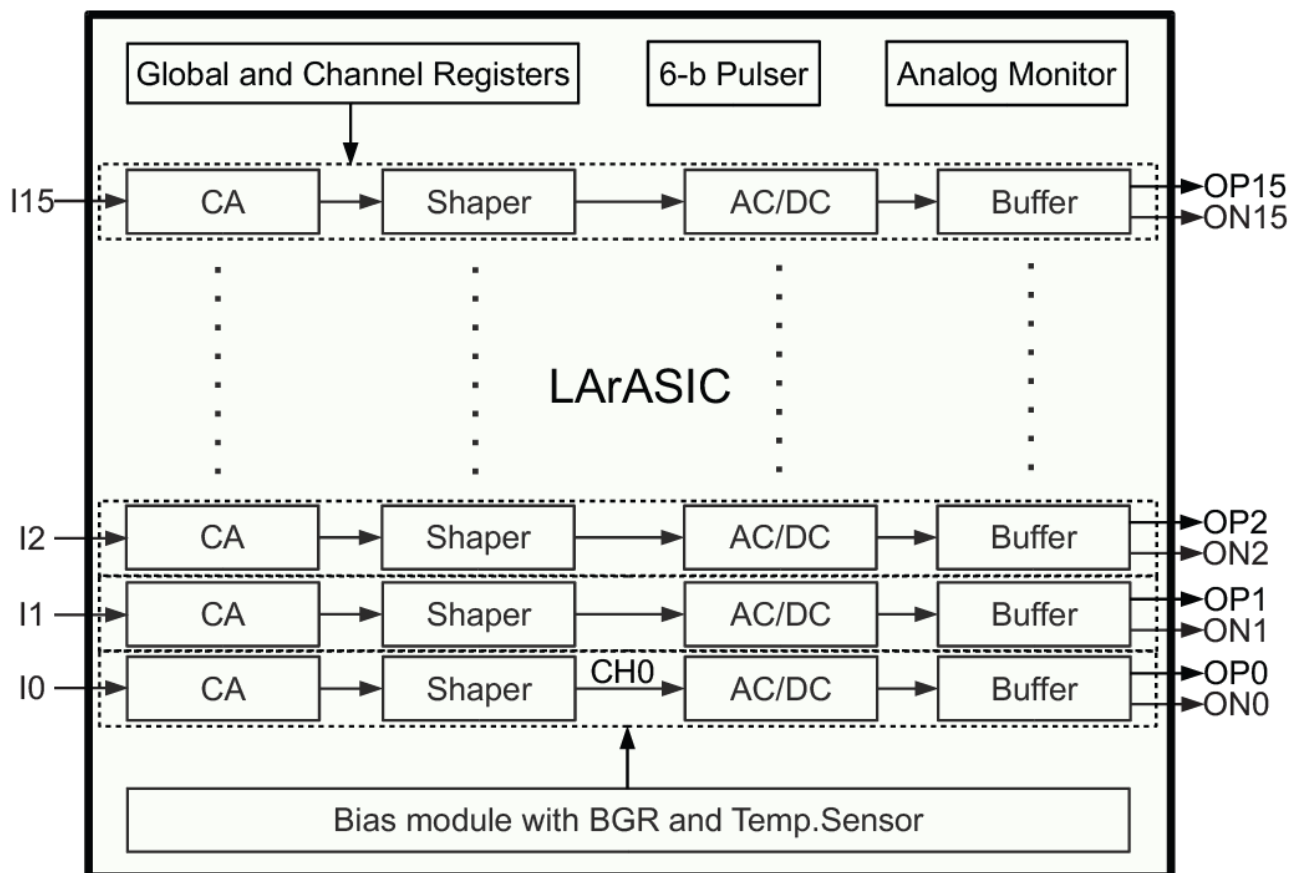


Figure 4.52: LArASIC block diagram, showing 16 channels and shared circuitry including a Band Gap Reference (BGR) circuit.

<sup>6</sup>Cadence Liberate™.

<sup>7</sup>Cadence Innovus™.

Each LArASIC [63] receives signals from 16 CRP strips, amplifies and shapes the signals, and outputs the signals to a ColdADC for digitization. LArASIC is designed to minimize noise for an input capacitance of approximately 150 pF. Figure 4.52 shows a block diagram of LArASIC, and a simplified block diagram of one channel of LArASIC is shown in Figure 4.53. LArASIC is implemented using a 180 nm CMOS process and was designed by engineers from Brookhaven National Laboratory (BNL).

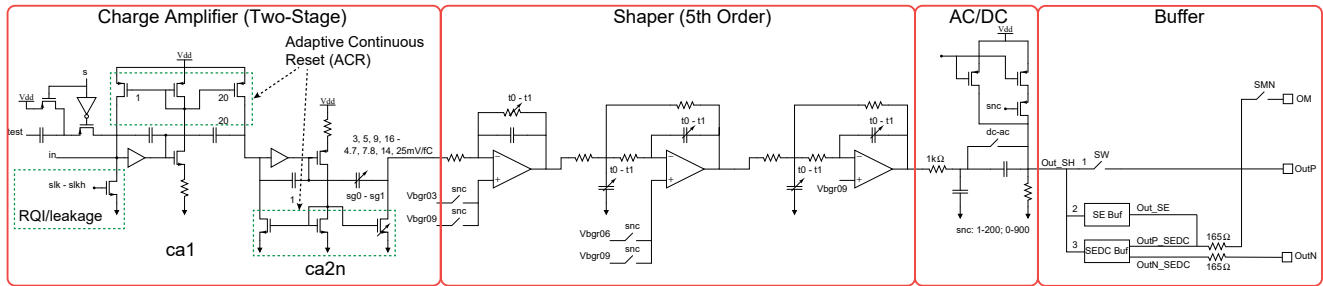


Figure 4.53: Channel schematic of LArASIC, which includes a two-stage charge amplifier and a 5<sup>th</sup> order semi-Gaussian shaper.

A two-stage charge amplifier with adaptive continuous reset is followed by a fifth-order shaping amplifier with complex conjugate poles that converts charge to voltage and performs shaping to maximize the signal-to-noise (S/N) ratio and provide an anti-aliasing filter for the ADC. The output of the shaper can be AC or DC coupled and an optional buffer can drive a long cable (for debugging purposes) or can provide a differential output.

Each channel can be independently configured by setting the gain, peaking time, and output baseline (assuming DC coupling). A bandgap reference circuit produces all of the required internal bias voltages and a six-bit digital to analog converter ( ) can provide a voltage level that can be used to test the channels using a charge injection capacitor. Figure 4.54 shows output pulses from test inputs for a variety of gain and shaping time settings.

A test output can be used to monitor the output of one channel, the bandgap reference voltage, or a voltage proportional to temperature.

#### 4.4.3.5 ColdADC ASIC

ColdADC is a low-noise ADC ASIC designed to digitize 16 input channels at a rate of  $\sim 2$  MHz. ColdADC requires two external clocks, the digitization clock and a master clock which is used by the ColdADC digital logic and must be 32 times the frequency of the digitization clock. DUNE will use a 62.5 MHz master clock, so the digitization frequency will be 1.953 MHz (1/512 ns). For convenience, the digitization clock is referred to as 2 MHz and the master clock as 64 MHz.

ColdADC is implemented in a 65 nm CMOS technology and has been designed by a team of engineers from Lawrence Berkeley National Laboratory (LBNL), BNL, and Fermilab. The ASIC uses a conservative, industry-standard design including digital calibration. Each ColdADC receives 16 voltage outputs from a single LArASIC chip. The voltages are sampled, multiplexed by eight, and input to two 15-stage pipelined ADCs operating at 16 MHz. The 16 MHz clock is generated internally in ColdADC by dividing the 64 MHz clock by four, and shares its rising edge with



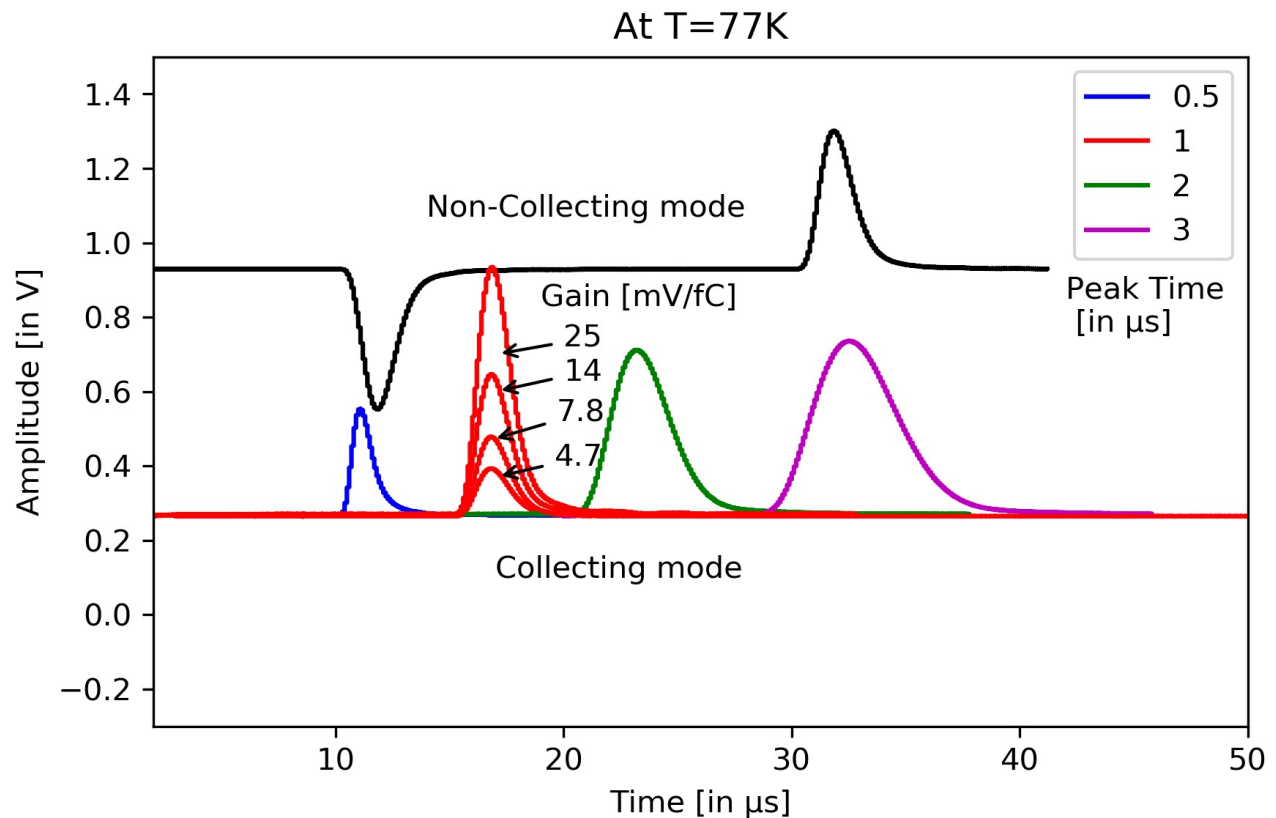


Figure 4.54: LArASIC output pulses recorded in response to test pulses input using the internal DAC. The black waveform is shown for a channel set to 14 mV/fC gain, 1 microsecond shaping time, and the 900 mV baseline intended for induction channels. The colored waveforms illustrate the various gain and shaping time settings with a channel set to the 200 mV baseline intended for collection channels.

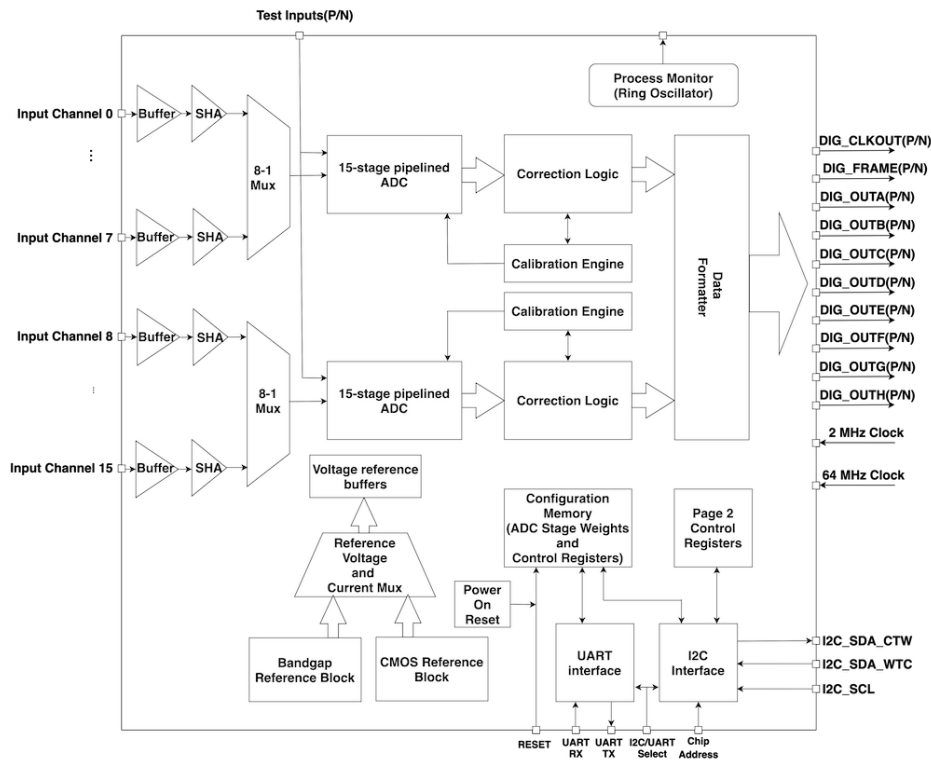


Figure 4.55: ColdADC block diagram.

the 2 MHz clock. The ADC uses the well known pipelined architecture with redundancy [64]. Digital logic is used to correct non-linearity introduced by non-ideal amplifier gain and offsets in each pipeline stage [65], and an automatic calibration procedure is implemented to determine the constants used in this logic. The ADC produces 16-bit output which is expected to be truncated to 12 or 14 bits.

The ADC is highly programmable to optimize performance at different temperatures. Many circuit blocks can be bypassed, allowing the performance of the core digitization engine to be evaluated separately from the ancillary circuits. A block diagram of the chip is shown in Figure 4.55. A detailed circuit description is given in reference [66].

ColdADC is designed to be very low noise so that it will contribute a negligible amount to the noise of a digitized waveform even when LArASIC is operated at its lowest gain setting. At liquid nitrogen temperature, the noise (measured either with open channels or with a constant voltage at the inputs) is  $\sim 0.75$  14-bit ADC counts with differential inputs and  $\sim 1.5$  14-bit ADC counts with single ended inputs. The noise is quite uniform channel to channel.

The static linearity of ColdADC has been measured both using a very slow linear ramp and using a sine wave input, with consistent results. Typical results are shown in Figure 4.56. The differential nonlinearity (DNL) is small and there are no missing codes, but the integral nonlinearity (INL) is larger than was expected and has a characteristic shape. It is believed this is due to dielectric absorption in the capacitors used in the switched capacitor circuits of the sample and hold amplifiers and in the pipeline ADCs [66].

The INL varies systematically channel to channel and to a lesser extent chip to chip and can be corrected with a polynomial function. The result of fitting a third-order polynomial to the INL of the ADC channel depicted in Figure 4.56 and using the fit function to correct data from the same channel taken on a different day (after multiple temperature cycles) is shown in Figure 4.57.

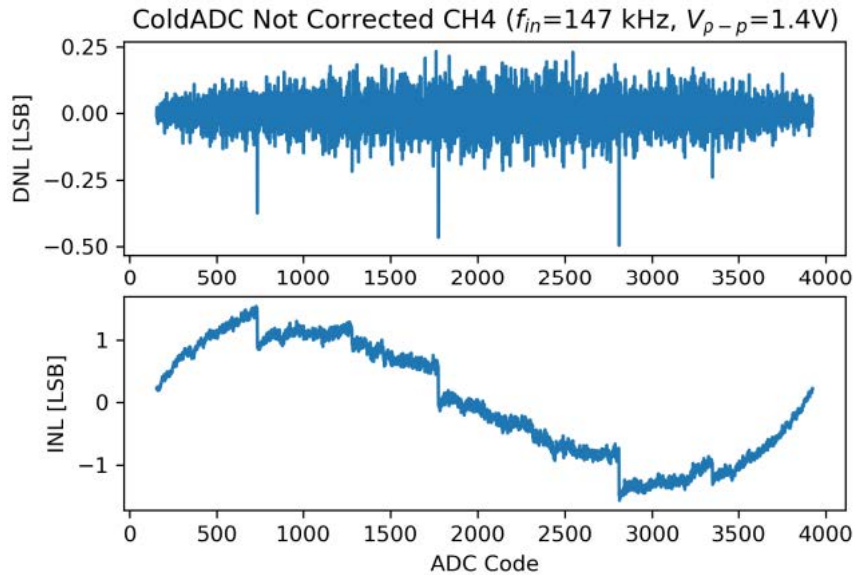


Figure 4.56: Typical static nonlinearity of a ColdADC channel differential inputs at 77 K. The INL shows a marked polynomial shape that suggests it could be corrected with a cubic (or another odd-order polynomial)

The structure in the INL that is attributed to dielectric absorption is very stable with time. Linearity correction has been found to be stable for at least several months, but in practice the transfer function of each channel will be measured in situ from time to time using the LArASIC test input.

The dynamic linearity of ColdADC has been measured using sine wave inputs. Figure 4.58 shows a typical Fourier-transformed output spectrum collected at 77 K using differential inputs. The measured dynamic performance as a function of input frequency is shown in Figure 4.59. The  $-3$  dB bandwidth of LArASIC is  $\sim 410$  kHz when the shortest shaping time of  $0.5 \mu\text{s}$  is selected and  $\sim 205$  kHz when the shaping time is  $1 \mu\text{s}$ .

ColdADC exceeds its effective number of bits (ENOB) requirement of 10.3 bits across the required input frequency range.

The crosstalk of ColdADC has also been measured by injecting a signal into one channel at a time and recording the ADC codes from all 16 channels (see Figure 4.60). The peak crosstalk is  $\sim 0.06\%$  and is observed in the next channel in the multiplexing cycle, indicating that most of the crosstalk is associated with the multiplexer. This level of crosstalk is small enough that no correction is expected to be needed in the analysis of DUNE data.

As detailed in Table 4.9, ColdADC dissipates approximately 332 mW in a typical configuration

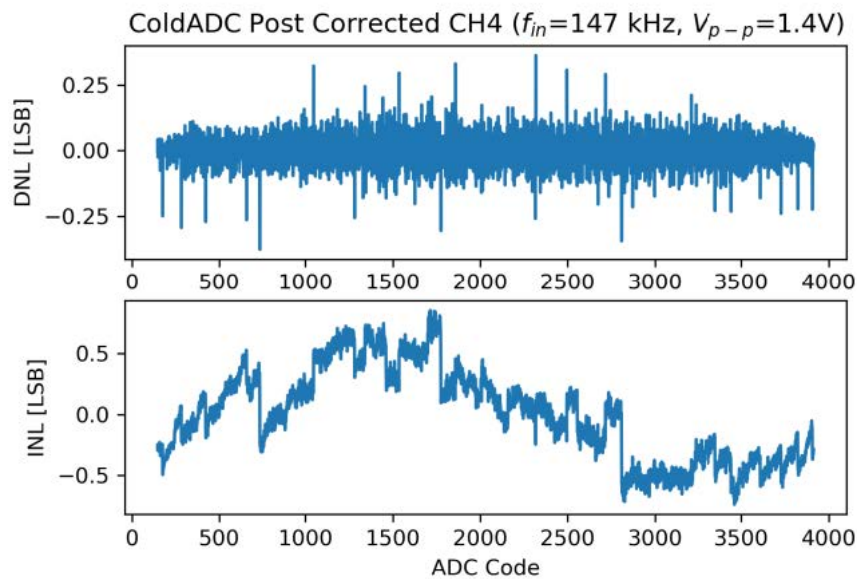


Figure 4.57: Post-correction static nonlinearity of a separate measurement (on a different day) of the same ColdADC channel shown in Figure 4.56. The INL is improved by use of a cubic fit to the INL shown in Figure 4.56.

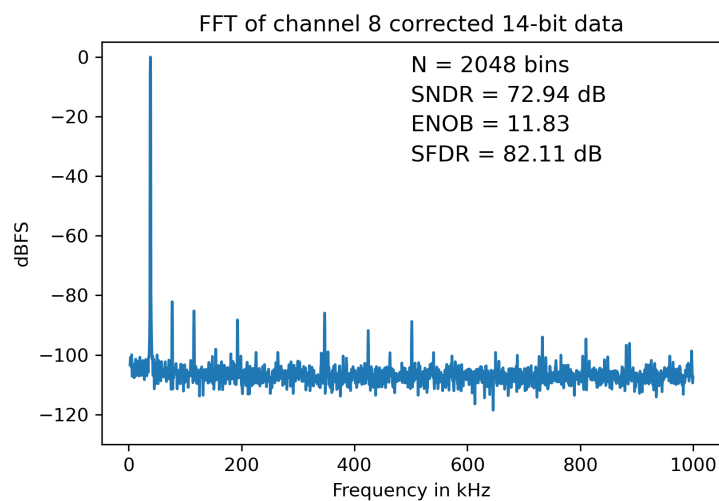


Figure 4.58: Typical frequency spectrum of ADC output codes (with differential inputs at 77 K) after polynomial correction. The input frequency was  $\sim 38.6$  kHz

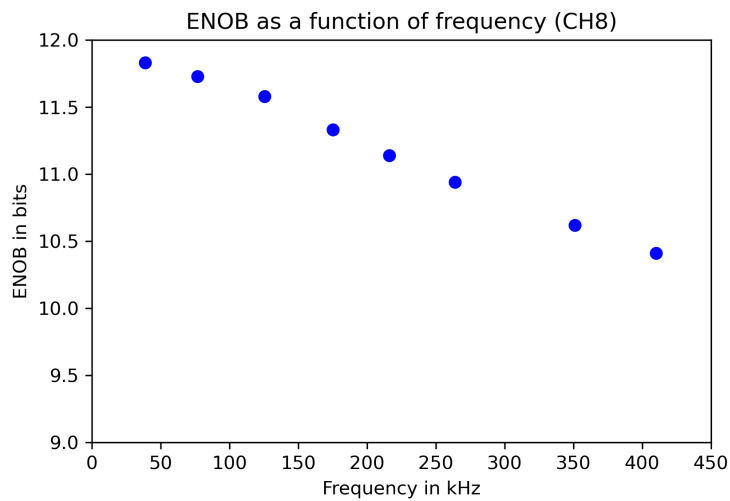


Figure 4.59: Typical ENOB as a function of input sinewave frequency (differential input, 77 K)

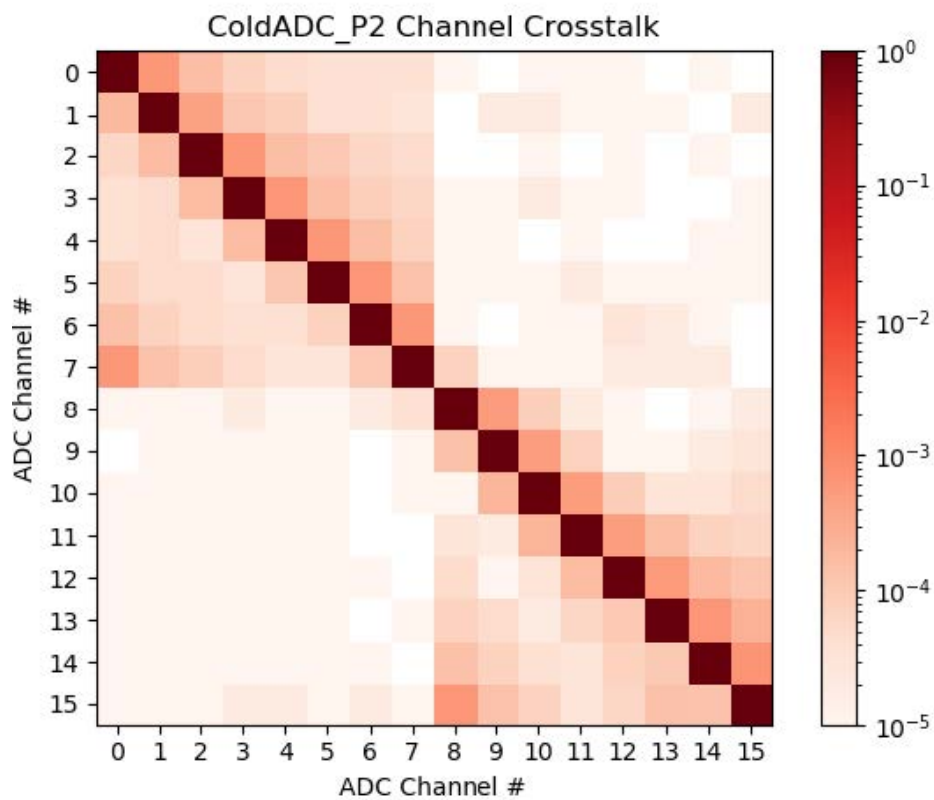


Figure 4.60: Channel-to-channel crosstalk in ColdADC measured with differential inputs at 77 K

(differential inputs with input buffers bypassed) at 77 K.

Table 4.9: ColdADC power dissipation at 77 K.

Power Domain	Description	Voltage (V)	Power Dissipation (mW)
VDDA2P5	Analog Circuitry	2.25	286
VDDD2P5	ADC Digital Logic and Switches	2.25	11.9
VDDD1P2	Digital Logic	1.10	1.3
VDDIO	ESD Ring, LVDS, CMOS I/O	2.25	32.6
Total			331.8
Per Channel			20.7

### 4.4.3.6 COLDDATA ASIC

COLDDATA is a control and communications ASIC designed to control four LArASIC front end ASICs and four ColdADC ASICs and to merge data from four ColdADCs. It transmits data to a WIB over two 1.25 Gbps links. COLDDATA receives commands either from a WIB or from another COLDDATA ASIC. It either responds to commands directly (if they are intended for it) or relays the commands to their destination and relays responses from the destination back to the WIB.

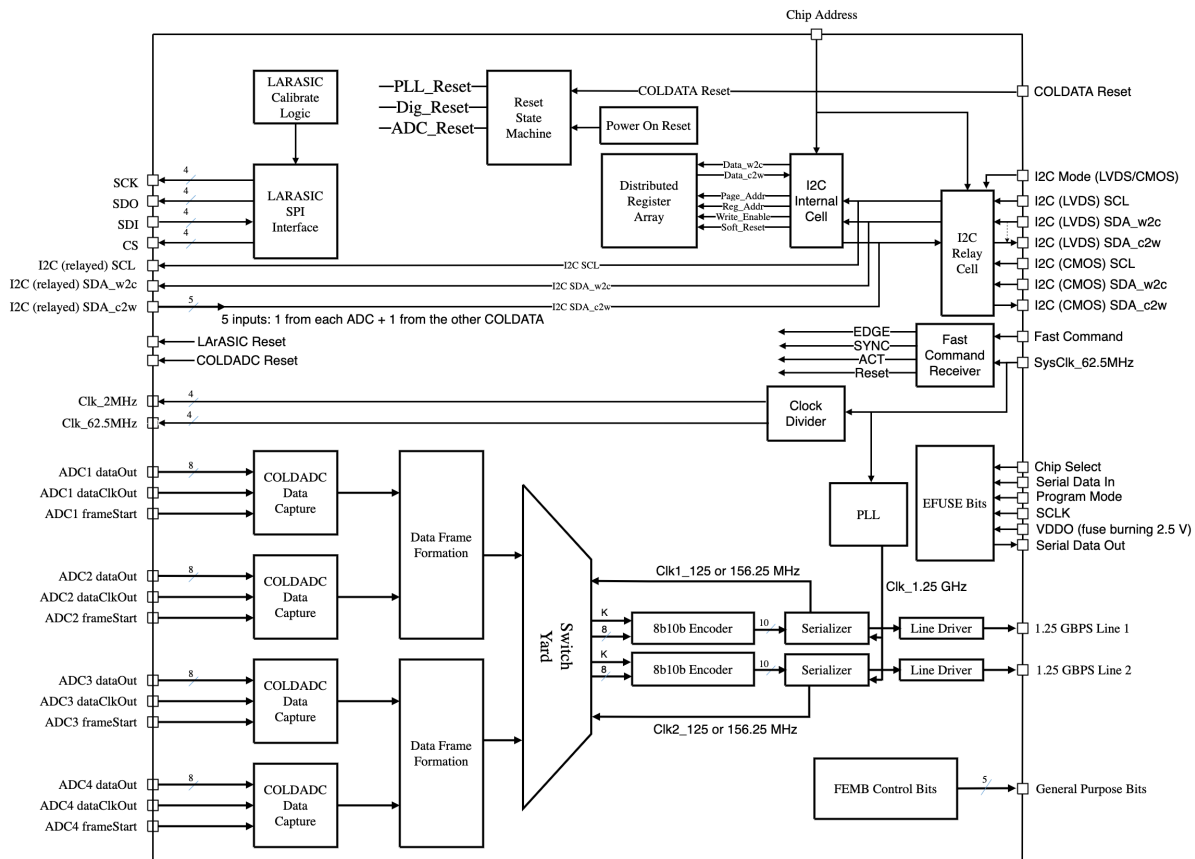


Figure 4.61: COLDDATA block diagram.

A block diagram of COLDDATA is shown in Figure 4.61. COLDDATA is implemented in a 65 nm

CMOS technology and was designed by a team of engineers from Fermilab, Southern Methodist University, and BNL.

COLDATA's control communication protocol is based on Inter-Integrated Circuit (I2C) [67] protocol. The major difference between COLDATA "I2C" and standard I2C is that COLDATA uses two separate SDA (Serial Data) lines, rather than one bidirectional line. This is motivated by the fact that COLDATA's control communications must travel over long cables between the WIBs and the FEMBs. Consequently, for these signals, canonical I2C signaling is replaced by differential. Since LVDS is not amenable to bidirectional communication, the bidirectional SDA (serial data) line is replaced by two data lines, one from Warm to Cold (I2C-SDA-w2c) and one from Cold to Warm (I2C-SDA-c2w). To reduce power dissipation on the FEMBs, single ended CMOS signaling rather than differential LVDS is used for "I2C" communication on the FEMBs. The COLDATA data sheet contains a full description of the protocol that is implemented.

Time-sensitive commands are sent from the WIB to COLDATA in the form of DC balanced 8-bit "Fast Command" words. Fast Command words are bit-aligned with the rising edge of the 62.5 MHz system clock and captured by COLDATA using the falling edge of the system clock. An example of a Fast Command is the "Edge" command, which is used to move the rising edge of the ADC sample clock to the next rising edge of the 62.5 MHz system clock. This command, along with another feature of COLDATA that allows the time delay on the cable between the WIB and the FEMB to be measured, is used to synchronize the sample time of all ColdADCs.

The 1.25 Gbps hybrid-mode Line Driver is designed with current-mode transmitter equalization and voltage-mode pre-emphasis to drive 25-35 meter long twin-axial cables. The current-mode transmitter equalization circuit uses a finite element response (FER) filter to distort the data pulse to compensate for the large frequency-dependent signal loss over a long twinax cable with low dynamic power consumption. The voltage-mode main driver and pre-emphasis circuit uses source-series-terminated (SST) output stages to provide a large output voltage swing and low static power consumption. The Line Driver is highly programmable and can also be operated in a pure current-mode or a pure voltage-mode. The pure current-mode with no equalization or pre-emphasis is appropriate for use with short cables. Figure 4.62 shows eye diagrams for a PRBS7 pseudorandom bit pattern driven (at room temperature) over 25 m and 35 m lengths of Samtec twinax cable. PRBS-7 has approximately the same degree of imbalance as is provided by the 8b10b encoding that is used by COLDATA. The cable insertion loss is less significant at cryogenic temperature, so the eyes become even more open when the cables are cold.

#### 4.4.3.7 Infrastructure Inside the Cryostat

Each FEMB is enclosed in a CE box which is connected to the ground of the FEMB and provides mechanical support for the FEMB and cable strain relief (see Figure 4.63). A 0.25 inch copper braid provides the electrical connection between the CE box and the CRP copper reference plane, as discussed in Section 4.4.3.1.

Twelve FEMBs are mounted on each half CRP and connected to patch panels (also mounted on the half CRPs) by 2.5 m long power cables and 2.5 m long miniSAS data cables as shown in Figure 4.64. 25 m long power and data cables are connected to the patch panels. These cables are 3 m longer than the power and data cables used in FD1-HD but otherwise identical. The long

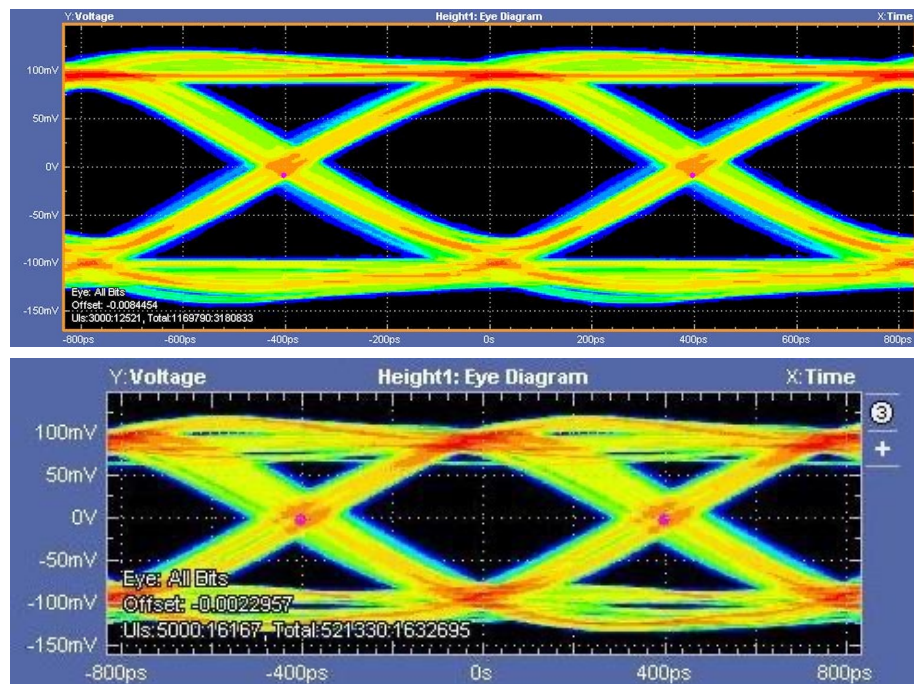


Figure 4.62: PRBS7 eye measurements made at room temperature using COLDATA with a 25 m length of Samtec twinax cable (top) and a 35 m length (bottom). The eye height is approximately 150 mV with a 25 m cable and slightly more than 100 mV with a 35 m cable.

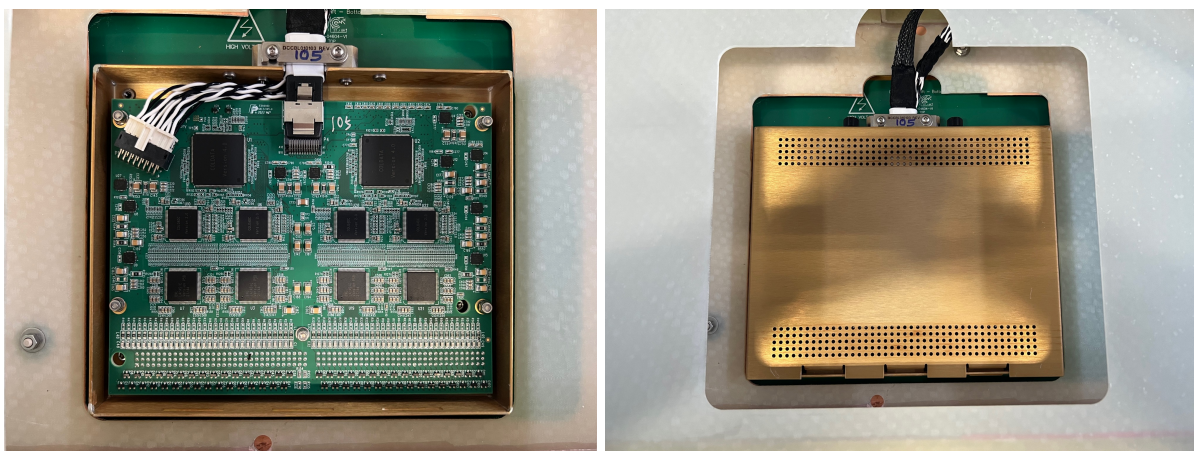


Figure 4.63: Picture of an open CE box (left) and a CE box with the lid on (right) mounted on a CRP.



cables will be routed from the patch panels on the CRPs along the floor of the cryostat to the long walls. They will be supported by “rope ladders” on the side of the cryostat and routed to penetrations located close to the long side of the cryostat.

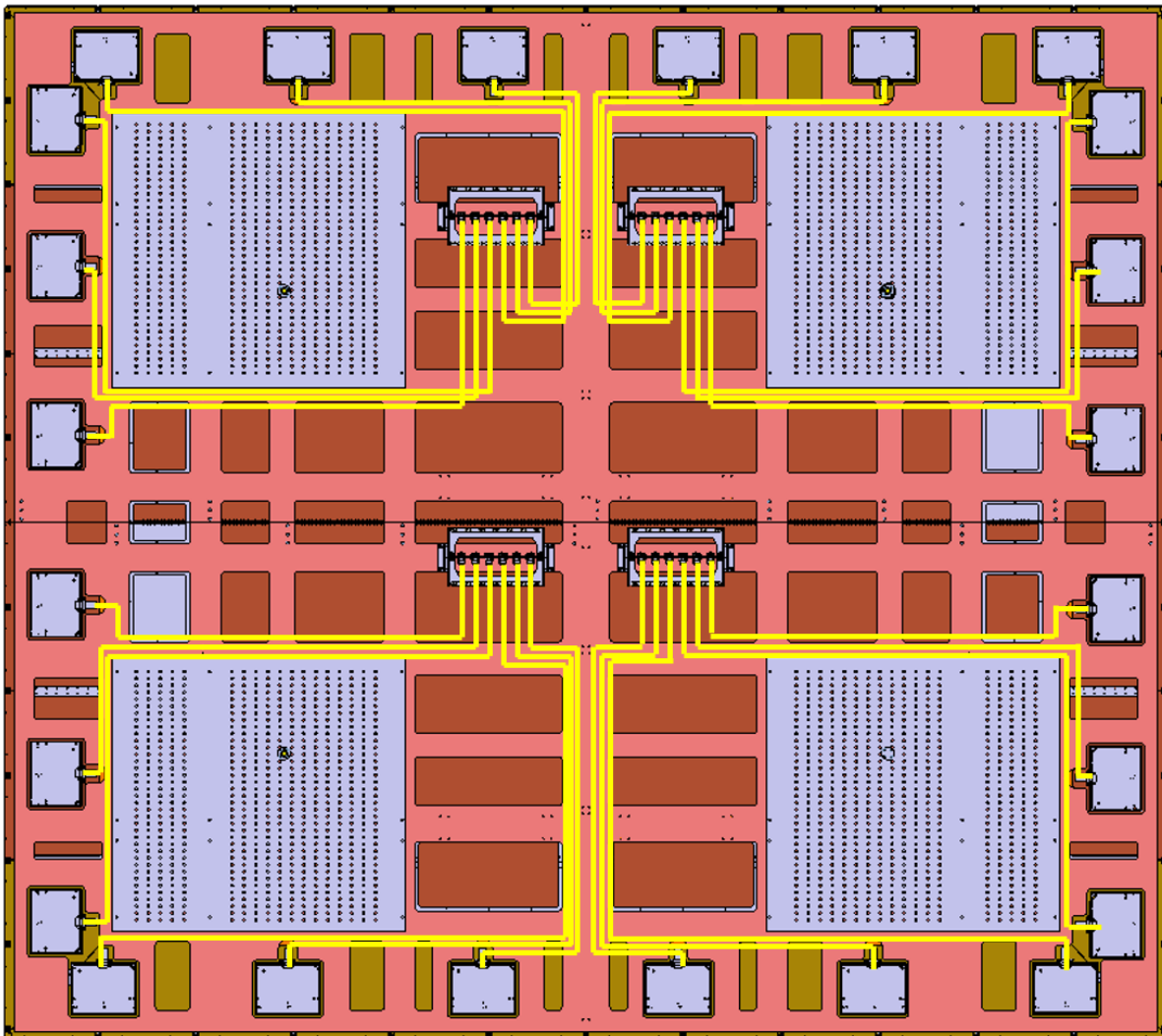


Figure 4.64: Cable routing between FEMBs and patch panels on a CRP.

#### 4.4.3.7.1 Cold Cables and Cold Electronics Feedthroughs

All cold cables originating inside the cryostat connect to the outside warm electronics through penetrations in the top of the cryostat. A fixture holding four threaded rods and a T-shaped spool piece are mounted on top of the cryostat penetration “crossing tube.” The threaded rods support a cable strain relief fixture positioned at the bottom of the crossing tube inside the cryostat (see Figure 4.65). BDE cold signal and power cables connect to feedthrough boards mounted on flanges on two of the three ports of the spool piece. The third port is for photodetector cables and cables associated with cryogenic instrumentation and calibration systems.

Data and control cable bundles send system clock and control signals from the signal flange to the FEMBs and high-speed data from the FEMBs to the signal flange. Each of the 24 FEMBs on one CRP connects to a flange via one data cable bundle. Ten low-skew shielded twin-axial cables

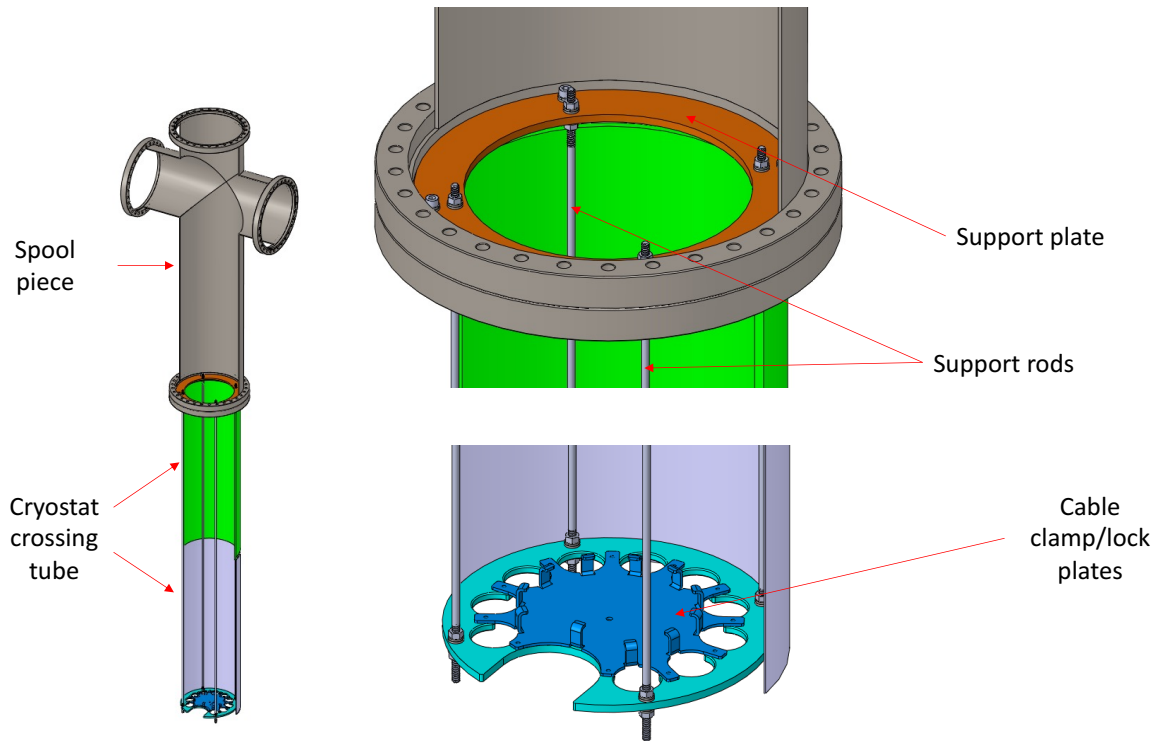


Figure 4.65: BDE cryostat feedthrough. Warm Electronics Interface Crates mount on the two horizontal flanges of the spool piece. The top flange is for photodetector cables and fibers. A fixture at the bottom of the crossing tube provides strain relief for the cable bundles.

transmit the following signals between the WIB and the FEMB:

- four differential 1.25 Gbps data links (two from each COLDATA);
- one 62.5 MHz system clock (sent from the WIB);
- one fast command line;
- three I2C-like control lines (clock, data-in, and data-out);
- one multipurpose pair of lines (described below in the section on the WIB).

The power is passed from the flange to the FEMB by bundles of 16 20 AWG twisted-pair wires, with half of the wires serving as power feeds and the other half as returns. The bulk of the power consumed on a FEMB is used by the analog section of ColdADC, which operates at 2.25 V. Most of the balance of the power is consumed by LArASIC, which operates at 1.8 V. For this reason, four wire pairs are devoted to supply voltage to the ColdADC low dropout (LDO) linear regulators and two pairs are used to supply voltage to the LArASIC LDOs. One pair is used to supply voltage to the COLDATA LDOs and one pair provides the 5 V required by the LDOs themselves.

The cable plant for one CRP in the LAr also includes the cables that provide the bias voltages applied to the shield, first induction, and collection plane strips. The voltages are supplied through three of eight safe high voltage (SHV) connectors mounted on the signal flange. RG-316 coaxial cables carry the voltages from the signal flange to a filter box mounted on the CRP.

### 4.4.3.8 Warm Interface Electronics

The warm interface electronics provide an interface between the CE and the DAQ, timing, and slow control systems. warm interface electronics crates (WIECs) are attached directly to the CE flanges. A WIEC, shown in Figure 4.66, contains one power and timing card (PTC), six WIBs, and a passive power and timing backplane (PTB) that fans out clock signals and LV power from the PTC to the WIBs. The WIEC provides a Faraday shield and robust ground connections from the WIBs to the detector ground (Section 4.4.3.1). Only optical connections are used for the communication to the DAQ and the slow controls.

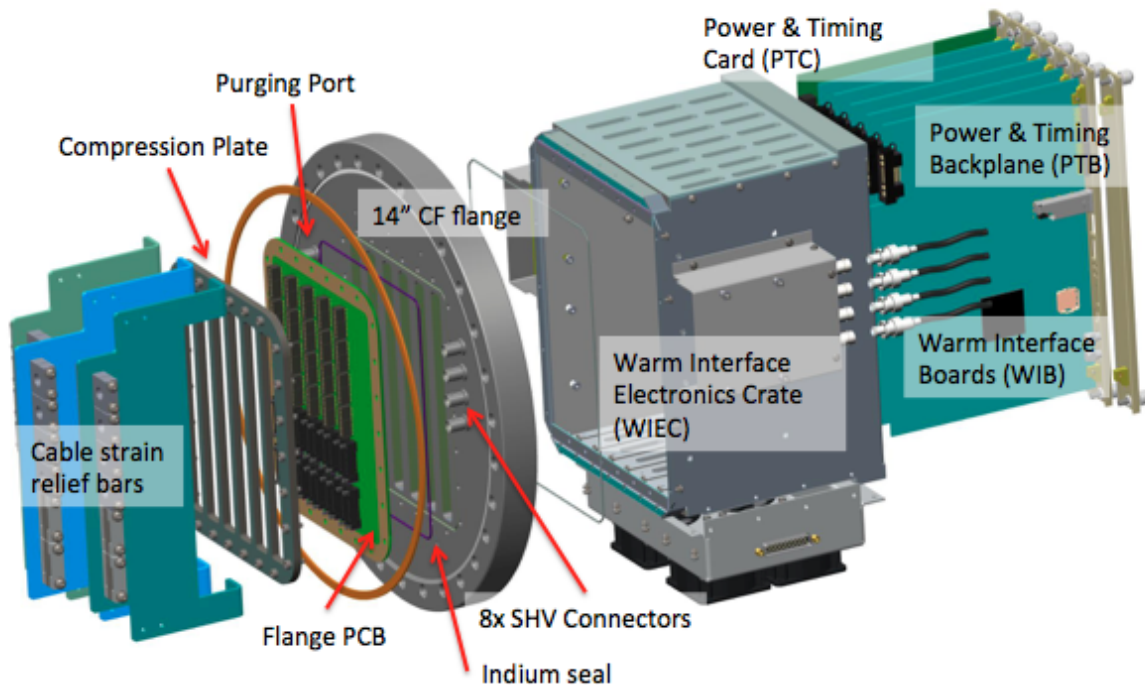


Figure 4.66: Exploded view of the CE signal flange.

#### 4.4.3.8.1 Power and Timing Card

The PTC receives 48 V LV power and steps the 48 V down to 12 V. Filtered 12 V is output from the PTC to the WIBs on point-to-point connections on the PTB. The WIBs in turn power the FEMBs (see Figure 4.67). The PTC also contains a bidirectional fiber interface to the timing system. The PTC fans out the encoded clock signal to the WIBs via the PTB.

#### 4.4.3.8.2 Warm Interface Board

A block diagram of the WIB is shown in Figure 4.68. The WIB receives the system clock and control signals from the PTC that allow it to synchronize the FEMBs and appropriately time stamp data received from the FEMBs. Each WIB provides power to and controls four FEMBs and receives high-speed serial data on 16 1.25 Gbps links from the FEMBs. It reformats these data and transmits data to the DAQ using two 10 Gbps optical links. A 1 Gbps Ethernet interface provides connectivity between the WIB and the slow controls system and also the configuration, control, and monitoring component of the data acquisition system.

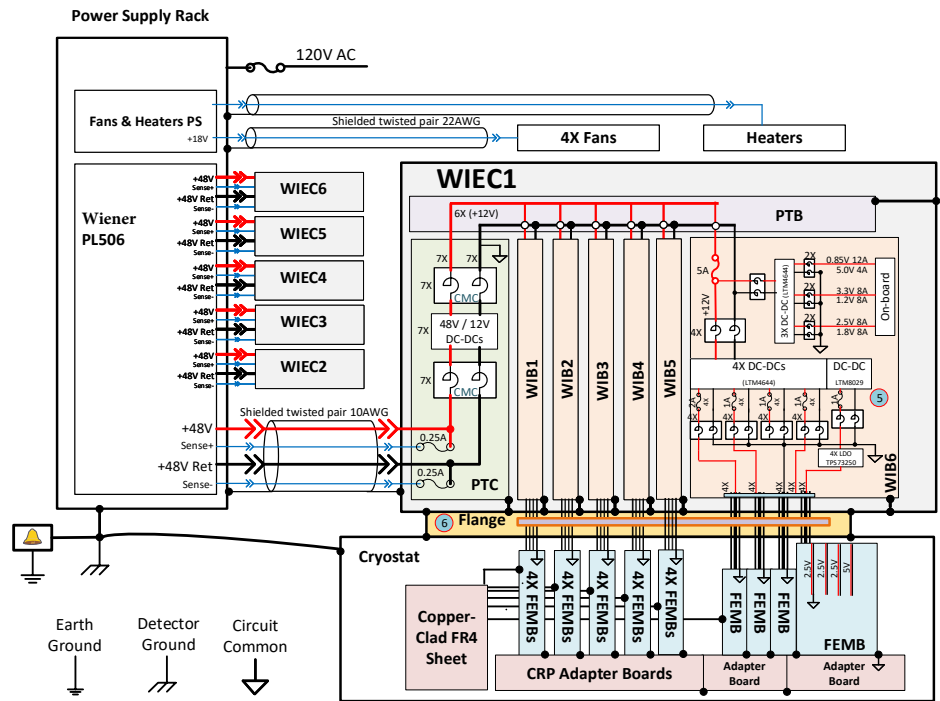


Figure 4.67: LV power distribution to the WIB and FEMBs.

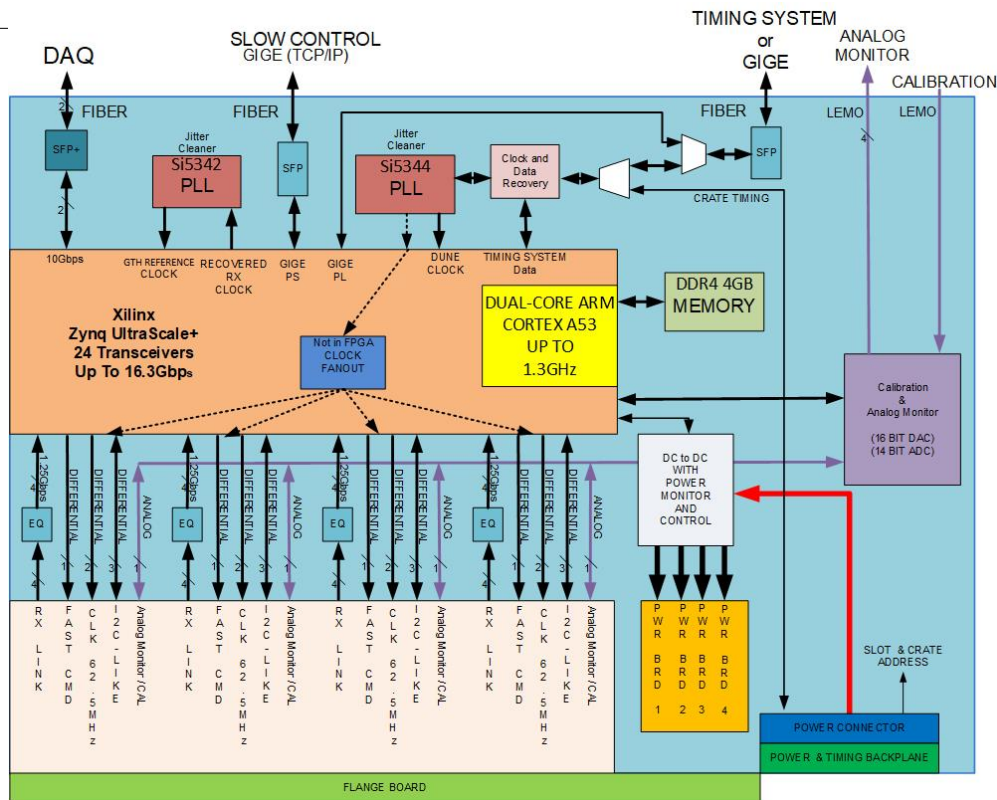


Figure 4.68: WIB block diagram including the fiber optic connections to the DAQ backend, slow controls, and the timing system, as well as the data readout, clock, and control signals to the FEMBs.

The WIBs are attached directly to the TPC CE feedthrough on the signal flange. The feedthrough board is a multilayer PCB with surface mount connectors on both sides electrically connected to one another using offset blind vias so there are no holes through the PCB. Cable strain relief for the cold cables is provided from the back end of the feedthrough.

All WIB functions are controlled by a Xilinx Zynq Ultrascale+ system-on-a-chip. Time-critical functions are implemented in the programmable logic and most other functions are implemented in software. Communication between software and firmware is done via a memory map (“REG” in Figure 4.69). The software framework for the WIB is based on a client server model. A server process (written in C) running on the WIB’s ARM cores provides a network API for client software running on other machines, either as part of DUNE DAQ or in a simpler bench-top setting. An OPC/UA server is also implemented to allow DUNE Slow Controls to access the WIB server. The WIB logical blocks and their interconnections are illustrated in Figure 4.69.

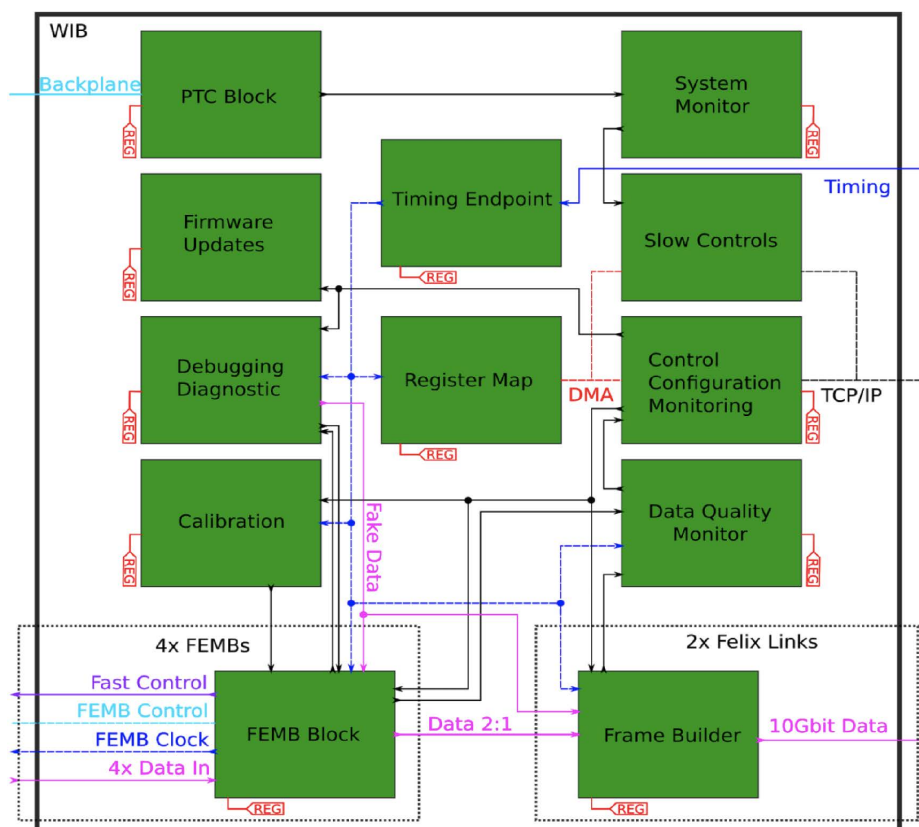


Figure 4.69: WIB logical blocks and interconnects.

#### 4.4.3.9 Services on Top of the Cryostat

Each PTC receives 48 V from a Wiener PL506 power supply installed on the top of the cryostat. Four wires are used for each PTC module; two 10 AWG, shielded, twisted-pair cables for the power and return; and two 20 AWG, shielded, twisted-pair cables for the sense. The primary protection is the over-current protection circuit in the LV supply modules, which is set higher than the  $\sim 10$  A current draw of the WIEC. Secondary sense-line fusing is provided on the PTC. The power cable shields can be connected at one or both ends of the cable. In tests of the first full-scale CRP in June 2022, good noise results were obtained with the shields connected at both ends. This will be

verified in FD2-VD Module 0 running.

Switching power supplies controlled by the slow controls system provide power to the heaters (12 V) and the fans (24 V) that are installed on the CE flanges. Temperature sensors mounted on the flanges, and power consumption and speed controls from the fans are connected to the interlock system that is part of the DUNE detector safety system (DDSS), in addition to being monitored by the slow controls system.

RG-58 coaxial cables connect the strip bias voltages from bias voltage supplies provided by the high voltage consortium to the standard SHV connectors that are machined directly into the CE feedthrough and insulated from the low voltage and data connectors.

Optical fibers are used for all connections between the WIECs and the DAQ and slow control systems.

To support the electronics, fan, and heater power cables, as well as optical fibers on top of the cryostat, cable trays are installed below the false flooring on top of the cryostat. All the necessary LV supplies and the bias voltage supplies are installed in these racks. Patch panels for the optical fiber plant used for the control and readout of the detector are also installed on the detector mezzanine.

#### 4.4.3.10 Summary of Differences between BDE and FD1-HD TPC Electronics

The BDE are almost identical to the FD1-HD TPC electronics. The only differences are:

- BDE FEMBs uses miniSAS data connectors rather than Samtec data connectors.
- The BDE uses longer cold cables than are used in FD1-HD and patch panels on the CRPs. The patch panels allow the FEMBs to be installed on the CRPs and cabled to the patch panels at the CRP factories, and also allow the long cold cables to be installed into FD2-VD before the CRPs are installed.
- Short mini-SAS data cables carry signals between the FEMBs and the patch panels.
- The routing of cold cables in FD1-HD and FD2-VD is different.
- The method of strain relieving the cold cables at the bottom of the cryostat crossing tubes is slightly different in FD1-HD and FD2-VD.
- Six WIBs are used in each FD2-VD WIEC and five WIBs are used in each FD1-HD WIEC.

#### 4.4.4 Performance with CRP

As detailed in Section 3.8.1, the first full-scale CRP prototype was built so that one half of the CRP could be read out using BDE and the other half TDE. Since monolithic FEMBs were not yet available, -style FEMBs were used for tests of this CRP. Tests were carried out in two phases. During the first phase, the BDE suffered from a relatively high level of coherent noise. The second phase of running included improved grounding and the BDE performed well with very little coherent noise.

One half of CRP-5, instrumented with 12 monolithic FEMBs, has been tested in LN2 in a cold

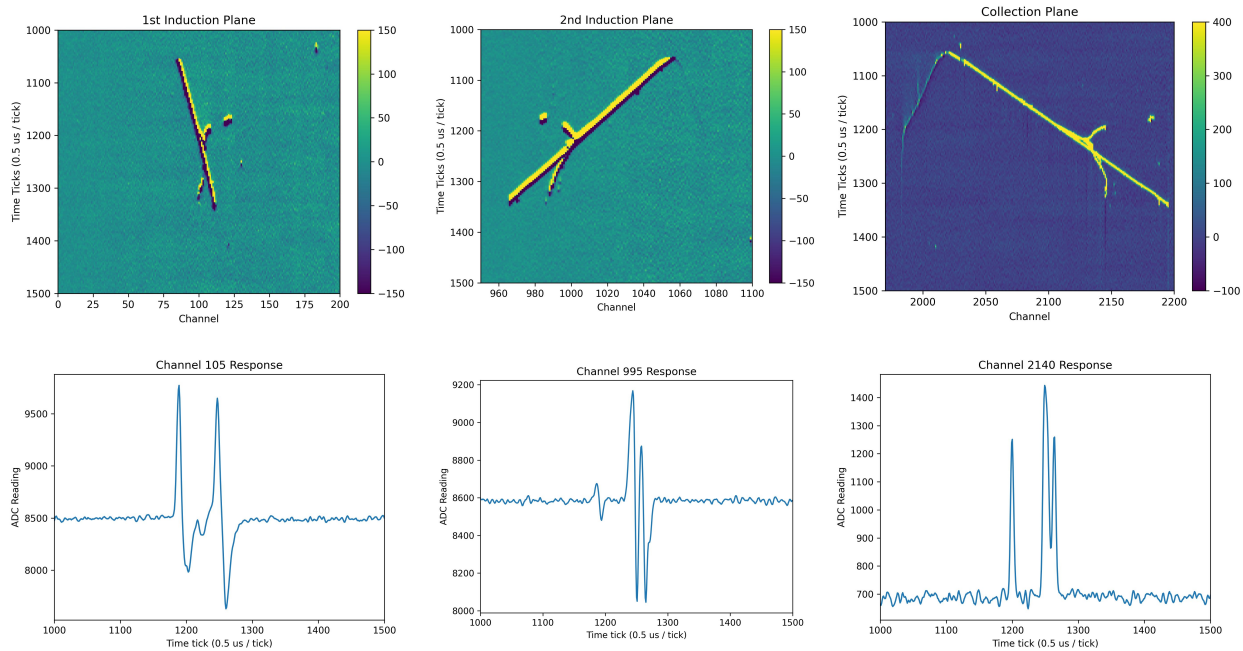


Figure 4.70: A sample cosmic ray track recorded using CRP-4 read out with BDE. The individual channel waveforms shown are for strips that recorded ionization from multiple tracks.

box at BNL. The noise performance was in line with expectations. The average noise (before coherent noise removal) for full length strips from the first and second induction layers is  $\sim 585 e^-$  and  $\sim 560 e^-$  and the average noise for collection strips is  $\sim 465 e^-$ . Recently, CRP-5 and CRP-4 have been tested in the cold box at NP02 using the final BDE. The measured noise in these cold box runs was also in line with expectations and very little coherent noise was observed. A sample event taken with CRP-4 (without coherent noise removal) is shown in Figure 4.70.

#### 4.4.5 Quality Assurance

DUNE aims to maximize the number of readout channels in FD2-VD that achieve the performance specifications discussed in Section 4.2. Particular care must be used for the CE components that will be installed inside the cryostat, since they cannot be repaired or replaced once the cryostat is closed.

A complete QA plan starts with ensuring that the designs of all detector components fulfill the specification criteria, considering also system aspects, i.e. how the various detector components interact among themselves and with the detector components provided by other consortia. Section 4.4.5.1 discusses design validation. The other aspects of the QA plan involve documenting the assembly and testing processes, storing and analyzing the information collected during the QC process, training and qualifying personnel from the consortium, monitoring procurement of components from external vendors, and assessing whether the QC procedures are applied uniformly across the various sites involved in detector construction, integration, and installation. The TPC electronics consortium plan involves having multiple sites using the same QC procedures, many of which will be developed as part of system design tests during the QA phase, with the possibility

of a significant turnover in the personnel performing these tasks. To avoid problems during most of the production phase, training as well as documentation of the QA plan will be emphasized. Reference parts will be tested at several sites to ensure consistent results. At a single site, some parts will be tested repeatedly to ensure that the response of the apparatus does not change and that new personnel involved in testing detector components are as proficient as more experienced personnel.

#### 4.4.5.1 Initial Design Validation

As described in Section 4.4.3, three ASICs have been developed for the DUNE FD TPC readout (LArASIC, ColdADC, and COLDATA). As each new prototype ASIC was produced, the groups responsible for the ASIC design performed the first tests of ASIC functionality and performance. Some of these tests used bare chips mounted directly on a printed circuit board and wire bonded to the board while others used package parts. The goal of these tests was to determine the extent to which the ASIC functions as intended, both at room temperature and at LN<sub>2</sub> temperature. For all chips, these tests included exercising digital control logic and all modes of operation. Tests of FE ASICs included measurements of noise levels as a function of input capacitance, baseline recovery from large pulses, cross-talk, linearity, and dynamic range. Tests of ADCs included measurements of the effective noise levels and of differential as well as integral non-linearity. Tests of the COLDATA ASIC included verification of both the control and high-speed data output links using cables with lengths up to 35 m. After the initial functionality tests, the ASICs were mounted on FEMBs so measurements could be repeated with varying input loads and with real anode plane assemblies.

#### 4.4.5.2 Cryogenic Tests

Tests of ASICs and FEMBs in a cryogenic environment are performed in LN<sub>2</sub> instead of LAr for cost reasons, ignoring the small temperature difference. These tests can be performed immersing the detector components in a dewar containing LN<sub>2</sub> for the duration of the tests. Condensation of water from air can interfere with the tests or damage the detector components or the test equipment, particularly during their extraction from the LN<sub>2</sub>. A test dewar design developed by Michigan State University, referred to as the (Cryogenic Test System), has been developed to avoid this problem. Several CTS units were deployed at BNL during the ProtoDUNE-SP construction and used for the QC on the ASICs and FEMBs for ProtoDUNE-SP. Later they were also used to perform similar tasks during the construction of the electronics for . Several other CTS units have been deployed to institutions involved in developing ASICs to test the first prototypes of ASICs and FEMBs for the DUNE FD as well as for QC tests.

Two CTS units in operation at BNL are shown in Figure 4.71.

#### 4.4.6 Reliability Studies

The TPC CE system of the DUNE FD2-VD FD must meet stringent requirements, including a very small number of failures (< 1% of the total number of channels) for components installed on the detector inside the cryostat during the 20 years of detector operation.

A few detectors have operated without intervention for a prolonged period, with few readout channel losses, in extreme conditions that are similar to those in the DUNE FD cryostats:





Figure 4.71: Cryogenic Test System (CTS): an insulated box is mounted on top of a commercial LN<sub>2</sub> dewar. Simple controls allow the box to be purged with nitrogen gas and LN<sub>2</sub> to be moved from the dewar to the box and back to the dewar.

- The NA48/NA62 liquid krypton (LKr) calorimeter has 13,212 channels of JFET pre-amplifiers installed on the detector. It has been kept at LKr temperature since 1998. The total fraction of failed channels is < 0.2% in more than 24 years of operation.
- The ATLAS LAr accordion electromagnetic barrel calorimeter has approximately 110,000 readout signal channels, with up to seven connections and different circuit boards populated with resistors and diodes inside the cryostat. This calorimeter has been cold since 2004, for a total of 18 years of operation. So far, the number of readout channels that have failed is approximately 0.02% of the total channel count.
- The ATLAS LAr hadronic endcap calorimeter has approximately 35,000 GaAs pre-amplifiers summed into 5,600 readout channels that are mounted on cold pre-amplifier and summing boards. The ATLAS LAr hadronic endcap calorimeter CE have been in cold since 2005, with < 0.1% of the channels failing during 17 years of operation.

Neither NA48/NA62 nor the ATLAS LAr hadronic endcap calorimeter uses CMOS electronics; however, the procedures used in the construction and QC of PCBs and for the selection and QC of connectors and discrete components mounted on the PCBs are directly relevant for the DUNE FD.

A list of reliability topics to be studied (including some that have already been completed and others that have started) for the TPC electronics operated in LAr environment are:

- For COTS components, accelerated lifetime testing, a methodology developed by [68] will be used to verify the expected lifetime of operation at cryogenic temperatures. A COTS ADC has undergone this procedure and has been qualified as a solution for the SBND experiment [69].
- The custom ASICs incorporate design rules intended to minimize the hot-carrier effect [70,71], which is recognized as the main failure mechanism for integrated circuits operating at LAr temperature. Extensive lifetime studies of individual transistors used in LArASIC were performed early in its development [70,72]. The lifetime of ColdADC has been verified using the accelerated lifetime testing methodology, and a similar verification of the lifetime of

COLDATA will be completed before the production order for ColdADC and COLDATA is placed.

- Printed circuit board assemblies are designed and fabricated to survive repeated immersions in LN<sub>2</sub>.
- In addition to the QA studies noted above, a very detailed and formal set of QC checks of the production pieces will be required in order to ensure a reliable detector. The QC plans for the BDE detector components are discussed in Section 4.4.7.4.

## 4.4.7 Production and Quality Control

This section, discusses the production and assembly plans, including the plans for the spares required during the detector construction and for operations, for procurement, assembly, and quality control.

### 4.4.7.1 Spares Plan

The bottom anode of the FD2-VD will consist of 80 CRPs. This means that at least 1920 FEMBs with the corresponding bundles of cold cables will be required for the integration. APAs). To have spare FEMBs, the TPC electronics consortium plans to build 2100 FEMBs, about 10% more than required to instrument 80 CRPs. If more spares are needed during the QC process or during integration, additional FEMBs can be produced quickly as long as any components that have long lead times are on hand. For these components, it is planned to keep on hand a larger number of spares. The ASICs require a long lead time; a plan for those spares is discussed below.

In the case of LArASIC, the number of spare chips is driven by concern that it may soon become impossible to have devices fabricated using the 180 nm CMOS process. Consequently, it was decided to hold a production readiness review (PRR) for LArASIC and purchase chips. The review committee recommended the immediate purchase of 250 wafers using the mask set for the engineering run of LArASIC. Each wafer contains 310 final-design LArASICs, so this is a sufficient number for both of the first two DUNE far detector modules, even making pessimistic assumptions of chip yield.

In the case of ColdADC and COLDATA, the number of spares expected is driven by the fact that these two designs are implemented on the same wafer and that production wafers must be purchased in batches of 25. The expected number of chips per wafer is about 850 for ColdADC and 275 for COLDATA.

Assuming an overall yield of 85% (5% loss in dicing and packaging and approximately 10% failure rate in the QC testing), 34 wafers are required for the FD1-HD. Since wafers must be fabricated in batches of 25, 50 wafers will be purchased for FD1-HD. It is planned to purchase another batch of 25 wafers for FD2-VD.

In general, for other components, it is planned to procure between 5 and 10% additional components for spares for the construction of the FD2-VD module. More spares will be needed for components that have a larger risk of damage during integration and installation.

The components on top of the cryostat (power supplies, bias voltage supplies, cables, WIECs

with their WIB and PTC boards) can be replaced while the detector is in operation. For these components, additional spares may be required during the 20 years operation period of FD2-VD. The plan is to purchase 10% additional components for spares.

#### 4.4.7.2 Procurement of Parts

The construction of the detector components for DUNE requires many large procurements that must be carefully planned to avoid delays. For the ASICs, the choice of vendor(s) is made at the time the technology used in designing the chips is chosen. For almost all other components, several vendors will bid on the same package. Depending on the requirements of the funding agency and of the responsible institution, this may require a lengthy selection process. The cold cables used to transmit data from the FEMBs to the WIBs represent a critical case. In this case a technical qualification, including tests of the entire chain (from the FEMB to the receiver on the WIB) is required.

#### 4.4.7.3 Assembly

The TPC electronics consortium plans to minimize the amount of assembly work at any one of the participating institutions. For instance, all printed circuit boards will be assembled by commercial fabricators. One of the few exceptions is the assembly of WIECs, since this involves the integration of the power and timing backplane and installation on a feedthrough flange.

#### 4.4.7.4 Quality Control

Once the CRPs are installed inside the cryostat, only limited access to the detector components will be available to the TPC electronics consortium. After the temporary construction opening (TCO) is closed, no access to detector components will be available; therefore, they should be constructed to last the entire lifetime of the experiment (20 years). This puts very stringent requirements on the reliability of these components, which has been already addressed in part through the QA program discussed in Section 4.4.5. The next step is to carefully apply stringent QC procedures for detector parts to be installed in the detector. All detector components installed inside the cryostat will be tested and sorted before they are prepared for integration with other detector components prior to installation. A preliminary version of the QC process is being used as parts are fabricated for use in FD2-VD Module 0. These processes will be further developed and fully documented before the PRRs for each specific part.

Some of the requirements for the QC plans can be laid out now based on the lessons learned from constructing and commissioning the ProtoDUNE-SP detector. A small but significant fraction ( $\sim 4\%$ ) of the LArASIC chips produced for ProtoDUNE-SP passed QC tests at room temperature but failed when immersed in LN<sub>2</sub>. Based on that experience, it is planned to test all ASICs in LN<sub>2</sub> before they are mounted on the FEMBs. If the fraction of ASICs that fail cold after passing QC tests at room temperature proves to be very low, this plan will be reconsidered.

Based on experiences at ProtoDUNE-SP, discrete components like resistors and capacitors need not undergo cryogenic testing before they are installed on the FEMBs.

ASIC testing is performed with dedicated test boards that allow tests of the functionality of the chips. The dedicated test boards reproduce the entire readout chain where the input to

the FE amplifier or to the ADC is replaced by an appropriate signal generator, and some parts of the backend may be replaced by a simple FPGA that is directly connected to a computer. Tests of the FEMBs can be performed by connecting them directly to a standalone WIB, as discussed in Section 4.4.3.8. Given the large number of ASICs and FEMBs required for one DUNE, corresponding QC activities will be distributed among multiple institutions belonging to the TPC electronics consortium. Up to six test sites are needed for the ASICs plus an additional five sites for the FEMBs, with each test equipped with a cryogenic system such as the CTS. All tests will be performed following a common set of instructions.

The choice of distributing the testing activities among multiple institutions has been made based in part on the experience gained with ProtoDUNE-SP, where all associated testing activities were concentrated at BNL. While this approach had some advantages, like the direct availability of the engineers that had designed the components, a strict conformance to the testing rules, and a fast turn-around time for repairs, it also required a very large commitment of personnel from a single institution. Personnel from other institutions interested in the TPC electronics participated in the test activities but could not commit for long periods of time. For this reason, it is planned to distribute the QC testing activities for ASICs and FEMBs among multiple institutions belonging to the TPC electronics consortium. It should be noted that this approach is used in the experiments for detector components like the silicon tracker modules where both the assembly and QC activities take place in parallel at multiple (of the order of ten) institutions. To ensure that all sites produce similar results, emphasis will be placed on training experienced personnel that will oversee the testing activities at each site, and a reference set of ASICs and FEMBs will be initially used to cross-calibrate the test procedures among sites and then to check the stability of the test equipment at each site.

Criteria will be developed for the acceptance of ASICs and FEMBs. The procedures adopted for detector construction will evolve from the experience gained with ProtoDUNE-SP and the Module 0s. The QC procedures will be reviewed before the PRR that triggers the beginning of production. During production, the results of the QC process will be reviewed at regular intervals in production progress reviews. The yields and acceptance rate of the production will be centrally monitored and compared among different sites. In case of problems, the failures will be analyzed and root cause analyses will be performed. If necessary, production and/or the test program will be stopped at all sites while issues are being investigated, followed by changes in the procedures if necessary. All data from the QC process will be stored in a common database.

Since the number of ASICs to be tested is very large, a robotic system is being developed at Michigan State University that includes a pick-and-place robot and a modified version of the CTS.

After assembly, each FEMB will be tested in LN<sub>2</sub> using the current CTS design.

In the test, each channel of the FEMB is connected to a 150 pF capacitive load. This allows connectivity checks for each channel as well as measurements of the waveform baseline and of the channel noise level. Calibration pulses will be injected in the front-end amplifier, digitized, and read out. The test setup requires one WIB and a printed-circuit board similar to those used on the cryostat penetration, allowing simultaneous testing of four FEMBs. A standalone 12 V power supply is required, and the readout of the WIB uses a direct Gb Ethernet connection to a PC. The setup used for ASIC testing is similar. In both cases, the data can be processed locally on the

PC, and the results from the tests and calibrations are then stored in a database. The plan is to have the capability to retrieve these test and calibration results throughout the entire life of the experiment. As in the case of ASIC testing, the test results will be monitored to ensure that all sites have similar test capabilities and yields and to identify possible problems during production.

The tested FEMBs will be installed on CRPs and cabled to patch panels mounted on the CRPs at the CRP factories. The BDE consortium will provide a WIEC with six WIBs, and a PTC to each CRP factory. The BDE consortium will also provide the necessary firmware, software, and training so that CRP consortium members can verify the successful installation and cabling in warm and cold tests.

Stringent requirements must be applied to the cryostat penetrations in order to ensure that the liquid argon is not contaminated by nitrogen or oxygen. The cryostat penetrations have two parts: the first is the crossing tube with its spool pieces, and the second one is the three flanges used for connecting the power, control, and readout electronics to the CE and photon detection system (PDS) components inside the cryostat. On each cryostat penetration there are two flanges for the CE and one for the PDS. The crossing tubes with their spool pieces are fabricated by industrial vendors and pressure-tested and tested for leaks by other vendors. The flanges are assembled by institutions that are members of the TPC electronics and PDS consortia; the flanges must undergo both electrical and mechanical tests to ensure their functionality. Electrical tests comprise checking all of the signals and voltages to ensure they are passed properly between the two sides of the flange and that there are no shorts. Mechanical tests involve pressure-testing the flange itself, including checking for leaks. Further leak tests are performed after the cryostat penetrations are installed on the cryostat and later after the TPC electronics and PDS cables are attached to the flanges. These leak tests are performed by releasing helium gas in the cryostat penetration and checking for the presence of helium on top of the cryostat. Similar tests were performed during the ProtoDUNE-SP installation.

All other detector components that are a responsibility of the TPC electronics consortium can be replaced, if necessary, even while the detector is in operation. Regardless, every component will be tested before it is installed in Sanford Underground Research Facility (SURF) to ensure smooth commissioning of the detector. The WIECs will be assembled and tested with all of the WIBs and PTC installed. Testing requires a slice of the DAQ back-end, power supplies, and at least one FEMB to check all connections. All cables between the bias voltage supplies and the end flange, as well as all of the cables between the low-voltage power supplies and the PTCs will be tested for electrical continuity and for shorts. All power supplies will undergo a period of burn-in with appropriate loads before being installed in the cavern. Optical fibers will be tested by measuring the eye diagram for data transmission at the required speed. All test equipment used for qualifying the components to be installed in the detector will be either transported to SURF or duplicated at SURF in order to be used as diagnostic tools during operations.

#### **4.4.8 Installation, Integration, and Commissioning**

The installation of BDE components consists of four steps:

- Install power supplies and DDSS components in the detector mezzanine.

- Install 40 cryostat penetrations (spool pieces and crossing tubes) and 80 WIECs.
- Install 25 m long cold cables from the WIECs to the bottom of the cryostat.
- Connect the cold cables to the patch panels on the bottom CRPs as they are installed.

The installation of power supplies and DDSS components in the detector mezzanine can take place as soon as the mezzanine is available and will be the first step in BDE installation.

The FSII team will provide the transport crate and mobile gantry used in the installation of the cryostat penetrations. They will also do the installation of the penetrations and spool pieces. A BDE crew will install the flanges, WIECs, WIBs, and PTCs. After each WIEC is installed, the BDE crew will verify that the WIBs and PTC are functional.

Cold cables will arrive at SURF pre-assembled into cable bundles fastened to rope ladders wound onto large reels. Each reel will hold the cables associated with one WIEC. The FSII team will install the cables and two BDE teams will test the cables after installation. The rope ladder will be attached to the cryostat wall and the cable bundles will be hoisted through a penetration using a lift. A BDE team on the cryostat roof will strain relief the cables and connect them to a warm electronics flange. A second BDE team will connect FEMBs to the cables on the floor of the cryostat where a CRP will be installed. The BDE team on top of the cryostat will verify that every FEMB is powered properly and can be read out, and then the FEMBs will be disconnected.

The half CRPs will be moved into the cryostat by FSII and CRP consortium members. Two half CRPs will be joined to form a full CRP, moved into position, and placed on a support truss that will hold the CRP approximately 1.2m off the floor. BDE crew members will connect cold cables to the CRP patch panels and perform readout tests to verify that all of the cables are connected properly and the full readout chain works. The FSII crew will then remove the truss and lower the full CRP into its final position.

Quality control tests will be performed at each step of the installation. After the WIECs are installed, test patterns will be read out from each WIB. After the cold cables are installed, four (data cable, power cable) pairs at a time will be connected to FEMBs inside the cryostat and read out through a WIB on top of the cryostat. After each half CRP is transported to the clean room, a BDE crew will connect cold cables to the CRP patch panels and use a test system to verify that all FEMB channels are working. Any FEMB with a dead channel will be replaced before the half CRP is moved to the cryostat. Finally, after a full CRP is positioned, it will be read out through the normal readout chain. If any dead channel is observed and the CRP installation schedule allows, the CRP will be raised back onto support trusses and the faulty FEMB will be replaced.

#### 4.4.9 Interfaces

Table 4.10 contains a list of all of the interfaces between the BDE consortium and other consortia or groups, with references to the current version of the interface documents in EDMS.

Table 4.10: TPC electronics system interfaces.

Interfacing System	Description
CRP	Mechanical (connections of CE boxes and cable routing) and electrical (bias voltages, FEMB–copper plane connection, grounding scheme)
DAQ	Data output from the WIB to the DAQ back-end, clock signal distribution, controls and data monitoring responsibilities
HV	Grounding, bias voltage distribution, installation and testing
PDS	Electrical (cable routing, installation, and grounding scheme), cold flange
Installation	Integration and installation activities at SURF, equipment required for TPC electronics consortium activities, material handling

#### 4.4.10 Safety

The leadership of the TPC electronics consortium will work with the LBNF and DUNE enterprise (LBNF/DUNE) environment, safety and health (ES&H) manager and other relevant responsible personnel at the participating institutions to ensure that all consortium members receive the appropriate training for the work they are expected to perform and that all preventive measures to minimize the risk of accidents are in place. Where appropriate, BDE will adopt the strictest standards and requirements from among the different institutions. Hazard analyses will be performed, and the level of personnel protective equipment (PPE) will be determined appropriately for each task. The scientists in charge of the BDE activities at each site will be responsible for monitoring the training of personnel at their site.

ES&H plans for the activities to be performed in various locations, including all universities, national laboratories, and SURF, are discussed in the review process (Preliminary Design, Final Design, Production Readiness, Production Progress) that takes place during the construction of the detector.

It is also important to protect the detector components during testing, shipping, integration, installation, and commissioning. The most important risk during construction is damage induced by ESD in the electronics components, followed by mechanical damage to parts during transport and handling. Appropriate preventive measures will be documented and enforced during all phases, and QC procedures and integration tests will ensure full functionality of the components and system.

To avoid unsafe conditions for the BDE during operations, the DDSS will include hardware interlocks to prevent operating or even powering up detector components unless conditions are safe both for the detector and for personnel. Interlocks will be used on all low-voltage power and on bias voltage supplies, including inputs from environmental monitors both inside and outside the cryostat.

## 4.4.11 Management and Organization

### 4.4.11.1 Institutions

Table 4.11 lists the institutions participating in the joint FD1-HD/FD2-VD BDE consortium.

Table 4.11: Institutions participating in the joint FD1-HD/FD2-VD TPC electronics (CE) consortium

Institution
Brookhaven National Laboratory
University of Cincinnati
Colorado State University
University of California, Davis
Fermilab
University of Florida
University of Hawaii
Iowa State University
University of California, Irvine
Lawrence Berkeley National Laboratory
Louisiana State University
Michigan State University
University of Pennsylvania
SLAC National Accelerator Laboratory
Stony Brook University

Institutional responsibilities for FD2-VD BDE are summarized below:

- LArASIC design and procurement: BNL
- LArASIC QC: BNL, Michigan State U., Stony Brook
- ColdADC design and procurement: LBNL, Fermilab, BNL
- ColdADC QC: LBNL, LSU, UC Irvine
- COLDATA design and procurement: Fermilab, BNL
- COLDATA QC: Fermilab, UC Irvine
- ASIC test stand development: BNL, LBNL, Fermilab
- FEMB test stand development: BNL
- Development of cryogenic and robotic test systems: Michigan State U.
- FEMB design and procurement (including cold boxes): BNL
- FEMB QC: BNL, Fermilab, Cincinnati, Iowa State, U. Florida
- Cold cable specification and procurement: BNL
- Cable tray and cryostat penetration design and procurement: BNL
- Flange design and procurement: BNL
- WIBs design, procurement, and QC: BNL, U. Penn
- WIB firmware and software: U. Florida, U. Penn, BNL



- PTCs design, procurement, and QC: U. Penn
- PTC firmware and software: U. Penn, U. Florida
- Interface to DDSS: Fermilab
- Low voltage and bias power supplies specification and procurement: Fermilab
- Warm cable and fiber procurement: Fermilab
- Support for CRP integration tests using the cold boxes at NP02: BNL, LBNL, LSU, UCI, Fermilab
- Installation at SURF: All institutions in the consortium
- Detector monitoring during installation at SURF: All institutions
- Detector commissioning: All institutions

#### 4.4.11.2 Milestones

The milestones of the FD2-VD BDE TPC electronics consortium for 2022 and beyond are listed in Table 4.12.

Table 4.12: Milestones of the BDE TPC electronics consortium.

Milestone	Date
Start of FD2-VD Module 0 CE installation	November 2022
Completion of FD2-VD Module 0 CE installation	May 2023
Completion of BDE Final Design Review	June 2023
Completion of Production Readiness Review	February 2024
Start of ColdADC/COLDATA ASIC production	November 2024
Start of cold cable procurement	October 2024
Start of FEMB production	October 2024
Start of production of WIECs, WIBs, and PTCs	June 2025
Start of production of cryostat penetrations	April 2025
Completion of ASIC QC	February 2026
Completion of cold cable QC	September 2026
Completion of FEMB QC	July 2026
Completion of WIEC, WIB, and PTC QC	November 2026
Completion of cryostat penetration QC	March 2026
Start of power supply, penetration, and WIEC installation at SURF	September 2026
Start of cold cable installation inside FD2 cryostat	July 2027
End of cold cable installation inside FD2 cryostat	September 2027
Start of FD2-VD bottom CRP installation inside FD2 cryostat	February 2028
End of FD2-VD bottom CRP installation inside FD2 cryostat	April 2028

A more detailed schedule for production and installation of the complete FD2-VD drift readout electronics is found in Figure 4.72.

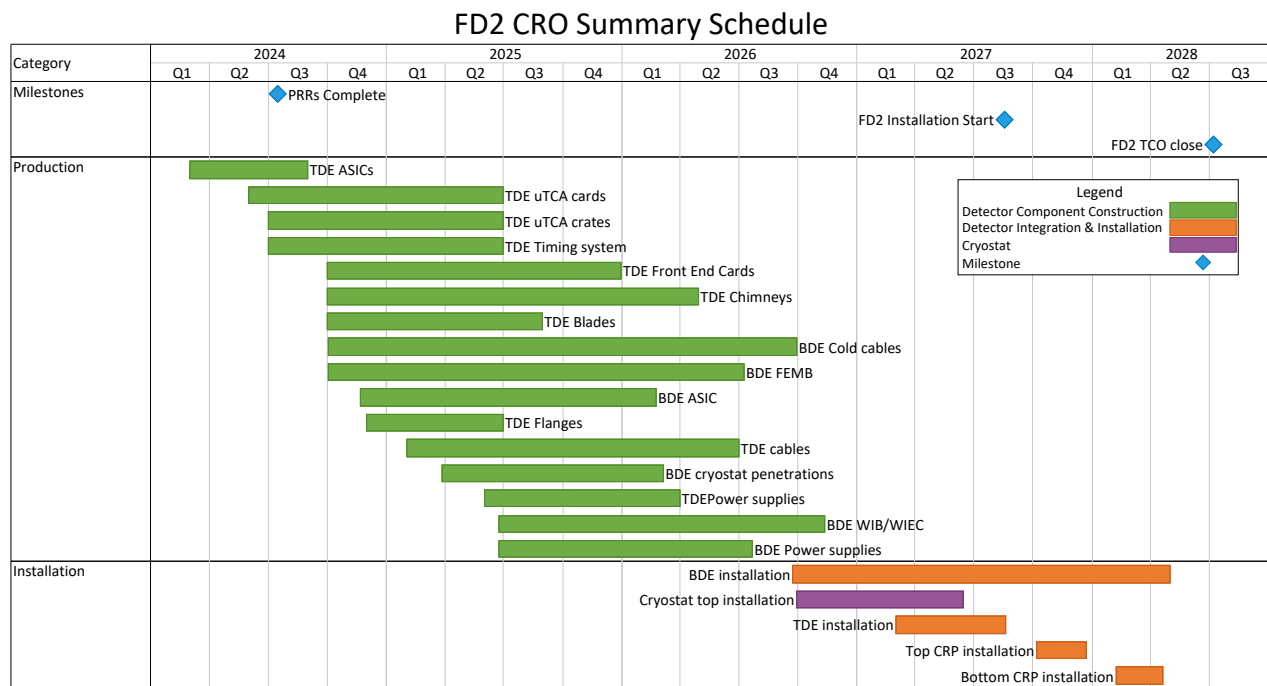


Figure 4.72: Key CRO milestones and activities toward the FD2-VD in graphical format (Data from [53]).

FD2-CRO\_Summary\_Schedule\_v3.xlsx

Snapshot Date: 3/13/2023

Created in OnePager® Express

# Chapter 5

## High Voltage System and Drift Field

### 5.1 Introduction

A liquid argon time-projection chamber (LArTPC) uses an electric field (E field) to drift ionization electrons through liquid argon (LAr) to an anode sensor plane. The system that drives these electrons consists of an equipotential cathode plane biased at a negative high voltage (HV), parallel to and a distance away from the anode plane, and an interior E field that is maintained uniform by a system that surrounds the detector active volume.

The DUNE LArTPC detector module design for vertical drift detector module (FD2-VD) encompasses two drift volumes of equal (maximum) drift distance 6.5 m and has a nominal uniform E field of 450 V/cm. A flat horizontal cathode plane spans the detector at mid-height and is held at a negative voltage. The two horizontal s (biased at near-ground potentials) span the top and bottom of the detector, as described in Chapter 3.

The high voltage system (HVS) is divided into the supply and delivery system, and the distribution system. The supply and delivery system consists of a negative high-voltage power supply (), HV cables with integrated resistors to form a low-pass filter network, a HV feedthrough (), and a 6 m long extender inside the cryostat to deliver  $-294$  kV to the cathode inside the time projection chamber (TPC). The distribution system consists of the cathode plane, the field cage, and the field cage termination supplies. Figure 5.1 is a schematic circuit diagram of the high-level components of the HV system.

The FD2-VD cathode plane is 60 m long, 13.5 m wide, and 6 cm thick. It is tiled from an array of  $20 \times 4$  cathode modules with highly resistive top and bottom panels mounted on fiber-reinforced plastic () frames. The purpose of the high-resistivity surfaces is to slow the voltage swing on the cathode in case of a discharge, thereby reducing the peak current injection into the front-end electronics connected to the anode readout strips (Section 3.3).

The field cage, in conjunction with the cathode and anode planes, defines the detector drift volumes and is designed to ensure uniformity of the E field in the vertical direction. The field cage



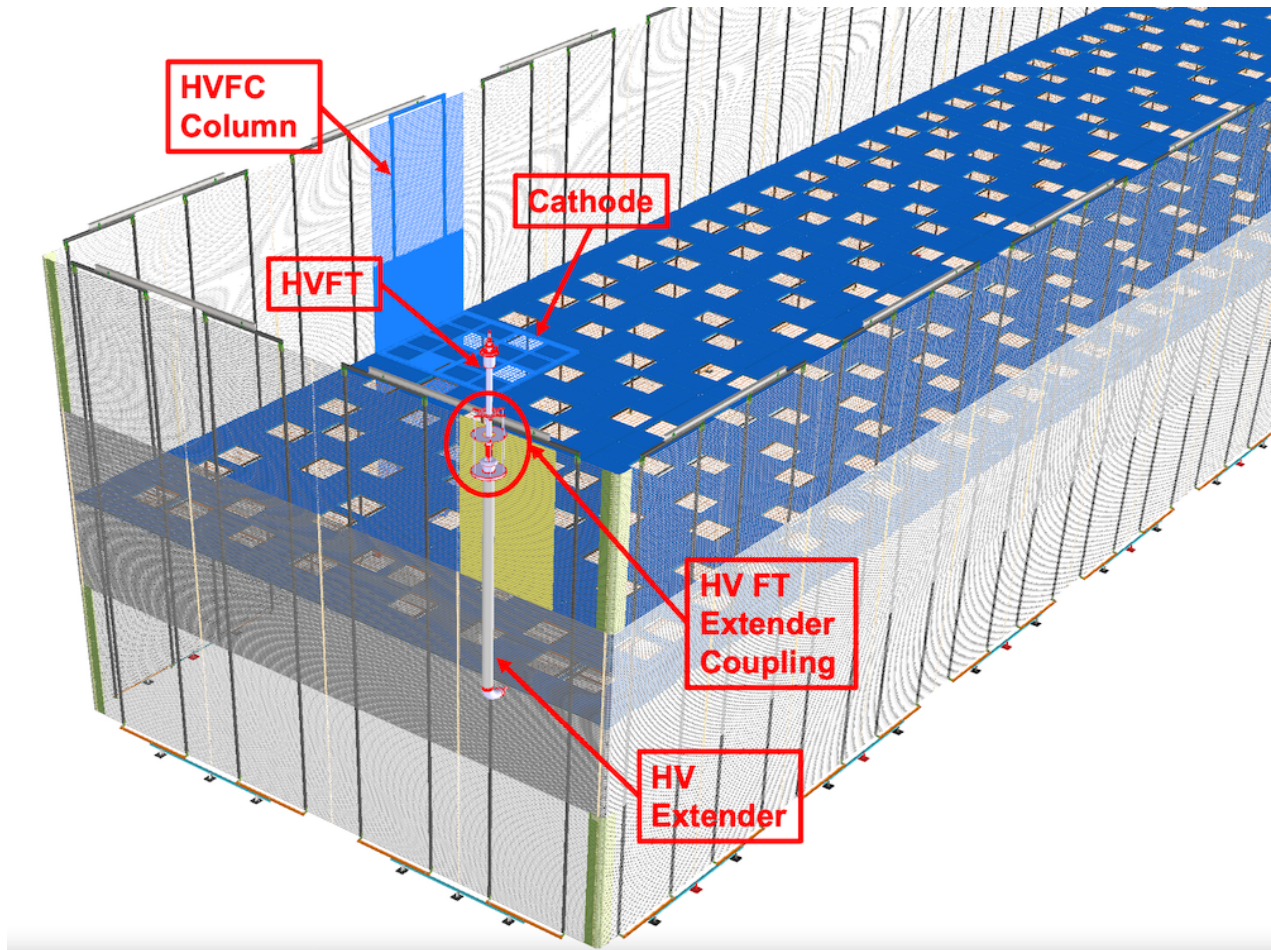


Figure 5.2: A birds-eye view of the field cage, with one full-height field cage column (highlighted in cyan) that extends the entire height, the HV feedthrough and extender (in the foreground), and the cathode (with one cathode module highlighted in cyan). The field cage profiles are mechanically and electrically independent. The figure distinguishes between the 70% optical transparency portion that spans the vertical ranges  $2.5 < y < 6.3$  m and  $-6.3 < y < -2.5$  m and the standard portion.

## 5.2 Requirements and Specifications

The high-level design requirements and specifications of the HVS are as listed in Table 5.1. All are common to both FD modules except FD2-HV-3, which is specific to FD2-VD.

Table 5.1: HV specifications

Label	Description	Specification (Goal)	Rationale	Validation
FD-1	Minimum drift field	$> 250 \text{ V/cm}$ ( $> 450 \text{ V/cm}$ )	Lessens impacts of $e^-$ -Ar recombination, $e^-$ lifetime, $e^-$ diffusion and space charge.	ProtoDUNE
FD-11	Drift field nonuniformity due to HVS	$< 1\%$ in 99.8% of active volume	High reconstruction efficiency.	ProtoDUNE and simulation
FD-12	Cathode HV power supply ripple contribution to system noise	$< 100 e^-$	Maximize live time; maintain high S/N.	Engineering calculation, in situ measurement, ProtoDUNE
FD-17	Cathode resistivity	$> 1 \text{ M}\Omega/\text{square}$ ( $> 1 \text{ G}\Omega/\text{square}$ )	Detector damage prevention.	ProtoDUNE
FD-24	Local electric fields	$< 30 \text{ kV/cm}$	Maximize live time; maintain high S/N.	ProtoDUNE
FD-29	Detector uptime	$> 98\%$ ( $> 99\%$ )	Meet physics goals in timely fashion.	ProtoDUNE
FD-HV-1	Maximize power supply stability	$> 95\%$ uptime	Collect data over long period with high uptime.	ProtoDUNE
FD-HV-2	Provide redundancy in all HV connections.	Two-fold (Four-fold)	Avoid interrupting data collection or causing accesses to the interior of the detector.	Assembly QC
FD2-HV-3	Provide optical transparency to the photon detectors on the membrane	$\geq 70\%$	Enable photons detectors outside the field cage to collect light with efficiency similar to those mounted in the cathode.	VD Module-0

All these specifications were met during operation. In particular, the HV stability was tested at  $-300 \text{ kV}$  on the cathode (about  $500 \text{ V/cm}$  in the  $6 \text{ m}$  drift) during the long-term stability test performed from fall 2021 through early 2022 in the cryostat at the European Laboratory for Particle Physics (CERN) Neutrino Platform.

## 5.3 HV Delivery System

This section describes the baseline design of the FD2-VD HV delivery system, which has been derived from the system developed for the dual-phase (DP) LArTPC proposal [73]. The FD2-VD design has undergone a design optimization process, and reflects the lessons learned from the long-term HVS stability test, where the new concept of the HV extender and its coupling to the HVFT were extensively tested at  $-300 \text{ kV}$ . This provides confidence that the design improves long-term reliability and stability at the FD2-VD operation voltage.

### 5.3.1 HV Power Supply and Cable

Low-noise  $-300$  kV HV power supplies (HVPS) and dedicated  $>300$  kV cables are commercially available. The baseline design uses the Heinzinger PNChp300000-05 <sup>1</sup> as the HVPS of choice. It has a residual ripple of  $10^{-5}$  (corresponding to 3 V at the maximum voltage of 300 kV) at an absolute precision in nominal voltage of  $\pm 50$  mV, with a typical frequency of 30 kHz. The cable is Dielectric Sciences type 2236 <sup>2</sup>, which is designed and certified to operate at 320 kV DC.

Given the  $100e$  noise ceiling requirement on the HVS, the upper limit of the ripple voltage on the cathode is found by dividing the noise charge by the capacitance between the cathode and the longest readout strip on the first induction plane. Using a conservative assumption that the coupling is a simple parallel plate capacitor, and factoring in the shielding effect of the shield plane in front of the first induction plane (calculated from a finite element analysis (FEA) using the perforated anode geometry), the cathode voltage ripple limit is found to be 15 mV. As a consequence, at  $-300$  kV output voltage and the typical HVPS frequency of 30 kHz, the required noise reduction from 3 V to 15 mV is a factor 200 ( $\sim 46$  dB). Note that this number is much greater than that for the horizontal drift detector module (FD1-HD) (0.9 mV) for several reasons: a larger drift distance, a smaller area covered by a charge-readout plane (CRP) readout strip compared to that of an anode plane assembly (APA) wire (due to the wires' length), and the presence of a much more effective shielding electrode.

The additional filtering is achieved with a resistor at the output of the HVPS and the capacitance of the HV cable. Assuming cable lengths of at least 20 m, calculations and experience confirm that a resistance as low as a few  $M\Omega$  yields the required noise reduction.

As shown in Figure 5.3, the Heinzinger PNChp300000-05 features a  $17 M\Omega$  output resistance  $R_O$ , with an internally compensated voltage drop. The primary low-pass filtering, aimed at reducing the 30 kHz voltage ripple on the output of the power supply, can be achieved by using this output resistance plus the 2 nF capacitance from the 20 m long HV cable ( $\sim 100$  pF/m). The corner frequency of this low-pass filter is 4.7 Hz, hence the noise attenuation at 30 kHz is expected to be  $\sim 76$  dB (well above the minimum required noise reduction of  $\sim 46$  dB). This minimal layout of the ripple noise filter was implemented in the HV delivery system of the NP02 HV long-term stability run: as expected, no HVPS-induced ripple was ever observed on the CRP read-out electronics.

No additional characteristic frequencies are expected from the HVPS. Very low frequency oscillations (e.g., 50 Hz), if present, would be difficult to identify as they would appear as tiny baseline variations during the full drift time of 4.2 ms. The preamplifier bandwidth is expected to further attenuate the baseline fluctuations.

To further increase the ripple filtering capability a HV-rated resistor  $R_1$  in a custom housing is inserted in the HV cable termination (HVPS side) (Figure 5.3). A second  $R_2$  is installed in the opposite cable termination (HVFT side); it serves as a current-limiting resistor to restrict sudden energy dumps from the HVPS and the long cable into the TPC in the event of a discharge.

<sup>1</sup>Heinzinger <https://www.heinzinger.com/en/applications>

<sup>2</sup>Dielectric Sciences <https://catalog.dielectricosciences.com/item/all-categories/wire-cable-2/item-1260?plpver=1001>

To ensure a drift field of 450 V/cm over the 6.5 m drift, the voltage to be provided to the cathode is 294 kV. Hence, the maximum voltage drop across the ripple filter resistors is 6 kV. Based on the total current drawn by the entire field cage ( $\sim 104 \mu\text{A}$ ), the sum of  $R_1$  and  $R_2$  can be as high as 57 M $\Omega$ . The actual value of each resistor can be tuned, but the baseline assumes equal values of about 25 M $\Omega$ . This filtering scheme, with similar power supplies, has been used successfully in other LArTPC experiments, such as  and , more recently, it has been demonstrated in  and ProtoDUNE-DP. Figure 5.3 shows the HV supply circuit.

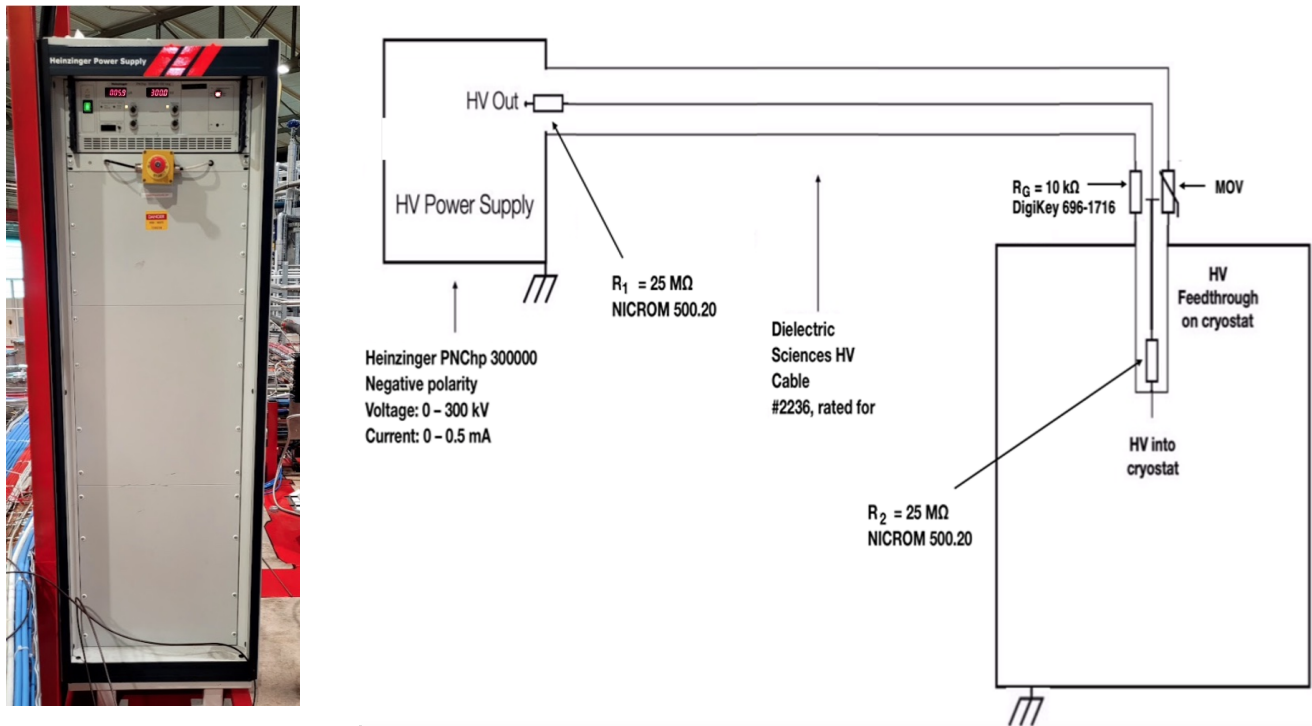


Figure 5.3: Left: The  $-300$  kV Heinzinger power supply. Right: A schematic showing the HV delivery system to the cryostat. Two filter resistors are included in the HV cable terminations:  $R_1$  sits near the power supply, and  $R_2$  near the HVFT. The 10 k $\Omega$  ground-loop breaking resistor  $R_G$ , placed at the HVFT termination, is also shown.

The cylindrical filter resistors are located in the termination tips of the HV cable, which in turn are inserted into the HVPS and HVFT cable receptacles. The resistor must withstand a large over-power condition. Resistors withstanding up to 150 kV are commercially available and were used in ProtoDUNE-DP. The filter layout allows for easy and rapid replacement of the resistors in case of damage. A breaking circuit to avoid ground loops is implemented on the cable termination shield at the level of HVFT plug.

### 5.3.2 HV Feedthrough

The HV feedthrough (HVFT) is based on the successful ICARUS design [8], and scaled to hold to  $-300$  kV. The voltage is transmitted by a stainless steel center conductor. On the warm side of the cryostat, this conductor mates with a cable end. Inside the cryostat, the end of the center conductor has a spring-loaded tip that ensures contact to the receptacle cup mounted on the HV extender, delivering HV to the cathode and the field cage. The 40 mm diameter center



conductor of the feedthrough is surrounded by an ultra-high molecular weight polyethylene (UHMWPE) insulator cylinder. The insulator is surrounded by a tight-fitting stainless steel ground tube. A Conflat industry-standard flange is welded onto the ground tube for attachment to the cryostat. On the under (cold) side of the HVFT, the UHMWPE cylinder extends beyond the edge of the outer ground shield by about 20 cm, along the length. This exposed cylindrical surface is corrugated with grooves to increase surface path length between the protruded center conductor below and the grounded shield above, as depicted in the top left and top right photos in Figure 5.4. The central conductor is equipped with a spring-loaded tip (10 cm excursion) to ensure electrical contact with the connected electrode.

A doughnut ( $\sim 20$  mm annular thickness) is added to the bottom edge of the outer stainless steel cylinder ground shield of the HVFT, as shown in Figures 5.5 and 5.4 to minimize the local E field strength. On the top (warm) side of the HVFT, a receptacle with a depth of  $\sim 80$  cm and a diameter of 38 mm receives the cable (Dielectric Science type 2236) from the HVPS.

Three HVFTs were built for ProtoDUNE-SP and ProtoDUNE-DP, and all functioned properly at  $-300$  kV on a short-term basis in dedicated test stands. One of these HVFTs was also successfully used in the second part of the ProtoDUNE-DP HV stability run (for more than three months), where the detector was operated at the nominal voltage of  $-300$  kV delivered from the HVPS under very stable conditions.

Following the long-term operation in both ProtoDUNE-SP and the two ProtoDUNE-DP runs, it was found that the HVFT was affected by ice formation at the cable receptacle. The cable tip was reaching the depth of the inner cryostat membrane, thus subject to a quite low temperature. Investigation showed that although the cable receptacle was flushed continuously with dry N<sub>2</sub>, it was insufficient to prevent ice formation over the long term. The formation of ice did not affect the performance of the HV distribution, given its good insulating properties. However, it would prevent potential extraction of the cable, which might be required at some point during the decades-long operation of FD2-VD. An improved version of the HVFT was initially used in the ProtoDUNE-DP HV stability run. This HVFT, conceptually similar to the original ones, but one meter longer on the warm end to keep the cable receptacle in the warm section of the HVFTs, was designed and built at UCLA. It was extensively tested in the U.S. up to  $-200$  kV and was then tested at CERN at  $-300$  kV prior to its use in the HVS long-term stability test. The UCLA HVFT performed stably at  $-300$  kV for more than two months in the early part of the stability test, at which point a failure due to impurities found in the UHMWPE insulation cylinder required its replacement by one of the original HVFTs for the remainder of the test at  $-300$  kV.

To prevent a similar failure, a new HVFT was designed as shown in Figure 5.5 for FD2-VD Module 0. This HVFT will be the prototype for both FD1-HD and FD2-VD; its components were built in 2022 and, as of this writing, the HVFT has been assembled via cryogenic insertion. Validation in LAr at 300 kV will be carried out in Q2 2023. It is similar to the UCLA design but longer (4 m), with the “warm” side of it that contains the cable receptacle extending above the cryostat roof by about 1 m. It is also thicker (150 mm instead of 100 mm) to improve the insulation reliability. X-ray inspection of the UHMWPE purity will be performed before assembling the parts. The inner conductor will also be thicker (40 mm diameter) to limit the E field strength at the conductor surface.



Figure 5.4: Components of the full scale HV long-term stability test in the NP02 cryostat. Top: two views of the doughnut and the sphere of the extender head with the HVFT tip connected. The gold colored ring in the top left photo is the sleeve to confine the gas bubbles produced by the heat input from the HVFT and evacuate them to the gas phase close to the HVFT ground skin. Bottom left: the tip of the extender in front of the field cage. Bottom right: Detail of the extender connection to the field cage.

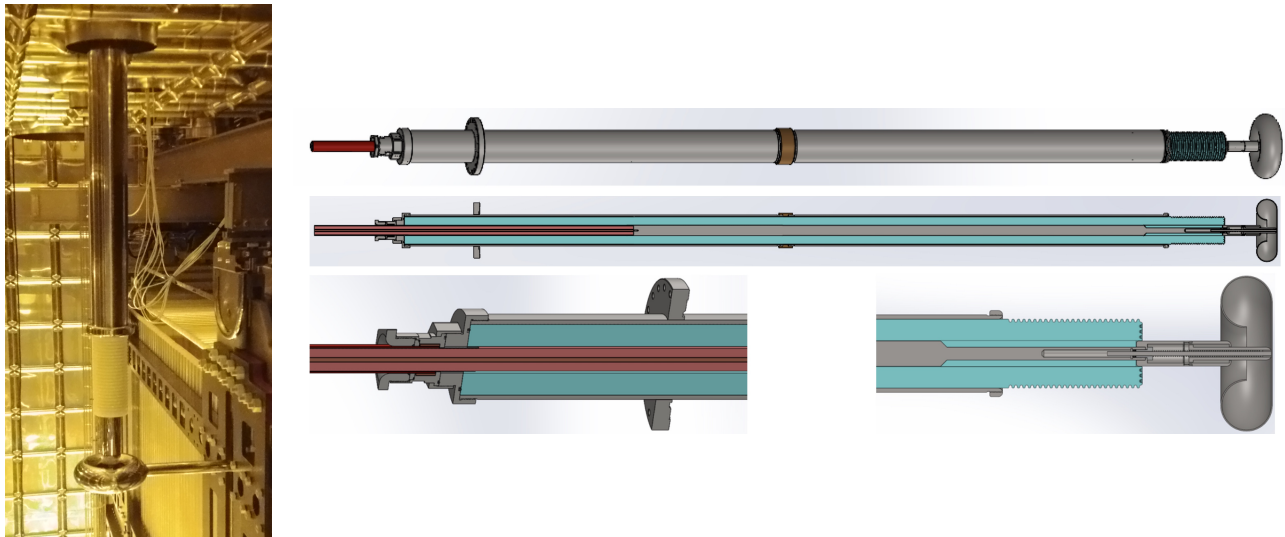


Figure 5.5: Photograph and drawings of a HVFT. The photograph shows the ProtoDUNE-SP installation with the “cold” HV tip in the doughnut cup that is connected to the top of the (vertical) cathode; no extender is necessary for the horizontal drift detectors. A 3D view and vertical cross sections of the HVFT are on the right, illustrating the cable insertion and the HV tip touching the doughnut cup. The HV cable (brown) is inserted about 1 m into the HVFT. The exposed UHMWPE insulator (aqua) near the “cold” HVFT tip is about 40 cm long and is corrugated. The insulator diameter is 150 mm. The diameter of the inner conductor is 40 mm. As in the FD1-HD HVFT, the spring-loaded tip of the HVFT makes contact with the center part of the doughnut cup, which is part of the HV extender.

Given the thickness of the far detector (FD) cryostat outer structure and insulation layers, and the depth of the gas ullage ( $\sim 150$  cm in total), the bottom rim of the HVFT ground shield will be immersed in LAr to a depth of at least 40 cm. This depth minimizes the risk of gas pocket formation below the ground shield doughnut from heat dissipation by the metallic components of the HVFT itself; gas bubbles generally form closer to the surface (in the top  $\sim 20$  cm of depth). To further mitigate this potential issue, holes are drilled in the HVFT outer shield cylinder a few cm above the doughnut at the tip, allowing any gas bubbles formed inside to easily escape.

The new design is illustrated in Figure 5.5. Detailed technical drawings of the HVFT can be found at [74]. The HVFTs are constructed by the same company that produced those for ICARUS, and

### 5.3.3 HV Extender and its Coupling to HVFT

An “HV extender” is introduced in the FD2-VD design to feed the cathode with the  $-300$  kV HV. It consists of a 20 cm diameter, 6 m long polished and passivated stainless steel pipe that is terminated at the top with a coupler to the HVFT and at the bottom with a  $90^\circ$  elbow for the connection to the cathode. The HV extender is supported by an insulating UHMWPE disk suspended from the cryostat roof using six insulating FR-4 rods. The extender exploits the surrounding LAr as the dielectric insulator.

The HVFT and the extender will be located on the side of the cryostat opposite the temporary construction opening (TCO) (Section 9.3.2), where the distance between the field cage profiles and

the flat face of the cryostat membrane is 1.1 m. The knuckles and corrugations of the membrane with small radii of curvature could be covered by a vertical band of flat conductive sheet to further smooth the E field in case future tests indicate that this is necessary. The internal cryogenic pipes on this end of the cryostat will be placed away from the HV extender. A FEA has shown that a conductive cylinder at  $-300$  kV with a diameter between 200 mm and 400 mm placed in the center of a 1 m gap between two grounded parallel planes will have a maximum surface E field of 17 kV/cm. This is well below the 30 kV/cm E field limit required for safe operation in LAr.

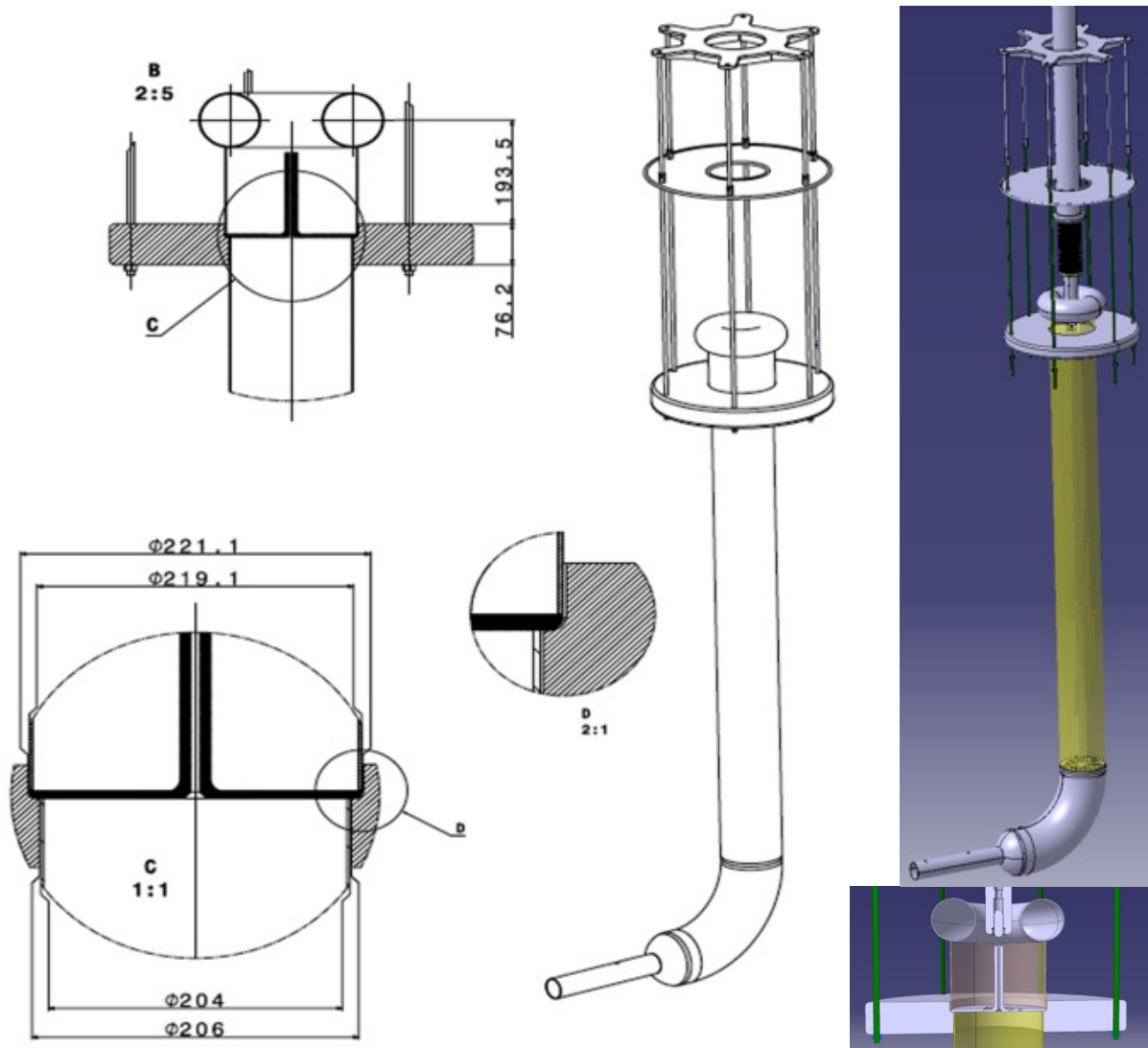


Figure 5.6: Left: Schematic diagrams of the optimized metal tube extender assembly showing the  $90^\circ$  elbow connection to the cathode, with details of the coupling to the HVFT and to the support disk. Right: (top) 3D model of the extender with HV tip inserted into doughnut and (bottom) detail of the head and support disk.

Figure 5.6 shows schematic diagrams of the components of the optimized HV extender.

The new version of the UHMWPE support disk has a notch at the extender tube weld joint, as illustrated in the figure (shaded areas), avoiding the critical triple-point of the previous design [32] (where three different materials, LAr, UHMWPE and stainless steel meet with  $< 90^\circ$  angles).

Triple-point locations are subject to potential instabilities because the insulating surfaces could get charged up by free charges moving in LAr under the E field in the contact region; if the angle between the insulating material and the metal surfaces is larger than  $90^\circ$ , the charging up is highly suppressed. The notch in the new UHMWPE disk is required to support the extender and fully contains the weld joint inside the insulating plate, reducing this possibility. The extender head and the support disk will be tested together with the new HVFT before installation in the upcoming FD2-VD Module 0.

## 5.4 HV Distribution System

The two main components of the HV distribution system are the cathode plane and the . Together with the top and bottom anode planes, they define a uniform drift E field in each of the two active volumes. The nominal bias voltage on the anode shield plane is  $-1.5$  kV. Therefore, in order to achieve the goal of  $450$  V/cm drift field, the cathode voltage needs to be set to  $-294$  kV for the  $6.5$  m drift distance.

The cathode plane is composed of 80 cathode modules identical in horizontal area to the CRPs. Since each cathode module will be adjacent to others at the same voltage, their outer edges are not directly exposed to a high E field region. The field cage, on the other hand, designed to cope with high E field outside the active volume, fully surrounds and shields the cathode plane.

The bias voltage to the cathode is delivered from the HVFT through the 6 m extender to a HV bus that is mounted on the inside of the field cage at mid-height. This bus connects to the resistor divider board ( ) chains on all the field cage columns and to the outer edges of the cathode plane to provide a constant voltage to the cathode plane, independent of the current flowing through each branch along a field cage column. Each chain of resistive HVDBs on the anode ends is brought out of the cryostat to a separate bias power supply that provides adjustable voltage for fine-tuning the drift field near the anode planes and monitors current.

In addition to the primary function of providing uniform E fields in the two drift volumes, both the cathode and the field cage designs are tailored to accommodate photon detectors (PDs), according to the configuration described in Chapter 6. In the baseline design, each cathode module is designed to hold four double-sided modules that are exposed through highly transparent wire mesh windows to the top and bottom drift volumes. PDs will also be mounted along the full perimeter of the cryostat walls, limited to the vertical ranges  $2.5 < y < 6.5$  m and  $-6.5 < y < -2.5$  m (vertically separated from the cathode plane by 2.5 m above and below). The field cage is designed to provide approximately 70% optical transparency, at normal incidence, over this vertical range.

### 5.4.1 Cathode

The cathode plane, while modular like both the ProtoDUNE cathodes, requires an all new design due to the unique requirements that the FD2-VD design imposes on it, such as integrating the PDs into it. A cathode module is illustrated in Figure 5.7.

A single cathode module has the same footprint as a CRP module, with dimensions of  $2.988$  m  $\times$   $3.366$  m  $\times$  62 mm. The weight of a cathode module, including the integrated PDs, is required to

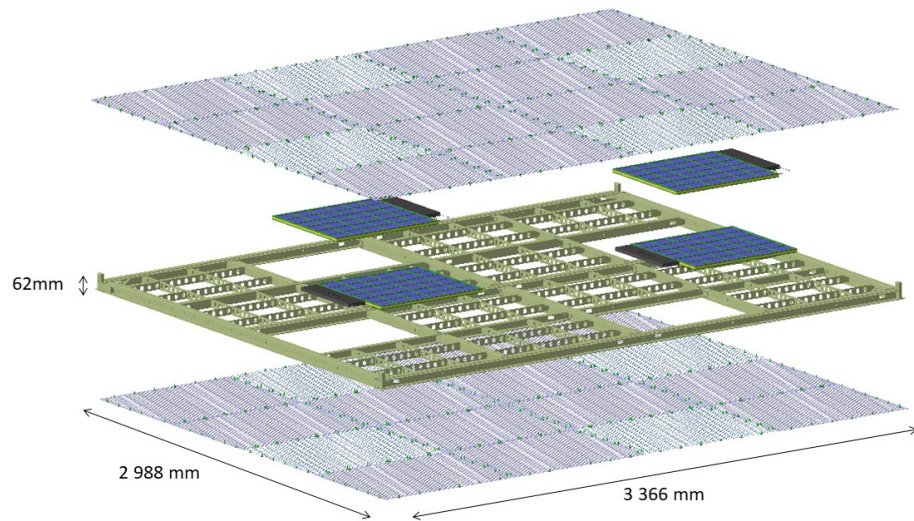


Figure 5.7: Diagram of a cathode module. The cathode module frame is constructed of FRP beams. One double-sided PD module (blue) is integrated into each of four dedicated openings. Each PD is covered on both sides by a metallic mesh with high optical transparency while the rest of the top and bottom faces of the cathode frame is reinforced with cross ribs that support perforated resistive panels (not shown) on both sides. For the modules placed along the cryostat perimeter, the PDs that would be located close to the cryostat wall are moved one slot away from it (see Section 6.4.1).

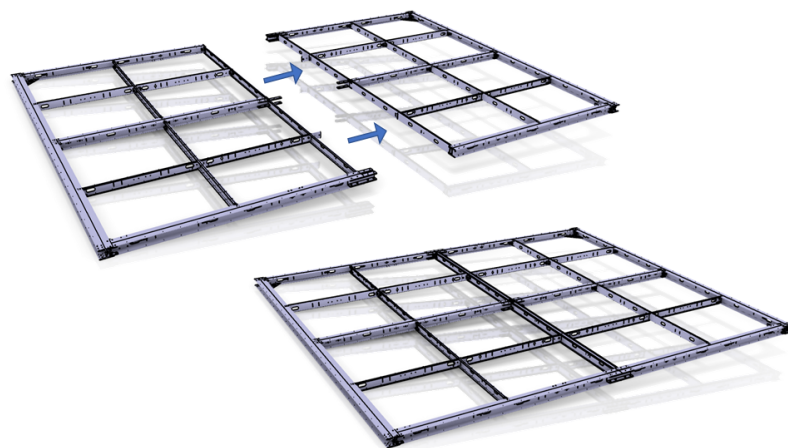


Figure 5.8: Two identical half frames are assembled to form a complete cathode module frame.

be less than 150 kg ( $15 \text{ kg/m}^2$ ) in air to minimize deformations of the CRP superstructure from which it hangs. The current estimate is 128 kg. To facilitate transportation, the frame consists of two identical half-frames (Figure 5.8) that, after transport underground, are joined in the in front of the cryostat, and then assembled into a cathode module.

To remain below the maximum deformation constraint of 20 mm across the entire surface of each cathode module in LAr, the cathode is constructed from FRP I-shaped and C-shaped beams (Figure 5.9).

The dimensions of the overall frame are:  $2948.3 \text{ mm} \times 3326 \text{ mm}$ ; this accommodates the field cage supports, allowing use of the same frame design for both perimeter and inner cathode modules. While the cathode frame is slightly smaller than the CRP footprint, the perforated resistive panels that deliver the E field will be machined to exactly match it since the shapes of the perforations have no impact on the mechanical behavior and they can be more easily machined than the frame. This simplifies the production and reduces the overall cost.

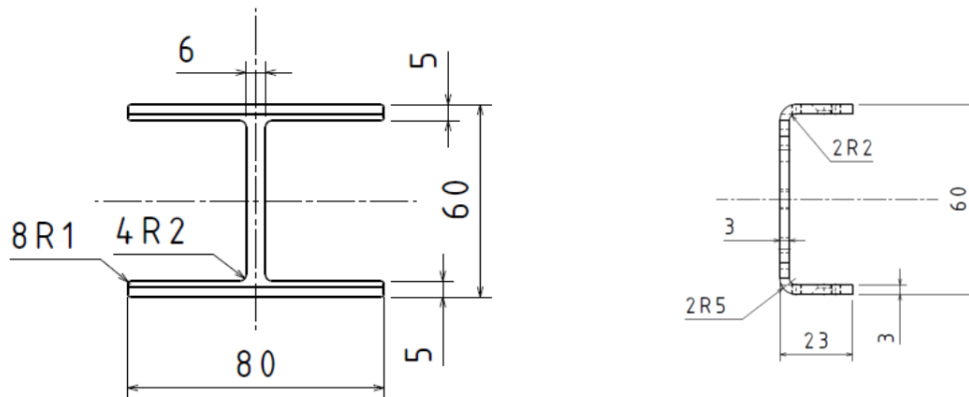


Figure 5.9: Dimensions of the I-shape and C-shape beams used for cathode frame construction.

According to the simulations that correctly predicted the measurements made on the prototype currently used in the NP02 cold box (with beams of 50 mm depth), the expected deformations of the frame are given in Table 5.2:

Table 5.2: Expected cathode deformation

Position on Cathode	In Air, z deformation (mm)	In LAr, z deformation (mm)
Center	-26.9	-8.5
Middle of Long Side	-14.3	-4.5
Middle of Short Side	-10.4	-3.3

These numbers are applicable for a single cathode module as well as for a six-module cathode supermodule configuration, described below (see Figure 5.10), and assume placement of all the PDs at the center of each cathode module, which would cause the most deformation; i.e., worst case.

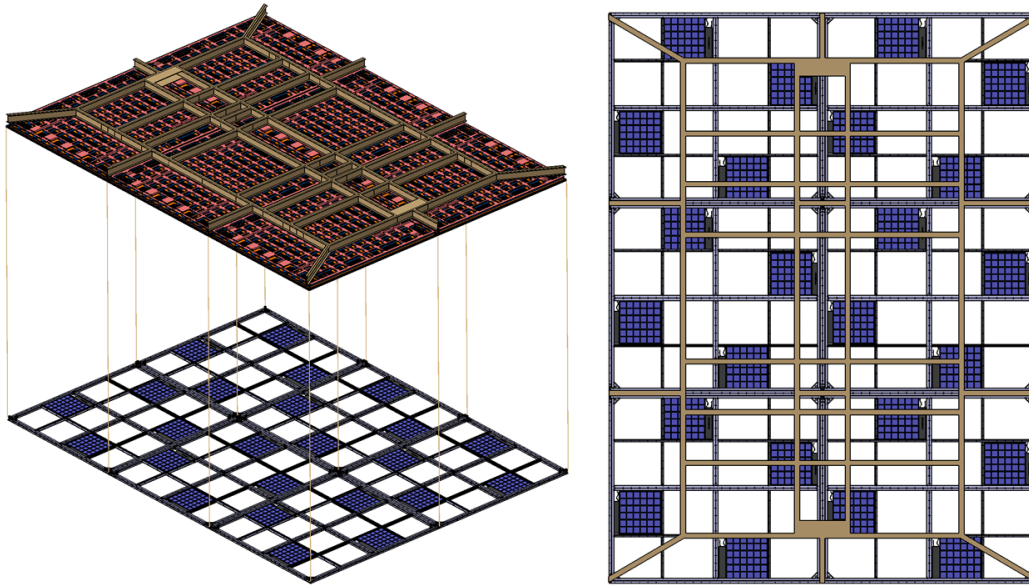


Figure 5.10: Conceptual view of a six-module cathode supermodule suspended from a CRP superstructure. Left: side view. Right: top view overlaid with a CRP superstructure and the embedded PD X-ARAPUCA modules in blue squares.

After production, the deformation of the frames will be measured with the expected loads (using meshes and dummy PD modules) to check compliance with the requirement (FD-11 in Table 5.1). The measurements will be done before and after a plunge in liquid nitrogen in order to check the impact on them of sudden cooling to cryogenic temperatures. A visual inspection of the beams and connections will also be done to check for any non-conformity.

The frame for each cathode module has 16 openings, four of which are dedicated to PDs. The four openings are all of slightly different sizes ( $635 \times 730$  mm,  $635 \times 812$  mm,  $696 \times 730$  mm and  $696 \times 812$  mm), all of which can accommodate the active part of the PD module, which is  $621 \times 621$  mm.

The four openings containing the double-sided PD modules are covered on both sides by stainless steel wire-mesh panels of optical transparency above 86.5% at normal incidence. A mesh of this type that satisfies all the DUNE requirements is commercially available. A set of meshes has been produced and installed on the cathode prototype in the cold box and has exhibited no issues throughout the duration of the tests.

To ensure the planarity of the perforated resistive panels and the wire meshes, which are quite flexible due to their high transparency, additional supporting cross ribs are provided in all cathode frame openings; these do not change the mechanical properties of the frame. The cross ribs in the four openings for the PD are integrated into the PD mechanical design (see Figure 5.13), and have been successfully tested in the cold box. The cross-ribs in the remaining 12 openings support



Vetronite EGS 619 AS resistive panels from Von Roll<sup>3</sup> (which is like G10) on both sides. The panels are perforated to reduce their weight and allow LAr flow. The square shaped perforations ( $25 \times 25$  mm spaced by 2.5 mm) are machined by water-jet cutting. Small hooks hold the panels.

The resistivity measurement of the Vetronite is  $16 \text{ M}\Omega/\text{sq}$ , in agreement with the requirements. An optical transparency (due to the perforations) of 75% has been achieved while maintaining good mechanical properties and achieving sufficient LAr flow across the cathode plane. The use of resistive material both reduces the peak current flow along the cathode in the event of a HV discharge and slows down the associated voltage swing, which reduces any potentially dangerous charge injection into the readout electronics. The PDs would be protected from a dangerous large spatial voltage gradient across their surface by the stainless steel meshes that cover them.

By analyzing the spatial distribution of the hits recorded in the cold box, it has been possible to measure the small variations in E field intensity (at the level of few percent) close to the cathode surface. This non-uniformity is due to the perforated structure and to the plates supporting the PD electronics. The measurements are in good agreement with the simulations of the cathode performed in-house.

The pitch of the mesh wires covering the PDs is 25 mm, chosen to avoid significant distortions of the E field. As shown in Figure 5.11, obtained from a COMSOL simulation of the cathode, the E field component along the drift direction is within 1% of its nominal value beyond 5 cm from the cathode plane (top plot). The amplitude of the transverse component of the E field is smaller than 1% of the longitudinal one beyond 3 cm (bottom plot).

For a given specification on the drift field uniformity, the simulation also allows computation of the fraction of the drift volume for which the specification is satisfied. Figure 5.12 shows that the difference between the nominal drift field and that generated by the cathode is less than 1% over  $\sim 99.4\%$  of the drift volume.

To maintain the entire cathode at the same voltage, adjacent resistive panels are interconnected at regular intervals both laterally and across opposite sides of the cathode to ensure good electrical connections with sufficient redundancy. The top and bottom interconnects of the wire meshes also offer some electrostatic protection to the PD modules mounted in between. Similar electrical interconnects between adjacent cathode modules and to the neighboring field cage modules are made through flexible hookup wires.

To reduce the amount of work in the underground environment, mounting hardware and local cables and fibers are pre-installed into the cathode module at the cathode assembly site. The beams in the frame have several openings (Figure 5.14) for routing the PD cables and fibers from any location in the cathode frame. The PD modules are installed into the cathode module shortly before the cathode is attached to the CRP superstructure once in the cryostat. The optical fibers that carry power and signal for the PDs, described in Section 6.6.2.1, are routed from the cable trays on the bottom of the cryostat, up the FRP box beams on the bottom half of the field cage below the cathode, and along the sides of the cathode frame to the designated cathode module. Section 9.8.3 provides details on cable and fiber routing.

---

<sup>3</sup>Von Roll <https://www.vonroll.com/en/>

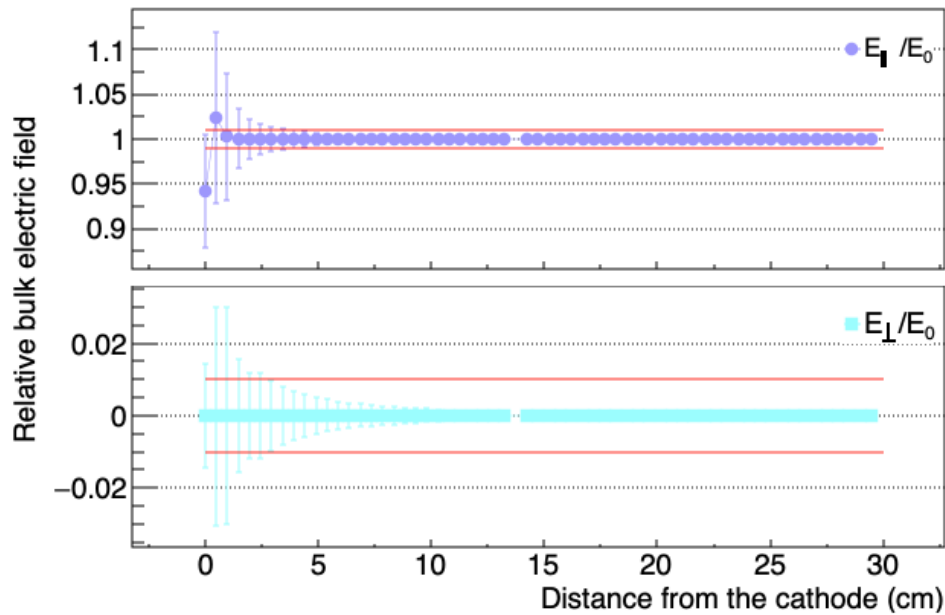


Figure 5.11: E field (normalized to the nominal value) close to the cathode surface. The top figure shows the uniformity of the E field component along the vertical direction, while the bottom shows the relative amplitude of the component in the horizontal plane. The error bars give the range of variation at a given distance. The red lines indicate the 1% specification.

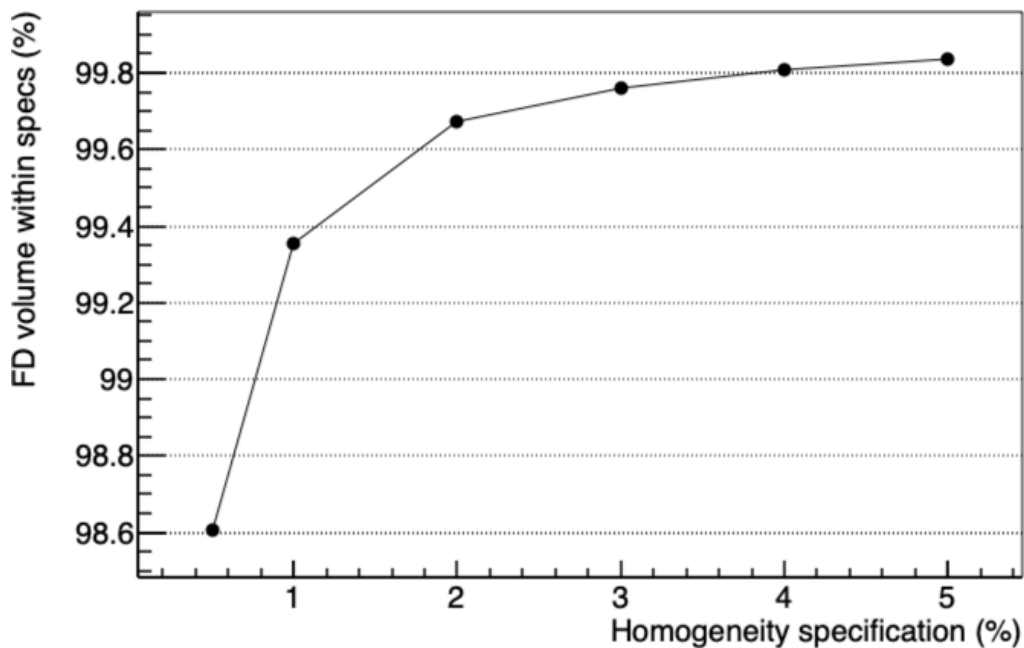


Figure 5.12: Volume within specification vs field homogeneity specification

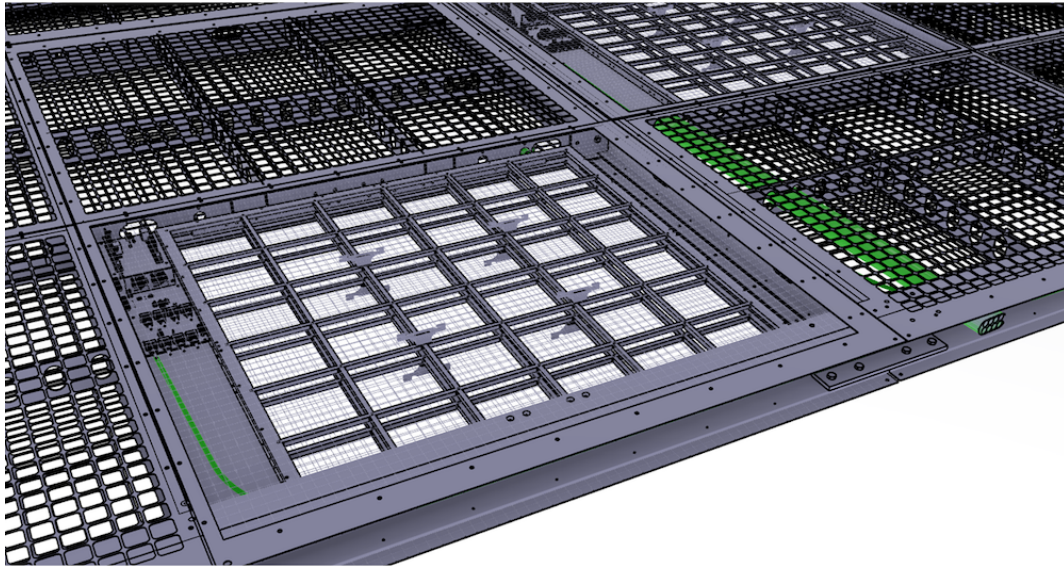


Figure 5.13: View of a portion of a cathode module. The opening in the foreground (and the one in the right rear) hosts a PD module (not visible in the image) covered on both sides by a stainless steel wire mesh (shown as light gray), with its electronics box at left. The openings in the left rear and on the right show the cross ribs and the (75%) perforated resistive panels, one on each side; the green bar is the fiber bundle.

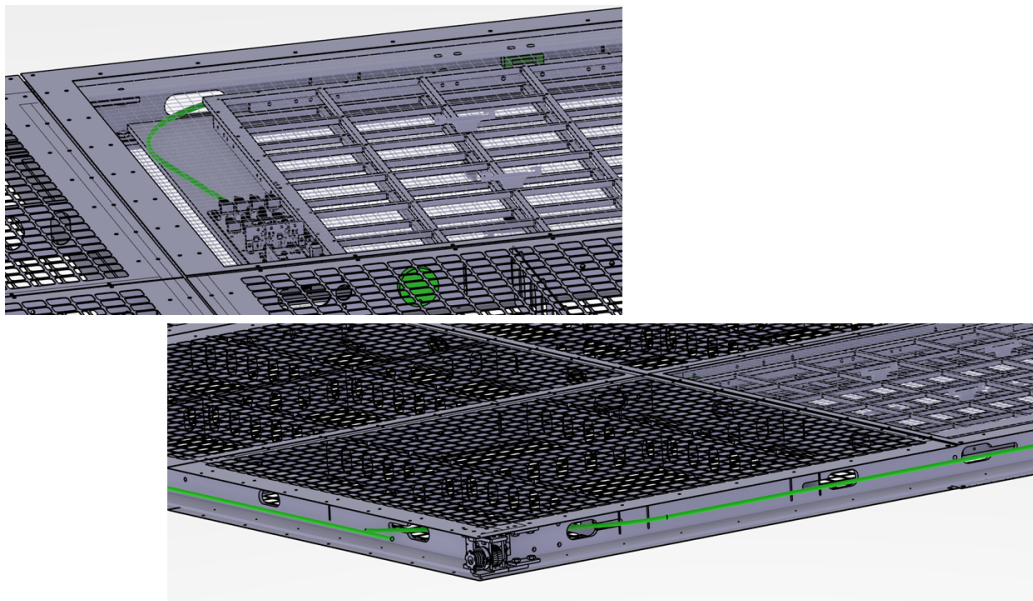


Figure 5.14: View of the frame openings designed for PD fiber and cable routing

The cathode plane consists of 80 cathode modules total, assembled into a set of 16 supermodules (12 six-module and four two-module), matching the modularity of the CRP superstructures (see Section 3.5) to simplify the installation. The six-module supermodules are in  $2 \times 3$  formation, and the two-module supermodules are  $2 \times 1$ . To form the entire cathode, the 12 six-module supermodules are arranged  $2 \times 6$ , each with the three-cathode-module (long) side oriented lengthwise along the cryostat and two (2) two-cathode-module supermodules along each end wall arranged with their long sides against the end wall.

Each six-module cathode supermodule is suspended from the ten CRP superstructure extensions along its perimeter and two junctions near its center using 12 non-conductive cables (“ropes”), as illustrated in Figure 5.10. The ropes are made of 3.35 mm diameter Dyneema DM20, produced by Corderie Lancelin<sup>4</sup>, which was chosen because it has one of the highest strength-to-weight ratios and, critically, according simulations done with the simulation tool of the Dyneema provider, maintains a very stable length over ten years of use at cryogenic temperatures. The suspension configuration limits the distortion to about 8.5 mm in LAr and 26.9 mm in air across the entire surface of each cathode supermodule.

Figure 5.15 presents a conceptual view of the suspension system. Each of the ten long ropes (about 6 m) that support the cathode supermodule from the top of the CRP superstructure is attached to a top adjusting device (TAD). At the bottom of the long rope, short ropes (one, two or four according to the position of the rope and the number of connected cathode modules) will be attached to the long rope via a shackle, and connected to the cathode supermodule frame using the length adjusting device (LAD).

The TAD shown in Figure 5.16 is the anchor point of the rope. The TAD provides an approximate large-scale tuning of the rope length as well as the precise positioning of the rope as it goes through a  $20 \times 20$  mm square space at the corner between the CRP superstructures.

Uniformity of the rope production, in particular the reproducibility of the rope lengths after load, has been validated with a joint R&D program between Physics Laboratory Irène Joliot-Curie, Paris (IJClab) and the rope producer. The dispersion on these lengths has an impact on the tuning range of the TAD and the LAD.

Several ropes were extensively tested at room temperature in late 2022. Some preliminary behavior tests at cryogenic temperatures have also been performed, and more recently quantitative measurements were carried out on a dedicated test bench. The rope stretches quite linearly with respect to the load, with a measured elongation coefficient of about 0.33 mm per kilogram. Measurements made over the course of a few months show reproducibility to about 1 mm, which is the precision of the current test setup. In LAr, the ropes are expected to stretch by  $\sim 14$  mm due to thermal expansion at low temperature (Dyneema has a negative  $\alpha$  of about  $-10^{-5}/K$ ). The buoyant forces, however, will reduce the load, so the rope length will depend on the number of supported cathodes, at about  $\sim 12.5$  mm per cathode. Table 5.3 presents the estimated length difference for the three possible cases (rope supporting one, two or four cathode supermodules):

Since there is no way to adjust the rope lengths once the cryostat is closed, it is essential to

---

<sup>4</sup>Corderie Lancelin <https://lancelin.com/>

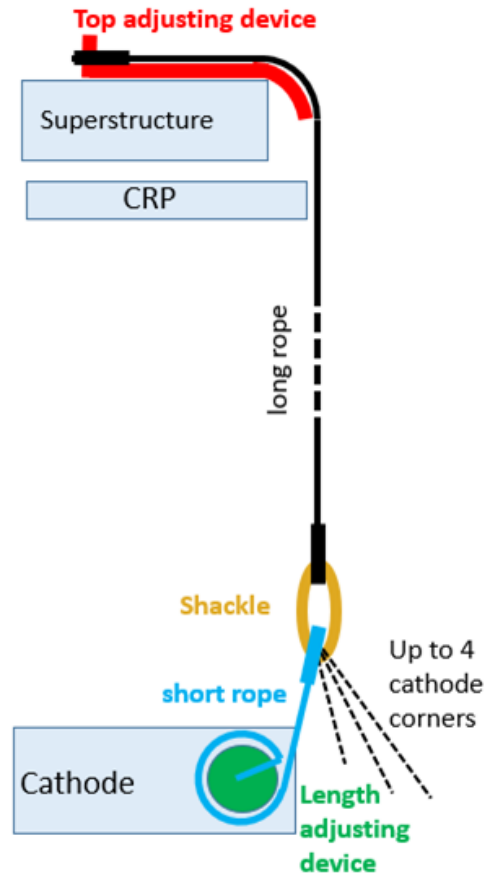


Figure 5.15: Conceptual view of the cathode suspension system composed of five elements: the top adjusting device (TAD), a long rope (about 6 m), a shackle, short ropes (1, 2 or 4) and the length adjusting device (LAD).

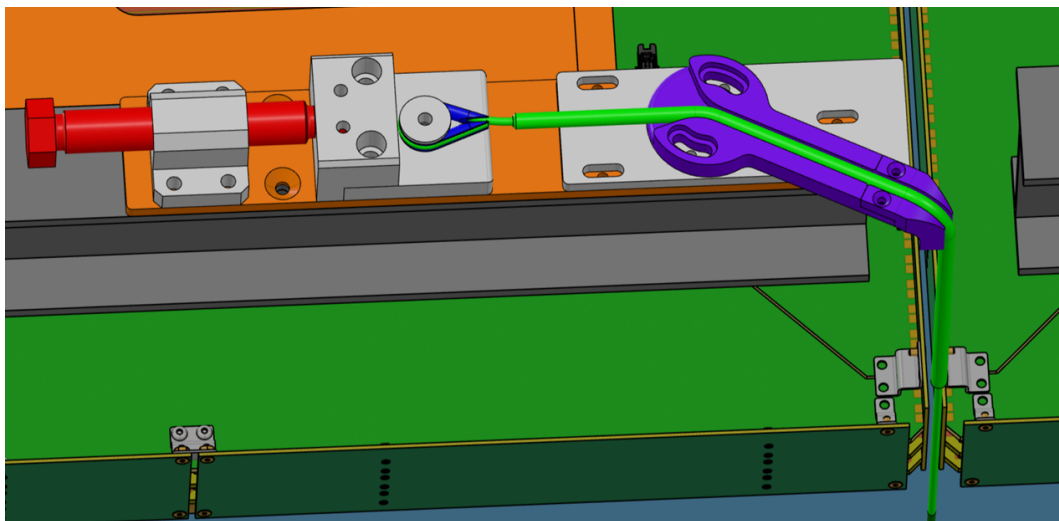


Figure 5.16: Model of the cathode top adjusting device (TAD) on the CRP superstructure

Table 5.3: Estimated length differences of ropes supporting the cathode

<b>Number of supported cathode supermodules</b>	<b>Length Difference (in mm) between installation and running conditions (+ in up direction)</b>
1	-1.5
2	11
4	36

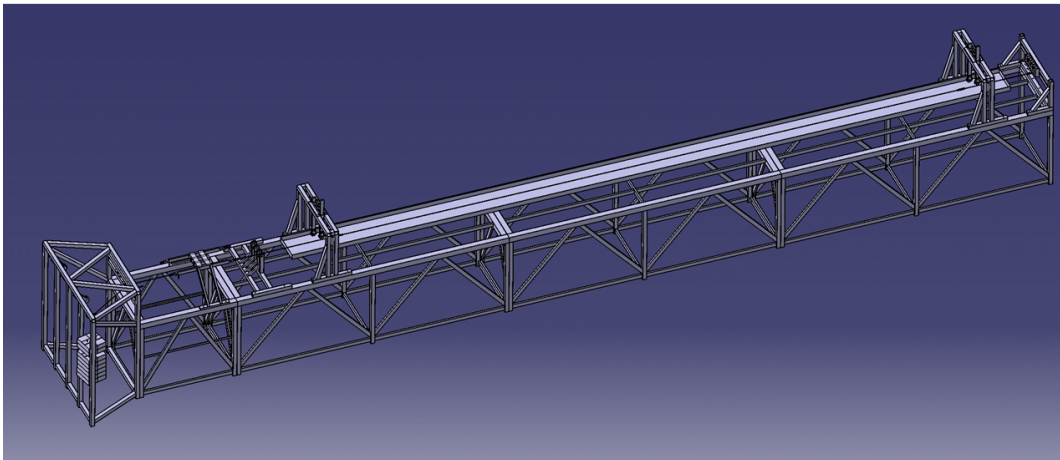


Figure 5.17: A conceptual view of the test bench under construction to be used for the quantitative characterization of the ropes (elongation under load and thermal elongation)

know precisely the rope's elongation behavior due to load and thermal factors. A dedicated bench (Figure 5.17) is under construction to measure each of the 168 6 m long ropes and the 192 50 cm long ropes needed to support the full set of cathode supermodules. The coupling between the long and the short ropes is performed through the standard Dyneema shackle.

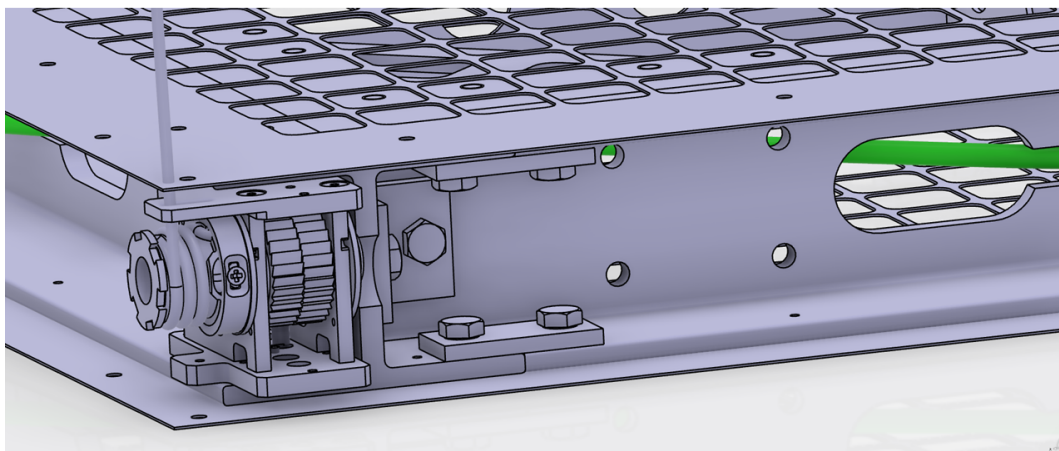


Figure 5.18: A model of the cathode length adjusting device (LAD) placed in the cathode supermodule frame.

For the connection to the cathode and the fine-tuning of the rope length, a dedicated device has been designed called the length-adjusting device (LAD), shown in Figure 5.18. The LAD is installed inside the I-shaped beam of the cathode frame to ensure the correct transmission of the stress. A system of two gears allows length tuning with a 1.5 mm precision and a range of  $\pm 5$  cm.

A LAD prototype was produced that successfully passed load tests in air. Figure 5.19 shows the prototype connected to a Dyneema rope with a load of 200 kg. No measurable deformation has been observed after one week of stress under the load. The LAD was also tested in a cryogenic bath and showed no deformation. The next step is to perform a load test in liquid nitrogen once the test bench illustrated in Figure 5.17 becomes available.

All elements described in this section (frame, resistive panel and metallic mesh, ropes, the TAD, the LAD, etc.) will be produced for FD2-VD Module 0 with their current designs, which are expected to be final. Some of the tools needed for installation will also be produced for and tested during FD2-VD Module 0 installation. Due to the limited size of NP02 and to the different CRP and cathode support structure under the cryostat ceiling, the actual full assembly test of the CRP superstructure hanging six cathode modules will require a dedicated mock-up to tune the final installation procedure and the associated tools.

## 5.4.2 Field Cage

ProtoDUNE-DP demonstrated the simplicity of installing a field cage in a vertical drift TPC, and ProtoDUNE-SP, whose field cage had identical design fundamentals, operated successfully. The



Figure 5.19: A photograph of the cathode LAD and a Dyneema rope under test in air. The system is loaded with a 200 kg weight. (The measuring stick shows inches.)



lessons learned in ProtoDUNE-SP have led to an updated field cage design for the FD1-HD, in which all insulating materials on the side of the field cage facing the grounded cryostat membrane wall are removed to improve HV stability. The updated FD2-VD design, illustrated in Figure 5.20, implements these features, and aims to achieve both improved performance and an even simpler field cage assembly.

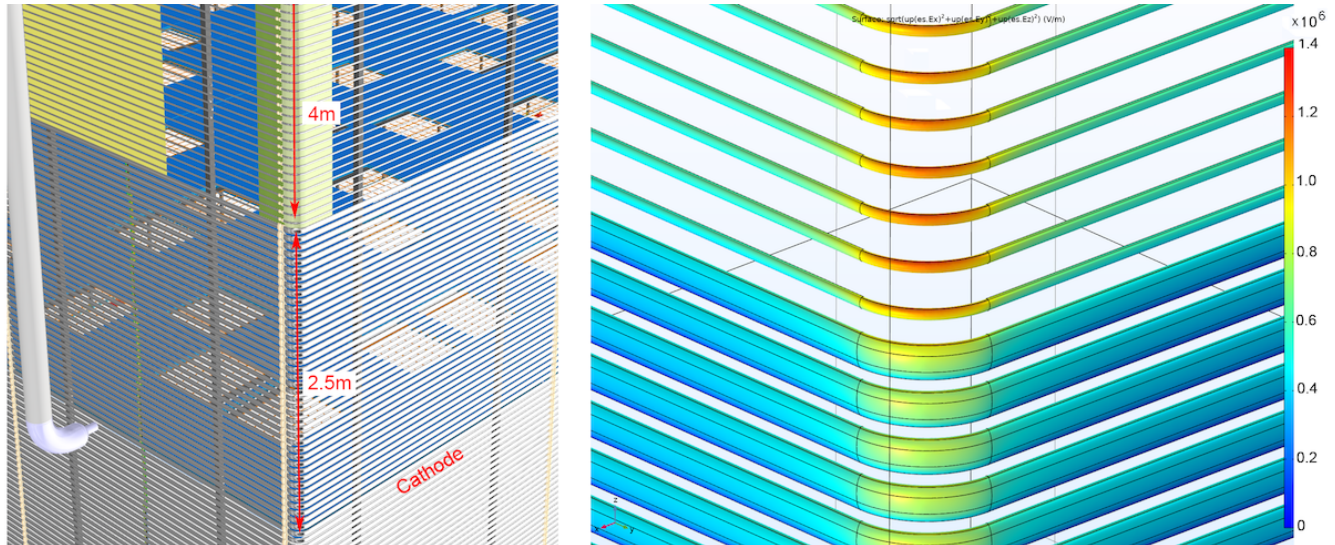


Figure 5.20: Left: A corner view of the field cage baseline design with 70% optical transparency along the four cryostat walls, starting at 2.5 m away from the cathode plane. Right: FEA calculation of the E field (V/m) of the corner without the additional insulation shield. The maximum value on the color scale is  $1.4 \times 10^6$  V/m.

#### 5.4.2.1 Geometry, Mounting and Support

The field cage modules for the long walls are 3.0 m wide  $\times$  3.24 m high, and for the endwalls, 3.38 m wide  $\times$  3.24 m high, the widths of their aluminum electrode profiles matching the CRPs' edges. Each field cage module consists of 54 extruded aluminum profiles stacked vertically at a 6 cm center-to-center spacing. The profiles are mounted on two  $5 \times 5$  cm<sup>2</sup> square cross section FRP box beams of length 3.24 m, spaced 1.8 m apart from each other. A subset of the profiles are fixed on both box beams at regular intervals to define the spacing between the box beams. The rest of the profiles are fixed only on one beam and are allowed to slide on the other (see discussion below on shrinkage). On the side of each endwall profile that meets one of the four corners of the cryostat, the profiles are bent 90° with a 10 cm bending radius to connect to the adjoining long-wall profiles and to avoid charge buildup on the insulating caps at the corners. Figure 5.21 shows the proposed FD2-VD field cage long wall module design with the HVDBs shown in green. The weight of a field cage module varies between 35 kg for the thin profile long wall type and 60 kg for the mixed profile end wall type.

Two columns of four field cage modules each form a field cage supermodule, 6.0 m(W)  $\times$  13 m(H) for the long walls and 6.76 m(W)  $\times$  13 m(H) for the endwalls. Each long wall has 10 adjacent supermodules and each endwall has two; together these 24 supermodules form the field cage that surrounds the two active drift volumes. Each field cage supermodule hangs from a stainless steel I-beam shown in Figure 5.22 with two lifting rods, each going through one of the 48 roof penetrations

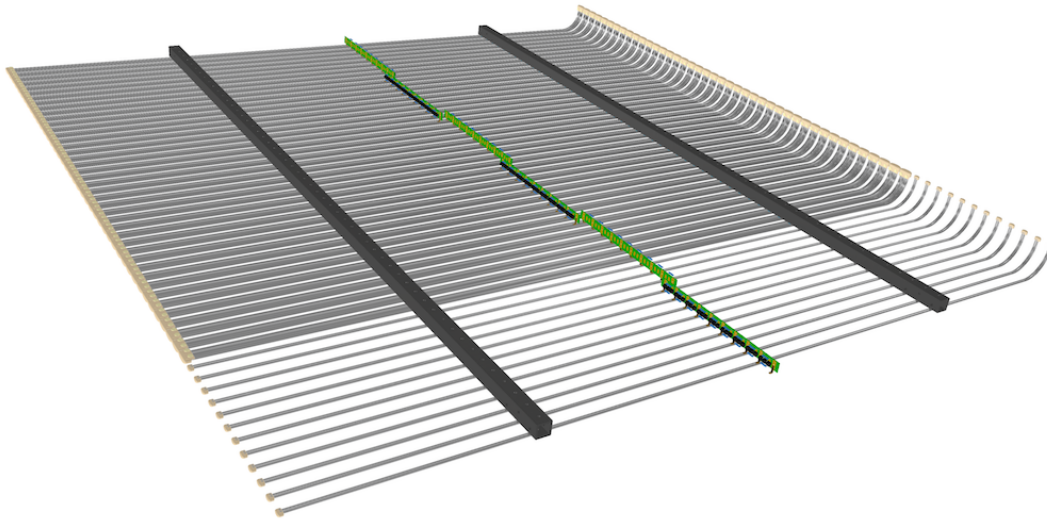


Figure 5.21: A long-wall field cage module to be placed at a corner. Its profiles are bent to  $90^\circ$  on the corner side to minimize the local field and to align with the field cage module along the adjoining end wall. Note the 12 thin profiles at the bottom of the figure; a module containing only thin profiles will be installed below the one in the picture and the two together will be part of the field cage of the bottom drift region. On each module, six HVDBs are mounted along a vertical line passing through its center of gravity.

provided for support of the field cage, as described in Chapter 9. Each mechanical feedthrough flange on top of these penetrations, described in Section 5.4.4, are designed to allow the field cage lift rods to be pulled up and anchored on the flange. The field cage support flange has a mechanism to allow the supermodule to be moved laterally by a few centimeters to avoid interference with the CRP during the field cage installation.

The cryostat roof is expected to deform downward by up to 13 mm after the cryostat is filled with LAr, and upward by about 6 mm before safety relief valves open [75]. Because of this, a pair of field cage supermodule support points on the roof could have a height differential up to 3.5 mm, or an equivalent rotation of 1 milliradians, which translates into a 13 mm lateral swing at the bottom of a 13 m tall field cage column. To maintain perpendicularity of each field cage column and to ensure even load balance on each field cage module, each top module of the two field cage columns is connected to the field cage support beam through an intermediate aluminum yoke at a single point located directly above the center of gravity of the assembled field cage column. At the bottom of each column, a stabilizer prevents the field cage column from lateral movement while permitting overall shrinkage in the vertical direction. The bottom stabilizer construction mirrors that of the top support structure. With its middle foot glued down to the membrane, which has little lateral movement during cool-down, it will keep the columns vertical even if the field cage construction is slightly asymmetrical in weight distribution.

#### 5.4.2.2 Shrinkage during Cool-down

At LAr temperature, the bottom of the field cage will shrink up by about 23 mm from a combination of FRP and stainless steel structure thermal contractions. This movement needs to be accounted for when setting the bottom CRP plane height. The top of the field cage moves more or less in

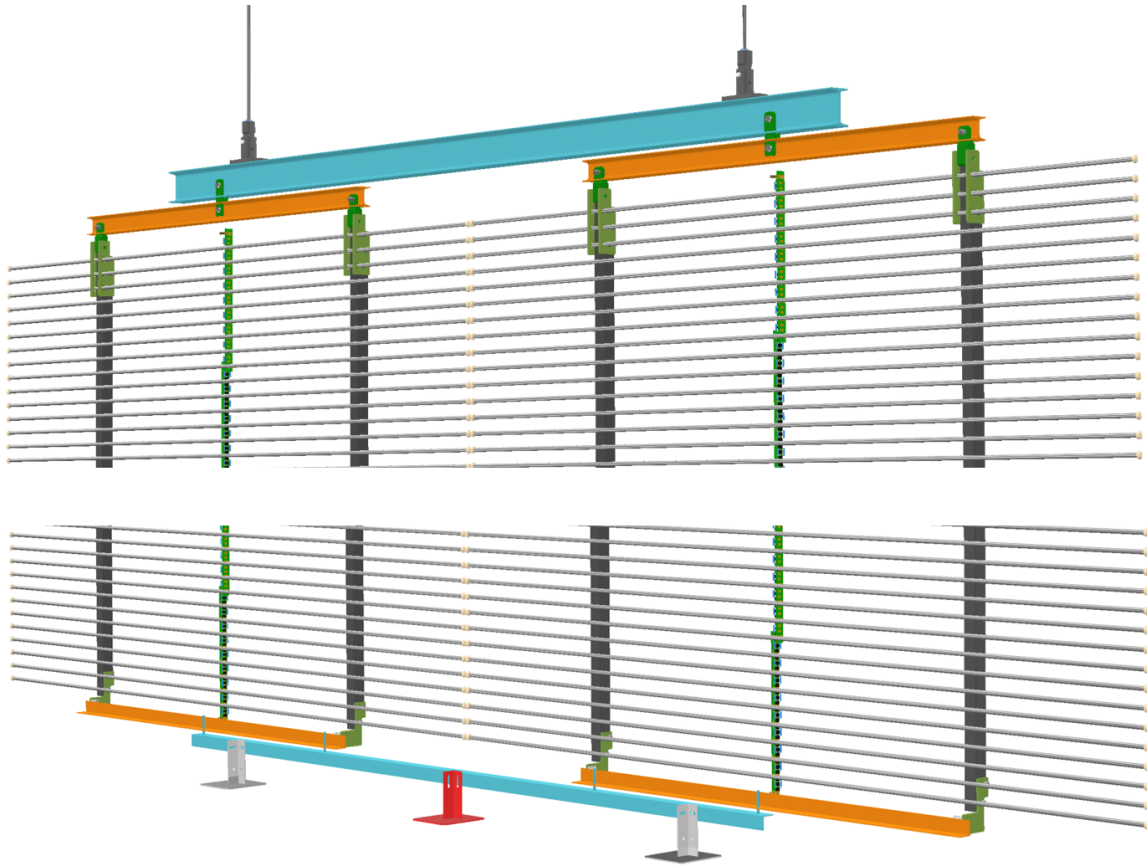


Figure 5.22: Top: Top field cage support beam and yoke structure for a field cage supermodule. A stainless steel I-beam (cyan) is suspended by two lift rods that are each lowered through a field cage support penetration in the cryostat roof. Each end of the beam is connected to an aluminum yoke (orange) at a single pivot point. The two ends of the yoke are attached to the two box beams of a field cage column. Bottom: Bottom field cage stabilizer. One stainless steel angle beam (cyan), and two aluminum angles (orange) mirror the beam and yoke structure at the top of the field cage column to ensure parallel lateral shrinkage of the column. The aluminum angles have clearance holes in the middle, and slots at the ends that slide along the vertical pins mounted on the stainless steel angle. The three feet are glued onto the membrane floor to prevent lateral sway while allowing contraction in the vertical direction. The middle foot (red) only allows vertical motion of the stainless steel angle while the other two feet allow its horizontal contraction.

sync with the top CRP since they both mostly shrink at the rate of the stainless steel support structures. Along the long walls of the cryostat, the (horizontal) gaps between field cage columns on adjacent supermodules will increase by about 20 mm due to shrinkage of both the stainless steel support beams and the aluminum profiles. The gaps between field cage modules on the same supermodule will see a smaller increase of about 3 mm, however, due only to the difference in the shrinkage between the two metals. The corresponding two values along the end walls will be 10% greater due to the larger span of both the beams and profiles. Perpendicular to the field cage, the (horizontal) gaps between the field cage and the anode/cathode will increase by about 7 mm. The 20 mm increase in field cage module gaps is expected to cause E field non-uniformity exceeding the 1% limit in small volumes of LAr near the field cage gaps at the outer edges of the active volume. The total fraction of the impacted LAr is negligible compared with the active mass of the TPC.

Since most of the FD2-VD components are oriented horizontally and occupy relatively narrow slices of vertical space, they are quite insensitive to vertical temperature gradients. The field cage, however, is an exception. The amount of contraction in the lengths of the aluminum field cage profiles at different heights will vary due to the vertical temperature gradient during the initial cool-down and LAr filling period. To avoid excess stress buildup in the field cage modules, most profiles are fixed on only one of the two FRP box beams in a field cage module and can slide on loosely tightened but secured slip nuts. To maintain the box beam spacing, a subset of profiles at large vertical intervals are fixed on both box beams. The interval is determined by the expected temperature gradient (from CFD studies and ProtoDUNE results) above the LAr surface, and the maximum stress the box beam and aluminum profiles can tolerate. This will be finalized as part of the ongoing field cage stress analysis. This configuration, in which the profiles are fixed only on one box beam, increases the field cage modules' tolerance to a higher vertical temperature gradient, and therefore reduces some constraints on the cryogenics system for cryostat cool-down and filling.

### 5.4.2.3 E field Uniformity and Field Cage Transparency

The field cage profiles are positioned 5 cm away from the boundary of the anode planes. This buffer zone ensures a sufficient E field uniformity at the boundaries of the sensitive volume, avoiding the highly modulated pattern very close to the discrete field cage electrodes.

The 5 cm vertical gap between the cathode and the field cage is in the transition region between the two drift fields in opposite directions. Due to the lack of well-defined electrodes in this gap, a non-uniform E field extends into the active volume. To improve the field uniformity, a set of aluminum strips is mounted on the field cage profiles at the cathode height, effectively extending the cathode surface to the field cage. Figure 5.23 shows the position of the field-shaping strip and the improved field uniformity at the edge of the cathode plane. The additional field-shaping strips essentially form a 5 cm × 5 cm channel between the field cage and the outer perimeter of the cathode plane.

The middle two rows of field cage profiles at the cathode level form a HV bus (see Figure 5.24) that distributes the cathode bias voltage to all cathode modules as well as all the field cage columns. Unlike what has been done for FD1-HD, this HV bus has interleaved resistive elements to retard large voltage swings of the cathode modules in case of a discharge to reduce the risk of damages to the cathode mounted PD modules.

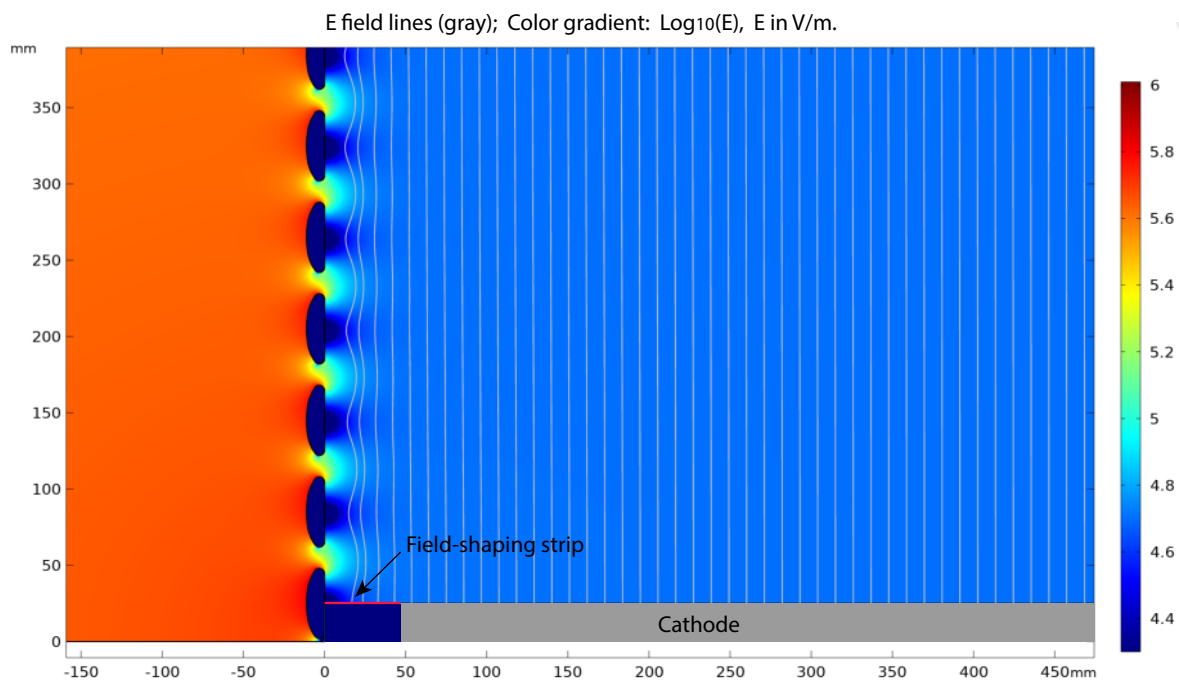


Figure 5.23: E field uniformity near the cathode and field cage intersection. A field-shaping strip is installed in the gap between the outer edge of the cathode and the field cage electrodes to extend the cathode surface to the field cage. The E field lines inside the TPC are shown in gray, and the color gradient represents the E field strength (V/m) in a logarithmic scale. The dark blue half-ellipses closest to the cryostat wall (left) represent the field cage profile cross sections. The calculations were made with a drift field of 500 V/cm, which can be scaled linearly down to the goal drift field value of 450 V/cm.

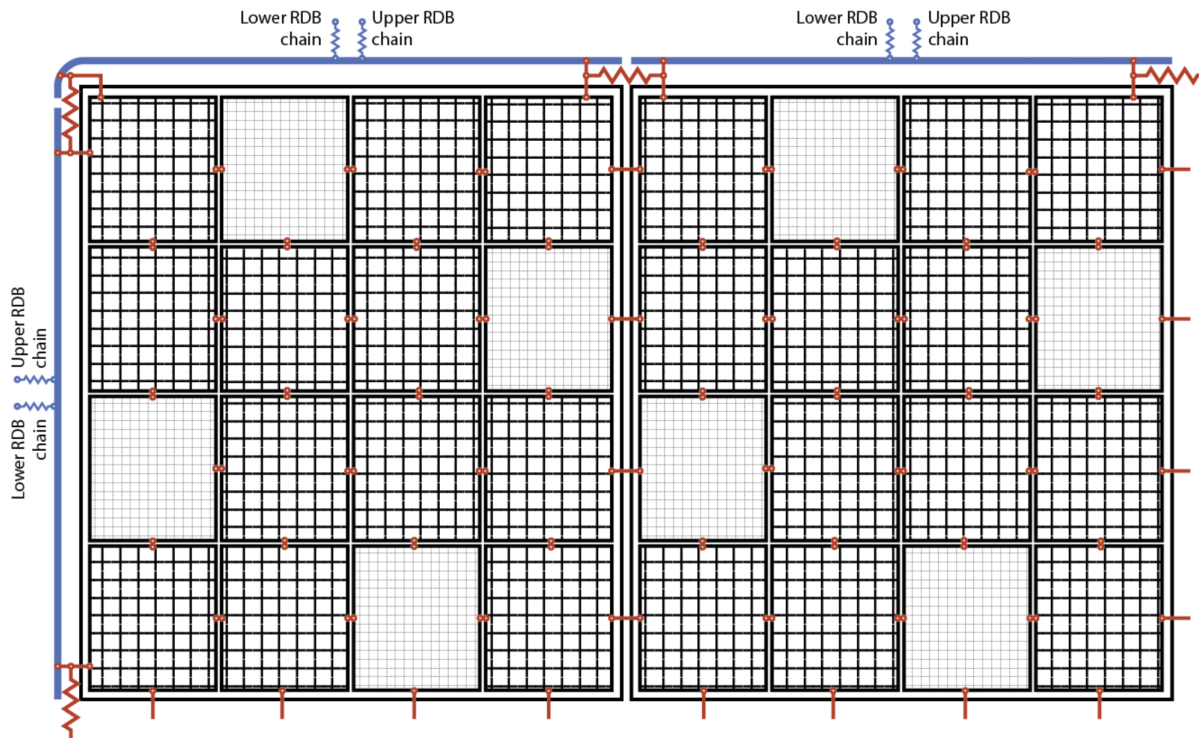


Figure 5.24: A schematic diagram illustrating the interconnects between field cage profiles (blue), HV bus resistors, and the resistive (black) and conductive (light gray) mesh panels on the cathode modules in a corner of the cathode plane. The two rows of field cage profiles at the cathode level serve as conductive segments of the HV bus, interconnecting the outer edges of the cathode modules. Custom resistor modules are mounted between two adjacent profile segments to form a complete loop around the cathode.

In the PDS baseline design, a large fraction of the PDs are mounted on the cryostat wall to collect photons transmitted through the field cage. A highly transparent field cage is therefore desired to allow as much light as possible to reach these PDs. This could be accomplished either using narrower field cage profiles or a larger profile spacing. Both of these options will increase the surface E field on the profiles toward the grounded membrane wall, which increases the risk of HV instabilities on the field cage. Additionally, increasing the profile spacing would require a deeper buffer zone for the E field to reach good uniformity. Therefore, using narrow profiles at the same spacing has been selected as the design choice.

The profiles have elliptical surfaces facing the outside of the TPC, yielding a relatively low E field on the surface. The narrow profile of 15 mm width at 6 cm spacing provides a maximum 70% optical transparency, taking into account all the other field cage structures. The cross section of this profile is shown in the top left of Figure 5.25. A comparison of this and the conventional profile (labeled “FD1 profile”) is shown on the right.

The lower left of Figure 5.25 shows the E field distribution surrounding the narrow profile when it is positioned as the profile immediately next to the cathode plane. The peak E field at this position is 13 kV/cm, well below the 30 kV/cm limit imposed on all electrodes. Nevertheless, it is about 50% higher than that of the conventional 46 mm profiles at the same position. To mitigate this potential risk of higher E field on the field cage surface, the narrow profiles will only be used to cover field cage surfaces further away from the cathode plane where the bias voltages of the profiles are much lower. For this reason, only the profiles in the range  $\pm 2.5$  m to  $\pm 6.5$  m away from the cathode plane (taken as  $y = 0$ ), namely within the 4 m of the top and bottom anode planes, have 15 mm width, while the remaining profiles are the standard 46 mm version, in the field cage baseline design. This configuration accommodates the PDS baseline design, described in Chapter 6.

At the  $90^\circ$  bend at the corners of the field cage, the standard 46 mm width profiles have a maximum local E field of 17 kV/cm, which is higher than in other areas on the field cage, but much lower than the 29 kV/cm value that would result from  $90^\circ$ -bent narrow profiles. A 3D FEA of the E field at the corner section of the field cage at and above the cathode plane is shown in Figure 5.20, right.

The mixing of the narrow and standard profiles introduces a discontinuity in the electrode coverage distribution, and results in an increase in E field non-uniformity at the transition region. See Figure 5.26 (left). Modifications to the standard HVDB resistance are needed to largely eliminate this local degradation; the implementation details are described in Section 5.4.3. The FEA shows that the least drift line distortion is achieved when the voltage steps beyond the third narrow profiles are about 0.7% higher than those of the standard profiles. Without this slight increase, there is a subtle divergence of E field lines near the edges of the field cage up to 2 cm over the 6.5 m full drift, although the E field amplitude remains within the requirement. To implement this small correction, we need to use about 40% of resistors with 0.7% lower value on the divider boards for the wide profiles. Since the tolerance on these resistors is  $\pm 1\%$ , we plan on sorting all resistors after their cold test at the QC stage and dividing the resistors into two groups with their mean values approximately 0.7% apart.

The distance of the field cage profiles from the surface of the flat part of the membrane is  $\sim 700$  mm.

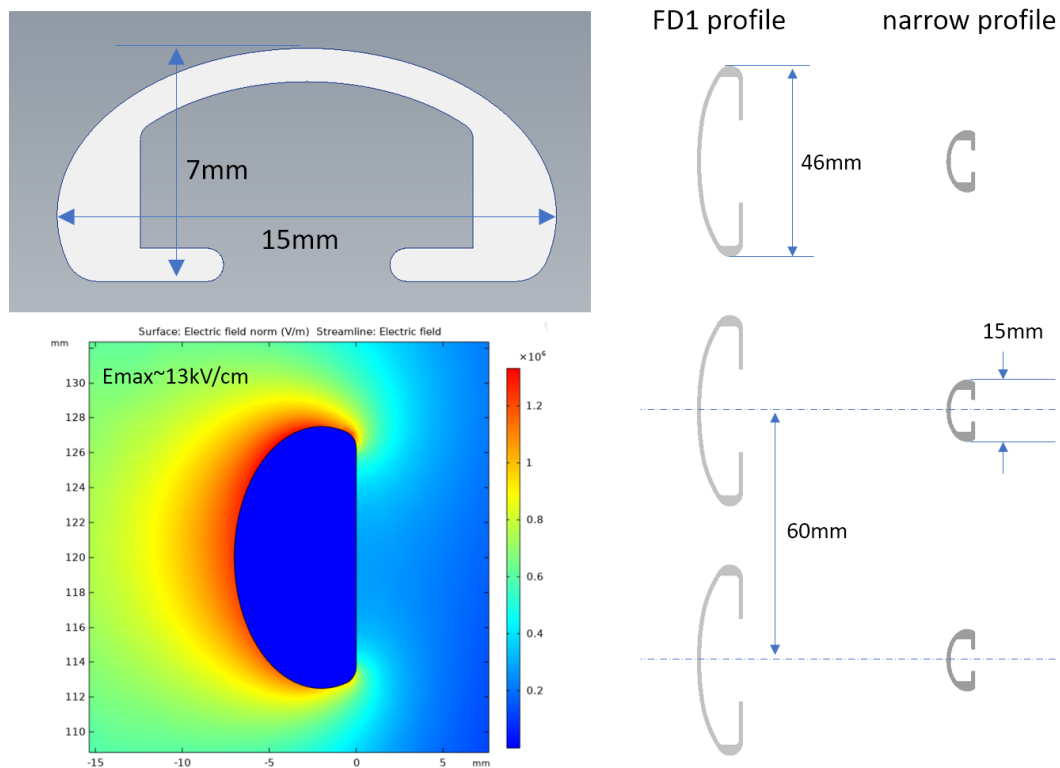


Figure 5.25: Top left: a cross section of a narrow aluminum profile. Bottom left: local E field of a narrow profile when positioned next to the cathode plane. Right: cross sections of the standard and narrow profiles, with dimensions.



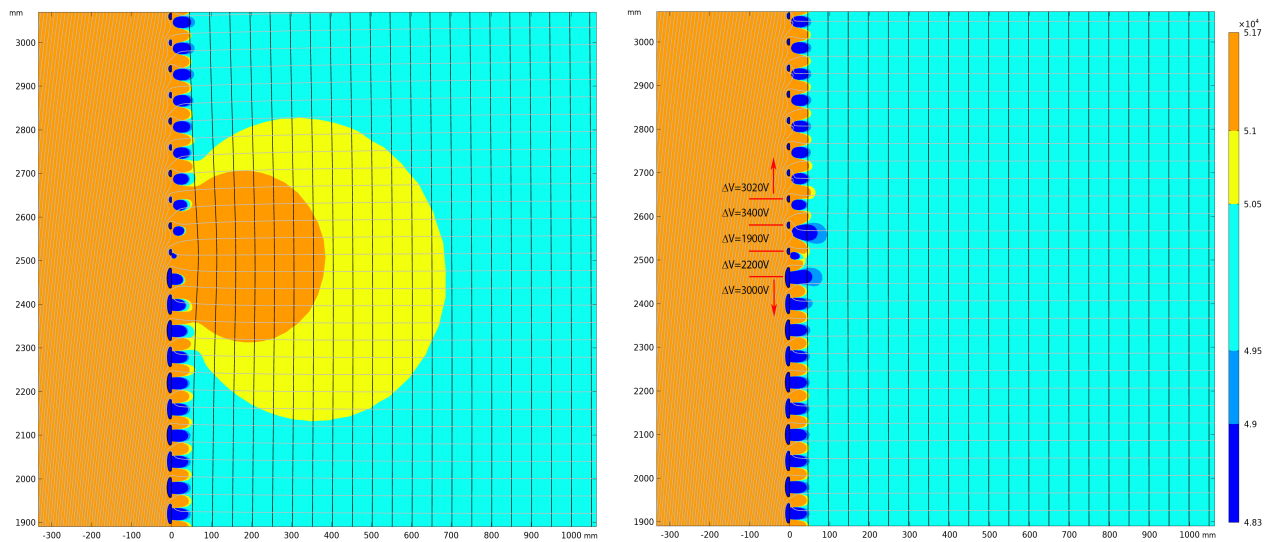


Figure 5.26: Comparison of the drift field uniformity near the transition region of the field cage profiles. Left: All field cage profiles are biased with a linear voltage gradient of 3000 V (for a 500 V/cm drift field); Right: A simple correction scheme that eliminates most of the field non-uniformity near the transition region. E field values are in units of V/m. The active volume starts at  $x > 50$  mm. A number of E field lines (vertical), and equipotential lines (horizontal) are also shown. The calculations were made with a drift field of 500 V/cm, which can be scaled linearly down to the goal drift field value of 450 V/cm. The region colored in yellow (orange) corresponds to a deviation in the range +1 to +2% (beyond +2%) in the E field intensity. The light blue (dark blue) regions correspond to deviation from the nominal E field in the range -1 to -2% (beyond -2%).

Once the height of the “knuckles” in the membrane (the intersections of the vertical and horizontal corrugations) and the depth of the cable trays for the bottom CRPs are taken into account, this distance is reduced to  $\sim 620$  mm. Extrapolating from the ProtoDUNE-SP HV experience, this is a safe separation for operation at  $-294$  kV on the cathode. The hydrostatic pressure from the  $\sim 7$  m of LAr also helps the stability of the field, suppressing the formation of gas bubbles at the cathode level.

### 5.4.3 High Voltage Divider Boards (HVDB)

The resistive chain for voltage division between the field cage aluminum profile electrodes provides the voltage gradient between the cathode and the top-most and bottom-most field-shaping rings. This chain is critical because it determines the uniformity of the E field inside the active volume of the TPC. The chain is constructed with a column of high voltage divider boards (HVDBs) to provide voltage divisions to each column of the field cage, independently. The HVDBs are PCBs with nine stages, each of them consisting of two  $5\text{ G}\Omega$  resistors in parallel, for intra-board redundancy and to keep the overall current of the system low, and three varistors of threshold voltage  $1.7\text{ kV}$ , which will act as a  $5.1\text{ kV}$  voltage clamp in case of a sudden discharge, and protect the resistors from failure due to excessive voltages across them [76]. Given a  $\sim 2.7\text{ kV}$  voltage differential between each stage, the total expected current is  $\sim 1.08\text{ }\mu\text{A}$  along each HVDB chain on a  $6.45\text{ m}$  high field cage column. With a total of 48 columns surrounding the active volume, each with its own resistor chain, the total current per active volume is  $\sim 52.0\text{ }\mu\text{A}$ . The two drift volumes are in parallel, so the field cage for the entire FD2-VD will draw  $\sim 104.0\text{ }\mu\text{A}$ .

Figure 5.27 shows a section of a HVDB board mounted on a section of the field cage in the 70% optical transparency region. The boards can be mounted either on the profiles with each of the electrical pads making direct contact as in the FD1-HD field cage, or through a set of right-angle metal brackets such that the boards are edge-on to the field cage surface and the electrical pads making contact with the profiles indirectly through the bracket.

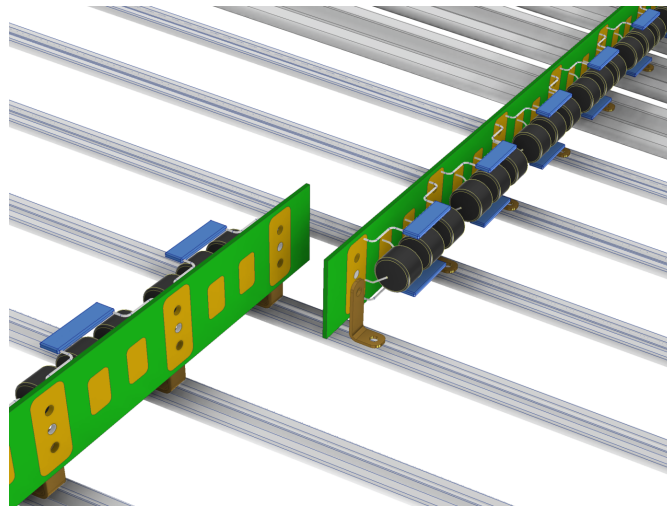


Figure 5.27: Illustration of the resistor divider board mounted edge-on to the field cage to improve the light transmission to the wall-mounted PDs.

To implement the local correct scheme over the wide-to-thin profile transition region, preliminary analysis has shown (see Figure 5.26) that the voltage drops in this region need to be:  $V_n = 73\% V_s$ ,

$V_{n+1} = 63\% V_s$ , and  $V_{n+2} = 113\% V_s$ , where  $n$  is the gap between the last wide and the first narrow profiles, and  $V_s$  is the nominal voltage between adjacent profiles. The resistor values across these gaps must be adjusted accordingly by adding a special, short correcting PCB over this transition region. This strategy keeps all HVDBs uniform but enables finer adjustments.

The field cage voltage divider chains for both the top and bottom active volumes are terminated through wired connections outside of the cryostat to a set of power supplies that can control the termination bias voltages and can measure and record the current flowing through each HVDB chain. The voltage adjustment provides the capability for fine-tuning the drift field near the edges of the CRPs, and recording the current has proven to be a valuable diagnostic tool. Provision for transmitting these signals has been made on the feedthrough for the bottom anode plane readout, as described in Section 5.4.4.

#### 5.4.4 Field Cage Support Feedthroughs

The field cage is suspended from the roof of the cryostat independently of the top anode and the cathode structures. A total of 48 dedicated penetrations are available on the roof of the cryostat: 20 along each long wall, and four along each end wall to support the 24 field cage supermodules.

As shown in Figure 5.28A, the vertical crossing tube has a 150 mm outer diameter (OD) and 10 mm wall thickness to support half the weight of a supermodule ( $\sim 600$  kg). Directly on top of the crossing tube is an oversized base flange (300 mm diameter) to serve as a platform for the lateral adjustment of the field cage anchor point. A slider plate with an O-ring groove underneath it is placed on top of the base flange. This slider plate has a keyhole-shaped opening and a hemispherical cradle to allow the ball end of a field cage support lift rod to pass through from below and sit on top. This slider plate can be pushed around by the four jacking screws on the base plate while maintaining a tight seal by the bottom O-ring. A very slim lifting adapter is attached to the threaded portion at the top of the field cage lifting bar.

A winch mounted on a tripod above the penetration is used to pull the field cage lift rod through the larger opening of the keyhole on the slider plate. This large opening is oriented away from the interior of the TPC to provide an offset of about 5 cm during the lifting of the field cage supermodule to provide added clearance between the field cage and the cathode or top CRPs. Once the ball end of the field cage lift rod emerges through the keyhole (Figure 5.28B), it is settled into the cradle, and the weight of the field cage is transferred to the base flange (Figure 5.28C). Before the final adjustment of all TPC component positions, the field cage support feedthroughs can be left in this state (with the cover flange loosely placed for protection).

To provide a leak-tight seal of the opening in the slider plate, a slider sealing plate is added on top. This plate has an O-ring groove at the bottom face (for O-ring 2 in Figure 5.28A), and another inside a hemispherical cavity (for O-ring 3). Combined with O-ring 1, these three O-rings provide a hermetic seal at the top of the penetration (Figure 5.28D). In this state, the field cage support rod can still be adjusted in all directions. The vertical adjustment is done by rotating the lift rod against a threaded connection at its bottom end. During normal operation, the cover flange is sealed against the base plate. The volume inside the cover flange can either be evacuated or purged together with the crossing tube below.

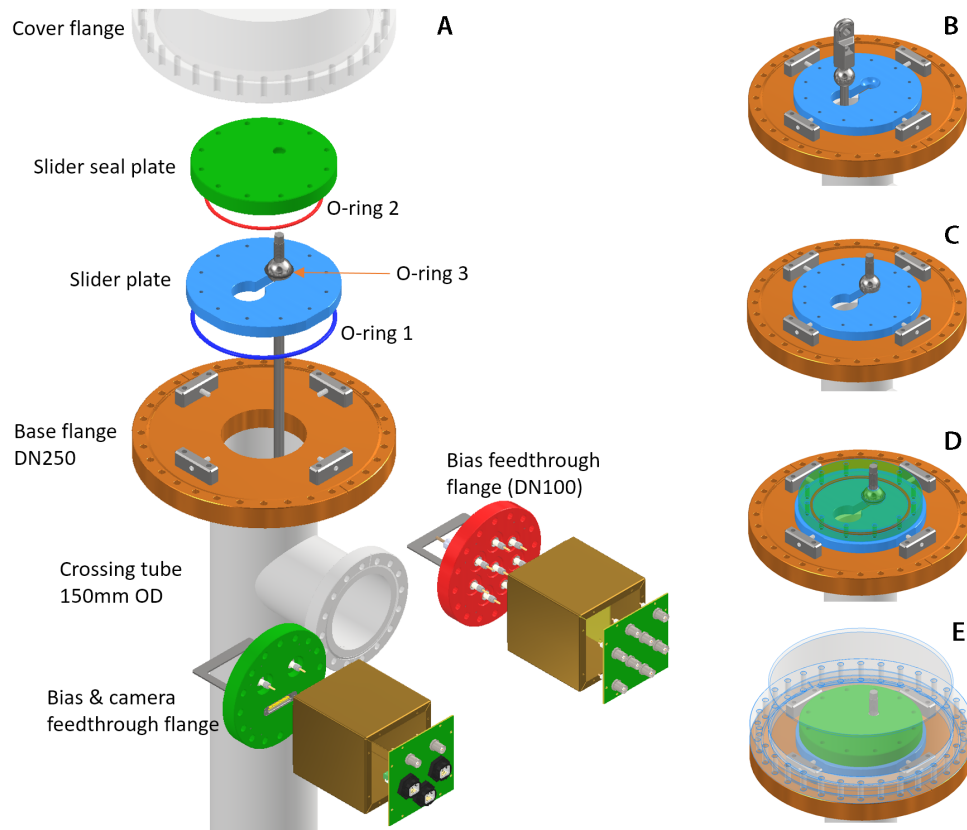


Figure 5.28: Conceptual design of a field cage support penetration and the associated feedthrough flanges for both mechanical support and electrical connections. Left (A): exploded view of the components of the field cage support penetration. Right (B – E) views of the top feedthrough flange at different stages of the installation.

As shown in Figure 5.28, the crossing tubes of field cage support penetrations have electrical flanges on their side, designed to bring out the field cage termination bias voltage cables, the cold camera data cables and the top anode bias voltage cables.

Two types of signal feedthrough flanges are designed for these ports. Along the long walls of the cryostat, two field cage termination lines and six top anode bias lines are needed. A DN100 Conflat flange with eight SHV feedthroughs are used here (see the red flange in Figure 5.28A). Along the end walls, there are two field cage termination lines per penetration, but no anode bias lines. Cameras will be placed inside the cryostat for monitoring of the HV components. A different flange with two SHV and one DB25 connector is used for the camera signal (see the green flange at the bottom of Figure 5.28A). The filter boards inside a shielded enclosure are mounted on the signal feedthrough flange to remove noise pickup inside the cryostat.

The top anode bias voltage lines are routed through the field cage support penetrations and secured to the side ports before the field cage installation. The bottom field cage termination cables are embedded inside the cable trays mounted on the cryostat wall, running from floor to ceiling. The upper ends of the cables are pulled through the field cage support penetrations while the rest of the cable bundles are installed into the cable trays. The top field cage termination cables are tied to the field cage lift rods at installation, and carefully detached as the lift rods pass through the top flange. Continuity checks are made at every step of the cable connections.

### 5.4.5 Field Cage Assembly and Installation Procedure and Tools

Detailed field cage unit module assembly and field cage super module installation procedures have been developed and were presented at the in May 2022. The assembly procedure includes mounting of the HVDB. This section briefly describes these procedures and the tools required for them.

Figure 5.29 shows several tools designed for the field cage installation process. Each of the 3.24 m tall field cage modules will be assembled vertically on the assembly station (A) to minimize stress and deformation of the profiles as the module is lifted after assembly. The storage cart (C) accommodates eight completed field cage modules, i.e., enough for one supermodule. Once it is full, the storage cart will be transported into the cryostat for installation of the supermodule. Each module is moved to the installation cart (B) and positioned under the stainless steel I-beam hanging on the cables attached to the installation tripod (D) on the cryostat roof. The two modules in the same row of a supermodule are installed, then the completed row is raised by about 3.5 m for the installation of the next row. This process is repeated until all four rows are installed.

## 5.5 Design Validation

After the ProtoDUNE-DP run, the most critical item of the vertical drift design was determined to be the HV delivery system, in particular the HV extender and its coupling to the HVFT.

**Delivery System.** The overall design of the extender was highly simplified with respect to the ProtoDUNE-DP version, and it was the subject of the dedicated R&D campaign in spring/summer 2021 in small scale cryostats (ICEBERG R&D cryostat and electronics (ICEBERG) at Fermi National Accelerator Laboratory (Fermilab) and the two-ton vessel at CERN). The main outcome

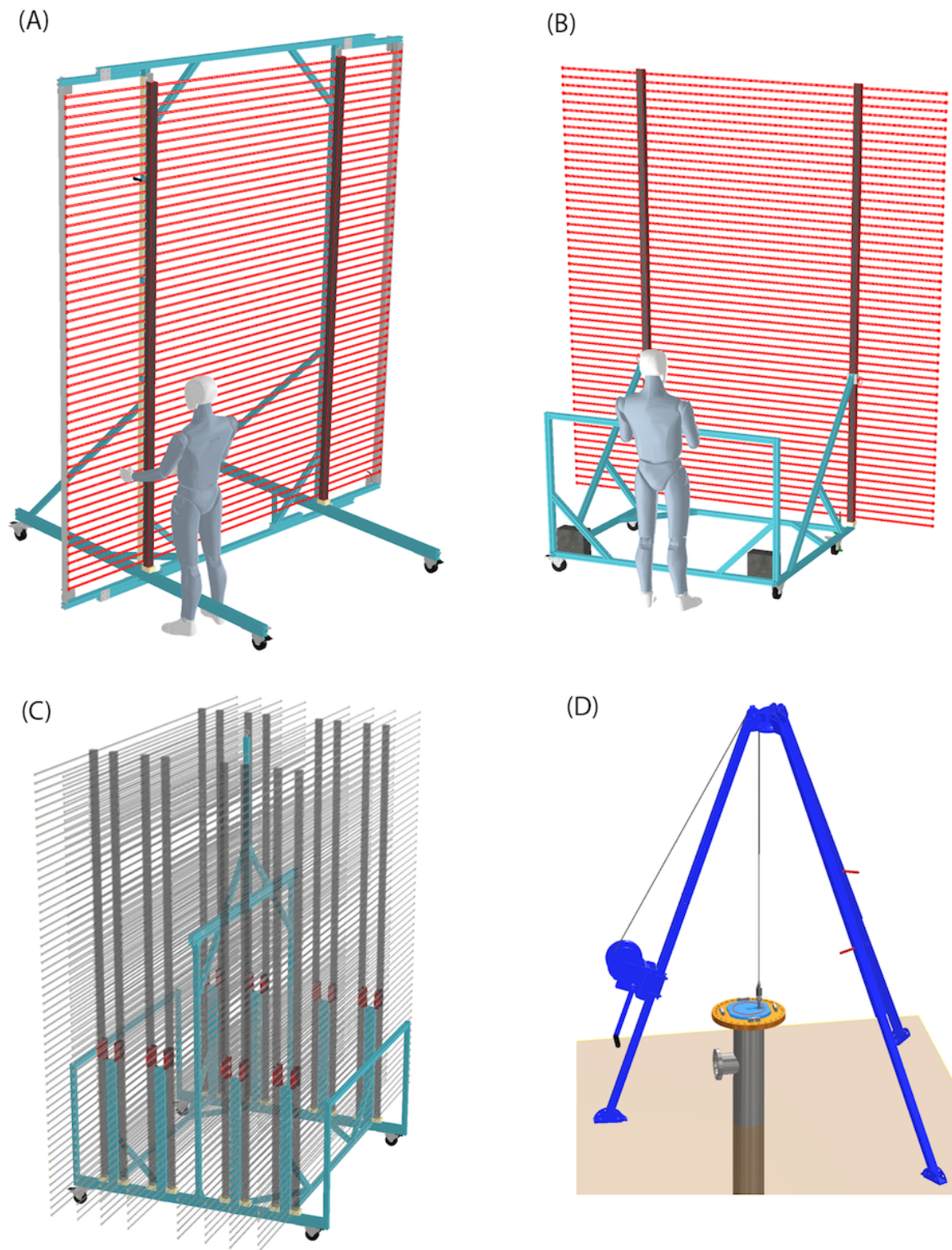


Figure 5.29: Tools for the field cage (FC) assembly and installation process - (A) FC module assembly station; (B) FC module installation cart; (C) FC module storage cart; (D) tripod for raising field cage supermodule assembly

of the R&D was a further optimization of the extender-to-HVFT coupling to minimize the E field at the extender surface and the charging up on insulating elements such as the exposed HVFT UHMWPE and the extender support disk. The material of the extender support disk was also selected to be UHMWPE against the FR-4 because of its homogeneity and better dielectric rigidity. Operation at  $-300$  kV in pure argon was achieved and maintained for the full test duration (several days) in these R&D campaigns.

The validation of the HV delivery system was performed during the NP02 HV long-term stability run in 2021-2022 in which operation at  $-300$  kV in ultra pure LAr was demonstrated (up-time  $> 99.9\%$  over two periods of about two months each of continuous operation). At the end of this run, cosmic rays tracks were also recorded with the DP CRP readout system, demonstrating that 6 m drift distances are feasible and that the newly designed HV delivery system introduces no detectable noise from residual ripple or leakage currents.

The down-time intervals of the HVS in this run occurred at a rate of about one every two hours for few seconds each ( $< 0.1\%$  of the time on average); they have been identified as HV current glitches located at the junction between the extender support UHMWPE disk and the metallic head of the extender-to-HVFT coupler. These glitches are most likely due to instability of the charged-up layer on the insulating surface of the support disk. While they were of limited duration with no visible degradation over the test run, a design optimization to further reduce the down-time was introduced and discussed in Section 5.3.3. Tests in the two-ton cryostat for this new design are in progress.

**HV feedthrough and HV cable.** The HV cable and the HVFT experienced a failure during the NP02 long-term HV stability run. In-depth investigations have been carried out in collaboration with the CERN experts of the “Materials, Metrology and Non-Destructive Testing” group with tools such as the electron microscope, computerized tomography, and X-rays. A crack in the cable insulation was most likely caused by pre-existing mechanical stress due to handling issues (e.g., bending the cable more acutely than its prescribed limit or making a small cut during the preparation of the cable termination). This incident is feeding into updates to the cable installation procedure.

Regarding the HVFT, the investigation points to pollution of the UHMWPE insulating cylinder by extraneous filaments during extrusion as the most probable explanation. Cracks progressively developed along these filaments and eventually opened a path for current flow. (Note that this problem occurred only in one 300 kV HVFT out of four available.) The mitigation consists of selecting very pure extruded UHMWPE. A certificate will be required; CT examination of a sample of the UHMWPE cylinder will also be an option. Since X-rays can be used to detect the filaments in UHMWPE, the full cylinder can be examined this way.

**HVFT length.** During the long-term runs of the original 300 kV HVFTs built for NP02 and , ice formed at the cable receptacle, which reached the depth of the cryostat roof inner membrane and was subject to a quite low temperature. Ice formed as a consequence, despite continuous flushing of the cable receptacle with dry nitrogen. This was confirmed in the NP02 stability run when the failed HVFT was replaced by the one previously used on the ProtoDUNE-DP run. Ice formation does not affect the HVS performance, given its good insulating properties, however it prevents extraction of the cable, which might be required in FD2-VD over the decades-long operation.

The new HVFT initially installed in NP02 for the long-term HV stability run was about 80 cm longer on the warm side to keep the cable receptacle temperature above 0 °C, avoiding freezing and frost buildup, which caused instability during NP04 operation. This allowed the cable to be easily extracted when the failure occurred after about two months of operation. The design of the HVFTs under construction maintains the “warm” cable receptacle, keeping it fully above the cryostat insulation skin. This results in a HVFT length longer than 3 m; at present the design is 4 m, which is feasible with the extruded UHMW-PE cylinders commercially available.

**Cathode.** The challenging features of the FD2-VD cathode design that require dedicated testing are the FRP frame and the suspension system. A prototype of the cathode module in 1:1 scale, has been built and installed in the NP02 cold box for the CRP test program, with integrated X-ARAPUCA cells and electronics. The cathode module was placed on feet resting on the cold box floor. Although some details of the design were not final, (the FRP frame was made from C-shaped beams glued together instead of H-shaped beams, that were 5 cm thick instead of 6 cm, and a metallic rather than resistive perforated panel for the first semester of tests; resistive meshes are currently in operation) the cathode operated properly and stably up to 15 kV as planned in all the test runs (from November 2021 through November 2022). No impact on the field uniformity from any possible sag has been measured.

Based on these first results, the final design of the cathode is proceeding as defined, with the first final prototypes to be built for FD2-VD Module 0.

Investigations are ongoing at IJClab concerning the behavior of the Dyneema rope used in the suspension system. The preliminary creep data acquired on several ropes show a reproducible and predictable elongation within a few cm precision, limited by the setup. A cryogenic and more precise (mm precision) setup at IJClab is undergoing validation and will be used for FD2-VD Module 0.

**Field Cage** The design of the field cage based on C-shaped aluminum profiles and supported by FRP beams is well established, and its validity was confirmed by the operation of ProtoDUNE-SP and more recently in the NP02 long-term HV stability run. The configuration in which narrower cross-section aluminum profiles are used along portions of its height (closer to the anode planes) has undergone preliminary tests in NP02. It has a 2 m × 2 m window integrated into the existing DP field cage. No issues were recorded, but due to the 1 m distance of the field cage to the membrane (instead of 70 cm) and the location of the window close to the anodes, the nominal E field expected around the profiles close to the cathode was not reached.

A dedicated test is planned with a mini-field cage in the 50 liter cryostat at CERN. Its field cage is made of aluminum profiles similar to those of the 70% transparent design. With a distance from the cryostat vessel as close as 3.5 cm and a HV as high as 25 kV on the cathode, the E field at the surface of the aluminum profiles can be as high as in the FD2-VD design close to the cathode.

## 5.6 Production, Handling and Quality Control

The production and handling of HV components must be approached with great care to avoid scratching and potentially compromising the electrical components. Part production is to be



carried out so as to avoid introducing sharp edges wherever possible. The aluminum field-shaping profiles are particularly prone to scratches and must be packaged and handled so as to avoid direct contact with other profiles and materials. Kapton strips are used to separate the profiles from the FRP of the field cage frames as they are inserted in order to protect against scratching or removal of the profile coating. Any scratches found in the FRP beams are covered with epoxy to prevent fibers from escaping into the LAr.

Quality control (QC) tests have been conducted on HV modules and individual components at every step: parts procurement, production, integration, and installation, and will continue to be conducted as production for FD2-VD proceeds. Documented procedures, including QC procedures, come with checklists that must be completed for component parts at each step. Printed copies of the checklists completed in the procurement and production stages were and will continue to be included as travelers in shipping crates. To ensure that nothing is compromised during transport, QC tests are repeated on individual components and assembled pieces after shipping.

Resistance between steps on the resistor divider boards is measured and verified to be within specification both after production and after delivery to CERN. Once the resistor divider boards are mounted onto an assembled field cage module, the resistance between adjacent profiles is measured to verify sound electrical connection. These QC checks of connections between cathode modules and between the cathode and field cage modules, that have been completed for the received parts, will also be performed after installation.

QC tests on the HV components of ProtoDUNE required many measurements with several different testing devices. Extrapolating these measurements to the scale of FD2-VD will require development of dedicated tools to optimize the QC process at each step.

## 5.7 Interfaces

The major interfaces of the HV system are shown in Table 5.4. They are all well advanced, although not fully finalized. The interface with the PDS is most critical since it concerns the routing of the fibers along the field cage modules and within the cathode modules, which may require some design changes to accommodate it.

Table 5.4: HV interface descriptions and links to full interface documents.

System	EDMS #	Description
CRP	2619003	Field cage to CRP clearance, CRP bias power supplies & cables
BDE	2726647	Bottom CRP bias voltage feedthroughs
PDS	2619007	Mounting of the PD modules on the cathode, routing of the PD fibers off the cathode, providing transparency in the field cage for wall mounted PDs.
I&I	2648558	Installation requirements and procedures.

## 5.8 Production Timetable

A timetable for HVS component procurement and assembly has been developed, as shown in Table 5.5 and feeds into the schedule outlined in Chapter 10.

Table 5.5: HV system production timetable

Deliverable	Production type	Dates
field cage profiles	commercial	Q2 2024 – Q3 2025
field cage divider boards production	<ul style="list-style-type: none"> <li>▪ component selection: in-house</li> <li>▪ board production: commercial</li> </ul>	Q1 2024 – Q4 2025
field cage box beams and hardware	<ul style="list-style-type: none"> <li>▪ fabrication: commercial</li> <li>▪ QC: in-house</li> </ul>	Q2 2024 – Q1 2025
cathode frame fabrication	commercial	Q2 2024 – Q3 2026
cathode frame integration and QC	in-house	Q1 2025 – Q3 2026
HVPS and HVFT	commercial	Q2 2024 – Q2 2025
remainder of HV delivery system	commercial and in-house	Q2 2024 – Q4 2024

## 5.9 Organization and Management

### 5.9.1 Institutional Responsibilities

The HVS joint consortium is responsible for the design, construction and assembly of the HV systems for both FD1-HD and FD2-VD. It currently comprises several US institutions and CERN. One French institution is participating in FD2-VD only. All the participating institutions are involved in construction and operation of and FD2-VD Module 0.

CERN is committed to a significant role in terms of funding, personnel, and the provision of infrastructure for R&D and detector optimization for the s. Moreover, CERN will be responsible for a significant fraction of FD2-VD subsystem deliverables.

In the current HVS consortium organization as listed in Table 5.6, each institution is naturally assuming the same responsibilities that it assumed for ProtoDUNE-SP and ProtoDUNE-DP. The consortium organizational structure includes a scientific lead (from CERN), a technical lead (from Brookhaven National Laboratory (BNL)), technical design report (TDR) editor (from UTA), and a HVS design and integration lead (from Argonne National Laboratory (ANL)).

The successful experience gained with ProtoDUNE-SP, ProtoDUNE-DP and the recent R&D with the NP02 Coldbox has demonstrated that the present HVS consortium organization and the number of institutions are appropriate for the construction of the HV system for both the FD1-HD and the FD2-VD.

The consortium is organized into working groups (WG) that address the design and R&D phases of development, and the hardware production and installation.

- WG1. Design optimization for FD1-HD and FD2-VD modules: assembly, system integration, detector simulation, physics requirements for monitoring and calibrations.
- WG2. R&D activities, R&D facilities.
- WG3. FD1-HD cathode plane assembly (CPA): Procurement of resistive panels, frame strips, electrical connections of planes; assembly, QC at all stages, and shipment of these parts.
- WG4. FD2-VD cathode and suspension system: material procurement; construction, assembly, shipment to South Dakota Warehouse Facility (SDWF), quality assurance (QA) and QC.
- WG5. FD1-HD top/bottom and endwall field cage modules, FD2-VD field cage modules: procurement of mechanical and electrical components, assembly and shipping to SDWF.
- WG6. HV supply and filtering, power supply, and cable procurement, R&D tests, filtering and receptacle design and tests.

Taking advantage of identified synergies, some activities of the FD1-HD and FD2-VD working groups are merged: HV feedthroughs, voltage dividers, aluminum profiles, FRP beams, and assembly infrastructure.

Table 5.6: Institutions participating in the HVS consortium

Institution	Country	Detector & Deliverables
European Organization for Nuclear Research (CERN)	Switzerland	FD1 & FD2: System design, HV R&D, HV distribution system & monitoring, components procurements (FC, CPA, HV), ProtoDUNE installation & operation
Argonne National Lab	USA	FD1: System design & analysis, CPA production and installation; FD1 & FD2: QA/QC
Brookhaven National Laboratory	USA	FD1 & FD2: System design & analysis, project management, interfaces, cold cameras
Kansas State University	USA	FD1: HV bus & interconnects, GP monitoring system
Louisiana State University	USA	FD1: Resistive divider boards, FC termination boards, end-wall FC production & installation
SUNY Stony Brook University	USA	FD1: Top field cage production & installation
University of Texas Arlington	USA	FD1: Bottom field cage production & installation; FD2: field cage production & installation
College of William and Mary - Virginia	USA	FD1: CPA production & installation; FD2: Resistive divider boards, FC assembly & installation.
Laboratoire de Physique Irène Joliot-Curie	France	FD2: Cathode design, construction, assembly & tests

## 5.9.2 High-level Schedule

Table 5.7 lists the most high-level milestones for the design, testing, production, and installation of the FD2-VD HVS. Dates in this tentative schedule are based on the assumed start of installation of the FD2-VD at Sanford Underground Research Facility (SURF). The dates for the HVS production of a FD2-VD are included as a reference.

The production scenario for the schedule presented in Table 5.7 assumes one factory site for the cathode construction and two for the field cage components, namely UTA and W&M with the field cage profiles supplied by CERN. Given the present starting date for FD2-VD installation, this assumption is fully compatible with the time available after the operation of FD2-VD Module 0 and with a reasonably large float in the production schedule.

Table 5.7: High level milestones and schedule for the production of the HVS of FD2-VD

Milestone	Date
Complete FD2-VD HVS Final Design Review	April 2023
Complete HVS installation of Module 0	April 2023
Module 0 commissioning	Fall 2023
Post Module 0 Review	Jan – March 2024
FD2-VD HVS production readiness review	March – April 2024
FD2-VD HVS component production	April 2024 – Aug 2026
Start of FD2-VD HVS TPC installation	July 2027
End of FD2-VD HVS TPC installation	April 2028

A more detailed schedule for production and installation of the FD2-VD is found in Figure 5.30.

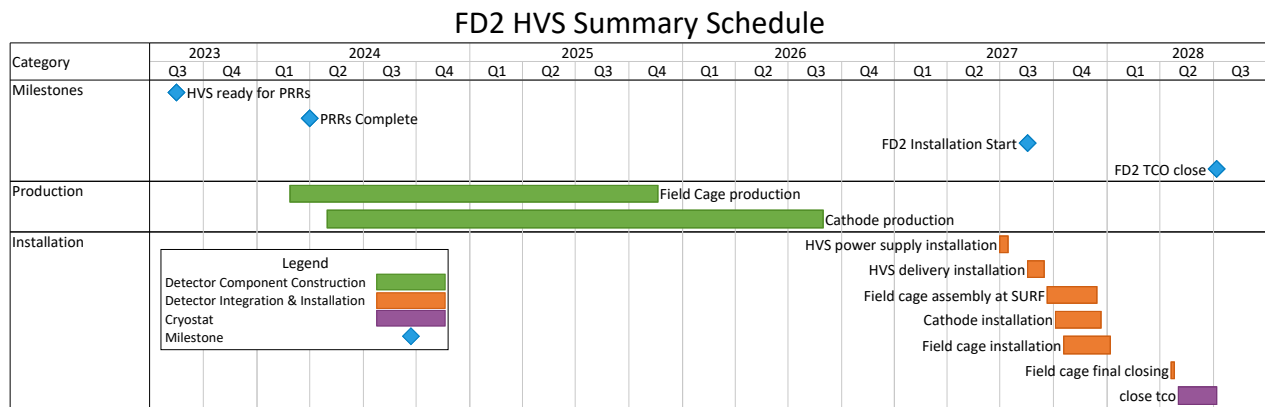


Figure 5.30: Key HVS milestones and activities toward the FD2-VD in graphical format (Data from [53]).

# Chapter 6

## Photon Detection System

### 6.1 Introduction

Energy deposition from the passage of high energy charged particles in liquid argon (LAr) yields both free charge from ionization and fast scintillation light. In fact, LAr is an excellent scintillator producing  $\sim 25,000$  photons per MeV of energy deposited by a minimum ionizing particle (MIP) in the presence of an electric field (E field) of 500 V/cm. Scintillation light provides information on three key detection aspects of the experiment: event triggering, event (and sub-event) precision time reconstruction, and event energy reconstruction as discussed in Chapter 2.

The mechanism for light production is quite well understood. Ionized and excited argon atoms combine on a picosecond timescale to produce  $Ar_2^*$  singlet or triplet excimer states that rapidly decay (about 25% with a time constant of  $\tau_s = 6$  ns, and 75% with  $\tau_t = 1.5$   $\mu s$ ) yielding a characteristic scintillation of 128 nm wavelength [77, 78]. In the environment of LAr doped with a small amount of xenon, the slow argon scintillation component is almost entirely shifted to 175 nm [79, 80]. This has the effect of increasing the scattering length for that component to approximately eight times higher than for 128 nm light with the impact that a higher amount of light is collected by the detector for sources beyond  $\sim 4$  meters [81]. Xenon doping is assumed for the vertical drift detector module (FD2-VD) and this effect is included in all relevant simulations.

The presence of nitrogen impurities in LAr affects both scintillation light production and propagation. Nitrogen affects the light output of argon through non-radiative collisional reactions that destroy the argon excimers before deexcitation, thus quenching scintillation light production. This process particularly affects the long-lived triplet excimer states, effectively reducing the amplitude of the slow component of the argon scintillation light [82]. In argon doped with xenon, the vast majority of the argon light that would otherwise be quenched by nitrogen impurities (via  $Ar_2^* + N_2 \rightarrow 2Ar + N_2$ ) can be recovered (via the competing process  $Ar_2^* + Xe \rightarrow ArXe^* + Ar$ ). The impact of nitrogen on scintillation light propagation is that it can absorb VUV photons, reducing argon transparency. Here again, xenon doping helps to mitigate this detrimental effect of nitrogen, since the photoabsorption cross-section by nitrogen is higher at 128 nm than at 175 nm [83].

Photon detectors (PDs) are implemented in liquid argon time-projection chamber (LArTPC) experiments to exploit the information provided by scintillation light and thereby both improve and expand the capabilities of the apparatus. The physics motivation for the system capabilities is presented in Section 2.3. In the FD2-VD proposal for the second DUNE far detector module, the implementation of a robust PDS is an important feature of the design.

The FD2-VD design will implement the same photon detection system (PDS) technology as the horizontal drift detector module (FD1-HD) design [84] but with a modified configuration. Functionally, an X-ARAPUCA module is a light trap that captures wavelength-shifted photons inside boxes with highly reflective internal surfaces until they are eventually detected by silicon photomultipliers (SiPMs). The wavelength-shifted photons are converted to electrical signals by SiPMs distributed evenly around the perimeter of the wavelength-shifting (WLS) plate. Figure 6.1 shows a full-scale X-ARAPUCA PD module prototype.

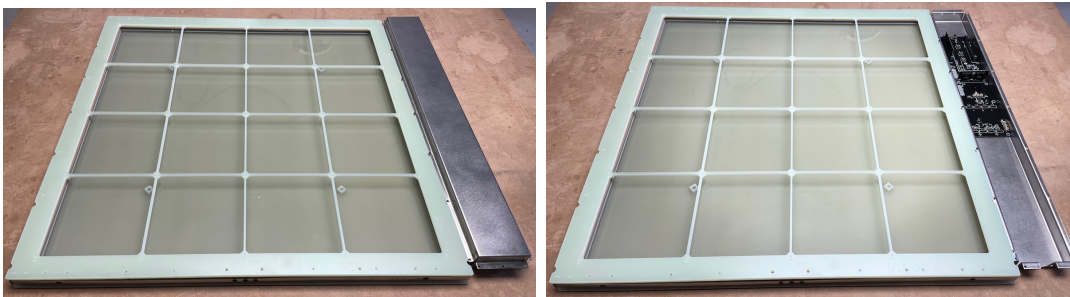


Figure 6.1: Full-scale prototype of the X-ARAPUCAs with (left) and without (right) the electronics cover.

In the vertical drift time projection chamber (TPC) configuration, even though the charge-readout plane (CRP) structure is perforated, it is effectively opaque to light and therefore does not allow for PD installation at the anode (ground) side of the TPC volume. This has the consequence that the PDs can only be installed on the cathode plane, on the walls or on the cryostat membrane walls behind the field cage, provided that the latter is sufficiently transparent to light.

In the FD2-VD PDS design, X-ARAPUCAs are mounted on all four membrane walls (at ground potential) and within the cathode plane structure, as shown in Figures 6.2 and 6.3. Cathode-mount PDs are at the cathode voltage, so there can be no conductive path to ground.

While membrane-mount PDs will adopt the same copper-based sensor biasing and readout techniques as FD1-HD, cathode-mount PDs require new solutions to meet the challenging constraint imposed by operation in a high voltage (HV) environment. The cathode-mount PDs are powered using non-conductive power-over-fiber (PoF) technology [17], and the output signals are transmitted through non-conductive optical fibers, i.e., signal-over-fiber (SoF) technology. This solution provides voltage isolation in both signal reception and transmission. PoF is a well established technology, but its extensive use in a cryogenic detector will be a new application.

Another important difference of the FD2-VD design with respect to FD1-HD, which has smaller optical volumes, is the doping of LAr with xenon at the level of  $\mathcal{O}(10 \text{ ppm})^1$ . Results from large-

<sup>1</sup>Although the baseline FD1-HD design does not call for xenon doping, the cryogenics system allows the option for addition of a xenon injection port as a potential mitigation for nitrogen contamination.

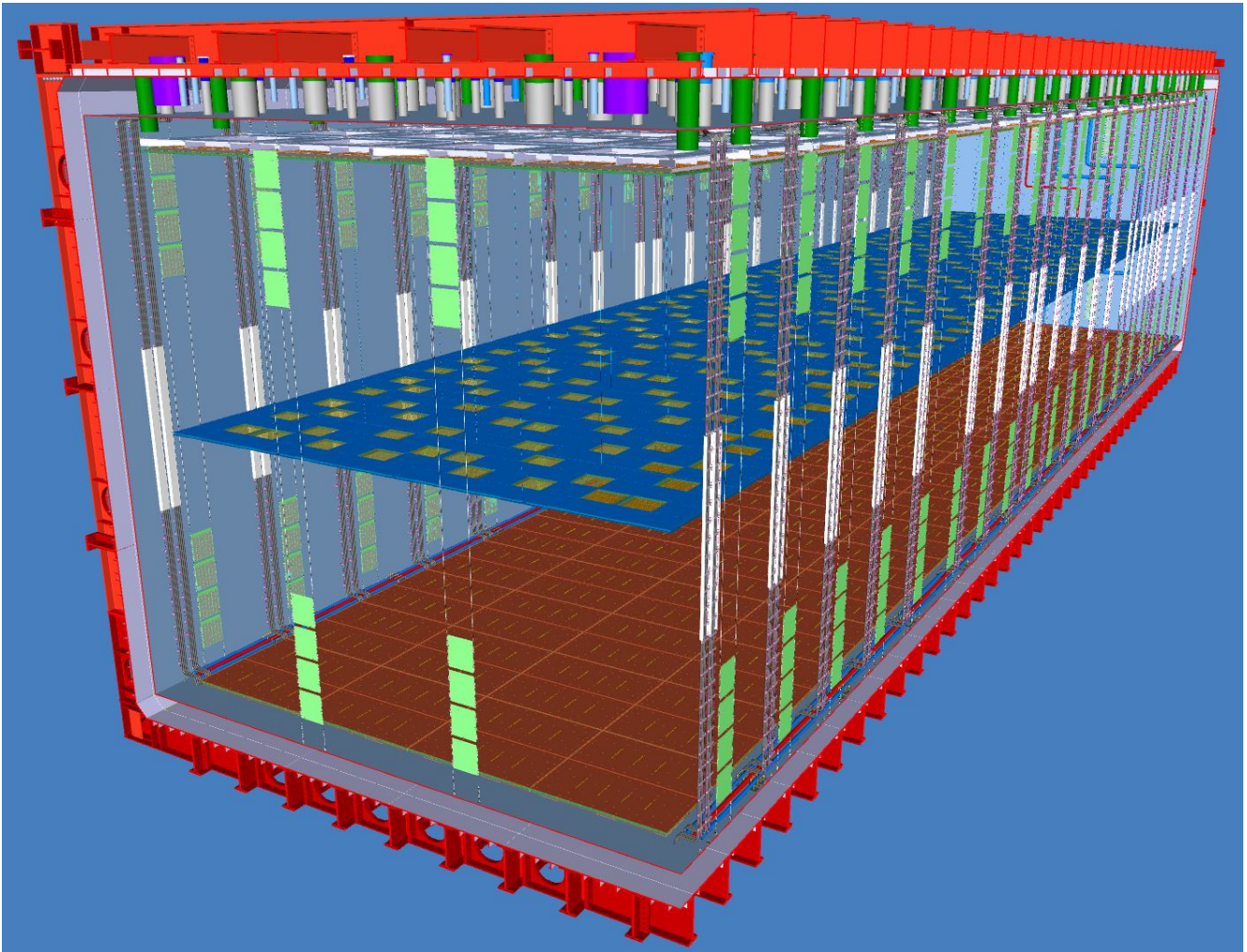


Figure 6.2: Perspective view of X-ARAPUCA modules locations on the horizontal cathode plane and on the vertical cryostat membrane walls behind the field cage.

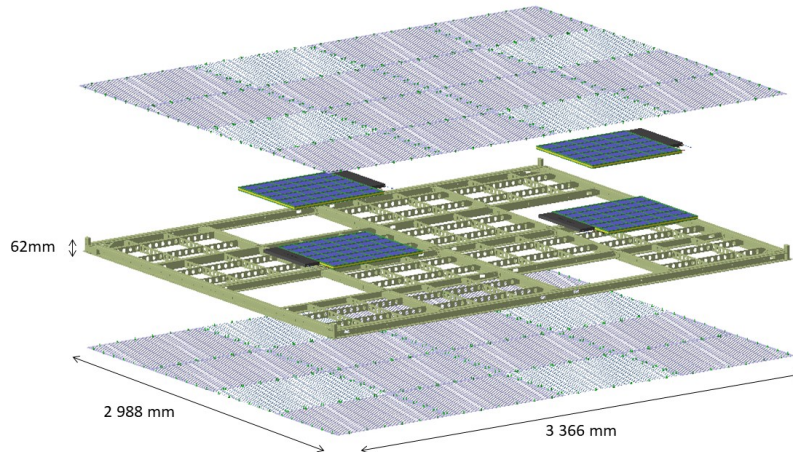


Figure 6.3: A cathode plane module showing the placement of the four FD2-VD PDS X-ARAPUCAs in the central modules (blue squares). In the cathode plane modules adjacent to the field cage, there are no PD modules abutting the field cage to minimize potential discharge effects. The cathode module has a resistive skin over most of the surface, except for a conductive mesh of 90% optical transparency over the X-ARAPUCAs.

volume measurements with and are summarized in Section 6.8.1. This feature will ensure improved light detection uniformity (see Figure 6.4) and will make the system more resilient to nitrogen contamination. In particular, the ratio of minimum-to-average light yield (LY) in the  $z=0$  plane of the active volume improves from 0.16 for pure argon to 0.51 for Xe-doped argon.

As shown in Section 6.2.1, the FD2-VD PDS configuration, with uniformly distributed PD coverage across the cathode and partial coverage on all four membrane walls near the anode planes, produces significantly better overall light yield and light yield uniformity across the entire TPC active volume when compared to the FD1-HD design for a comparable cost.

## 6.2 Design Specifications, Performance and Scope

### 6.2.1 Specifications and Performance

The detector specifications for the FD2-VD PDS are the same as for the FD1-HD system. Selected specifications, those with a direct connection with physics performance, are reproduced here in Table 6.1. The proposed system will exceed these requirements, as summarized in Table 6.2 and described below, providing a robust margin against unexpected degradation and may enhance the system performance for some physics studies.

The light yield (LY, detected photons per unit deposited energy) is the most important PDS specification in Table 6.1 (first row). Both the average LY from light emission anywhere in the detector volume, and the lowest detectable light level from the dimmest part of the detector, are relevant. For PDs located on a single detection surface, the LY variation across the volume would present a large gradient along a perpendicular axis to this plane. Placing photosensors along the four membrane walls in addition to the cathode, as in this system design, significantly reduces the



Table 6.1: Key FD2-VD PDS specifications.

No.	Description	Specification	Rationale
1	Light yield	$>20$ PE/MeV (avg), $>0.5$ PE/MeV (min)	Gives PDS energy resolution comparable to that of the TPC for 5-7 MeV supernova (SN) $\nu$ 's, and allows tagging of $> 99\%$ of nucleon decay backgrounds with light at all points in detector.
2	Time resolution	$< 1 \mu\text{s}$ Goal: $< 100$ ns	Enables 1 mm position resolution along drift direction.
3	Spatial localization in plane perpendicular to drift	$< 2.5$ m	Enables accurate matching of PD and TPC signals.
4	Single PE pulse height divided by baseline noise RMS	$> 4$	Signal-to-noise sufficiently high to keep data rate within electronics bandwidth limits and to ensure efficient trigger.
5	Dark rate per electronics channel	$< 1$ kHz	Dark noise sufficiently low to keep data rate within electronics bandwidth limits and to ensure efficient trigger.
6	Fraction of beam events with saturating channels	$< 20\%$	Sufficient dynamic range is needed to reconstruct the energy calorimetrically, but a small amount of saturation can be mitigated.

Table 6.2: FD2-VD PDS estimated performance and basis for estimates (see text for details).

No.	Description	Estimated Performance	Basis for Estimate
1	Light yield	$\simeq 39$ PE/MeV (avg), $\simeq 16$ PE/MeV (min)	Geant4-only simulations.
2	Time resolution	$\simeq 4$ ns	ProtoDUNE-SP cosmic-ray data.
3	Spatial localization in plane perpendicular to drift	$\simeq 0.75$ m at 400 MeV	Liquid Argon Software (LArSoft) simulations of nucleon decay events.
4	Single PE pulse height divided by baseline noise RMS	6	Cold box tests at CERN and ganging tests in standalone facilities.
5	Dark rate (DCR) per electronics channel	$\simeq 0.2$ kHz	Standalone tests at 77 K for 80 ganged SiPMs (verified for both vendors).
6	Fraction of beam events with saturating channels	2% of beam events with $> 5\%$ saturated channels	LArSoft simulations of beam neutrino interactions.

LY non-uniformity along the drift ( $y$ ) direction.

A dedicated study using a Geant4-only simulation has been performed to determine the LY map of the reference PDS design. Compared to the LY studies that also relied on a -only simulation, several simulation assumptions affecting the detector geometry, the light production in LAr and the reflectivity of detector materials have been updated. The result is a realistic simulation, based on essentially the same optical assumptions included in the end-to-end LArSoft event processing chain discussed in Section 2. The advantage of the standalone Geant4 simulation over the LArSoft simulation framework is a much faster turnaround for LY studies for different PDS layout geometries or optical simulation assumptions.

In the Geant4-only simulation used to estimate the LY, the full FD2 geometry is simulated, including the most relevant detector components from the PDS point of view. In particular, the geometry of the thin ( $\sim 70\%$  transparent) and thick (optically opaque) field cage profiles, as well as the location of all cathode-mount and membrane-mount X-ARAPUCAs, is accounted for. The average light transmission of the conductive mesh that covers the cathode-mounted module windows is taken to be 90%.

For scintillation light production in LAr, we use 12,700 photons/MeV at 175 nm, plus 7,300 photons/MeV at 128 nm, as inferred from ProtoDUNE-DP Xe-doping data (at 10 ppm Xe). For light propagation in LAr, an absorption length of 80 m (20 m) and a Rayleigh scattering length of 8.5 m (1 m) are assumed at 175 nm (128 nm). This absorption length corresponds to a level of  $N_2$  impurities in the LAr of about 3 ppm, see [85]. The reflectivity at 175 nm and 128 nm of the anode PCB, the field cage profiles, and the membrane cryostat wall materials are accounted for in the simulation. Finally, motivated by prototype measurements and simulations [16, 29, 86, 87], the X-ARAPUCA detection efficiency is set to the target value of 3% at both 175 nm and 128 nm. In the light yield plots (Figure 6.4) the detection efficiency is a scale factor, as discussed below.

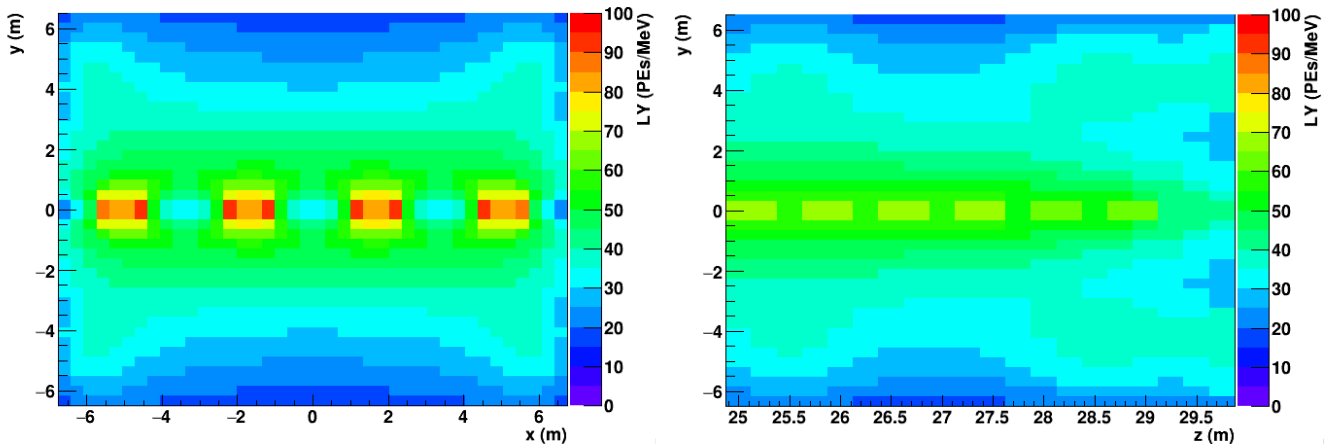


Figure 6.4: (Left) Map of the light yield (LY) in the central  $(x, y)$  transverse plane at  $z = 0$  for the reference configuration. (Right) Map of LY in the central  $(z, y)$  longitudinal plane at  $x = 0$ , close to the detector boundary at  $z = 30$  m in front of one of the membrane short walls, for the same PDS configuration.

The light yield  $LY(x, y)$  for the central transverse plane at  $z = 0$  inside the target volume was

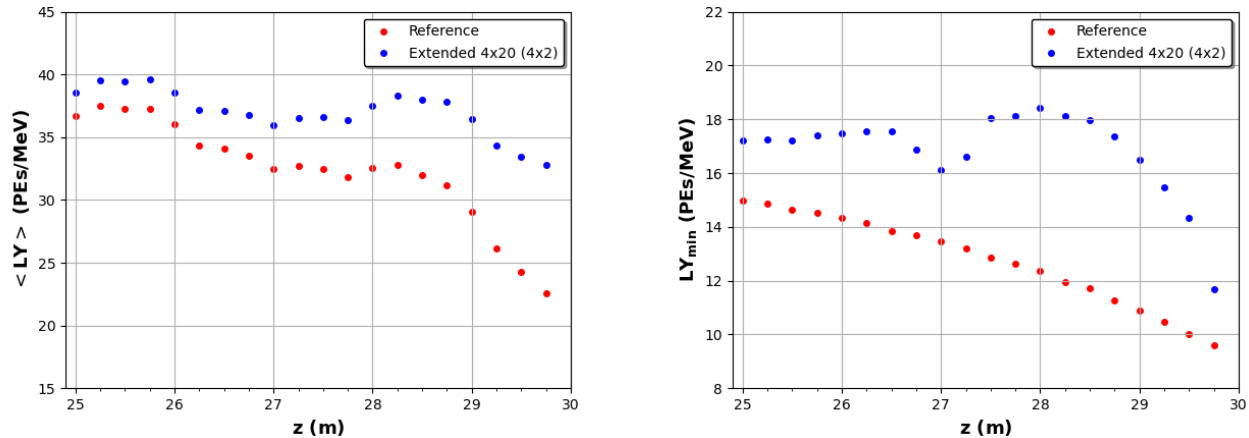


Figure 6.5: Values for average (left) and minimum (right) LY in  $(x, y)$  planes as a function of the  $z$  direction, obtained close to the detector boundary at  $z = 30$  m. Light yield values for two detector configurations are shown: reference configuration including X-ARAPUCAs on the membrane short walls in blue, without short wall X-ARAPUCAs in red.

evaluated and is shown in Figure 6.4 (left).<sup>2</sup> The  $(z, y)$  projection of LY for  $x = 0$  and near the detector end-wall at  $z = 30$  m is shown in Figure 6.4 (right). As is evident in both projections, the LY is highest near the cathode plane at  $y = 0$ , and lowest near the non-instrumented anode planes at  $y = \pm 6.5$  m. The average LY value for events in the  $0 < z < 3$  m detector portion near the central transverse plane at  $z = 0$  is  $\langle \text{LY} \rangle \simeq 39$  PE/MeV, as reported in Table 6.2. Boundary conditions close to either ends of the detector volume at  $z = \pm 30$  m also affect the LY.

As shown by the red data points in Figure 6.5, a clear decrease for both average (left) and minimum (right panel) LY per  $z$  slice would be observed along the  $z$  direction at both detector ends if no X-ARAPUCAs were installed on the membrane short walls. The presence of 32 X-ARAPUCAs in the reference design on the end walls ensures a more uniform LY response along  $z$  near the detector boundaries, as shown by the blue points in Figure 6.5. The goal of this modest (5%) coverage increase, compared to the option with non-instrumented end walls, is to enlarge the FD2 fiducial volume for analyses relying on PDS information.

These values significantly exceed the LY specifications of Table 6.1. They are also much better than the FD1-HD PDS values, particularly with regard to the spatial uniformity of the detector response. While these simulation results assume our target X-ARAPUCA detection efficiency of 3%, light yield estimates for the FD2-VD PDS scale linearly with efficiency. Light yield specifications would thus be met even under the worst-case X-ARAPUCA detection efficiency that would satisfy requirements, that is 2% (see Sec. 6.4). As discussed in Table 6.1 and in Section 2, this high and uniform light yield will ensure a PDS energy resolution comparable to that of the TPC at supernova neutrino burst (SNB) energies, SNB event triggering using PDS information alone, and efficient tagging of nucleon decay backgrounds anywhere in the LAr active volume.

<sup>2</sup>We use the FD2-VD coordinate system:  $z$  is parallel to the Far Detector Module's long dimension, aligned with the incident neutrino beam;  $y$  is the vertical drift direction; and  $x$  is along the module's narrow horizontal dimension. The origin is at the geometric center of the module.

Preliminary time resolution results for an X-ARAPUCA-based PDS have been obtained using the 12 X-ARAPUCA channels in APA6 of ProtoDUNE-SP at CERN. Photons coming from the same cosmic-ray muon track are detected by two separate (nearby) channels. TPC crossing cosmic-ray muon tracks nearly parallel to APA6 are used, such that differences in photon arrival time to the two nearby channels become negligible. To reduce the effect of the 6.67 ns sampling time, the waveforms' rising edges are fitted to extract the time at which the amplitude crosses one photoelectron (PE) for each channel. The difference in time measured by the two channels provides a direct estimate of the single-channel time resolution, measured to be about 4 ns. The time resolution of the optical flashes, being a collection of time-coincident and space-correlated optical hits, is better than 4 ns.<sup>3</sup> Even though this result was obtained with ProtoDUNE-SP data, the similar PDS technology and sampling time ensure that a similar time resolution is expected in FD2-VD, exceeding the time resolution requirement by a large margin.

Initial results on spatial resolution in the FD2-VD and in the plane perpendicular to the drift direction were obtained with a Geant4-only simulation of point-like energy deposits at SNB energies (tens of MeV) and a pseudo-reconstruction relying on the barycenter of the light pattern, see [88]. A spatial resolution in the transverse plane of about 0.5 m was obtained. These results have now been confirmed with full LArSoft simulations of nucleon decay events.

For this study, the simulation and reconstruction of  $10^5$  events has been carried out. The events include GENIE-generated  $p \rightarrow K^+ \bar{\nu}$  decays, one decay per simulated event, uniformly distributed in the LAr volume and depositing about 400 MeV of energy on average. They also model the detector activity due to radiological backgrounds, according to the model in Table 2.3. The radiological model introduces a rate of reconstructed optical flashes of about 200 kHz, or about 800 flashes throughout the 4 ms long event time window. For the position reconstruction study, we define the signal-like flash in each event as the flash of highest charge among those with a timing consistent (within  $\pm 1 \mu\text{s}$ ) with the nucleon decay time.

As in our earlier study, the reconstructed position of the nucleon decay candidate event in the plane perpendicular to drift is reconstructed using a simple barycenter algorithm, using position and detected charge information from PDs located on the cathode. The reconstructed position is then compared to the true position of the MC simulated nucleon decay vertex. A spatial resolution of about 75 cm is obtained. This expected performance is significantly better than the 2.5 m spatial resolution required.

The single-photoelectron pulse height divided by the baseline noise root mean square (RMS) (or signal-to-noise (S/N) ratio, in the following<sup>4</sup>) and the dark rate per electronics channel (rows 4 and 5 in Table 6.1), have been studied with ProtoDUNE-SP PDS data, with CERN cold box data, and with dedicated setups. Since the initial cold box runs in August 2022, light leakage from PoF receivers and fibers have been reduced to negligible levels. The S/N ratio measured in a cold box run in February 2023 for a PD module with PoF and SoF readout was 5.9, as shown in Figure 6.29, significantly higher than the specification of 4.

<sup>3</sup>The current PDS reconstruction assumes a 1.5 PE threshold to reconstruct an optical hit, and a 3.5 PE threshold to construct an optical flash.

<sup>4</sup>The S/N ratios quoted throughout the chapter refer to the smallest possible signal of interest for one PD channel, which is a single-photoelectron pulse. Most physics event categories in DUNE will typically produce much larger signals.

The dark count rate at 77 K of the SiPMs under consideration for FD2-VD (see Section 6.5) has been measured to be about 60 mHz/mm<sup>2</sup>, corresponding to about 0.2 kHz per electronics channel, which is well within requirements.

Table 6.1 specification No. 6, the maximum fraction of beam events with saturating channels that impacts energy resolution, has been demonstrated in full LArSoft simulations of beam electron neutrino interactions and assuming a 14-bit dynamic range, see Section 2. It was found that only a 2% (0.2%) of events have more than 5% (10%) PDS channels overflowing the ADC range. Also, this dynamic range induces a mean reduction in the determination of the total deposited energy per event, estimated from the reconstructed charge sum over all optical hits, of only 2%. In other words, PDS channel saturation level in FD2-VD is expected to be within requirements. It is also lower compared to the saturation studies presented in the FD1-HD [7], which assumed a 12-bit digitizer.

## 6.2.2 PD Consortium Scope

The DUNE PD Consortium (see Section 6.14) will provide a photon detector system for FD2-VD that meets the performance requirements established by the DUNE collaboration as presented in Table 6.1. The scope of the consortium activity includes selecting and procuring material for, and the fabrication, testing, delivery and installation of light collectors (X-ARAPUCA), photosensors (SiPMs), electronics, and a calibration and monitoring system. The reference design components are listed in Table 6.3.

Table 6.3: PDS reference configuration

Component	Description	Quantity
Light collector	X-ARAPUCA	352 single-sided modules (160 per long-dimension wall, 16 per short-dimension wall), 320 double-sided modules (cathode plane); 672 total. Light collection area 3600 cm <sup>2</sup> /module/side
Photosensor	Hamamatsu and FBK 6 mm SiPM×6 mm	160 SiPMs per module; 107 520 total
SiPM signal summing	5 groups (in series) of 4 SiPMs (in parallel) per flex PCB	8 flex PCBs per module; 5376 total
Readout electronics	Analog signal conditioning circuit	2 channels/module; 1344 total
Calibration and monitoring	Pulsed UV via field cage-mounted fibers	15 fibers per roof penetration; 20 penetrations per side; 600 total

Although the configuration of the FD2-VD and FD1-HD led to structurally different solutions for the PDS, many of scientific and technical issues are similar. A common consortium facilitates the sharing of information and helps to exploit the similarity of these two detectors, as appropriate.

## 6.3 Photon Detector System Overview

Scintillation light detection in the FD2-VD module is based on the X-ARAPUCA technology developed for the FD1-HD module, with the photocollector design modified to match the different FD2-VD mechanical and electrical constraints. The PDS consists of a large number of photon detection units distributed on or behind the surfaces delimiting the LArTPC active volume. The basic unit is the X-ARAPUCA detector module with a light collecting area of approximately  $600 \times 600 \text{ mm}^2$ . The modules have light collection windows on either one (single-sided) or two (double-sided) faces, depending on the location in the active volume. The wavelength-shifted photons are converted to an electrical signal by 160 SiPMs distributed evenly around the perimeter of the module. Groups of SiPMs are electrically connected to form just two output signals, each corresponding to the sum of the response of 80 SiPMs.

The FD2-VD PDS topology consists of 320 double-sided X-ARAPUCA modules evenly distributed across the cathode plane (cathode-mount modules) and 352 single-sided modules mounted behind the field cage onto the cryostat walls (membrane-mount modules), as illustrated in Figure 6.2. The 352 membrane-mount modules includes 32 modules on the cryostat end-walls<sup>5</sup>.

The cathode-mount X-ARAPUCAs are embedded in the mechanical frames of the central cathode plane, as illustrated in Figure 6.3. They will have two optical surfaces, one facing upward into the top FD2-VD volume, the other facing downward into the bottom volume. Operating photodetectors on a HV surface requires electrically floating photosensors and readout electronics, i.e., power (in) and signal (out) transmitted via non-conductive cables. This is achieved with the use of PoF technology and optical transceivers for communication via SoF technology.

Membrane-mounted X-ARAPUCAs will be arrayed in columns along all four walls of the cryostat. They will face inward from behind the field cage, spanning the vertical ranges  $3.3 < y < 6.3 \text{ m}$  and  $-6.3 < y < -3.3 \text{ m}$  as measured from the cathode plane, respectively, where the field cage is approximately 70% transparent (Section 5.4.2). They will be supported on hanging vertical mechanical structures, each holding four modules mounted near the top anode plane and four near the bottom. There will be 20 columns on each of the long walls and two columns on each short wall. The column structures are electrically referenced to detector ground and thus do not require PoF and optical transceivers; standard transmission through copper cables will be used for both power and signal, leveraging the FD1-HD experience.

A conceptual diagram of the the SoF and PoF routing for the cathode-mount modules and the copper-based routing for the membrane-mount modules is shown in Figure 6.6.

To optimize the light collection uniformity, the LAr is doped with  $\mathcal{O}(10 \text{ ppm})$  xenon, which like argon, is a high-yield scintillator. Several studies have demonstrated its beneficial light production properties when used as a low concentration dopant [79, 80, 89, 90]. Motivated by these studies done on smaller LAr volumes, DUNE tested xenon doping in the detectors, and concluded that it will provide greater light yield uniformity and allow photon detection recovery from accidental nitrogen contamination for multi-meter drift-path TPCs (see Section 6.8.1).

<sup>5</sup>These were not part of the Conceptual Design Report design, but were added to provide better light-yield uniformity throughout the active volume.

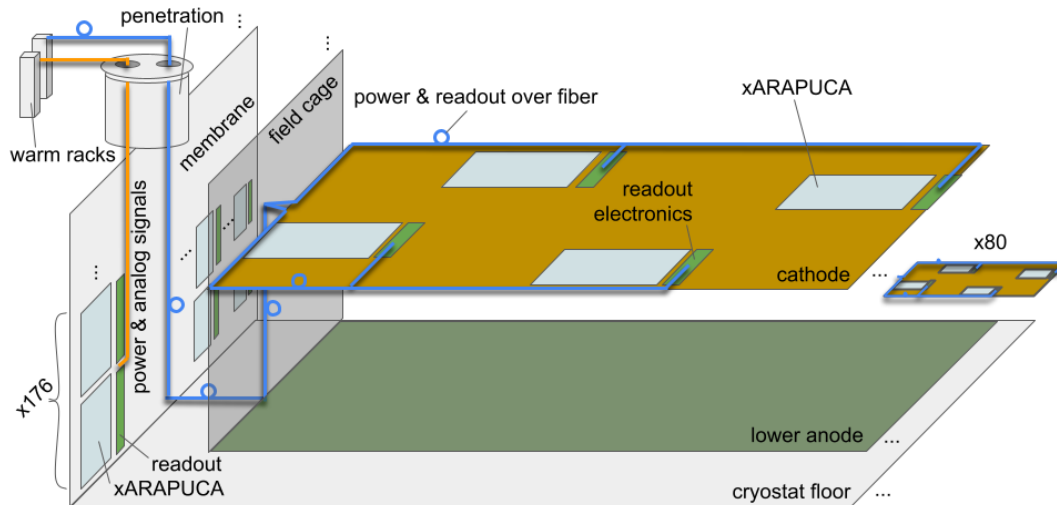


Figure 6.6: Conceptual diagram of power and signal routing. One of the 80 cathode four-module groups (see Figure 6.3) is shown on a greatly expanded scale; fibers pass through holes in the cathode modules, down along the field cage and over to the membrane wall, en route to penetrations on the top surface of the cryostat. More detailed drawings are provided in Section 6.6.2.3.

A concentration of  $\mathcal{O}(10 \text{ ppm})$  is sufficient for the Ar triplet scintillation component to be fully transferred to the xenon emission wavelength (175 nm), which reduces the Rayleigh scattering rate of the wavelength-shifted light and so increases collection efficiency for light emitted at a far distance from the PDs. It also mitigates the risk due to inadvertent nitrogen contamination of the LAr. The time response of the PD modules to scintillation light will be used to monitor the xenon content in LAr. ProtoDUNE-SP data have demonstrated that the shape of the average PD modules' waveforms is very sensitive to the xenon concentration.

The basic properties of the scintillation medium, photon collectors, photon sensors and associated electronics for the FD2-VD PDS are summarized in Table 6.4.

The FD2-VD PDS design of 320 cathode mounted X-ARAPUCAs provides  $105.6 \text{ m}^2$  photodetector coverage out of the  $810 \text{ m}^2$  cathode area, for 13.0% optical coverage. The assemblage of 320 X-ARAPUCAs mounted on the long walls of the cryostat membrane gives  $105.6 \text{ m}^2$  coverage which is about 6.8% of the field cage area. Finally, the optical coverage on the cryostat membrane short walls is  $10.6 \text{ m}^2$  out of  $351 \text{ m}^2$  for 3.0%. Figure 6.7 (left) is a 3D rendering of the FD2-VD showing the top two rows of PDs X-ARAPUCAs (blue) on one long wall and those in the cathode frame. The view is from the opposite cryostat wall, behind the field cage, in the top drift volume.

The field cage electrodes in the foreground are  $\sim 70\%$  transparent to light, allowing transmission to the PD detector modules behind it. This configuration provides the FD2-VD PDS with a photon detection performance that meets the experiment's requirements, as presented in Chapter 2 and Section 6.2.

Table 6.4: Summary of FD2-VD PDS scintillation medium and reference design technology.

Item	Description
Liquid argon Scintillator	Ar+Xe (10 ppm). Residual impurity: $[N_2] < 1$ ppm, $[O_2] < 50$ ppt. Absorption length: $\lambda_{abs} \geq 30$ m. Photon yield (MIP, nominal E field =500 V/cm): 25,000 ph/MeV. (Ar-Xe) Energy transfer reaction: Ar triplet scintillation component fully transferred to Xe $\Rightarrow Y_{ph}(Ar) \simeq 6,000$ ph/MeV, $Y_{ph}(Xe) \simeq 19,000$ ph/MeV. Rayleigh scattering length: $\lambda_R(Ar) \simeq 1$ m, $\lambda_R(Xe) \simeq 8.5$ m.
Photon collector	X-ARAPUCA (light trapping by dichroic filters and two-stage WLS). Sensitive to both Ar light (128 nm) and Xe light (147 and 175 nm). Detection efficiency $\epsilon_D \simeq 3\%$ (detected PEs per photon impinging upon the optical surface of the detector).
Photosensor	SiPM $6 \times 6$ mm <sup>2</sup> area, single-photon sensitive. Requirements at nominal voltage: PDE(450 nm) >35%, dark count rate <200 mHz/mm <sup>2</sup> , cross-talk <35%, afterpulse < 5%, gain $> 2 \times 10^6$ . Cold electronics (CE) read-out (active ganging, shape and noise filtering). $S/N \geq 4$

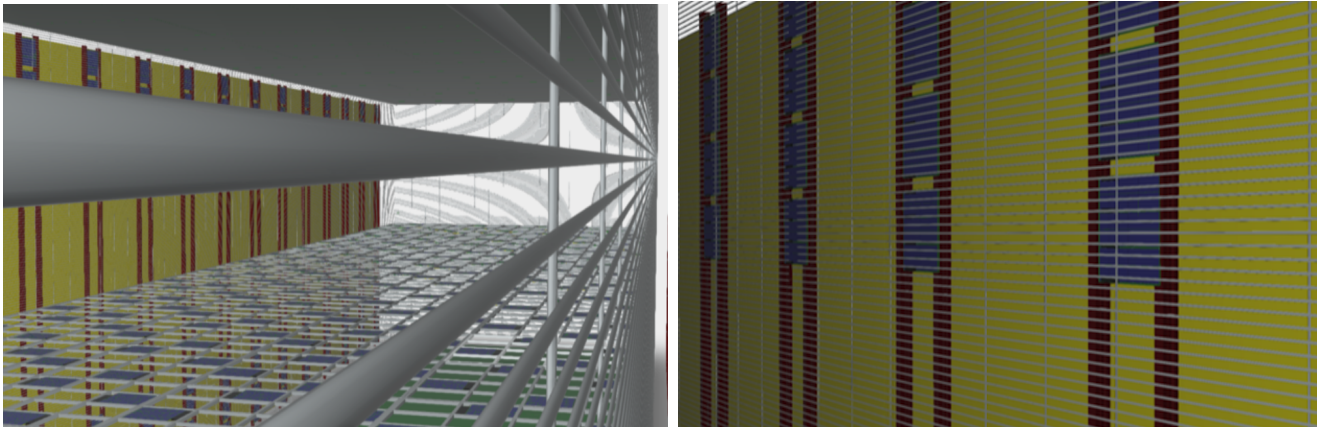


Figure 6.7: X-ARAPUCA detector modules (indigo) on the cathode plane and on the field cage walls – view through  $\sim 70\%$  transparent field cage into detector volume (left); view of the membrane-mount X-ARAPUCA detector modules from inside the active volume (in this close-up view, the field cage bars are visible in front of the modules) (right).



Table 6.5: FD2-VD PDS components.

Item	Quantity	Detector surface
X-ARAPUCA modules	320 double-sided	Cathode plane
	320 single-sided	Membrane long walls
	32 single-sided	Membrane short walls
Dichroic filters	17,856	
WLS plates	672	
Photosensors (SiPMs)	51,200	Cathode plane
	51,200	Membrane long walls
	5,120	Membrane short walls
Signal channels	640	Cathode plane
	640	Membrane long walls
	64	Membrane short walls
SiPMs per channel	80	
Optical Area	$105.6 \text{ m}^2 \times 2$	Cathode plane
	$105.6 \text{ m}^2$	Membrane long walls
	$11.5 \text{ m}^2$	Membrane short walls
Active coverage	13.0%	Cathode plane
	6.8%	Membrane long walls
	3.0%	Membrane short walls

## 6.4 Light Collectors

The X-ARAPUCA developed for the FD1-HD has been adopted for use in FD2-VD. It offers compact and flexible design geometry and has a very small impact on the LArTPC active volume. The X-ARAPUCA module has an excellent ratio of optical to inactive surface areas (68%), a good , a moderate fabrication cost, and is relatively easy to integrate into the TPC layout. Table 6.5 itemizes the components of the PDS.

The basic unit of the PDS is a module as depicted in Figure 6.8 with dimensions provided in Table 6.6.

It is a tile-shaped thin module with overall dimensions  $653 \times 653 \times 29.9 \text{ mm}^3$  plus an attached electronics box  $645 \times 89.6 \times 42.4 \text{ mm}^3$ , bringing the total outside dimensions to  $742.6 \times 653 \times 42.4 \text{ mm}^3$ . PD modules are composed of three basic design elements:

- one (single-sided) or two (double-sided) dichroic window frame assemblies composed of 16 -coated dichroic filters mounted in frames – the dichroic window dimension establishes the active area of the module as  $575 \times 575 \text{ mm}^2$ ,  $0.33 \text{ m}^2$ ;
- one frame and Faraday cage shielding assembly consisting of a WLS-doped acrylic plate onto which the SiPMs are coupled (a three-sided conducting box protects the SiPMs from induced currents due to a potential cathode HV discharge, see Section 6.4.1); and
- one cold electronics/PoF/SoF electronics enclosure, mounted to one side of the basic module following assembly.

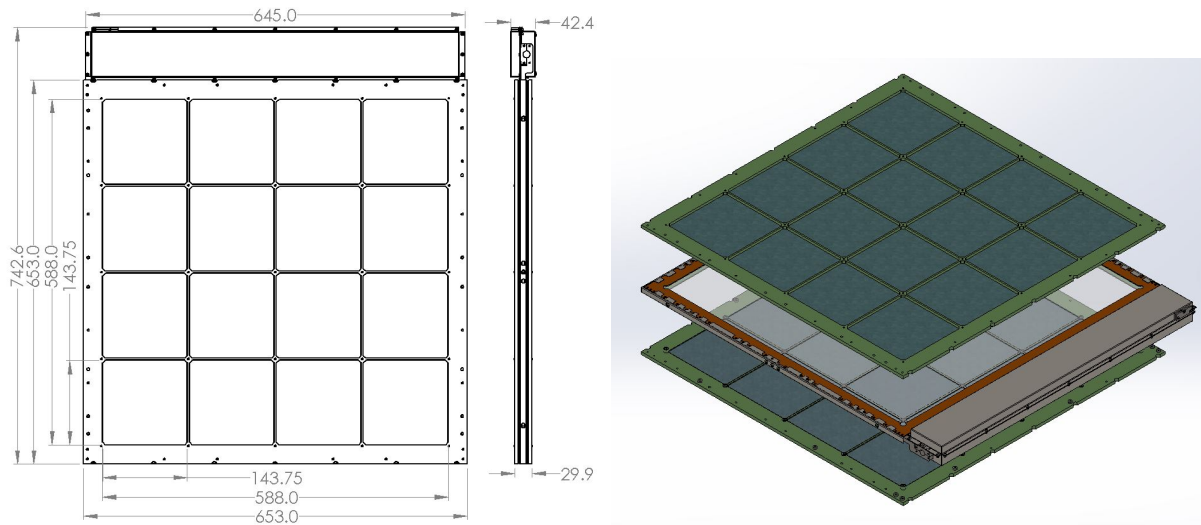


Figure 6.8: (Left) Dimensioned drawing of a FD2-VD PDS detector module. (Right) Exploded view showing major design elements. The double-sided module concept to be used in the cathode is shown (with dichroic filter windows on both sides of the module). For the membrane mount modules, the windows on the side facing the cryostat wall are replaced with a reflector-coated G-10 sheet. [A photograph of a module that will be tested in the cold box at CERN is shown in Figure 6.1.]

Table 6.6: PD basic unit: X-ARAPUCA module.

Item/Parameter	Quantity	Dimensions
Light collection module area (excluding electronics box)	1	$653 \times 653 \text{ mm}^2 = 0.43 \text{ m}^2$
Module thickness	1	29.9 mm
Weight	1	$\sim 8.6 \text{ kg}$
Active Area	2 (two-sided)	$0.33 \text{ m}^2$ per side
Dichroic filters	$16 \times 2$ sides	$143.8 \times 143.8 \text{ mm}^2$
WLS plate	1	$607 \times 607 \times 3.8 \text{ mm}^3$
SiPMs	160	$6 \times 6 \text{ mm}^2$
Read-out channels	2	
SiPMs per channel	80	

The square modular geometry optimizes the ratio of the light collecting area to the SiPM area and the module mechanical design allows use of the same structure for both the cathode-mount and membrane-mount configurations. In the case of the single-sided membrane-mount modules, the rear side (facing the cryostat wall) window frame assembly is removed and replaced by a single sheet of G-10 coated with 3M Vikuiti™ reflective material.

The WLS plate acts as a secondary shifter, serving three main functions: providing the wavelength shift required to trap the photons within the X-ARAPUCA volume, matching the SiPMs wavelength sensitivity, and as a light guide – the optical-grade surfaces enable efficient uniform light collection over a large area. Prototype WLS plate have been manufactured at a casting reactor at UniMIB, while for the large scale production, the Glass to Power s.p.a. company (G2P)<sup>6</sup> G2P has been identified as an industrial partner.

The mechanical properties of acrylic plates have been tested extensively in both the FD1-HD and FD2-VD PDS geometries. ProtoDUNE-SP (the Horizontal Drift ProtoDUNE) included 38 acrylic bars (externally coated with TPB) and showed no indication of surface cracking after more than a year of continuous immersion in LAr. Each of the 20 Glass to Power bars installed in were been submerged in LAr and inspected following testing, with no signs of surface degradation. Finally, full-size FD2-VD WLS plates have been tested through multiple cooling cycles (up to 4 cycles for the V1 module) with no observed degradation. will provide the final long-scale validation of these full-size bars.

A spring-loaded SiPM mounting system (see Figure 6.9) makes a dynamic connection between the WLS plate and the G-10 frame to allow for relative thermal contraction of the WLS plate and frame.

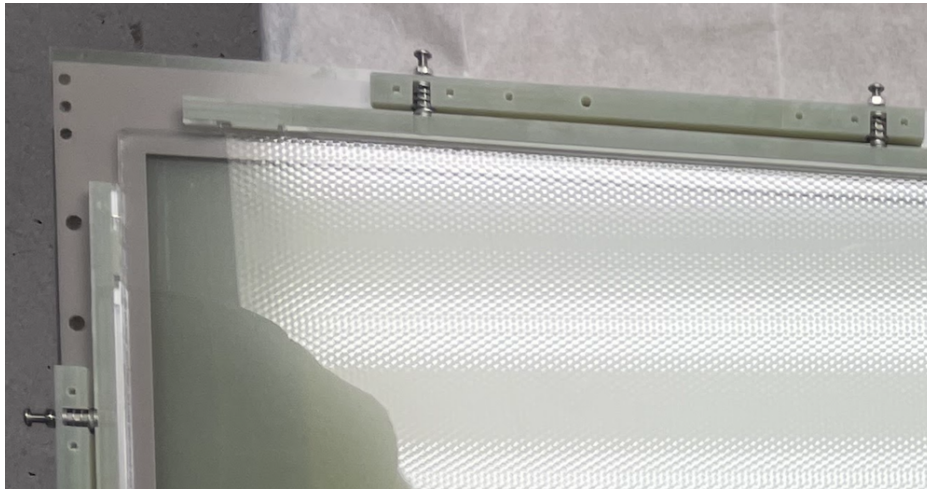


Figure 6.9: WLS plate centered in G-10 frame, held by spring-loaded dynamic mounting system. Coil springs (16 total, three visible in this image) maintain physical contact between the WLS plate and the SiPM face throughout cool-down. Screws (seen in this figure) passing through the springs are used to allow controlled application of force while the SiPMs are installed, then removed following installation.

The SiPMs have dimensions  $6\times 6\text{ mm}^2$  and are mounted in a series of five adjacent units of four SiPMs, each passively ganged on one flexible Kapton PCB strip (i.e., one 30 cm flex circuit has

<sup>6</sup>Glass-to-Power - Italy <https://www.glasstopower.com>.

20 SiPMs; see Figure 6.10, left). The SiPMs are positioned symmetrically with respect to the mid-plane of the plate<sup>7</sup>.

Each flex circuit mates through a connector to a shielded twisted-pair cable 130 cm long that passively routes the flex circuit signal to the module interface board where a stage of signal shaping and buffering prepares the signal for readout. There are eight such flex circuits along the perimeter of the WLS plate, for a total of 160 SiPMs. The SiPMs are grouped into two readout channels of 80 SiPMs each; two channels offer a level of redundancy for the module.

The strips of SiPMs are held against the WLS plate edges by an array of low-strength coil springs. The use of a spring-loaded backing plate and flexible PCBs for mounting (Figure 6.10) the SiPMs combined with dynamic supports for the WLS plate inside the G-10 provides accommodation for the roughly 1% relative thermal contraction between the WLS plate and the G-10 frame during cool-down. A Vikuiti reflector adhered to the Kapton flexi PCB covers the plate edge between adjacent SiPMs.

A possible enhancement of the reference PD module design to enhance the efficiency of photon extraction from the WLS plates onto the SiPMs would be to include cutouts in the WLS plates at the location of the SiPMs. The performance and cost-effectiveness of three different cutout shapes and associated production costs are being evaluated as part of the final module evaluation, with a final decision as to their inclusion decided prior to the production readiness review (PRR).



Figure 6.10: 20 SiPMs mounted to flexible PCB (left). Flexible PCB positioned against a dummy WLS plate (white block) with spring-loaded dynamic mount (right).

The required PDE for the PD modules is 2% with a target value of 3%, similar to the best achieved by the FD1-HD X-ARAPUCA [16, 29, 86, 87]. Measurements of PDE have not yet been made on full-sized FD2-VD PD modules but the fundamental design of the X-ARAPUCA is the same as for FD1-HD, so we expect similar performance. Nonetheless, there are differences that directly affect the PDE, most significantly the ratio of photosensors per light collection area is reduced by a factor of 2.4 compared to FD1-HD. Simulations indicate that this factor is compensated for by the more efficient WLS plates, spring-loading of the SiPM to WLS plate mounting to ensure mechanical

<sup>7</sup>Simulation of two additional SiPM geometries with the same active area ( $4 \times 9 \text{ mm}^2$  and  $3 \times 12 \text{ mm}^2$ ) in the FD1-HD PD module bar configuration showed no substantial difference in the detection efficiency that would justify a custom geometry for the SiPM.

contact, and reflective X-ARAPUCA frames. An additional enhancement may come from inclusion of light-concentrating cutouts in the edge of the WLS plates that simulations indicate increases the photon collection efficiency - validation studies will be completed prior to design baselining in summer 2023.

### 6.4.1 Cathode Modules HV Discharge Protection

Having the cathode modules mounted in the cathode plane exposes them to a risk of damage from a discharge event of the -300 kV HV system.

Two independent studies, one at Brookhaven National Laboratory (BNL) and one at Fermi National Accelerator Laboratory (Fermilab), agreed that the original design presents an unacceptable risk of damage to the X-ARAPUCA modules' electronics from a discharge, especially for the configuration in which multiple modules share power and signal, but that an open faced conductive enclosure around the SiPM flexible PCBs and readout cables, together with a complete enclosure of the cold readout electronics, provides sufficient risk mitigation.

As a result of these studies, the X-ARAPUCA module design has been modified to include a three-sided Faraday cage composed primarily of copper-clad surrounding the SiPMs, flexible readout boards, and readout cables for all PD modules. Additionally, the readout electronics, and PoF in the case of the cathode mount modules, are enclosed in the Faraday cage. Details of this cage can be seen in Figure 6.11. The opening in the Faraday cage is  $593.4 \times 593.4 \text{ mm}^2$ , matching the coverage of the dichroic filter windows.

This design will be tested and improved in test benches that will emulate the cathode discharge, with progressively increasing charge injection amounts to identify weaknesses. In FD2-VD Module 0 we will test the design on both shared/distributed power and signal system and independently powered X-ARAPUCAs. At the end of the FD2-VD Module 0 run, discharges will be induced from maximum cathode HV.

The final design will be validated in a cold box run in advance of the Production Readiness Review."

### 6.4.2 Membrane Modules Suspension System

The membrane-mount portion of the PDS is composed of 20 columns of 8 PD modules on each of the two long walls of the cryostat, plus 2 columns of 8 PD modules on each of the two short walls, for a total of 352 modules. Each PD column is supported by two suspension lines. The suspension lines are made of three connected stainless steel pieces: a top rod bar (5 mm diameter, 3.7 m length) fixed on the cryostat roof, a central tube (12 mm diameter, 6 m length) in the central part of the detector, and a bottom rod bar (5 mm diameter, 3.7 m length) fixed on the cryostat floor. The top and bottom rod bars have eye bolts to be fixed on the M10 membrane bolts welded on the cryostat. The central tube has a larger (12 mm) diameter in order to avoid inducing large field gradients in the high voltage region near the cathode plane. The central tube is fixed between the two rod bars by shackles. There is a jaw to jaw straining screw and spring on the bottom rod bar, in order to compensate for differences between nominal and real line dimensions (75 mm adjustment range), to pre-load the spring, and to absorb the thermal expansion.

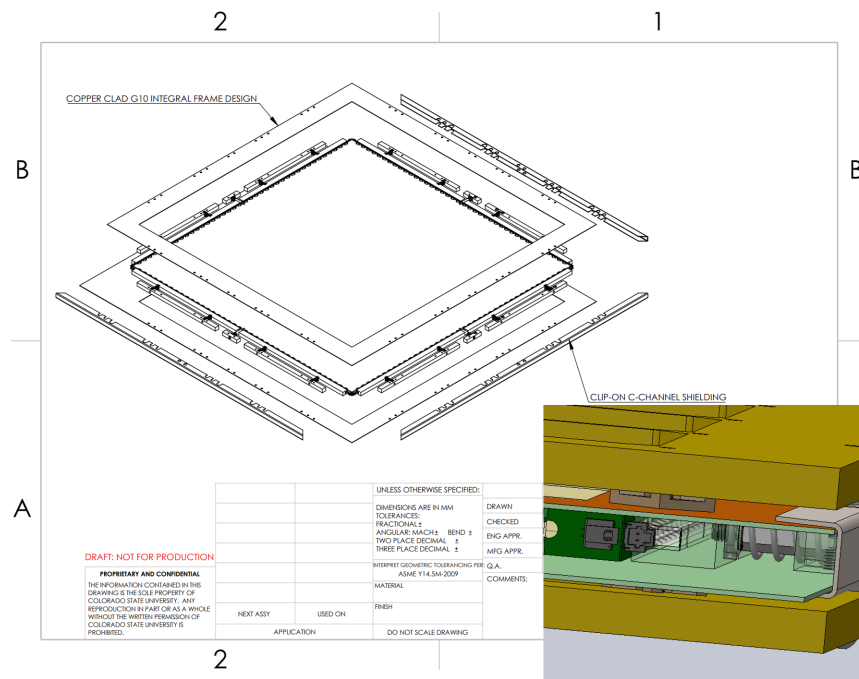


Figure 6.11: Copper-clad G-10 frames and formed stainless-steel external covers provide a 3-sided discharge shield for SiPMs.

Each PD module has four attachment points, two on each suspension line, as shown in Figure 6.12 (left). The fixation points are made of wire rope grips pre-positioned along the 5 mm rod bars. Figure 6.12 (right) shows a zoomed image of one fixation point. Signal cables are routed along the rod bars toward the cryostat roof and floor, and then exit on the cables tray. The estimated weight of each PD module column, including 8 X-ARAPUCA modules, electronics, cables, fixation elements, and rod bars/tube lines, is about 110 kg. Several prototype suspension lines have been produced.

## 6.5 PDS Module Signal

### 6.5.1 Silicon Photosensors

The photosensors of choice for the FD2-VD are SiPMs. This choice is driven by the use of the X-ARAPUCA as the underlying technology for photon collection and the experience leveraged from the FD1-HD module development. The sensors developed in collaboration with the two main vendors of cryogenic SiPMs (Fondazione Bruno Kessler (FBK) and Hamamatsu Photonics (HPK)) fulfill the sensor specifications listed in Tables 6.1 and 6.4. Several candidate devices from these vendors have undergone extensive evaluation by the DUNE team over several years. The typical breakdown voltage for Si-photosensors at cold temperature is in the few tens of volts ( $\sim 42$  V for Hamamatsu and  $\sim 27$  V for FBK SiPM). They will be operated at +3 to +5 V overvoltage, with a typical PDE at room temperature of 45% at 430 nm.

The SiPM development needed for the FD2-VD PDS was modest. Thanks to the experience gained in the construction of FD1-HD Module 0, we know that the failure rate is well below 0.5% and the dark count rate is marginal compared with the expected contribution from  $^{39}\text{Ar}$  and other

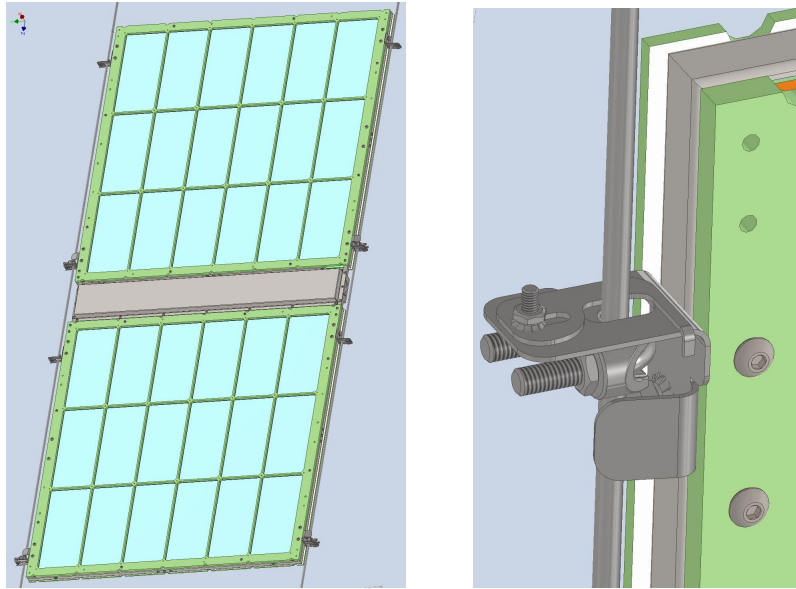


Figure 6.12: Fixation system for membrane-mount PD modules. (Left) Each X-ARAPUCA module is supported using four fixation points on two vertical suspension lines. (Right) Detail of one fixation point.

radiological backgrounds<sup>8</sup>.

For optical coupling of the SiPMs to the WLS plate, both gluing and non-adhesive positioning were investigated. The results indicate that a spring loading system (see Section 6.4) provides an optimal solution. This solution was successfully validated in laboratory test-stands and during the cold box tests. The associated risks related to the thermal stress are mitigated by the flexible boards that host the SiPMs.

The baseline SiPMs choice is to use the S13360-5075HD-HQR (HPK) for the membrane modules and the NUV-HD-CRYO triple-trench (FBK) for the cathode modules. This solution benefits from the lower operating voltage of the FBK sensors to be biased by the PoF. Both types of sensors have been tested with the PoF system and achieved the expected performance.

As a consequence, the choice of SiPM models is mostly driven by cost-effectiveness and the performance of the cold electronics described in Section 6.6. The SiPMs do not represent a significant risk source for the design of the FD2-VD module.

### 6.5.2 Signal Ganging

The PD module SiPMs are mechanically pressed against a WLS plate and electrically connected to a flexible Kapton(R) PCB where 20 SiPMs are passively ganged to sum their electrical response. Summed signals from four flex PCBs are fed into the amplifier stage (active ganging, biased at +5 V), so a single electronic channel provides a readout of the combined response of 80 ganged

<sup>8</sup>Our background simulation (where <sup>39</sup>Ar is the dominant contribution) yields a flash rate of about 200 kHz for a flash reconstruction threshold of 3.5 photoelectrons. This is much larger than the flash rate induced by SiPM dark counts alone, and for the same 3.5 PE threshold.

SiPMs; there are two such channels per X-ARAPUCA. Both passive and active ganging stages are cold. This double-stage ganging solution, adopted for both cathode-mount and membrane-mount modules, represents an extension of the scheme adopted for the FD1-HD PD electronics where eight boards of six SiPMs are summed in a single-stage cold amplifier. Commercial components are used for the ganging signal conditioning circuit.

A flexible PCB is host to the passive ganging of 20 SiPMs of the FD2-VD PDS. Five groups of four SiPMs connected in parallel are connected in series, as shown in the equivalent circuit of Figure 6.13. advantage of allowing all the SiPMs to be biased at the same voltage while keeping the overall capacitance of the system low, thus ensuring a short This circuit has the advantages of ensuring the same potential on the surface of the SiPMs, and a small capacitance, hence a lower noise and generally faster response time. The ganged signal is read in differential mode in order to increase the S/N ratio.

Figure 6.14 shows four flexible PCBs ganged to make a single PDS channel (there are two such channels per module) that have been used successfully in the CERN cold box.

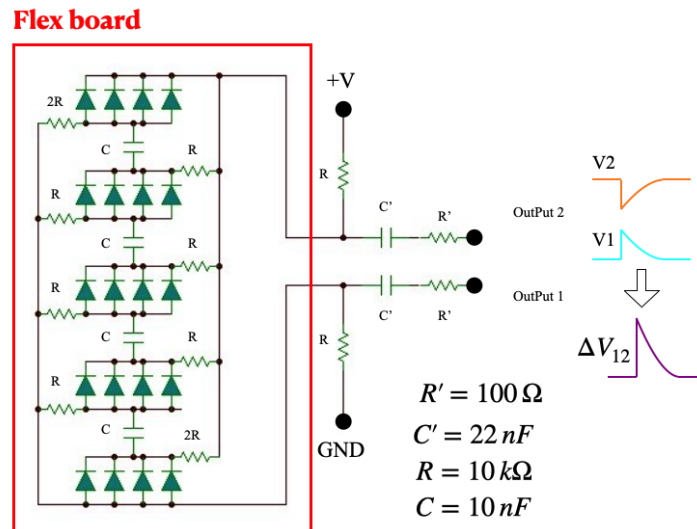


Figure 6.13: Equivalent circuit for the passive ganging of 20 SiPMs of the FD2-VD PDS.

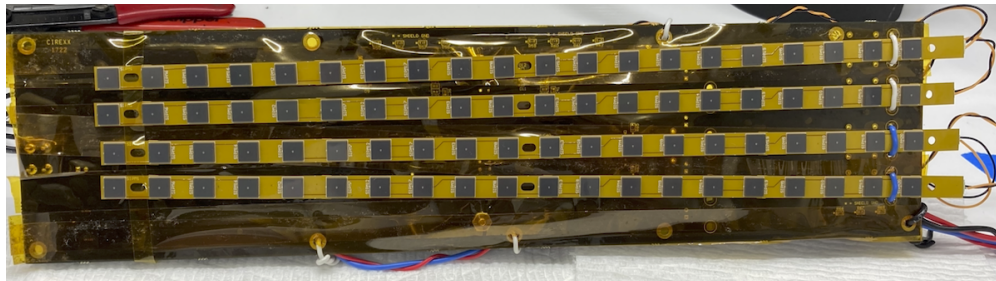


Figure 6.14: Four flexible boards with the 80 ganged SiPMs of a single FD2-VD PDS channel. The X-ARAPUCA light collector to which the four flexible boards are coupled is not shown in this figure.



## 6.6 Sensor Biasing and Signal Readout

### 6.6.1 Membrane Mount Modules

The FD2-VD design calls for 56,320 SiPMs and 704 signal transmission electronics channels (two signals per light collector module) to read out membrane mount modules.

The membrane-mount X-ARAPUCAs and associated readout electronics are at ground, so the readout solution developed for FD1-HD PDS, with power and signal transmitted over conductive cable, is a viable solution with minor changes and is adopted as the reference design. In parallel, a study is in progress to determine whether a more effective solution is to adapt the board containing the signal summing and amplifier stage developed for the cathode modules for use with the membrane system; power and signal would be over copper for the membrane modules. This would have the benefit of maximizing the similarity for the first stage signal processing of the subsystems.

The warm electronics ( digitizer), and associated interface to data acquisition (DAQ), are adopted from the existing FD1-HD PDS solution [7].

### 6.6.2 Cathode Mount Modules

The cathode-mount modules will float at the cathode HV, requiring power and signal transmission via non-conductive cables. Liquid immersion, low temperatures, long maintenance-free lifetime, and HV isolation requirements combine for a particular challenge for the electronics.

#### 6.6.2.1 Power-over-Fiber for Active Devices on the Cathode

Power-over-fiber (PoF) is a power delivery technology that delivers electrical power by sending laser light through robust, lightweight, non-conductive optical fibers to a remote photovoltaic receiver or photovoltaic power converter ( ) to power remote sensors or electrical devices. This innovative technology provides three major benefits: (1) noise immunity, (2) voltage isolation, and (3) spark-free operation.

The current FD2-VD design consists of discrete PoF units that include a laser transmitter module on the warm side, a fiber link, and a PoF receiver on the LAr side. Figure 6.15 shows the basic block layout of a single PoF system. The laser transmitter is made of photonic power modules (PPMs), which are laser modules with fiber pigtailed. The fibers are passed through a bearing sensor wire compression seal ( ) rubber cork feedthrough. The PoF receivers, called PPCs or optical photovoltaic converters (OPCs), deliver power to readout electronics and bias generation circuits.

The first silicon-based transmitter control unit (PPM module) consisted of a switching power supply, laser interlocks, controls and five Class 4, 971 nm wavelength, laser transmitters that each had fused fibers. This compact power housing unit is shown in Figure 6.16 and has been fully tested. A final, improved, design of the transmitter module that includes both local system communication capability and remote control is underway. An improved system will be deployed that includes eight, 2 W power capable and 808 nm wavelength, gallium arsenide (GaAs) lasers per control unit; the operational laser power target is 0.4 W. The control unit will have the same

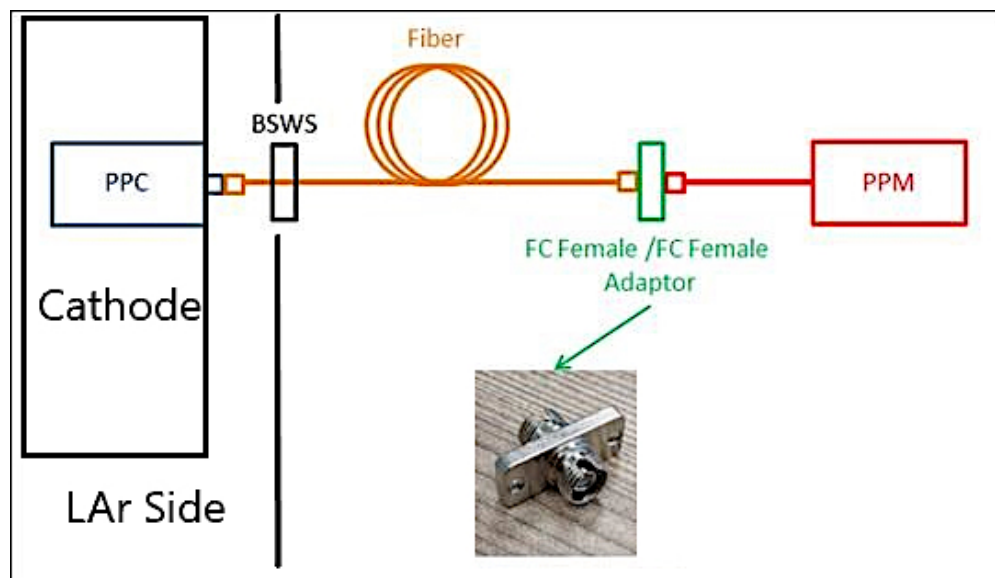


Figure 6.15: A block diagram of a single power-over-fiber (PoF) system with the vacuum feedthrough (BSWS) separating the LAr and warm sides.

basic design, but the laser's compact footprint allows up to eight lasers per box.

The BSWS feedthrough leak rate with optical readout and PoF fibers has been tested at Fermilab in a stand-alone test bed with silicone potting by pumping against a small sealed volume to  $10^{-6}$  Torr and conducting leak tests with a leak checker. The results were satisfactory ( $e-10$  atm-cc/sec). The BSWS flange prototype with silicone potting has also been successfully tested in the NP02 cold box test bed, demonstrating the ability to reach the required LAr purity. The full-scale FD2-VD PDS flange with epoxy potting will be tested in FD2-VD Module 0 allowing for final design validation well ahead of DUNE FD2-VD installation.

The readout electronics system voltage is 6 V and 450 mW power. To deliver the low voltage for the readout electronics, GaAs PPC receiver units [91] are deployed in parallel to provide sufficient current supply and redundancy. The voltage and power needs of the readout electronics must be closely monitored during cold box and FD2-VD Module 0 operation, as changes in power delivery requirements could imply changes to the PoF full system topology and a possible re-optimization for performance and cost. Compared to the silicon option, the GaAs PPC systems have higher efficiency at LAr temperatures at a similar, if not lower, cost. In LAr, the commercial silicon options deliver 200 mW at 12 V, while the commercial GaAs options deliver 200 mW at 6.5 V or 400 mW at 6.5 V. Specifications of the single PPC modules that have been considered are summarized in Table 6.7. Because of its higher efficiency, the GaAs technology is our chosen option for FD2-VD PoF.

All PPC systems can be assembled in parallel or series sets, like batteries, in combination with Zener diodes, to achieve the required voltage and current. Figure 6.17 shows the basic block layouts of arranging PoF power systems. The PDS cathode-mounted module readout electronics motherboard, DUNE Cold Electronics Motherboard (DCEM), as shown in Figure 6.18, has been designed to accommodate the PPC units on G10 standoffs, with a heat sink with through-hole vias to provide power connection to the signal conditioning and bias generation circuitry. Up to

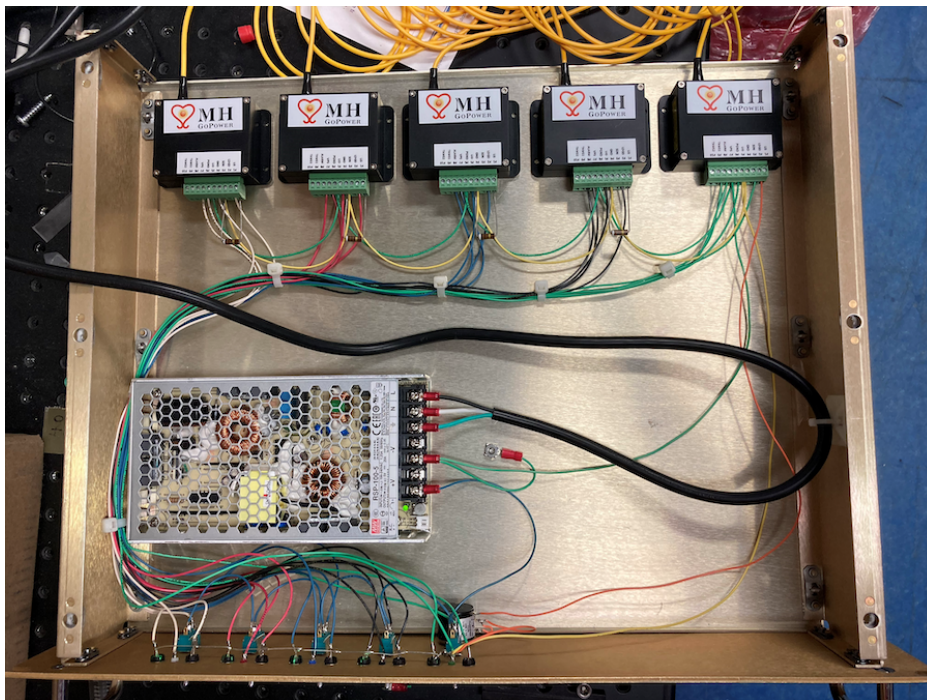


Figure 6.16: Photograph of the fully tested PoF transmitter module showing five 971 nm lasers.

Table 6.7: Power estimates for PoF cathode SiPM systems. Numbers refer to individual PPC modules.

Del. Power (W)*	Type	Wavelength (nm)	Current (mA)	Voltage (V)**	Usable Power (W)	Eff. (%)
0.6	GaAs warm	808	70	5.5	0.40	65
0.4	GaAs cold	808	30	6.5	0.20	50
0.8	Si warm	971	70	5.5	0.40	50
1	Si cold	971	16	12.0	0.20	20

\* The power delivered is not all converted to usable power; e.g. for Si cold, the efficiency is about 20% in LAr.

\*\* Each PPC module voltage can vary about 3%.

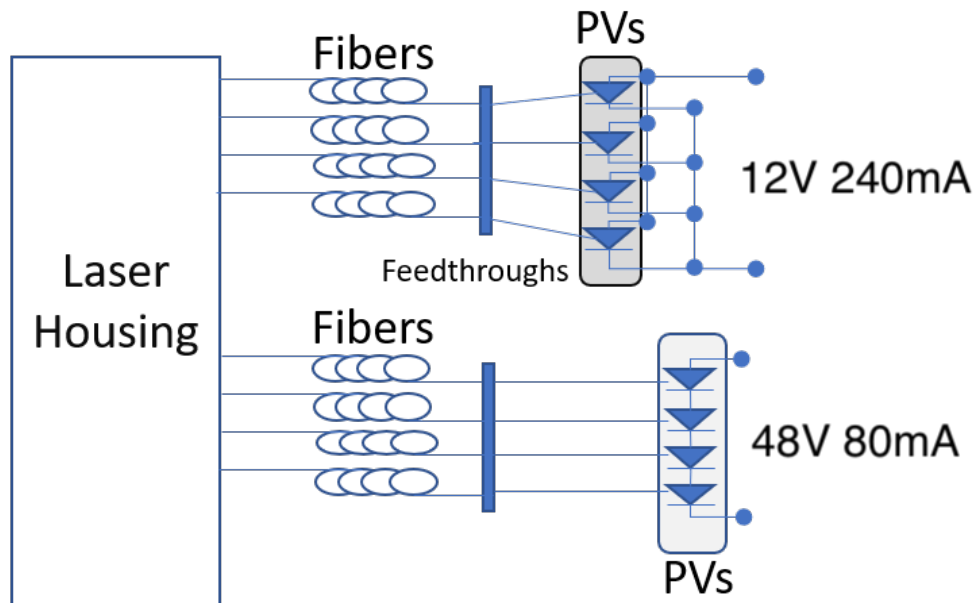


Figure 6.17: PoF receiver options. The photovoltaic (PV) components are housed in a small metal field cage-style unit called a PPC or OPC (optical photovoltaic converter). The series and parallel connections shown are for illustrative purposes only, assuming each unit is 12V/80 mA. The actual number of photovoltaic components used will depend upon the semiconductor choice. For example, GaAs PPCs have lower voltage but higher current compared to silicon-based ones.

four PPCs can be established in parallel on the motherboard PCB. The parallel mounting of three GaAs PPCs on the readout electronics motherboard is shown in Figure 6.18.

While sensor biasing and signal readout electronics will operate in cold, validation in warm conditions after installation is a requirement of the system, see Section 6.12.4. The SiPM bias is established with a DC-to-DC step-up converter to generate a bias voltage derived from the low voltage delivered by the redundant, parallel GaAs PPC units. The step-up converter is designed as a daughtercard to the readout electronics motherboard. The step-up converter can be tuned separately to the desired bias voltage for the SiPMs which is 20 V to 50 V in LAr depending on the SiPM type, see Section 6.5.1. A critical constraint for SiPM bias comes from the risk of high voltage discharge by the cathode; that is, the collapsing of the -300 kV on the cathode, which could occur due to arcing at the HV feedthrough. If not for this risk, SiPMs bias voltage could be shared among multiple X-ARAPUCAs, thus reducing the cost and complexity of the FD2-VD power distribution.

However, as discussed in Section 6.4.1, a conductive distributed power system elevates the risk of damage to the readout electronics to unacceptable levels. Although a well-designed electrical shielding should provide sufficient protection, the safest option is to power each X-ARAPUCA independently in addition to shielding. To optimize costs, generating the bias through the use of PPC units in series was abandoned in favor of local bias generation using DC-to-DC step-up conversion.

A concern for the use of PoF in the vicinity of very sensitive photodetectors is related to photons

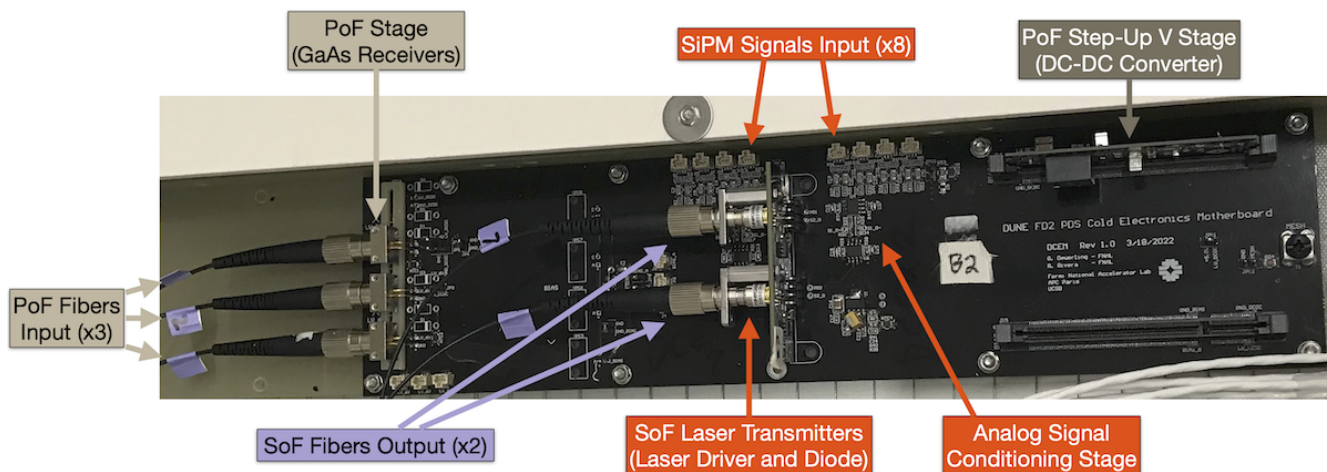


Figure 6.18: DUNE Cold Electronics Motherboard (DCEM) for the FD2-VD PDS. The labels indicate the main components. The board has been used in cold box tests at CERN.

leaking from the high intensity system. The selected black-jacketed fibers<sup>9</sup> were found to reduce the leakage of IR photons to undetectable levels using high-sensitivity thermal cameras. The PoF fibers are also routed through dedicated black polytetrafluoroethylene (PTFE) tubing (sloped and periodically slit to allow trapped gas to escape) and silicon potting may be employed at the terminations, providing further optical isolation.

Tests at the CERN cold box have shown that black-jacketed fibers and potted terminations are successful at preventing light leakage. FD2-VD Module 0 operation will confirm that the power delivery does not introduce an unacceptable background. More than one type of conduit, tubing, or braided sleeving will be deployed at FD2-VD Module 0 to compare background measurements for different solutions.

### 6.6.2.2 Signal Transmission

Analog optical transmission of the signal has been selected as the reference design based on numerous factors<sup>10</sup>. A similar parallel development by the DarkSide experiment showing promising results served as proof that analog transmission in LAr is possible, and therefore achievable within the constrained timescale of the development. The simplicity of design reduces risk associated with long-term cold qualification and affords a straightforward approach to PD module redundancy by increasing the number of analog transmitter channels per PD module.

As shown in Figure 6.19, the analog signals on the cathode are transferred, via a cold optical transceiver, over optical fiber to the external DAPHNE warm electronics for digitization and recording (the same system as the membrane modules). The FD2-VD topology calls for 51,200 SiPMs and 640 signal transmission electronics (two signals per light collector module) on the cathode.

<sup>9</sup>MH GoPower 62.5  $\mu\text{m}$  core diameter, 1.5mm OD, 40 m length, black PTFE coating.

<sup>10</sup>A digital optical transmission was investigated but could not be validated on the appropriate timescale.

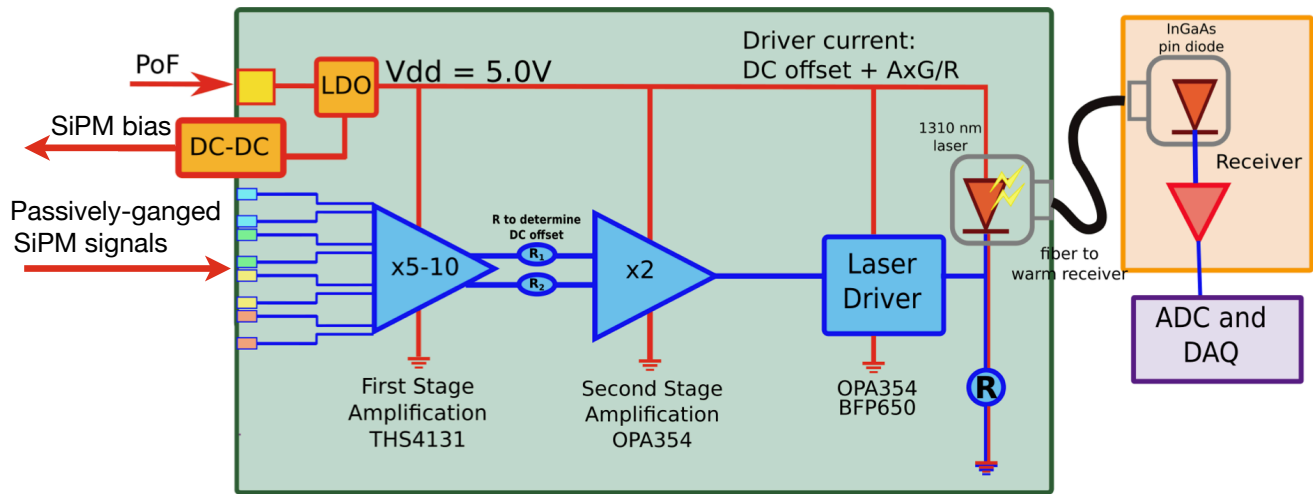


Figure 6.19: Readout electronics for cathode-mount PD modules - optical transmission of the analog signals to digitizers outside the LAr cryostat. The green box represents the cold readout components for one analog readout channel. The differential input on the left of the figure corresponds to 80 ganged SiPMs, hence two analog optical transmitters and two receivers per PD module are required.

Commercial transceivers are operated and certified only for temperatures greater than 233 K. Converting electrical signals to optical signals at LAr temperatures is thus recognized as a critical aspect of the readout of the PDS. Analog optical transceivers have been developed to operate at such temperatures previously [92]. In particular, the DarkSide Collaboration has developed a prototype transmitter for their experiment that shows satisfactory results [93].

An analog optical transceiver has been developed for FD2-VD. These transceivers are based upon commercially available discrete analog components, and the light source can be either a LED or a laser. A laser is used in the FD2-VD PDS, owing to its higher optical output efficiency in cold. Compared to DarkSide, the FD2-VD optical driver has no major radiopurity constraints but must serve a detector with a larger dynamic range. The design aims to reduce risks by implementing a minimum topology of discrete components that are known to have adequate behavior in cold, while attempting to match as well as possible the dynamic range of the signals coming from the X-ARAPUCA and minimizing power consumption.

The signals of each analog channel (80 SiPMs) are first amplified (signal shaping stage), then converted to a current signal (laser driver). Both stages are based on high-bandwidth operational amplifiers. The bandwidth of the transmitter circuit is one of the key aspects for properly transmitting the ganged signal of the SiPMs. With a rise time of around 50 ns, a bandwidth of at least 20 MHz is desirable in order to transmit the signal without significant deformations. In addition, the expected signal level for the single photoelectron is about 30-50  $\mu\text{V}$  and hence requires amplification on the transmitter board. An appropriate balance between gain and bandwidth must be reached, given that a configuration with larger gain reduces the bandwidth capabilities of the circuit components.

Although it has been found that operation in cold reduces the performance of the driver with

respect to operation at room temperature, an adequate bandwidth of 50 MHz in cold has already been achieved. The circuit drives current through an edge-emitting laser diode coupled to an optical fiber. Edge-emitting lasers show satisfactory behavior, with a threshold lasing current reduced to only a few milliamps in cold and with good linearity.

The linearity of the electrical-to-optical conversion and transmission for the analog signals in the dynamic range of expected signals is a crucial feature of the SoF system, and has been tested in detail with satisfactory results. Commercially available Fabry-Pérot laser diodes have been shown to work well as an optical signal source at cryogenic temperatures, with a lower threshold current in cold

laser  
current  
of I

### 500 $\mu$ W Defocused FC Receptacle with 40 m 62.5 $\mu$ m MMF Deep LAr (>20 inches)

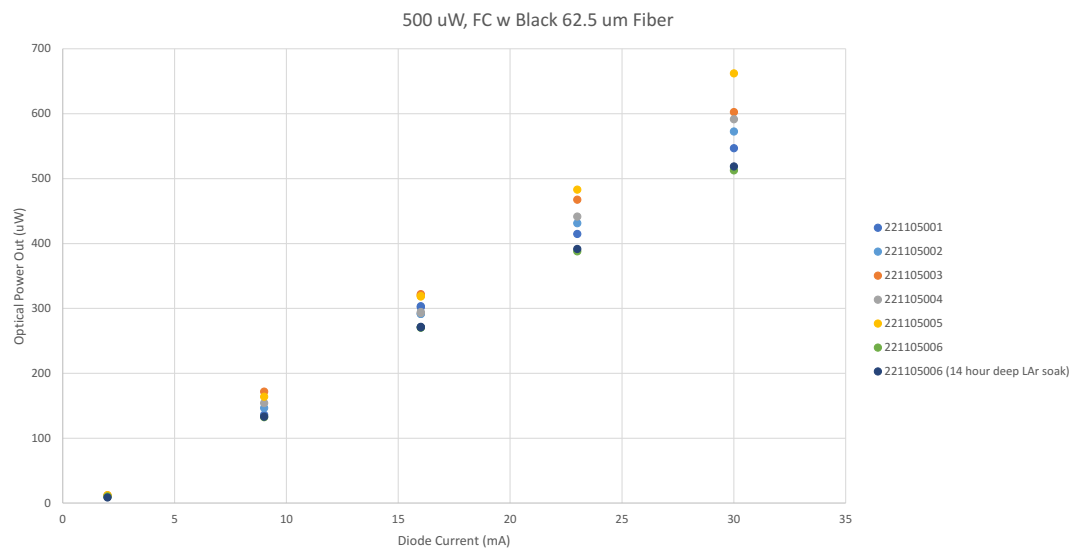


Figure 6.20: Linearity of response for a sample of six Lasermate Fabry-Pérot laser diodes from acceptance tests in deep LAr at Fermilab Proton Assembly Building (PAB). The optical power transmitted through the fiber is shown as a function of excitation input current (2.1 mA threshold). This test is for 500  $\mu$ W devices over 40 m of 62.5  $\mu$ m diameter multimode fibers, and read out via an optical power meter.

An annotated photograph of the DCEM is shown in Figure 6.18. One such board per X-ARAPUCA will be used. As shown by the labels in the figure, this single integrated board operating at LAr temperatures includes circuitry for PoF, analog signal amplification and conditioning, delivery of SoF and SiPM bias.

Power dissipation from the DCEM is within the specification from the HV group that limits the heat load to less than 1 W/cm<sup>2</sup> in order to avoid bubbles. We estimate a power dissipation of 400 mW across the two, 50% efficient, PPC modules needed per X-ARAPUCA PoF. The local heat load from the PPC modules does not exceed 200 mW/cm<sup>2</sup> at any location, and is hence within specifications. The DCEM board itself uses an additional 400 mW of power, yielding a maximum local heat load of 130 mW/cm<sup>2</sup>, also within specifications. Total power consumption across the entire cathode mount X-ARAPUCA system is about 300 W.

At the other end of the signal fibers and outside the cryostat, the analog optical receivers will operate at room temperature. The photodiodes to be used are , since they have the optimal sensitivity to the 1310 nm light being used in the transmitter on the DCEM. The radius of the photosensor should be well adapted to the fiber core diameter; currently 300  $\mu\text{m}$  is planned, since it would be appropriate for any of the fiber core diameters used, and it is a commercially available standard size. These devices have a responsivity<sup>11</sup> power-to-current conversion that depends on the incident light wavelength; for 1310 nm light this is close to 0.8 A/W.

The photodiode is followed by a fast, low-noise amplification circuit. A carefully selected high-gain transimpedance operational amplifier is the basis of this stage. The gain should be such that the smallest signals expected from the transmitter, the single photoelectrons (SPE), are correctly digitized by the ADC that follows. This is a 14-bit ADC currently used in the DAPHNE digital electronics board, with a 1 V maximum input. The goal is to adapt the gain of the entire transmitted/receiver path to achieve both a good S/N in SPE signals and the readout of large signals. The analog signal targets a 1-to-2000 photoelectron dynamic range, the upper bound being dictated by the range of signals expected in beam-induced neutrino events.

Simulations have been performed to determine the occurrence of ADC saturation events for such a dynamic range. ADC saturation within specifications was achieved, see Section 6.2. Knowing the DC level of the transmitter signal is important, since it allows for checking that the transmitter circuit is working and functioning correctly. For this reason, DC coupling in the receiver and digitizer stage is desirable.

A commercial solution for the analog signal receiver, the Koheron PD100, has been in use since the first prototype. Despite its excellent noise performance and robustness, its gain is too large to be used in combination with an analog-to-digital converter (ADC) like that in DAPHNE, and its power input saturation point of 600  $\mu\text{W}$  is too low. An in-house receiver is being developed that will allow the receiver stage to be fully configurable and adapted to the specific needs of this application. It will also enable a cost reduction in the final construction, and will better integrate with DAPHNE. The final design will be installed in FD2-VD Module 0, final optimizations will be made based on the installation experience during summer 2023. Since the receiver is external to the cryostat, it can be optimized even at a later time.

### 6.6.2.3 Power and Signal Fiber Routing

Figure 6.21 provides a 3D rendering of the routing of the PDS signal and power optical fibers for the cathode mount modules. From the module, they run internally to the cathode grid over to the edge next to the field cage vertical supports. From there, they run down to the cryostat floor into the cables trays provided for the bottom CRP detector electronics. These run up to the PDS flanges (Figure 6.22) on 32 of the penetrations that also carry feedthroughs for 4 CAT-6 cables, each of which serves 2 membrane-mounted PD modules, while the remaining 8 flanges will each carry 8 CAT-6 feedthroughs.

---

<sup>11</sup>Output signal (typically voltage or current) of the detector produced in response to a given incident radiant power falling on the detector.



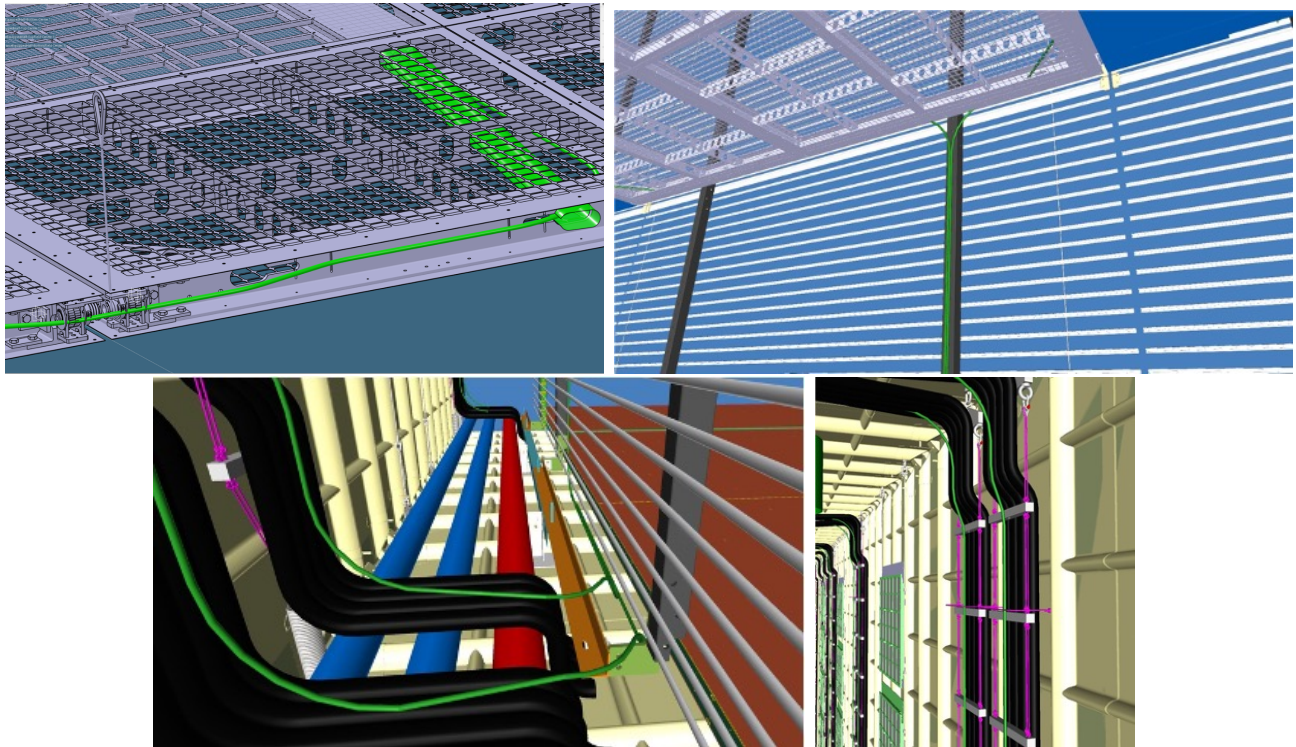


Figure 6.21: Cathode module optical fiber routing: Internal to cathode plane to the edge (top left); from the cathode plane edge to the field cage vertical supports then down to the floor (top right); (bottom left) transfer into bottom detector electronics cables conduit on the membrane walls; up the membrane walls and over to flanges on the cryostat top.

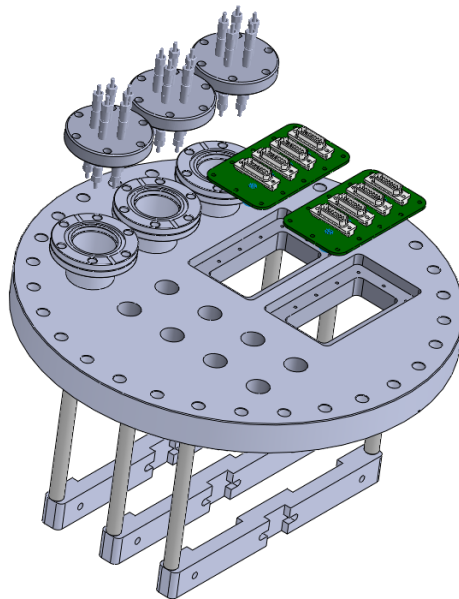


Figure 6.22: PDS flange with 3 feedthroughs for light response monitoring fibers, (top-left), 8 feedthroughs for fibers for cathode-mounted PDS modules (left), and feedthroughs for CAT-6 cables (right). Of the 40 flanges, 32 will have 4 CAT-6 feedthroughs, with the remaining 8 flanges having 8 CAT-6 feedthroughs as shown.

## 6.7 Light Response Monitoring and SiPM Calibration

The PDS will incorporate a pulsed UV-light system to calibrate and monitor PD response over time. The calibration system produces UV light flashes with a variable pulse amplitude, pulse width, repetition rate, and pulse duration. The calibration data recorded by PDS will be used to characterize and calibrate the PD gain, crosstalk, time resolution, channel-to-channel timing, and PDS stability over time. Examples of potential time instabilities to be monitored include dissolution of PTP coatings over time, or drifts in the power of the readout electronics lasers.

The system design, which has both warm and cold components, is very similar to that designed for the FD1-HD PDS and operated in ProtoDUNE-SP [34] where all the primary components of the system have been validated. A significant difference between ProtoDUNE-SP and FD2-VD is the typical distance between the point-like light source locations in the cold volume and photon detectors. However, illumination of a large area ( $6 \times 6 \text{ m}^2$ ) of PMTs from a fiber placed at the top of the field cage in ProtoDUNE-DP demonstrated that there will be sufficient intensity for these longer distances.

Based on ProtoDUNE-SP prototyping and operational experience, the system hardware for FD2-VD calibration and monitoring system consists of both warm and cold components.

Fibers with diffuse fiber-end points mounted on the support structure around CRPs' perimeter above the field cage strips and at locations behind the field cage strips will serve as point-like light sources, used to illuminate the PDs mounted at the cathode and on the cryostat membrane walls. Quartz fibers transport light from the optical feedthrough (at the cryostat top) to the diffuse fiber-end points. In this configuration the light emission points are about 6.5 m away from the cathode surface. Warm components of the system include electronics boards with controlled pulsed-UV source (currently 275 nm and/or 365 nm) and warm optics. Cold and warm components are interfaced through an optical feed-through, optimized for the number of calibration fibers and for the size of the cryostat flange. Figure 6.22 illustrates the top, horizontal flange, which provides eight fiber feedthroughs each serving up to eight PoF and SoF fibers for one cathode-mount PD module, three optical feedthroughs serving up to 15 Response Monitoring System diffusers.

Most of the design of the FD1-HD calibration system will be reused for FD2-VD. The primary differences with respect to the ProtoDUNE-SP system are the number and location of the fibers and its diffuse end-points, the lengths of the optical fibers, and the addition of a monitoring photodiode within the LED light source. The diffuse fiber end-points will be Figure 6.23. attached at support structure around the CRP perimeter at locations indicated in Figure 6.23. Each of these point-like diffuse sources will illuminate the cathode and membrane-mount X-ARAPUCAs using pairs of fibers. In each pair, one fiber will be pointing inward toward the cathode-mount PD modules and one fiber will be pointing outward toward the membrane-mount modules. The calibration system will have 24 pairs close to the top CRPs, and another 24 pairs closer to the bottom CRPs. These fibers run to the flanges at the top of the cryostat, where the electronics modules with light sources will be located.

The optical fiber, fiber routing scheme and optical feedthrough components, as well as light source electronics, have been designed for FD1-HD and will be tested in FD1-HD Module 0. For FD2-VD, the diffuse light point design and distribution will be optimized for light coverage of PD units

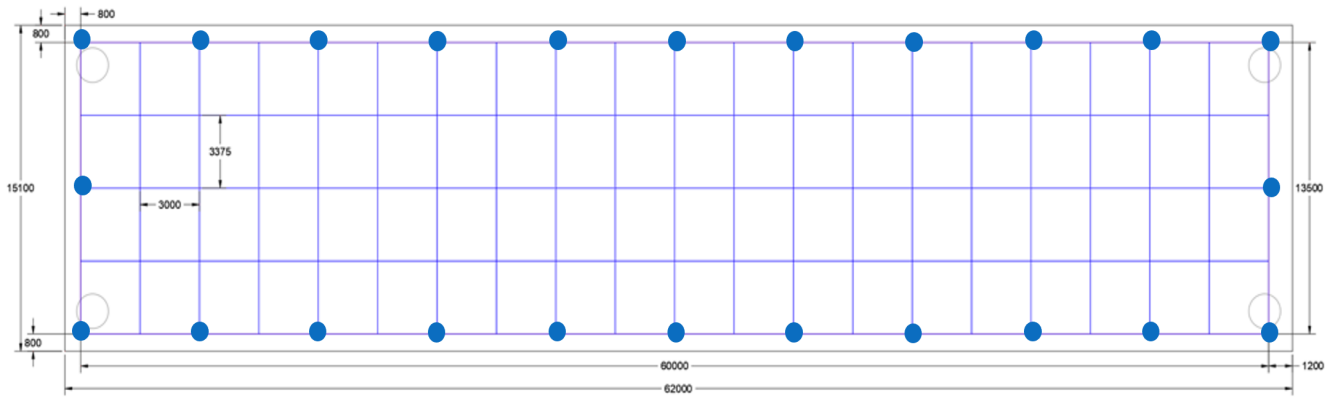


Figure 6.23: Location of the calibration system optical fibers with diffusers at the ends. They are installed along the perimeter of the CRP (viewed from above) and illuminate the PDs mounted on the cathode and cryostat walls.

located across the cathode and on the cryostat membrane walls. Design options include use of a bare fiber end as a diffuse light point, and/or installation of a small quartz light diffuser at the fiber end to provide a more uniform illumination (see Figure 6.24).

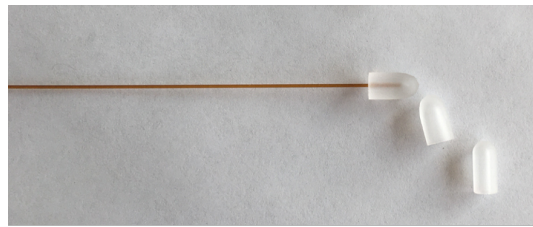


Figure 6.24: Diffuser (6.0 mm diameter) attached to bare fiber (0.7 mm diameter).

The FD2-VD Module 0 will be used to validate the design and evaluate the performance of the calibration system for FD2-VD. The FD2-VD Module 0 system provides ten calibration fiber-end diffuse ends. Calibration light is diffused from six light emission points attached to upper CRPs support structure with four diffuse-end points to illuminate cathode PDs, and two diffuse-end points to illuminate membrane wall PDs. There are four light emission points attached to lower CRPs support structure with two diffuse-end points to illuminate cathode PDs, and two diffuse-end points to illuminate membrane wall PDs. A test will be performed to determine if the light emitting points at fibers-end may diffuse light via either bare fiber-end or with the designed diffuser unit attached to it as shown in Figure 6.24. One of the top fiber-end emission points will be instrumented with the diffuser unit.

Multiple quartz fiber types will be tested for the light transport and diffusion characteristics in FD2-VD Module 0: two types of fibers with different resistance of the quartz core (200 and 400  $\mu\text{m}$  core diameter), and the third type already selected for FD1-HD Module 0 (600  $\mu\text{m}$  core diameter, which is expected to have a negligible solarization effect). Two fiber jacketing options are considered depending on fiber installation route constraints: PTFE jacket, or stainless-steel jacket.

The system has no active components within the cryostat. The active system component consists of a 1U rack-mount light calibration module (LCM) at warm temperature. The LCM electronics system generates light pulses that propagate through a quartz fiber-optic cable to the diffusive fiber-end to distribute the light across the PDs. The current calibration module design consists of a field programmable gate array (FPGA) based control logic unit coupled to an internal LED pulser module (LPM) and an additional bulk power supply.

The LPM uses multiple digital outputs from the control board to control the pulse amplitude, pulse multiplicity, repetition rate, and pulse duration. Analog-to-digital converter (ADC) channels internal to the LCM are used to read out a reference photodiode used for pulse-by-pulse monitoring of the LED light output. The output of the monitoring diode is available for monitoring and for normalizing the response of the SiPMs in the detector to the calibration pulse. Hardware components for the far detector (FD) modules will be costed based on the prototyping cost and expertise gained with FD2-VD Module 0.

Complementary to the monitoring system, a calibration of the absolute energy scale as a function of position within the detector will be pursued. The goal is to derive the position-dependent LY in the detector, in units of detected photoelectrons per unit energy deposit, from the data themselves. Several options are under consideration, including cosmic ray tracks, radioactive sources (at fixed positions or diffused into the LAr volume), pulsed neutron generators, and ionization lasers.

## 6.8 Design Validation

This section summarizes the results of the R&D and prototyping plan carried out for the FD2-VD PDS following the Conceptual Design Report and the on-going design validation program.

### 6.8.1 Xenon doping in ProtoDUNE-SP

A xenon-doping campaign was carried out in ProtoDUNE-SP a few months after an incident with a gas recirculation pump had let an unknown amount of air inside the detector volume. Oxygen and water were efficiently removed by the purification loop, but nitrogen cannot be removed by the purification filters. A residue of nitrogen ( $\sim 5.4$  ppm in mass) remained in the LAr with the result that the scintillation light was effectively quenched. Although it was not originally foreseen to do xenon testing in the presence of nitrogen contamination, its presence presented the opportunity to demonstrate light recovery due to xenon doping and a large scale.

The doping run consisted in doping argon with up to 18.8 ppm of xenon, in steps. The amount of detected light increased as a function of concentration up to around 16 ppm, after which the gain flattened. This trend was consistent across the three types of light detectors in ProtoDUNE-SP PDS. The results were corroborated by measurements taken with two prototype X-ARAPUCA detectors inserted for this run in the non-active TPC region behind one of the APAs. A paper on this work is in internal review.

Initial small-scale tests and the procedure used for ProtoDUNE-SP demonstrated that the doping of xenon and the mixing with argon must happen in gas phase, before condensation of the fluid. Indeed, since xenon liquefies at 165 K and solidifies at 161 K, creating a solution with liquid argon

must be performed with extreme care, in order to avoid its freezing. Several mixing ratios were tested, showing that the Ar/Xe ratio must be above  $10^3$ , to avoid xenon solidification on the walls of the argon condenser. This *freeze-out* effect can be easily observed since, at the highest xenon concentrations, the pipes of the condenser get clogged and the argon recirculation stops.

For ProtoDUNE-SP, the xenon injection point was placed on the gas recirculation system; on the line collecting the chimney boil-off, after the argon gas purification filter but some distance before the condenser. This allows for full mixing within the gas flow. The maximum xenon mass flow rate was set to 36 g/h, to be well within the Ar/Xe ratio limit mentioned above; this corresponds to 50 ppb/hour in the ProtoDUNE-SP detector. Based on a numerical computational fluid dynamics (CFD) simulation of the LAr flow within the ProtoDUNE cryostat, the xenon injected at this rate is expected to be uniformly distributed in LAr within few hours.

Here we summarize the main results of the successful run:

- Since one of the two X-ARAPUCA detectors was fitted with a quartz window, which makes it insensitive to 128 nm photons, it is possible to disentangle the contribution of the xenon photons alone from the total emitted light. Comparison of the signal from the two detectors clearly shows that the amount of light above the quartz window cut-off, “xenon light”, increases with xenon concentration. The ratio of the xenon-to-total argon light collected by the two detectors, as a function of xenon concentration, is shown in Figure 6.25.
- The data shows that the effect of xenon is similar across the several detector technologies which are at different locations in ProtoDUNE-SP. This indicates good uniformity of the doping throughout the TPC volume. Time stability of the mixture is observed at the level of few weeks after the last doping event (afterwards, the run was stopped).
- Light attenuation curves show that the amount of detected light increases more further from the detectors, demonstrating the usefulness of the doping for very large volume TPCs (Figure 6.26). This is even more evident in a subsequent xenon-doping campaign in the ProtoDUNE-DP, which features a larger drift distance [33].
- In the ProtoDUNE-SP configuration, the increase of light with xenon concentration starts flattening out at around 16.6 ppm.
- No detectable deterioration of the charge collection performance, i.e., of the imaging capability of the TPC, was observed during the doping campaign.

In addition to the ProtoDUNE-SP run, ProtoDUNE-DP was partially emptied and refilled with the doped argon transferred from ProtoDUNE-SP. The amount of nitrogen was increased in order to reproduce the conditions of ProtoDUNE SP. The measurements taken in ProtoDUNE-DP also show an increase in the amount of collected light, which is becoming more and more evident with increasing distance from the detectors (due to the larger Rayleigh Scattering length). This result is published in the overall paper on the performance of the ProtoDUNE-DP light detection system [33].

The results of the two campaigns cannot be directly compared due to the significantly different TPC configurations and light collection technologies. However, both demonstrate that xenon doping will provide greater light yield uniformity and allow photon detection recovery from accidental nitrogen

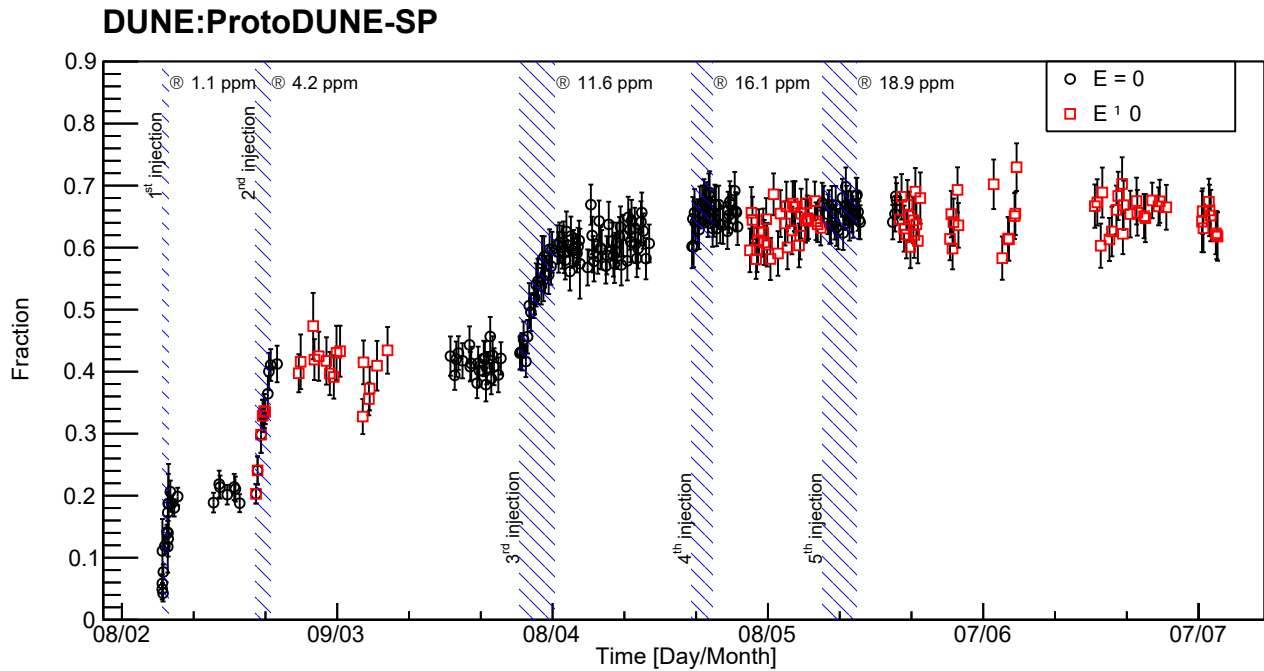


Figure 6.25: Fraction of light collected by the xenon light-only sensitive X-ARAPUCA in ProtoDUNE-SP, with respect to total light collected by the other device:  $\frac{X_e}{Ar+X_e}$ . The ratio increases with the doping concentration and reaches a plateau around 0.65 for xenon concentration greater than 16.1 ppm. The red points correspond to data collected with the nominal TPC electric field (500 V/cm), while black points refer to data with no electric field. Shaded areas indicate xenon injection periods.

contamination for multi-meter drift-path TPCs.

## 6.8.2 X-ARAPUCA Module Optical and Mechanical Development

The X-ARAPUCA concept of the FD2-VD PDS module is the same as that of FD1-HD. Though the design benefited greatly from the FD1-HD development through to the final design, an R&D program was pursued in those aspects most impacted by the significantly different geometrical layout of the FD2-VD modules.

The development of the FD2-VD module focused on:

- Production of large area WLS plates of  $607 \times 607 \times 3.8 \text{ mm}^3$  dimensions compliant with cryo-resilience, optical grade, and thickness requirements;
- SiPM mounting onto flexible kapton PCB (instead of rigid FR4 PCB pin coupled to FR4 routing boards) utilized for both the SiPM mechanical support and the signal routing;
- Spring-loaded mounting of the WLS/SiPM photon collector structure inside a G-10 frame, to compensate for their differential thermal shrinking (about 1%);
- Optimization of the dichroic filters optical density and reflectivity at specific angle of incidence (maximized for 45deg, the average angle of the Lambertian emission angle distribution) and wavelengths;
- Development of larger size ( $202 \times 97.5 \text{ mm}^2$  and  $143.75 \times 143.75 \text{ mm}^2$ ) dichroic filters to min-

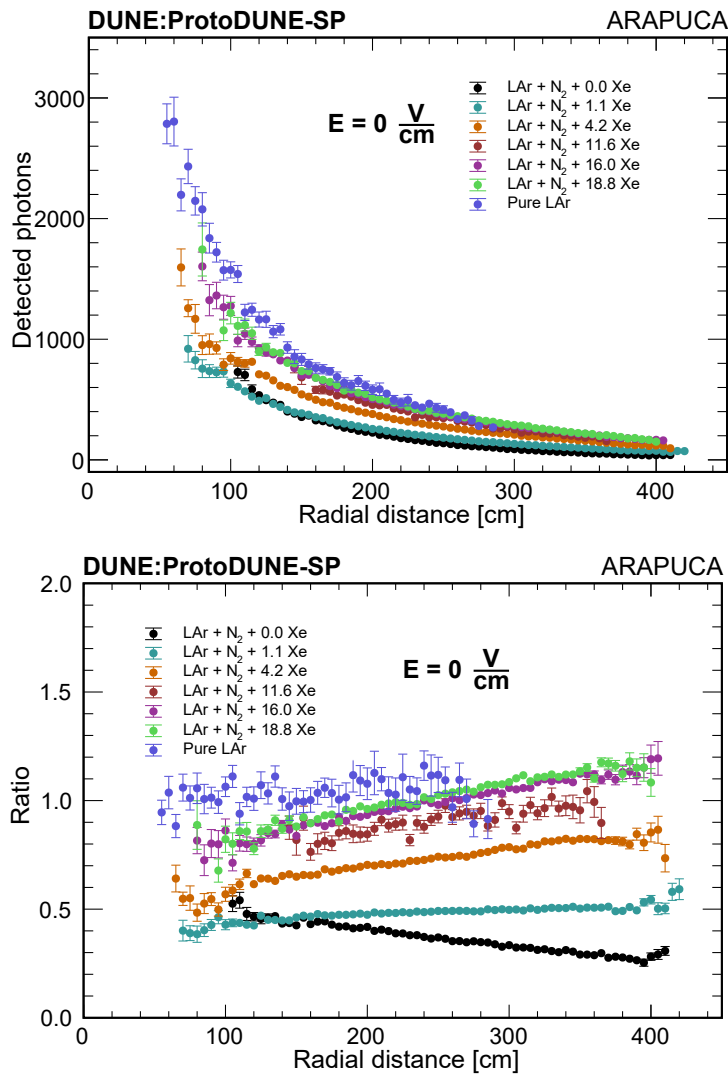


Figure 6.26: Light recovery is demonstrated through attenuation curves after xenon injection in the nitrogen-polluted ProtoDUNE-SP. Data collected with the non-beam side. The left plot shows the collected light versus distance from the detector; the right plot shows the ratio of collected light with nitrogen (black points) and with nitrogen+xenon, with respect to non-polluted LAr (blue points). Data refer to runs with no active electric field. The right plot shows how the increasing concentration of xenon enhances light recovery further from the photon detectors.

imize the surface area of the non-active holder frame profiles of the dichroic filters.

- Optimization of PTP coating on large size filters;
- SiPM coupling via optical grade epoxy to a WLS plate forming an integrated readout structure;
- Laser cutting of the WLS tile edges with cutouts of rectangular/elliptical shape, to improve the photon collection as they exit the lightguide and to mitigate SiPM gluing.

### 6.8.3 Cryogenic PD Testing Facility for FD2-VD Module 0

In late 2022 a cryogenic facility was constructed at the Neutrino Platform facility at CERN EHN1 building to test full size X-ARAPUCA modules and read-out electronics, see Figure 6.27. This facility provides final functionality check and validation in cold prior to deployment in the FD2-VD Module 0 cryostat and detector integration. The  $4 \times 4 \text{ m}^2$  test area is located at CERN building 887/R-291 Salève side, in front of the ground floor PDS Lab barrack, where the assembly of the X-ARAPUCA PD modules is performed.

A 70-cm diameter  $\times$  120-cm tall open air Dewar contains a (non-purified) LAr bath, which can be sealed with a custom-made lid that ensures light tightness and free exit for gaseous argon boil-off. A trolley with a winch allows insertion and extraction of a PD module. To minimize the usage of liquid argon and ensure safe warm-up and fast operation turnaround, a stainless steel box that can accommodate the X-ARAPUCA module is inserted inside the Dewar and filled with LAr.

At the end of a test, when extracting the module while it is still cold, nitrogen gas flowing under the box contained by a polyethylene skirt, prevents frost condensing on the modules. Cables and optical fibers routed via dedicated feedthroughs on the lid allow for cold electronics readout during test and calibration with a LED pulsed flasher installed inside the Dewar. Temperature sensors and a slow control system are used to monitor the LAr level and temperatures at different heights inside the inner vessel.

All 16 X-ARAPUCA modules for FD2-VD Module 0 were tested, and qualification data acquired, analyzed, and stored.

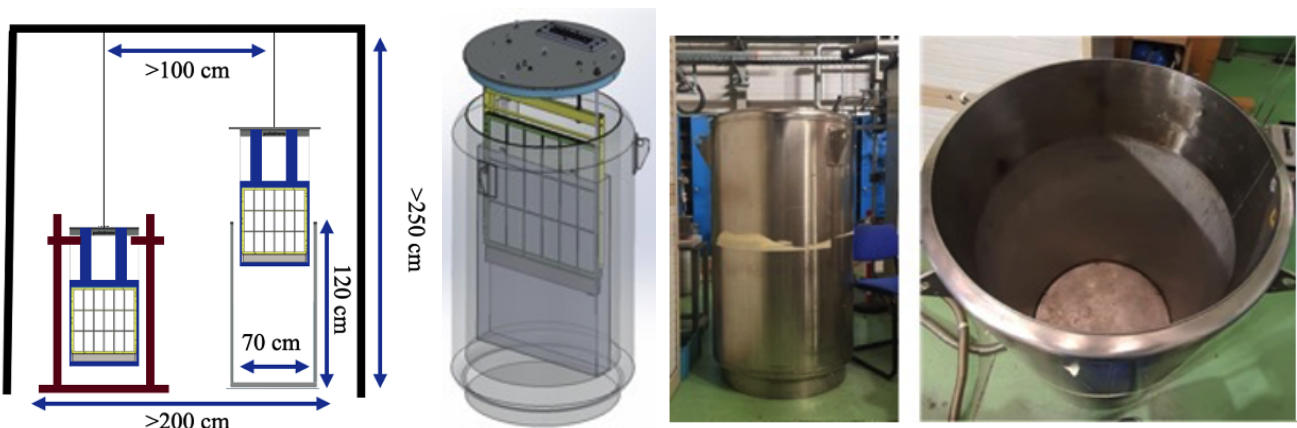


Figure 6.27: Schematic (left) and Dewar photos (right) of the mini-cold box at CERN, for testing X-ARAPUCA modules prior to installation in FD2-VD Module 0.



## 6.8.4 PD Module Validation

During 2021 and 2022, all the components were developed and prototypes fabricated. Integration techniques and procedures were developed and tested.

Fully-instrumented X-ARAPUCA modules have been tested both at the Proton Assembly Building at Fermilab, which serves as a test-bed for cryogenic electronics and PoF development, in a test facility at CERN commissioned in later 2022 (described in Section 6.8.3), and in the cold box demonstrator, in at CERN, starting in summer 2021 and continuing through to 2023, see Table 6.8.

Three prototype versions (X-ARAPUCA.V1, X-ARAPUCA.V2, and X-ARAPUCA.V3) have been deployed and operated in the cold box demonstrator, as can be seen in Figure 6.28. The V4 and V5 prototypes were validated in the EHN1 FD2 cold box ahead of FD2-VD Module 0 installation: these versions integrate different technologies of electronics shielding, SiPM-to-WLS coupling, and WLS edge shaping. An independent module mechanics design committee set up by the FD2-VD PDS consortium management evaluated the designs and down-selected from the two options (V4 and V5) to a single option (essentially V5) that is deployed in FD2-VD Module 0. These value engineering efforts are aimed at increased manufacturability, reduction of fabrication costs, and optimization for shipping.

Table 6.8: PD module prototypes.

Version	Description
V1	First full-size FD2 PD module. 3-sheet filter frame design, coil springs for pressing SiPMs against WLS plate.
V2	Changes primarily to dichroic filter frames, incorporating leaf springs to press SiPMs against WLS, Single-sheet filter frame with spring-loaded filter plates.
V3	Evolution of V2 design, making improvements to filter frame assembly.
V4	Final version of leaf-spring SiPM mounting design with spring-loaded filter windows in single-piece frame. Evaluated as part of Module-0 mechanical design process.
V5	Final version of coil-spring SiPM mounting design with Teflon washers mounting filter windows in single-piece frame. Evaluated as part of Module-0 mechanical design process.

## 6.8.5 Cathode-Mount Module Cold Electronics Validation

Numerous tests of the electronics developed for the SiPM signal read-out of the cathode-mount PD modules V1 to V5 have been performed in the cold box, starting from the earliest prototypes (Dec. 2021) to the latest fully integrated final design board (Dec.22-Feb.23 - DCEM board shown in Figure 6.18). In this section first results are reported on the read-out electronics response characterization validating the final design of the DCEM board.

For the analysis of the electronics response, a pulsed LED calibration system is implemented in the cold box. It consists of a board that drives a 310 nm LED flasher, into a quartz fiber ending

## ckups

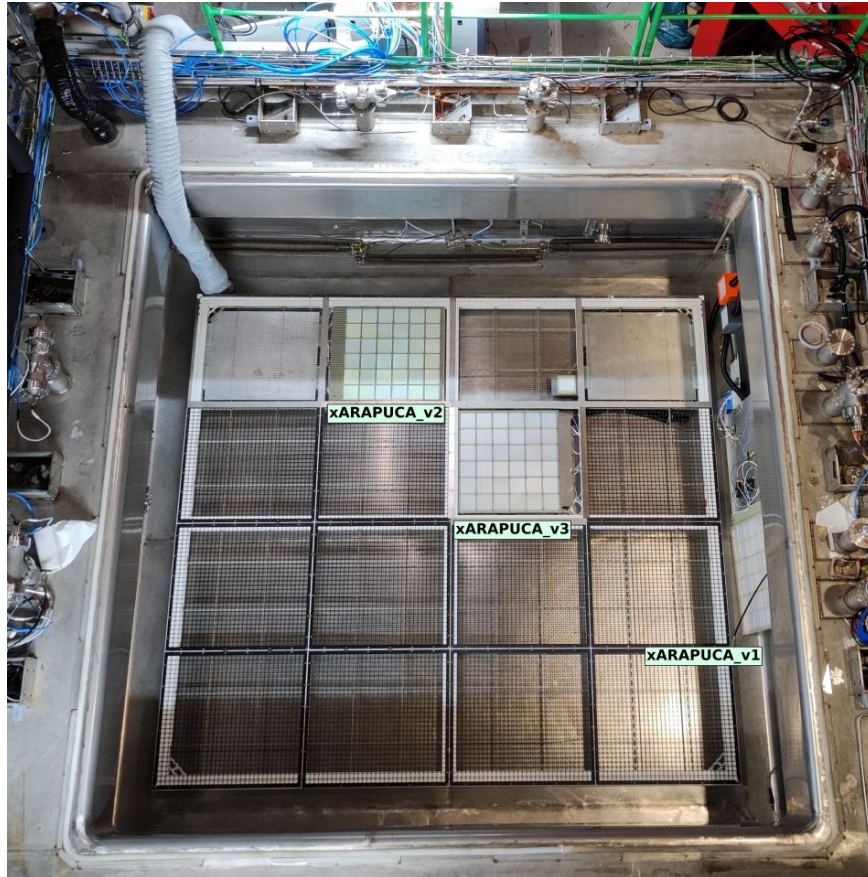


Figure 6.28: Top view of the cold box demonstrator at CERN, showing three X-ARAPUCA prototypes installed. The first prototype is mounted on the cryostat wall, while the second and third prototypes are mounted on the cathode.

into a light diffuser placed in the LAr bath inside the cold box. The intensity and the width of the LED pulse can be selected, down to about 20 ns minimum duration.

The DCEM board in its final configuration is made of three main stages, the PoF stage (with two OPCs, optical-to-electrical power converter, and a bias circuit transforming the OPC low output voltage to the high SiPM bias voltage), the signal amplification and conditioning stage, and the 2-channel SoF transmitter (laser diode and its driver for signal transmission over optical fiber). The board, with input cable connections from the SiPM flex boards, is placed within a Faraday shielding metallic box along one side of the X-ARAPUCA module.

The first key milestone achieved is the demonstration of a signal-to-noise ratio (SNR) above the requirement of 4. Figure 6.29 shows the charge spectrum obtained with minimum LED pulse amplitude illumination, with peaks representing the charge distribution for 1-PE to 6-PE, above the first noise (0-PE) peak. From the multi-Gaussian fit, the ratio of the 1-PE peak position to the width of the 0-PE peak  $\text{SNR}=5.9$  is obtained. This SNR is obtained operating the X-ARAPUCA module (V4) on the cathode at high voltage, during TPC operation. The DCEM read-out board is powered by PoF laser power via optical fiber and SiPM electrical signals are converted into optical signals and transmitted by SoF laser diode via optical fiber. Signal and noise levels were stable during the cold box run.

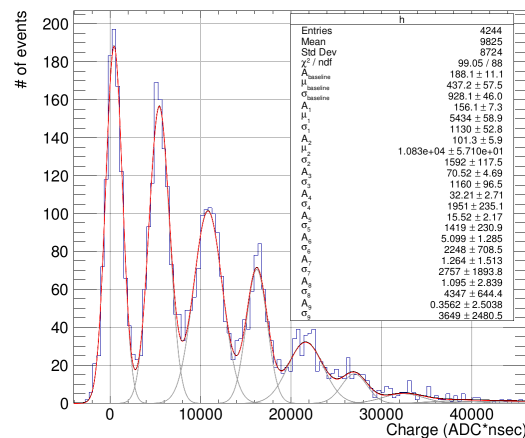


Figure 6.29: Photoelectron charge distribution for a full cathode module, obtained with the data from February 2023 cold box test with PoF and SoF. An SNR of  $\sim 5.9$  was obtained.

The impulse response function of the readout electronic chain, SiPM signal summing, cold DCEM analog signal conditioning and warm signal optical-to-electrical conversion (commercial Koheron PD100 board) and digitization, is obtained by  $\sim 20$  ns narrow LED flasher pulsing. Figure 6.30 shows the average of 500 signals obtained with fixed amplitude LED pulse. The relevant characteristics are highlighted on the plot, namely the rise time and discharge time measured between the 10% and 90% of the pulse amplitude, of 40 ns and about 400 ns respectively. The rise-time obtained is that expected from 80-ganged SiPMs, indicating that the bandwidth of the transmitter is adequate.

Linearity of the SoF electronics was first demonstrated with lab test-bench measurements over a limited range of signal amplitude, corresponding to few tens of PEs. Using data acquired at the cold box, it has been possible to evaluate the linearity of the entire readout chain, from the

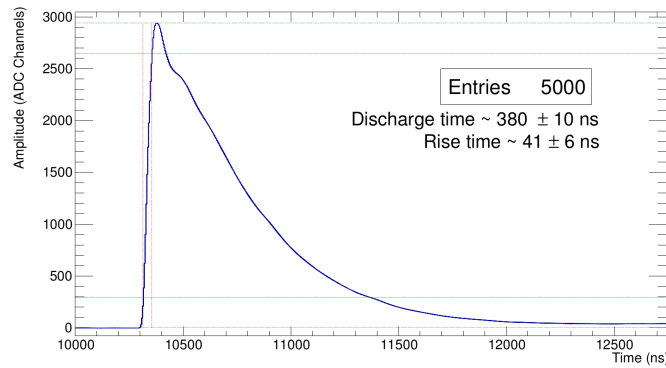


Figure 6.30: Average of 500 pulses obtained from the cathode modules. The rise time measured between 10% and 90% amplitude is  $\sim 40$  ns, while the discharge time is around 380 ns.

photosensor to the warm receiver, for a much larger dynamic range.

Signal waveforms were recorded with LED calibration flasher pulsed from minimum to maximum amplitude settings. The linear correlation between amplitude of the signal waveform (pulse height expressed in ADC counts) and signal waveform integral (after charge-to-PE calibration is applied) for various LED flasher amplitude setting is shown in Figure 6.31. The pulse amplitude of the recorded signals is limited to a maximum of about 1.5 V ( $\sim 13000$  ADC), since the warm receiver is saturated at this point. The linearity shown in Figure 6.31 demonstrates that the signal maintains the expected shape without distortions over the dynamic range of interest. A slight non-linearity of the LED calibration system signals appears at higher LED pulse amplitude settings that does not occur for scintillation signals from cosmics for all amplitudes. This residual non-linearity of the LED calibration system has to be taken into account.

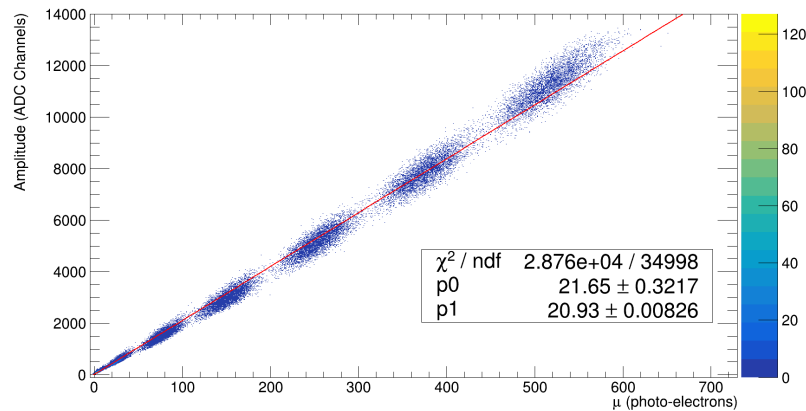


Figure 6.31: Linear growth of signal amplitude as a function of the number of PE, estimated from the integral of the SPE charge. The groups of data correspond to LED voltage levels. The saturation is due to the warm receiver's maximum input limit.

The full dynamic range was evaluated in a special channel of a DCEM board with lower light output also tested in cold box for V4 X-ARAPUCA module read-out, without the saturation limitation of the warm receiver (whose gain will be adjusted for the in-house receiver under development to replace the commercial Koheron board). The resulting measurement, going up to almost 2000 PE equivalent signal amplitude, is presented in Figure 6.32.

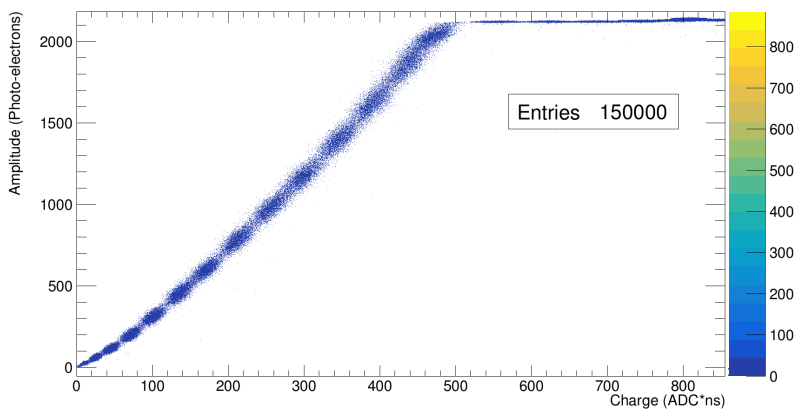


Figure 6.32: The dynamic range of the system has been demonstrated from the SPE level to over 2000 PE.

The X-ARAPUCA detectors have a very small, but non-zero, sensitivity to the 808 nm infrared light of the PoF laser. This means that the PoF fibers and connectors at OPC receivers must be adequately shielded. Potential light leakage is effectively mitigated by potting the OPC receivers and connectors on the DCEM boards with electronic grade silicone paste and also by the metallic Faraday boxes surrounding the electronic boards. Light leakage from the PoF fibers becomes negligible when black jacketed fibers are bundled in the protective black tubes used for fiber routing from PD modules on the cathode to the feedthrough flanges at the top of the cryostat. Lab tests have demonstrated optical noise due to PoF light leakage decreases to sub-PE levels with these measures.

The level of detectable light leakage at the cold box was evaluated by measuring the rate of single PE signals with an independent X-ARAPUCA module mounted on the wall (V1). Data were taken while both the cathode X-ARAPUCA modules (V4 and V5) with PoF lasers were turned ON and OFF. No difference was found in the number of detected single-photon signals with PoF ON compared to PoF OFF (no laser light injected in cold box). The noise distribution evaluated from baseline fluctuations from the V1 membrane-mount X-ARAPUCA module on the wall before and after turning on PoF lasers is shown in Figure 6.33 and demonstrates no significant noise increase. It is concluded the light leakage has been reduced to inconsequential levels.

Interactions between the PDS system and the rest of the detector were evaluated. The noise levels on the PDS system were compared with the cathode HV voltage ON (10 kV) and OFF. Figure 6.34 shows the Fourier transform of the data collected from a cathode module; the peak around 30 MHz corresponds to the frequency domain of the signals detected. No difference was observed due to the state of the HV. The TPC CE also evaluated the noise level with PDS on and off, finding no differences.

Lastly, the time resolution of the PDS system is evaluated by comparing the measured time of arrival of signals from two channels for the same X-ARAPUCA; the result is shown in Figure 6.35. The convoluted time dispersion of both channels is found to be of the order of a few nanoseconds. It should be noted that the result is preliminary in that a fixed threshold is applied and with no correction for time-walk.

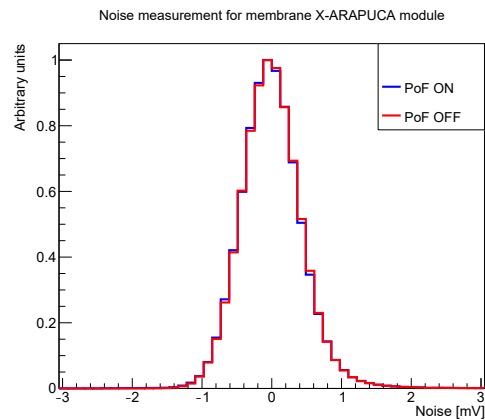


Figure 6.33: Distribution of baseline noise for membrane V1 X-ARAPUCA (DCEM v1.0 coaxial cable readout) with PoF OFF and ON for February 2023 cold box data.

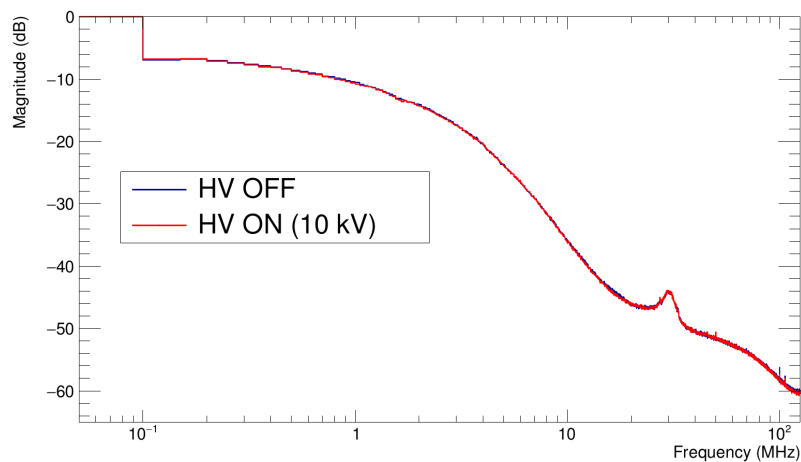


Figure 6.34: Fourier transform plot of the baseline signal of the PDS readout with the high voltage of the cathode ON and OFF. No difference is found.

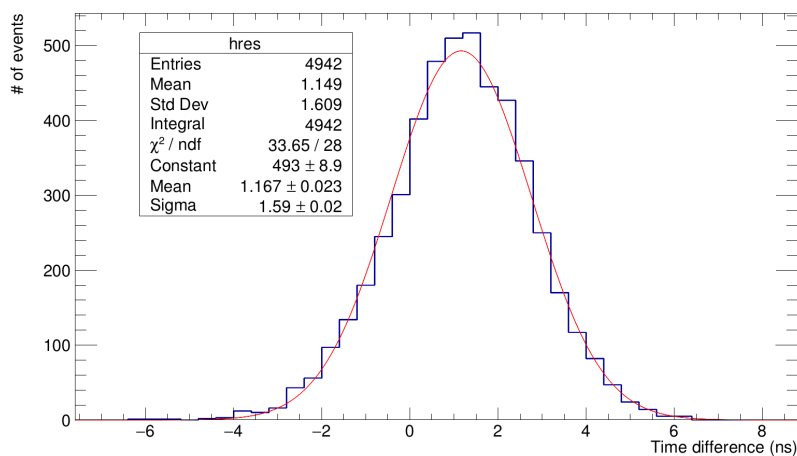


Figure 6.35: Histogram of the time difference between signals from the two channels of one X-ARAPUCA detector.

## 6.9 Production and Assembly

The FD2-VD PDS production phase will be launched after a successful PRR, which should be completed in early 2024.

Production procurement will be split into three phases: an initial 10% phase to establish the quality assurance (QA)/quality control (QC) procedures with vendors and FD2-VD PDS assembly centers, followed by two 45% time-sequential phases. This sequence of fabrication stages is initially envisioned to allow for an initial 10% production startup phase followed by two main production phases to control cost envelopes over fiscal years. It also provides a handle for multiple sites and/or multiple vendors, as a secondary benefit. Once production begins, the schedule drivers for FD2-VD PDS are procurement handling, vendor lead-time, and production site throughput rate. No schedule logic that interfaces to other subsystems will be present until installation begins.

The reference design calls for using several similar or identical components for FD2-VD PDS as used in FD1-HD: photosensors, dichroic filter plates, WLS plates, and membrane-mount conductive cables. Dealing with the same vendors as the FD1-HD should mitigate production delay concerns on these components. Schedule risk is significantly mitigated by a two-vendor strategy for both photosensor and WLS plate fabrication. Multiple vendors of high-quality dichroic filters have also been identified.

Planning for module assembly is based on the experience with the ProtoDUNE-SP PDS. The modules were designed to be factorizable into multiple free-standing sub-assemblies, thereby increasing the number of assembly sites that can operate independently. SiPMs already mounted to flexible PCBs will be procured from vendors, simplifying the logistics chain while reducing the number of required QC tests. Dichroic filter plates will be procured, tested and assembled into sub-assemblies as shown in Figure 6.8. These sub-assemblies will be assembled into PD modules at multiple production sites. Studies of assembly rate for FD2-VD PD modules will be conducted as part of the cold box and FD2-VD Module 0 validation efforts. Preliminary tests at CSU, NIU and at CERN all suggest that module assembly times (from a complete set of components) of one module per day using a two-person assembly team are reasonable. Particular care will be taken to understand the impact of coupling the SiPMs to the WLS plates, which is likely to have the most significant impact on production rate.

The reference plan is for 672 detector modules for the FD2-VD PDS. Potential production sites at collaborating institutions have been identified. At least two production sites will be selected, possibly more, depending on interest from collaborators and the ability to meet production requirements. These production sites will be supplied from multiple sub-assembly sites, the number of which will be determined by collaborator interest and the required production rate. It is planned to launch production orders over three years beginning in 2024 and for fabrication of core components (SiPM, WLS plates, dichroic filters etc.) with a ramp up during summer of 2024. After the ramp-up period, the target production rate for modules is eight per week. In the reference schedule, detector module assembly begins in early 2025 and should be completed by Q2 2027.

For cold electronics readout, commercial vendors will fabricate custom PCBs. On-board components will be qualified for long-term cold operation following a peer-reviewed process. PoF assembly is currently planned to involve custom assembly by collaborating institutions on the transmitter

side and for individual receiver mounting to the cold readout electronics motherboard. There is an opportunity to explore turnkey vendor assembly of the PoF rack mount transmitter units and cold receiver units. The PoF fiber optical power converter receiver unit is fabricated by commercial vendors, as is the SoF transmitter unit.

The readout electronics in warm is a custom module assembly of commercial digitizer and aggregator electronics.

## 6.10 Interfaces

Table 6.9 summarizes the PDS interfaces to the other FD2-VD systems. Each interface is discussed in more detail in the following sections.

Table 6.9: PDS interface descriptions and links to full interface documents.

Interfacing System	Description
CRP	Response Monitoring System diffuser placement (potential, TBD), routing of PDS fibers at bottom of cryostat.
BDE	Shared use of cable trays and cryostat penetrations.
TDE	None.
HVS	Mechanical and electrical contact between cathode and PD modules, fiber routing in cathode, fiber routing along field cage, field cage transparency, PDS fiber diffuser placement, high voltage system (HVS) camera lighting.
DAQ	High-speed data links, timing signals.
I&I and SC	Membrane-mounted PD module support, fiber installation process, grounding, rack infrastructure, power, PDS readout configuration, power supply control and monitoring, PDS Response Monitoring system control and monitoring.
CALCI	None.
SWC	Software and databases to support data-taking and offline analysis.

### 6.10.1 Charge Readout Plane (CRP)

Previously, a potential interface between the PDS and CRP was identified as arising from the possible installation of PDS Response Monitoring System optical fibers on the central long axis of each CRP. As of the drafting of this report, it is believed that the optical fibers placed between the field cage and cryostat wall will provide sufficient coverage of all PDS modules in the system, thus eliminating this interface. This will be verified with the FD2 FD2-VD Module 0 run scheduled to take place in 2023, and the potential interface revisited accordingly.

The precise routing of bundles of fibers for the PDS PoF and SoF systems for cathode-mounted modules is a potential mechanical interface with the CRP. The interface will be further defined to ensure that the fiber bundles at the bottom of the cryostat are neither damaged by nor impede the placement of the CRP during its installation.



## 6.10.2 Bottom Drift Electronics (BDE)

The interfaces between BDE and PDS stem from overlapping cable and fiber paths for the two systems. As described in Section 4.4.3.7.1, the two systems share 40 penetrations through the cryostat roof, each consisting of a four-way cross-shaped spool piece. Two vertical flanges indicated in Figure 4.65 serve BDE, with the top horizontal flange serving PDS.

The design elements required for the routing of BDE and PDS cables and fibers through the penetrations, and the responsibilities for finalizing them, are laid out in the Interface Control Document.

The routing of cables and fibers in shared cable trays along the cryostat membrane presents another interface between PDS and BDE.

## 6.10.3 Cathode Plane Assembly and High Voltage System (HVS)

The mechanical and electrical contact between the cathode and FD2-VD PDS as described in Sections 5.4.1 and 6.1 presents several interfaces between the PDS and HVS. The electrical contact with the cathode will be a critical consideration due to field uniformity and the risk of cathode high voltage discharge as described in Section 6.4. The reference design envisions that each cathode module contains four PD modules with an independent set of optical fibers to provide power to each module, eliminating the risk of discharge damage resulting from transient potentials between modules. An alternative mitigation using custom-designed balun circuits as part of a conductive distribution of SiPM bias voltage between PD modules on a single cathode module is under investigation, targeting a demonstration at Module-0. Individual PD modules are further protected from the effects of discharge by a conductive mesh covering each side of the cathode openings which house PD modules and by a Faraday cage enclosing the electrical components of each cathode-mounted PD module as shown in Figure 6.11.

Mechanical supports connecting cathode-mounted PD modules to the cathode structure have been designed and deployed successfully in CERN cold box prototyping runs, and will be updated as the PDS mechanical design is finalized. Both the dry and buoyant weight of cathode-mounted PD modules must remain below their respective maxima determined by cathode flatness specifications. The cathode suspension system must be calibrated in accordance with the PD module weight; 12kg is the dry weight limit per X-ARAPUCA.

As shown in Figure 6.6, the FD2-VD PDS fiber routing from the cathode modules is expected to go along the cathode to the field cage, down along the field cage, from the anode over to the membrane wall where cathode cable routes will join PDS membrane module cable routes up to penetrations at the cryostat roof.

The process of fiber installation represents an interface with HVS in the placement of fibers along the field cage cable tray, the proximity of fiber handling, and the installation of fibers in the cathode. The fiber installation in the cathode will take place *in situ*.

The light yield specification (Table 6.1) implies a design interface with HVS through the transparency of the field cage and its impact on light collection by the membrane-mounted PD modules.

All membrane-mounted PD modules are positioned within the region of 70% FC transparency.

The PDS response and monitoring system has a potential interface with the HVS through the possible mounting of light sources (diffusers and fibers) on field cage elements, respectively. This interface will be updated as the monitoring system design is finalized after the operation of FD2-VD Module 0.

A final interface with HVS is presented by infrared LEDs providing illumination for inspection cameras in HVS scope. The resulting risk of damage to powered SiPMs requires a system, to be designed, to prevent operation of SiPM bias while the camera LEDs are in use.

#### 6.10.4 Data Acquisition (DAQ)

The FD2-VD PDS interfaces with the DAQ system through high-speed links and timing signals connected to a layer of warm readout electronics that is in FD2-VD PDS scope. The DAQ high-speed links and timing signal cables and fibers are not in FD2-VD PDS scope, nor is the supporting infrastructure such as racks, rack power, and rack monitoring. The FD2-VD PDS warm readout electronics will handle extracting timing signals and distributing them to the detector readout electronics, as well as aggregating and formatting detector data in the DAQ event structure.

#### 6.10.5 Cryogenics Instrumentation and Slow Control (SC)

has several interfaces with PDS:

- SC control (configuration) and monitoring of the DAPHNE modules used for PDS readout.
- SC control (voltage level, current limits, and on/off state) and monitoring (current draw, sense voltage, on/off state) of low-voltage direct-current power supplies powering the DAPHNE crates.
- SC control and monitoring of power distribution units (PDUs) controlling distributing of AC power to PDS direct-current power supplies and PoF transmitter units.
- SC control and monitoring of the flashers for the PDS response monitoring system.

These interfaces will require implementation of software modules to reflect configuration options yet to be determined.

#### 6.10.6 Facility, Integration and Installation Interfaces (I&I)

The PDS has an interface with Integration and Installation (I&I) in the design and execution of the installation and process. The completion of routing of fibers for PoF, SoF, and the Response Monitoring System will require coordination with other systems via I&I, as well as careful consideration for Class-4 laser safety protocols during testing of PoF functionality in place.

The reference voltage of the cold electronics for the 352 membrane-mounted PD modules will be tied to detector ground at the cryostat penetration. The reference voltage of the 320 cathode-mounted PD modules will be connected via a 1 M $\Omega$  resistor to the conductive mesh that covers each cathode cell housing a PD module.

The PDS-I&I interface also includes 40 27u racks on the cryostat roof, close to the penetrations, housing PoF transmitter boxes and DAPHNE readout cards. An additional 4 LV power supply racks serving PDS will be located among the detector racks, approximately 25 m from the penetrations.

### 6.10.7 Calibration and Monitoring

While early versions of the -PDS anticipated light sources potentially capable of damaging powered SiPMs and lasers capable of damaging WLS components in PDS, the scope of CALCI does not currently include such components.

### 6.10.8 Physics, Software and Computing

The interfaces of FD2-VD PDS with physics, software, and computing are identical in form to those for FD1-HD, impacting

- Operations
- Data products
- Database schema and management
- Software design
- Computing power.

The PDS system is expected to contribute a very small fraction of the data that is selected to be transferred to and stored at Fermilab. Data products, algorithms, and database schemas provided by for FD2-VD PDS data will require different treatments of geometrical information for FD1-HD and FD2-VD. PDS will be responsible for ensuring that the technical geometry description of the FD2-VD PDS remains up-to-date.

## 6.11 Transport and Handling

A storage facility near the far detector (FD) site (the South Dakota Warehouse Facility (SDWF)) will be established to allow storage of materials for detector assembly until needed. Transport of assembled and tested PD modules, electronics, cabling, and monitoring hardware to the SDWF is the responsibility of the PD consortium.

Following assembly and quality management testing at FD2-VD PDS construction centers, the PD modules with associated cold readout electronics will be packaged and shipped to an intermediate cryogenic testing facility for final full-chain testing including operation in LN<sub>2</sub> to validate detector performance. Following this, the modules will be stored in their shipping containers in the SDWF. Cables, warm readout electronics, and monitoring hardware will be shipped directly to the SDWF and stored until needed underground for integration.

Packaging plans are informed by the FD1-HD PDS experience. X-ARAPUCAs will be packaged in groups of 4 modules (matching the installation pattern), approximately 1 m × 1 m × 50 cm. These

shipping boxes may be gathered into larger crates to facilitate shipping. The optimal number per shipment is being considered.

Documentation and tracking of all components and PD modules will be required. Well-defined procedures are in place to ensure that all components/modules are tested and examined prior to, and after, shipping. These procedures will be presented during the FD2 PDS Final Design Review and posted in EDMS.

Information coming from testing and examinations will be stored in the DUNE hardware database. Each X-ARAPUCA will be labeled with a text and barcode label, referencing the unique ID number for the X-ARAPUCA contained, and allowing linkage to the hardware database upon unpacking prior to integration in cathode modules and membrane-mount support systems underground.

Tests have been conducted and continue to validate environmental requirements for photon detector handling and shipping. The environmental condition specifications for lighting (no exposure to sunlight), humidity (<50% RH at 70 degF), and work area cleanliness (Class 100,000 clean assembly area) apply for surface and underground transport, storage and handling, and any exposure during installation and integration underground.

Details of PD integration into the cathode and installation into the cryostat, including quality management testing equipment, tests, and documentation are included in Chapter 9.

## 6.12 Quality Assurance and Quality Control

The QA and QC programs as well as the design-phase quality assurance and validation plans are based on our experience with the ProtoDUNE-SP. The FD2-VD PDS quality assurance program is focused on final specifications and drawings, and developing a formal set of fabrication procedures including a detailed set of QC procedures.

During fabrication, integration into the detector, and detector installation into the cryostat, the FD2-VD PDS QC plan will be carefully followed, including incoming materials and other inspection reports, fabrication travelers, and formal test result reports entered into the DUNE QA/QC database.

Steps in this process are detailed below.

### 6.12.1 Design Quality Assurance

PD design QA focused on ensuring that the detector modules meet the following goals:

- Physics goals as specified in the DUNE requirements document;
- Interfaces with other detector subsystems as specified by the subsystem interface documents; and
- Materials selection and testing to ensure non-contamination of the LAr volume.

QA for full system prototypes is underway at multiple cryogenic test sites during the design to ensure the module design achieves requirements. In particular, a series of tests is ongoing at the CERN cold box at NP02, as detailed in Section 6.8.

In addition, the lifetime of all electrical components that will be located inside the cryostat must be established. Most electronics failure mechanisms can be characterized by a (positive) activation energy and are greatly suppressed at cryogenic temperatures. One notable exception is the hot electron effect [62] that can limit the lifetime of NMOS transistors. For this reason, all CMOS circuits must either be designed to mitigate this damage mechanism, or be operated at reduced bias voltage. Another exception is damage to components caused by material CTE mismatch; this mechanism is especially important for capacitors [68].

The circuit used to read out cathode-mounted PDS units includes a CMOS operational amplifier that may be difficult to qualify for resistance to the hot electron effect. High priority will be given to qualifying this part [69] or finding a replacement part. A number of capacitor failures have occurred during cold box tests. High priority will also be given to establishing a procedure for selecting and qualifying capacitors.

The PDS consortium will perform design and fabrication of components in accordance with applicable requirements as specified in the relevant LBNF-DUNE QA plan. If an institution (working under the supervision of the consortium) performing the work has a previously-existing documented QA program meeting PD consortium requirements, work may be performed in accordance with their own existing program. As part of the final design review and PRR process, the reviewers will be charged to ensure that the design demonstrates compliance with the goals above.

### 6.12.2 Production and Assembly Quality Assurance

The PDS will undergo a QA review for all components prior to completion of the design and development phase of the project. The FD2-VD Module 0 test will represent the most significant test of near-final PD components in a near-DUNE configuration, but additional tests will also be performed. The QA plan will include, but not be limited to, the following areas:

- Materials certification (in the Fermilab materials test stand and other facilities) to ensure materials compliance with cleanliness requirements;
- Cryogenic testing of all materials to be immersed in LAr, to ensure satisfactory performance through repeated and long-term exposure to LAr. Special attention will be paid to cryogenic behavior of fused silica and plastic materials (such as filter plates and wavelength-shifters), SiPMs, cables and connectors, optical fibers and connections, and all electronics and optics operated cryogenically. Testing will be conducted both on small-scale test assemblies (including small cryostats and dewars at institutions throughout the consortium) and full-scale prototypes (including mechanical testing at the large CDDF dewar at CSU, and operational testing at CERN cold boxes, ICEBERG R&D cryostat and electronics (ICEBERG) at Fermilab, and other large cryostats available to the consortium).
- Mechanical interface testing, beginning with simple mechanical go/no-go gauge tests, followed by installation into the FD2-VD Module 0 system, and finally full-scale interface testing of the PDS into the final pre-production TPC system models; and

- Full-system readout tests of the PD readout electronics, including trigger generation and timing, including tests for electrical interference between the TPC and PD signals.

Prior to beginning construction, the PDS will undergo a final design review and PRR, where the planned QA tests will be reviewed, and the system declared ready to move to the production phase.

### 6.12.3 Production and Assembly Quality Control

Prior to the start of fabrication, a manufacturing and QC plan will be developed detailing the key manufacturing, inspection, and test steps. The fabrication, inspection, and testing of the components will be performed in accordance with documented procedures. For example, vendors will provide the I-V curve of each SiPM at room temperature and test 10% of each lot (1 lot is about 100 flexi boards) at 77 K. The PDS consortium will test the boards before and after three thermal cycles and check the I-V curve in reverse bias and the single SiPM response to LED light of the flexi-boards.

The work will be documented on travelers and applicable test or inspection reports. Records of the fabrication, inspection and testing will be maintained. When a component has been identified as being in noncompliance to the design, the nonconforming condition shall be documented, evaluated, and dispositioned as: *use-as-is* (does not meet design but can meet functionality as it is), *rework* (bring into compliance with design), *repair* (will be brought to meet functionality but will not meet design), and *scrap*. For products with a disposition of accept, as is, or repair, the nonconformance documentation shall be submitted to the design authority for approval.

All QC data (from assembly and pre- and post-installation into the cryostat) will be directly stored to the DUNE database for ready access of all QC data. Monthly summaries of key performance metrics (to be defined) will be generated and inspected to check for quality trends.

Based on the FD1-HD PDS model, we expect to conduct the following FD2-VD PDS production testing:

Prior to shipping from assembly site:

- Dimensional checks of critical components and completed assemblies to ensure satisfactory system interfaces;
- Post-assembly cryogenic checkouts of SiPM mounting flex PCBs (prior to assembly into PD modules);
- Module dimensional tolerances using go/no-go gauge set;
- Room temperature scan of complete module using motor-driven LED scanner (or UV LED array), with the final electronics in place. The readout electronics for cathode-mount PD modules will be modified to allow them to be tested at room temperature; and
- DAQ tests using DAPHNE: communication check of a test pattern generated inside DAPHNE, confirmation of SiPM bias voltage settings, and a check of the digitization of known injected charges.

Following shipping to the US reception and checkout facility but prior to storage at SDWF:

- Mechanical inspection;
- Room temperature scan (using identical scanner to initial scan); and
- Cryogenic testing of completed modules (in CSU CDDF or similar facility).

#### 6.12.4 Installation Quality Control

PDS pre-installation testing will follow the model established for FD1-HD PDS. Prior to installation in the cathode and on the membrane walls, PD modules will undergo a room temperature scan in a scanner identical to the one at the PD module assembly facility and the results compared to results collected during fabrication. In addition, the module will undergo a complete visual inspection for defects and a set of photographs of selected critical optical surfaces taken and entered into the QC record database.

Following installation into the cathode, an immediate check for optical fiber continuity will be conducted. Spare fibers will be installed in every feedthrough, so if a bad fiber is found at this point, a spare will be used (before the cathode is raised). Following the mounting of the PD module on the membrane wall, an immediate check of cable continuity will be conducted. During this test, the PDS system will undergo a final integrated system check for expected warm response for all channels, electrical interference with other electronics, compliance with the detector grounding scheme, and power consumption.

### 6.13 Safety

Safety management practices will be critical for all phases of the FD2-VD PDS assembly, and testing. Planning for safety in all phases of the project, including fabrication, testing, and installation will be part of the design process. The initial safety planning for all phases will be reviewed and approved by safety experts and the DUNE safety management team in the Project Office as part of the Final Design Review and the PRRs. All component cleaning, assembly, testing, and installation procedure documentation will include a section on safety concerns relevant to that procedure and will also be reviewed during the design reviews.

Areas of particular importance to the FD2-VD PDS include:

**Hazardous chemicals and cleaning compounds:** All potentially hazardous chemicals used (particularly WLS chemicals such as PTP used in filter plate coating) will be documented at the consortium management level, with materials data safety sheets (MSDS) and approved handling and disposal plans in place.

**Class-4 laser hazards associated with the PoF installation:** Class 4 is the highest and most dangerous class of laser; by definition, a class 4 laser can burn the skin, or cause devastating and permanent eye damage as a result of direct, diffuse or indirect beam viewing. These lasers may ignite combustible materials, and thus may represent a fire risk. Class 4 lasers must be equipped with a key switch and a safety interlock. All class 4 laser operation, particularly

as part of installation testing when personnel from other subsystems will be present, will be documented at the consortium management level and activities will carefully coordinated with the safety experts.

**Liquid and gaseous cryogens used in module testing:** Full hazard analysis plans will be in place at the consortium management level for all module or module component testing involving cryogenic hazards, and these safety plans will be reviewed in the appropriate pre-production and production reviews.

**High voltage safety:** Some of the candidate SiPMs may require bias voltages above 50 VDC during warm testing (although not during cryogenic operation), which may be a regulated voltage as determined by specific laboratories and institutions. Fabrication and testing plans will demonstrate compliance with local HV safety requirements at the particular institution or laboratory where the testing or operation is performed, and this compliance will be reviewed as part of the standard review process.

**UV and light exposure:** Some QA and QC procedures used for module testing and qualification may require use of UV and/or VUV light sources, which can be hazardous to unprotected operators. Full safety plans must be in place and reviewed by consortium management prior to beginning such testing.

**Working at heights, underground:** Some aspects of FD2-VD PDS module fabrication, testing and installation will require working at heights or deep underground. Personnel safety will be an important factor in the design and planning for these operations, all procedures will be reviewed prior to implementation, and all applicable safety requirements at the relevant institutions will be observed at all times.

## 6.14 Organization and Management

The PD consortium benefits from the contributions of many institutions and facilities in Europe and North and South America. Table 6.10 lists the member institutions.

### 6.14.1 Consortium Organization

Table 6.10: PDS consortium institutions.

Member Institute	Country
Federal University of ABC <sup>†</sup>	Brazil
Federal University of Alfnas Poços de Caldas	Brazil
Centro Brasileiro de Pesquisas Físicas	Brazil
Federal University of Goiás	Brazil
Brazilian Synchrotron Light Laboratory LNLS/CNPEM	Brazil
University of Campinas <sup>†</sup>	Brazil
CTI Renato Archer	Brazil
Federal Technological University of Paraná	Brazil



Instituto Tecnológico de Aeronáutica <sup>†</sup>	Brazil
University Antonio Nariño <sup>†</sup>	Colombia
Universidad del Atlántico <sup>†</sup>	Colombia
University EIA <sup>†</sup>	Colombia
Universidad Sergio Arboleda	Colombia
Institute of Physics CAS	Czech Republic
Czech Technical University in Prague	Czech Republic
Laboratoire APC <sup>†</sup>	France
University of Bologna and INFN <sup>†</sup>	Italy
University of Milano and INFN <sup>†</sup>	Italy
University of Milano Bicocca and INFN <sup>†</sup>	Italy
University of Insubria and INFN	Italy
Laboratori Nazionali del Sud	Italy
University of Naples "Federico II" and INFN <sup>†</sup>	Italy
University of Ferrara and INFN <sup>†</sup>	Italy
INFN Padova	Italy
INFN Pavia <sup>†</sup>	Italy
Nikhef <sup>†</sup>	Netherlands
Universidad Nacional de Assunción <sup>†</sup>	Paraguay
Comisión Nacional de Investigación y Desarrollo Aeroespacial <sup>†</sup>	Perú
Pontificia Universidad Católica Perú	Perú
Universidad Nacional de Ingeniería <sup>†</sup>	Perú
Chung Ang University <sup>†</sup>	South Korea
CIEMAT <sup>†</sup>	Spain
IFIC (CSIC and University of Valencia) <sup>†</sup>	Spain
University of Granada <sup>†</sup>	Spain
Edinburgh University	UK
Argonne National Laboratory <sup>†</sup>	USA
Boston University <sup>†</sup>	USA
Brookhaven National Laboratory <sup>†</sup>	USA
University of California, Santa Barbara <sup>†</sup>	USA
Colorado State University <sup>†</sup>	USA
Fermilab <sup>†</sup>	USA
University of Illinois - Urbana-Champaign <sup>†</sup>	USA
Indiana University <sup>†</sup>	USA
University of Iowa <sup>†</sup>	USA
Lawrence Berkeley National Laboratory <sup>†</sup>	USA
University of Michigan <sup>†</sup>	USA
Northern Illinois University <sup>†</sup>	USA
South Dakota School of Mines and Technology <sup>†</sup>	USA
Stony Brook University <sup>†</sup>	USA
Syracuse University	USA

The PDS consortium has an organizational structure as follows:

- A consortium lead provides overall leadership for the effort and attends meetings of the DUNE Executive and Technical Boards.
- A deputy consortium lead, who provides support to the consortium lead and has specific responsibility for oversight of the FD2-VD PDS.
- Two technical leads, one with primary responsibility for mechanical systems, and one with primary responsibility for electronic and electrical systems. The technical leads provide technical support to the consortium lead and deputy, attend the Technical Board and other project meetings, oversee the project schedule and work breakdown structure (WBS), and oversee the operation of the project working groups.
- A Project Management Board composed by the project leads from the participating countries, the consortium leadership team and a few *ad hoc* members. The Board maintains tight communication between the countries participating in the consortium construction activity.

Below the leadership, the consortium is divided up into six working groups, each led by two or three working group conveners. Each working group is charged with one primary area of responsibility within the consortium, and the conveners report directly to the Technical Lead regarding those responsibilities. Responsible institutions have been identified for all aspects of PDS detector fabrication as indicated in Table 6.11. A Memorandum of Understanding has been signed by representatives of all participating institutions and international supporting funding agencies with commitments for delivery on schedule.

The working group conveners are appointed by the PDS consortium lead and technical lead; the structure may evolve as the consortium matures and additional needs are identified.

Table 6.11: PDS deliverables and responsible institutions

Subsystem	Description	Contributing Institutions
Photosensors (SiPM)	Validation, procurement and component testing for all cathode and membrane modules.	INFN-MiB, INFN-Bo, CIEMAT, IFIC, U. Granada, U. Prague
Dichroic Filters	Validation, procurement, primary wavelength shifting thin-film deposit, and component testing for all cathode and membrane modules.	INFN-MiB, INFN-Na, CIEMAT, IFIC, U. Granada, UNICAMP, UFABC, ITA
WLS Plates	Validation, procurement, groove milling and component testing for all cathode and membrane modules.	INFN-MiB, INFN-Na

X-ARAPUCA Mechanical Frames	Procurement, fabrication, construction.	CSU, Iowa, NIU
SiPM Mounting and Ganging Cold Electronics	Validation, procurement, cold FlexBoards fabrication and testing, cold FlexBoard Integration (SiPM mounting & ganging electronics) for all cathode and membrane modules.	UCSB, INFN-MiB
Signal-Shaping Cold Electronics	Component down-select, validation, procurement, cold motherboard integration (signal conditioning stage) of all cathode and membrane modules.	FNAL, UCSB, APC-Paris, LBL, U. Mich, Iowa, NIU
SoF: Electrical-to-Optical Conversion Cold Electronics	Component down-select, procurement, cold motherboard integration (SoF stage – analog signal transmitters and driver circuitry) for cathode modules.	FNAL, UCSB, APC-Paris
SoF: Optical-to-Electrical Conversion Warm Electronics	Component down-select, procurement, warm board fabrication, construction, integration (analog signal optical-to-electrical conversion stage) for cathode modules.	APC-Paris
Signal Digitization Warm Electronics	Warm board construction (signal digitizer, DAQ interface, online software) for cathode and membrane modules.	INFN-MiB, INFN-Bo, CIEMAT, IFIC, U. Granada, SBU
PoF: Warm Transmitter and Cold Receiver	PoF Laser Module down-select, procurement, Warm Laser Box fabrication and integration, Photovoltaic power converter design, selection, procurement, cold motherboard integration (PoF stage – power optical-to-electrical conversion) for cathode modules.	FNAL, UIUC, SDSMT
PoF: Step-Up Cold Electronics	PoF Voltage StepUp Cold Electronics.	FNAL, Iowa, LBL, BNL, INFN-Mi
Cathode PDS Fibers, Cables, Flanges	Procurement, fabrication, construction, integration of all fibers, flanges, and feedthroughs for cathode modules.	FNAL, NIU, UMich, SDSMT, SBU, CAU
Membrane PDS Fibers, Cables, Flanges	Procurement, fabrication, construction, integration of all cables, flanges and feedthroughs for membrane modules.	CIEMAT, IFIC
Cathode PDS Integration in Cathode systems	Procurement of electrical (cables & balun) and mechanical cathode mounting solutions, interface mechanics, integration of cathode modules.	BNL, FNAL, CSU, NIU, Iowa
Membrane PDS Support Structure Mechanics	Procurement and fabrication of cryostat mounting solutions, interface mechanics, integration of membrane modules.	CIEMAT

Cathode PDS Response and Monitoring System	LED flashers and diffuser procurement, fabrication, integration of fibers, flanges, and feedthroughs for cathode response and monitoring system kit.	ANL, CIEMAT, SDSMT
Membrane PDS Response and Monitoring System	Procurement, fabrication, construction, integration of all fibers, flanges and feedthroughs for the response and monitoring system kits.	ANL, CIEMAT
Detector Components Qualification in Cold	Test Stands (7) construction and operation: 1. Cold electronics components 2. SiPM cold FlexBoards 3. PoF and fibers components 4. Cold motherboards signal cables	BNL, SBU, INFN-MiB, UCSB, SDSMT, FNAL, NIU, UMich
Production QA	SiPM, WLS, Dichroic Filter.	INFN-Bo, INFN-FE, INFN-MiB, INFN-Na, CIEMAT, IFIC, U. Granada, UNICAMP
X-ARAPUCA Integrated Module and Electronics Assembly	Cathode and membrane modules.	NIU, CIEMAT, U. Granada
Production QC	Test Stand construction and operation: 1. X-ARAPUCA integrated cathode Modules 2. X-ARAPUCA integrated membrane Modules	1. CSU, FNAL, NIU 2. CIEMAT, INFN-Na, INFN-Pv, INFN-MiB

### 6.14.2 High-Level Schedule

Table 6.12 lists key milestones in the design, validation, construction, and installation of the FD2-VD PDS. This list includes external milestones indicating linkages to the main DUNE schedule (highlighted in color in the table), as well as internal milestones such as design validation and technical reviews.

In general, the flow of the schedule commences with a 60% design review based on module performance testing at PDS consortium test stands and integration testing at the CERN cold box. Additional similar design validation follows, leading to a final design review (FDR). Following the FDR, 16 X-ARAPUCAs and required electronics, cabling, fibers, and PD monitoring system components for FD2-VD Module 0 will be built, installed, and validated at CERN. Once the data from FD2-VD Module 0 have undergone initial analysis, production readiness reviews will be conducted and module fabrication will begin.

Some parts of the FD2-VD PDS system have a long procurement cycle and will require an ac-

celerated design review process, as shown in the milestone table. This is the case for the SiPMs, required in mid-2024 for flex PCB assembly.

Table 6.12: Photon Detection System Milestones

Milestone	Date
Ready to begin PDS install at CERN FD2-VD Module 0	Dec 2022
PDS installation complete at CERN FD2-VD Module 0	Mar 2023
<b>Ready for Final Design Review</b>	<b>Apr 2023</b>
Full Detection-to-Digitization Test complete	Oct 2023
Ready for SiPMs Production Readiness Review	Jan 2024
Ready for X-ARAPUCA Production Readiness Review	Mar 2024
Ready for Warm Electronics Production Readiness Review	May 2024
Ready for Fibers, Cables, and Feedthroughs Production Readiness Review	July 2024
<b>All Production Readiness Reviews complete</b>	<b>Aug 2024</b>
Warm electronics units construction complete	Feb 2026
Cold electronics (Sof & PoF) construction complete	Sep 2025
Cathode and Membrane X-ARAPUCA modules construction complete	May 2027
<b>Photon Detection System Ready for Installation</b>	May 2027
Membrane X-ARAPUCA and Response and Monitoring system installed	Oct 2027
Cathode X-ARAPUCA installed	Feb 2028
<b>Photon Detection System commissioned</b>	<b>May 2028</b>
<b>Photon Detection System project complete</b>	<b>Jul 2028</b>

A more detailed schedule for production and installation of the FD2-VD is found in Figure 6.36.

### FD2 PDS Summary Schedule

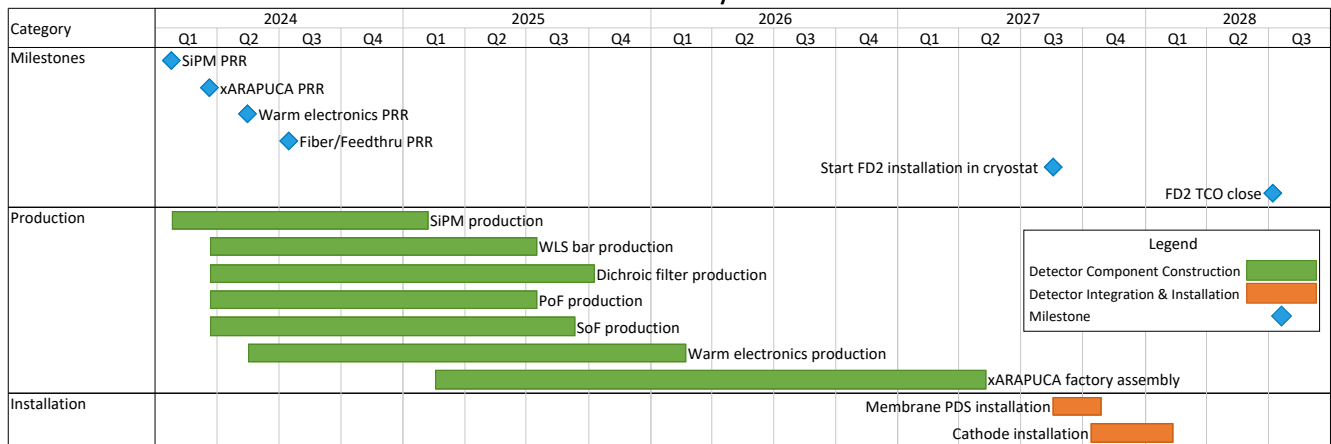


Figure 6.36: Key PDS milestones and activities toward the FD2-VD in graphical format (Data from [53]).

# Chapter 7

## Trigger and DAQ

### 7.1 Introduction

The trigger and data acquisition (DAQ) system is responsible for receiving, processing, and recording data from the DUNE experiment. For the vertical drift detector module (FD2-VD) this system:

- provides timing and synchronization to the detector electronics and calibration devices;
- receives and buffers data streaming from the time projection chamber (TPC) top and bottom electronics and the photon detection system (PDS);
- extracts information from the data at a local level to subsequently form s;
- builds s, defined as a collection of data and metadata from selected detector space-time volumes corresponding to a trigger decision;
- carries out additional data reduction and compression as needed; and
- relays trigger records to permanent storage.

The main challenge for the DUNE TDAQ lies in the development of effective, resilient software and firmware that optimize the performance of the underlying hardware. The design is driven not only by data rate and throughput considerations, but also—and predominantly—by the stringent uptime requirements of the experiment.

The TDAQ is subdivided into a set of subsystems. Figure 7.1 shows the different subsystems and their relationships. All subsystems rely on the functionality provided by the *DAQ control, configuration and monitoring subsystem (CCM)* and *data quality monitoring (DQM)*, that is the glue of the overall TDAQ, transforming the set of components into a coherent system. The *DAQ trigger subsystem (DAQ TS)* and *Data filter* are in charge of the selection and compression of data. The *Dataflow* subsystem provides the communication layer to exchange data (i.e., it is used by the other subsystems intersecting it in the diagram). In addition, it implements the data collection functionality, i.e., the logic for building trigger records as well as the organization of data into files. The *DAQ readout subsystem (DAQ RO)* receives the data streams from the TPC and PDS,

processes them to extract information for the trigger, and buffers data while the trigger is forming a decision. The *DUNE timing and synchronization subsystem (DTS)* is in charge of distributing the clock, synchronizing the s, as well as applying timestamps to hardware signals that may be used for triggering, such as calibration pulses. The *Detector electronics software* is not part of the TDAQ responsibility: it is shown in the diagram to indicate that detector experts will develop the software to configure, control, and monitor the electronics using the tools provided by the *CCM* subsystem.

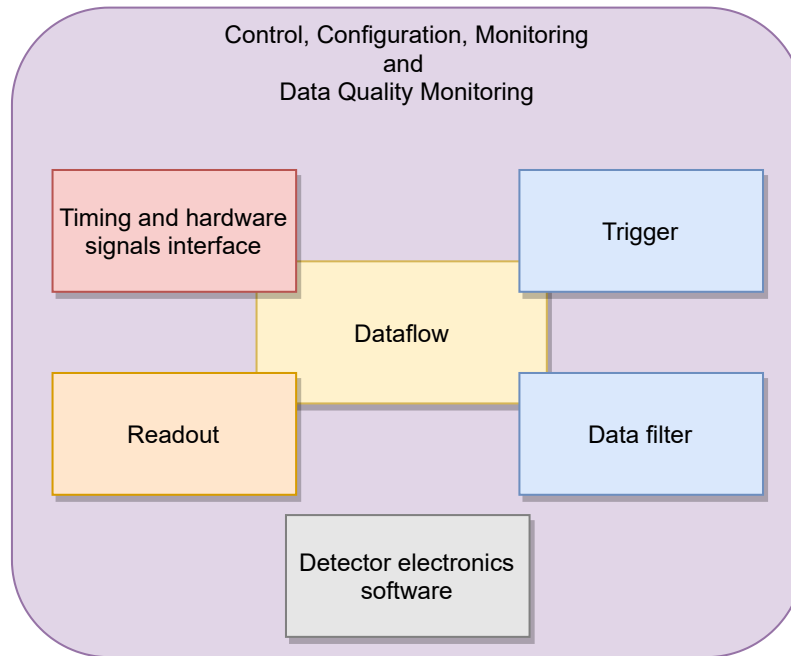


Figure 7.1: Diagram showing the relationships between TDAQ subsystems. Overlaps indicate dependence on another subsystem, e.g., readout depends on the software communication layer provided by dataflow. All subsystems rely on control, configuration and monitoring libraries and framework provided by CCM. It also shows, in grey, the detector electronics software, which is not part of TDAQ but will be developed fully embedded into the CCM environment.

The physical components of the TDAQ are primarily commercial off-the-shelf (COTS) components—servers, switches, fibers, etc.—as shown in Figure 7.2. A high performance Ethernet network interconnects all the elements and allows them to operate as a single, distributed system. At the output of the TDAQ the high-bandwidth Wide Area Network (WAN) allows the transfer of data from the Sanford Underground Research Facility (SURF) to Fermi National Accelerator Laboratory (Fermilab).

The TDAQ for the whole of DUNE is designed and developed coherently by a joint team for both far detector (FD) and near detector (ND). The TDAQ systems for the ND and the different FD modules differ only in minor details so as to support the electronics and the data selection criteria for each.

In particular, the FD2-VD module TDAQ system will be very similar to that for the horizontal drift detector module (FD1-HD) detector module, but with customizations for the top and bottom anode planes and the photon detector (PD) electronics readout, as well as for the data selection



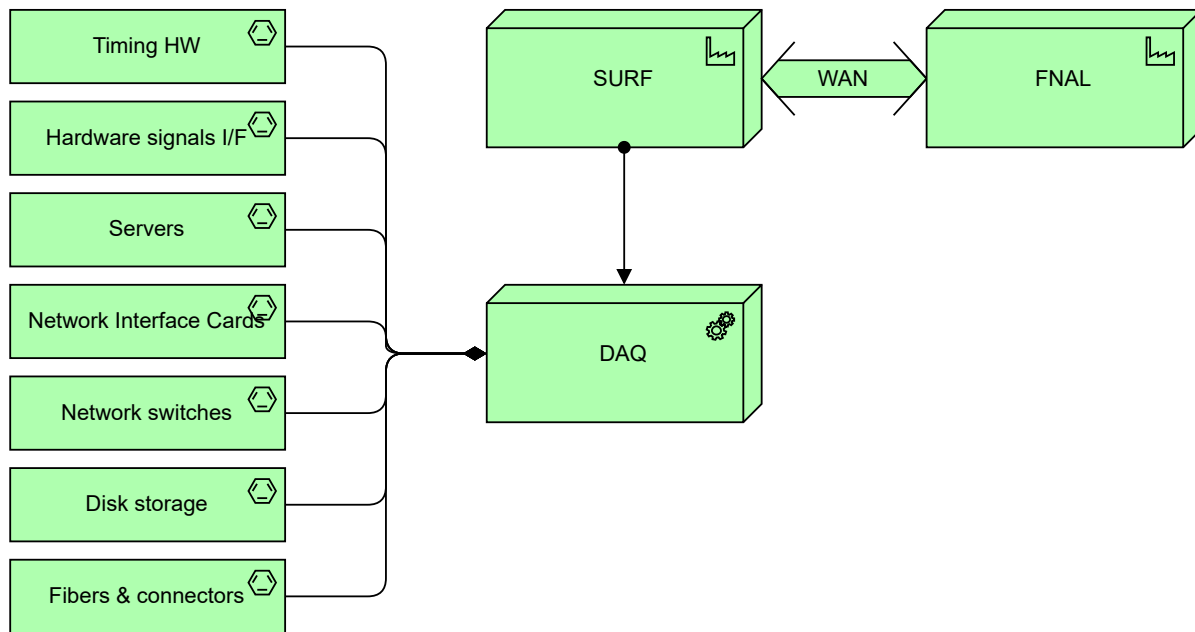


Figure 7.2: Physical view diagram of the TDAQ system. At SURF, the hardware components are distributed across the detector caverns and the surface DAQ room. The TDAQ data are transferred to Fermilab over a WAN connection.

algorithms, which will be tuned to the module's geometry. The main TDAQ features for the FD are described in Volume IV of the DUNE [84].

The chapter begins with an overview of the DAQ design requirements (Section 7.2) that the design must meet and specifications for interfaces between the DAQ and other DUNE FD systems. Subsequently, Section 7.4, which makes up the majority this chapter, describes the design of the FD DAQ in greater detail. Section 7.5 describes design validation efforts to date, as well as future design development and validation plans. At the center of these efforts is the DAQ system (described in Section 7.5.2), which has demonstrated several key aspects of the DUNE FD DAQ design and continues to serve as a platform for further developing and validating the final design. The chapter finishes with Section 7.8, which detail the management of the DAQ project, including the schedule for completing the design, production, and installation of the system, as well as risk considerations.

## 7.2 Requirements and Specifications

The specifications for the TDAQ derive from higher-level requirements [14]. Table 1.1 lists the specifications that are critical to the FD performance, including two relating to the TDAQ (FD-22 and 23). These two and the additional TDAQ specifications are listed in Table 7.1. Note that the differences in TDAQ requirements due to detector configuration and technology between the FD1-HD and FD2-VD are very limited, amounting only to a slightly larger total data rate of 1.8 TB/s for FD2-VD as opposed to 1.4 TB/s for FD1-HD, and the necessity of incorporating the . The requirement for data rate to tape of 30 PB/year is across all FD modules.

Table 7.1: TDAQ specifications

Label	Description	Specification (Goal)	Rationale	Validation
FD-22	Data rate to tape	< 30 PB/year	Cost. Bandwidth.	ProtoDUNE
FD-23	Supernova trigger	Efficiency for a SNB producing at least 60 interactions with a $\nu$ energy > 10 MeV in 12 kt of active detector mass during the first 10 s of the burst.	> 95% efficiency for SNB within 20 kpc	Simulation and bench tests
FD-DAQ-1	DAQ readout throughput: The DAQ shall be able to accept the continuous data stream from the TPC and PDs.	1.8 TB/s per FD module	Specification from TPC and PDS electronics	Modular test on ProtoDUNE; overall throughput scales linearly with number of APAs
FD-DAQ-2	DAQ storage throughput: The DAQ shall be able to store selected data at an average throughput of 10 Gb/s, with temporary peak throughput of 100 Gb/s.	10 Gb/s average storage throughput; 100 Gb/s peak temporary storage throughput per single phase detector module	Average throughput estimated from physics and calibration requirements; peak throughput allowing for fast storage of SNB data ( $\sim 10^4$ seconds to store 180 TB of data).	ProtoDUNE demonstrated steady storage at $\sim 40$ Gb/s for a storage volume of 700 TB. Laboratory tests will allow to demonstrate the performance reach.
FD-DAQ-3	DAQ readout window: The DAQ shall support storing triggered data with a variable size readout window, from few $\mu$ s (calibration) to 100 s (SNB), with a typical readout window for triggered interactions of 4.25 ms.	$10 \mu$ s < readout window < 100 s	Storage of the complete dataset for up to 100 s is required by the SNB physics studies; the typical readout window of 4.25 ms is defined by the drift time in the detector; calibration triggers can be configured to read out data over much shorter time intervals.	Implementation techniques to be validated on the ProtoDUNE setup and in test labs.

FD-DAQ-4	<p>Calibration trigger: The DAQ shall provide the means to distribute time-synchronous commands to the calibration systems, in order to fire them, at a configurable rate and sequence and at configurable intervals in time. Those commands may be distributed during physics data taking or during special calibration data taking sessions. The DAQ shall trigger and acquire data at a fixed, configurable interval after the distribution of the commands, in order to capture the response of the detector to calibration stimuli.</p>	<p>Calibration is essential to attain required detector performance comprehension.</p>	<p>Calibration techniques for these purposes have been operated successfully in MicroBooNE and ProtoDUNE.</p>
FD-DAQ-5	<p>Data record: Corresponding to every trigger, the DAQ shall form a data record to be transferred to offline together with the metadata necessary for validation and processing.</p>	<p>Needed for offline analysis.</p>	<p>Common experimental practice.</p>
FD-DAQ-6	<p>Data verification: The DAQ shall check integrity of data at every data transfer step. It shall only delete data from the local storage after confirmation that data have been correctly recorded to permanent storage.</p>	<p>Data integrity checking is fundamental to ensure data quality.</p>	
FD-DAQ-7	<p>High-energy Trigger: &gt;100 MeV The DAQ shall trigger and acquire data on visible energy deposition &gt;100 MeV. Data acquisition may be limited to the area in which activity was detected.</p>	<p>Driven by DUNE physics mission.</p>	<p>Physics TDR. 100 MeV is an achievable parameter; lower thresholds are possible.</p>

FD-DAQ-8	Low-energy Trigger: The DAQ shall trigger and acquire data on visible energy deposition $> 10$ MeV of single neutrino interactions. Those triggers will normally be fired using a pre-scaling factor, in order to limit the data volume.	$>10$ MeV	Driven by DUNE physics mission.	Physics TDR. 10 MeV is an achievable parameter; lower thresholds are possible.
FD-DAQ-9	DAQ deadtime: While taking data within the agreed conditions, the DAQ shall be able to trigger and acquire data without introducing any deadtime.	(Zero deadtime)	Driven by DUNE physics mission.	Zero inter-event deadtime is achievable. A small deadtime would not significantly compromise physics sensitivity.

Putting these into context, these specifications can be viewed as falling into four categories:

- Synchronization:
  - The timing system shall provide a common timestamp to all FD2-VD detector systems.
  - It shall be able to align the timestamp across the FD2-VD TPC and PDS to better than 10 ns at all times (set by PDS).
  - It shall be able to distribute synchronization, calibration, and control commands to FD2-VD systems.
- Data selection:
  - The FD shall be  $>90\%$  efficient for any interaction that leaves  $>100$  MeV of visible ionization energy inside the fiducial volume.
  - The DAQ TS shall be capable of recognizing a supernova neutrino burst (SNB) from a nearby supernova based on a threshold of more than 60 interactions within 10 seconds, with neutrino energy deposition above 10 MeV each, with an efficiency  $>95\%$ .
  - The FD shall have high efficiency for any interaction leaving  $<100$  MeV of visible ionization energy inside the fiducial volume, and for single interactions with visible energy deposit  $>10$  MeV. The lowest-energy of these may be pre-scaled.
- Data throughput:
  - The TDAQ shall be able to receive digitized data from the detector electronics ( $\approx 1.8$  TB/s) and buffer them for up to 10 seconds awaiting a trigger decision.
  - It shall be able to store data for up to one week without interrupting the DAQ, in case of delays in the data transfer from SURF to Fermilab.
  - It shall provide enough disk I/O capacity for driving the WAN link at 100 G/s.
  - It should be able to transfer SNB trigger records ( $\approx 180$  TB) from the FD2-VD detector cavern to the DAQ components on the surface within one hour ( $\approx 400$  Gb/s).

- Uptime: Each FD module shall have an uptime of at least 95%, and the FD as a whole shall have an uptime of at least 98%, during which at least one module is operational. Since a few days per year of downtime for infrastructure maintenance cannot be avoided, and individual hardware failures (electronics, servers, disks, ...) may occur, this translates into a very strong requirement for the TDAQ. The TDAQ shall operate continuously, dynamically adjust to changing conditions, tolerate faults, and recover from errors autonomously.

The electronics parameters essential for dimensioning the FD2-VD TDAQ system are shown in Table 7.2. The individual TDAQ component counts for the FD2-VD are shown in Table 7.3.

Table 7.2: Summary of detector parameters driving the DAQ design.

Parameter	Value
TPC channels	491520
TPC channel count per charge-readout plane (CRP)	3072
TPC top electronics 40 G links	320
TPC bottom electronics 10 G links	960
TPC analog-to-digital converter (ADC) sampling rate	1.953125 MHz
TPC ADC dynamic range	14 bits
PDS channels	1280
Max localized event record window (1 drift length)	4.25 ms
Extended event record window	100 s
Maximum size of TPC localized event record (uncompressed)	8 GB
Full size of TPC extended event record (uncompressed)	180 TB

Table 7.3: TDAQ component counts for FD2-VD. All servers are interconnected via 10G/100G Ethernet network.

Parameter	Count
Clock speed	62.5 MHz
Timing endpoints	$\approx 120$
Readout switches (10G/100G)	20
Readout switches (40G/100G)	8
TPC readout cards	80+80
PDS readout cards	4
Readout servers	84
Trigger servers	20
Data collection, storage servers	8
Data filter servers	20
TDAQ control and monitoring servers	25

## 7.3 Interfaces

The overview diagram in Figure 7.3 shows the main external interfaces of the TDAQ, with the external systems depicted in grey. Brief descriptions of these follow; they are detailed in referenced interface documents. The components' external interfaces are summarized in Table 7.4.

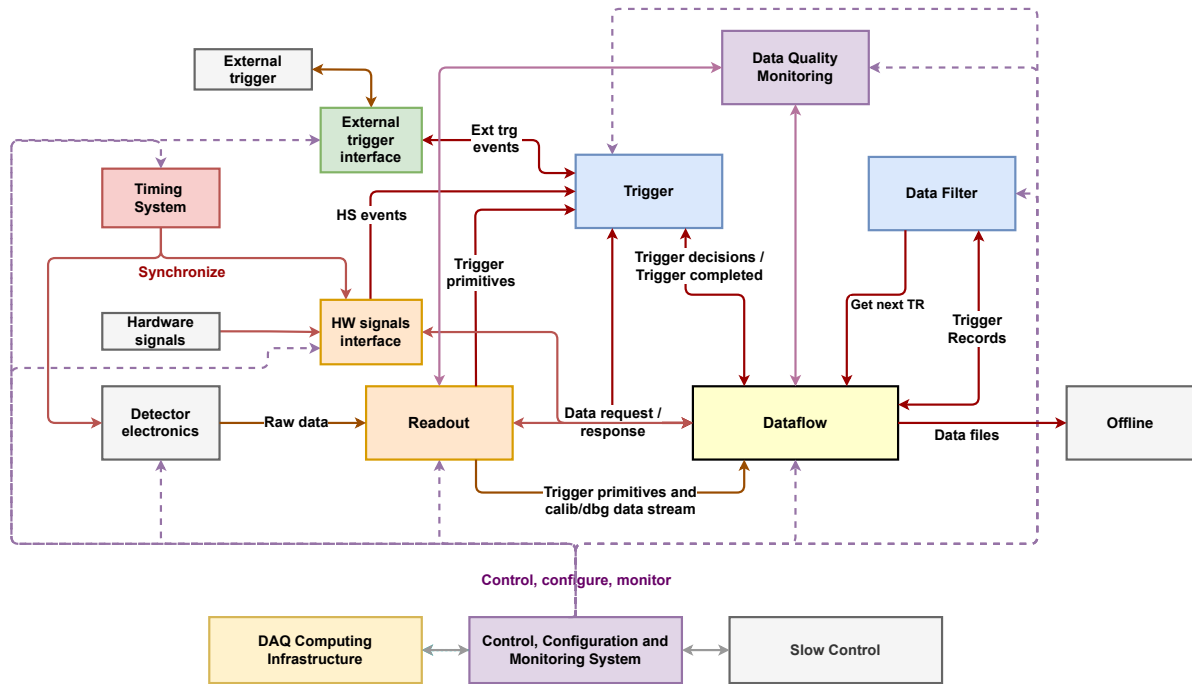


Figure 7.3: Conceptual overview of TDAQ system functionality for a single FD module. External systems are depicted in grey while the TDAQ subsystems are represented using the same color scheme as in Figure 7.1. The external interfaces are described in Section 7.3 while the flow of data and messages is described in Section 7.4. Acronyms used in the figure: HW=hardware, HS=hardware signal, TR=trigger record, ICT=information and communication technologies

**TPC Electronics and Photon Detection** The DAQ readout subsystem (DAQ RO) (Section 7.4.2) receives raw data from the various detector electronics devices. The interface to the top TPC electronics is described in [57] and the interface to the bottom TPC electronics is in [94]. The interface to the PDS electronics is in [95]. These documents describe the physical interface of the electronics to the DAQ system through optical links, as well as the expected data formats and transfer protocols.

**Calibration** The hardware signals interface injects timestamped hardware signals, e.g., from calibration systems, into the TDAQ data selection chain. The interface to calibration systems is through the DTS and the interfaces are described in [96].

**External Triggers** The DAQ trigger subsystem (DAQ TS) (Section 7.4.3) receives external timestamped trigger messages (e.g., from other FD modules) to initiate data collection irrespective of any activity inside the module.

**Computing** The data collection (Section 7.4.4) interfaces to the offline computing, for the purpose

of transferring raw data and metadata for permanent storage. The interfaces are described in [97].

**Slow Control** The DAQ relies on the Slow Control system to control and monitor the power distribution units in the server racks and to provide a user interface to remotely turn on/off computers (in addition to the network-based interface). Furthermore, DAQ and Slow Control will exchange information about the status of different components. Details of the interaction are still to be worked out, but will occur purely on a software-data-exchange basis.

**Information and Communication Technologies** The DAQ transfers a large amount of data across networks within clusters of computers in certain locations, between computer cluster locations, and between the detector site and Fermilab central computing. The responsibilities of the DAQ and of Fermilab Networking are described in [98].

Table 7.4: Brief description of TDAQ components' external interfaces. References to interface documents are given in the text.

TDAQ Component	Interface description
Timing	1000-BaseBX single mode fiber with custom protocol
Readout - TPC bottom electronics	10 G Ethernet, UDP/IP protocol
Readout - TPC top electronics	40 G Ethernet, UDP/IP protocol
Readout - PDS	10 G Ethernet, UDP/IP protocol
Trigger - external trigger sources/output	Ethernet I/O of timestamped signals from calibration devices, or from/to other FD modules or SNEWS
Transient data store - offline computing	WAN ethernet connection for transfer of HDF5 raw data files. HDF5 raw data format specifications.
CCM - offline computing	databases with the archive of run configurations and conditions
CCM - slow control	Ethernet based inter process communication to exchange status information
CCM - detectors software	Software libraries and tools for the implementation of the control, configuration and monitoring of the detector electronics

## 7.4 Trigger and DAQ (TDAQ) System Design

The FD TDAQ system is physically located at the FD site, SURF. It uses space and power in each underground detector cavern (on top of the cryogenics mezzanine), and above-ground, in the main communications room (MCR) within the Ross Dry building. The upstream part of the system, responsible for raw detector data reception, buffering, pre-processing, and triggering, resides underground. The back-end, which is responsible for trigger-records-building, data storage, and data filtering, resides at the surface. Some elements of the TDAQ span both locations, i.e., the timing, control, configuration, and monitoring systems (DTS and CCM). See Section 9.3.3 for information on the electrical infrastructure. The connectivity between all TDAQ elements is provided through a distributed and redundant 10G/100G/400G Ethernet network, which is outside the scope of the

DAQ consortium. The link between upstream and back-end elements is implemented over the redundant dual-fiber run in the Ross and Yates shafts described in Section 9.3.3, ensuring the operation of the TDAQ system even in the event of accidental damage to one of the two runs. Data flow through the DAQ from upstream to the back-end and then offline. Most raw data are processed and buffered underground, thus controlling consumption of available data bandwidth to the surface.

All the detector modules and their subsystems are synchronized and timed against a common global clock, provided by the DTS. Cross-module communication and communication to the outside world for data selection (trigger) purposes is facilitated through an external trigger interface (ETI).

The TDAQ system must acquire data from the both the TPC and the PDS in order to satisfy the requirements placed on it that derive from the experiment's physics objectives. Ionization charge measurement by the TPC for any given activity in the FD requires a nominal recording of data over a time window determined by the drift speed of the ionization electrons in liquid argon (LAr) and the detector dimension along the drift direction (6.5 m). Given a target drift E field of 450 V/cm, the time window is set to 4.25 ms. The activity associated with beam, cosmic rays, and atmospheric neutrinos is localized in space and particularly in time; SNB neutrinos are associated with activity that extends over the entirety of the detector and lasts between 10 and 100 s.

The detector data flow from the electronics output links, on top of the cryostat, through the TDAQ system to permanent storage at Fermilab. Two stages of data selection allow reduction of the overall data volume from  $\sim 1.8$  TB/s produced by the FD2-VD module to  $\sim 30$  PB/year for all FD modules: triggering the collection of data only for interesting detector regions and time windows, and applying data compression algorithms. Data selection strategies are defined in close collaboration with the DUNE physics groups, the offline processing team, and the detector subsystem and calibration experts.

Figure 7.3 depicts the flow of data within the TDAQ system, left to right. Raw data produced by the detector electronics is streamed into the readout (DAQ RO). Here data are processed to produce information, and stored for up to 10 s. The trigger subsystem (DAQ TS) receives trigger primitives, timestamped hardware signal events, and external trigger events, and combines this information to form a trigger decision. Trigger decision messages containing a list of time windows and detector locations are forwarded to the data collection component and an acknowledgment is sent back; data collection is in charge of requesting the relevant data from the DAQ RO and the DAQ TS, forming trigger records, and storing them to disk. Trigger records are dispatched by data collection to the data filter for further data reduction. The data filter returns the modified trigger records to the data collection component for both storage and transfer to the offline computing system at Fermilab. The whole DAQ process is orchestrated by the CCM; the quality of the raw data is continuously monitored by the DQM (Section 7.4.6).

The TDAQ can be partitioned—that is, multiple instances of the system can run on physically distinct regions of the detector, with each instance referred to as a . This allows, for example, part of the module to be calibrated while other parts continue to collect physics data, maintaining the high uptime requirements of the system.

In the following sections the different TDAQ components shown in Figure 7.3 and the external



TDAQ interfaces are described in more detail.

### 7.4.1 Timing and Clock Distribution

The DUNE timing and synchronization subsystem (DTS) provides services to allow the accurate synchronization of sampling and data processing for all elements of the FD. The primary function is the distribution of clock and synchronization to front-end (FE) electronics, such that every data sample may be tagged with a 64-bit timestamp. These DTS timestamps, which are unique across the lifetime of the experiment, are used for data processing and event building within the TDAQ, and are included within the recorded data sample to support event reconstruction within and across detector modules, and the correlation of DUNE data with external events (e.g., beam spills or astronomical observations).

All the electronics for the FD2-VD module are synchronized to a common clock, derived from a single Global Positioning System (GPS)-disciplined source. Individual detector channels are synchronized to a fraction of the timestamp granularity. Initial bench tests show this to be  $<1$  ns, and the expected final synchronization will be determined during the tests. Due to the extended physical size of the DUNE far detector modules, consistency of timing alignment is ensured by both hardware- and software-based feedback loops, calibrating propagation delays on the timing links. The requirement on the absolute accuracy of timestamps with respect to is one microsecond, though in practice is expected to be much better.

The consistent timing synchronization of all detector channels is continuously monitored and checked at multiple levels: within the timing distribution systems themselves; within the DAQ system against calibration signals; and offline against physics signals. As critical infrastructure for data-taking, the timing distribution systems are designed for robustness and fault-tolerance. All electronic components of the system for which failure would affect a large detector volume have redundant components contained in separate crates with redundant power and network links. Two independent GPS systems are used, with antennae at the Ross and Yates shaft entrances respectively, and are able to operate in a hot-spare configuration.

The DTS provides a common interface to timing “endpoints” in the readout systems. The endpoints provide a 62.5 MHz master clock and 64 bit timestamp. Synchronization information is transmitted on single-mode optical fibers. Passive optical splitters are used to provide the ability to drive multiple timing endpoints from a single fiber. Passive optical combiners allow the use of two independent timing master systems. One timing master system is in operation at any one time, with the other available as a redundant hot-spare. The DTS measures, and compensates for, the propagation delays from timing master to endpoints in the readout systems.

The bottom drift electronics ( $\mu$ ), and the PDS, have the same interface to the timing system as the corresponding systems in FD1-HD module. The top drift electronics were designed with an embedded timing distribution system based on the IEEE-1588/White Rabbit (WR) standard, which, starting from a 10 MHz clock and 1 pulse-per-second hardware signals distributes a timestamp to the digitization units in the Micro Telecommunications Computing Architecture ( $\mu$ TCA) crates (Section 4.3). Tests in the WR lab at European Laboratory for Particle Physics (CERN) have shown that it is possible to synchronize a WR “island” from the DTS. Tests at larger scales will be done with the FD2-VD cold boxes and Module 0 detectors.

## 7.4.2 Readout

The DAQ readout subsystem (DAQ RO) is responsible for receiving data from the electronics. It interfaces with the top and bottom drift TPC electronics and the PDS electronics via optical fibers that connect the detector electronics on the cryostat roof with a set of Ethernet switches on the cryogenics mezzanine, inside the DAQ barrack. The switches aggregate traffic on 100G Ethernet links which are fed into the DAQ front-end (FE) readout units.

Each top-drift electronics charge readout (CRO)  $\mu$ TCA crate aggregates raw data from twelve advanced mezzanine cards (AMCs) into a 40 Gbit/s optical link to the DAQ, for a total of 768 CRPs channels per crate, and of 320 links to the DAQ FE readout. The typical effective throughput of a data link is expected to be around 22 Gbit/s.

Each bottom-drift electronics warm interface boards (WIBs) sends data via two 10 Gbit/s optical links to the DAQ. A total of 960 links is expected; the typical effective throughput of a data link is around 7.2 Gbit/s.

As the digitization rates of the charge electronics are directly streamed to readout, the rate of events does not change the bandwidth necessary between the electronics and the readout boards; the number of links is set to allow some redundancy in case of transmission failures.

Each PDS electronics board sends data on one 10 Gbit/s optical link to the DAQ. A total of 40 links is expected; the typical effective throughput of a data link is estimated to be around 3.5 Gbit/s.

As the PDS electronics include zero-suppression, more overhead is allocated for the bandwidth of the system to account for variations in the event rate.

The basic component of the readout subsystem is a , of which there are 84 responsible for reading out FD2-VD. A DAQ readout unit consists of a high-end server hosting two e cards which provide the high-bandwidth data connection to the FE. Each DAQ readout unit processes and buffers the data coming in from a portion of the detector (two CRPs or 25% of the PDS).

Figure 7.4 shows an expanded view of the readout subsystem in the context of the overall DAQ. The DAQ FE readout units store the raw data stream from detectors in a circular memory buffer after data checking for at least 10s, and perform a first stage of preprocessing. DAQ readout units respond to data requests from the event builder by providing the data fragments corresponding to the selected from the temporary memory buffers.

In the event of an SNB trigger firing, the DAQ readout units will stream the content of the temporary memory buffer to local storage for a total duration of 100 second. Afterwards, each DAQ readout unit makes the stored SNB record available to the data collection system for transfer to the surface storage.

DAQ readout units perform the first stage of trigger processing on incoming data to generate local elementary trigger information (see trigger primitives in Section 7.4.3), to minimize the raw data transfer over network. The trigger primitives are streamed to both the DAQ TS for further

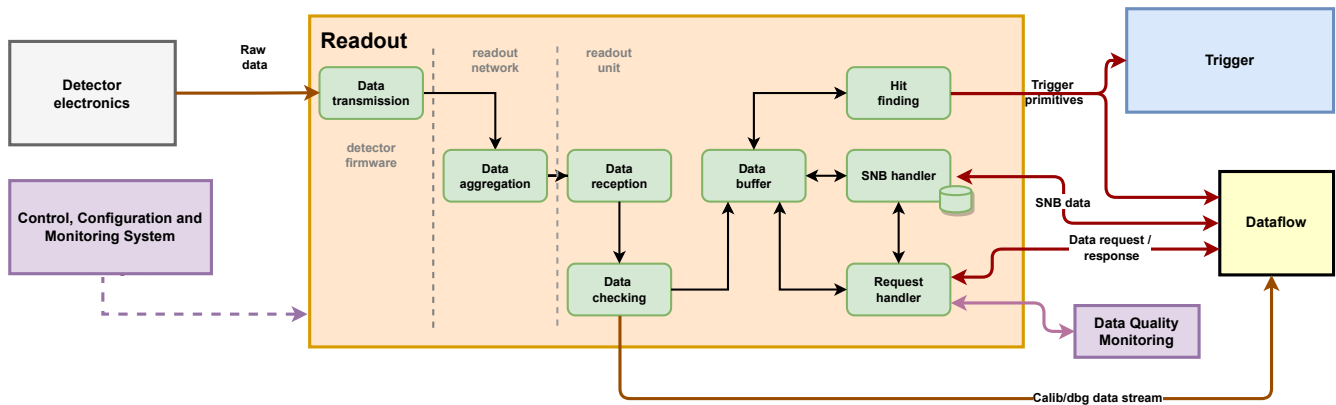


Figure 7.4: Diagram of the readout portion of the DAQ, showing the path of data movement and buffering, including SNB data.

processing, and to data collection for semi-permanent storage.

In addition to handling the main data path, DAQ FE readout provides extra functions to support debugging, calibration and quality assessment. Specifically it:

- supports the BDE calibration with a dedicated raw data stream during calibration cycles;
- generates a reduced raw data stream for a configurable subset of channels, on demand, for debugging purposes; and
- samples and extracts basic DQM information.

At a prototype implementation of the readout subsystem using a simplified communication protocol and custom Front-End Link eXchange (FELIX) PCIe cards was demonstrated, and is described in [7].

The need of finding a common solution for reading out all the different detector electronics (including the TDE), justified a change in the implementation choice for the readout. Ethernet and the UDP/IP protocol are used as the underlying technologies for this change. Network switches and 100 G smart network interface cards are the hardware components that allow to implement it. The switches multiplex several FE data streams—320x40 G links for the TDE and 960x10 G links for the BDE—into 80 100 G links for each type of that are fed into the readout units. Thanks to recent technology advances it is possible to use exclusively commercial components for the implementation of this subsystem, thus reducing the complexity of (and the risks in) this area of the TDAQ.

From a design point of view the system remains largely unchanged and much of the code developed for the FELIX based solution can be reused. In order to speed-up the evaluation of the readout implementation two prototypes have been developed, with a different balance of resources usage on the server or network interface cards. Those are being finalized and tested in a laboratory environment. The first integration with the BDE and TDE are planned before the TDAQ final design review, while the integration with the PDS electronics will occur later. During the transition

phase the existing FELIX based solution will continue being supported.

### 7.4.3 Trigger and Data Filter

#### 7.4.3.1 Strategies for Data Retention

This section summarizes the strategies that have been devised to maximize the retention of interesting data while respecting the data volume that can be permanently stored long-term for the DUNE FD ( $\sim 30$  PB/y). The goal is to be as inclusive as possible; at high energies ( $> 100$  MeV) it is important to accept all possible events with as high an efficiency and as wide a region-of-interest () in channel and time space as possible, regardless of event type. As energies approach 10 MeV, when radiological backgrounds (including neutron captures,  $^{42}\text{Ar}$ , and  $^{39}\text{Ar}$  pileup) become dominant, the system should be semi-inclusive, leveraging the topological capabilities of the TPC data to provide some discrimination of low-energy physics signals.

To facilitate partitioning, the DAQ trigger and data filter can be instantiated several times, and multiple instances can operate in parallel. Within any given DAQ partition, the DAQ trigger and data filter will also be informed and aware of current detector configuration and conditions and apply certain masks and mapping on subdetectors or their fragments in its decision making. This information is delivered by the CCM system.

All digitized charge collection data are sent to the readout subsystem and processed. For each strip on a CRP layer, a hit-finding algorithm allows identification of activity above the electronic noise; the threshold and time above threshold will be configurable. With the expected noise of the TPC electronics, the hit-finding threshold is expected to be such that hits will be generated for a large fraction of the  $^{39}\text{Ar}$  decays; the spectrum endpoint is at 0.5 MeV. Every hit generates a so-called trigger primitive.

Similarly, PDS electronics boards send waveform data for any channel that passed an internal threshold; trigger primitives are also formed from these data.

The trigger primitives serve two purposes:

- They are the basic elements used to form a trigger decision in the TDAQ system.
- They are stored as unbiased (at the “event” level) summary information that can be used for trigger, calibration, low-energy physics studies, etc.

To provide good sensitivity to different track topologies, each trigger primitive contains information such as the time-over-threshold of the waveform, its peak, and its total charge, as well as the timestamp of the start of the waveform. To date, our TPC trigger studies have been done using collection view only; exploitation of induction views is under development but is not seen as needed to satisfy any of DUNE’s triggering requirements.

Trigger primitives generated from charge collection channels and the PDS will be stored on disk by the TDAQ system. This data set is very important for carrying out trigger studies but can also be used for calibration purposes, as well as fast data analysis. After compression and minimal clean-up, it is estimated that a few PB/year will be sufficient to store them. It is thus an option for

DUNE to not only store the trigger primitives temporarily (a few months) for specific studies, but to make them part of the data that will be stored permanently. This data stream is particularly interesting in view of its role in potentially extending the low-energy physics reach of DUNE beyond its core program; it will also contain summary information for individual interactions with very low visible deposited energy. Depending on the achieved signal-to-noise (S/N) on the collection strips, the trigger primitive threshold is expected to be around 250 keV.

For triggering purposes, the trigger primitives are the basic elements used by the TDAQ to form a trigger record and initiate the collection and storage of raw waveform data. The system takes trigger primitives generated locally and looks for clusters in time and space. These clusters represent what is called “trigger activity.” Clusters of trigger activity are then passed to algorithms downstream, which determine whether any particular set of trigger activity clusters should be promoted to a . Trigger candidates then are sent to trigger decision logic, which apply criteria that include both configuration parameters (e.g., which triggers are accepted in this data run) and dynamic decisions (e.g., does a TPC trigger candidate come after an existing PDS trigger candidate?). The data selection work flow is shown in Figure 7.5.

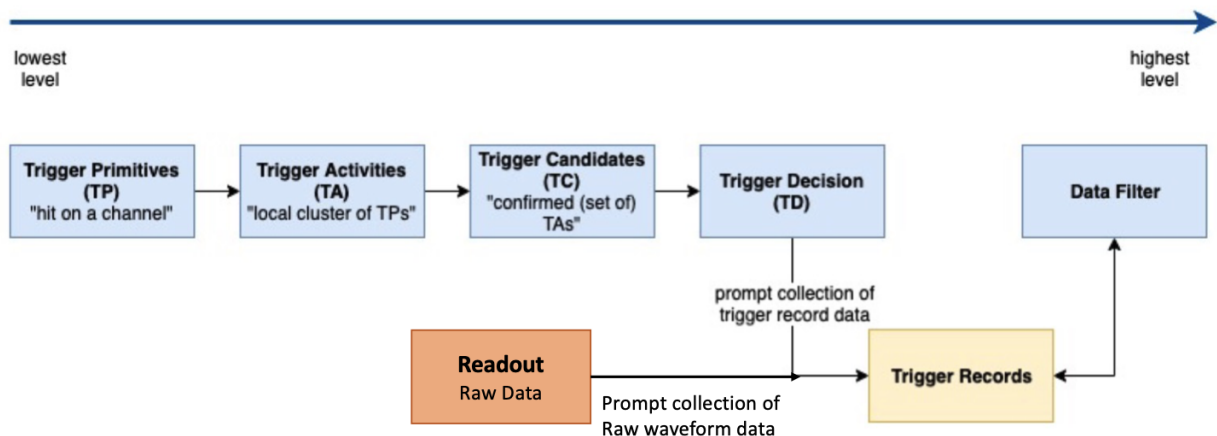


Figure 7.5: The data selection work flow. The trigger system is responsible for the decisions and algorithms in the blue boxes, and the dataflow system is responsible for drawing raw data and trigger system output into the trigger records.

There are two different raw data collection modes foreseen for the DUNE FD:

- A trigger decision based on trigger activity consistent with a single interaction or internal decay that includes a list of CRP and/or PD channels to be collected and their associated time window(s). The TDAQ uses this information to collect the relevant raw data from its temporary buffers, form trigger records, and store them persistently. The data files may be further trimmed or compressed through a data filter stage before being transmitted to Fermilab for permanent storage.
- When the trigger identifies several trigger activity clusters within a few seconds that are inconsistent with the expected fluctuations from background in rate and energy, it fires a special trigger decision indicating a SNB candidate. For the FD2-VD the total collected raw data from a SNB will be about  $\sim 180$  TB of raw data. Thus, while the effective burst threshold

must be set low enough to satisfy DUNE’s requirements on SNB detection efficiency, it is important to not fire too frequently on background fluctuations. The present assumption is that the trigger conditions will be adjusted such that statistical fluctuations cause on the order of one SNB candidate trigger per month. It will take about one hour to transfer the data from this trigger event from the detector caverns to the storage on surface, and several additional hours to transfer those data to Fermilab. Upon inspection, fake SNB trigger records will be discarded.

Each trigger prompts the collection of data from the DAQ RO to form a trigger record. In the extreme case of an SNB trigger, data from the whole module is collected over a time window of 100 s. In most other cases, data from only a few CRPs and PDs will be collected over much shorter times ( $\ll 10$  ms).

The data filter acts on already-stored trigger records. It processes them with the aim of further reducing the data volume to be transferred to Fermilab. Initially, the Data Filter was conceived as back-end “insurance” in the event that instrumental events (such as high-voltage “streamers”) increased the data volume to unmanageable levels, and needed to be removed with more sophisticated algorithms than are possible upstream in the system. It has become clear, however, that the Data Filter can also filter the data volume by imposing, if desired, various region-of-interest criteria on tracks and hits, thus reducing the data volume and allowing for more inclusive triggers. Such regions-of-interest may be as simple as narrow (e.g.,  $\sim 100\mu\text{s}$ ) windows in time around hits, to rudimentary track reconstruction, or even machine learning approaches. The interface between the data filter and the rest of the DAQ is specified so that events that get passed to it can equally well come off of the network, or from disk, so that algorithms can be tested offline and with little or not change, be included within the online Data Filter. Development of Data Filter algorithms will be ongoing as experience with prototypes and the as-installed detector progresses.

A final component to the trigger system, not shown in Figure 7.5, is the ETI. It is intended to allow triggering of various modules off of one another within DUNE, triggering of modules due to external signals from Long-Baseline Neutrino Facility (LBNF) or calibration systems, publishing SNB triggers to SuperNova Early Warning System (SNEWS), or even triggering by different detectors locally should various collaborations agree to this possibility. In the hierarchical design of the DUNE Data Selection system, the External Trigger thus represents the most “global” level.

Beam information from LBNF or calibration systems can be used to judge if trigger candidates may come from beam or calibration activity, which may be helpful, for example, in allowing the Data Filter to decide on the ROI for the event. The beam time information can also be distributed to components of the calibration system to avoid producing activity in the detector that may interfere with activity from beam neutrinos.

The ETI may also be useful as a way of increasing the sensitivity of SNB triggering by requiring fewer events per module and summing events across all far detector modules. In the case of future FD modules with complementary physics capabilities to FD2-VD and FD1-HD, the ETI will enable this complementarity.

### 7.4.3.2 Trigger Performance Studies

Studies of the performance of the FD2-VD trigger have been done on simulated data as well as on cold box data. Extensive performance studies have also been done for the FD1-HD module, with which the trigger primitive–trigger activity–trigger candidate–trigger decision chain was initially developed and validated. Performance of trigger primitive generation on FD2-VD simulation has also been done, albeit with a relatively early version of the model of its channel signal and noise. With this simulation, the FD2-VD sensitivity to triggering on a SNB neutrino flux has been studied, detailed in Section 2.4.1.1. Further evaluation of the performance will be done with low-energy energy deposits in when data taking begins.

For example, Figure 7.6 shows the work done to validate the (software) trigger primitive algorithm on ProtoDUNE-SP collection-channel data and on Monte Carlo (MC) simulations for FD1-HD which performs similarly to FD2-VD. As the figure shows, identification of hits to generate trigger primitive is relatively easy with the algorithm, including adjustments for noise and baseline variations. The middle plot of Figure 7.6 shows the efficiency for detecting hits and generating trigger primitives, as a function of threshold, for a gain that is roughly twice what the ProtoDUNE-SP channel gains were. The right side of Figure 7.6 shows the trigger primitive rates for various physics sources: Model of Argon Reaction Low Energy Yields (MARLEY) events are hits from SNB neutrinos, and the others are radiological backgrounds. At a threshold of about 7 ADC counts, the trigger primitive rate is entirely dominated by  $^{39}\text{Ar}$  decays, which in the far detector modules will be about 10 MBq per 10 kt module.

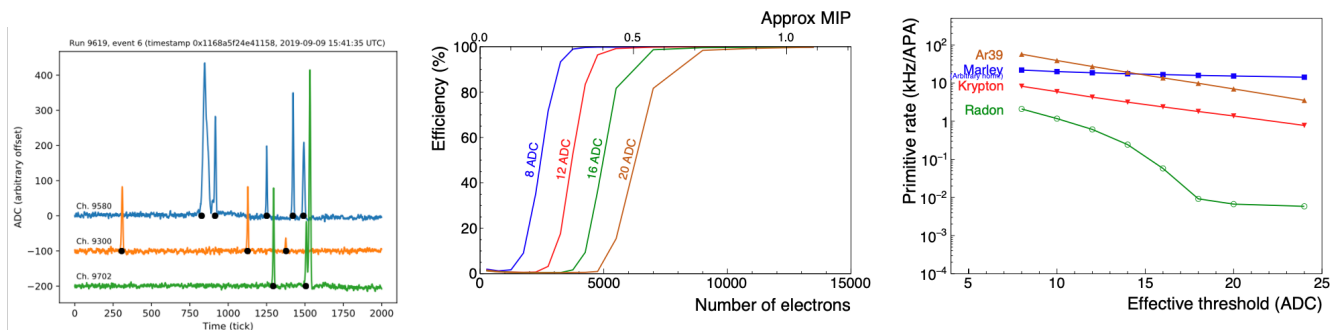


Figure 7.6: (Left) Identification of trigger primitive hits in collection channels in ProtoDUNE-SP, using a software version of the trigger primitive generation algorithm. (Middle) Efficiency curves for trigger primitive identification as a function of threshold and number of electrons in a hit (or minimum ionizing particle (MIP)-equivalent energy). (Right) Rates of trigger primitives expected in FD1-HD for various radiological backgrounds and SNB neutrino events (MARLEY) as a function of trigger primitives threshold in ADC counts.

Moving from identifying hits to identifying events, the effective energy threshold for the trigger is driven by the limits on total data volume. With a very conservative assumption that for every triggered event we write out an entire module’s worth of data for twice the drift time, the event energy threshold is limited by the expected rates of background events, most notably neutrons, which yield roughly 6 MeV of energy in a  $\gamma$  cascade. As shown in Figure 7.7, with a purely inclusive trigger—cutting on windows of trigger activity by requiring clusters to have a minimum total and peak charge, a maximum time-over-threshold that exceeds a certain minimum, and a minimum hit multiplicity—the resultant efficiency curves pass through 50% at 6 and 12 MeV, depending on

the requirement of hit multiplicity. The agreement between FD1-HD and FD2-VD is very good. This satisfies requirement SP-DAQ-8 (high efficiency above 10 MeV) and, with high efficiency above 40 MeV, requirement SP-DAQ-7 (>90% efficiency above 100 MeV) is met for events more energetic than those observed in a SNB. As shown in section 2.4.1.1, we achieve > 95% triggering efficiency for 50 events in 10 kt of argon, performing better than requirement SP-FD-23. The effective threshold for SNB events can be even lower due to burst structure of the neutrinos.

Simple performance studies have also been done with data using the vertical drift cold box. For surface detectors like the cold boxes and the Module 0s, an inclusive trigger does not make a lot of sense, because the cosmic ray rates are so high. Fortunately, the software approach using TPC topological information is naturally adaptable to creating exclusive triggers for low-rate event classes. For the vertical drift cold box, we implemented both a “horizontal muon trigger” (which essentially just counted collection-wire hits) and a trigger for Michel-like events. While efficiency studies in a configuration like the vertical drift cold box are difficult to do (there is no precise normalization for the flux of horizontal cosmics, for example), the trigger performed well at selecting events with the expected topologies. These tests were not just tests of selection purity, however, they also showed that the latencies are small and are accommodated easily within the system, and that the entire trigger generation chain functioned smoothly.

Figure 7.8 shows both an event display of an event triggered by the Horizontal Muon Trigger (HMA) in the vertical drift cold box, and distributions of the reconstructed angles of triggered tracks versus all tracks, for two different thresholds on the collection-wire hit multiplicity (60 and 100). As the right plot shows, increasing the trigger threshold enriches the data set with horizontal-going muons, despite the enormous flux of downward ( $180^\circ$ ) cosmics.

Figure 7.9 shows the trigger catching a Michel in simulation on the left, and a Michel candidate from the vertical drift cold box on the right.

#### 7.4.4 Data Collection

The role of the data collection system is to handle the flow of data coherently from their sources to local storage, to provide inputs to data filtering, to collect the filtering result, and to interface with computing for data transfers to permanent storage. It is the only interface to the local DAQ storage at SURF, and is responsible for ensuring consistency, traceability and reliable handling of the data at all times until they are moved to offline computing at Fermilab. Figure 7.10 shows a detailed diagram of the data collection flow.

The data collection strategy varies based on the specific readout mode: interaction triggers, SNB triggers, or streaming.

Once an interaction trigger decision is formed, the data collection system gathers data fragments from the readout units into coherent trigger records. Intermediate trigger objects that contributed to the trigger decision are added to complement the information. Trigger records are stored on disks prior to being served to the high-level filter system for further data reduction. The high-level filter forms modified trigger records that the storage system saves on disk, awaiting their successful transfer to Fermilab.



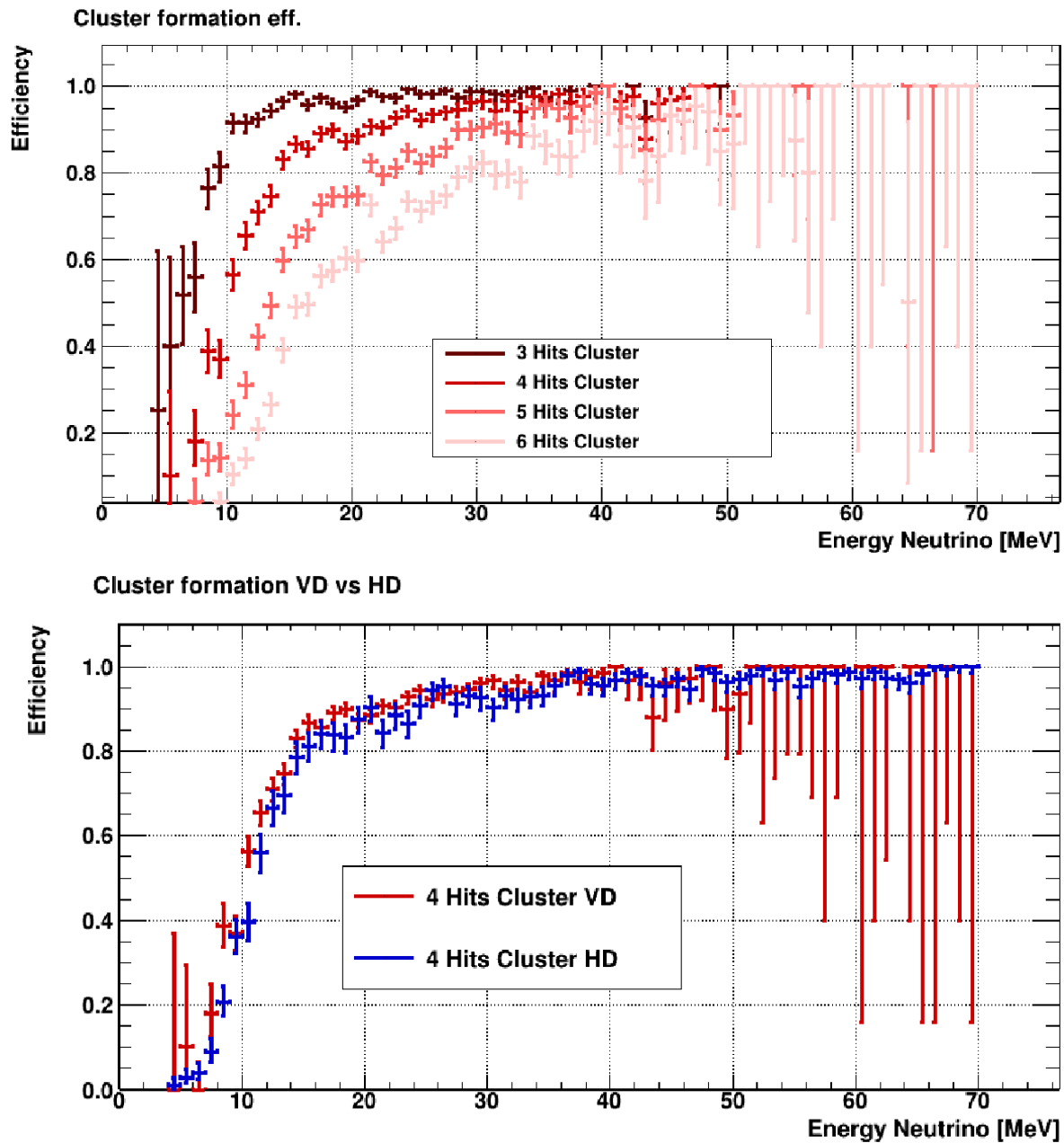


Figure 7.7: (Top) Trigger efficiency curves as a function of cluster size of trigger primitive hits for and (bottom) a comparison of the trigger efficiency curves between vertical drift and simulations.

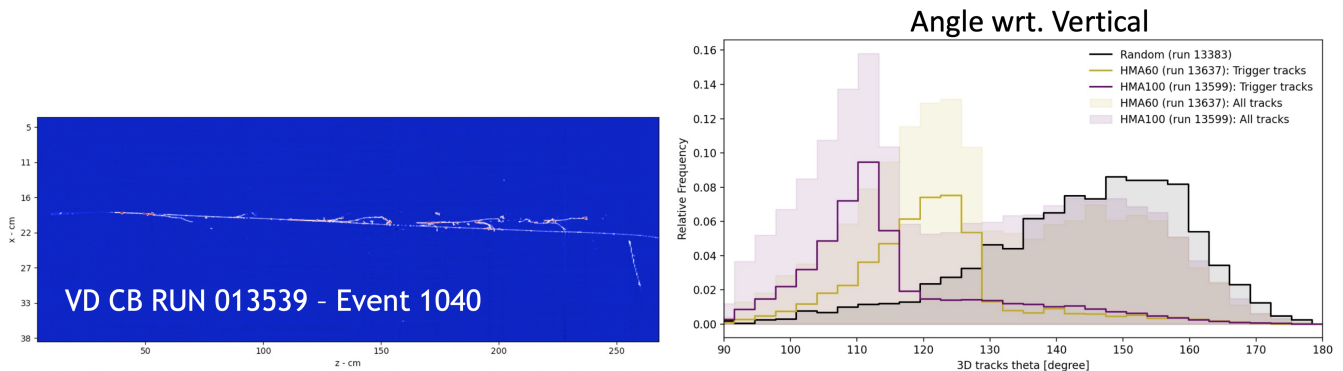


Figure 7.8: (Left) A horizontal muon in the vertical drift cold box captured by the very simple hit-counting trigger. (Right) Reconstructed angles of muons for all tracks and tracks triggered by counting either 60 (HMA60) or 100 (HMA100) hits. Here, downward-going events have angles of 180°. As can be seen, the imposition of the higher hit multiplicity preferentially selects events closer to horizontal.

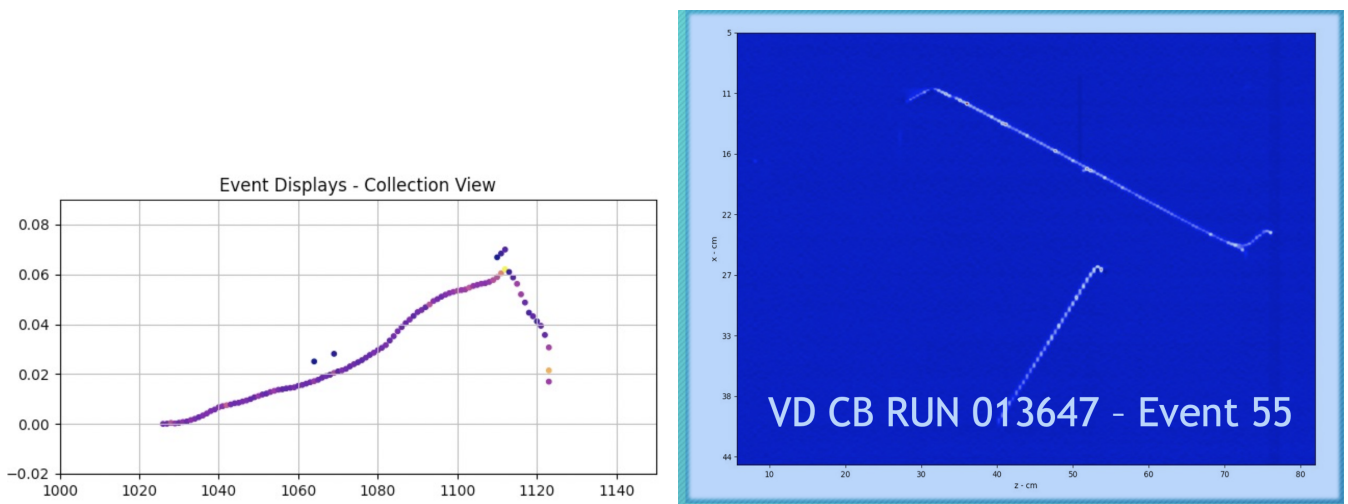


Figure 7.9: (Left) A Michel event triggered in simulation of the vertical drift cold box (Right) A Michel candidate from the exclusive Michel trigger in vertical drift cold box data.

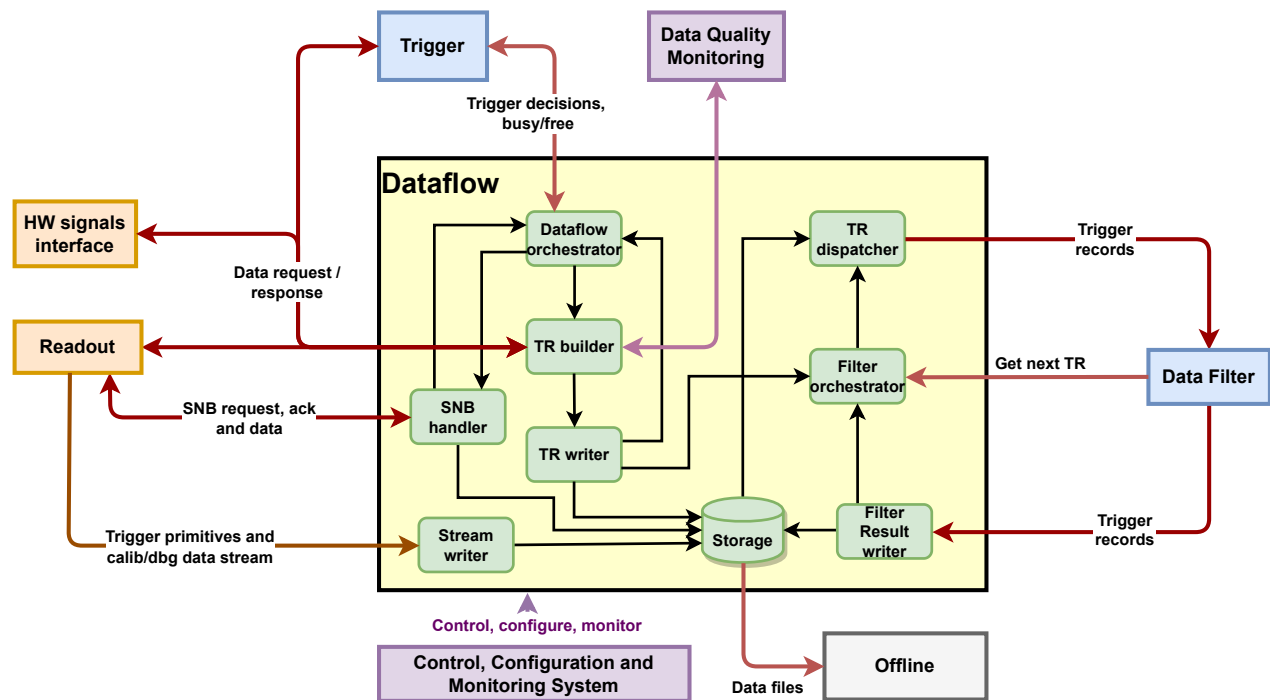


Figure 7.10: A schematic diagram of the DAQ with detailed data collection flow, showing the different paths to local storage (cylinder) for triggered data, SNB triggers, and trigger primitive storage.

The SNB records require a different approach due to their size: the data collection system instructs DAQ readout units to initiate the raw streaming to local storage on the DAQ readout unit. Afterwards, it transfers SNB record fragments to the surface storage servers with high priority, compatibly with the available bandwidth and without interfering with the collection of interaction triggers, which continues in parallel. From the surface storage, the SNB record is transmitted to Fermilab computing over the 100 Gbps WAN link. To minimize the transfer time, which is expected to be a few hours, the data collection system will start uploading as soon as SNB raw data reaches the surface buffer.

The trigger primitives are continuously streamed during data taking. The data collection system is responsible for keeping a copy of the stream in the surface temporary storage for a time period of at least a few months. The trigger primitive stream records will be made available on demand.

#### 7.4.5 Run Control, Configuration and Monitoring

The DAQ control, configuration and monitoring subsystem (CCM) subsystem is in charge of controlling, configuring, and monitoring the TDAQ system, as well as the detector components participating in data taking. It provides a central access point for the highly distributed TDAQ components, allowing them to be treated and managed as a single coherent system through their corresponding subsystem interfaces. It is responsible for error handling and recovery, which is achieved through a robust and autonomous fault-tolerant control system. The main goal is to maximize system uptime, data-taking efficiency and data quality, taking into account that the system will encounter changes in data-taking conditions, both programmatic (e.g., calibrations)

and unplanned (e.g., hardware failures or software faults).

The CCM provides an access point that delegates the user's actions, defined as any kind of human interaction, to internal function calls and procedures. It protects the direct access to detector and infrastructural resources. It also controls authentication and authorization, which limits different functionalities to certain groups and subsystems. As an example, only individuals authorized as detector experts can modify the FE configuration through the configuration interfaces, or exclude a CRP from the readout.

The control component validates, distributes and executes commands on the TDAQ, and is in charge of keeping the system in a coherent state. It consists of several components, such as access manager, process manager, resource manager and run control to carry out its tasks and also implements the intelligence required to automatically maintain the system in a properly functioning state or to alert operators if any parts malfunction and cannot be automatically recovered. The smallest unit of a detector that can be controlled independently is referred to as a DAQ partition.

The configuration component provides several key elements for the configuration management of the TDAQ components and detector FE electronics. It provides descriptions of system configurations, the ability to define and modify configurations, and graphical user interfaces for the human user to access the data. Data access libraries will hide the technology used for the database's implementation. The configuration component is also responsible for the archiving and bookkeeping of any used configurations.

Highly scalable and efficient operational monitoring is essential during data-taking periods. Any malfunctioning component of the experiment must be identified and reported as soon as possible. The monitoring component is intended to probe the TDAQ components, services, and resources, collect and archive the obtained status information, and provide aggregation and visualization tools.

The types of monitoring information vary greatly, ranging from log/error messages to metrics of different types. The monitoring infrastructure must therefore be flexible enough to seamlessly accommodate additions and modifications, and provide an aggregated view of the system behavior. The monitoring subsystem is a data source for the control subsystem that makes use of the information to automatically optimize the data taking conditions or recover from errors. Monitoring data is stored in databases and can be viewed through dashboards by the end user. The database structure continues to evolve as experience is gained in what is necessary to monitor.

The CCM must also be flexible enough to be able to deploy the DAQ on a number of different test stands, prototypes, and production systems with varying sizes of server clusters, and manage the computing loads on these systems.

The requirements on the CCM led to an investigation of systematic solutions, and Kubernetes [99] was chosen as the path forward. Kubernetes is an open-source system for deploying and controlling applications running within containers, used very widely in the technology industry. There were several motivations to choose this approach for the DUNE DAQ system, driven, for example, by the location of the DUNE FD and the uptime requirements for the experiment. These include:

- Reliability engineering: Considering the stringent uptime requirement for the DUNE detector and looking to industry to see how comparable performance is achieved, cloud technology providers have similar or more stringent requirements for large data centers. The container orchestration paradigm is used throughout this industry, with Kubernetes the system of choice in almost all cases.
- Provision of services: In addition to the DUNE DAQ applications for dataflow and triggering, the system relies on a large number of commercial and custom services, e.g., databases, visualization dashboards etc., which must be kept running reliably. Kubernetes provides a robust and convenient way to define and deploy such services and to expose them in a simple way such that they may be used by other applications.
- Test-stand support: In addition to the FD at SURF and larger test facilities, such as those based at Fermilab and CERN, there is a need to provide DAQ functionality to small test stands located in labs at institutes around the world. A failure to provide coherent infrastructure for this use case would likely lead to homegrown testing scripts that duplicate some features of the DAQ software.
- Resource management and networking: Kubernetes provides many tools that are required by the DAQ system, e.g., fail-safe process control, resource management to ensure validity of configuration and avoid clashes of hardware requirements, and a networking system that allows for improved flexibility compared to typical networking.
- System administration: given the location of the DUNE FD, remote system administration is required. Running applications in containers gives some level of independence from the underlying operating systems on the DAQ nodes themselves, since the operating system and dependencies for applications can be distributed alongside the applications in their containers. This reduces the need for disruptive large-scale system upgrades.

Given the strong motivation to consider container-based systems, with Kubernetes as the most obvious choice, an R&D program was initiated in mid-2021. The starting point was the development of a single-node cluster configuration, providing some key services required by the DAQ, such as the databases for storing operational monitoring and logging data, and the Grafana dashboard server for viewing this data. The development addressed the test-stand and provision-of-services requirements. After successful testing of the prototype by many DAQ developers, the decision was taken to continue this development to meet the full needs of the DAQ.

The next step was to set up a test cluster at the facility at CERN, with about five nodes. This cluster has been used as the main development facility for over a year and has allowed us to scale up the early developments to an intermediate size and make use of realistic hardware systems. A key test was to benchmark the dataflow performance using the FELIX hardware as an example of a hardware readout card to pass data to applications running within containers. Tests have shown that the performance is not affected by the use of containers, which was a potential concern, and have led to the cluster design shown in Figure 7.11.

Continuing work concentrates on scaling up the system from a small number of nodes to a larger, more production-like system, with input from multiple readout cards, output to multiple disk servers, distribution of applications over a larger number of nodes, and corresponding monitoring of this larger system. Future plans include continuing to develop expertise in Kubernetes and leverage the wealth of features it provides, and development of a supervisor control layer, likely

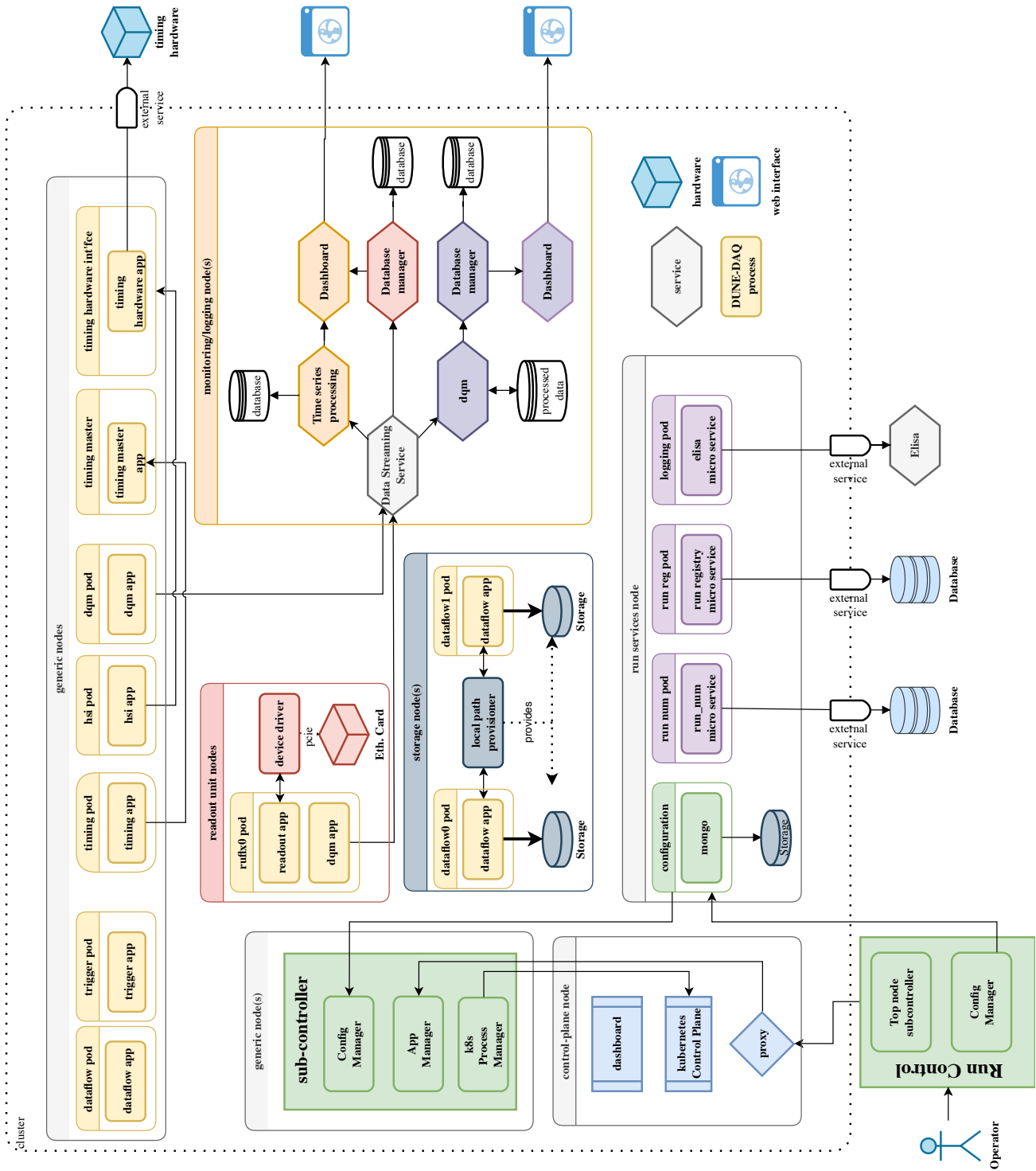


Figure 7.11: A schematic diagram of cluster design based on the Kubernetes system. “Pods” are sets of containers running on servers (nodes); the pods run applications that carry out various functions of the DAQ, though not all nodes will run all applications simultaneously. Specialized nodes interface with readout hardware and with storage. Pods can connect to external services that can, e.g., provide logging services. Other services can be deployed on nodes natively. The run control interface allows the human user to configure and control apps across the cluster.

based on an expert system, to provide automated responses to common problems.

### 7.4.6 Data Quality Monitoring

The DQM subsystem is complementary to the monitoring component of the CCM. Instead of collecting counters, rates and logs, the DQM analyses samples of raw data and compares the results with the expectations, thus assessing the quality of the data themselves, rather than the quality of the DAQ process.

The DQM consists of three parts: the local processing module, the remote analysis module, and the web platform. Their interactions are shown in Figure 7.12.

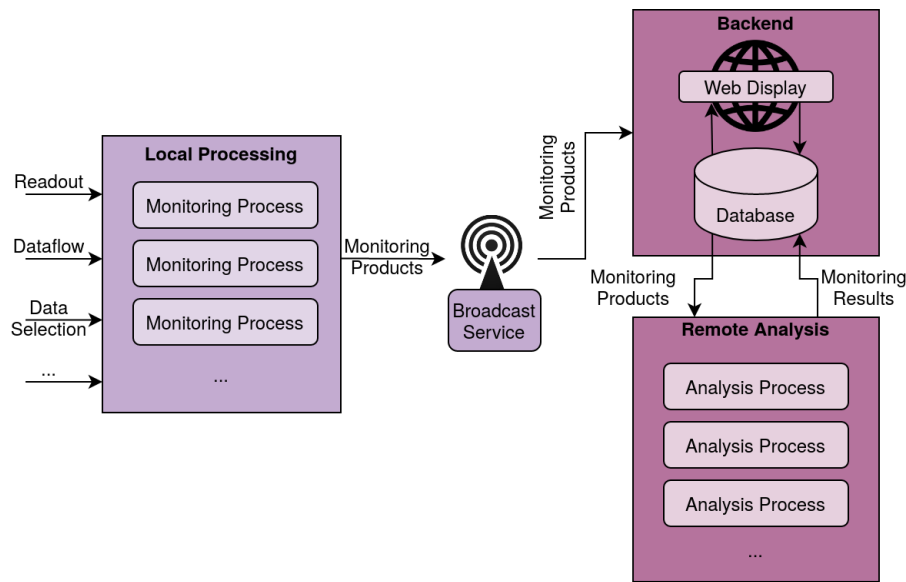


Figure 7.12: A schematic diagram of the DQM system showing the major components. Components at left plus the broadcast service are underground and those at right are aboveground.

The local processing module is directly connected to the rest of the DAQ, and will run underground at the FD site. It samples data in parallel from across the DAQ, at configurable rates designed to keep processing requirements below 1 core per CRP. From these data, it produces monitoring products summarizing the data quality (such as histograms and Fourier transform), which are transmitted to the surface via an Apache Kafka broadcast service.

The web platform will be hosted on servers operating at the surface. It receives the monitoring products transmitted by the local processing, and indexes them in its own dedicated database. This database is connected to a web user interface, accessible to collaborators anywhere in the world, that allows users to navigate each detector subsystem and examine both live and historical data quality conditions. A data retention scheme will be developed to manage the total data volume in this database by down-sampling the time resolution of old run periods, keeping maximum granularity for current data quality conditions while ensuring that data quality records remain for the full run history of the experiment.

The remote analysis module will be hosted on the same surface-level servers as the web platform. It will monitor the DQM database as it is filled, and perform automated assessment of the monitoring

products produced by the local processing. These assessment algorithms will generate alerts that can be passed directly to operators and experts through the web platform, or to the control subsystem in order to execute automated recovery actions. This module is designed to continuously evolve as understanding of the detector broadens during commissioning and early operation, and as detector conditions evolve and stabilize, allowing for the easy addition and removal of parallel analysis algorithms.

Prototyped versions of the local processing module and web platform have been tested at the CERN cold boxes. Development of the algorithms for the remote analysis model will be developed with experience running detectors to define “normal” operations.

## 7.5 Design Validation and Development

The validation and development of the DAQ design uses multiple test stands to prototype, develop, and test the performance of the system. This development is closely linked to the development of the electronics, and testing of the two systems goes hand-in-hand.

### 7.5.1 CERN Cold box

As described in Chapter 8 the readout electronics for FD2-VD are being tested at CERN's . This test provides the opportunity to test the integration of the TDE with the DAQ to ensure that the interface between the electronics and the upstream readout units is working correctly, as well as the CCM.

### 7.5.2 Module 0

The primary large-scale test of the DAQ will be via the FD2-VD Module 0 activities, where the DAQ will be tested for both the FD1-HD and FD2-VD detectors.

## 7.6 Hardware Procurement and QA/QC

The TDAQ system relies on COTS items, except for the custom built DTS. This section describes the approach to procurement as well as the quality assurance (QA)/quality control (QC) plans. The DTS hardware and the COTS items are treated separately.

### 7.6.1 Timing System

The timing system consists of three items of custom hardware, supported by COTS components. The custom components need to be produced, tested first individually and then as part of a system. Detailed procurement schedules and testing procedure documents are being developed, and will be available in the second quarter of 2023

#### 7.6.1.1 Custom Components

Table 7.5 lists the custom components for the timing system that will be in operation in the first two far detector modules.



Table 7.5: Summary of custom hardware items in DTS

Description	Quantity in service	Quantity of spares
GPS Interface Module. One at the top of each access shaft	2	2
$\mu$ TCA Interface Module. One per $\mu$ TCA crate. Two crates per far detector module	4	2
Fiber Interface Module. Ten per $\mu$ TCA crate	40	5

### 7.6.1.2 COTS Items

Table 7.6 lists the COTS components for the timing system that will be in operation in the first two far detector modules.

Table 7.6: Summary of COTS items in DTS

Description	Quantity in service	Quantity of spares
$\mu$ TCA crate: Either Vadatech or Schroff/nVent	4	1
$\mu$ TCA fan trays	8	2
$\mu$ TCA MCH: Crate controllers. One per crate	4	1
$\mu$ TCA PSU: Power supply modules. Redundancy. Hot swappable	8	2
$\mu$ TCA JSM: JTAG service modules (for reflashing FPGA firmware)	4	1
COTS FPGA based AMC that houses fiber interface board	40	4
GPS interface board PSU: 12V/3A output , 120V input external power supply	2	1

### 7.6.1.3 Timing System QA/QC

Production modules will be tested and “burnt in” in the UK before shipping to SURF, where they will undergo brief testing after installation. A plan for the testing of production modules will be documented in the second quarter of 2023, and will include a detailed testing procedure document, a daily testing schedule and manpower allocations specifying those responsible for various testing aspects.

The testing schedule provides one-year contingency to allow for another production batch in case some components fail any of the specified tests. The fiber patch panels and passive optical splitters on the top of the cryostats will be installed by the infrastructure installation team, and tested together with the detector readout data and control fibers.

## 7.6.2 TDAQ COTS Items

The remaining TDAQ hardware consists of computers and network switches, interconnected through either CAT6 copper cables or optical (, and Single Mode) fibers.

The computers themselves can be split into four categories as shown in Table 7.7.

Table 7.7: Summary of COTS items in TDAQ

Item	Description	Quantity in service	Quantity of spares
Readout servers	high-end servers with 2x100G Ethernet network interface controllers (NICs), 2x10G Ethernet NICs, at least 768 GB of DDR5 RAM, at least 4 TB of fast Non-volatile memory express (NVMe) storage and at least 32 physical CPU cores @2.5 GHz	167	8
Storage servers	used for data flow through the DAQ, with large storage and high performance I/O capacity	12	1
Data processing servers	used for DAQ TS, data flow, DQM, with optimized CPU for processing	102	5
General purpose servers	used for CCM, TDAQ infrastructure, ETI, etc., with a balanced configuration for I/O, processing and storage	40	2
Readout switches	Ethernet aggregator switches to multiplex the detector links into 100G links for DAQ reception	71	4

### 7.6.3 Procurement Process

The TDAQ infrastructure at the Experiment Hall North One (EHN1) is currently instrumental for the testing of hardware samples: it is used to finalize the hardware specifications prior to launching the procurement.

The main characteristics of the required hardware have been clarified through the prototype implementations of the TDAQ components described in Sections 7.6.1 and 7.6.2, such that realistic cost estimates could be made. Nevertheless, the pace of technology and products evolution is at present so high that detailed specifications for the computers and their peripherals will only be made closer to the purchasing date. For example, new motherboards supporting PCIe Gen 5 and dynamic random access memory (DRAM) DDR5 have only recently been launched by both Intel and AMD, with important consequences on memory, storage and network performance.

The aim is to have a complete set of specifications in 2024, for procurement in 2024-2025 and installation of the pre-series hardware at the SURF in 2025-2026 for FD1-HD and 2027 for FD2-VD. The pre-series hardware makes up approximately 25% of the final quantities, and will be used for detector integration and testing. The remaining hardware (approximately 75%) will be installed closer to the date scheduled for the filling of the detector with LAr.

The specifications documents will be checked during a production readiness review (PRR) prior to launching the procurement. The aim of this review is to give the final green light for the material spending.

Part of the procurement process is to test combinations of potential equipment together to eliminate

compatibility problems in advance. Candidate hardware will thus be installed in the ProtoDUNE TDAQ barracks at CERN, as part of the qualification step during the procurement process.

#### 7.6.4 Quality Assurance and Control

Vendors of computing equipment have a set of standard QA/QC procedures to ensure the quality of their products. Nevertheless, during the tendering process it is possible to require additional tests to certify that the functionalities meet specifications. This is particularly important since the plan is for the equipment to be shipped directly to the South Dakota Warehouse Facility (SDWF), ready to be moved from the storage area to SURF when needed.

For the FD TDAQ computers the following tests (with the corresponding test result documents) will be required:

- installation of an agreed version of the BIOS firmware,
- adjustment of the BIOS settings,
- installation of a Linux operating system image provided by Fermilab,
- stress testing of CPUs using an agreed utility,
- stress testing of DRAM using an agreed utility,
- stress testing of disks using an agreed utility adapted to the type of storage,
- stress testing of network I/O using an agreed utility,

The test reports will contain not only the information about pass/failed tests but also the monitoring values of temperatures and power consumption during the tests.

In order to catch problems that might have circumvented the manufacturer's QC process, acceptance testing will be done also *in situ*, at the SURF. This eliminates the additional time, logistics, and handling that would be needed if this were done elsewhere. To reduce the impact of items which fail the acceptance testing, spares (which are needed anyway) will be included in the initial order, allowing head room to return any defective hardware without impacting the installation schedule.

Acceptance testing for COTS computing and networking hardware is part of the installation. A 24h burn-in procedure will be run to catch cases of infant mortality. For computers, a standard Linux burn-in/test suite will be run (largely overlapping with the tests carried out at the manufacturer's premises).

The network switches will be tested by routing data through them at the full load, using industry standard tools.

For other COTS components procured by the TDAQ, the plan is to rely on the manufacturer's QA/QC standards only: this is in particular valid for optical transceivers, pre-terminated fibers and CAT6 cables, patch panels, passive optical splitters.

## 7.7 Assembly, Installation, and Integration

The installation of the DAQ must be carefully timed to support the activities of the rest of the detector components, since the DAQ is required to check whether the installation and integration of the detector is proceeding well. The physical activities of the DAQ installation are not extensive in comparison to other subsystems, but the timing of the activities is critical to the overall success of the detector.

The interface document describing the interface between the DAQ system and the facilities is in [100].

### 7.7.1 DAQ Facilities and Infrastructure

The DAQ for FD2-VD will inhabit similar space to that for FD1-HD. Note that the location of DAQ infrastructure has changed since the publication of the FD1-HD TDR [84]. The DAQ computing infrastructure for each far detector module will be located on the cryogenics mezzanine on top of each detector module rather than all together in the central utility cavern (CUC). Servers central to all modules will be in the Ross Dry basement at the surface, and all modules will connect to the fiber trunk running up the shaft in the CUC's MCR room, where central networking equipment will be located. Additionally, GPS antennae for the timing system will be located at the top of both the Ross and Yates shafts.

### 7.7.2 Ross Dry Basement

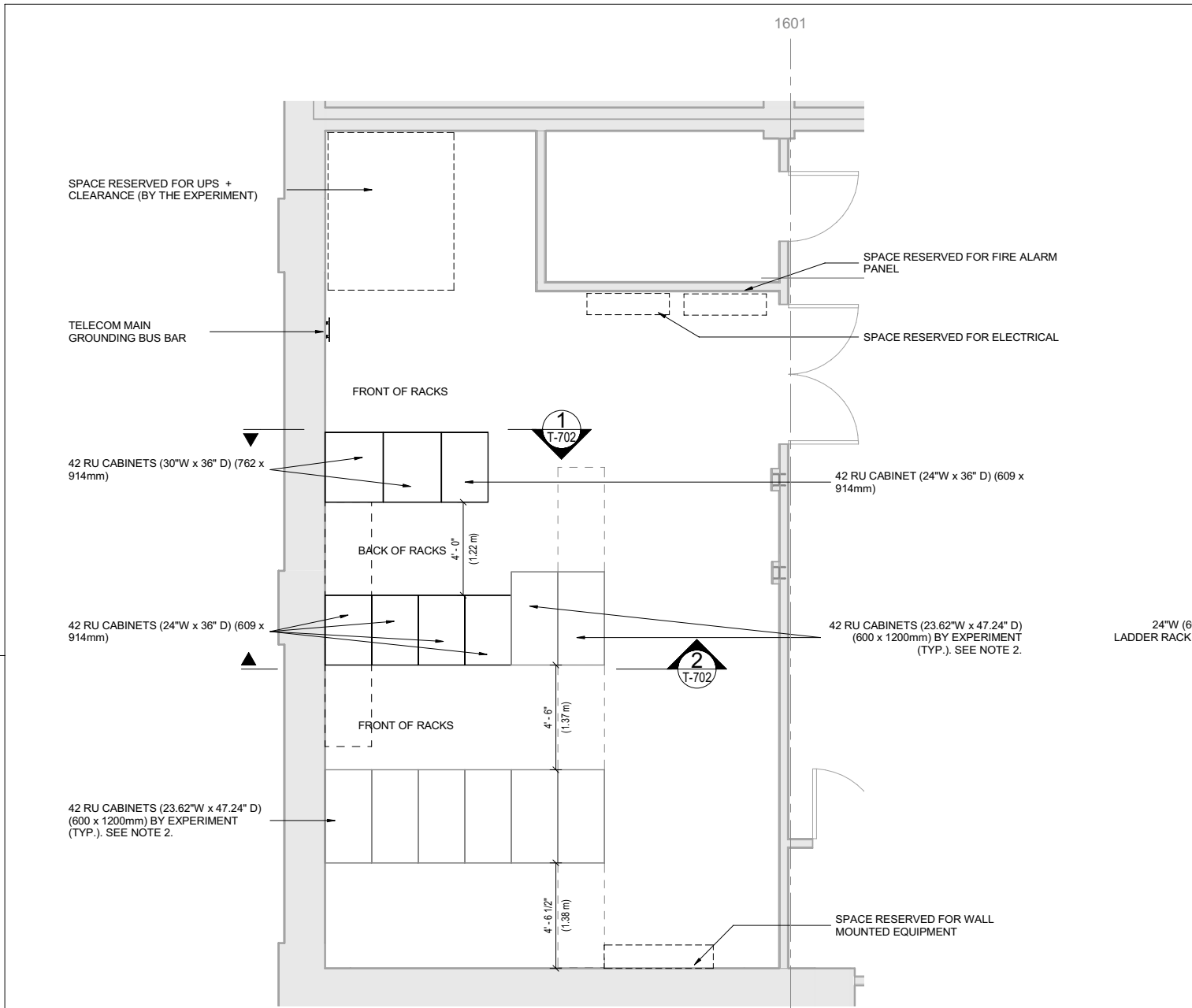
The southwest corner of the Ross Dry basement area (Figure 7.13) at the surface will contain not only networking and central IT related gear, but eight 42U DAQ racks. These will house the data collection servers and transient storage, the data filter farm, and servers for DAQ services common to all far detector modules (web services, databases, and so on). The shaft fibers connect to this room, as does the connection to the WAN. For this site, 50 kVA of power and cooling, the racks, and cable trays will be installed by the fall of 2024, and the minimal installation of DAQ administrative machines needed to facilitate further work underground will be installed by the summer of 2025.

### 7.7.3 The MCR in the CUC

The MCR in the CUC is the connectivity hub where all the far detector modules connect to the network out of the underground via Fermilab central networking routers. While this is facility space, it will be available to the DAQ consortium in the spring of 2025, well before either the surface or detector DAQ spaces will have need of it.

### 7.7.4 The DAQ Barracks

The main site for each detector module's DAQ infrastructure will be a barrack built on the cryogenics mezzanine above its cryostat. This space will contain 16 42U racks air cooled via a traditional data center hot/cold aisle arrangement. Fibers will run from the warm electronics atop each detector module to patch panels in the barracks, then into the readout servers. This arrangement ensures that the electronically noisy DAQ computing infrastructure is galvanically isolated from



NOTES:  
 1. CLEARANCE TO ACTIVE WASTE LINE TO BE MINIMUM 3' 6" (1066mm)  
 2. RACKS TO BE FURNISHED AND INSTALLED BY EXPERIMENT.

Figure 7.13: Layout of the DAQ area in the Ross Dry Basement.  
**ROSS DRY MCR ROOM LAYOUT**

SCALE: 3/8" = 1'-0"

REV.	DATE	DESCRIPTION
6	11/20/20	100% FD UPDATE
5	10/01/20	90% FD UPDATE
4	05/03/19	100% FD SUBMISSION
3	02/22/19	90% FD SUBMISSION
2	11/16/18	60% FD SUBMISSION
1	07/27/18	30% FD SUBMISSION
REVISIONS		

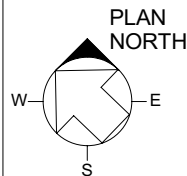
**ARUP**

Arup USA Inc.  
 77 Water Street, New York NY 10005, T 212 896 3000  
 www.arup.com

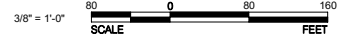
**DKa**  
 Dangermond  
 Keeler Architecture  
 LLC  
 167 10th Avenue St.  
 60610 Kansas City, MO

**TSP**  
 TSP, Inc.  
 600 Kansas City St.  
 64620 Overland Park, KS  
 phone: (816) 343-6100  
 fax: (816) 343-7159  
 www.teamtsp.com

**RESPEC**  
 CONSULTING & SERVICES



SCALE:



the sensitive detector electronics. Data will then be transferred via fiber to the MCR to be sent out to the surface components of the DAQ.

Each DAQ barrack will have 150 kVA of power and cooling. Pallet staging and storage space is available on the cryogenics mezzanine floor nearby, and there is a separate small room suitable for people to work outside the hostile environment of a server room.

Figure 7.14 shows the layout and 3D model of the barracks.

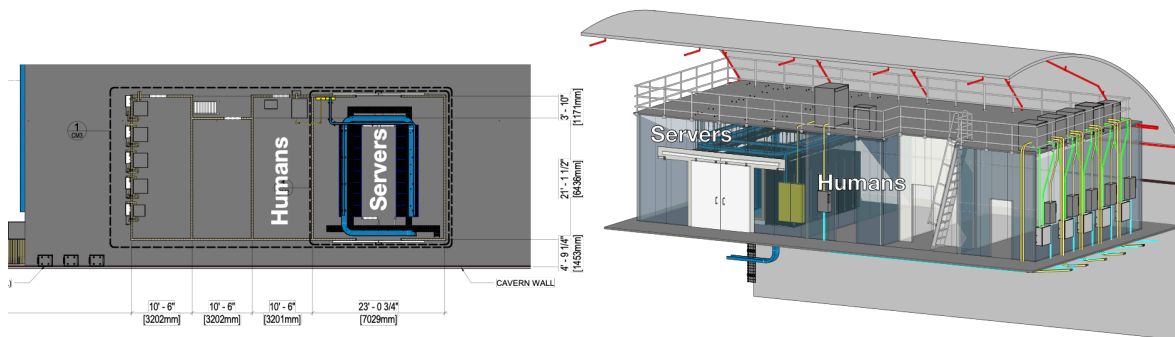


Figure 7.14: Left: Overhead view of the DAQ barracks on the cryo mezzanine. Right: 3D model of the DAQ barracks. The server rooms and working areas are labeled.

## 7.7.5 Installation Schedule

The DAQ installation schedule is driven by when the warm electronics need to be connected to computers to test their readouts. The FD1-HD barracks will be available complete with fiber connection to the MCR, racks, cooling, and power early in 2026. At that point servers can be installed in the racks and fibers laid in cable trays on the detector top to the warm electronics chimneys. Three full months are foreseen in the schedule to finish the DAQ computing installation, configuration, and testing before it is needed to service detector electronics.

Both FD1-HD and FD2-VD fit into the same computing envelope, so the installation plan is the same for both detectors, offset by their installation schedules. The FD2-VD barracks will be available for DAQ installation well after the FD1-HD DAQ installation is in the “service anode plane assembly (APA) installation” mode.

Items that go underground need to arrive at SURF at least three months before they are needed. Thus, procurement is planned at present with ample headroom.

## 7.7.6 Installation Scheme

All three locations described here will need small crews of approximately six people for a limited time to rack in servers and switches, cable them up, and perform tests to validate the installation. After that, a fractional will be needed occasionally onsite to be hands-on, but the system is designed to be operated remotely, with remote console logins and power distribution units. The remote operation is being developed and tested at CERN’s NP04 site for and at Fermilab’s ICEBERG R&D cryostat and electronics (ICEBERG) prototype, and will be replicated at test

stands at multiple sites before the installation at SURF, by which point any problems will have been solved.

### 7.7.7 Networking

The TDAQ relies largely on the network infrastructure provided by LBNF/DUNE at SURF.

The Wide Area Network (WAN) for DUNE at SURF will be contracted and managed by Energy Sciences Network (ESNet), the network infrastructure and service provider funded by the Department of Energy Office of Science. The existing 10Gb/s VLAN circuit, provided by the Research, Education and Economic Development (REED) Network, will be upgraded to redundant links with a 100Gb/s primary path and at least 10Gb/s guaranteed bandwidth backup path provided by ESNet. The redundant, full-bandwidth WAN will be available by the start of FD1 DAQ commissioning, June 2028.

DUNE networks at SURF share a high performance, redundant aggregation backbone provided by modular chassis switches/routers on the surface, in Ross Dry and Yates buildings, and underground in the MCR. The network equipment will be installed underground and in surface buildings. It will be configured, tested, managed and monitored by the Network Services group in Fermilab's Core Computing Division and will have the capacity to support both FD1 and FD2 detectors.

DUNE DAQ requirements specify distinct, interconnected (via central hubs) networks with different performance and bandwidth needs: the Experiment and Technical networks. There is also a General Purpose network provisioned for other computers and user network access, and a separate management network infrastructure to manage all DUNE network devices. Fermilab Core Computing will configure all VLANs and provision ports for access switch uplinks for both FD1 and FD2 detectors before FD1 is ready for commissioning.

Core IT services such as DNS, DHCP, NTP, Kerberos and Active Directory/LDAP will run on a small virtual machine cluster co-located in the Ross Dry and Yates building computer rooms for redundancy. This infrastructure will be implemented in a fault tolerant scheme and is shared between FD1 and FD2. Access controls to the networks and to systems on the network will be applied on the basis of user roles and controlled centrally via Core IT applications managed by Fermilab Core Computing and will be built during the start of the initial DAQ surface installation, or before, in a standalone, locked rack temporarily placed outside the computer room in the Ross Dry lower level.

The DAQ consortium is responsible for the network used in the DAQ RO. Figure 7.15 illustrates the part of the overall network that will be used by TDAQ for FD1-HD and FD2-VD. At the bottom of the diagram the readout switches are included.

### 7.7.8 Rack Layout

The rack layout and design is at a preliminary stage and shown in Figure 7.16, for the FD2-VD underground DAQ. Since the servers will be commodity hardware, specification and procurement of this hardware will happen closer to the time it is needed in order to manage costs and extend the lifetime of the equipment. Once the final number, dimensions, and cooling needs for the servers

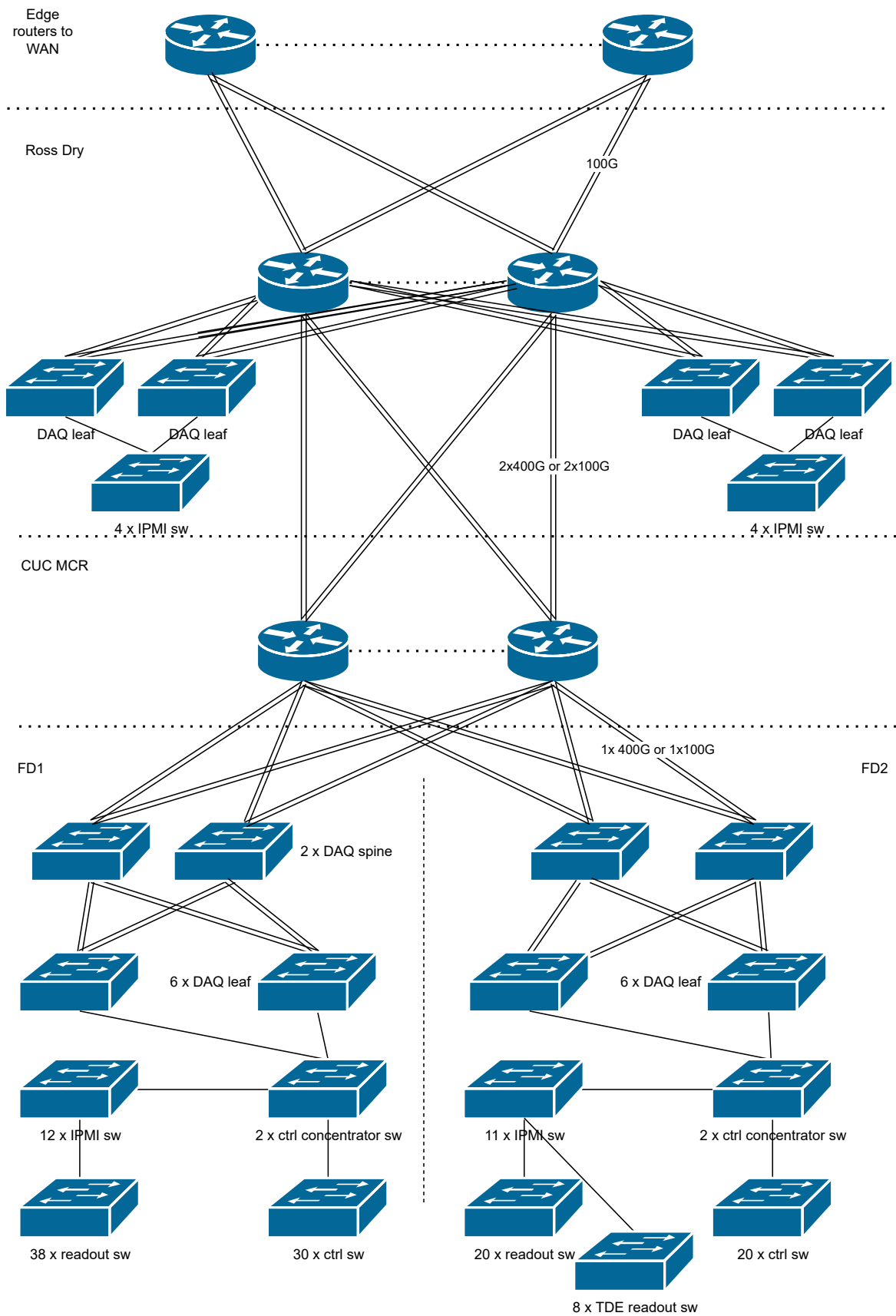


Figure 7.15: Preliminary layout of the TDAQ network.



are known, detailed rack design will be undertaken.

## 7.8 Organization and Schedule

### 7.8.1 TDAQ Consortium

The TDAQ consortium was inaugurated in 2017, with responsibility for delivery of the DAQ and trigger systems for all DUNE detector systems at the far and near sites. The management and working group structure of the consortium have evolved in the intervening time, and the current organization is shown in Figure 7.17. The working groups have responsibility for the TDAQ subsystems described above. The data selection working groups have responsibility for both the design of the subsystem and the development of software and simulation tools to evaluate and optimize the physics performance of the overall system. Another working group is dedicated to the specification and design of the supporting infrastructure at SURF — including computing services – and planning the integration and installation steps required to deliver a working system.

The management team comprises the consortium leader, who is the liaison to the DUNE executive board (EB), and technical leads for far and near detector systems who are members of the DUNE technical board (TB). They are supported by a resources coordinator with responsibility for resource and schedule management, liaising with the resources board. The funding agencies supporting the consortium are represented in the Management Board, which has ultimate responsibility for approving the project plan, monitoring progress, tracking changes, and ensuring that the necessary personnel and resources are committed to the project. A breakdown of consortium institutes and deliverables is shown in Table 7.8. Many of these deliverables are common to all FD modules, and so do not represent tasks specific to FD2-VD; however, the quantities of hardware components quoted below are those required for the FD2-VD system alone.

Table 7.8: TDAQ deliverables by institution

Component	Description	Quantity (FD2)	Institutions	Funding Agencies
TDAQ software & firmware management	Administration of code repositories; Development and maintenance of build tools; Coordination, preparation, and distribution of SW/FW releases		Fermilab, RAL	DOE, STFC
Infrastructure servers	DAQ computing infrastructure (file servers, databases, etc)	8	Fermilab	DOE
Computing administration and support	Development and testing of system configuration, management, and administration tools; DAQ hardware inventory system administration		Fermilab, UMN Duluth	DOE
Timing system	$\mu$ TCA-based system to synchronize and distribute clock and timestamp to all electronics endpoints	2	Bristol, RAL	STFC
External trigger interface	Server dedicated to the exchange of trigger messages with external systems (e.g. SNEWs) or other FD modules	1	Bristol, RAL	STFC

Readout system cards	PCIe cards interfacing the DAQ to the detector electronics	200	Oxford, RAL	STFC
Readout system SNB storage	Fast storage system for SNB data	200	Oxford	STFC
Readout system servers	Servers hosting the readout cards and SNB storage, used to buffer data and transfer triggered data to the dataflow system	100	CERN	CERN
Readout system firmware and software	Development and testing of FW and SW for the readout subsystem		Toronto, CERN, Birmingham, Bristol, Oxford, RAL, Sussex, UCL	Canada, CERN, STFC
Dataflow servers	Servers and storage to collect data and store them before final transfer to Fermilab	8	Fermilab	DOE
Trigger servers	Servers to carry out the first stage of data selection	20	CERN	CERN
Trigger software	Software development and testing to support the trigger algorithms execution		Bristol, Oxford, RAL, Sussex	STFC
Data filter servers	Servers to carry out the second stage of data selection; software to support the filtering algorithms execution	20	Fermilab	DOE
Data filter software	Software development and testing to support the filtering algorithms execution		CERN, Oxford, RAL, Sussex	CERN, STFC
CCM & DQM servers	Servers to control, configure and monitor the system	20	RAL	STFC
CCM SW	Development and testing of software to control, configure and monitor the system		Birmingham, Imperial, Liverpool, RAL, CERN, Fermilab	STFC, CERN, DOE
DQM SW	Software development and testing to support the execution of data quality monitoring algorithms and visualize results		Edinburgh, Imperial, UCL	STFC, CERN
Algorithms, performance, simulation	Simulation and performance studies to devise optimal data selection strategies; development and testing of data selection and monitoring algorithms		Toronto, Imperial, Oxford, Sussex, UCL, Columbia, Pennsylvania, BNL	Canada, STFC, DOE
Fibers and cabling equipment	Patch panels, patch cords, timing connections, cable ties, labels		RAL	STFC
HW for Module 0	DAQ hardware for Module-0 in NP02		Toronto, CERN	Canada, STFC, CERN
HW for FD2 coldbox	Extensions to the ProtoDUNE-SP DAQ system for VD cold box		Toronto, CERN	Canada, STFC, CERN
Installation, integration, and support for Module 0	Effort to support the integration, commissioning, and operations of Module 0		All TDAQ institutions	

Support for detector test setups	Effort to support the integration and commissioning of detector electronics and DAQ at detector test labs	All TDAQ institutions
DAQ hardware installation and commissioning at SURF	Effort to install DAQ hardware, test it and carry out integration and commissioning	All TDAQ institutions
DAQ integration and operations support at SURF	Effort to support the integration and commissioning of detector electronics and DAQ during the construction and commissioning phase	All TDAQ institutions

## 7.8.2 Schedule

### 7.8.2.1 Scheduling Approach

The TDAQ development schedule is driven by the requirements of other DUNE FD subsystems through the various stages of their development, construction, installation and commissioning for physics.

- During the development phase, primarily at test cryostats and at the Module 0s, TDAQ must support timing, readout and data storage functions adequate for reliable running and capture of data.
- Detector construction will be supported through provision of small-scale readout and timing systems at production sites as required.
- Early installation of TDAQ components at the FD2-VD site will allow control, testing and evaluation of detector components and electronics during installation.
- Detector commissioning under warm and cold conditions will be supported by a fully functional TDAQ system, with continuing development of data selection algorithms as the detector performance is understood and optimized.

The majority of resources in the TDAQ project are devoted to software and firmware development, integration and testing. Moreover, the “hard problems” associated with development of a complex distributed real-time system lie to a large extent in the interfaces between components and the evolution of their specifications as the behavior and performance of the system is understood in detail.

For these deliverables, an agile-inspired approach to scheduling is therefore appropriate, and has been used with success during the development period leading up to the Module 0s. This approach mandates the incremental development of software and firmware components in parallel, with emphasis on frequent integration leading to functional releases. The target feature set for each release is treated flexibly to account for the evolution of component specification. It is the responsibility of working group leaders to ensure that the overall schedule for the TDAQ system is met, and moreover that the testing and development of hardware is adequately supported by mature software, as required. It is anticipated that continuous improvements will be made to TDAQ software and firmware until DUNE physics running.

	Rack 1	Rack 2	Rack 3	Rack 4	Rack 5	Rack 6	Rack 7	Rack 8	Rack 9	Rack 10	Rack 11	Rack 12	Rack 13	Rack 14	Rack 15	Rack 16
U42																
U41																
U40	Patch Panel	Patch Panel	Patch Panel	Patch Panel	Patch Panel						Ctrl SW UP		Patch Panel	Patch Panel	Patch Panel	Patch Panel
U39											SC server		Patch Panel	Patch Panel	Patch Panel	Patch Panel
U38	Ctrl SW	Ctrl SW	Ctrl SW	Ctrl SW	Ctrl SW	Ctrl SW UP					SC server		Ctrl SW	Ctrl SW	Ctrl SW	Ctrl SW
U37																
U36	Ctrl SW	Ctrl SW	Ctrl SW	Ctrl SW	Ctrl SW	SC server										
U35																
U34	Ctrl SW	Ctrl SW	Ctrl SW	Ctrl SW	Ctrl SW	SC server										
U33											IPMI SW					
U32	IPMI SW	IPMI SW	IPMI SW	IPMI SW	IPMI SW	IPMI SW							IPMI SW	IPMI SW	IPMI SW	IPMI SW
U31																
U30											DAQ leaf		DAQ leaf			
U29																
U28	Readout sw	Readout sw	Readout sw	Readout sw	Readout sw	DAQ spine					DAQ spine		TDE readout SW	TDE readout SW	TDE readout SW	TDE readout SW
U27																
U26	Readout sw	Readout sw	Readout sw	Readout sw	Readout sw	Readout sw										
U25																
U24	Readout sw	Readout sw	Readout sw	Readout sw	Readout sw	Readout sw										
U23																
U22	Readout sw	Readout sw	Readout sw	Readout sw	Readout sw	Readout sw										
U21																
U20	CCM server	CCM server	CCM server	CCM server	CCM server	Facility server										
U19																
U18	Readout spare	Readout server PDS	Readout spare	Readout server PDS	Readout spare	Mon server					Mon server		Readout server	Readout server	Readout server	Readout server
U17																
U16	Readout server	Readout server	Readout server	Readout server	Readout server	Mon server					Mon server		Readout server	Readout server	Readout server	Readout server
U15																
U14	Readout server	Readout server	Readout server	Readout server	Readout server	Mon server					Mon server		Readout server	Readout server	Readout server	Readout server
U13																
U12	Readout server	Readout server	Readout server	Readout server	Readout server	DFO server					DFO server		Readout server	Readout server	Readout server	Readout server
U11											MLT server		Readout server	Readout server	Readout server	Readout server
U10	Readout server	Readout server	Readout server	Readout server	Readout server	MLT server					MLT server		Readout server	Readout server	Readout server	Readout server
U9																
U8	Readout server	Readout server	Readout server	Readout server	Readout server	TRG server					TRG server		Readout server	Readout server	Readout server	Readout server
U7																
U6	Readout server	Readout server	Readout server	Readout server	Readout server	TRG server					TRG server		Readout server	Readout server	Readout server	Readout server
U5																
U4	Readout server	Readout server	Readout server	Readout server	Readout server	TRG server					TRG server		Readout server	Readout server	Readout server	Readout server
U3																
U2	Readout server	Readout server	Readout server	Readout server	Readout server	TRG server					TRG server		Readout server	Readout server	Readout server	Readout server
U1																

Figure 7.16: Preliminary layout of the underground racks for FD2-VD. Network devices use the same nomenclature as in Figure 7.15.

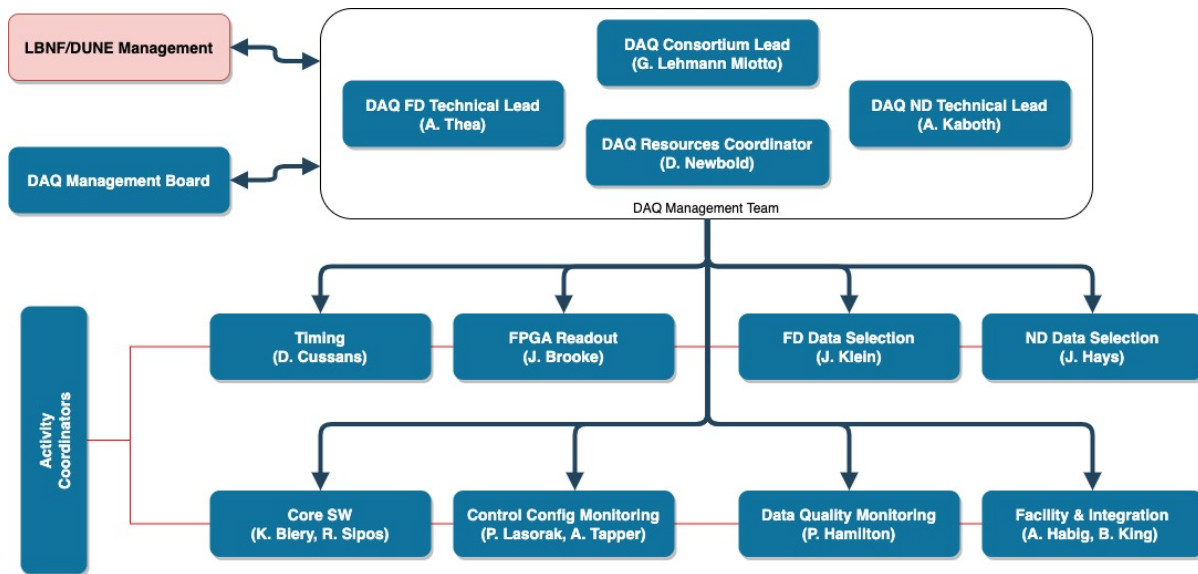


Figure 7.17: TDAQ Consortium Management Structure

For hardware deliverables (either custom electronics or COTS computing and networking), the development and evolution of the system stops at installation. Therefore, a more traditional scheduling approach is taken, involving steps of prototyping, integration and testing, pre-production, and production. Here the schedule is driven by the requirement to have all TDAQ hardware available by the time of beneficial occupancy of the FD site (surface and then underground areas respectively). Owing to risks associated with delays in hardware production, supply chain issues, or logistical problems, a conservative approach is taken, with explicit schedule contingency of up to six months for packaging and transatlantic shipping of goods, and three months allowed for logistics and handling at SURF.

### 7.8.2.2 Milestones

The TDAQ project is a single common activity for all DUNE detector elements, and is planned so as to obtain maximum efficiency and cost saving from use of common technical approaches, choice of components, and integration and validation steps. The vast majority of development and integration activities are therefore common to FD1-HD and FD2-VD, and the project is planned around a single common set of milestones, also ensuring that no conflicts exist between the installation and commissioning steps for these two detector modules. The main FD2-VD-specific deliverables are:

- Elements of online and offline software and timing system hardware which are required to support the top drift electronics;
- Data selection algorithms optimized for the FD2-VD charge readout and PDS geometry and performance;
- The installation campaign for FD2-VD.

Table 7.9 shows the top-level TDAQ-specific milestones. These are largely driven by ready-by dates for infrastructure and facilities at SURF, and by need-by dates for installation.

Table 7.9: TDAQ Top-level milestones focused on FD2-VD

Milestone	Date	Driver
Far detector final design review passed	March 2023	Procurement schedule
Ready for NP02 running	May 2023	FD2-VD Module 0 Schedule
Procurement Readiness Review passed	September 2024	Procurement schedule
Initial DAQ surface installation complete	September 2025	Surface beneficial occupancy
Timing, readout, trigger, monitoring HW procurement complete	December 2026	FD1/FD2 installation schedule
Dataflow and Data Filter HW procurement complete	June 2027	FD1/FD2 installation schedule
FD2 DAQ underground installation complete	August 2027	FD2 installation schedule
FD2 DAQ surface installation complete	Oct 2027	FD2 installation schedule
Ready for FD2 commissioning	October 2028	FD2 cool-down schedule

A summary schedule is shown in Figure 7.18.

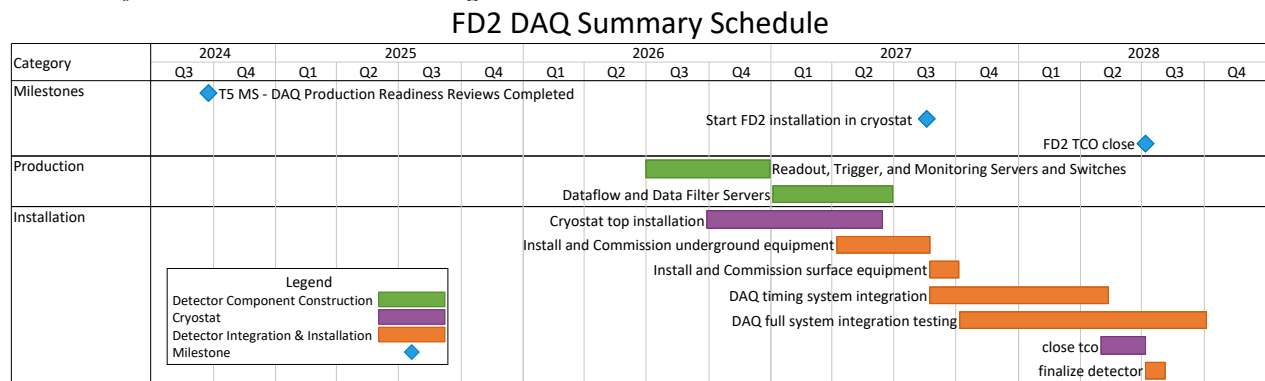


Figure 7.18: Key DAQ milestones and activities toward the FD2-VD in graphical format.

# Chapter 8

## FD2-VD Module 0

### 8.1 Introduction

The detector is a full scale demonstrator of the DUNE vertical drift detector module (FD2-VD). Assembly of the detector in the cryostat at the Neutrino Platform Facility at the European Laboratory for Particle Physics (CERN) began in fall 2022 after decommissioning of the detector; Figure 8.1 shows the inner volume of the NP02 cryostat during installation of the FD2-VD Module 0 detector. There is currently some uncertainty as to when sufficient liquid argon (LAr) will be available in Europe to fill the detector. The CERN cryogenics group is in monthly contact with all LAr vendors in Europe for the  $\sim$ kton of LAr that is needed. Our current understanding is that liquid oxygen production is very limited until steel production ramps back up. The price of delivery of LAr to CERN from the U.S. is quite high.

The active components (CRPs, photon detection systems (PDSs), cathode, etc.) are all tested in smaller cryostats (the cold box or the dedicated photon detector (PD)-cold box) to qualify the production process and detector performance. In the cold box, all time projection chamber (TPC) features (anode, cathode, PDS, E field) are reproduced at a reduced drift length. The cold box and its tests are presented in Section 8.2. More detailed discussion of cold box test results have been presented in the corresponding detector system chapters.

Section 8.3 introduces the FD2-VD Module 0 concept. Its goal is to demonstrate the high-level complete functional system integration of all FD2-VD components. Prior to filling, tests at warm will verify all connectivity and grounding issues. The cold box tests have already demonstrated the performance of detector systems in an operational environment in LAr. Given the uncertainty of LAr availability in Europe in 2023, it is possible that full tests at cold in FD2-VD Module 0 may not occur until 2024 and may be after the production readiness review (PRR) process has been initiated.

Once filled, FD2-VD Module 0 is planned to be exposed to charged particle beams from the CERN beamline. The beam test will provide valuable data to fully characterize the response and performance of the detector and complement the hadron-argon cross sections measured with .



Figure 8.1: The inner volume of NP02 during installation of the FD2-VD Module 0 detector. The two top charge-readout planes (CRPs) are visible, along with one cathode equipped with four sensors, the downstream cathode is temporarily elevated and two X-ARAPUCAs on the upstream wall are visible behind the upstream field cage (the downstream membrane wall X-ARAPUCAs are not visible). All of the X-ARAPUCAs are covered by temporary bags.



## 8.2 Cold box Test Facility

Before CRPs or PDs are installed in FD2-VD Module 0, they are tested in either the cold box located immediately next to the NP02 cryostat or the dedicated PD-cold box. The cold box makes use of the NP02 cryogenics facility. The typical cold box installation requires 4–5 days. The top-cap of the cold box acts as its roof, and the CRP is attached to it. Before installation on the cold box, the top-cap, equipped with all necessary feedthroughs, is positioned in the dedicated Faraday cage, where all connections can be debugged and the grounding tested. This Faraday cage facility is also served by the data acquisition (DAQ) system, and therefore the entire CRP can be read out and qualified prior to installation. Figure 8.2 shows a photograph of the cold box during an installation, where the roof of the cold box is shown with an attached CRP to be tested. The cathode (with an X-ARAPUCA) is visible at the bottom of the cold box.

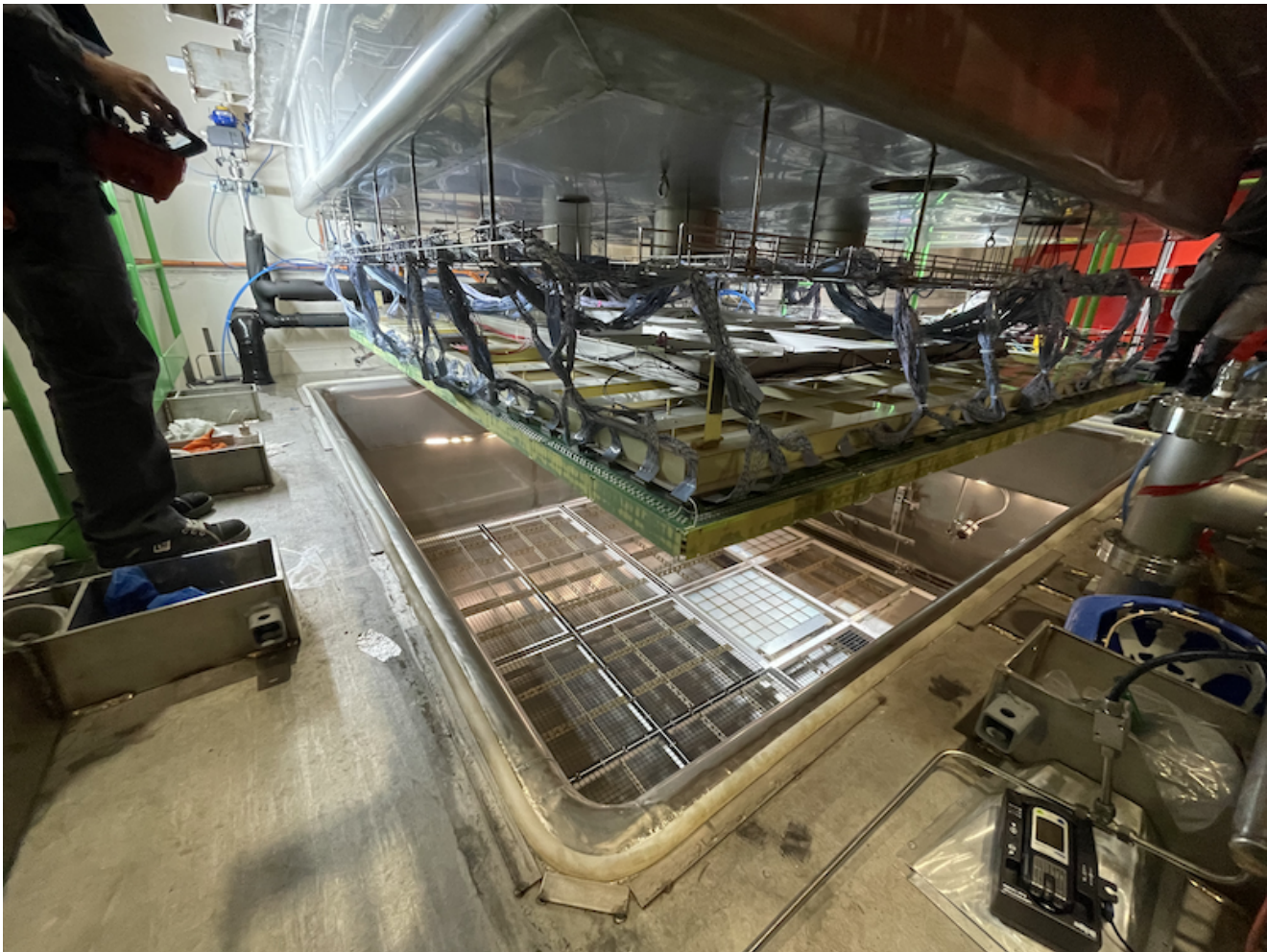


Figure 8.2: The cold box during installation of a CRP. The cathode is visible on the bottom, with an X-ARAPUCA installed.

Figure 8.3 shows the schematic layout of the cold box. Visible in yellow is the support structure of the CRP and services. Just below the CRP is an empty volume of about 25 cm for drift, and on the floor of the cold box is the cathode with the PDS. Typically the cathode sits at  $-10$  kV. Once the cold box is tested for leaks and closed, it is purged of air and filled with LAr above the yellow support structure. Then the LAr re-circulation is started, achieving a typical purity above 1.5 ms.

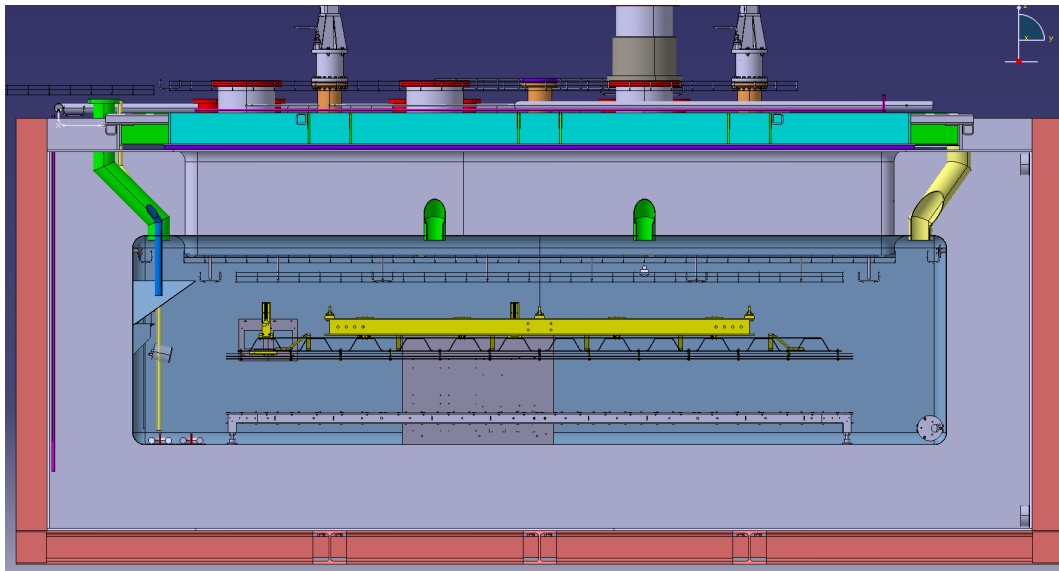


Figure 8.3: Schematic layout of the detector components inside the cold box. The top-cap (cyan), the CRP, a drift of  $\sim 25$  cm and the cathode (grey) with the X-ARAPUCA PD on the bottom at HV.

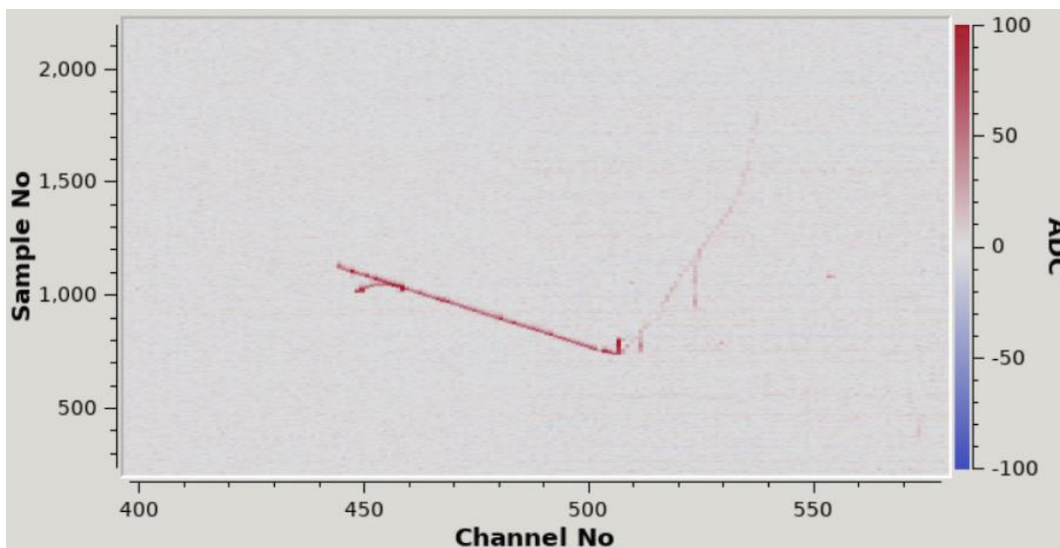


Figure 8.4: Typical raw data event display showing the quality of the reconstructed image. The image shows a muon track crossing the full drift volume from anode (the first hit at low drift times) to cathode (the top most hit at higher drift times). The faint hit signals visible to the right of the main track are due to the ionization in the LAr above the CRP, where a weak residual E field is present. The signals are weaker due to the higher electron-ion recombination, while the apparent track angle is steeper due to the slower drift velocity in the low E field above the CRP.

This purity corresponds to an attenuation length of about 2 m, well beyond the 25 cm drift length. Once the DAQ and slow control are activated, it is normal that cosmic muons appear immediately in the event displays such as the one shown in Figure 8.4.

Five pre-production CRPs will have been tested through this process. The first hybrid CRP tested in 2021 (CRP-1) was equipped with both types of electronics (half top and half bottom electronics — and ). A second test of CRP-1 in 2022 had improved grounding and some modification of the electronics layout. The second CRP (CRP-2) (top CRP with full TDE readout) was tested in summer 2022 and retested in early fall 2022 with a strip continuity issue resolved. The third CRP (CRP-3), (also full TDE) was tested in fall 2022. The first bottom CRP (CRP-5) (equipped with full cold BDE) was tested in February 2023 and the last one (CRP-4, with full BDE) was tested in March 2023. All CRPs tested reflect the layout and readout characteristics defined in the relevant chapters of this report.

The preliminary tests in the cold box have required the following operational steps (time estimate given for each step):

1. installing CRP under the top-cap of the cold box, cabling and preliminary testing of the connections: four to five days;
2. purging, cooling down and filling the cold box: three to four days;
3. turning on detector and running DAQ; and
4. emptying, warming up, and opening the cold box: five days.

In addition, a progression of X-ARAPUCA prototypes (v.1-v.4) toward the final design have been installed and tested in cold box runs throughout 2022–2023. Some runs were parasitic to CRP tests and some were dedicated to PDS. Several versions of cold PDS read-out motherboard (DCEm v.1.0 to v.2.0) including new generations of power-over-fiber (PoF) receivers and signal-over-fiber (SoF) transmitters were tested and progressively optimized. A pulsed calibration system permanently installed in the cold box allowed a diagnostic, debugging and complete characterization of the response function of the new cold PDS readout system, toward the reference design presented in this report. More detailed description of these tests can be found in Chapter 6.

The new dedicated PD-cold box in a smaller cryostat has enabled much faster turnaround on PDS testing and greatly expanded the testing capabilities for the PDS.

For the bottom CRP cold-tests in the U.S., a cold-box was built at BNL. As described in Section 3.8.2.3, it has been used for the cold-tests of CRP-5a at BNL and the cold-tests of CRP-4 at Yale.

## 8.3 FD2-VD Module 0

The FD2-VD Module 0 will validate the following aspects of the FD2-VD far detector module, which are not covered in either the cold box or the NP02 HV tests:

- The bottom CRP in the design position with the supports on the cryostat floor;

- Cathode suspension system;
- Cathode modules in their final design as in FD2-VD;
- The  $\sim 70\%$  transparent ;
- The symmetric top and bottom drifts;
- The mechanical structures of PDSs on the cryostat wall and the cable layout testing and installation; and
- PDS operation at the nominal high voltage (HV) on the cathode.

Figure 8.5 shows a model of FD2-VD Module 0 inside the NP02 cryostat.

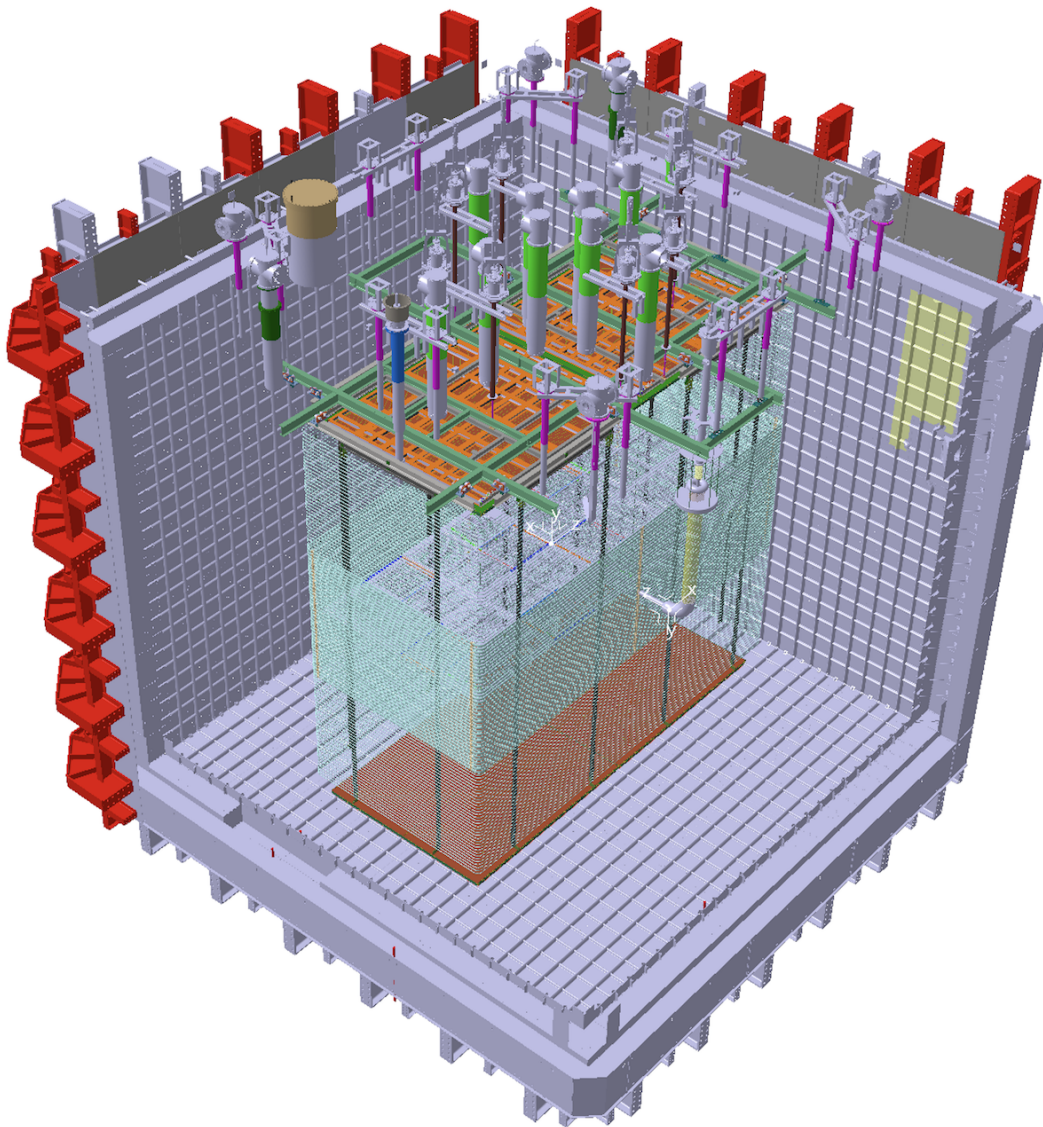


Figure 8.5: A 3D model of the FD2-VD Module 0 layout to be installed inside the NP02 cryostat.

The FD2-VD Module 0 detector design must accommodate the constraints set by the existing setup, most notably the NP02 cryostat and its roof penetrations. The interface structures are therefore required to match the positions of the various detector components with the positions of the penetrations.

### 8.3.1 Charge-readout Planes (CRPs)

FD2-VD Module 0 contains an upper and a lower drift volume, each of which has two CRPs to read out the drift charge.

#### 8.3.1.1 Top CRPs

The FD2-VD Module 0 detector top anode plane consists of two top CRPs that have already been tested in the cold box. They hang from dedicated stainless steel beams supported from roof penetrations (see Figure 8.6) as used by ProtoDUNE-DP. They are installed next to each other in the center of the cryostat, forming the TPC active area of  $3\text{m} \times \sim 6.7\text{m}$ . In this configuration, the distance between the CRP on the short side and the cryostat wall is about 73 cm, close to the value in FD2-VD.

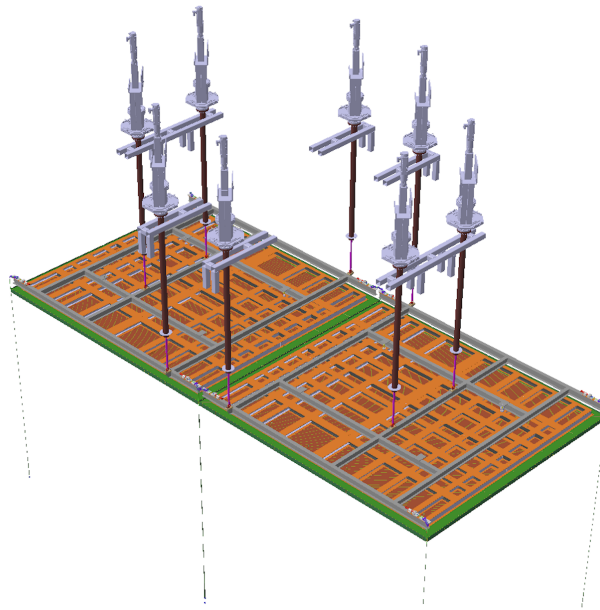


Figure 8.6: Top CRP mechanical support structure connected to the support feedthroughs.

The TDE will use the signal feedthroughs (signal feedthroughs (SFTs)) built for ProtoDUNE-DP, as shown in Figure 8.7. They are conceptually identical to what is envisaged for FD2-VD, but they differ in the size of the flange separating the clean argon volume and the volume of the SGFT. This difference is dictated by the availability of the roof penetrations in NP02.

#### 8.3.1.2 Bottom CRPs

Two bottom CRPs will be installed directly on the corrugated membrane of the cryostat, as envisaged for FD2-VD. The support structure is shown in Figure 8.8.

The bottom CRPs are identical in their layout and technology to the top CRPs. The difference lies in the readout electronics and interface boards connecting the BDE front-end mother boards (FEMBs) to the the anodes strips. The cables from the bottom CRPs will be routed on cable trays along the walls of the cryostat as shown in Figure 8.9.

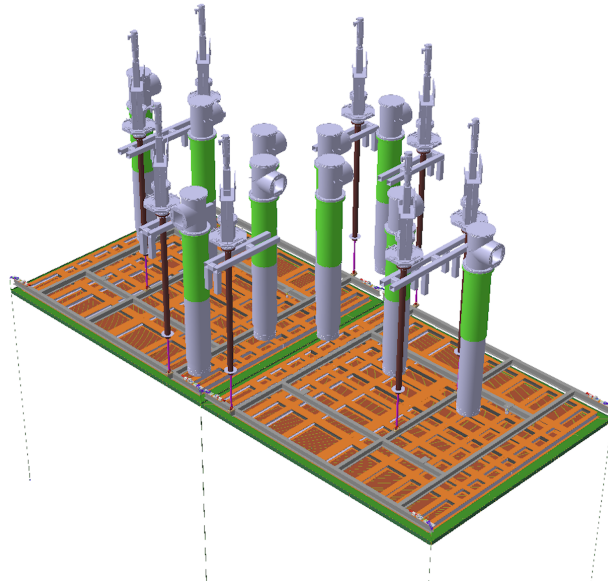


Figure 8.7: Top CRP signal feedthroughs (SFTs)

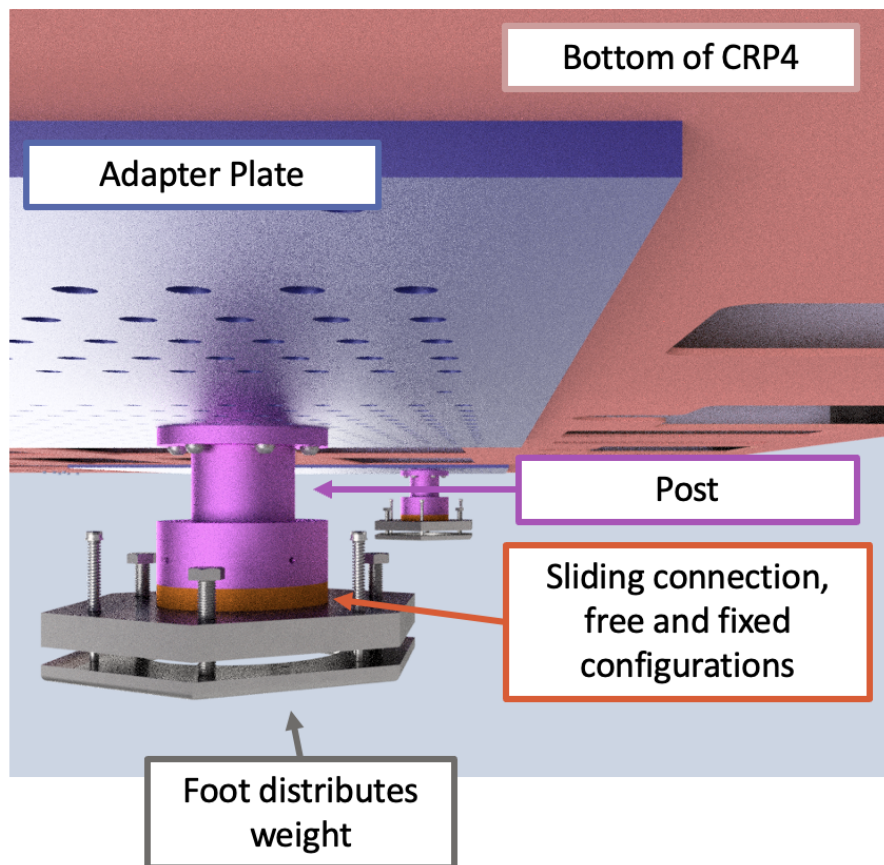


Figure 8.8: Bottom CRP supports

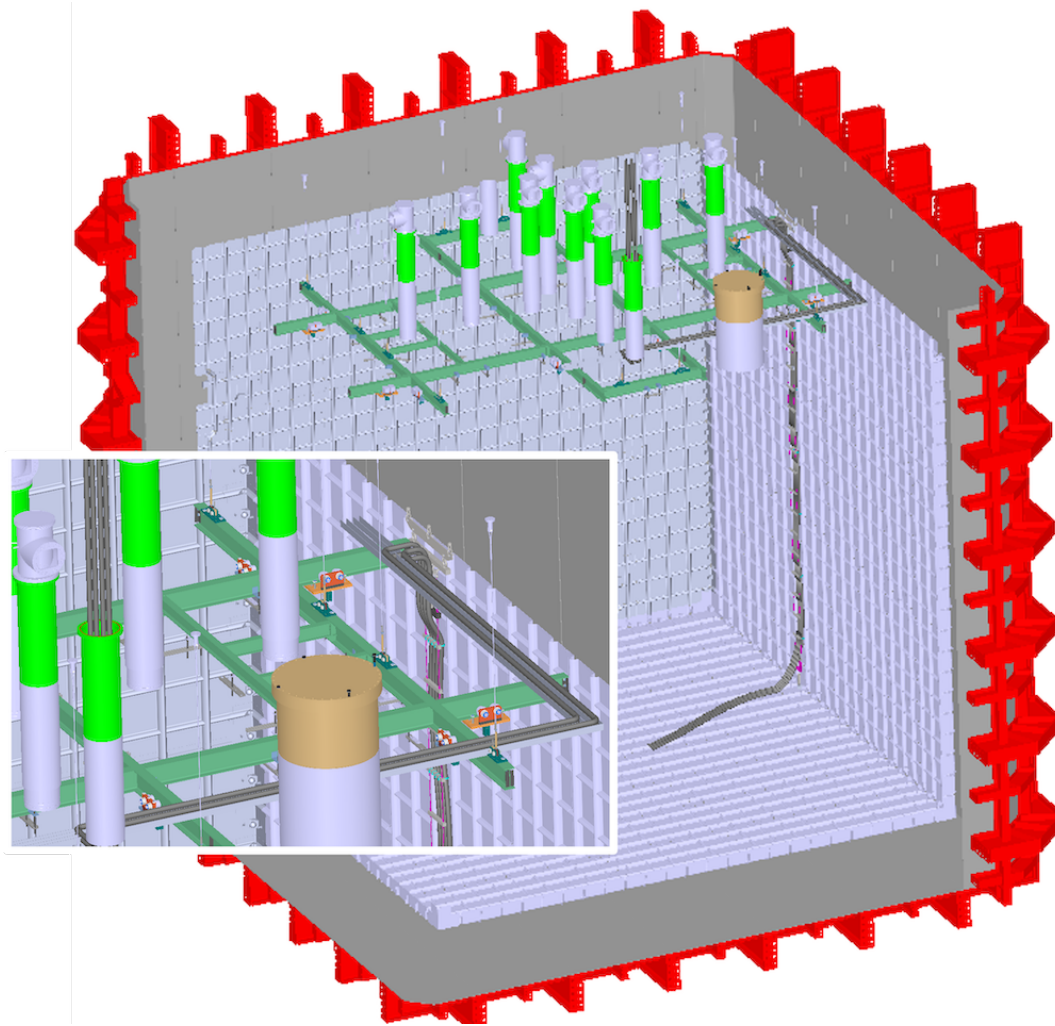


Figure 8.9: Bottom CRP cable routing in FD2-VD Module 0. The insert provides an expanded view of the cable routing near the roof. The CRPs are not shown.

## 8.3.2 HV System

The HV delivery system builds on the successful demonstration of  $-300$  kV in the NP02 HV test. The cathode consists of two modules (dimensions are the same as the CRP) suspended from the top CRP superstructure with supports at the four corners of each module at half-height of the active volume. Each cathode module will be instrumented with four X-ARAPUCAs, operating at the cathode HV and electrically isolated via PoF and SoF. The two cathode modules will be electrically connected to the field cage. The field cage design is the same as that for FD2-VD, except for the support structure which is tailored for the FD2-VD Module 0 cryostat roof penetrations. The top and bottom drift will be symmetric, with the maximum drift length of 3.2 m in both directions. To achieve the nominal E field in the drift region, half of the FD2-VD voltage will be applied in FD2-VD Module 0.

### 8.3.2.1 HV Delivery

The nominal drift field of 450 V/cm will be achieved with approximately  $-160$  kV applied to the cathode. Operation at the full DUNE  $-300$  kV was already achieved with the HV stability test in the NP02 HV test and the FD2-VD Module 0 is capable of operating the cathode at the full DUNE voltage to validate the operation at the nominal  $-300$  kV value of the fully integrated FD2-VD. Simulations indicate that the FD2-VD Module 0 is robust against HV breakdown at  $-300$  kV. FD2-VD Module 0 will provide an even more stringent test of the field cage transition region than required for FD2-VD.

For this reason — and similar to the operation in the NP02 HV test — the voltage will be provided by a commercial  $-300$  kV power supply, fed into the cryostat through a vacuum-tight HV feedthrough ( ) rated for more than 300 kV, and brought to the cathode depth by the HV extender.

The main improvements of the HV delivery system with respect to the NP02 HV stability test, where the functionality of the HV extender was successfully demonstrated, are described in Chapter 5. In summary, they consists of a new, longer and wider HVFT to avoid icing in the receptacle that receives the HV cable on the warm side, and a modified HVFT-to-extender coupling (replacing the spherical head with a cylinder and including a suspension disk adapted to support the new coupling) redesigned to mitigate the residual discharge events most likely due to the charging up of the supporting disk insulating surfaces. For the FD2-VD Module 0 detector, the straight section of the extender will be shortened to about 3 m to match the cathode depth in LAr. A dedicated test of the new HVFT and the new extender coupling is planned to validate the design improvements.

The installation of the HV extender occurs after the completion of the TPC with the procedure already tested in NP02 in the HV stability test. It will be followed by the insertion of the HVFT, the electrical connection of the cathode to the HV bus and the electrical continuity checks.

### 8.3.2.2 Cathode

The two cathode modules are constructed and installed exactly as planned for FD2-VD as described in Chapter 5. Each module has the same foot print as the CRPs and consists of two 6 cm thick half frames that will be connected together on a dedicated cart in the NP02 clean room. This is followed by the mounting of the perforated resistive panels on both surfaces of the frames and



the metallic meshes in the locations where the X-ARAPUCA are inserted. X-ARAPUCA fiber routing through the frames follows the procedure depicted for FD2-VD.

As described in Chapter 5, the Length Adjusting Devices (LADs) are hosted in the four corners of the cathode frame. Being part of the suspension system, these devices receive the insulating suspension cables and allow for fine-tuning of the cathode level when hanging from the CRP support structure.

The other end of the suspension cables is connected to the Top Adjusting Device (TAD) on the top of the CRP superstructure. Both the adjusting devices and the insulation cables are being validated for cryogenic operation in extensive dedicated tests ongoing at IJCLab.

The suspension on the CRP structure for will follow closely the one depicted for the FD2-VD, except for the fact that each CRP supporting structure holds a single CRP and a single cathode module.

Figure 8.10 shows the two cathode modules hanging from the CRP suspension structures. Figure 8.11 shows details of the cathode hanging device, the X-ARAPUCA location and the resistive panels with their supports to ensure planarity.

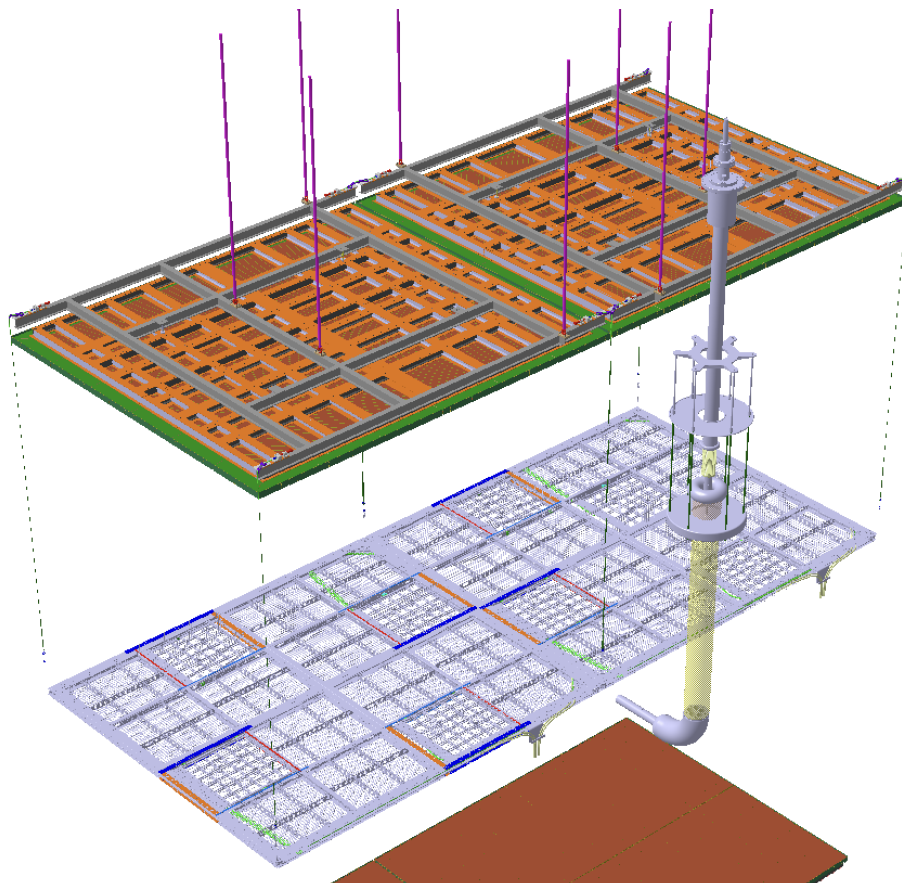


Figure 8.10: The two-module cathode supermodule hanging from the CRP suspension structures. The HV extender is also shown.

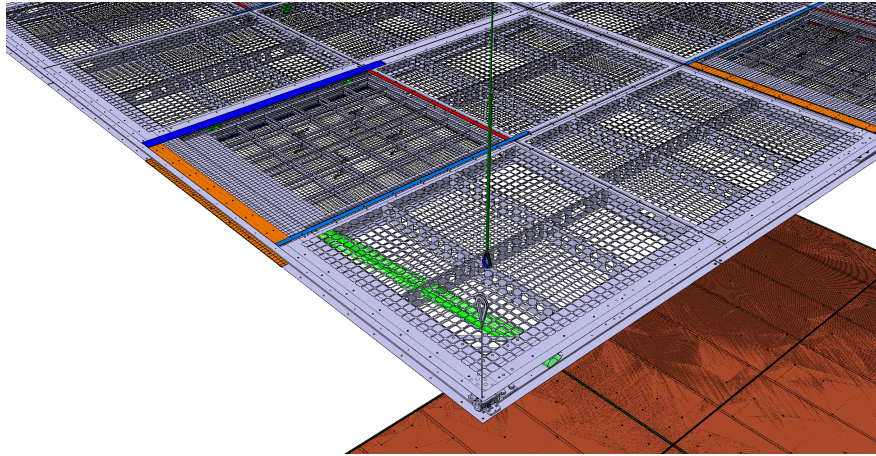


Figure 8.11: Detail of the cathode hanging device and the X-ARAPUCA locations.

### 8.3.2.3 Field Cage

The FD2-VD Module 0 field cage is designed to match as closely as possible that for FD2-VD, described in Chapter 5. It will consist of six independent columns, each of which is made of two field cage panels hanging one below the other and connected together at the cathode level. Figure 8.12 gives a global view of the field cage layout for the FD2-VD Module 0.

Each panel is 3.2m tall and hosts twenty-one 4.6 cm thick profiles, starting from the cathode level, followed by 33 thinner profiles (1.5 cm thick) to complete the field cage column to the CRP. The spacing between two neighboring field cage profiles is 6 cm (center-to-center) for both the thin and standard-thickness profiles. The profiles are kept in place with two FRP box beams (50 mm×50 mm in cross section). This scheme allows for a 70% optically transparent field cage in front of PDSs placed on the cryostat membrane, where the vertical height of the thick profile and thin profile regions are scaled by the ratio of heights of FD2-VD Module 0 and FD2-VD. The two columns on the short sides of FD2-VD Module 0 are made of 3 m long straight profiles, and their distance from the cryostat membrane is set to be  $\sim 750$  mm as planned in FD2-VD. The four columns composing the long sides of FD2-VD Module 0 host 3.4 m long profiles bent at  $90^\circ$  on one end, to minimize the local E field and to smoothly meet the profiles on the short sides. A finite element analysis (FEA) for the FD2-VD shows that this layout results in a uniform E field including the corners of the active drift volume.

Each profile will be terminated with end caps. A 3D printed version, whose compatibility with LAr and HV was previously tested, has been made for the thin profiles.

Each field cage column is equipped with high voltage divider boards (s) where each step between two neighboring profiles is made of two  $5\text{ G}\Omega$  resistors connected in parallel with a series of four varistors clamping at 1.74 kV each. This scheme was used in ProtoDUNE-DP. Most of the boards from ProtoDUNE-DP test will be reused after being refurbished with new resistors. The implementation of four varistors instead of three, as planned for FD2-VD (see Section 5.4.3), is to allow testing the vertical drift layout with  $-300$  kV applied on the cathode (the  $\Delta V$  between the profiles will be as high as 5400 V), as will be the case in FD2-VD.

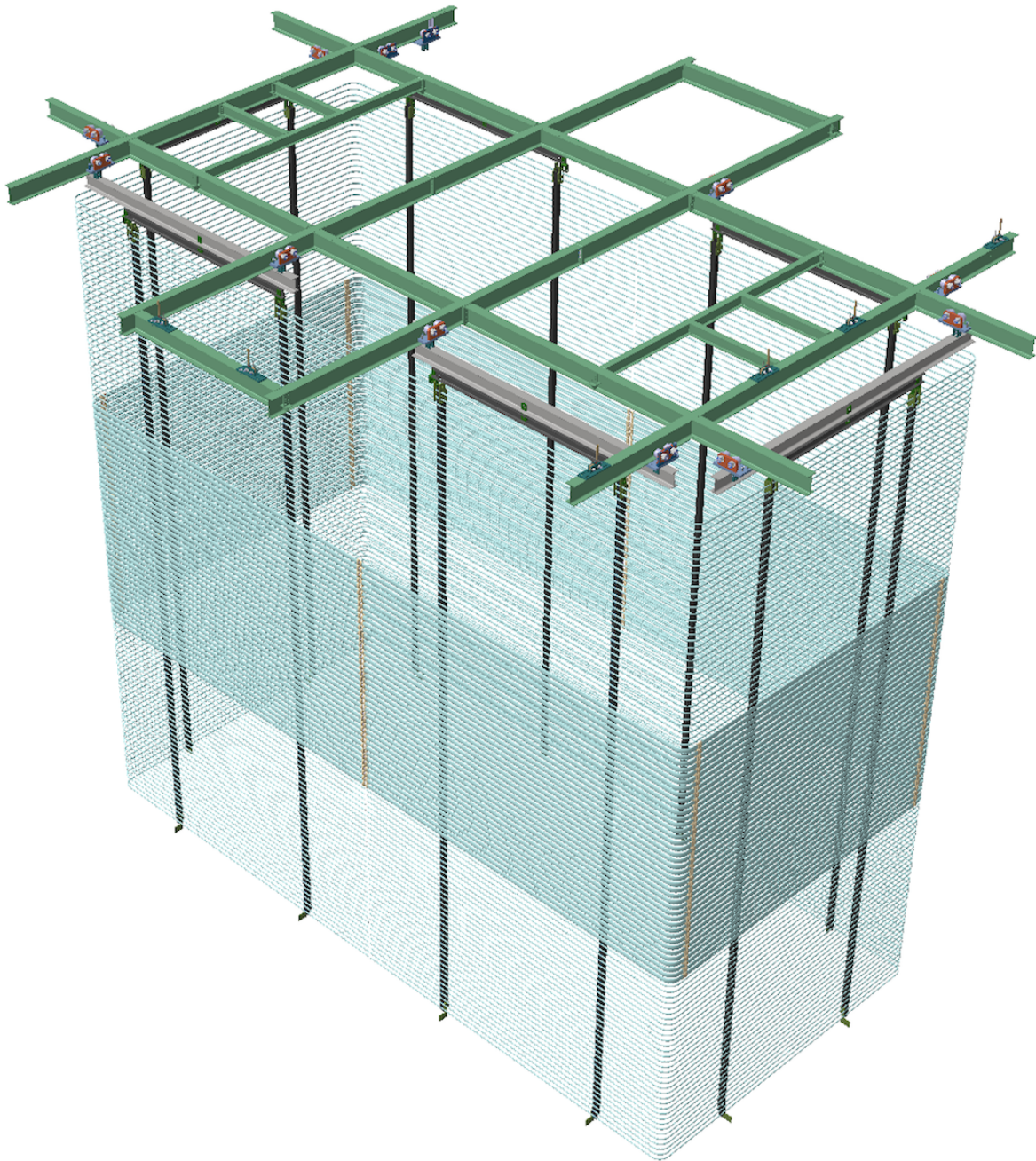


Figure 8.12: The field cage layout in the FD2-VD Module 0 design to provide two 3.2 m drift regions, above and below the cathode, with the E fields applied in opposite directions.

Each field cage column is supported at the top by an aluminum yoke, from which the FRP box beams hang. At the bottom, a ‘field cage stabilizer’ that sits on the cryostat membrane is connected to the FRP beams to avoid uncontrolled swinging of the field cage columns (details are found in Section 5.4.2). The yoke is connected at a single point to a stainless steel beam which in turn is supported by the field cage support system (FCSS) by means of trolleys. This supporting scheme ensures the verticality of the field cage columns even in case of roof/FCSS deformation. In addition, the use of trolleys allows for assembling the field cage columns away from the CRPs and cathode, and positioning them in their final location once quality control (QC) has been completed (including, possibly, the fiber routing of for the X-ARAPUCAs on the cathode).

At the cathode the field cage columns are connected together with a low-resistivity ‘HV bus’ (see Section 5.4) to distribute the HV, provided by the extender, to the outer boundary of the cathode plane.

The total dry weight of each field cage column (including the yoke, the FCSS beam and the trolleys) will not exceed 200 kg. The FRP connections between the yoke and the FRP beams have been tested to hold more than 1300 kg without failing.

The assembly of the field cage panels will be performed in the NP02 and clean rooms. Prototypes of the assembly station and the related tooling, described in Section 5.4.5, were constructed in late 2022, including the profile-bending tool, adapted from that used for NP04, and the storage cart designed to transport the field cage panels inside the NP02 cryostat.

### 8.3.3 Photon Detectors

The PDS consortium has delivered eight X-ARAPUCAs with dedicated PoF and SoF for the two cathode modules (4+4). The detailed description is in Chapter 6. Similarly, the PDS consortium has delivered four X-ARAPUCAs for the top membrane locations and plans to deliver four more X-ARAPUCAs for the bottom membrane locations (four covering the top drift and four covering the bottom drift).

### 8.3.4 Data Acquisition (DAQ)

The DAQ system as developed for ProtoDUNE-SP has been used for the cold box operations and will be used for FD2-VD Module 0.

### 8.3.5 Beam Plug

The dedicated tertiary beamline from the SPS-H2 line crosses the FD2-VD Module 0 cryostat diagonally (in the horizontal plane). It is inclined slightly downward and is fully contained in the top drift volume. It enters the field cage 96 cm above the cathode and exits  $\sim 36$  cm above it. Before entering the active volume, the total path length crossed by beam particle in inactive LAr (from the cryostat membrane to the field cage) is  $\sim 4.3$  m.

To enable data-taking with particles of well-known energy in the low-energy region of interest () to Deep Underground Neutrino Experiment (DUNE), the present plan is to reduce the inactive LAr along the beamline inside the cryostat by inserting two consecutive ‘beam plugs’ similar to

the one built and installed in NP04 for . Figure 8.13 shows a layout of the beam plug concept integrated into the NP02 FD2-VD Module 0 detector. Figure 8.14 shows the beam plug installed in the NP04 cryostat.

The first beam plug, close to the cryostat membrane, could be made of a fully metallic vacuum pipe with metallic end caps. The length would be  $\sim 2.5$  m and the diameter 25 cm. The second one, in line with the first and reaching the field cage wall, will be a vacuum pipe made of insulating material with metallic end caps; its material, length, diameter and suspension system will be similar to those for the FD1-HD Module 0 version.

The beam plug could be operated under vacuum or filled with nitrogen gas. In either case, the material budget encountered by the beam particles consists essentially of the thickness of the stainless steel end caps ( $\sim 4$ – $5$  mm each). This thickness will ensure that a sizable fraction of the low-energy beam electrons will reach the active volume before showering.

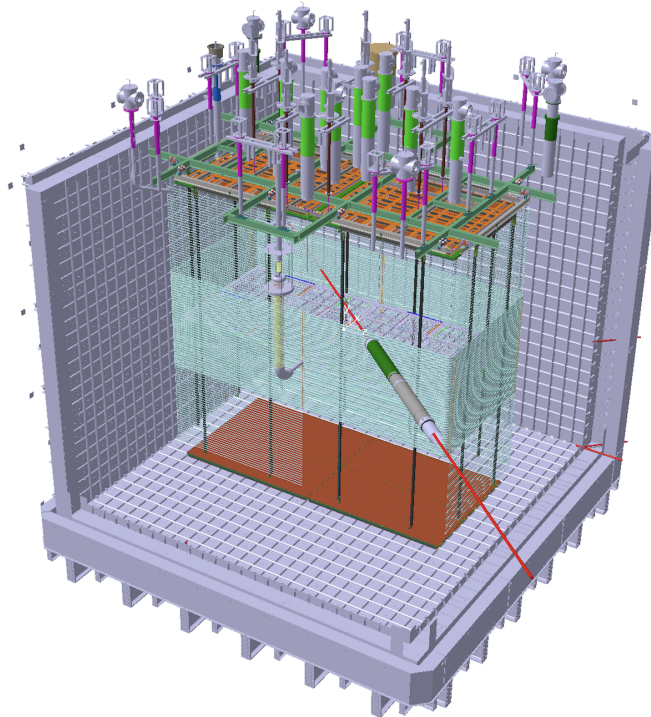


Figure 8.13: Beam plug concept for the FD2-VD Module 0 detector

### 8.3.6 Installation

The decommissioning of the current HV test setup in NP02 and the opening of the cryostat were completed in fall 2022. Installation of the detector started in December 2022 and will continue through spring 2023.

The installation sequence is as follows:

1. Install the FCSS.
2. Install top CRPs.



Figure 8.14: Photo of the beam plug realized and installed in the FD1-HD Module 0

3. Connect the cables and bias to the existing feedthroughs.
4. Install the top four membrane PDs and run the services to the feedthroughs.
5. Install the vertical cable trays.
6. Install the PDS in the two cathode modules.
7. Connect the two cathode modules to the suspension wires from the CRP supports.
8. Bring the PDS services to the cable trays and onward to the related feedthroughs.
9. Install the bottom CRPs and run the cables via the vertical cable trays to the dedicated feedthroughs.
10. Install the field cage and the HV system.
11. Install the four bottom membrane PDS and run the services to the feedthroughs.
12. Install the beam plug.
13. Clean the cryostat.
14. Close the temporary construction opening (TCO).

The slow control system remains in place from ProtoDUNE-DP and will be available for dedicated debugging activities after each component is installed. Detector component tests are described in their respective chapters in this report. All of the installation steps will go through the standard CERN planning and review, with dedicated environment, safety and health (ES&H) documentation to be prepared and accepted in advance for each step. All components installed in FD2-VD Module 0 are pre-production units.

### 8.3.7 Infrastructure

The cryogenics is unchanged. The grounding scheme is based on full electrical isolation of all components on the cryostat and of the cryostat itself, with respect to the building ground.

- Cryogenics instrumentation;
- Grounding scheme;
- Slow control;
- TCO opening and closure approach;
- Cryogenics scheme and operation.

The TCO closing is similar to that of ProtoDUNE-SP and ProtoDUNE-DP. The slow control is essentially unchanged. The cryogenics instrumentation (temperature and purity) is similar, with some upgrades.

### 8.3.8 Timeline and Strategy for Fill and Operation

The filling schedule of FD2-VD Module 0 depends on the market availability of LAr ( $\sim 1$  kt) at reasonable cost. At the time of writing this report, no firm offer is available from any vendor in Europe. When LAr becomes available, the present plan is to fill the NP04 cryostat for FD1-HD Module 0 first and then to transfer that LAr to the NP02 cryostat for FD2-VD Module 0 once FD1-HD Module 0 has been tested and qualified, probably five months after filling. Discussions are ongoing as to whether to reverse the sequence and start with NP02. The DUNE collaboration will make this decision once the availability of the necessary quantity of LAr is known. If the cost allows, it could even be possible to fill both cryostats at the same time.

The FD2-VD Module 0 is simpler to fill since no requirement exists on the maximum temperature gradient during filling, as is the case for FD1-HD Module 0. The level of LAr should reach the height of the FCSS or above.

Slow control monitoring systems will follow the entire operation from the beginning. Dedicated dimensional and stress probes will be operational on the external wall of the cryostat to monitor abnormal behaviors. Once the NP02 cryostat is full, the next step is to turn on the required HV and the various biases to the electronics, followed by the DAQ systems.

Exposure to the dedicated H2 tertiary beam is planned. With the filling plan described above, this will most likely happen in 2024. The beam time request to CERN will be refined and submitted toward the end of 2023.

# Chapter 9

## Integrated Engineering and Installation

### 9.1 Introduction

The will provide facilities on the surface and underground at the Sanford Underground Research Facility (SURF) to house and support the DUNE far detector modules, and once DUNE obtains acceptance for use and possession (AUP), the Fermi National Accelerator Laboratory (Fermilab) Fermilab South Dakota Services Division (SDSD) will assist the LBNF/DUNE-US far site integration and installation () team with the integration and installation of the detector and its safe and productive operation, providing logistical, electrical, mechanical, cyber, and environmental support.

The FSII team has responsibility for integration engineering at the far site. Section 9.3 describes the integration engineering and it also describes the critical services the FSII team provides: warehousing, transportation, and logistics support. The FDC physical deliverables include the detector cryostat, cryogenics system, and installation infrastructure (Figure 9.1); FSCF-BSI provides the initial electrical infrastructure. Section 9.8 outlines the installation process.

### 9.2 Requirements and Specifications

The principal requirements and specifications for these activities are listed in Table 9.1.

Table 9.1: Installation specifications

Label	Description	Specification (Goal)	Rationale	Validation
INST-1	Compliance with the SURF Material Handling Specification for all material transported underground	SURF Material Handling Specification	Loads must fit in the shaft be lifted safely.	Visual and documentation check



INST-2	Coordination of shipments with construction manager/general contractor (CMGC); DUNE to schedule use of Ross Shaft	2 wk notice to CMGC	to	Both DUNE and CMGC need to use Ross Shaft	
INST-3	Maintain materials buffer at logistics facility in SD	> 1 month		Prevent schedule delays in case of shipping or customs delays	Documentation and progress reporting
INST-4	Installation cleanroom Specification	ISO 8		Reduce dust (contains U/Th) to prevent induced radiological background in detector	Monitor air purity
INST-5	UV filter in installation cleanrooms for PDS sensor protection	filter < 400 nm for > 2 wk exp; < 520 nm all else		Prevent damage to PD coatings	Visual or spectrographic inspection

The FSII team requires that all materials to be immersed in LAr be validated in a liquid argon (LAr) test stand in order to satisfy FD-5 in Table 1.1. This is the responsibility of the consortia.

## 9.3 Detector Integration

### 9.3.1 Responsibilities and Activities

The detector integration is the responsibility of the FSII team in cooperation with the various Deep Underground Neutrino Experiment (DUNE) consortium technical leads. It comprises the activities listed below and involves several specialized engineering skills and groups within the LBNF/DUNE-US, e.g., the review office (RO), the compliance office (CO), and safety professionals.

- 3D model integration,
- mechanical conflict detection,
- interface drawings,
- integration with FSCF-BSI,
- interface to integration deliverables,
- warehousing and logistics,
- scheduling and planning,
- detector slow control,
- material transport underground,
- integration with cryostat, and
- management and oversight of underground work.

A configuration control office provides all modeling and its verification, including all interfaces to the civil engineering activities of FSCF-BSI.

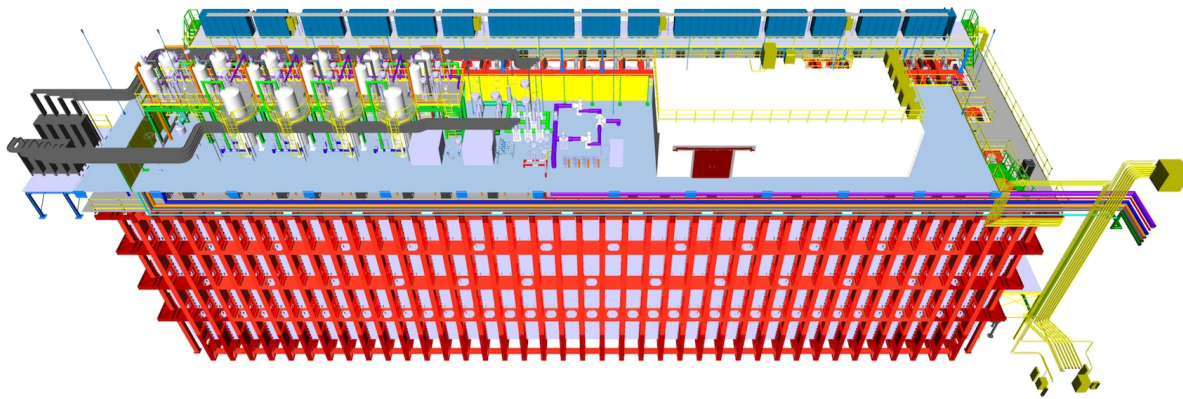


Figure 9.1: Model of cryostat outer structure and the mezzanines above its roof. The cryogenics mezzanine (60.5 m × 11.3 m) appears in the foreground, the detector electronics mezzanine (61.5 m × 3.6 m) appears behind it.

The RO, led by four senior physicists and engineers, will perform centralized technical reviews of the various aspects of the detector throughout the design process, ending with operational readiness reviews (ORRs).

The CO enforces the rules and codes that apply to the design of each component and verifies the validity of the structural analyses. The SDS is responsible for material and component receipt and logistics, and for the final delivery of materials to the appropriate underground cavern. This responsibility includes the hiring and management of underground work managers, a crew for basic services (electricity, ventilation, networking), and safety inspectors.

## 9.3.2 Cryostat and Cryogenics Systems

### 9.3.2.1 Cryostat Design Overview

The vertical drift detector module (FD2-VD) cryostat will be constructed using membrane cryostat technology, as for the horizontal drift detector module (FD1-HD) and the two ProtoDUNE cryostats. In the cryostat design, described in [101], a 1.2 mm thick, corrugated stainless steel membrane forms a sealed container for the LAr, with surrounding layers of thermal insulation and vapor barriers. Outside these layers, a free-standing steel frame forms the outer (warm) vessel, the bottom and sides of which support the hydrostatic load. The roof of the cryostat supports most of the components and equipment within the cryostat. The design differs between FD1-HD and FD2-VD largely in two areas: the number and location of the roof penetrations, and the size of the temporary construction opening (TCO).

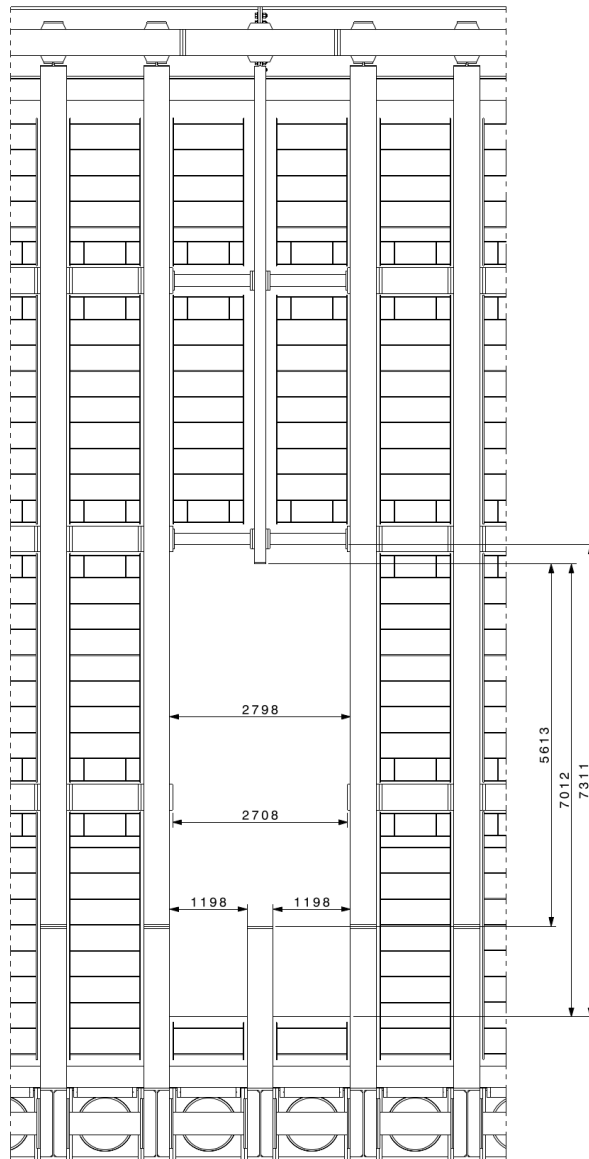


Figure 9.2: View of part of cryostat endwall from exterior, showing TCO layout and dimensions.

The detector penetration details were finalized in November 2021. The cryostat engineering firm, GTT, provided an updated design for the cryostat in accordance with the new penetration specifications, an updated list of materials to be procured, and appropriate testing and installation procedures. The European Laboratory for Particle Physics (CERN) holds the engineering contract with GTT for the cryostats, and this contract accommodates these updates.

### 9.3.2.2 Detector Assembly within Cryostat

Given the sizes, relative robustness and modularity of the FD2-VD components, much of the detector assembly work can be done inside the cryostat. The TCO height can therefore be reduced by about half relative to the FD1-HD design, to 7.3 m (see Figure 9.2), which will reduce the time needed to close it. Closing the TCO from the exterior will be tested in 2023 on the cryostat; experience gained from this will further simplify and shorten the procedure for FD2-VD as well as eliminate the risks and difficulties associated with performing work inside the cryostat after the detector is fully installed.

### 9.3.2.3 Cryostat Roof Penetrations: Parameters and Uses

The cryostat roof penetration locations and parameters are given in Figure 9.3 and Table 9.2. Together, the 293 penetrations on the cryostat roof accommodate all the cabling, wiring, and instrumentation needed by the charge-readout plane (CRP) superstructures, the time projection chamber (TPC) and photon detection system (PDS) readout, and the interior cryogenics instrumentation. The 64 CRP support penetrations (orange-colored in Figure 9.3 and Table 9.2) can be motorized in order to control the position and the planarity of the detector elements after LAr filling. Four of the penetrations (violet-colored in the diagram), one on each corner, are access holes that will allow continued access to the interior once the TCO is closed and until everything is ready for the purge and cool-down process to start. During the detector installation, clean air will be injected into the cryostat through these access holes.

### 9.3.2.4 Cryogenics Infrastructure in the Cryostat

The cryogenics system is described in detail in the Cryogenics Design Report [101]. The cryogenics system has been scaled and designed to perform similarly to the systems at CERN. Excellent purity was achieved in , and simulations [54] indicate that FD2-VD should perform in a similar manner, limiting impurities to <30 ppt, thereby reaching the specification goal listed in FD-5 (see Table 1.1). These simulations concluded that any possible effects from superheating of the LAr would be confined to the top layer of the liquid.

As the cryostat dimensions and corresponding external heat loads are identical for the FD1-HD and FD2-VD detector modules, and the heat load from the electrical power and the roof penetrations are similar, the primary cryogenics plant in the central utility cavern (CUC) was designed for and will service both. This system is described in detail in [101].

The FD2-VD design does not require fine control of the temperature gradient during cool-down, therefore no sprayers are needed on the short end walls, reducing the amount of internal cryogenics needed relative to the FD1-HD. In addition, pipes for flushing gaseous argon (GAr) and distributing LAr are needed only along the outer edges of the cryostat floor and up the long walls in this design,

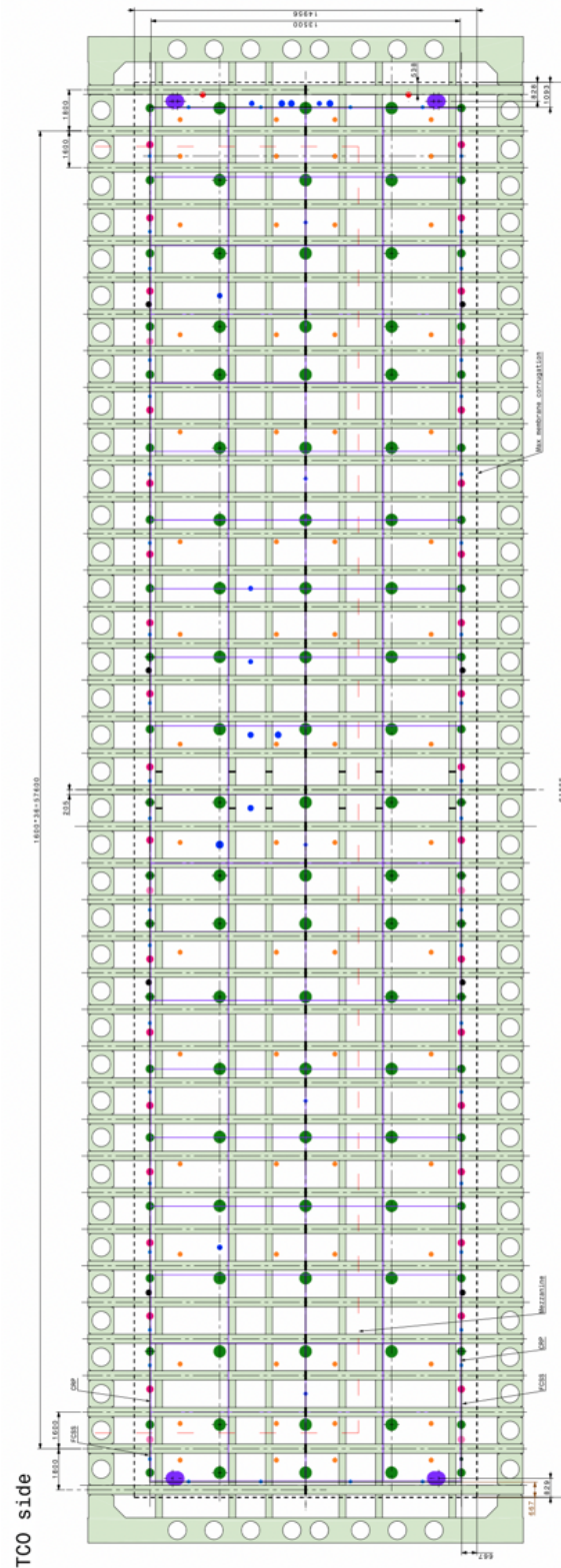


Figure 9.3: The layout of penetrations on the cryostat roof. The major dimensions (in meters) are 62.00 and 15.10 (primary membrane length and width), 60.02 and 13.50 ( length and width). See Figure 9.4 for a detail of the top right corner.

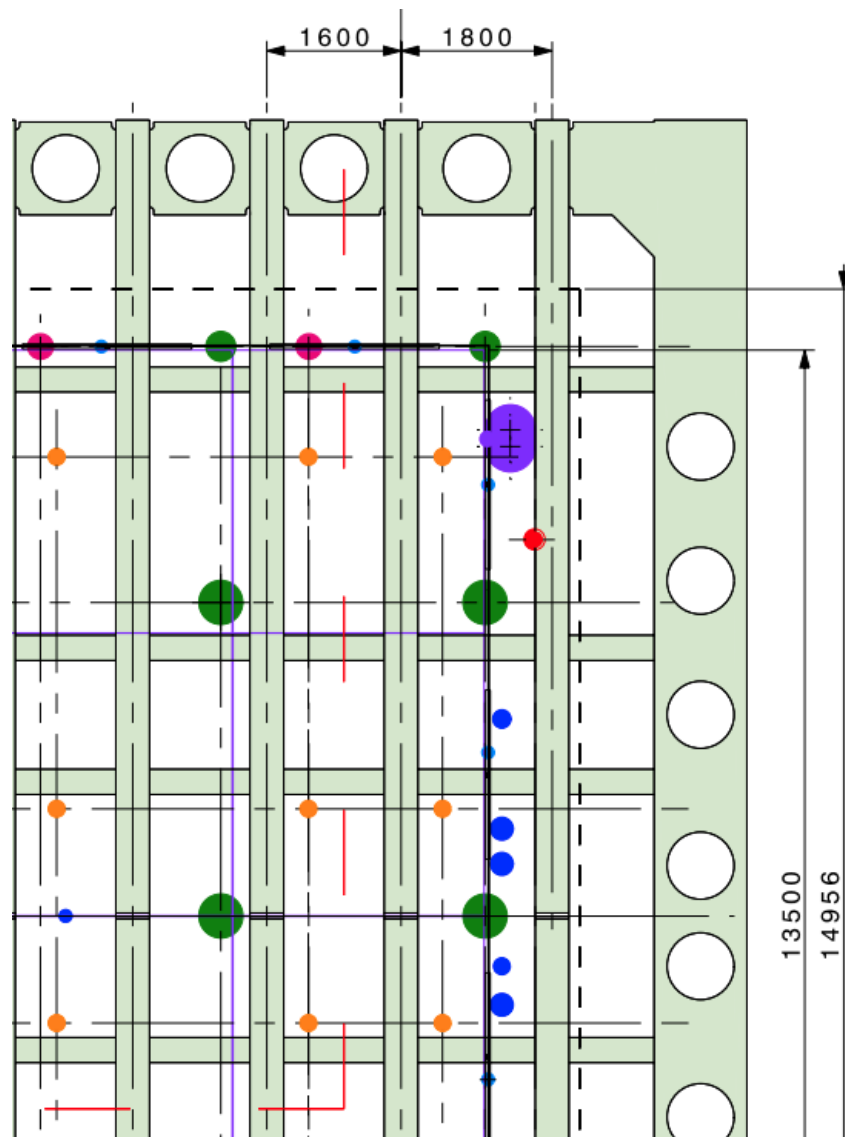


Figure 9.4: Detail of the cryostat roof penetrations showing the end opposite from TCO (top right corner of Figure 9.3).

Table 9.2: Cryostat roof penetration parameters; colors correspond to Figures 9.3 and 9.4.

Color	Diam. (mm)	Quantity	Description
orange	200	64	CRP supports
green	526	63	Top center CRP cables
green	355.6	42	Top side CRP cables
dark pink	304.8	34	Bottom CRP cables + PDS
light pink	304.8	6	Bottom CRP cables
red	250	2	High voltage
black	250	8	Laser
violet	800	4	Access hatches
light blue	150	48	FC supports
light blue	250	4	
blue	250	2	Water trap
blue	200	3	Spares
blue	152	5	GAr controlled vent
blue	273	1	GAr boiloff
blue	324	1	
blue	273	3	LAr return
blue	219	3	GAr purge; GAr make up

as shown in Figures 9.5 and 9.6. This allows flexibility in optimizing the vertical position of the detector within the cryostat.

### 9.3.2.5 Cryogenic Instrumentation

The FD2-VD cryogenics instrumentation is designed to provide real-time measurements of the state of the LAr (i.e., purity, temperature, level) and in particular, to provide prompt indications of any changes in its state. As in the FD1-HD module, external purity monitors will be installed immediately downstream of the filtration system to signal any deterioration in the performance of the filters, and space is reserved for a purity monitor immediately upstream of the filtration system to measure the quality of the argon as it leaves the cryostat.

#### 9.3.2.5.1 Purity Monitors

Four purity monitors will be installed inside the cryostat, one pair on each of the upstream and downstream ends, one outside the upper drift volume and the other outside the lower. Each purity monitor requires quartz optical fibers that deliver xenon UV light to the gold photon cathode and are protected in a flexible fiber-bellow-hose, and traditional coaxial cables that provide high voltage (HV) and signal readout. There are no dedicated roof penetrations for the purity monitors. Instead, the access hole covers will be used as feedthroughs for the monitor fibers and cables. On each end of the detector, one (upper) purity monitor will be mounted to the bottom of the access hole radiation shielding (see Figure 9.7), and the other will sit on a simple stand on the cryostat floor. The cables and fibers for both will be routed up through the radiation shielding, and for the lower monitor, they will continue down the corner of the cryostat and then across the floor to the

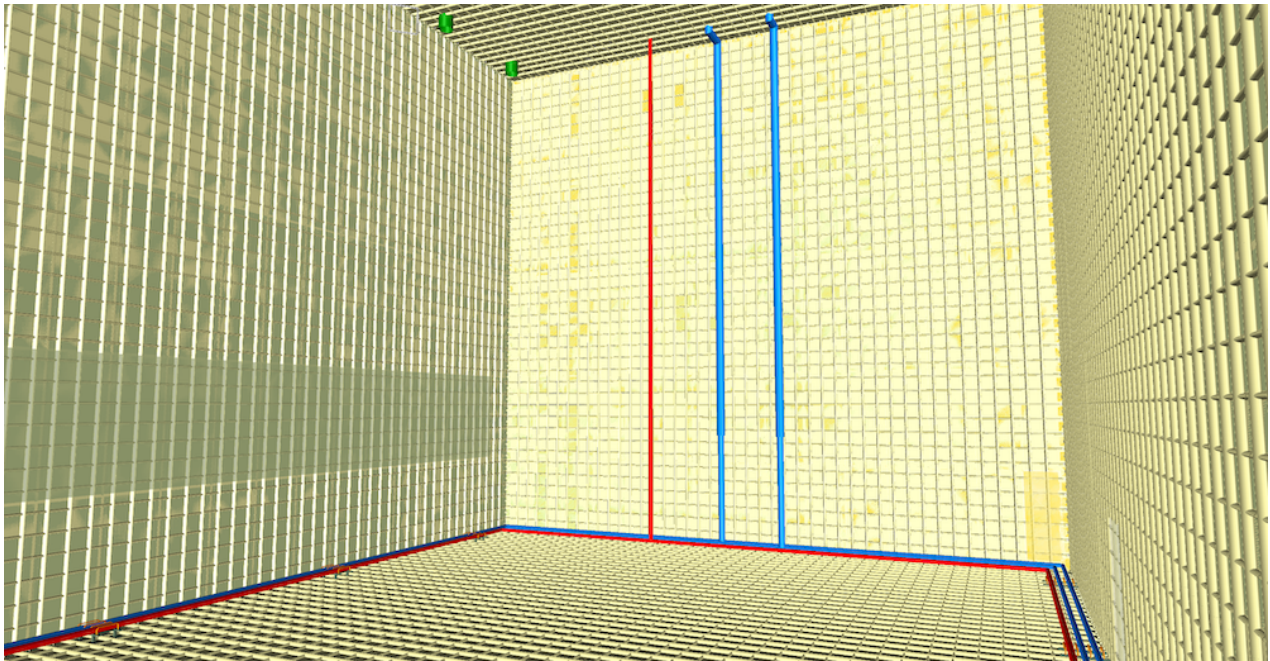


Figure 9.5: Internal cryogenic piping at the top. The red pipe is the gas purge line and the two blue pipes are the liquid return lines.

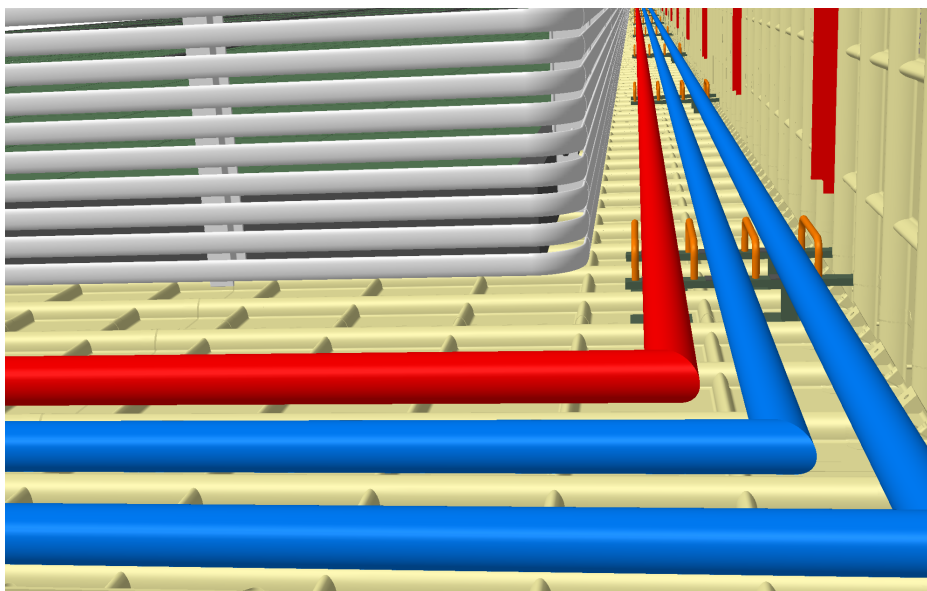


Figure 9.6: Internal cryogenic piping and floor supports.



lower monitor.

The installation procedure of a purity monitor (PrM) assembly is as follows:

1. The cables and fibers are routed along the corner of the wall of the cryostat and placed near the roof so they can be reached at the completion of the detector installation.
2. After the top CRP and cathode are installed, but before installation of the east endwall field cage (endwall FC), the east lower purity monitor is installed and connected to its cables. It will become inaccessible after this point.
3. After the west endwall FC is in place, the west lower purity monitor is installed along with its stand, and cabled.
4. Immediately before closing the TCO, the top purity monitors are mounted to the radiation shields attached to the bottom of the sealing flange to the access ports, the cables inside the detector near the access holes are pulled up and attached to the purity monitor feedthrough that is welded to the access hole cover flange, and the access holes are closed.

#### 9.3.2.5.2 Temperature Monitors

Plans to measure the temperature of the LAr entering the cryostat will be formulated based on the details of the cryogenic piping. The baseline design assumes a total of 16 precision RTDs, deployed in pairs, with four sensors per pipe at opposite cryostat corners.

The temperature of the LAr leaving the cryostat will be also monitored, with two sensors near each of the four pumps at the bottom of one of the short walls. Finally, one RTDs above and below each purity monitor will facilitate the study of correlations between temperature and purity.

The temperature of the gas argon at the top of the cryostat (in the ullage) will be monitored using arrays of 18 sensors at ten different locations above the CRPs. The top 14 sensors will be standard RTDs since the temperature gradient will be very large. The four sensors at the bottom, which are expected to be below the LAr surface, will be precision RTDs.

All systems described above have been prototyped in ProtoDUNE-SP.

A prototype of a system to measure the LAr vertical temperature gradient in the proximity of the active volume will be deployed in .

Vertical arrays of standard RTDs will be epoxied to the cryostat membrane in two opposite corners of the cryostat with the aim of monitoring the membrane temperature during cool-down and filling.

The thermometry is installed in the first phase of the detector installation when the cryostat false floor is in place but the walls are accessible using the scissor lifts.

#### 9.3.2.5.3 Alignment Monitors

A laser-based alignment system is not part of the FD2-VD baseline design, but active prototyping is ongoing. This system would provide artificial straight tracks used for mechanical alignment. Six penetrations will be available to accommodate a future laser-based alignment system and physical

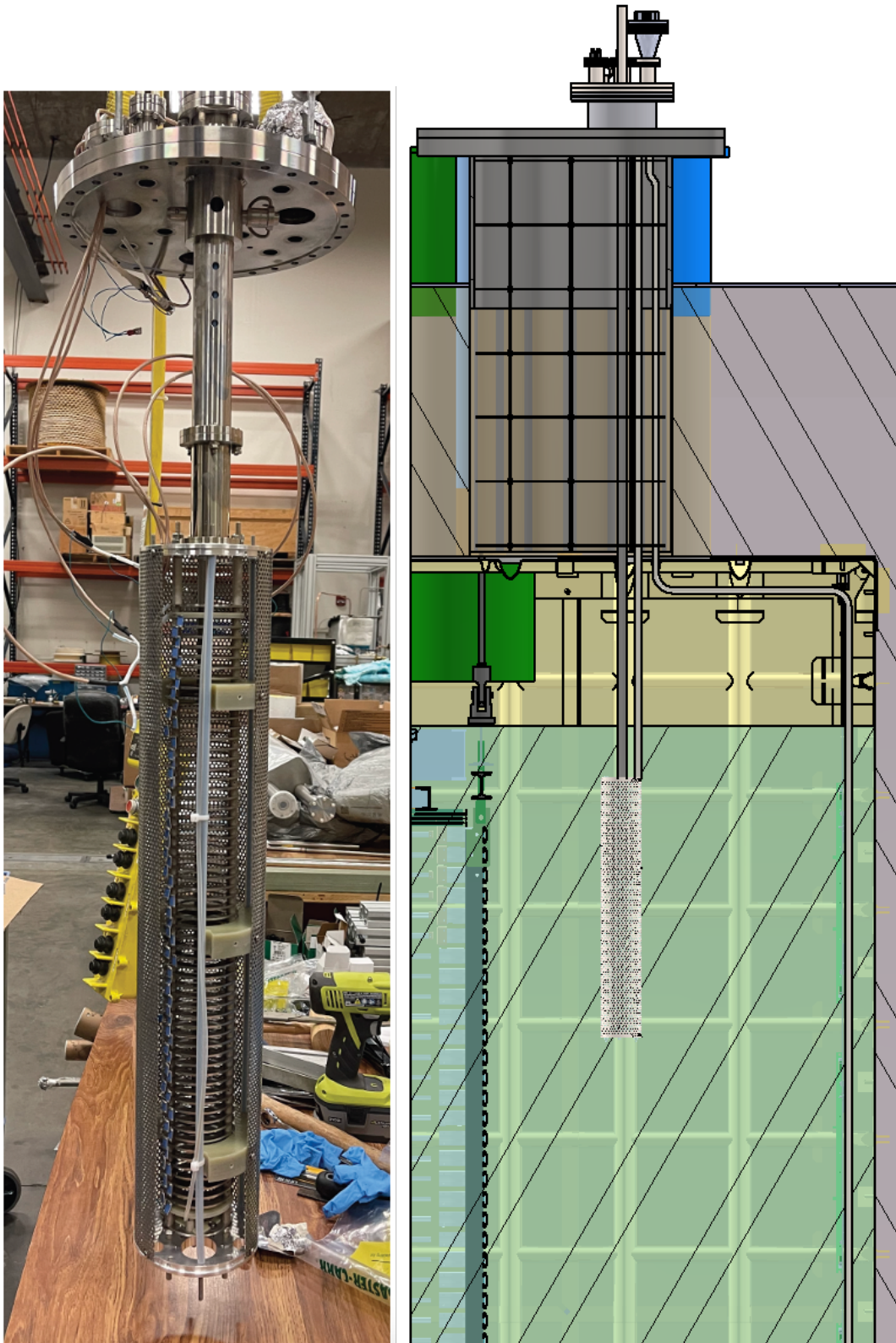


Figure 9.7: Left: Photograph of a purity monitor. Right: 3D model of a purity monitor mounted under an access port.

space is reserved.

### 9.3.3 Electrical Infrastructure

In addition to that provided by FSII, after gaining AUP of the caverns the FDC subproject will provide additional electrical infrastructure. This includes the installation of detector power and ground, power and cooling for data acquisition (DAQ) racks, readout racks located both on the detector and on the detector rack mezzanine, optical fiber distribution for both data and network, and a DUNE detector safety system (DDSS).

#### 9.3.3.1 Grounding and Detector Power

The grounding strategy provides each detector module with an independent ground to minimize any environmental electrical noise that could couple into detector readout electronics either conductively or through emitted electromagnetic interference. The plan includes a separate detector ground, separated from the rest of the facility, for each of the four planned detector modules. The detector ground will primarily consist of the steel containment vessel, cryostat membrane, and connected readout electronics.

For safety reasons, a saturable inductor must connect the detector ground to the facility ground. This saturable inductor provides an impedance to any AC environmental noise on the facility ground as well as a safety path for any DC fault current that could damage equipment or harm personnel.

Power for the FD2-VD will be provided through transformers located in the CUC electrical room. (FSCF-BSI will supply a 1000 kVA transformer for each cavern.) Power from these initial transformers will be run through special double-shielded transformers, which allows for separation of facility power and ground from detector power and ground. The saturable inductor will be located close to these double-shielded transformers and provide the safety ground.

Power to each detector module will be de-rated to no more than 75% of total power available (500 kVA) at the electrical distribution panels. Consumption per detector module is planned to remain at or below 375 kW. AC power will be distributed from the DAQ barracks on the cryogenics mezzanine to approximately 80 detector racks located on the detector rack mezzanine and to 320 Micro Telecommunications Computing Architecture ( $\mu$ TCA) crates distributed on top of the FD2-VD cryostat. Figure 9.8 shows the anticipated load of the FD2-VD to be approximately 300 kW.

#### 9.3.3.2 Detector Readout Electronics

A DAQ barrack, to be located on top of the cryogenics mezzanine, will be referenced to facility ground. Only fiber optic cables will be allowed to run between the detector electronics and the DAQ barrack in order to maintain the ground separation of facility and detector electronics. DAQ will install 16 racks in this room with an expected load of 125 kW. A transformer to provide this power will be located on the roof of the barrack, along with a cooling unit to maintain the required temperature and humidity levels. All DAQ power will be UPS backed, with a requirement of 10 minutes of standby power to protect the DAQ servers.

Detector electronics are installed on detector feedthroughs, in 27U racks close to feedthroughs,

Power Loads for DUNE FD2						
<b>TDE</b>		<b>(KW)</b>	<b>(KW)</b>	<b>BDE</b>	<b>(KW)</b>	<b>(KW)</b>
Qty (320) uATC @500W		160		Qty (14) LVDC PS 3U @ 3KW	42	
Qty (20) LVDC PS 7U @ 1KW		20		Qty (14) Heater PS @ 0.5KW	7	
Qty (19) White Rabbit 1U @ 200W		3.8		Qty (14) Fan PS @ 0.5KW	7	
Qty (11) Calibration 2U @ 100W		1.1		Qty (14) BDE Safety System @ 0.3KW	4.2	
			<b>184.9</b>			<b>60.2</b>
<b>Rack Infrastructure</b>				<b>HV</b>		
Network switch qty (76) @ ~240W		18.24		300kV power supply	1	
Rack Protection/PDU (76) @ ~200W		15.2		cold camera power supplies	0.1	
			<b>33.44</b>	CRP Bias PS (480 ch)	7.68	
				Field Cage Termination PS (96 ch)	1.92	
				(144 ISEG chan Module ~1920W)		<b>10.7</b>
<b>PDS</b>						
Qty (40) LVDS PS channels @50W for DAPHNE		2				
Qty (40) LVDS PS channels @50W for Light Calibartion Unit		2				
Qty (80) POF crates @50W		4				
			<b>8</b>			
				<b>Total Power</b>		<b>297.24</b>

Figure 9.8: Power budget table.

and in taller racks located on a detector mezzanine. The detector rack mezzanine will hold approximately 80 racks and be referenced to detector ground, allowing easy access for maintenance and reducing complexity on top of the detector. These racks will include cooling fans, a rack protection system, smoke detection and a power distribution unit. If smoke is detected within a rack, a hardware interlock will shut power off to the rack.

The DUNE experiment requires a number of fiber optic pairs to run between the surface and the . These fibers serve as the pathways for data, networking, and slow controls. A total of 96 fiber pairs, which will accommodate both DUNE and FSCF-BSI needs, will be supplied through redundant paths with bundles of 96 pairs coming down both the Ross and Yates Shafts. The individual fibers are specified to allow for transmission of 100 Gbps. The fibers run between the surface main communications room (MCR) and a central location in the CUC and then to each DAQ barrack. From the MCR, they connect to the WAN and ESnet to get to Fermilab. Figure 9.9 shows the fiber plan for the detector.

## 9.4 Safety

The LBNF/DUNE Integrated environment, safety and health (ES&H) Plan [12] outlines the requirements and regulations that DUNE work must comply with, whether (1) at Fermilab, (2) in areas leased by Fermilab or the , (3) in leased space at SURF, or (4) at collaborating institutions.

### 9.4.1 Documentation Approval Process

DUNE implements an engineering review and approval process for all required documentation, including structural calculations, assembly drawings, load tests, hazard analysis (HA), and proce-

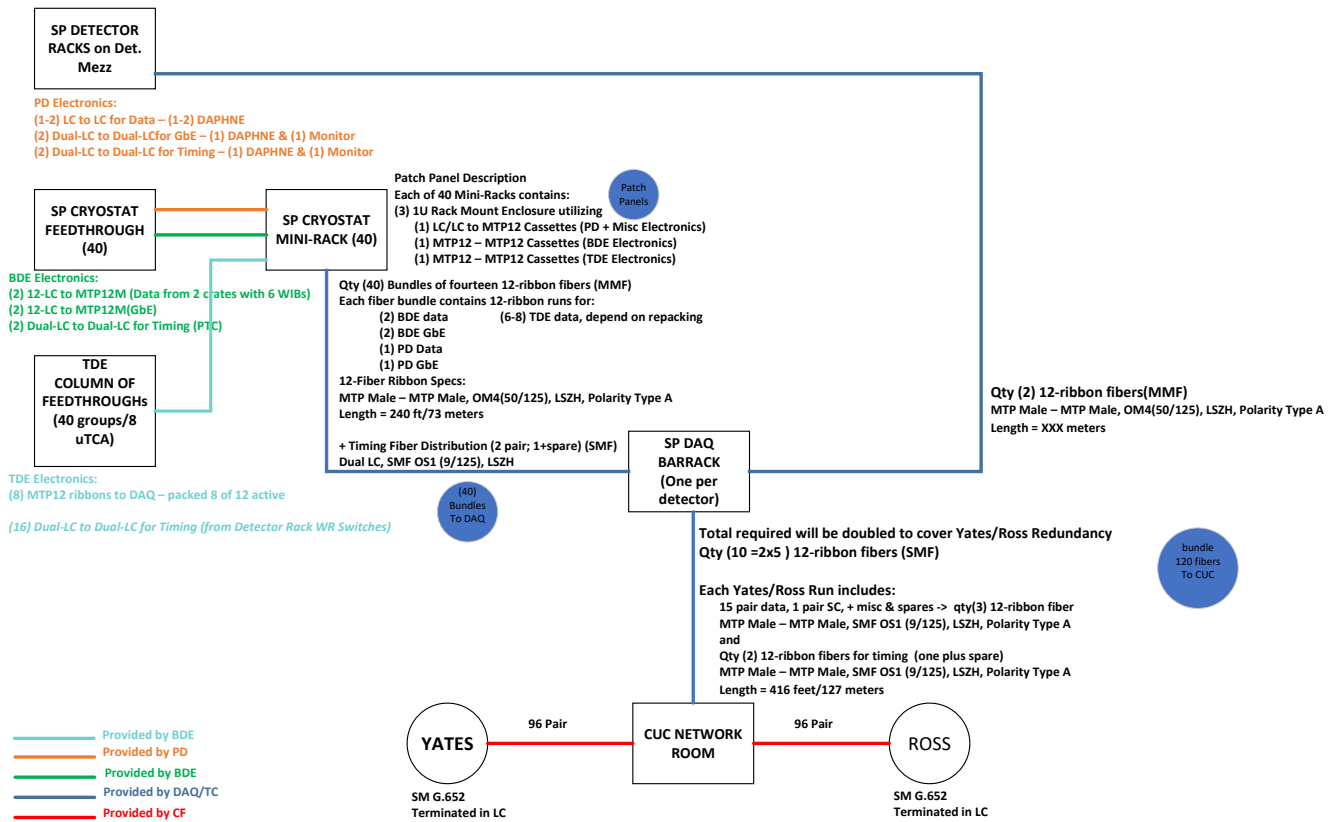


Figure 9.9: Summary of the number and routing of the optical fibers.

dural documents for a comprehensive set of identified individual tasks. As for ProtoDUNE-SP, all these documents are stored in the engineering document management system (EDMS) at CERN. For the larger operations and systems like TPC component factories, the detector support system (DSS), cleanroom, and assembly infrastructure, DUNE safety also reviews the documentation then visits the site to conduct an ORR, which includes a demonstration of the final operations. The ORRs are listed in project schedule.

Structural calculations, assembly drawings and proper documentation of load tests, hazard analyses, and procedures for various items and activities will require review and approval before operational readiness is granted.

### 9.4.2 Support and Responsibilities

The ES&H coordinator for each shift, who will report to the DUNE project ES&H manager, has overall ES&H oversight responsibility for the DUNE activities at the South Dakota Warehouse Facility (SDWF) and on the SURF site. This person coordinates any ES&H activities and facilitates the resolution of any issues that are subject to the requirements of the DOE Workers Safety and Health Program, Title 10, Code Federal Regulations (CRF) Part 851 (10 CFR 851). The on-site ES&H coordinator facilitates training and runs weekly safety meetings. This person is also responsible for managing ES&H-related documentation, including training records, HA documents, weekly safety reports, records on materials-handling equipment, near-miss and accident reports, and equipment inspections.

If the ES&H coordinator is absent, the shift supervisor acts in this capacity. All workers have work stop authority in support of a safe working environment.

### 9.4.3 Safety Program

The on-site ES&H coordinators will guide the far detector (FD) installation safety program, using the following:

1. the Fermilab Environment, Safety and Health Manual (FESHM);
2. the DUNE Installation ES&H Plan [102], which includes the fire evacuation plan, fire safety plan, lockdown plans, and the site plan;
3. work planning and controls documentation which includes both hazard analysis and procedures;
4. Safety Data Sheets (SDS);
5. the respiratory plan, as required for chemical or oxygen deficiency hazard (ODH) hazards; and
6. the training program, which covers required certifications and training records.

During the installation setup phase, as new equipment is being installed and tested, new employees and collaborators will be trained to access the facility and use the equipment. At the end of this phase, two shifts per day will be required.

The DUNE installation team will develop an ES&H plan for detector installation that defines the

ES&H requirements and responsibilities for personnel during assembly, installation, and construction of equipment at SURF. It will cover at least the following areas:

**Work Planning and HA:** The goal of the work planning and HA process is to initiate thought about the hazards associated with work activities and plan how to perform the work. Work planning ensures the scope of the job is understood, appropriate materials and tools are available, all hazards are identified, mitigation efforts are established, and all affected employees understand what is expected of them. The work planning and HA program is documented in Chapter 2060 in the FESHM.

The shift supervisor and the ES&H coordinator will lead a work planning meeting at the start of each shift to (1) coordinate the work activities, (2) notify the workers of potential safety issues, constraints, and hazard mitigations, (3) ensure that employees have the necessary ES&H training and personnel protective equipment (PPE), and (4) answer any questions.

**Access and training:** All DUNE workers requiring access to the SURF site must (1) register through the Fermilab Users Office to receive the necessary user training and a Fermilab identification number, and (2) they must apply for a SURF identification badge. The workers will be required to complete SURF surface and underground orientation classes. Workers accessing the underground must also complete 4850L and 4910L specific unescorted access training, and obtain a trip action plan (TAP) for each trip to the underground area; this is required as part of SURF's Site Access Control Program. A properly trained guide will be stationed on all working levels.

**PPE:** The host laboratory is responsible for supplying appropriate PPE to all workers.

**Emergency response team ():** The South Dakota Science and Technology Authority (SDSTA) will maintain an emergency response incident command system and an ERT. The guides on each underground level will be trained as first responders to help in a medical emergency.

**Guides:** The shift supervisor and lead workers will be trained as guides.

**House cleaning:** All workers are responsible for keeping a clean organized work area. This is particularly important underground. Flammable items must be in proper storage cabinets, and items like empty shipping crates and boxes must be removed and transported back to the surface to make space.

**Equipment operation:** All overhead cranes, gantry cranes, fork lifts, motorized equipment, e.g., trains and carts, will be operated only by trained operators. Other equipment, e.g., scissor lifts, pallet jacks, hand tools, and shop equipment, will be operated only by people trained and certified for the particular piece of equipment. All installation equipment will be electrically powered.

## 9.5 Detector Safety

The DUNE detector safety system (DDSS) is intended to detect abnormal and potentially harmful operating conditions and provide interlocks, thereby protecting the experimental equipment. The system will recognize when conditions are not within the bounds of normal operating parame-

ters and take pre-defined protective actions. Protective actions are hardware- or programmable logic controller (PLC)-driven. DUNE technical coordination works with the consortia to identify equipment hazards and ensure that harmful operating conditions can be prevented, or detected and mitigated. Potential hazards include, e.g., smoke in racks, ODH, a drop in the cryostat LAr liquid level, or over- or under-voltage conditions. The DDSS will receive alarms via cables from the various detector racks and provide input to the 4850L fire alarm system. This alarm system is part of the life safety system and will play an integral role in detecting and responding to an event, as well as notifying occupants and emergency responders. This system is the responsibility of the host laboratory (Fermilab) and SDSTA.

## 9.6 CRP and Cathode Support Structures

The CRP superstructure, which supports the top anode plane and the cathode, is described in Section 3.5. It is designed by the CRP consortium and the design will include an engineering note with the quality control (QC) requirements. The FSII team will be responsible for its fabrication and assembly, execution of the QC, and installation.

The assembled CRP superstructures are either  $3\text{ m} \times 7\text{ m}$  or  $7\text{ m} \times 9\text{ m}$ , i.e., too large to fit down the shaft in a single piece. The structures are designed to be brought underground in  $3\text{ m} \times 3.4\text{ m}$  sub-assemblies, with final cleaning, assembly, and QC testing underground by FSII.

## 9.7 Installation Infrastructure

The installation infrastructure consists of the temporary equipment needed to install the detector, which is removed after the installation is complete. Installation infrastructure provided by the FSII team includes the outside the cryostat with associated changing room, temporary cryostat and gray room ventilation, the false floor inside the cryostat, temporary power and lighting in the cryostat and gray room, scissor lifts capable of reaching 12 m work height, material transport equipment from the gray room to the cryostat, rigging equipment on the cryostat roof for the TDE and equipment, and miscellaneous tools and rigging equipment. A crane will be in the cavern; there will be no fixed cranes in the gray room or the cryostat except for the hoist beam through the TCO.

The FSII team is also responsible for planning the material flow into the cryostat and budgeting the clean workspace provided by the cryostat and the gray room for assembly, testing, and installation. Figure 9.10 shows these spaces during the early phase of the CRP installation, the period that requires the most clean workspace because of the activities going on in parallel. The floor of the cryostat measures 62 m by 15.1 m, offering a large available work area to be used for CRP assembly and testing. The field cage assembly area, the photon detector (PD) testing area, and the cathode assembly area will be in the gray room, as shown in the bottom of Figure 9.10. This set of activities determines the space requirements for the gray room, which will be 15.5 m deep by 17.45 m wide. To enclose the cryostat's TCO (the bottom of which is 2 m off the ground), the gray room height is set at least 9.82 m.

A light-weight construction technique is used for the gray room as there are no physical require-



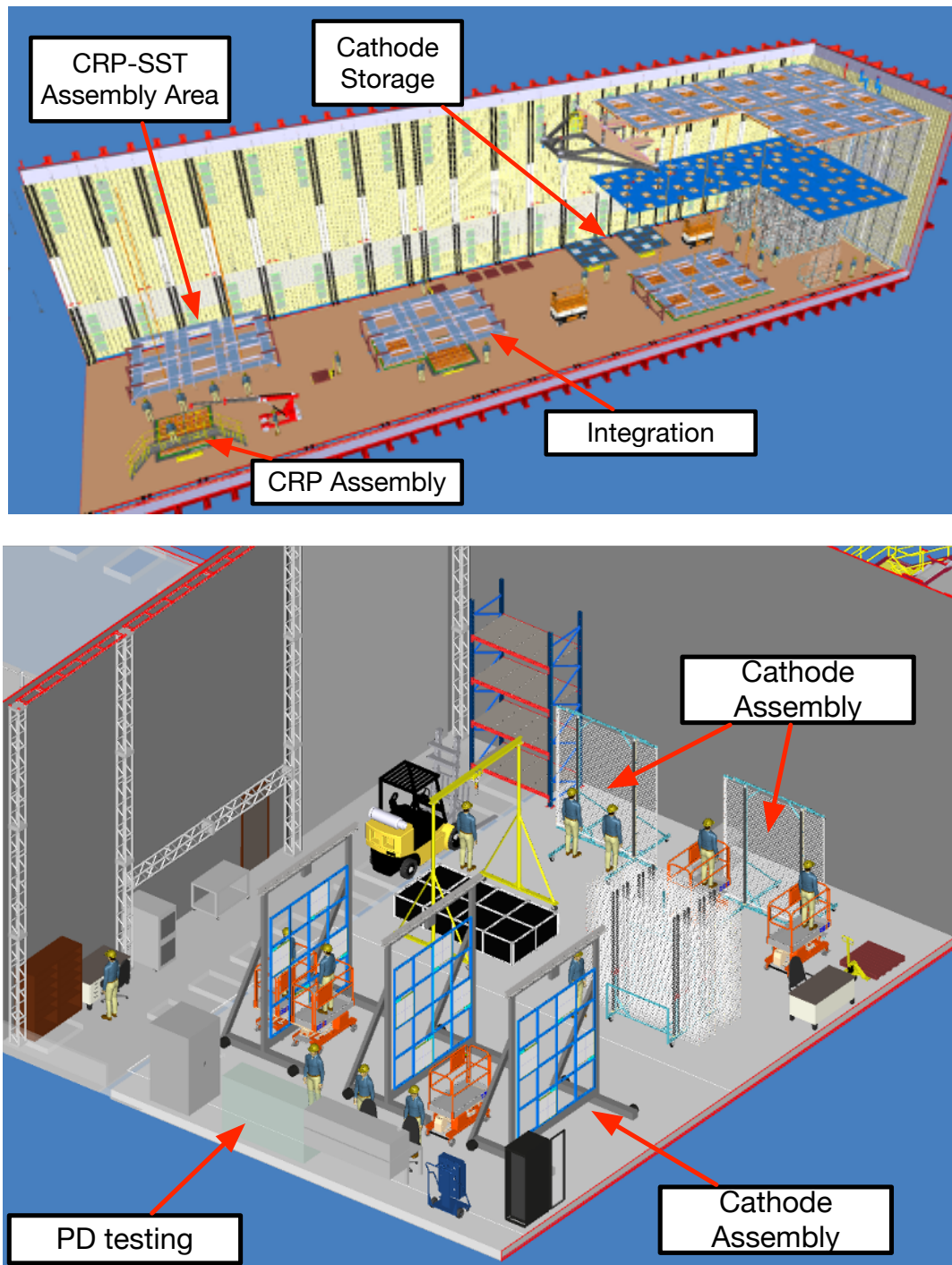


Figure 9.10: Top: Image of the cryostat during week 8 of CRP installation, showing the main space allocations inside the cryostat. Bottom: gray room work area and space allocations.

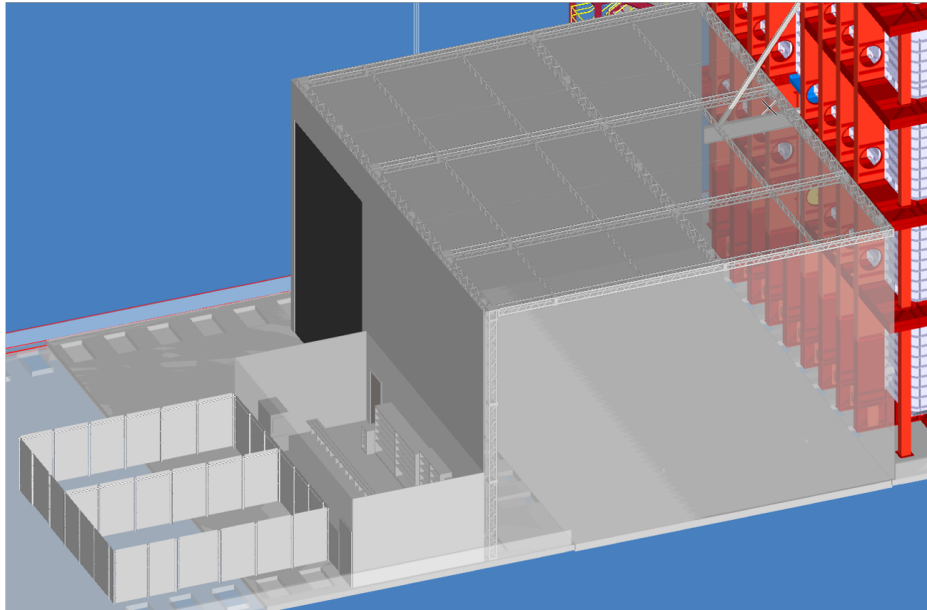


Figure 9.11: gray room for the installation of the FD2-VD detector module. The small structures to the left of the gray room are the changing room and fenced areas for storage, and a small machine shop.

ments beyond preventing dust migration and blocking UV light from entering. As shown in Figure 9.11, the gray room support frame will be constructed of the same lightweight aluminum trusses that are used for the west wall of the FD1-HD cleanroom. The frame will be covered with fiber-reinforced plastic sheets. Materials will enter the gray room through a 6.1 m by 8.3 m opening in the west wall, which is normally closed with a pair of tarps. Since little sensitive electrical work will be performed inside the gray room during this period, the floor will not be protected. The BDE consortium is planning to use this area for testing at the end of the installation and they will install temporary ESD mats at that time. A small battery-operated forklift is used to move materials inside the gray room. Temporary lighting and power are distributed in the area. In order to transport equipment from the gray room through the TCO into the cryostat a custom hoisting beam (TCO-Beam) has been designed (Figure 9.12). As there are no mechanical connection points inside the cryostat this beam must be supported from the outer steel and cantilevered inside. To minimize the cantilever inside the cryostat, the area directly in front of the TCO is kept free, and cryostat access during hoisting operations is via a fixed ladder. The hook coverage outside(inside) the cryostat is 2.2m(1.9 m), which is sufficient to lift the longest piece of equipment (lifted from the center). A 2-ton (US) ultra-low-profile hoist will give the maximum vertical hook clearance through the TCO of 4.5 m.

Inside the cryostat, a temporary false floor will protect the cryostat's thin steel membrane and provide a flat surface for the scissor lifts during installation. Pedestals will be placed between the cryostat membrane corrugations to provide level support for the fire-retardant plywood flooring. Commercial floor pedestals have been identified with sufficient load rating for the scissor lifts.

The design of the cryostat false floor (Figure 9.13) required consideration of the interfaces with the cryostat convolutions, the cryogenic piping along the wall, the bottom CRP installation footprint, and the cables and fibers for the bottom CRPs and the cathode PD modules, so it has to stop short

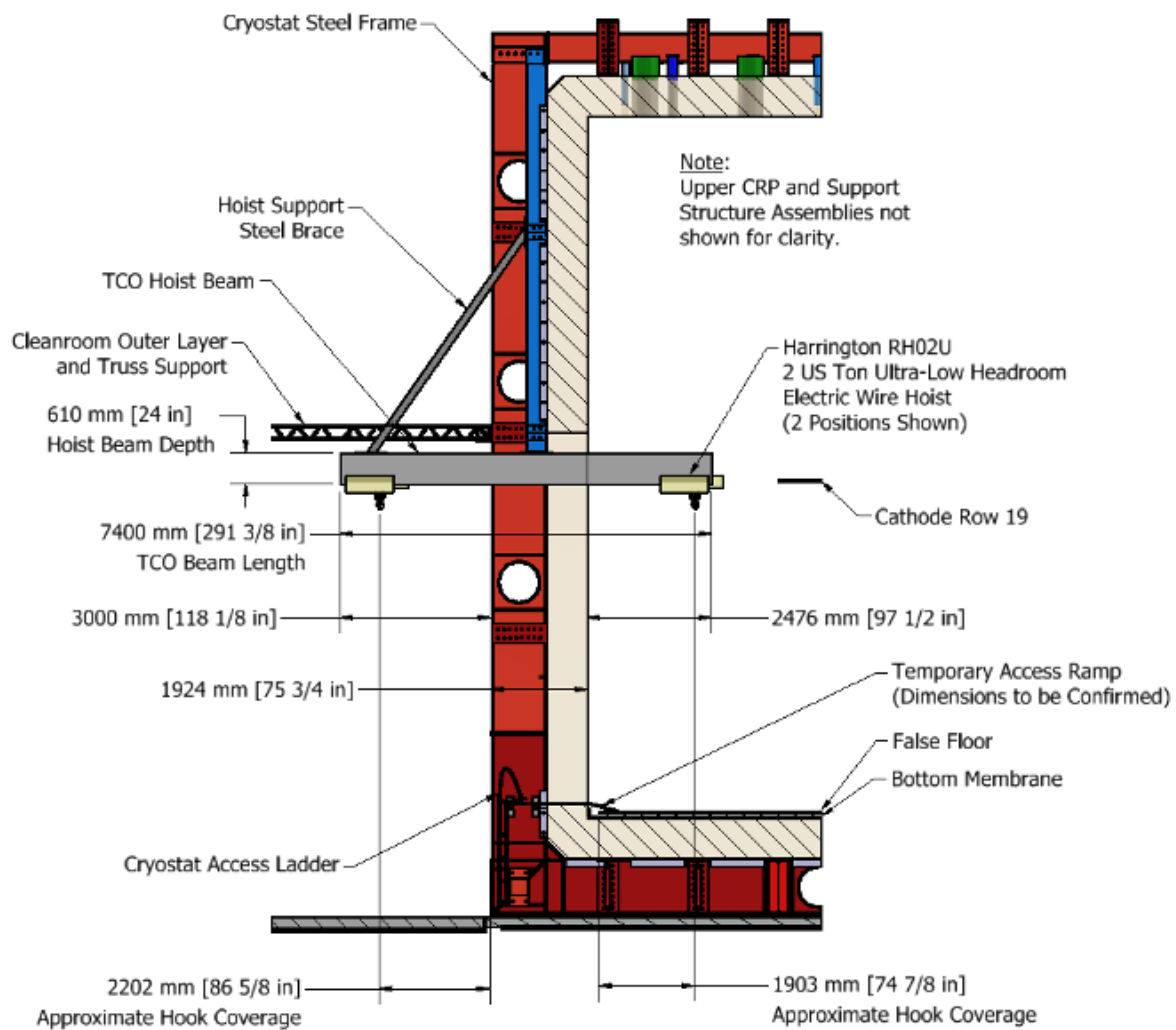


Figure 9.12: The hoist system for transporting equipment from the gray room into the cryostat through the TCO allows objects up to 4 m long to be brought in for installation.

of the vertical plane of the field cage modules. Figure 9.13 shows a 3D model of the temporary floor and the floor tested at Ash River.

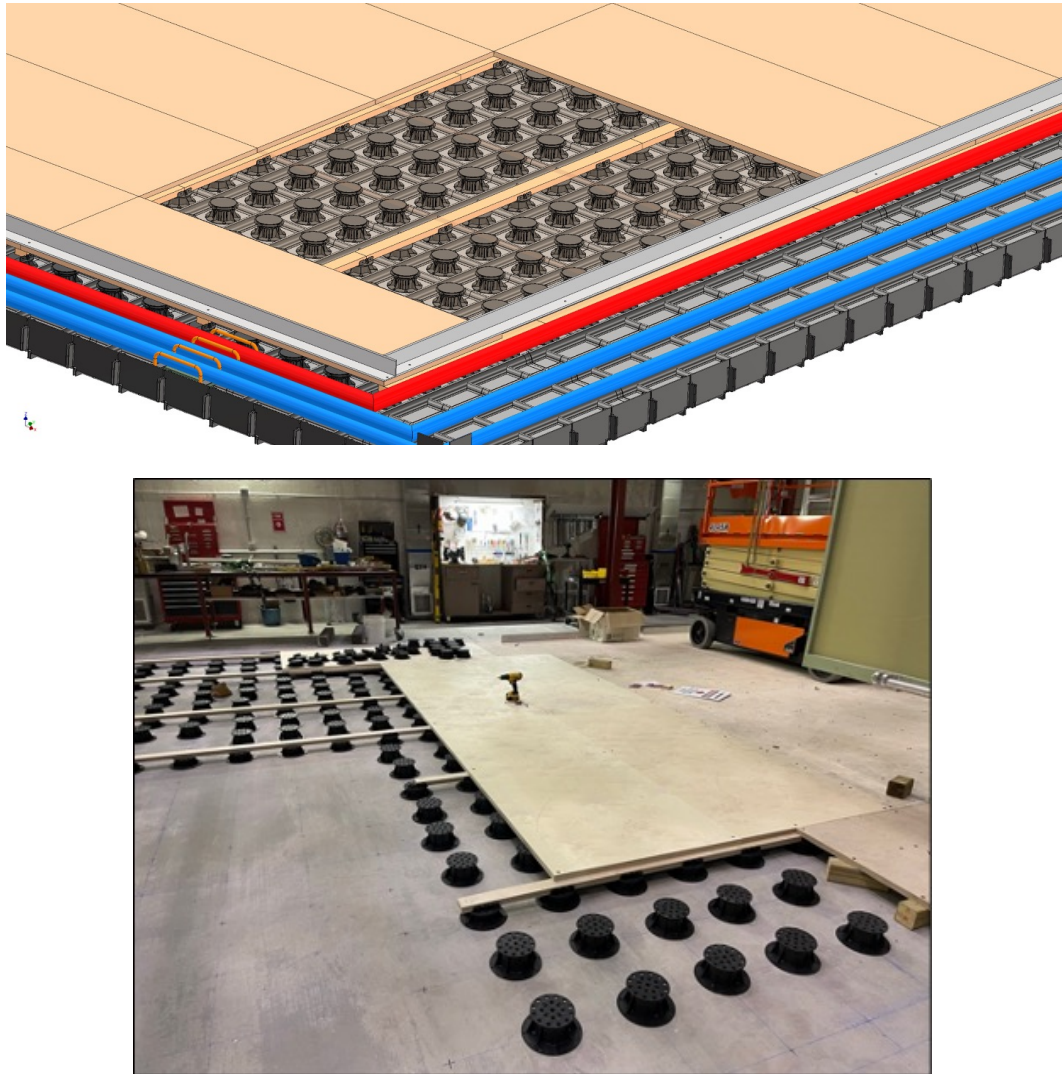


Figure 9.13: Top: 3D model of the cryostat temporary floor with a section of the plywood removed to show the support pedestals and the underlying membrane. Bottom: Photograph of the flooring test at Ash River.

Like the FD1-HD detector module, the FD2-VD module must be installed under relatively clean conditions. The radioactive decay of the naturally occurring  $\text{Ar}^{39}$  isotope in the detector means that under normal operation the TPCs will always have a steady background rate. Since the detector will be installed under ISO-8 (gray room) conditions, the  $\text{Ar}^{39}$  background will dominate. In order to keep the inside of the cryostat clean, pure High Efficiency Particulate Air (HEPA)-filtered air is forced into the cryostat at the east end, which then flows along the cryostat and out the TCO at the west end. This keeps the cryostat at an overpressure. The access hatches shown in Figure 9.3 are circular, 800 mm in diameter, and are 1.2 m in length. Using these ports as air ducts, an air flow of roughly 8,000 CFM (13,600  $\text{m}^3/\text{hr}$ ) through each is possible. The pressure in the cryostat will be sufficient to ensure outward airflow while work is performed around the flanges on the roof, and covers will be added over the work area to prevent objects from falling in. The outer surfaces and cover will be cleaned just before closing.

A computational fluid dynamics (CFD) model of the air flow in the cryostat was performed and the average lifetime of the air in the cryostat computed. Based on the results, the model was amended to assume eight additional portable air filter units placed in the cryostat at various locations and orientations, and the impact on the air stream age was re-computed. The best results are shown in Figure 9.14. The 16,000 CFM input airflow combined with an additional 16,000 CFM of local filtration resulted in an average air age in the cryostat of 15 minutes, which is anticipated to be sufficient given the low expected occupancy. Note that cleanroom design guidelines do not directly apply to the FD2-VD cryostat since the dimensions and occupancy are very different from standard cleanrooms. (Under typical cleanroom conditions a minimum of five air exchanges per hour are recommended.) If in situ measurements indicate additional measure will be required, then workers in the cryostat may be required to wear traditional cleanroom garb to reduce dust production and/or additional portable air filters can be installed. Experience from FD1-HD will also be taken into account.

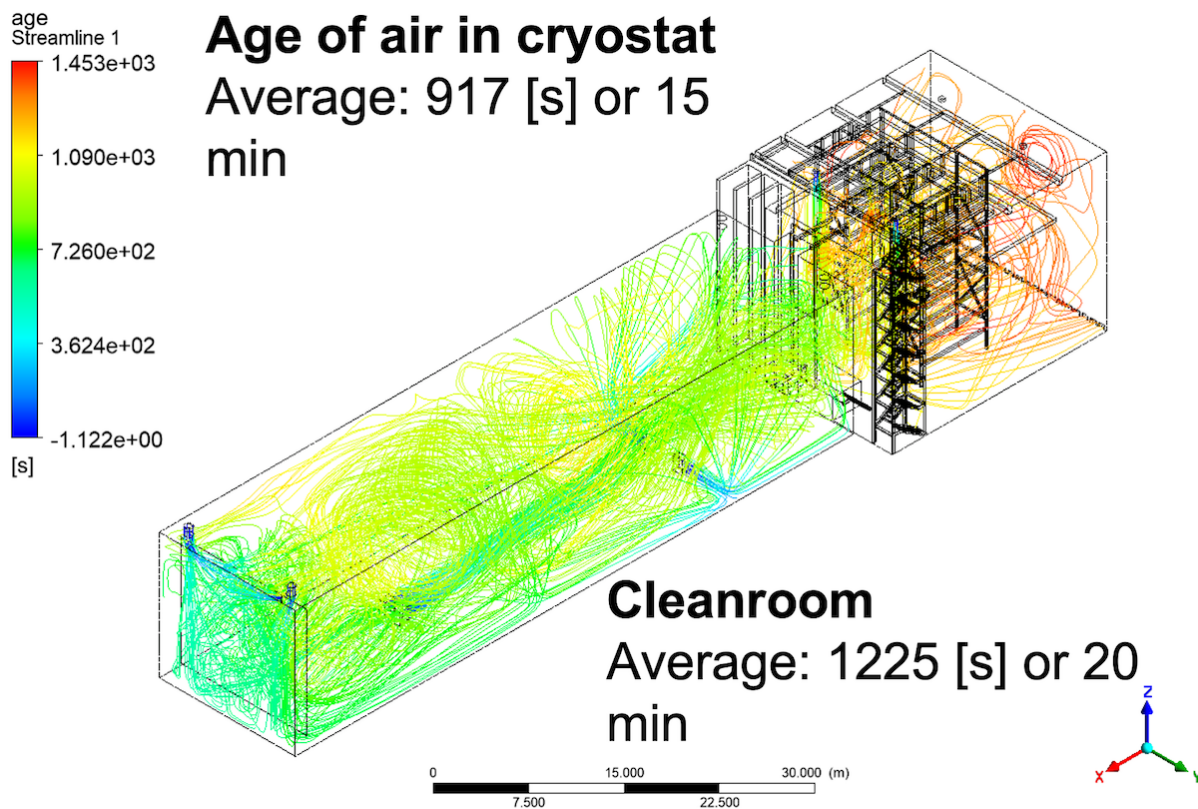


Figure 9.14: Finite element analysis (FEA) model of the air flow inside the cryostat with 16,000 CFM of pure filtered air entering through the east access hatches in the cryostat roof. The average duration of a given volume of air in the cryostat is 15 minutes. Plan view with TCO at right.

The air flow through the TCO was also investigated in the CFD model. The air velocity over a large majority of the surface exceeds 0.2 m/s, which, according to the ISO-14644-4 international standard, is sufficient to prevent dust from migrating from the gray room into the cryostat. Figure 9.15 shows the velocity of the air exiting the cryostat through the TCO.

Outside the gray room a changing room is required to give personnel space to put on lab coats and clean shoes before entering. This will be a modular pre-fabricated room that can be erected



Figure 9.15: CFD model of the air flowing out through the TCO with 16,000 CFM of pure filtered air entering through the West access hatches in the cryostat roof. The velocity is consistently above  $v_{air} > 0.2$  m/s.

and dismantled quickly.

The majority of the detector installation work takes place inside either the gray room or the cryostat. However the installation of the electronics and readout related equipment takes place primarily on top of the cryostat. The 0.5 m diameter TDE chimneys weigh 340 kg empty and are 2730 mm long, requiring rigging equipment for transport and installation. Given the large number of chimneys (105) and crosses (40), all of which are outside crane coverage, a custom gantry cart was designed to facilitate the installation.

Each chimney will be loaded into the gantry cart in the horizontal orientation using the cavern crane, and moved across the cryostat roof to the correct port. The cart is designed to fit under the cryogenics and detector mezzanines. It is equipped with a hydraulic cylinder that enables it to rotate the chimney to vertical, then integrated trolleys are used to adjust the position of the chimney over the flange. The chimney is lowered through the cryostat penetration using built-in hoists. These steps are shown in Figure 9.16.

Additional installation infrastructure provided by the FSII team includes temporary power and lighting in the cryostat, six scissor lifts capable of reaching a 12m work height, and miscellaneous tool and rigging equipment. This equipment is identical or very similar to what is required for the FD1-HD installation.

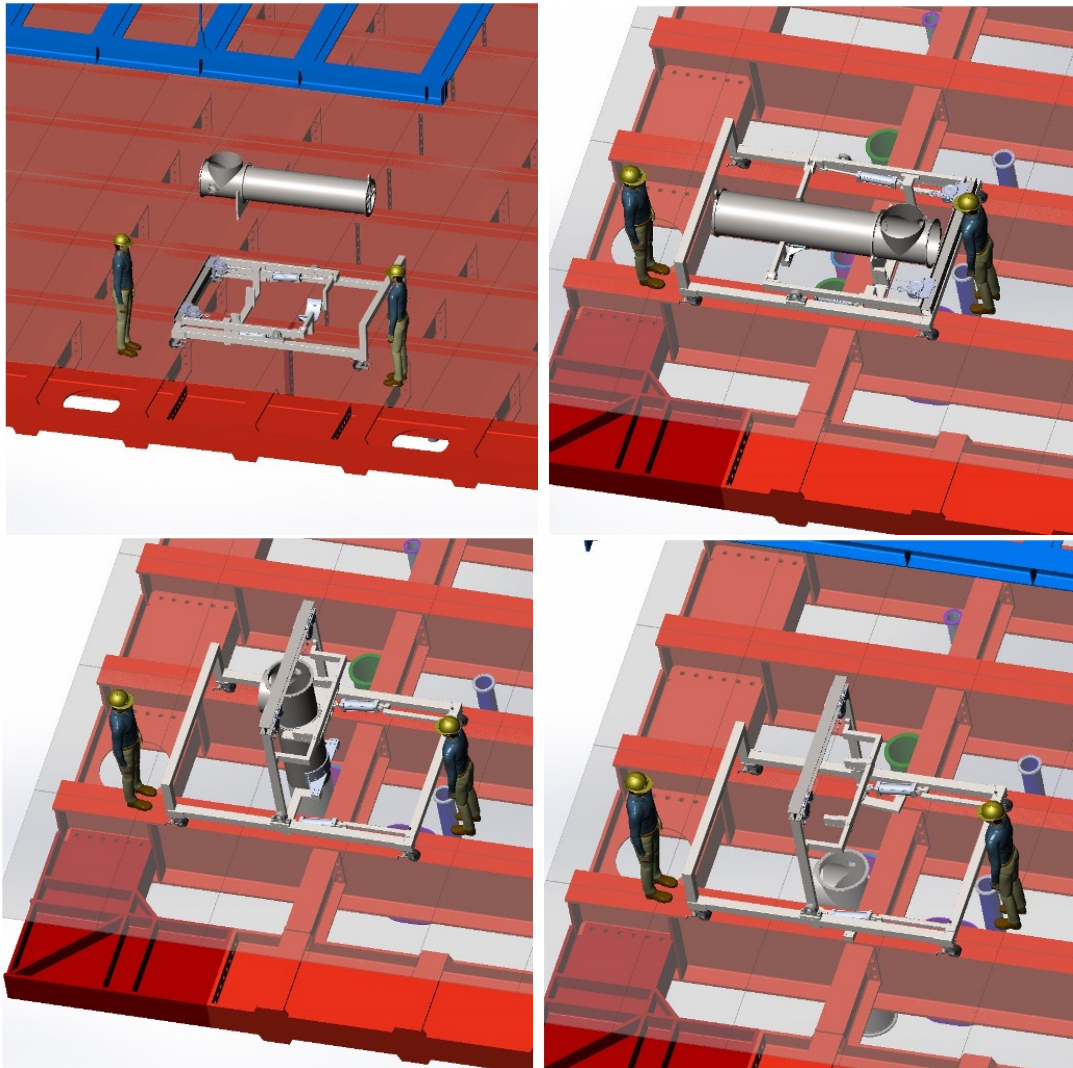


Figure 9.16: Images showing a custom gantry cart used to install the TDE chimney and the BDE crosses.

## 9.8 Detector Installation

The installation of the FD2-VD detector is the last major exercise at the far site for this . This makes it imperative that the work proceed as quickly as possible in order to minimize the installation cost and to bring the FD2-VD detector online as fast as possible. The FSII installation team will complete the mechanical portions of the installation, and DUNE consortium members will complete the activities related to connectivity, testing, geometrical positioning, and surveying. It is planned to install the detector module using two 10 hour shifts per day, six days a week.

In planning the installation work it is assumed that roughly half the time is available for productive work and the rest is spent bringing people underground, breaks, entering the gray room, safety meetings, returning to the surface, or general inefficiency of underground work. The 50% efficiency estimate is typical for underground work. The access to the underground area is limited on Sunday due to shaft maintenance and safety inspections.

### 9.8.1 Installations on Cryostat Roof

Work on installing the detector infrastructure and the equipment from the consortia begins in parallel with the installation of the cryostat insulation and stainless steel membrane. During this period the installation contractor will be working on the 4910 foot level both inside the cryostat and in the area outside. This leaves the roof of the cryostat free to begin installing the cryogenics and detector-related infrastructure. Installation of the cryostat cold structure (the membrane) will require one year of work, so the infrastructure on the roof can be completed before the cryostat work is complete. Both the cryogenics and detector mezzanines are installed at the beginning of the cryostat work, after which work on the proximity cryogenics system, barracks for the DAQ, the power infrastructure, and all the racks is performed. The DAQ barracks shown in Figure 9.17 was designed to host the 16 DAQ electronics racks. The section view of the room shows one side of the double-row of racks with associated cable trays. The barracks will be outfitted with HVAC compatible with the computer heat load, and a dry agent fire extinguisher due to the high electrical load in the room and the large monetary value of the servers. It is planned to have the infrastructure for the DAQ available three months before the start of detector installation to ensure ample commissioning time (taking into account that there will already be a functioning DAQ in the north cavern).

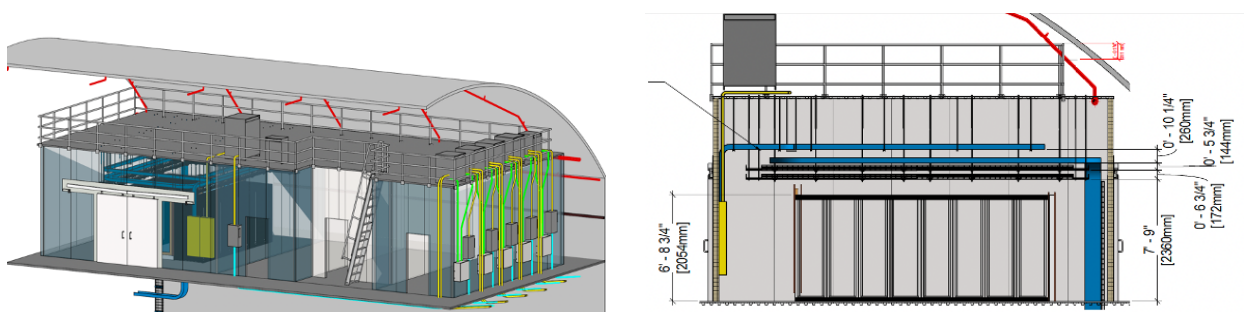


Figure 9.17: Left: Isometric model of the DAQ barracks with racks installed. Right: Section view of the barracks showing the rack placement

On the cryostat roof itself, decking is installed for easy access, the GAr purge system and all the cable trays are installed, and the ladders for accessing the outside of the cryostat steel are



installed. This completes all the heavy work and associated welding so the installation of the delicate detector elements can begin. The electronics modules that are located in the racks on the detector mezzanine can be installed and connected to the DDSS and slow-control readout. Installation of cables and fibers on the cryostat roof and mezzanines will progress as the electronics installation proceeds. In the last few months before the cryostat is finished, the top and bottom TPC electronics consortia can install the feedthroughs, chimneys, BDE crosses, and the cable trays for the CRPs, and connect the cables to the DAQ.

Once the chimneys and crosses are installed the installation of the TDE readout electronics and the BDE warm interface electronics crate (WIEC) can proceed. The installation of the electronics on the roof can progress in parallel with the detector installation work inside the cryostat.

### 9.8.2 Preparing the Cryostat Interior

Once the cryostat installation is complete and the cryostat has been leak-tested, the cleaning operation can begin. The hoisting beam in the TCO will be installed, 8,000 cfm (13,600 cubic m/hr) of purified air will be injected into the cryostat through the access hatches on the east end, the gray room will be closed and cleaned, and the detector installation can begin inside the cryostat. The first steps are:

1. Rough clean the cryostat floor and install the false floor.
2. Set up the temporary power and lighting in the cryostat.
3. Lift the five 12 m tall scissor lifts onto a temporary platform at the cryostat entrance using the hall crane and then drive them into the cryostat.
4. Wipe down the cryostat interior; with five scissor lifts and a crew of 12 people per shift, the cryostat can be wiped down and most of the dust removed in two days.

At this point detector installation can begin.

### 9.8.3 Detector Component Installation

Installation begins on the east end wall, and moves west, toward the TCO, in the order given here.

5. Remove the plastic sheet protecting the east wall and clean the membrane.
6. Install the two strings of membrane PD modules and route cables to the first of the roof penetrations on the side wall of the detector. See Figure 9.18.
7. Install the HV extender and test it for continuity to the power supply. (The HV extender must be installed before the top CRPs, as they will block access at the roof.)

Next, installation of the cables for the BDE, fibers for the cathode PD modules, and the membrane PD modules begins along the north and south walls of the cryostat. The BDE cables arrive underground on a large spool with the cable trays pre-attached. These cable trays are of a unique design based on a rope-ladder concept. Access to the roof penetrations is still required. A manual chain hoist is brought into the cryostat for this installation work.

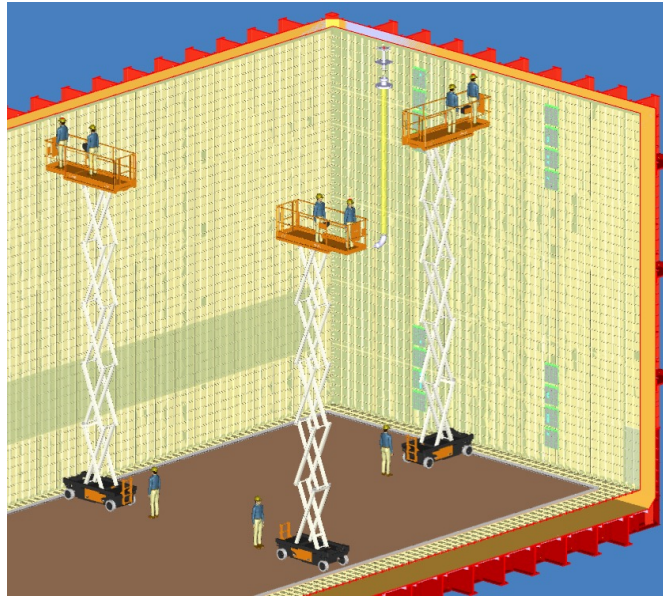


Figure 9.18: Model illustrating the installation of the PD modules on the east end wall and the HV extender.

Two crews, one on the north wall and one on the south wall, will work in parallel starting in the east corner and working west, to accomplish the following.

8. Remove the sheet protecting the cryostat membrane and clean the stainless steel surface including the roof.
9. Mount a hoisting fixture to the M10 corner bolts of the cryostat and hoist the cables up the wall.
10. Once in position, install a tensioning spring at the bottom and remove the hoist.
11. Route the cables through the roof penetrations and install the cathode-mount PD fibers down to floor level.
12. In parallel, install the strings of membrane-mount PDs.
13. In the  $\pm 2\text{m}$  region above and below the cathode, install a protective cover over the cable trays to prevent the cathode field from interacting with the thin conductors in the BDE cables.

Figure 9.19 illustrates the BDE cable and membrane PD installation. The image on the left shows the relative orientation of the PD modules and the BDE cables. Here the PD cables are not shown, but they will run from the PD modules to the same feedthrough.

14. After the cables are in place, install temporary BDE electronics and test the entire read-out chain through to the DAQ. Channel mapping, all electrical connections, and the warm readout are tested together.
15. After verification of the full functionality of the system, disconnect the BDE cables and store them below the temporary floor.

The process of installing the false floor, cleaning the walls, installing the cable trays, and installing the cables could be accomplished in eight weeks, but the work is spread over 11 weeks for resource-leveling reasons (once the CRP installation begins, the crew gets split in order to accomplish the work in parallel.)

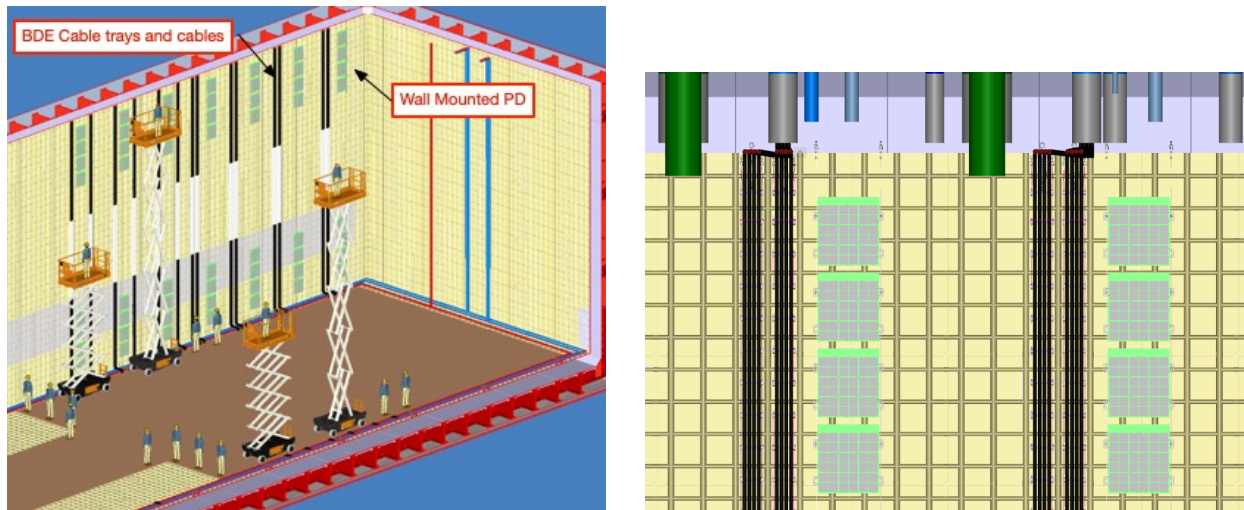


Figure 9.19: Left: Models of the installation of the wall PD modules and the BDE cables along the cryostat long walls. Right: Closeup showing the relation of the BDE cables and cable trays, the wall PD modules and the cryostat roof feedthrough.

Following the work on a portion of the north and south walls, but (for access considerations) before the CRPs are in place, the circular cable trays for the top CRPs for that area need to be installed. The large TDE chimneys service 50 flat ribbon readout cables, making the cable density in this area high. As the pitch of the major I-beams on the cryostat roof do not match the pitch of the internal detectors, the locations of the chimneys relative to the CRPs are not consistent. A circular cable tray, Figure 9.20, was designed that mounts on the chimney to hold the cables and a jig was designed to route each cable to the appropriate location.

16. The cables will be attached first on the ground using a custom cabling jig.
17. The assembly is lifted into location and attached to the chimneys.
18. Once attached, the cables are connected to the chimneys.
19. The cables connecting the CRPs to the readout electronics are installed.

Since the roof cabling work follows the wall PD installation, the cables will be in place before the top CRPs are installed.

After four weeks, enough of the wall-mount PDs will be installed to leave space to begin installation of the top CRPs. This procedure will differ in many respects from that used in , and will be prototyped in the FD2-VD Module 0 test at CERN. The FD2-VD top CRPs are connected to an intermediary steel support frame that supports either two or six CRP modules (see Section 3.5). This reduces the number of penetrations through the roof from three per CRP for ProtoDUNE-DP to four per support structure, greatly simplifying the cryostat design. However, to connect the cables, the area above the CRPs must remain accessible. A custom elevated workstation has

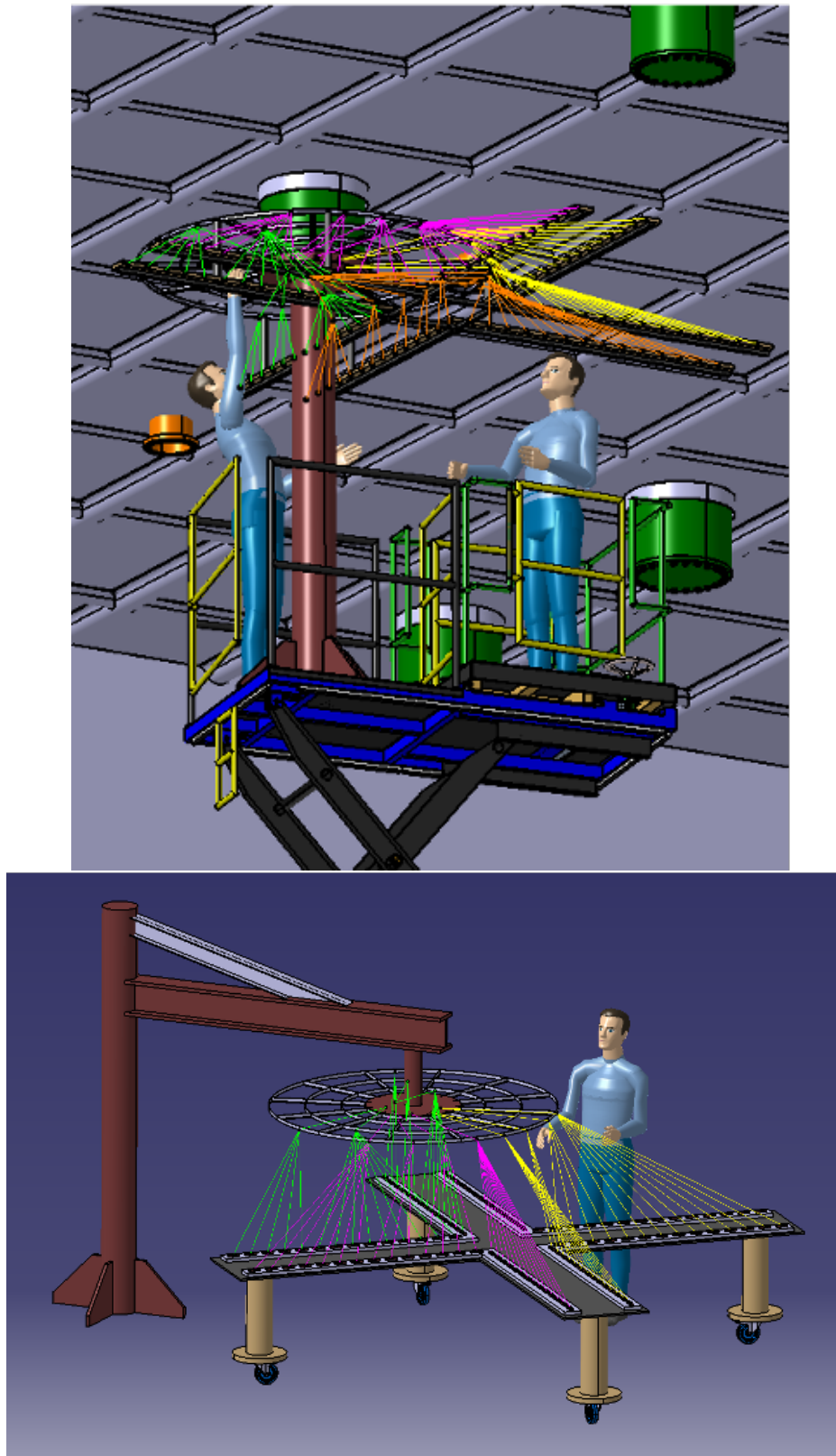


Figure 9.20: Top: Model of the installation of the circular cable trays for the top CRP. Bottom: Installation jig used to pre-route the cables and to install the trays.

therefore been designed that is supported through the cryostat roof and accessed from below via scissor lifts.

Figure 9.10 illustrates the layout of the gray room in this phase of the installation, where the cathode and PD module components are brought for assembly and integration together. These activities occur in this order.

20. Bring the pieces of the CRP support structures and the charge-readout units (CRUs), which will be assembled into CRP modules, directly into the cryostat and clean the components (Figure 9.21).
21. Assemble the CRP support structures and the CRPs at their respective work stations.
22. Affix two or six CRPs to a support structure using a series of linkages that must be adjusted to level the CRPs and position them relative to the support structure. The CRP support structures are equipped with temporary wheeled supports so they can be easily moved around inside the cryostat. (The 16 CRP superstructures will be assembled and tested for dimensional tolerances before the start of installation.)
23. Hoist the elevated workstation and attach it to the cryostat roof using an unused upstream CRP support feedthrough.
24. Wheel the set of two or six CRPs into location and hoist it.
25. Suspend the cathode plane from the CRP superstructure using several 3 mm Dyneema cables.

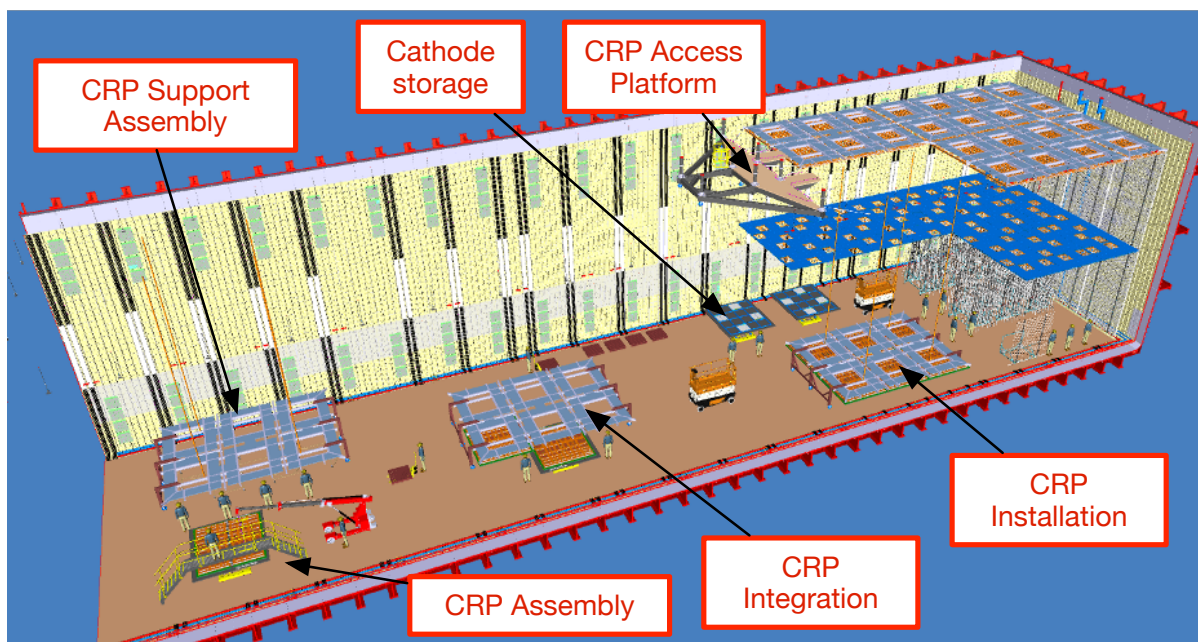


Figure 9.21: Layout of the equipment in the cryostat during top CRP installation. The main work areas are labeled.

In order to raise the superstructure, synchronized winches will be installed in place of the automated position system on top of the cryostat, as shown in Figure 9.20. The external support structure is designed to allow switching between the manual winches and the automated suspension system while under load.

Figure 9.22 illustrates the top CRP and cathode installation process, which proceeds as follows.

26. Install the hoisting system on the roof and lower the lifting cables through the CRP support penetrations.
27. When the cables are at roughly the correct height, move the assembly with the support structure and CRP modules into position and connect it to the lifting cables.
28. Remove the load from the support wheels, then remove the wheels.
29. Attach the cathode support cables and set them to the correct length.
30. Raise the CRPs to where the cathode support cables are at the height of a cathode module on its installation table.
31. Connect the support cables and set the gap to the CRP with a laser range finder.
32. Connect the cathode PD fibers to the PD modules.
33. Make the interconnections between cathodes and perform continuity tests.
34. Raise the CRPs and cathode together to cabling height and attach the elevated workstation. This workstation provides lateral support so the CRP structure does not sway when people are working on top of it.

A 14 week schedule for the combined installation of the CRPs and cathode modules has been developed.

The top surface of the CRP support structure is accessed by raising a scissor lift up to the access ladder attached to the elevated workstation (Figure 9.23). A system of fall restraint supports are integrated into the workstation and the CRP support structures; qualified personnel attach their fall restraint supports at the access ladder and climb onto the workstation.

The rails and attachment points are designed so a person can crawl out on the workstation and then onto the CRP support structure. Figure 9.23 shows the space between the cryostat roof and the work surface; it clearly illustrates the need to have the cables pre-positioned near the final connection point. Engineering related to the addition of a perimeter barrier along the outside edges of the CRP supports and access platforms is actively being investigated. Upon conclusion, additional safety barriers may be added to the design.

35. Manually connect the cables to the CRPs.
36. Once all the connections are made, evacuate the area and test the readout.
37. Installation of the adjacent CRP support structure can begin in parallel with the testing of the first set of CRPs.
38. When both sets of CRPs have been installed and tested, disconnect the elevated workstation, lower it to the floor, and re-install it for the next pair of support structures.
39. Raise the CRPs to the final height in the cryostat and monitor them regularly to ensure all the readout channels are functional.

The installation of the field cage can begin once the second pair of CRP super structures is installed. This provides sufficient time and space under the installed CRPs for the field cage installation team to work, and corresponds to four weeks after the start of CRP installation. Recall from Section 5.4.2

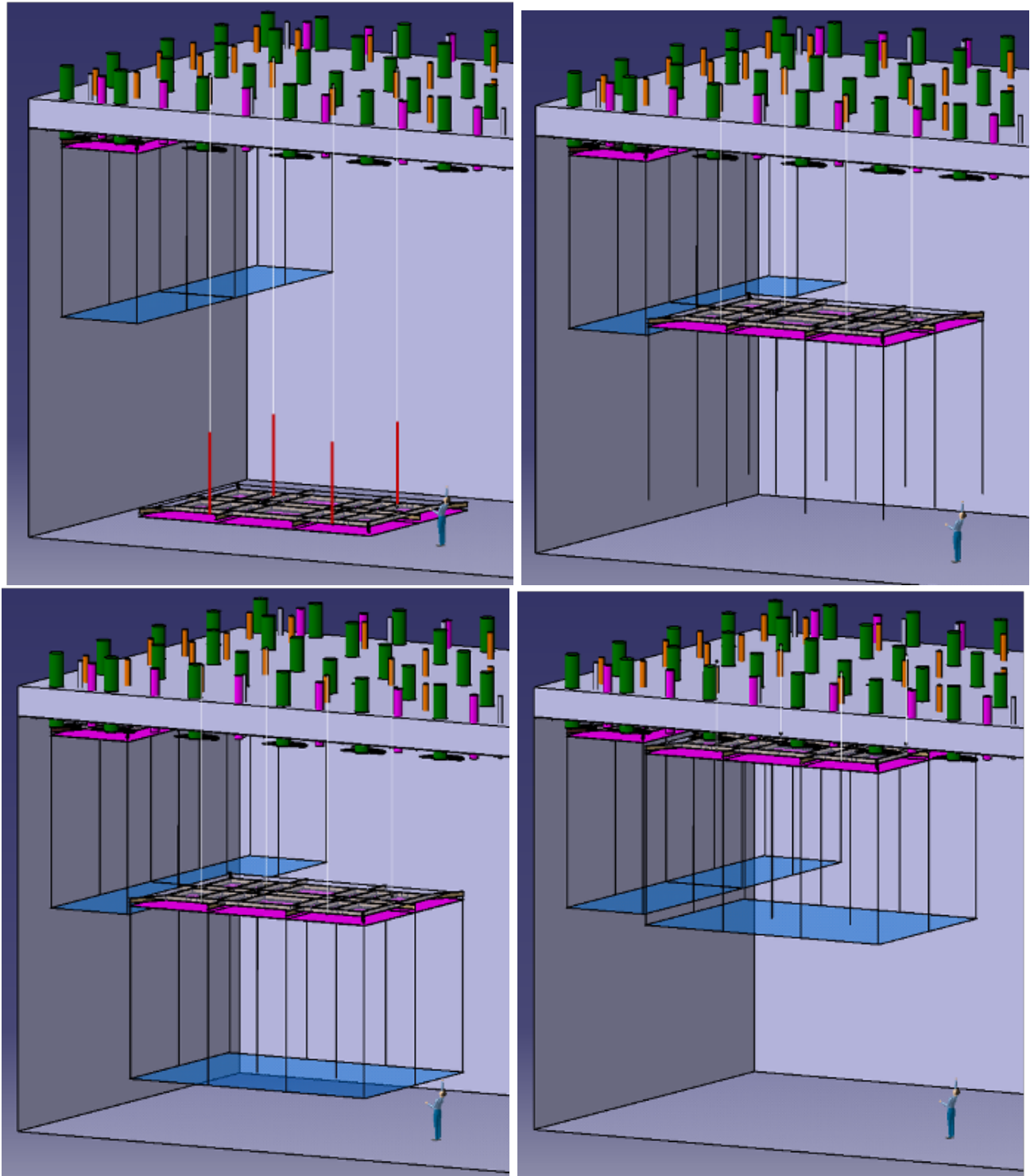


Figure 9.22: The installation sequence for the top CRP and the cathode modules is shown for a six-CRP superstructure unit. Top left: The CRP support superstructure is moved into position and attached to the lifting cables. Top right: The cathode support cables are attached and the CRPs are lifted 6 m. Bottom Left: The cathode modules (blue) are installed under the CRPs, and the cathode is suspended. Bottom Right: The entire assembly is lifted to cabling height where it is attached to the elevated workstation.

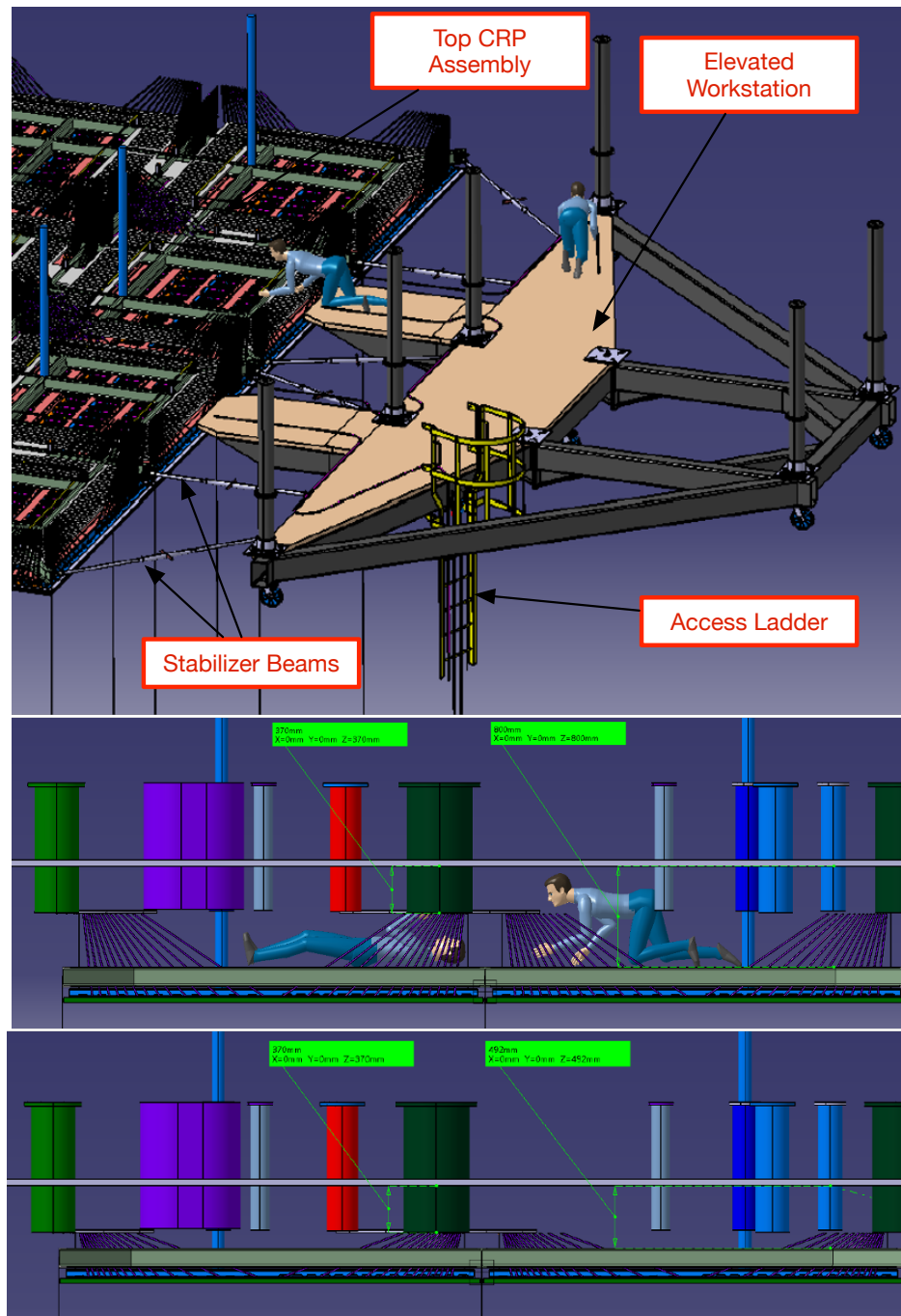


Figure 9.23: The cabling process for the top CRP. Top: The CRP support superstructure connected to the elevated workstation. Middle: Crawl space for connecting the cables to the CRP. Bottom: The space near the roof of the cryostat after the CRPs are raised to their final position.



that two columns of four field cage modules each (eight total) form a supermodule,  $6.0\text{ m(W)} \times 13\text{ m(H)}$  for the long walls and  $6.76\text{ m(W)} \times 13\text{ m(H)}$  for the end walls. Each field cage supermodule hangs from a  $6.4\text{ m}$  long field cage support beam assembly constructed of stainless steel I-beam and consists of a main spanning beam with two lift rods and two field cage spanning yokes, as shown in Figure 9.24. The support beams are brought into the gray room and cleaned and then transported into the cryostat. The support beams are hoisted from the floor in the cryostat first to their assembly heights and then to their final heights using winches and cables that raise the field cage lift rods. The flange and hoisting setup is designed so that while the FC support beam is lifted it is offset by  $50\text{ mm}$  from its final position. Since it will be lifted with hand winches that could be at slightly different levels, the offset is critical, as it allows the modules supported from the beam to swing in-plane somewhat. When assembly in the cryostat is complete, the beams are shifted to the final position and placed on a spherical indent on the roof flange. Details of the roof alignment and support flange are shown in Figure 9.24.

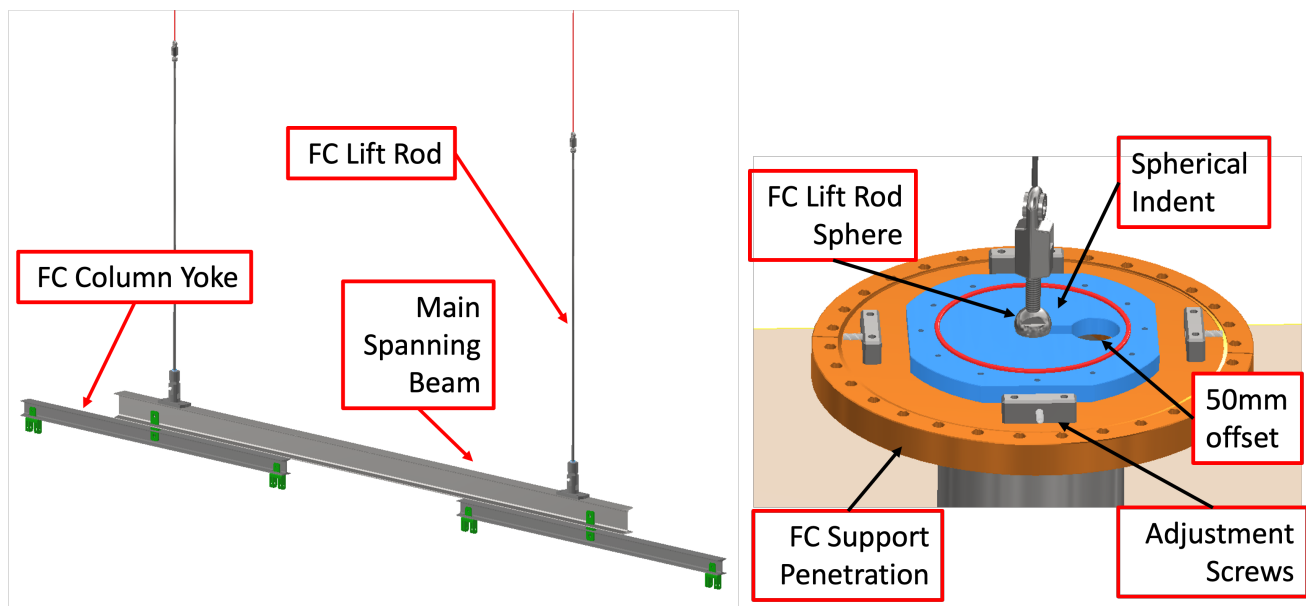


Figure 9.24: Left: field cage support beam showing the major sub-assemblies. Right: field cage roof penetration showing the  $x$ - $y$  position adjustment system, the penetration for lifting the support beam assembly, and the spherical socket for final positioning.

The four walls surrounding the two active drift volumes are formed by ten field cage supermodules each along the long walls, and two each along the end walls for a total of 24. The single field cage modules will be assembled in the gray room starting at the same time as CRP installation. All the parts for the field cages and assembly tooling are cleaned as they are brought into the gray room. As the modules are finished they will be transferred to custom storage carts (Figure 9.25) and hoisted into the cryostat. Once inside, the field cage is constructed one supermodule at a time. The field cage installation process is substantially faster than that for the CRP, so the field cage team will be primarily fabricating modules and then installing them as space behind the CRPs becomes available. In order to install the modules, a cantilevered cart was designed to hold a single field cage module (Figure 9.25). During installation the single modules will either be lifted from the storage cart by hand and placed on the installation cart or a gantry crane will be used. The field cage installation sequence for the field cage modules is shown in Figure 9.26 and enumerated below.

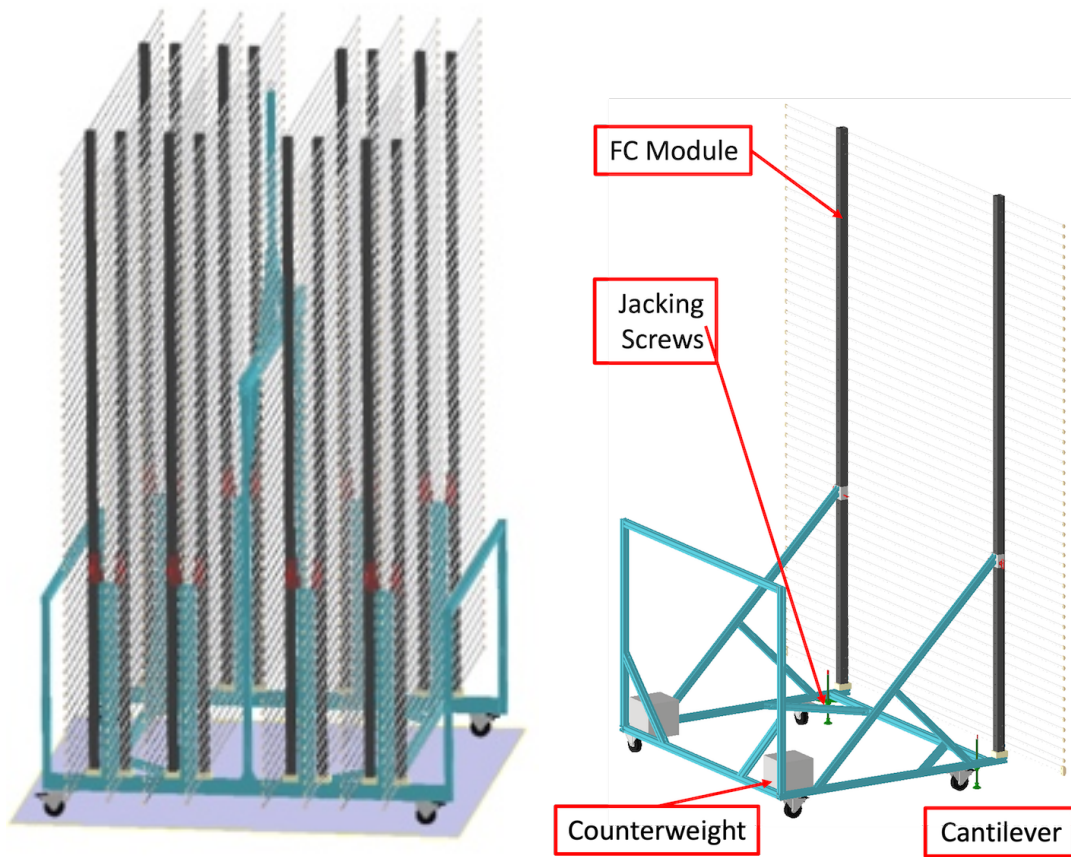


Figure 9.25: Left: field cage storage cart. Right: field cage installation cart.

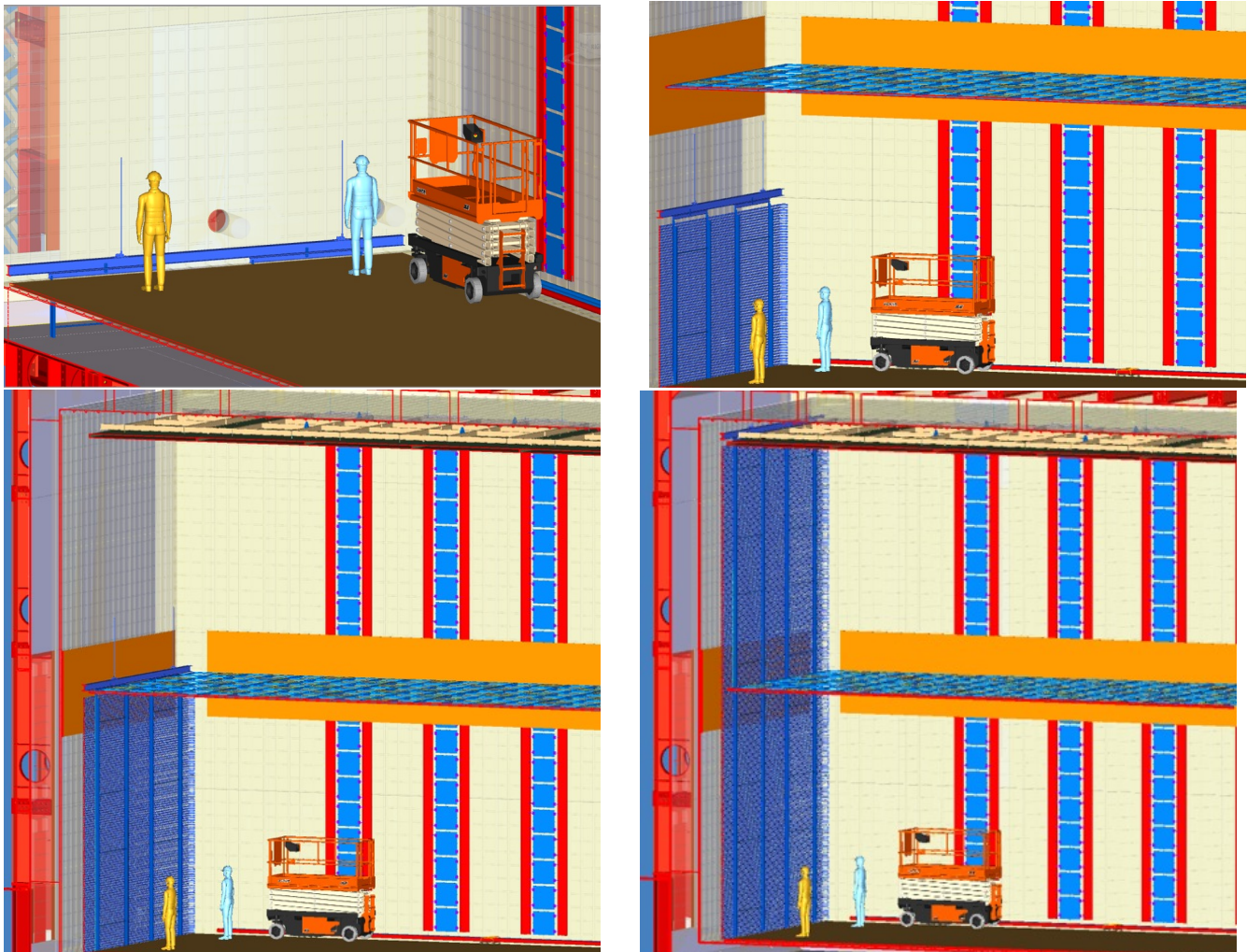


Figure 9.26: field cage installation sequence shown for an endwall panel. The top CRP superstructure and cathode are in position. Top Left: The support I-Beam is installed with support rods and field cage module supports. The vertical lifting cables are not shown. Top Right: the first two field cage modules (blue, at left) are installed. Bottom Left: the second set of modules is installed. Bottom Right: the full field cage supermodule is installed.

40. The installation of each field cage supermodule starts with moving one 6 m stainless steel field cage support I-beam into position.
41. Attach the stainless steel support rods and lower a pair of cables from the cryostat roof through the field cage roof penetrations.
42. Three options exist for hoisting the modules; the use of (a) hoists on tripods just above the feedthroughs, (b) the chimney installation gantry cart, or (c) a temporary I-beam, which can be mounted under the mezzanines with hoist attached. The simplest option may depend on mechanical interferences in the local area. The FC support I-beam is raised by about 3.5 m, high enough to position two field cage modules underneath it, side by side.
43. Once the two top modules are secured to the I-Beam, raise the partial supermodule again by the same amount to mount the next set (row) of two field cage modules under the top row, and to connect them, both mechanically and electrically. (These first two rows of the supermodule will be above the cathode).
44. Repeat this process for the third row of field cage modules; the profiles at the boundary of the second and third rows are at the cathode level and at a later stage will be connected to the cathode on its bottom-facing side.
45. Once the third row is constructed, raise the nearly complete supermodule again, this time to its final position, and connect the fourth row of field cage modules similarly to the others.
46. Transfer the load directly to the feedthrough flanges and remove the winch cables.
47. On the cryostat roof place a vacuum-tight cover over the roof penetration flange, make the electrical connections through a side flange on the roof penetration, and test the electrical connections. At the bottom of the cryostat, install a support brace to stabilize the superstructure. The final roof penetration assembly and floor brace is shown in Figure 9.27.
48. After the floor brace is secured, the PD fibers that are hanging from the cathode are attached to the vertical field cage support beams. Any excess slack is stored under the cryogenic piping at the edge of the cryostat.
49. Test the readout and cathode PD modules in location.

Once the next-to-final row of top CRPs and north-south wall field cages are installed, it will be necessary to remove the hoisting beam through the TCO to make room to install the last CRP row and the top 2/3 of the west field cage endwall. Afterwards, TCO hoisting beam is re-installed in a position below the cathode plane in preparation for the bottom CRP installation, the last major detector elements to be installed.

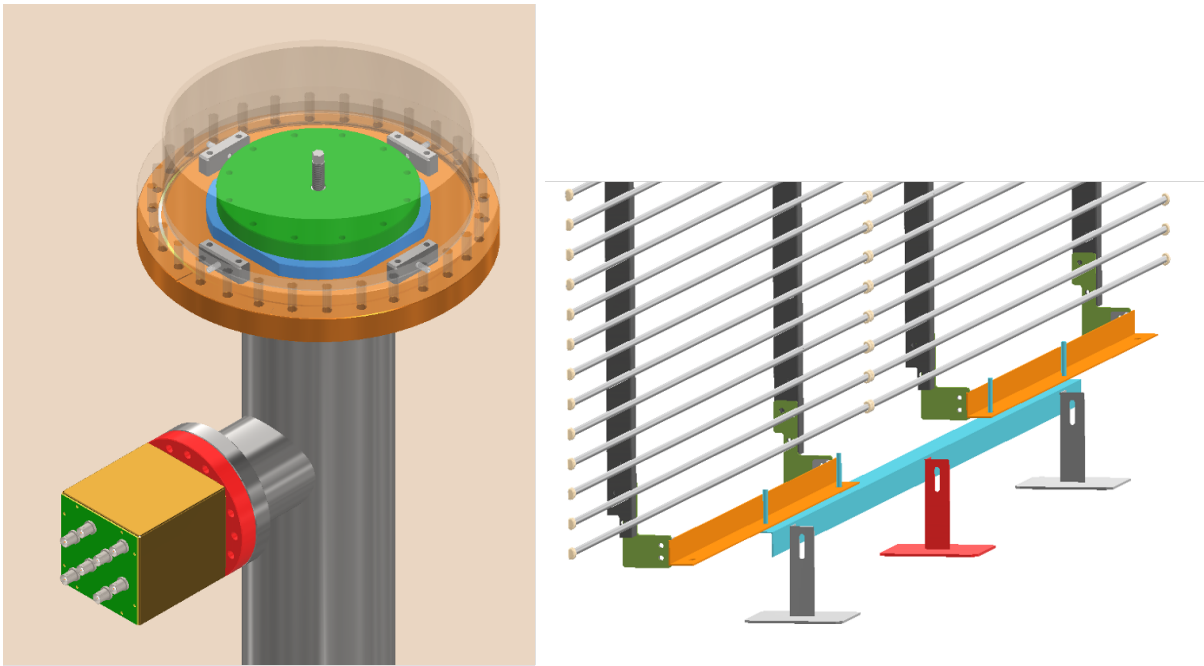


Figure 9.27: Left: Fully assembled field cage roof penetration. Right: Support brace to the cryostat floor.

Although the bottom CRPs are mechanically very similar to the top ones, they are installed individually (no superstructure), making the installation process completely different. Tooling to rotate and lift the CRPs will need to be designed and/or purchased. Each CRP weighs roughly 200 kg, making it too heavy to lift by hand, but this is well within the range of a light counterbalanced crane, many of which are on the market.

Like the top CRPs, the bottom CRPs are delivered to South Dakota as half-size CRUs in transport crates that can be rotated on-edge to fit down the Ross shaft. Unlike the top ones, however, the bottom CRP are delivered with the electronics pre-installed and the internal cabling complete. Both top and bottom CRP are bagged inside the shipping crates to prevent any dust accumulation. A dedicated area in the gray room will be set up with ESD mats for acceptance testing. The same lifting tooling in the gray room can be used for both top and bottom CRPs. The process is as follows.

50. Carry the shipping boxes into the gray room with the anodes facing down and the composite frame up.
51. Execute the tests.
52. Install the final support feet.
53. Move the CRU to the TCO using a simple cart, and hoist it into the cryostat.
54. Rotate the CRUs to have the anodes face up.
55. Lower them onto an assembly table and move them to an assembly area. Since one BDE will have one leg and the adjacent one two, the former will require shimming on the table.
56. Assemble the CRP in the cryostat by connecting the two sections of the composite frame and routing the downstream cables to the final patch panel.

The installation of the bottom CRPs will begin on the east end of the cryostat and single rows of bottom CRPs will be installed at a time.

57. Before installing each new row of bottom CRPs, remove the false floor and clean the region carefully. A protective bag over the cables to prevent dust contacting the cables is also removed.
58. Prepare the BDE cables that were stored under the floor for connection to the CRP.
59. Install a truss structure (Figure 9.28) that pre-loads the membrane floor.
60. Lift each CRP off the assembly table using a commercial counter-balanced crane with a custom 2.5 m long fork.
61. Place the CRP on the installation truss, level it and set it to the correct height.
62. Connect the BDE cables to the pre-installed patch panels and test the unit.
63. Using the same crane, remove the load from the truss and disassemble it.
64. Lower the CRP onto the cryostat floor (Figure 9.29).
65. Take measurements to determine the plane flatness and to verify the gaps between adjacent units.
66. Repeat this process until the installation reaches the last row in the detector, row 20.

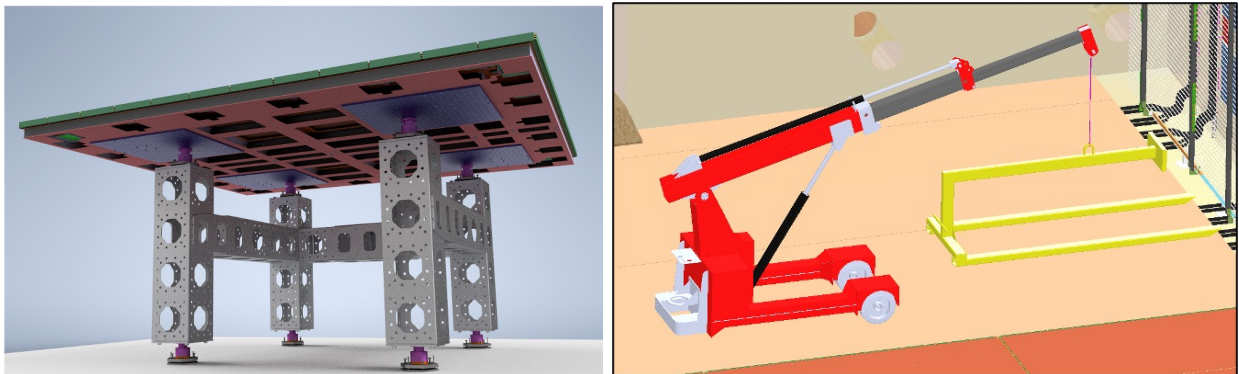


Figure 9.28: Left: CRP survey and leveling truss. Right: Crane and lifting fork.

The last row of the detector will be challenging to install due to the limited space available. On the downstream end of the cryostat only 700 mm of space exists between the field cage endwall and the cryostat membrane flat surface. This installation proceeds as follows.

67. Bring field cage storage carts with enough modules for the top 2/3 of the endwall into the cryostat.
68. Remove the TCO hoist and install the endwall panels.
69. Make final HV connections between that cathode and the endwalls from the bottom
70. Remove the scissor lift from the cryostat.
71. Attach a temporary jib crane to the cryostat entrance (Figure 9.30) for installation of the final row of bottom CRPs.
72. Position the CRP assembly table directly in front of the TCO opening, remove the floor under the north and south CRP, and clean the membrane areas.

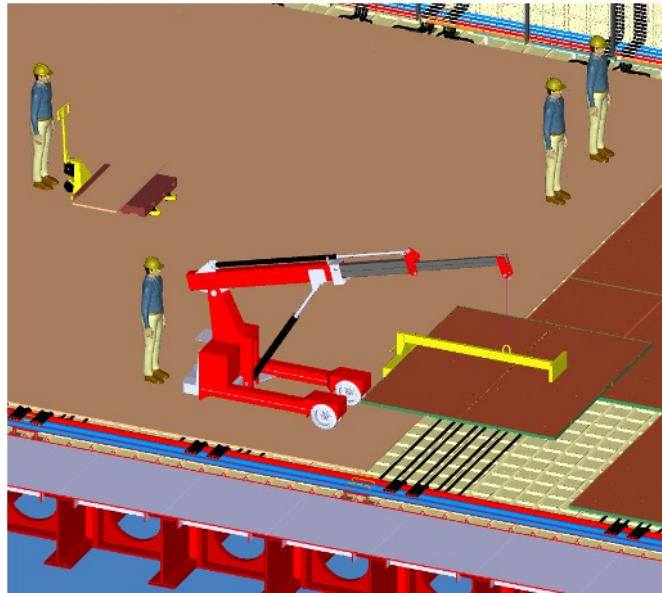


Figure 9.29: Bottom CRP being lowered into final position.

73. Move two CRUs into the cryostat using the jib crane and place them on the assembly table.
74. Assemble the two BDE.
75. The tines of the bottom CRPs lifting tool can then be placed under the CRP to lift it.
76. Move the table out of the way, place the CRP temporarily on the floor, and move the jib crane away.
77. Move the counterbalanced crane next to the CRP, lift it, and move it to its final position.
78. Repeat for the other outer CRP.
79. Finally, bring the last CRUs individually into the cryostat using the jib crane as shown in Figure 9.31. At this time only 700 mm of floor is left in the cryostat.
80. Carry in the last four field cage modules by hand. These modules have only a fraction of the aluminum profiles installed so as to keep the weight low.
81. Two technicians hold them in position while a third connects the supports at the top.
82. Once the modules are freely hanging, install the floor support and the final profiles.
83. The remaining profiles are then installed on the lower field cage modules.
84. Install the west purity monitors.
85. Remove the last of the floor, the protective covers over the end wall PD modules, and LAr valves.
86. Clean all reachable surfaces.

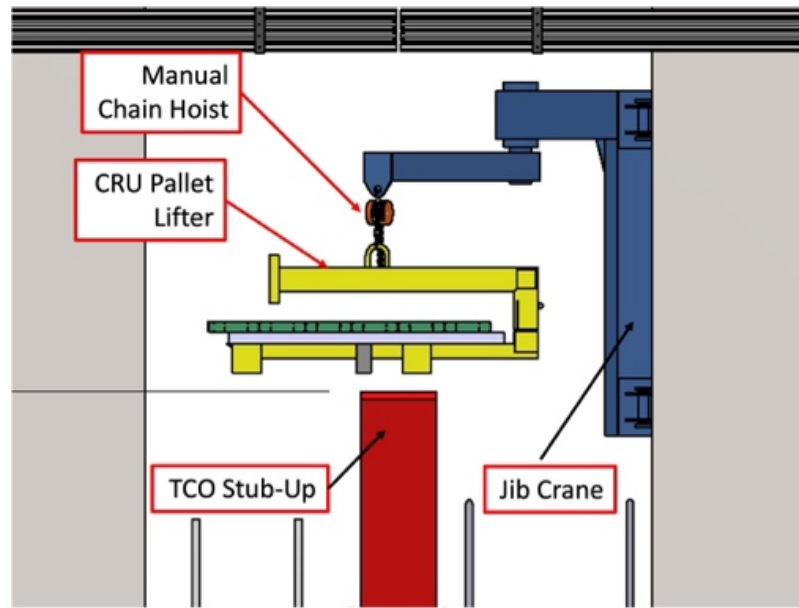


Figure 9.30: Jib crane for Row 20 installation.

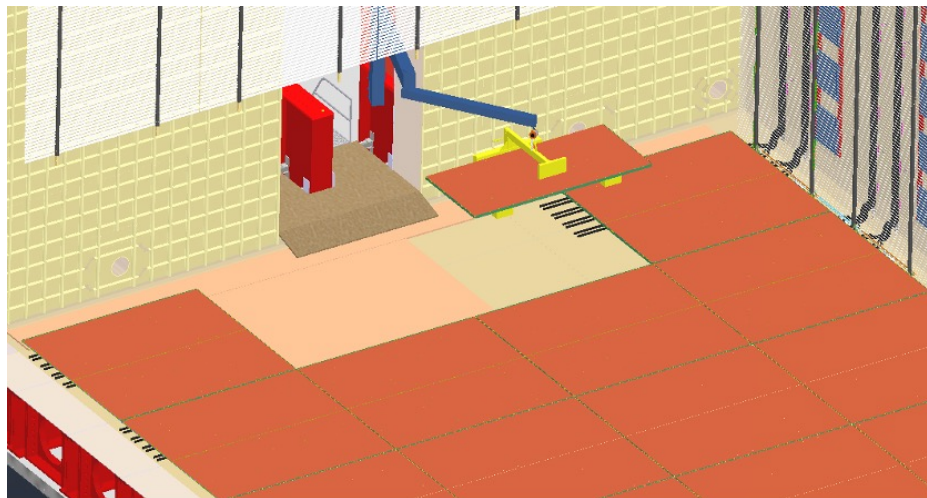


Figure 9.31: Installation of the last BDE.



Once detector installation completes, the process of closing the TCO begins. The cryostat vendor will perform the mechanical closure of the TCO as described.

87. First weld the remaining membrane panels in position and clean the local area.
88. Working from the outside, install the foam insulation and bolt the steel support structure in position with the tertiary 1 cm membrane.
89. Weld the tertiary membrane, sealing the TCO.
90. Remove the cryostat ventilation from the four access hatches in the cryostat roof, and seal them.
91. This completes the detector module installation.

## 9.9 Interfaces

The interfaces between FSII and the consortia are documented in a series of Interface Control Documents (ICD)s and interface drawings which are linked to left column in Table 9.3.

Table 9.3: Installation interface descriptions and links to full interface documents.

Interfacing System	Description
General	FSII interfaces with all consortia in the same manner. This document defines the fundamental roles and responsibilities between FSII and every consortium. Consortia specific interfaces are defined in the interface appendices below.
CRP	The CRP consortia designs the CRP supports. FSII will fabricate. CRP provides lifting fixtures and FSII provides commercial rigging equipment. CRP provides equipment to assemble the CRP from CRU in the cryostat.
BDE	FSII provides the cryostat roof penetrations, the racks for BDE modules and patch panels, cable trays and warm cables and optical fibers. BDE provides all cold cables, all electronics, all electrical testing equipment.
TDE	FSII provides equipment to install the chimneys, TDE provides tooling to connect to the chimneys. FSII provides the roof penetrations, cable trays, warm cables and optical fibers. TDE provides all electronics and electrical testing equipment.
HV	FSII will provide a gray room for field cage and cathode assembly. HV provides all equipment to do this work. FSII provides lifting equipment for raising the field cage support beams. Other equipment is provided by HV.
PDS	FSII provides the roof penetrations, racks, warm cables and cable trays. PDS provides the detector modules and supports, the readout and testing equipment. FSII will provide a gray room for assembling and testing the PD modules.
DAQ	FSII provides the barracks, racks, fire suppression, and cooling for the DAQ servers. FSII also provides the fibers running from the surface and fibers on the cryostat roof.
FSCF-BSI	Interfaces to FSCF-BSI are described in the document linked to the left. These interfaces include: power, ventilation, cooling, fiber infrastructure, mechanical interfaces, and egress.
Drawings	A collection of drawings defining the mechanical interfaces relevant to the installation process are collected in the folder linked to the right.

## 9.10 Organization and Management

### 9.10.1 Contributing Institutions

The DUNE institutions contributing to the FSII scope are listed in Table 9.4.

Table 9.4: FSII Institutions

Member Institute	Country
BNL	USA
CERN	Switzerland
FNAL	USA
U. Minn.	USA

### 9.10.2 High-level Schedule

Table 9.5: High level milestones and schedule for FD2-VD integration and installation.

Milestone	Date
FD2-VD cryostat start of construction	May 2025
SDWF ready to accept FD2-VD shipments	February 2027
Installation readiness review (IRR) all items for FD2-VD	February 2027
Top TDE/CRP assembly ready for installation	April 2027
FD2-VD cryostat complete; ready for detector installation	August 2027
FD2-VD fabrication and delivery of components to SURF – threshold (KPP)	August 2027
Bottom BDE/CRP assembly ready for installation	October 2027
FD2-VD installation complete – threshold KPP	August 2028
Final approval to operate cryogenics system #2	November 2028
All threshold KPPs met	September 2029
FD2-VD commissioning test complete – objective KPP met (30% filling)	October 2029
FD2-VD complete - objective KPP met	November 2029

# Chapter 10

## Project Management

### 10.1 Project Organization

#### 10.1.1 DUNE Collaboration and Consortia

The Deep Underground Neutrino Experiment (DUNE), shown in Figure 10.1, is led by two co-spokespersons overseeing the construction activities in three principal areas: horizontal drift detector module (FD1-HD), vertical drift detector module (FD2-VD) and near detector (ND). An overall institutional board () is responsible for the governance of the collaboration. DUNE is organized into several consortia, each of which is responsible for design, fabrication and commissioning of specific detector components and continue to maintain responsibility for these subsystems through the operations phase.

The DUNE spokespersons serve on the Experimental Facilities Interface Group (EFIG) that coordinates between the conventional and beamline facilities and the DUNE detector subprojects. DUNE has three technical coordinators, one for each of FD1-HD, FD2-VD, and ND, who coordinate the activities across their respective detector subsystem and provide the critical interface across the consortia. The technical coordinators are part of the DUNE management team as described in [103, 104] along with the spokespersons, resource coordinator, physics coordinators, computing coordinator and upgrade coordinator.

There is a high degree of overlap between consortium deliverables in design, prototyping, and fabrication for FD2-VD and FD1-HD. In many cases entire subsystems are identical, and in others many of the components are identical. In these cases, a single consortia working on multiple detector systems has been instituted to provide maximum efficiency, and this is represented by the horizontal dashed lines in Figure 10.1.

Each consortium is managed by a consortium leader and technical leads appointed by DUNE management. The consortium leader chairs a (consortium-specific) institutional board (IB) composed of one representative from each of the contributing institutions. Major consortium decisions such as technology selections and assignment of responsibilities to specific institutions pass through its

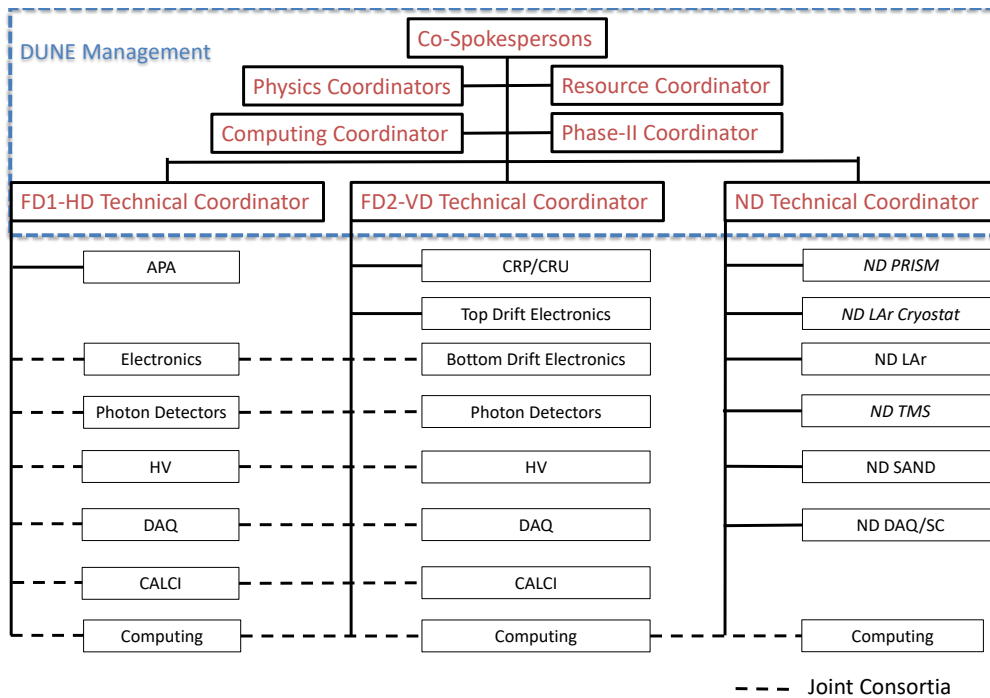


Figure 10.1: Organization of the DUNE consortia.

IB. These decisions are then passed as recommendations to the overall DUNE executive board (EB). (The DUNE EB consists of the Spokespersons, DUNE IB chair, technical coordinators, resource coordinator, computing coordinator, physics coordinators, phase-II coordinator, and consortia leaders.)

Consortia manage the design and construction of subsystem deliverables that may be supported by multiple funding agencies, where each funding agency is responsible for its own deliverables. To ensure coordination between the separate internal projects contributing to the consortia, technical leads are responsible for chairing consortium project management boards that incorporate managers from each of the internal projects.

A total of nine consortia have been formed to cover the subsystems required for FD1-HD and FD2-VD, as shown in Figure 10.1. In particular, two consortia focus exclusively on FD2-VD (charge-readout plane (CRP) and Top Drift Electronics) and another six consortia have responsibility for subsystems common to both detector technologies (Bottom Drift Electronics (combined with FD1-HD Electronics), photon detection system (PDS), high voltage (HV), data acquisition (DAQ), , and Computing). One consortium, anode plane assembly (APA), focuses exclusively on FD1-HD.

### 10.1.2 LBNF/DUNE Project

The LBNF and DUNE enterprise (LBNF/DUNE) has been organized as shown in Figure 10.2, with the LBNF/DUNE project (and project) subdivided into five subprojects.

LBNF/DUNE is led by a Project Director. The five subprojects are managed by Deputy Project Directors who report to the Project Director, and engage the Joint Project Office (JPO) to sup-

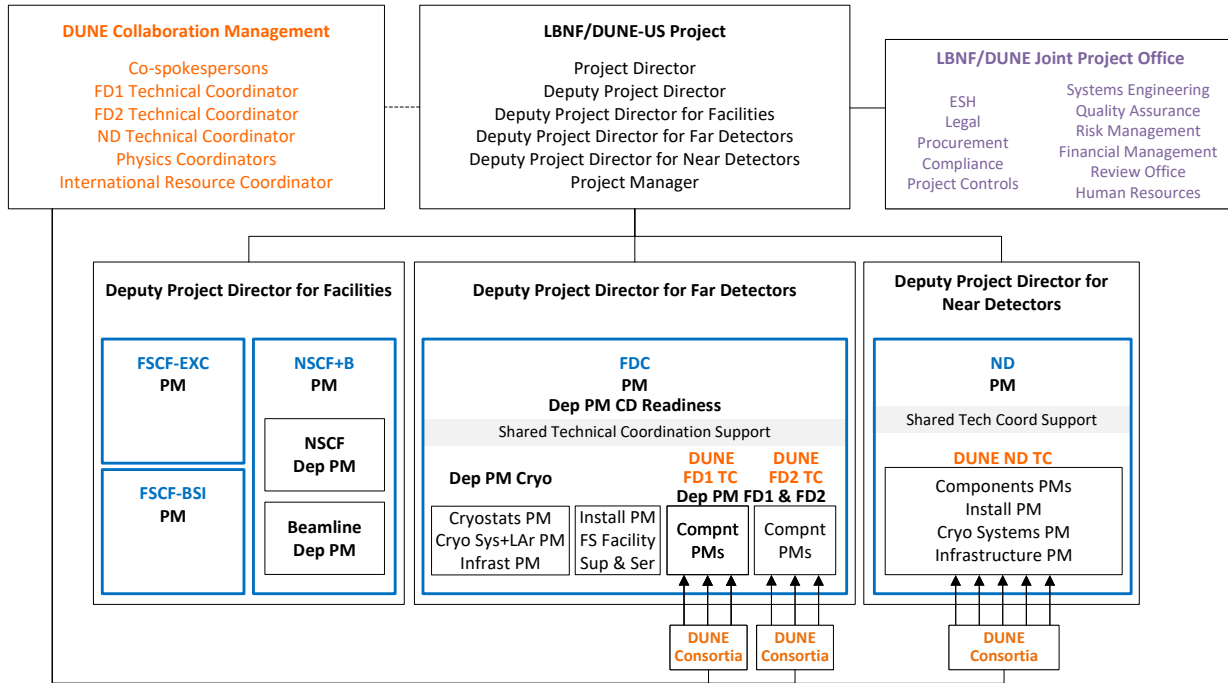


Figure 10.2: LBNF/DUNE organization showing the LBNF/DUNE and LBNF/DUNE-US (top, center) as comprising five subprojects (SP), delineated with blue boxes. The DUNE Collaboration Management (top, left), LBNF/DUNE and JPO (top, right) work closely together. The exclusive US project organization, FSCF includes two subprojects for excavation (EXE) and building and site infrastructure (BSI) that include the utilities. The far detector and cryogenics (FDC) subproject (both US and international) includes both detectors FD1–2 and the cryostats and cryogenics. PM refers to project manager. CD refers to critical decision (part of the DOE system). "Sup & Ser" refers to support and services. "Compnt PMs" refers to the different DUNE subsystems.

port various project functions. These management structures and functions are outlined in the LBNF/DUNE Project Management Plan [105]. Far Site Conventional Facilities (FSCF) includes two subprojects for excavation (EXE) and building and site infrastructure (BSI that include the utilities. The far detector and cryogenics (FDC) subproject includes both detectors FD1-2 and the cryostats and cryogenics.

### 10.1.3 Far Detector and Cryogenics (FDC) Subproject

The international Far Detector and Cryogenics subproject (FDC) is responsible for construction, assembly, installation and commissioning of the FD1-HD and FD2-VD far detector modules (including the supporting infrastructure: cryostats and cryogenics systems). Major parts of the detector are the responsibility of the DUNE consortia which are coordinated through the technical coordinators.

The FDC subproject is overseen by the Deputy Project Director for Far Detectors ( ) and is organized as shown in Figure 10.3.

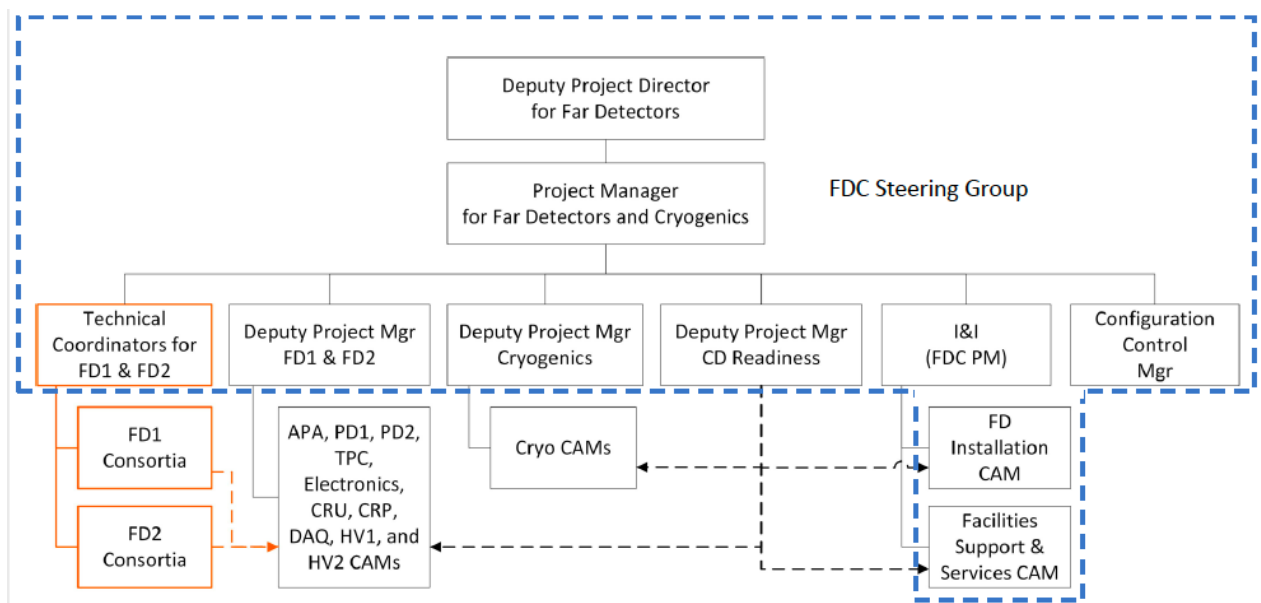


Figure 10.3: Far detector and cryogenic (FDC) subproject organization. CAM refers to control account manager, who is responsible for the budget and reporting.

The far site steering group (delineated by blue dashed line in Figure 10.3) is chaired by and advises the DPDFD; its members are the

- DPDFD,
- FD1-HD/FD2-VD technical coordinators (TCs),
- FDC subproject manager and deputies,
- FD1-HD/FD2-VD installation managers,
- cryogenics manager,
- configuration control manager,
- Fermilab South Dakota Services Division (SDSD) manager,

- LBNF/DUNE-US Project Director,
- LBNF/DUNE-US Project Manager,
- Co-spokespersons.

The steering group oversees the entire FDC subproject, including the design and fabrication of the detector modules, cryostats, cryogenics and support systems and their installation and commissioning at Sanford Underground Research Facility (SURF) following acceptance for use and possession (AUP).

The FDC subproject maintains several management tools, including the international FDC scheduling software and the FD2-VD schedule. The FD2-VD schedule was developed by the consortia contributing to FD2-VD and is maintained by the FDC project controls staff. The US FD2-VD L2 s are responsible for earned value management system (EVMS) on the US part of the schedule and track percent-complete and milestones with the consortia leaders for the rest of the schedule. The FDC subproject coordinates with and oversees the DUNE consortia in the design, fabrication, installation and commissioning of their detector components and manages the interfaces between detector components and the detector support infrastructure (Interface documents can be found in <https://edms.cern.ch/project/CERN-0000224744>). It coordinates with the review office (RO) and compliance office (CO) to ensure that all detector components meet specifications and are safe, and with the configuration control manager to ensure that the integrated detector model fits in the overall far site model, that installation envelopes are fully specified, and that detector component locations are understood when installed (at room temperature and dry) and during operations after the cryostat is filled with liquid argon (LAr). The FDC subproject coordinates with the consortia in the development of the FD2-VD detector cost estimate, basis of estimate, risk register, contingency estimate, requirements, interfaces, P6 schedule, milestones and for the U.S. scope of the project, EVMS. Requirements are managed at several levels and can be found in [106]. The FDC subproject includes the organization that is responsible for all installation activities at the far site, including FD1-HD, FD2-VD and cryogenics, as discussed in Chapter 9.

FD2-VD maintains a set of tools to document, manage and track risks developed by the consortia together with the U.S. CAMs. Risks are continually discussed and updated within each consortia and eventually approved by the LBNF/DUNE Risk Management Board and documented in the Fermilab Risk tool. A snapshot of the risk register is provided at [107] and the technical risks are summarized in Section 10.2. Regular risk workshops assess risks across the full scope of FDC.

#### 10.1.4 Technical Boards

Technical board meetings, chaired by the technical coordinators are the fora for resolving technical issues (e.g., how a and CRP may interfere during the installation process). Minutes are taken and made available to the collaboration so that issues that impact science are brought to the attention of the EB. Issues that impact project scope and schedule are brought to the consortia project management boards as needed. Two separate, but highly overlapping, far detector (FD) technical boards focus separately on FD1-HD and FD2-VD. The technical boards have expanded to incorporate additional project team members. These boards incorporate all parties needed to address issues arising across the full spectrum of detector-related activities and thereby ensure



tight coordination between the consortia. Each technical board consists of the following members:

- technical coordinator (chair),
- consortium leadership teams,
- technical coordination engineering teams,
- installation coordinators (lead engineers),
- cryogenics coordinators (project managers and lead engineers),
- SDSD (support service managers and logistics manager),
- configuration management team;
- project management (Deputy Directors for FDs and detector subproject managers), and
- collaboration spokespersons and LBNF/DUNE-US Project Director.

### 10.1.5 Joint Project Office

The JPO reports to the LBNF/DUNE Project Director as shown in Figure 10.2 and provides coordination across the LBNF/DUNE enterprise. Major functions provided by the JPO include environment, safety and health (ES&H), quality assurance (QA), systems engineering, and the review and compliance offices (RO and CO).

LBNF/DUNE is committed to protecting the health and safety of staff, the community, and the environment, as well as to ensuring a safe work environment for DUNE workers at all institutions and protecting the public from hazards associated with constructing and operating DUNE. Accidents and injuries are preventable, and the ES&H team works with the global LBNF/DUNE project and collaboration to establish an injury-free workplace. All work will be performed so as to preserve the quality of the environment and prevent property damage. The LBNF/DUNE ES&H program is described in detail in the LBNF/DUNE Integrated Safety and Health Management Plan [12], and more briefly in [108], Chapter 10.

The systems engineering group is responsible for the high-level project-wide management of requirements, interfaces and integration, and oversees configuration management and change management. Systems engineering works with all LBNF/DUNE design teams to incorporate individual CAD models into the global controlled model that is released in [109]. Configuration management establishes and maintains consistency across the entire LBNF/DUNE enterprise for project performance, function, and physical attributes via requirements, design models and drawing, and operational information for the duration of the project. The Systems Engineering Management Plan (SEMP) [110] describes the responsibilities and processes that support the design and implementation of configuration management. The main goal of the SEMP is to prevent unauthorized or uncontrolled changes to the engineering design or analysis, hardware, controlled documents, and controlled software. The latest official version of the requirements is stored in [14]. Change control processes are defined in the SEMP. Baseline change requests are catalogued and managed in the LBNF/DUNE change control tool according to thresholds defined in the Change Control Threshold and Authority Table [105, 110]. The integrated LBNF/DUNE change control board provides oversight of changes. The JPO engineering team reviews subsystem component documentation in order to manage the detector configuration. The consortia provide engineering data for their detector subsystems to the JPO team for incorporation into global configuration files. The inte-

gration of the FD2-VD detector is carried out by the technical coordination (TCN) engineering team working with the consortia and in the broader framework of the JPO central engineering team.

The LBNF/DUNE design review process, described in [111], is consistent with the Fermilab review process described in its ES&H manual [112]. Past and scheduled reviews are documented in [113]. Review reports are saved in [114]). The review process is an important part of the DUNE QA process, both for design and production. The review office (RO), in coordination with the TCN, reviews all stages of development and works with each consortium or subsystem to arrange reviews at key stages of the design (, and ) and production (production readiness review (PRR) and production progress review (PPR)). The office also conducts installation readiness reviews (IRRs) and operational readiness reviews (ORRs) of their subsystems. CDR, PDR and FDR are equated with 30%, 60% and 90% design. The review charge for each is set by the RO in coordination with TCN.

Full production of detector elements begins only after successful PRRs. Regular production progress reviews will be held once production starts. The PRRs will typically include a review of the first pre-production modules produced at each facility, which may include the production of components. Installation reviews will review the DUNE installation equipment, procedures, lifting fixtures and hazard analyses for the installation work. The ORRs will feed the Fermilab operational readiness clearance (ORC) process [112] and are the final safety checkout before equipment can be operated. Tracking review recommendations is part of the review process, with reports and recommendations maintained in [115].

The JPO compliance office (CO) has mechanical and electrical engineering experts from collaborating institutions and serves as the LBNF/DUNE engineering safety assurance team. The CO develops processes and procedures for evaluating engineering designs using accepted international safety standards. The codes and standards to which each system is designed will be reviewed as part of the PDR and FDR reviews. The CO verifies that the structural analysis presented by the various engineering partners in the project is correct and of sufficient quality.

DUNE technical coordination (TCN) monitors technical contributions from collaborating institutions and provides centralized project coordination functions with support from the JPO. Part of this project coordination is standardizing quality assurance (QA) and quality control (QC) practices, one facet of which is to assist the consortia in defining and implementing QA/lans that maintain uniform, high standards across the entire detector construction effort. The LBNF/DUNE QA program is described in detail in the project's Quality Assurance Plan [116] () and more briefly in [108], Chapter 9.

## 10.2 Risks

Table 10.1 lists the significant technical risks for the FD2-VD, along with the risk mitigations and their post-mitigation probabilities (P) and potential impacts on cost (C) and schedule (S). The impacts are designated as low (L), medium (M) or high (H) in each category. The impact values are assigned according to these criteria:

- Probability (%): L=0-19, M=20-39, H= $\geq$ 40;
- Cost (k\$ U.S.): L=0-100, M=100-500, H= $\geq$ 500;
- Schedule (months): L=0-2, M=2-6, H= $\geq$ 6.

Note that risks associated with delays, cost increases, insufficient personnel, or damages are not included. Two operational risks, BDE1 and HVS2, are included to emphasize that risk mitigation starts during the design phase, making design choices that go toward minimizing all operational risks.

Most of the risks have been determined to be low probability (P); the few that are currently set to medium (M) will be reduced prior to the final design review (FDR). This demonstrates the technical maturity of the design. The few risks designated high (H) (in cost or schedule only) are expected to decrease to low or medium prior to the PRR, once the production model is further understood and documented.

Table 10.1: FD2-VD Risks

ID	Description	Mitigation	P	C	S
CRP1	Bottom CRP support requires additional design consideration following Module 0 test.	Engineering by an experienced group is planned for Module 0 supports. Prototype testing will be done before installation in Module 0.	L	M	L
CRP2	Bottom CRP support requires additional design consideration following Module 0 test.	Engineering by an experienced group is planned for Module 0 supports. Prototype testing will be done before installation in module 0.	L	M	L
CRP3	Bottom CRP require additional cold testing at far site due to damage on receipt	Extensive tests of shipping process during prototyping stage to minimize damage	M	M	L
CRP4	Additional design iteration of CRP adapter cards needed to address noise issues	CRP adapter cards are extensively tested during cold box tests prior to PRR	L	L	M
CRP5	Additional design iteration of edge boards needed to address mechanical connection issues prior to PRR.	Edge boards are extensively tested during prototyping stage; additional design considerations are explored to improve mechanical integrity.	L	L	M
CRP6	Anode strip interconnect has some failure rate from handling and thermal cycle on the silver printing regions.	Identify alternative PCB panel building methods to eliminate the use of silver printing.	L	L	L
TDE1	Commercial components become obsolete	Procure components with sufficient spares in advance.	L	L	L
TDE2	Damage of front-end (FE) electronics due to HV discharges occurring at the level of CRP and/or field cage.	Design of suitable protection components on the FE card. Allow for replacement of cryogenic electronics via chimneys without contaminating LAr volume or switching off the other cards in the same or other chimneys.	L	L	L
TDE3	SFT chimneys do not fit in roof penetrations	Jointly with I&I, draft and execute validation procedure for chimney and penetration interface and tolerances.	L	L	L
TDE4	Nitrogen leaks into cryostat via the SFT chimneys	Before installation, leak-test each chimney by filling it with argon. Perform other tests in situ.	L	L	L

BDE1	Lifetime of TPC electronics components inside the cryostat.	Engineering of s follows design rules aimed at ensuring that the chips would work in LAr. The possibility of using redundant connections between the ASICs/front-end mother boards (FEMBs) and the warm interface boards (WIBs) is also being taken into account. Proper fabrication rules and QC tests for PCBs are being put in place based on the experience with other detectors that use cryogenic liquids.	L	L	H
BDE3	Incompatibilities with detector components provided by other consortia	Determine and agree on proper design of interfaces; extensive integration tests during prototyping stage	L	M	M
BD4	Single source vendor for BDE	Use fabrication technologies that are relatively recent and in widespread usage. Investigate alternative vendors. Purchase all the components as soon as the design is finalized.	L	H	L
HVS1	FD1-HD/FD2-VD HV experience in Module 0 leads to a significant redesign	If the HV performance during Module 0 does not improve upon performance, then there may be a significant redesign of the HV/cathode system	L	M	M
HVS2	Field cage profiles need coating	A method of applying a coating using chemical wipes has been found and can be implemented at SURF during field cage assembly	L	L	L
PDS1	Insufficient power-over-fiber (PoF) efficiency compared to baseline expectations.	Explore and compare PoF technologies from different vendors. Consider adding PoF transmitters, receivers, and fiber penetrations in the cryostat.	L	H	M
PDS2	Simulations show additional detection efficiency required	Explore and optimize geometries, optimize the number of silicon photomultipliers (SiPMs) to maintain efficiency. Conclude studies before FDR.	L	H	L
PDS3	PDS Components fail 30-year cold validation testing	Extensive lifetime tests of individual components and integrated module prior to FDR. Identify alternate vendor for several components in advance if issues arise during tests.	M	H	L
PDS4	Photon detector (PD) electronics generates noise on the TPC strips readout	Reasonable shielding and simulations will be conducted to minimize risk of inducing noise on TPC at critical frequencies. Prototype and Module 0 completion will improve confidence if there is no indication of noise in neighboring detectors.	L	M	M
DAQ1	Inability to efficiently perform DAQ work remotely	Tools developed to allow for remote access and for collaborative work between SURF personnel and remote DAQ experts; train SURF personnel to handle trouble-shooting issues independently	L	L	L
DAQ2	SURF infrastructure stability impacts DAQ uptime and server lifetimes	Communicate DAQ services requirements clearly, including those that affect stability. Develop a plan for operations support to monitor stability issues. Plan integration testing activities such that some instability will not cause a complete halt in work.	L	L	L
DAQ3	DAQ control, configuration and monitoring subsystem (CCM) and data quality monitoring (DQM) do not meet required specifications	Perform scaling tests at Module 0s to ensure CCM and DQM infrastructure can support full detectors with some headroom. Focus final development, integration, and review activities on achieving performance at scale.	L	L	M

DAQ4	Data filter is not optimized or deployed efficiently	Ensure data filter development work ends with full demonstration and integration with the DAQ well ahead of when it is needed for commissioning.	L	L	L
I&I1	Detector failure during cool-down	Cold testing of all components before installation and continuous monitoring during cool-down	L	H	H
I&I2	Missing scope due to poor interface definition at Far Site	Use systems engineering methodologies to identify and alleviate gaps in scope. Ongoing inter-project interface meetings/discussions to ensure scope alignment and clarity of expectations.	L	H	L
I&I3	Lack of agreement on international codes/standards affects partner design work	Use code equivalencies and international agreements to detail process for design and acceptance of non-U.S. components. Use design reviews to evaluate compliance to codes/standards applicable to the project; establishment of the integration project office / compliance office to resolve issues ahead of execution.	L	L	M
I&I4	Grounding and shielding errors induce electronics noise requiring additional mitigation.	Document and implement the DUNE grounding and shielding plan. Test all instrumentation during Module 0.	M	L	L
I&I5	Additional Installation testing required after Module 0	Provide for additional test setup during Module 0	M	L	M
I&I6	I&I Equipment requires major repair	Plan includes periodic maintenance and minor repair, including annual inspections, as appropriate.	M	M	L

### 10.3 Schedule

The FD2-VD detector was added to the overall LBNF/DUNE project in June 2021. The development steps of the FD2-VD project are summarized in Figure 10.4 as FD2-VD advances from conceptual design through preliminary and final design, and into production.

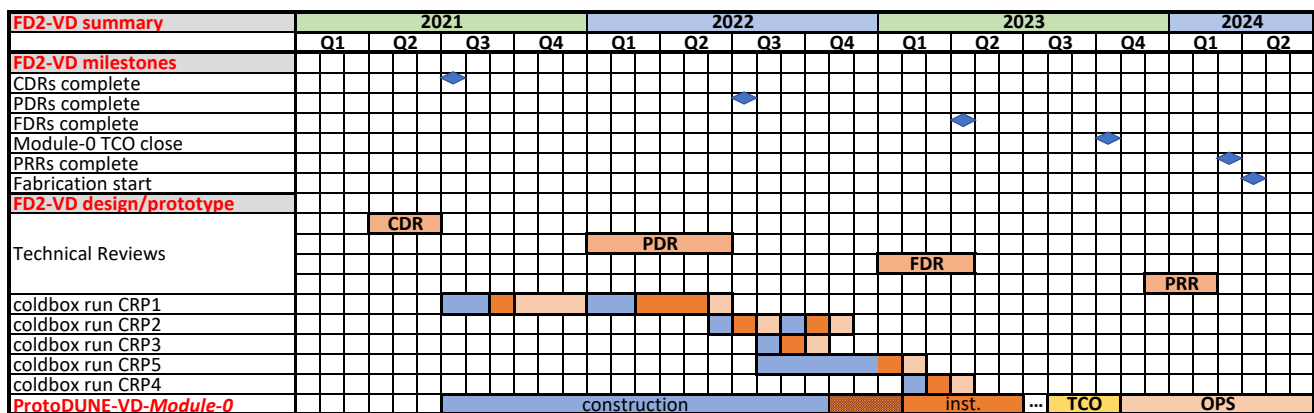


Figure 10.4: Project development plan for FD2-VD. The operation dates of FD2-VD Module 0 depend on the availability of LAr. The dedicated PD cold box runs are not shown.

The overall schedule includes the FD2-VD phased R&D plan starting with small-scale R&D tests from 2020 through 2022, advancing to large-scale tests in 2021–2022 (as discussed in Chapter 8) and the complete FD2-VD Module 0 detector in 2023–2024. FD2-VD Module 0 is composed of

pre-production components intended for production for FD2-VD. The conceptual design reviews (CDRs) for each consortium were completed in spring 2021, followed by the conceptual design report (also abbreviated as CDR) that was endorsed by the Long-Baseline Neutrino Committee (LBNC) and approved by the Fermilab director in January 2022. Preliminary design reviews (PDRs) for each consortium were completed by June 2022. Final design reviews (FDRs) are expected in the first half of 2023 after FD2-VD cold box runs have validated detector designs. The final full-scale pre-production components will be installed into FD2-VD Module 0 in early 2023. PRRs for each consortium are expected in early 2024 in anticipation of full-scale production of components that is expected to start in 2024–2025 with installation at SURF in 2026–2027. Near-term development milestones tracked by the LBNC are shown in Figure 10.5. These milestones will be expanded and implemented into P6.

### 10.3.1 Prototyping Schedule

The cold box tests of detector components are the key to demonstrating performance for the FDRs (and U.S. critical decision (CD)-2/3). These tests demonstrate system prototype performance in an operational environment and give confidence that the components can deliver the necessary performance in FD2-VD. The required steps that follow before launching PRRs and final production include qualification of production sites and QC, production processes and procedures. The FD2-VD Module 0 tests demonstrate a high level complete functional system integration of all FD2-VD detector components.

As discussed in the FD2-VD CDR [32], several key areas of R&D were advanced in small-scale test stands, including the 50 L test stand at the European Laboratory for Particle Physics (CERN), Fermilab’s ICEBERG R&D cryostat and electronics (ICEBERG), the Brookhaven National Laboratory (BNL)/Yale cold box and the 2 t cryostat at CERN, and this development will continue. Larger-scale demonstrations focus on the FD2-VD cold box and HV test in the large cryostat. The , coupler and HV extender were tested in test stands and in the large NP02 cryostat. This NP02 test has demonstrated that 300 kV can be delivered to a cathode 6 m under the LAr surface and that ionization electronics can be drifted 6 m; retiring significant risk for FD2-VD. The CRP anode designs were tested in the 50 L system and cold box at CERN. This prototyping establishes performance parameters, refines designs, develops vendors, and progresses FD2-VD to final design and Module 0. FD2-VD Module 0 installation started in early 2023 after component testing in the FD2-VD cold box. Operations are expected to start in 2024. The results may enable final adjustments for FD2-VD production if there are outstanding issues from the PRRs.

### 10.3.2 Production and Installation Schedule

The FDRs for FD2-VD components started in early 2023 and are expected to complete by May 2023. PRRs are anticipated in early 2024 after LBNF/DUNE-US obtains CD-3 approval. The production schedule is based on production estimates from each consortium as discussed in previous chapters; production is expected to occur in 2024–2026. The components for FD2-VD should be delivered to SURF in 2026–2027. The installation of FD2-VD, the second far detector module, at SURF is planned for 2026–2028. Additional details for the proposed installation procedure have been presented in Section 9.8. The overall production and installation schedule is shown in Figure 10.6.

<b>DUNE Vertical Drift (FD2-VD) Milestones (2020-2023)</b>					
System codes: M=management, H=HV, C=CRP, P=PDS, S=simulations					
	Date	System	Milestone	Accomplished or Revised	Status
	<b>2020</b>				
1	1-Nov-2020	C	Validate 2-view anode (0, 90) in 50l test	5/26/2020	done
2	30-Nov-2020	M,C,H,P,S	Technical proposal distributed to DUNE and LBNC	11/30/2020	done
3	1-Dec-2020	M,C,H,P,S	First reviews presented to LBNC, DOE and DUNE	12/12/2020	done
	<b>2021</b>				
4	31-Jan-2021	M,C,H,P,S	FD2-VD presented to DOE IPR	1/8/2021	done
5	30-Apr-2021	C	Validate 3-view anode (0, 48, 90) in 50l test	4/13/2021	done
6	31-May-2021	M,C,H,P,S	LBNC technical review complete	6/10/2021	done
7	20-Jun-2021	H	HV coupler and feedthrough verified for NP02 test	7/5/2021	done
8	30-Jun-2021	M,C,H,P	All internal conceptual design reviews complete	6/18/2021	done
9	15-Jul-2021	P	R&D on PDS at 300kV results reviewed, decision on cold-box PDS layout	8/4/2021	done
10	31-Jul-2021	C,P	Cold-box dry run completed and cold-box meets requirements	10/13/2021	done
11	31-Jul-2021	H	NP02 closed for 300 kV HV tests	8/3/2021	done
12	15-Aug-2021	C	Validate 3-view anode (30, -30, 90) in 50l test	2/4/2022	done
13	18-Sep-2021	M,C,H,P,S	CDR posted for CD1-RR with LBNC report	12/5/2021	done
14	30-Sep-2021	C,P	Cold-box closed with first full CRP+cathode+PDS	10/25/2021	done
15	30-Sep-2021	S	First full samples available with reference geometry and basic reconstruction	11/30/2021	done
16	30-Sep-2021	S	Initial studies of low energy physics improvements with PDS	7/15/2022	ongoing
17	15-Dec-2021	C	First validation of (0, 48, 90) CRP in cold-box test with HV and electron drift	11/10/2021	done
18	15-Dec-2021	P	First validation of PDS at HV in cold-box test	12/16/2021	done
19	31-Dec-2021	H	NP02 HV (300kV) stability validation, including 70% FC performance. Validate HV and 6m drift for <i>module-0</i>	9/15/2021	done
	<b>2022</b>				
20	31-Jan-2022	S	Tuned/validated 3D reconstruction ready	3/10/2022	done
21	31-Jan-2022	S	Newly trained CVN selection for beam events	3/20/2022	done
22	15-Feb-2022	C	Decision on CRP layout (not strip orientation), electronics for <i>module-0</i>	9/22/2021	done
23	28-Feb-2022	S	Tests of low energy tracking performance with reference geometry	5/4/2022	done
24	31-Mar-2022	C	Initial validation of (30, -30, 90) CRP in cold-box	7/22/2022	done
25	31-Mar-2022	C,S	Decision on viability of 2-view alternative based on simulation	-	done
26	30-Apr-2022	C,S	Decision on strip orientation for 3 <sup>rd</sup> and 4 <sup>th</sup> CRP for <i>module-0</i> based on simulation	2/23/2022	done
27	1-May-2022	P	Intermediate assessment of PDS in cold-box runs #1-2 and decision for CRP#3	6/1/2022	done
28	1-Jun-2022	H,P	Decision on <i>module-0</i> FC configuration	9/28/2022	done
29	31-Aug-2022	S	Simulation of (+-30,90) CRP geometry for TDR	8/8/2022	done
30	30-Sep-2022	C	Initial validation of full top CRP with mechanical support in cold-box	7/22/2022	done
31	30-Sep-2022	P	Decision on <i>module-0</i> PDS layout	10/14/2022	done
32	1-Oct-2022	M	Ready for baselining, including with all PDR design reviews complete	6/16/2022	done
33	15-Oct-2022	M	Warm cryostat and open TCO	10/20/2022	done
34	30-Nov-2022	C	Initial validation of full bottom CRP (from US factory) in cold	12/2/2022	done
	<b>2023</b>				
35	15-Jan-2023	C,H,P	Start <i>module-0</i> installation	11/28/2022	done
36	1-Mar-2023	M	All FDRs complete, ready for PRRs and construction start	5/1/2023	
37	30-Sep-2023	C,H,P	<i>Module-0</i> closed and start cool-down		
38	1-Nov-2023	P	Assess PDS performance in <i>module-0</i> and decide on DUNE PDS/FC configuration		
39	1-Nov-2023	C	Assess CRP performance in <i>module-0</i> and decide on DUNE CRP configuration		
40	31-Dec-2023	M,C,H,P,S	FD2-VD PPRs completed	3/15/2024	

FD2-VD\_DevelopmentMilestones\_230226

Figure 10.5: FD2-VD milestones tracked by the LBNC. Green status indicates that it was accomplished before the milestone date and yellow means it was after the initial date.

### FD2 TC Summary Schedule

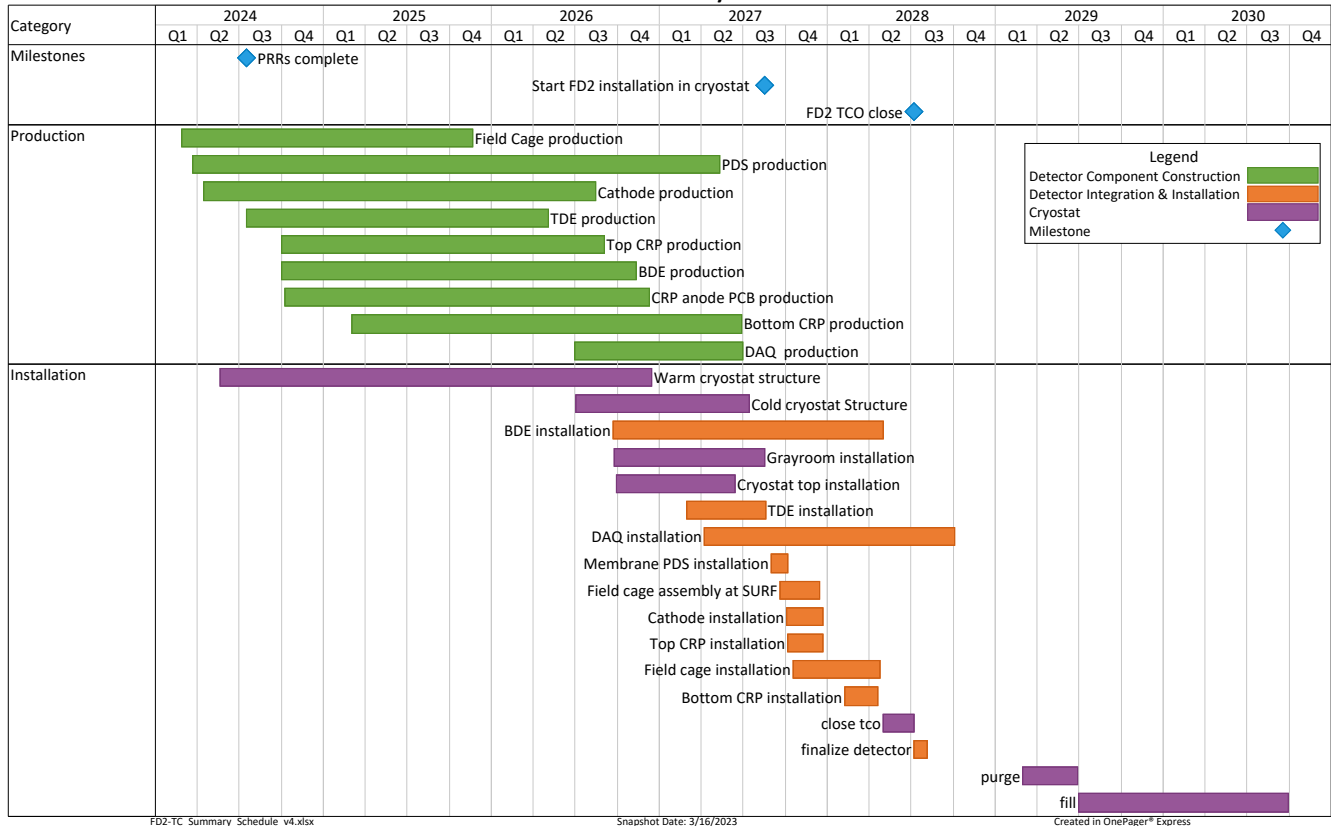


Figure 10.6: Vertical drift production and installation schedule, based on FD2-VD production estimates. Gap between TCO closing and purge/filling results from cooling power needs for FD1 filling. (Data from [53])



# Glossary

- Micro Telecommunications Computing Architecture ( $\mu$ TCA)** The computer architecture specification followed by the crates that house charge and light readout electronics; used in the vertical drift detector module (FD2-VD) and dual-phase (DP) technologies. 97, 101, 106, 111, 115, 132, 142, 146–148, 293, 351
- 4850L** The depth in feet (1480 m) of the access level for the DUNE underground area at SURF; called the “4850 level”. 4, 352, 356
- AC** Alternating Current; when used in the phrase “AC coupling” refers to a circuit element that filters out low-frequency components, such as constant offsets, leaving higher frequency signal components. The frequency filtering is determined both by a resistor and a capacitor. 154
- analog-to-digital converter (ADC)** A sampling of a voltage resulting in a discrete integer count corresponding in some way to the input. 102, 108, 110, 115, 125, 146, 150, 158, 174, 175, 178, 253, 289, 299
- advanced mezzanine card (AMC)** Holds digitizing electronics and lives in Micro Telecommunications Computing Architecture ( $\mu$ TCA) crates. 101, 102, 108, 110, 115, 132, 136, 138, 142, 146, 148, 294
- Argonne National Laboratory (ANL)** US national laboratory in Lemont, IL. 223
- anode plane** a planar array of charge readout devices covering an entire face of a detector module. 3, 12, 50, 55, 96, 152, 185, 213
- anode plane assembly (APA)** A unit of the horizontal drift detector module (FD1-HD) detector module containing the elements sensitive to ionization in the liquid argon (LAr). Each anode face has three planes of wires (two induction, one collection) to provide a 3D view, and interfaces to the cold electronics and photon detection system. 2, 56, 96, 174, 176, 189, 314, 385
- ARAPUCA** A photon detection system (PDS) design that consists of a light trap that captures wavelength-shifted photons inside boxes with highly reflective internal surfaces until they are eventually detected by silicon photomultiplier (SiPM) detectors or are lost. 260

- ASIC** application-specific integrated circuit. 97, 102, 139, 142, 147, 154, 155, 164, 174, 177, 182, 183, 392
- ATLAS** One of two general-purpose detectors at the . It investigates a wide range of physics, from the measurements of the Higgs boson properties to searches for extra dimensions and particles that could make up dark matter (DM). 156
- acceptance for use and possession (AUP)** Required for beneficial occupancy of the underground areas at Sanford Underground Research Facility (SURF) for Long-Baseline Neutrino Facility (LBNF) and Deep Underground Neutrino Experiment (DUNE). 340, 351, 388
- BDE** bottom detector electronics. 10, 11, 78, 90, 96, 122, 152, 167, 172, 173, 179–183, 243, 269, 293, 295, 296, 327, 329, 356, 365, 378
- boosted dark matter (BDM)** A new model that describes a relativistic dark matter particle boosted by the annihilation of heavier dark matter particles in the galactic center or the sun. 30
- Brookhaven National Laboratory (BNL)** US national laboratory in Upton, NY. 158, 174, 178, 223, 242, 394
- BSM** beyond the Standard Model. 25, 30
- BSWS** bearing sensor wire compression seal. 246–248
- CAD** computer aided design. 341, 389
- CALCI** Calibration and Cryogenic Instrumentation. 272, 347, 385
- CAM** control account manager. 388
- charged current (CC)** Refers to an interaction between elementary particles where a charged weak force carrier ( $W^+$  or  $W^-$ ) is exchanged. 4, 25, 27
- DAQ control, configuration and monitoring subsystem (CCM)** A system for controlling, configuring and monitoring other systems in particular those that make up the data acquisition (DAQ) where the CCM encompasses . 16, 283, 291, 296, 303, 307, 308, 310, 392
- critical decision (CD)** The U.S. DOE’s Order 413.3B outlines a series of staged project approvals, each of which is referred to as a critical decision (CD). 394
- CDR** Depending on context, either “conceptual design report,” a formal project document that describes the experiment at a conceptual level, or “conceptual design review,” a formal review of the conceptual design of the experiment or of a component. 78, 231, 390, 394
- cold electronics (CE)** Analog and digital readout electronics that operate at cryogenic tempera-

tures. 10, 11, 50, 58, 70, 77, 90, 96, 150, 154, 165, 169, 172–174, 179, 182, 237

**European Laboratory for Particle Physics (CERN)** The leading particle physics laboratory in Europe and home to the s and other prototypes and demonstrators, including the s. 7, 16, 78, 92, 111, 188, 191, 218, 223, 293, 305, 308, 311, 315, 323, 338, 339, 344, 394

**computational fluid dynamics (CFD)** High performance computer-assisted modeling of fluid dynamical systems. 258, 361

**construction manager/general contractor (CMGC)** The contracted company hired to manage overall construction, used by LBNF at the SURF site for the Far Site Conventional Facilities (FSCF) construction. 341

**CMOS** Complementary metal-oxide-semiconductor. 103, 156, 165, 175, 176

**compliance office (CO)** a team of engineers from multiple partners that provides clear direction for designing and constructing components that will be used during integration. 341, 342, 388–390

**ColdADC** A newly developed 16-channels providing analog to digital conversion. 155, 174, 176, 182, 183

**COLDATA** A 64-channel control and communications ASIC. 155, 174, 176, 182, 183

**COMSOL** General-purpose simulation software based on advanced numerical methods (comsol.com). 199

**commercial off-the-shelf (COTS)** Items, typically hardware such as computers, that may be purchased whole, without any custom design or fabrication and thus at normal consumer prices and availability. 16, 101, 175, 284, 308, 309

**charge conjugation and parity (CP)** Product of charge conjugation and parity transformations. 1, 24, 26

**cathode plane assembly (CPA)** The component of the FD1-HD detector module that provides the drift HV cathode. 224

**charge, parity, and time reversal symmetry (CPT)** product of charge, parity and time-reversal transformations. 31

**Charge Conjugation-Parity Symmetry Violation (CPV)** Lack of symmetry in a system before and after charge conjugation and parity transformations are applied. For charge conjugation and parity (CP) symmetry to hold, a particle turns into its corresponding antiparticle under a charge transformation, and a parity transformation inverts its space coordinates, i.e. produces the mirror image. 4, 26, 48

**charge readout (CRO)** The system for detecting ionization charge distributions in a detector

module. 11, 50, 96, 115, 139, 150, 294

**charge-readout plane (CRP)** An anode technology using a stack of perforated s with etched electrode strips to provide charge readout (CRO) in 3D; it has two induction layers and one collection layer; it is used in the FD2-VD far detector (FD) and DP designs. 7, 10, 12, 21, 35, 50, 54, 56, 60, 65, 70, 73, 78, 90, 91, 94, 96, 107, 137, 145, 147, 150, 154, 155, 165, 171, 172, 176, 177, 180, 183, 189, 195, 197, 200, 202, 205, 207, 208, 216, 220, 221, 227, 253, 255, 256, 269, 289, 294, 304, 323–334, 336–338, 344, 349, 356, 385, 388, 391, 394

**charge-readout unit (CRU)** In the FD2-VD design an assembly of the s plus adapter boards; two to a charge-readout plane (CRP). 10, 56, 70, 72, 369, 377

**CTE** coefficient of thermal expansion. 67, 204

**CTS** Cryogenic Test System. 174, 178

**central utility cavern (CUC)** The utility cavern at the 4850L of SURF located between the two detector caverns. It contains utilities such as central cryogenics and other systems, and the underground data center and control room. 2, 312, 344, 351

**convolutional visual network (CVN)** An algorithm for identifying neutrino interactions based on their topology and without the need for detailed reconstruction algorithms. 34

**DAC** digital-to-analog converter. 158, 159

**DAPHNE** Detector electronics for Acquiring PHotons from NEutrinos is a custom-developed warm front-end waveform digitizing electronics module derived from the readout system developed at Fermi National Accelerator Laboratory (Fermilab) for the Mu2e experiment. 246, 294

**data acquisition (DAQ)** The data acquisition system accepts data from the detector front-end (FE) electronics, buffers the data, performs a , builds events from the selected data and delivers the result to the offline . 2, 34, 36, 101, 115, 125, 142, 145, 150, 151, 169, 179, 181, 246, 271, 283, 288, 325, 327, 336, 339, 351, 364, 385, 392

**DAQ partition** A cohesive and coherent collection of DAQ hardware and software working together to trigger and read out some portion of one detector module; it consists of an integral number of s. Multiple DAQ partitions may operate simultaneously, but each instance operates independently. 292, 296, 304

**DAQ readout unit** The basic component of the DAQ readout subsystem (DAQ RO). 294, 295, 303

**DAQ readout subsystem (DAQ RO)** The subsystem of the DAQ for accepting and buffering data input from detector electronics. 283, 290, 292, 294, 298, 315

- DAQ trigger subsystem (DAQ TS)** The subsystem of the DAQ responsible for forming a trigger decision. 283, 288, 290, 292
- data selection** The process of forming a trigger decision for selecting a subset of detector data for output by the DAQ from the content of the detector data itself. Not to be confused with . 297
- DC** direct coupling. 154
- DUNE detector safety system (DDSS)** The hardware system responsible for the safety of the detector, implemented either via a programmable logic controller (PLC) or via custom hardware protections. 172, 179–181, 183, 351, 356, 365
- DOE** U.S. Department of Energy. 352, 354
- dual-phase (DP)** Distinguishes a liquid argon time-projection chamber (LArTPC) technology by the fact that it operates using argon in both gas and liquid phases; sometimes called double-phase. 7, 21, 50, 96, 104, 107, 108, 188, 220, 221
- DPDFD** Deputy Project Director for far detectors. 387
- data quality monitoring (DQM)** Analysis of the raw data to monitor the integrity of the data and the performance of the detectors and their electronics. This type of monitoring may be performed in real time, within the DAQ system, or in later stages of processing, using disk files as input. 16, 283, 292, 307, 310, 392
- dynamic random access memory (DRAM)** A computer memory technology. 310, 311
- diffuse supernova neutrino background (DSNB)** The term describing the pervasive, constant flux of neutrinos due to all past supernova neutrino bursts. 29
- detector support system (DSS)** The system of rails suspended from the cryostat ceiling in a used to support the anode plane assembly (APA)s, cathode plane assembly (CPA)s, and the endwall field cages (endwall FCs). 354
- DUNE timing and synchronization subsystem (DTS)** The portion of the DAQ that provides for timing and synchronization to various detector systems. 146, 284, 290–293, 308, 309
- Deep Underground Neutrino Experiment (DUNE)** A leading-edge, international experiment for neutrino science and proton decay studies; refers to the entire international experiment and collaboration. 1, 24, 336, 341, 352, 354, 383–385
- executive board (EB)** The highest level DUNE decision-making body for the collaboration. 317, 385, 388
- edge-emitting laser** a laser in which light is emitted from the edge of the substrate. 251

- engineering document management system (EDMS)** A computerized document management system developed and supported at the European Laboratory for Particle Physics (CERN) in which some DUNE project and collaboration documents, drawings and engineering models are managed. 354
- Experimental Facilities Interface Group (EFIG)** The body that provides a means to coordinate and discuss issues related to the interfaces within and between the facility and the DUNE detectors at both the Fermilab and SURF sites. 384
- Experiment Hall North One (EHN1)** Location at CERN of the and areas used for the Proto-DUNEs and for other test and prototyping activities for DUNE. 78, 125, 310
- endwall field cage (endwall FC)** The vertical portions of the near the end walls. 349
- effective number of bits (ENOB)** The effective number of bits is a measure of the dynamic range of an analog-to-digital converter (ADC) and its associated circuitry. The resolution of an ADC is specified by the number of bits used to represent the analog value, in principle giving  $2^N$  signal levels for an N-bit signal. However, all real ADC circuits introduce noise and distortion. ENOB specifies the resolution of an ideal ADC circuit that would have the same resolution as the circuit under consideration. 161
- ERT** emergency response team. 355
- elastic scattering (ES)** Events in which a neutrino elastically scatters off of another particle. 27, 29
- environment, safety and health (ES&H)** A discipline and specialty that studies and implements practical aspects of environmental protection and safety at work. 181, 338, 352, 354, 389
- ESD** electrostatic discharge. 107, 147, 181, 358, 377
- external trigger interface (ETI)** Interface between module trigger logics (MTLs) and external source and sinks of relevant trigger information. 292, 298, 310
- earned value management system (EVMS)** Earned Value Management is a systematic approach to the integration and measurement of cost, schedule, and technical (scope) accomplishments on a project or task. It provides both the government and contractors the ability to examine detailed schedule information, critical program and technical milestones, and cost data (text from the US DOE); the EVMS is a system that implements this approach. 388
- far detector module** The entire DUNE far detector design calls for segmentation into four modules, each with a total/fiducial mass of approximately 17 kt/10 kt. 178, 284, 364
- field cage support system (FCSS)** The support system suspended from the cryostat ceiling in the used to support the field cage. 336, 337, 339

- far detector (FD)** The 70 kt total (40 kt fiducial) mass LArTPC DUNE detector, composed of four 17.5 kt total (10 kt fiducial) mass modules, to be installed at the far site at SURF in Lead, SD, USA. 1, 4, 21, 24, 101, 174, 193, 272, 284, 285, 288–293, 296–298, 305, 307, 311, 317, 319, 321, 354, 388, 389
- horizontal drift detector module (FD1-HD)** LArTPC design used in FD1 in which electrons drift horizontally to wire plane anodes (anode plane assemblies) that along with the front-end electronics are immersed in LAr. 2, 24, 54, 56, 96, 98, 150, 165, 172, 176, 182, 189, 191, 205, 210, 223, 227, 272, 284, 285, 293, 298–300, 308, 310, 312, 314, 315, 321, 342, 347, 384, 385, 387, 388
- FD1-HD Module 0** The final pre-production ProtoDUNE instance for the DUNE FD1-HD, it will use the 800 t cryostat in NP04. 223, 240, 243, 255, 315, 337–339
- vertical drift detector module (FD2-VD)** LArTPC design used in FD2 in which electrons drift vertically to PCB-based anodes at the top and bottom of the LAr volume, with a cathode in the middle. 2, 3, 7, 9, 16, 21, 24, 50, 55, 60, 78, 96, 99, 107, 147, 148, 152, 173, 174, 176, 182, 183, 185, 186, 188, 191, 193, 195, 205, 210, 223–226, 283–285, 288, 289, 292–294, 298–300, 308, 310, 312, 314, 315, 317, 319–323, 327–329, 332–334, 342, 344, 347, 364, 367, 384, 385, 387, 388, 390, 393, 394
- FD2-VD Module 0** The final pre-production ProtoDUNE instance for the DUNE FD2-VD far detector module, it will use the 800 t cryostat in NP02. 16, 78, 90, 91, 99, 111, 122, 139, 146, 172, 177, 183, 186, 191, 205, 221, 223, 225, 240, 242, 248, 299, 308, 323–325, 327–329, 332, 334–339, 349, 367
- FDC** Far Detector and Cryogenics Subproject. 21, 340, 385, 387
- FDR** Depending on context, either “final design report,” a formal project document that describes the experiment at a final level, or “final design review,” a formal review of the final design of the experiment or of a component. 390, 391, 394
- front-end (FE)** The front-end refers to a point that is “upstream” of the data flow for a particular subsystem. For example the FD1-HD front-end electronics is where the cold electronics meet the sense wires of the TPC and the front-end DAQ is where the DAQ meets the output of the electronics. 96, 106, 108, 111, 113, 138, 142, 147, 154, 177, 293–295, 304, 391
- finite element analysis (FEA)** Simulation of a physical phenomenon using the numerical technique called Finite Element Method (FEM), a numerical method for solving problems of engineering and mathematical physics. 56, 64, 189, 194, 207, 214, 334, 361
- FEE** front-end electronics. 295
- Front-End Link eXchange (FELIX)** A high-throughput interface between FE and trigger electronics and the standard PCIe computer bus. 295, 305
- front-end mother board (FEMB)** Refers to a unit of the single-phase (SP) cold electronics (CE)

that contains the FE amplifier and ADC ASICs covering 128 channels. 90, 150–152, 154, 155, 165, 169, 172, 176, 180–183, 329, 392

**Fermi National Accelerator Laboratory (Fermilab)** U.S. national laboratory in Batavia, IL. It is the laboratory that hosts LBNF and DUNE, and serves as the experiment's near site. 1, 25, 157, 158, 182, 218, 242, 252, 261, 274, 284, 285, 288, 291, 292, 297, 298, 300, 303, 305, 311, 312, 315, 340

**Fermilab Environment, Safety and Health Manual (FESHM)** The document that contains Fermilab's policies and procedures designed to manage environment, safety, and health in all its programs. 354

**Fast Fourier Transform (FFT)** An algorithm that calculates the frequency components of a time-domain waveform in a computationally efficient manner. 126

**FHC** forward horn current ( $\nu_\mu$  mode). 42

**field cage** The component of a LArTPC that contains and shapes the applied E field. 2, 7, 12, 50, 73, 185, 186, 190, 193, 195, 200, 205, 208, 210, 214–216, 218, 222, 224, 227, 328, 332, 334, 336–338, 345, 376, 388, 392

**field programmable gate array (FPGA)** An integrated circuit technology that allows the hardware to be reconfigured to execute different algorithms after its manufacture and deployment. 115, 155, 178

**FR-4** Flame-retardant fiberglass-reinforced epoxy resin laminate used in making PCBs and other detector components. 242

**FRP** fiber-reinforced plastic. 12, 60, 185, 197, 200, 207, 208, 221, 222, 224, 332, 334, 336, 376

**Far Site Conventional Facilities (FSCF)** The conventional facilities (CF) at the DUNE far detector site, SURF, including all detector caverns and support infrastructure. 17, 387

**FSCF-BSI** subproject for far site conventional facilities, building and site infrastructure. 340, 351, 352

**FSII** far site integration and installation. 17, 90, 91, 144, 145, 180, 340, 341, 356, 364, 381, 388

**FTE** full-time equivalent. A unit of labor for the project. One year of work from one person. 314

**G-10** Non-flame-retardant fiberglass-reinforced epoxy resin laminate used in making PCBs. 238

**gaseous argon (GAr)** argon in its gas phase. 344, 364

**Geant4** A software toolkit for the simulation of the passage of particles through matter using Monte Carlo (MC) methods. 27, 231



- Generates Events for Neutrino Interaction Experiments (GENIE)** Software providing an object-oriented neutrino interaction simulation resulting in kinematics of the products of the interaction. 34
- GKVM** Gava, Kneller, Volpe, McLaughlin Supernova model. 29, 38
- Global Positioning System (GPS)** A satellite-based system that provides a highly accurate one-pulse-per-second signal (1PPS signal) that may be used to synchronize clocks and determine location. 118, 293, 312
- Grafana** add def. 304, 305
- gray room** ISO-8 clean room with a cleanliness level of 3.5M particles of 0.5 micron or less per cubic meter volume. ISO-8 clean rooms are referred to as grey rooms because at this level of cleanliness most standard clean room attire is not required.. 17, 197, 356, 364
- H2** CERN North Area hadron beamline used for and FD2-VD prototypes and demonstrators. 323, 336, 339
- hazard analysis (HA)** A first step in a process to assess risk; the result of hazard analysis is the identification of the hazards present for a task or process. 354
- HEP** high energy physics. 174
- High Efficiency Particulate Air (HEPA)** The High Efficiency Particulate Air filters are a type of air filter that remove 99.97% of particles that have a size greater than or equal to 0.3  $\mu\text{m}$ . 360
- horizontal drift** single-phase, horizontal drift LArTPC technology. 2, 301
- high voltage (HV)** Generally describes a voltage applied to drive the motion of free electrons through some media, e.g., LAr. 7, 50, 58, 73, 90, 107, 110, 185, 188, 190, 193, 195, 205, 210, 221, 222, 224, 227, 235, 242, 246, 252, 277, 328, 332–334, 336–339, 347, 385, 392, 394
- HVDB** HV divider board. 195, 207, 214, 215, 218, 334
- HVFT** HV feedthrough. 12, 185, 188, 190, 193, 195, 218, 220, 332, 394
- HVPS** high voltage (HV) power supply. 12, 185, 189, 191
- high voltage system (HVS)** The detector subsystem that provides the time projection chamber (TPC) drift field. 12, 15, 185, 186, 188, 191, 220, 222–224, 269, 270
- Inter-Integrated Circuit (I2C)** I<sup>2</sup>C or I2C is a synchronous, multi-master, multi-slave, packet switched, single-ended, serial computer bus widely used for attaching lower-speed peripheral ICs to processors and microcontrollers in short-distance, intra-board communication. 165

- Integration and Installation (I&I)** One of the three project areas in the LBNF/DUNE-US project, along with LBNF and DUNE-US. 271
- IB** institutional board; all institutions participating in DUNE are represented on this board. 384
- ICARUS** A neutrino experiment that was located at the Laboratori Nazionali del Gran Sasso (LNGS) in Italy, then refurbished at CERN for re-use in the same neutrino beam from Fermilab used by the  $\nu_{\mu}$  and  $\nu_{\tau}$  experiments at Fermilab. 2, 190, 193
- ICEBERG R&D cryostat and electronics (ICEBERG)** Integrated Cryostat and Electronics Built for Experimental Research Goals: a double-walled cryostat built and installed at Fermilab for liquid argon detector R&D and for testing of DUNE detector components. 218, 274, 315, 394
- InGaAs** Indium gallium arsenide is a room-temperature semiconductor commonly used as a high-speed, high-sensitivity photodetector for optical fiber telecommunications. 252
- interface document** Interface document. 272
- IPMI** Intelligent Platform Management Interface. 291
- installation readiness review (IRR)** A project management mechanism by which the plan for installation is reviewed. 383, 390
- Joint Project Office (JPO)** The framework used to facilitate close and coherent coordination across all elements with many shared management resources; JPO functions include systems engineering, procurement, environment, safety and health (ES&H), quality assurance (QA), finance, project controls, risk management, compliance, internal reviews, partner agreement management, document management, and administrative support. 387, 389
- key performance parameter (KPP)** Defined by critical decision (CD)-2 (U.S.) as characteristic, function, requirement or design basis that if changed would have a major impact on the system or facility performance, schedule, cost and/or risk. 383
- liquid argon (LAr)** Argon in its liquid phase; it is a cryogenic liquid with a boiling point of 87 K and density of 1.4 g/ml. 2, 3, 27, 50, 55, 56, 96, 155, 185, 193, 198, 208, 220, 222, 226, 233, 292, 310, 323, 326, 327, 332, 334, 336, 339, 341, 388, 392
- LArASIC** A 16-channel FE ASIC that provides signal amplification and pulse shaping. 155, 174-176, 182
- Liquid Argon Software (LArSoft)** A shared base of physics software across LArTPC experiments. 21, 31, 230
- liquid argon time-projection chamber (LArTPC)** A TPC filled with liquid argon; the basis for

the DUNE FD modules. 1, 2, 24, 42, 50, 54, 156, 185, 190, 227

**LARZIC** The cryogenic amplifier ASIC that is the principal component of the FD2-VD top drift FE analog cards. 102, 139, 147

**long-baseline (LBL)** Refers to the distance between the neutrino source and the FD. It can also refer to the distance between the near and far detectors. The “long” designation is an approximate and relative distinction. For DUNE, this distance (between Fermilab and SURF) is approximately 1300 km. 24, 41

**Long-Baseline Neutrino Committee (LBNC)** The committee, composed of internationally prominent scientists with relevant expertise, charged by the Fermilab director to review the scientific, technical, and managerial progress, plans and decisions associated with DUNE. 394

**Long-Baseline Neutrino Facility (LBNF)** Long-Baseline Neutrino Facility; refers to the facilities that support the experiment including in-kind contributions under the line-item project. The portion of LBNF/DUNE-US responsible for developing the neutrino beam, the far site cryostats, and far and near site cryogenics systems, and the conventional facilities, including the excavations. 298

**LBNF and DUNE enterprise (LBNF/DUNE)** Long-Baseline Neutrino Facility/Deep Underground Neutrino Experiment; refers to the overall enterprise or program including LBNF/DUNE-US, participating international projects, and the DUNE experiment and collaboration. 21, 181, 385, 389, 393

**LBNF/DUNE-US** Long-Baseline Neutrino Facility/Deep Underground Neutrino Experiment - United States; project to design and build the conventional and beamline facilities and the DOE contributions to the detectors. It is organized as a DOE/Fermilab project and incorporates contributions to the facilities from international partners. It also acts as host for the installation and integration of the DUNE detectors. 1, 17, 340, 385, 389, 394

**Lawrence Berkeley National Laboratory (LBNL)** US national laboratory in Berkeley, CA. 158

**LED** Light-emitting diode. 327

**large electron multiplier (LEM)** A micro-pattern detector suitable for use in ultra-pure argon vapor; LEMs consist of copper-clad PCB boards with sub-millimeter-size holes through which electrons undergo amplification. 50, 104, 107, 120, 122

**LHC** Large Hadron Collider. 178

**LN<sub>2</sub>** liquid nitrogen. 155

**light readout (LRO)** The system for detecting scintillation photons in a LArTPC detector module. 96

**LV** low voltage. 168, 169, 171, 269, 271

**LVDS** low-voltage differential signaling. 165

**light yield (LY)** detected photons per unit deposited energy. 21, 31, 41, 229, 231, 257

**Model of Argon Reaction Low Energy Yields (MARLEY)** Developed at UC Davis, MARLEY is the first realistic model of neutrino electron interactions on argon for energies less than 50 MeV. This includes the energy range important for supernova neutrino burst (SNB) neutrinos and also solar 8–boron neutrinos. 27, 35, 299

**Monte Carlo (MC)** Refers to a method of numerical integration that entails the statistical sampling of the integrand function. Forms the basis for some types of detector and physics simulations. 27, 33, 35, 37, 47, 299

**MicroTCA Carrier Hub (MCH)** A network switching device. 101, 111, 117, 146

**main communications room (MCR)** Space at the FD site for cyber infrastructure. 291, 312, 314, 352

**Fermilab Main Injector (MI)** An accelerator at Fermilab that provides a beam of high-energy protons to the the LBNF/DUNE-US beamline. 1

**MicroBooNE** A LArTPC neutrino oscillation experiment at Fermilab. 2, 35, 190

**minimum ionizing particle (MIP)** Refers to a particle traversing some medium such that the particle’s mean energy loss is near the minimum. 1, 111, 226, 299

**Module 0** The final pre-production instance of a detector; for the DUNE far detector modules, the s in the 800 t cryostats in NP02 and NP04 serve this purpose. 97, 178, 223, 293, 294, 300, 319, 333, 390, 391, 394

**MPPC** 6 mm×6 mm Multi-Pixel Photon Counters produced by Hamamatsu™ Photonics K.K. 243

**MSPS** megasamples per second. 117

**NASA** U.S. National Aeronautics and Space Administration. 175

**neutral current (NC)** Refers to an interaction between elementary particles where a neutrally charged weak force carrier ( $Z^0$ ) is exchanged. 25, 27, 29, 30, 43

**near detector (ND)** Refers to the collection of DUNE detector components installed close to the neutrino source at Fermilab; also a subproject of LBNF/DUNE-US that includes installation, infrastructure, and the cryogenics systems for this detector. 1, 16, 24, 30, 49, 284, 384

**network interface controller (NIC)** Hardware for controlling the interface to a communication network. Typically, one that obeys the Ethernet protocol. 310

- NIOS** network identity operating system. 115
- NP02** The CERN North Area in Experiment Hall North One (EHN1) intersected by the hadron beamline, the location of the 800 t cryostat used for ProtoDUNE-DP and for FD2-VD tests and prototypes; also used to refer to the 800 t cryostat in this area. 16, 21, 113, 120, 188, 189, 197, 205, 220, 262, 308, 323, 325, 327–329, 332, 336, 337, 339, 394
- NP04** The CERN North Area in EHN1 intersected by the hadron beamline, the location of and ; also used to refer to the 800 t cryostat in this area. 80, 220, 305, 315, 336, 337, 339, 344
- nonstandard interaction (NSI)** A general class of theory of elementary particles other than the Standard Model. 31
- Non-volatile memory express (NVMe)** A specification for an interface to storage media attached via PCIe. 310
- outer diameter (OD)** Outer diameter of a tube. 216
- oxygen deficiency hazard (ODH)** a hazard that occurs when inert gases such as nitrogen, helium, or argon displace room air and thus reduce the percentage of oxygen below the level required for human life. 354, 356
- OM3** Type of multi-mode fiber optic cable, typically capable of 10 Gbps data transmission at lengths up to 300 m. 310
- OM4** Type of multi-mode fiber optic cable, typically capable of 10 Gbps data transmission at lengths up to 550 m. 310
- operational readiness clearance (ORC)** Final safety approval prior to the start of operation. 390
- operational readiness review (ORR)** A project management mechanism by which the operational readiness is reviewed. 342, 354, 390
- P6** software framework used to plan and status the resource-loaded schedule of activities associated with LBNF/DUNE-US. 388, 394
- Proton Assembly Building (PAB)** Home of several LAr facilities at Fermilab. 252
- Pandora** The Pandora multi-algorithm approach to pattern recognition. 34
- PCB** printed circuit board. 3, 10, 16, 33, 35, 40, 50, 55, 60, 78, 80, 91, 110, 136, 154, 175, 189, 215, 391
- PCB panel** In the FD2-VD design, one of four PCBs of size  $1.5 \times 1.7$  m assembled into a charge-readout unit (CRU). 56, 78, 97

**PCI** Peripheral Component Interconnect. 294, 295, 310

**photon detector (PD)** The detector elements involved in measurement of the number and arrival times of optical photons produced in a detector module. 2, 15, 32, 41, 50, 186, 195–197, 227, 234, 284, 297, 323, 325–327, 338, 356, 365–367, 376, 392

**PDE** photo detection efficiency. 238, 241, 243

**PDR** Depending on context, either “preliminary design report,” a formal project document that describes the experiment at a preliminary level, or “preliminary design review,” a formal review of the preliminary design of the experiment or of a component. 73, 117, 218, 390, 394

**photon detection system (PDS)** The detector subsystem sensitive to light produced in the LAr. 3, 15, 21, 24, 25, 179, 186, 210, 222, 227, 283, 288, 290, 292–294, 296, 297, 321, 323, 327, 328, 334, 336, 338, 344, 385

**photoelectron (PE)** An electron ejected from the surface of a material by the photoelectric effect. 48, 233

**PEEK** Polyether ether ketone, a colorless organic thermoplastic polymer. 58, 82

**programmable logic controller (PLC)** An industrial digital computer that has been ruggedized and adapted for the control of manufacturing or other processes that require high reliability, ease of programming, and process fault diagnosis. 356

**Pontecorvo-Maki-Nakagawa-Sakata (PMNS)** A type of matrix that describes the mixing between mass and weak eigenstates of the neutrino. 1, 31

**power-over-fiber (PoF)** a technology in which a fiber optic cable carries optical power, which is used as an energy source rather than, or as well as, carrying data; this allows a device to be remotely powered, while providing electrical isolation between the device and the power supply. 15, 227, 233, 238, 246, 247, 261, 327, 332, 336, 392

**PPC** photovoltaic power converter. 246, 248–250, 252

**personnel protective equipment (PPE)** Equipment worn to minimize exposure to hazards that cause serious workplace injuries and illnesses. 181, 355

**production progress review (PPR)** A project management mechanism by which the progress of production is reviewed. 390

**ProtoDUNE** Either of the two initial DUNE prototype detectors constructed at CERN. One prototype implemented SP technology and the other DP. 7, 172, 193, 195, 210, 235, 285, 311, 344, 392

**ProtoDUNE-DP** The DP ProtoDUNE detector constructed at CERN in NP02. 7, 51, 70, 96, 98, 99, 109, 120, 137, 139, 146, 188, 190, 205, 218, 220, 223, 229, 231, 255, 258, 323, 329, 334,

338, 339, 367

**ProtoDUNE-SP** The FD1-HD ProtoDUNE detector constructed at CERN in NP04. 2, 35, 96, 122, 150, 155, 174, 177, 178, 190, 205, 221, 223, 229, 233, 255, 295, 299, 319, 325, 336, 339, 344, 354

**production readiness review (PRR)** A project management mechanism by which the production readiness is reviewed. 23, 176, 178, 241, 267, 274, 276, 311, 323, 390, 391, 394

**PSV** pressure safety valve. 347

**power and timing backplane (PTB)** Backplane used to connect the warm interface boards (WIBs) and the power and timing cards (PTCs) on the warm interface electronics crate (WIEC). Also connects the CE flange on the cryostat penetration. 169

**power and timing card (PTC)** Cards that provide further processing and distribution of the signals entering and exiting the SP cryostat. 169, 171, 177, 179, 180, 183

**PTP** Depending on context, either p-terphenyl, a wavelength-shifting (WLS) material, or Precision Time Protocol, a networking protocol that allows synchronizing of clocks to within a few  $\mu\text{s}$  of a time standard on a local network. 118, 238, 255, 259, 276

**quality assurance (QA)** The process of ensuring that the quality of each element meets requirements during design and development, and to detect and correct poor results prior to production. 10, 16, 91, 139, 173, 177, 224, 267, 308, 311, 389, 390

**QAP** quality assurance plan. 390

**quality control (QC)** The process (e.g., inspection, testing, measurements) of ensuring that each manufactured element meets its quality requirements prior to assembly or installation. 10, 16, 19, 73, 78, 92, 97, 110, 120, 148, 173, 176, 177, 181, 222, 224, 267, 308, 311, 336, 356, 390, 394

**RC** Depending on context, one of (1) resistive-capacitive (circuit), (2) run control, the system for configuring, starting and terminating the DAQ, or (3) resource coordinator, a member of the DUNE management team responsible for coordinating the financial resources of the project. 154, 189

**readout window** A fixed, atomic and continuous period of time over which data from a far detector module, in whole or in part, is recorded. This period may differ based on the trigger that initiated the readout. 294

**RHC** reverse horn current ( $\bar{\nu}_\mu \rightarrow \bar{\nu}_\mu$  mode). 42

**root mean square (RMS)** The square root of the arithmetic mean of the squares of a set of values, used as a measure of the typical magnitude of a set of numbers, regardless of their

sign. 41, 125, 233

**review office (RO)** An office within the that organizes reviews. 17, 341, 342, 388–390

**ROI** region of interest. 296, 298, 336

**signal-to-noise (S/N)** signal-to-noise ratio. 158, 233, 237, 245, 297

**SBND** The Short-Baseline Near Detector experiment at Fermilab. 174, 193

**SC** depending on context, either speakers committee or scientific computing. 271

**Fermilab South Dakota Services Division (SDSD)** A Fermilab division responsible providing host laboratory functions at SURF in South Dakota. 17, 340, 342, 388, 389

**South Dakota Science and Technology Authority (SDSTA)** The legal entity that manages SURF, in Lead, S.D. 17, 355, 356

**South Dakota Warehouse Facility (SDWF)** Warehousing operations in South Dakota responsible for receiving LBNF and DUNE goods and coordinating shipments to the access shaft (Ross Shaft) at SURF. 224, 272, 311, 354, 383

**SEMP** systems engineering management plan. 389

**signal feedthrough (SFT)** A cryostat penetration allowing for the passage of cables or other extended parts. 101, 111, 154, 329, 330

**signal feedthrough chimney (SFT chimney)** A volume above the cryostat penetration used for a signal feedthrough. 10, 11, 96, 97, 134, 138, 147

**safe high voltage (SHV)** Type of bayonet mount connector used on coaxial cables that has additional insulation compared to standard BNC and MHV connectors that makes it safer for handling HV by preventing accidental contact with the live wire connector in an unmated connector or plug. 91, 168, 172

**Signal Processing** The goal of TPC signal processing is to reconstruct the distribution of ionization electrons arriving at wire planes from the digitized TPC waveform. 35

**silicon photomultiplier (SiPM)** A solid-state avalanche photodiode sensitive to single photoelectron signals. 15, 227, 235, 237, 240, 243, 392

**supernova (SN)** Event that occurs upon the death of certain types of stars. 27, 36

**supernova neutrino burst (SNB)** A prompt increase in the flux of low-energy neutrinos emitted in the first few seconds of a core-collapse supernova. It can also refer to a trigger command type that may be due to this phenomenon, or detector conditions that mimic its interaction



signature. 1, 3, 21, 24, 27, 232, 288, 292, 299, 303

**SuperNova Early Warning System (SNEWS)** A global supernova neutrino burst trigger formed by a coincidence of SNB triggers collected from participating experiments. 36, 37, 39, 298

**SuperNova Observatories with GLoBES (SNOWGLoBES)** From the official description: SNOWGLoBES is public software for computing interaction rates and distributions of observed quantities for SNB neutrinos in common detector materials. 27

**signal-over-fiber (SoF)** a technology in which a fiber optic cable carries detector output that has been converted from an electrical to an optical pulse. 15, 227, 235, 238, 327, 332, 336

**solarization** Aging caused by exposure to UV-light, which can lead to increased attenuation. 256

**single-phase (SP)** Distinguishes a LArTPC technology by the fact that it operates using argon in its liquid phase only; a legacy DUNE term now replaced by `single-phase` and `single-phase`. 7, 21, 24

**Serial Peripheral Interface (SPI)** The Serial Peripheral Interface is a synchronous serial communication interface specification used for short distance communication, primarily in embedded systems. 104, 106, 109

**Simulation Program with Integrated Circuit Emphasis (SPICE)** a general-purpose, open-source analog electronic circuit simulator. It is a program used in integrated circuit and board-level design to check the integrity of circuit designs and to predict circuit behavior. 157

**Sanford Underground Research Facility (SURF)** The laboratory in Lead, SD, USA where the DUNE FD will be installed and operated; also where the LBNF/DUNE-US FSCF and the cryostat and cryogenics systems will be constructed. 1, 60, 67, 94, 179–181, 224, 284, 285, 288, 291, 300, 305, 310, 311, 314, 315, 317, 321, 322, 340, 388

**SWC** Software & Computing. 272

**TAI** International Atomic Time. 146, 293

**trip action plan (TAP)** A document required for any trip by a worker to the underground area at SURF, per that site's access control program; it describes the work to be accomplished during the trip. 355

**technical board (TB)** The DUNE organization responsible for evaluating technical decisions. 317

**technical coordinator (TC)** A member of the DUNE management team responsible for organizing the technical aspects of the project effort; is head of technical coordination (TCN). 387

**technical coordination (TCN)** The DUNE organization responsible for overall integration of the detector elements and successful execution of the detector construction project; areas of responsibility include general project oversight, systems engineering, QA and safety. 390

- temporary construction opening (TCO)** An opening in the side of a cryostat through which detector elements are brought into the cryostat; utilized during construction and installation. 17, 177, 193, 338, 339, 342, 349, 358, 365
- TDAQ** trigger and DAQ system. 15, 16, 283, 285, 290, 291, 303, 308, 310, 315, 317
- TDE** top detector electronics. 10, 11, 73, 78, 84, 90, 92, 96, 99, 108, 138, 147, 148, 172, 285, 295, 296, 308, 327, 329, 351, 356, 367
- TDR** Depending on context, either “technical design report,” a formal project document that describes the experiment at a technical level, or “technical design review,” a formal review of the technical design of the experiment or of a component. 3, 21, 23, 24, 234, 285
- time projection chamber (TPC)** Depending on context: (1) A type of particle detector that uses an E field together with a sensitive volume of gas or liquid, e.g., LAr, to perform a 3D reconstruction of a particle trajectory or interaction. The activity is recorded by digitizing the waveforms of current induced on the anode as the distribution of ionization charge passes by or is collected on the electrode. (2) TPC is also used in LBNF/DUNE-US for “total project cost”. 3, 4, 32, 78, 80, 96, 97, 154, 173, 174, 176, 181–183, 185, 205, 215, 216, 227, 283, 288–290, 292, 294, 296, 297, 300, 323, 329, 332, 344, 354, 360, 365
- trigger activation** a correlation (or cluster) in time and space within a stream of s. 39
- trigger candidate** Summary information derived from the full data stream and representing a contribution toward forming a trigger decision. 297, 299
- trigger decision** The process by which s are converted into s. 283, 288, 292, 299
- trigger primitive** Information derived by the DAQ FE hardware that describes a region of space (e.g., one or several neighboring channels) and time (e.g., a contiguous set of ADC sample ticks) associated with some activity. 37, 292, 299
- trigger record** a collection of data and metadata from selected detector space-time volumes corresponding to a trigger decision. 283, 288, 290, 292, 297, 300
- UHMWPE** ultra-high molecular weight polyethylene. 191, 193, 218, 334
- vertical drift** single-phase, vertical drift LArTPC technology. 146, 301
- VUV** vacuum ultra-violet. 277
- WA105 DP demonstrator** The 3m×1m×1m WA105 DP prototype detector at CERN. 110, 120, 139, 146
- Wide Area Network (WAN)** Computing network that interconnects Local Area Networks (LANs)

across relatively broad geographic areas. 284, 285, 288, 303, 312

**work breakdown structure (WBS)** An organizational project management tool by which the tasks to be performed are partitioned in a hierarchical manner. 279

**Wire-Cell Toolkit (WCT)** A software toolkit with data flow processing components for LArTPC noise and signal simulation, noise filtering, signal processing, and tomographic 3D ionization activity imaging. 35

**warm interface board (WIB)** Digital electronics situated just outside a FD cryostat that receives digital data from the front-end mother boards (FEMBs) (part of CE) over cold copper connections and sends it to the reconfigurable computing element (RCE) FE readout hardware. 150–152, 155, 164, 169, 177, 178, 180–183, 294, 392

**warm interface electronics crate (WIEC)** Crates mounted on the signal flanges that contain the WIBs. 169, 171, 172, 176, 180, 183, 365

**Wire-Cell** A tomographic automated 3D neutrino event reconstruction method for LArTPCs. 35

**wavelength-shifting (WLS)** A material or process by which incident photons are absorbed by a material and photons are emitted at a different, typically longer, wavelength. 15, 227, 238

**White Rabbit (WR)** A component of the timing system that forwards clock signal and time-of-day reference data to the master timing unit. 101, 117, 118, 132, 142, 146, 293

**WR grandmaster** White Rabbit grandmaster. 102, 120, 133, 146

**White Rabbit  $\mu$ TCA Carrier Hub (WR-MCH)** A card mounted in  $\mu$ TCA crate that receives time synchronization information and trigger data packets over White Rabbit (WR) network and distributes them to the advanced mezzanine card (AMC) over  $\mu$ TCA backplane. 101, 117, 120

**X-ARAPUCA** Extended design with WLS coating on only the external face of the dichroic filter window(s) but with a WLS doped plate inside the cell. 3, 31, 47, 195, 221, 227, 228, 235, 239, 324–327, 332–334, 336

# References

- [1] **DUNE** Collaboration, B. Abi *et al.*, “Deep Underground Neutrino Experiment (DUNE), Far Detector Technical Design Report, Volume II: DUNE Physics,” [arXiv:2002.03005 \[hep-ex\]](#).
- [2] **K2K** Collaboration, S. H. Ahn *et al.*, “Detection of accelerator produced neutrinos at a distance of 250 km,” *Phys. Lett. B* **511** (2001) 178–184, [arXiv:hep-ex/0103001](#).
- [3] **MINOS** Collaboration, D. G. Michael *et al.*, “Observation of muon neutrino disappearance with the MINOS detectors and the NuMI neutrino beam,” *Phys. Rev. Lett.* **97** (2006) 191801, [arXiv:hep-ex/0607088](#).
- [4] **T2K** Collaboration, K. Abe *et al.*, “The T2K Experiment,” *Nucl. Instrum. Meth. A* **659** (2011) 106–135, [arXiv:1106.1238 \[physics.ins-det\]](#).
- [5] **NOvA** Collaboration, P. Adamson *et al.*, “First measurement of muon-neutrino disappearance in NOvA,” *Phys. Rev.* **D93** no. 5, (2016) 051104, [arXiv:1601.05037 \[hep-ex\]](#).
- [6] **LBNE** Collaboration, C. Adams *et al.*, “The Long-Baseline Neutrino Experiment: Exploring Fundamental Symmetries of the Universe,” in *Snowmass 2013: Workshop on Energy Frontier Seattle, USA, June 30-July 3, 2013*. 2013. [arXiv:1307.7335 \[hep-ex\]](#). <http://lss.fnal.gov/archive/2014/pub/fermilab-pub-14-022.pdf>.
- [7] **DUNE** Collaboration, B. Abi *et al.*, “Deep Underground Neutrino Experiment (DUNE), Far Detector Technical Design Report, Volume IV: Far Detector Single-phase Technology,” *JINST* **15** no. 08, (2020) T08010, [arXiv:2002.03010 \[physics.ins-det\]](#).
- [8] **ICARUS** Collaboration, S. Amerio *et al.*, “Design, construction and tests of the ICARUS T600 detector,” *Nucl. Instrum. Meth. A* **527** (2004) 329–410.
- [9] **MicroBooNE** Collaboration, R. Acciarri *et al.*, “Design and Construction of the MicroBooNE Detector,” *JINST* **12** no. 02, (2017) P02017, [arXiv:1612.05824 \[physics.ins-det\]](#).
- [10] **DUNE** Collaboration, A. A. Abud *et al.*, “Design, construction and operation of the

- ProtoDUNE-SP Liquid Argon TPC,” *JINST* **17** no. 01, (2022) P01005, [arXiv:2108.01902](https://arxiv.org/abs/2108.01902) [[physics.ins-det](https://arxiv.org/archive/physics)].
- [11] A. Machado *et al.*, “The X-ARAPUCA: an improvement of the ARAPUCA device,” *JINST* **13** no. 04, (2018) C04026, [arXiv:1804.01407](https://arxiv.org/abs/1804.01407) [[physics.ins-det](https://arxiv.org/archive/physics)].
- [12] “LBNF/DUNE Integrated Environmental, Safety, and Health Management Plan.” <https://edms.cern.ch/document/2808692>.
- [13] **DUNE** Collaboration, B. Abi *et al.*, “Deep Underground Neutrino Experiment (DUNE), Far Detector Technical Design Report, Volume I: Introduction to DUNE,” *JINST* **15** no. 08, (2020) T08008, [arXiv:2002.02967](https://arxiv.org/abs/2002.02967) [[physics.ins-det](https://arxiv.org/archive/physics)].
- [14] “LBNF/DUNE Requirements and Specifications.” <https://edms.cern.ch/project/CERN-0000198204>.
- [15] **DUNE** Collaboration, B. Abi *et al.*, “The DUNE Far Detector Interim Design Report, Volume 3: Dual-Phase Module,” [arXiv:1807.10340](https://arxiv.org/abs/1807.10340) [[physics.ins-det](https://arxiv.org/archive/physics)].
- [16] C. Brizzolari *et al.*, “Enhancement of the X-Arapuca photon detection device for the DUNE experiment,” *JINST* **16** no. 09, (2021) P09027, [arXiv:2104.07548](https://arxiv.org/abs/2104.07548) [[physics.ins-det](https://arxiv.org/archive/physics)].
- [17] J. D. C. Vázquez, D. S. López-Cardona, I. Montero, P. C. Pérez, Lallana, and F. M. A. Al-Zubaidi, “Power over Fiber in Radio over Fiber Systems in 5G Scenarios,” *21st International Conference on Transparent Optical Networks (ICTON), 2019* (2019) 1–4.
- [18] **DUNE** Collaboration, B. Abi *et al.*, “Long-baseline neutrino oscillation physics potential of the DUNE experiment,” *Eur. Phys. J. C* **80** no. 10, (2020) 978, [arXiv:2006.16043](https://arxiv.org/abs/2006.16043) [[hep-ex](https://arxiv.org/archive/hep)].
- [19] **DUNE** Collaboration, B. Abi *et al.*, “Prospects for beyond the Standard Model physics searches at the Deep Underground Neutrino Experiment,” *Eur. Phys. J. C* **81** no. 4, (2021) 322, [arXiv:2008.12769](https://arxiv.org/abs/2008.12769) [[hep-ex](https://arxiv.org/archive/hep)].
- [20] **DUNE** Collaboration, B. Abi *et al.*, “Supernova neutrino burst detection with the deep underground neutrino experiment,” *Eur. Phys. J. C* **81** no. 5, (2021) 423, [arXiv:2008.06647](https://arxiv.org/abs/2008.06647) [[hep-ex](https://arxiv.org/archive/hep)].
- [21] “Nufit4.0.” <http://www.nu-fit.org/>.
- [22] L. Huedepohl, B. Muller, H.-T. Janka, A. Marek, and G. Raffelt, “Neutrino Signal of Electron-Capture Supernovae from Core Collapse to Cooling,” *Phys.Rev.Lett.* **104** (2010) 251101, [arXiv:0912.0260](https://arxiv.org/abs/0912.0260) [[astro-ph.SR](https://arxiv.org/archive/astro-ph)]. Erratum: *Phys.Rev.Lett.* **105** (2010) 249901.
- [23] “SNOwGLoBES.” [https://www.researchgate.net/publication/253613163\\_SNOwGLoBES\\_SuperNova\\_Observatories\\_with\\_GLoBES](https://www.researchgate.net/publication/253613163_SNOwGLoBES_SuperNova_Observatories_with_GLoBES).

- [24] “MARLEY (Model of Argon Reaction Low Energy Yields).” <https://www.marleygen.org/>.
- [25] S. Gardiner, “Simulating low-energy neutrino interactions with MARLEY,” *Comput. Phys. Commun.* **269** (2021) 108123, [arXiv:2101.11867](https://arxiv.org/abs/2101.11867) [nucl-th].
- [26] J. Gava, J. Kneller, C. Volpe, and G. C. McLaughlin, “A dynamical collective calculation of supernova neutrino signals,” *Phys.Rev.Lett.* **103** (2009) 071101, [arXiv:0902.0317](https://arxiv.org/abs/0902.0317) [hep-ph].
- [27] **Super-Kamiokande** Collaboration, K. Abe *et al.*, “Solar Neutrino Measurements in Super-Kamiokande-IV,” *Phys. Rev. D* **94** no. 5, (2016) 052010, [arXiv:1606.07538](https://arxiv.org/abs/1606.07538) [hep-ex].
- [28] J. F. Beacom, “The Diffuse Supernova Neutrino Background,” *Ann. Rev. Nucl. Part. Sci.* **60** (2010) 439–462, [arXiv:1004.3311](https://arxiv.org/abs/1004.3311) [astro-ph.HE].
- [29] E. Segreto, A. A. Machado, A. Fauth, R. R. Ramos, G. de Souza, H. V. Souza, V. L. Pimentel, M. C. Q. Bazetto, and M. A. Ayala-Torres, “First liquid argon test of the X-ARAPUCA,” *JINST* **15** no. 05, (2020) C05045.
- [30] F. Marinho, L. Paulucci, D. Totani, and F. Cavanna, “LArQL: a phenomenological model for treating light and charge generation in liquid argon,” *JINST* **17** no. 07, (2022) C07009, [arXiv:2202.08905](https://arxiv.org/abs/2202.08905) [physics.ins-det].
- [31] W. Mu, A. I. Himmel, and B. Ramson, “Photon detection probability prediction using one-dimensional generative neural network,” *Mach. Learn.: Sci. Technol.* **3** (2022) 015033, [arXiv:2109.07277](https://arxiv.org/abs/2109.07277).
- [32] **DUNE** Collaboration, “Fd2 vertical drift conceptual design report,” 2022. [https://edms.cern.ch/file/2709820/1/CDR\\_Vertical\\_Single\\_Phase\\_FD\\_Technology\\_Final.pdf](https://edms.cern.ch/file/2709820/1/CDR_Vertical_Single_Phase_FD_Technology_Final.pdf).
- [33] **DUNE** Collaboration, A. Abed Abud *et al.*, “Scintillation light detection in the 6-m drift-length ProtoDUNE Dual Phase liquid argon TPC,” *Eur. Phys. J. C* **82** no. 7, (2022) 618, [arXiv:2203.16134](https://arxiv.org/abs/2203.16134) [physics.ins-det].
- [34] **DUNE** Collaboration, B. Abi *et al.*, “First results on ProtoDUNE-SP liquid argon time projection chamber performance from a beam test at the CERN Neutrino Platform,” *JINST* **15** no. 12, (2020) P12004, [arXiv:2007.06722](https://arxiv.org/abs/2007.06722) [physics.ins-det].
- [35] V. Chepel and H. Araujo, “Liquid noble gas detectors for low energy particle physics,” *JINST* **8** (2013) R04001, [arXiv:1207.2292](https://arxiv.org/abs/1207.2292) [physics.ins-det].
- [36] S. Bricola, A. Menegolli, M. Prata, M. C. Prata, G. L. Raselli, M. Rossella, and C. Vignoli, “Noble-gas liquid detectors: Measurement of light diffusion and reflectivity on commonly adopted inner surface materials,” *Nucl. Phys. B Proc. Suppl.* **172** (2007) 260–262.

- [37] **MicroBooNE Collaboration** Collaboration, R. Acciarri *et al.*, “The Pandora multi-algorithm approach to automated pattern recognition of cosmic-ray muon and neutrino events in the MicroBooNE detector,” *Eur. Phys. J. C* (2017) , arXiv:1708.03135. <https://cds.cern.ch/record/2286065>.
- [38] **MicroBooNE Collaboration**, C. Adams *et al.*, “Ionization electron signal processing in single phase LArTPCs. Part I. Algorithm Description and quantitative evaluation with MicroBooNE simulation,” *JINST* **13** no. 07, (2018) P07006, arXiv:1802.08709 [physics.ins-det].
- [39] **MicroBooNE Collaboration**, C. Adams *et al.*, “Ionization electron signal processing in single phase LArTPCs. Part II. Data/simulation comparison and performance in MicroBooNE,” *JINST* **13** no. 07, (2018) P07007, arXiv:1804.02583 [physics.ins-det].
- [40] P. Antonioli *et al.*, “SNEWS: The SuperNova Early Warning System,” *New J. Phys.* **6** (2004) 114, arXiv:astro-ph/0406214.
- [41] **DUNE Collaboration**, B. Abi *et al.*, “Long-baseline neutrino oscillation physics potential of the DUNE experiment,” *Eur. Phys. J. C* **80** no. 10, (2020) 978, arXiv:2006.16043 [hep-ex].
- [42] **DUNE Collaboration**, A. Abud Abed *et al.*, “Low exposure long-baseline neutrino oscillation sensitivity of the DUNE experiment,” *Phys. Rev. D* **105** no. 7, (2022) 072006, arXiv:2109.01304 [hep-ex].
- [43] D. Brailsford, M. B. Brunetti, S. Alonso Monsalve, A. Blake, A. Chappell, J. Marshall, L. H. Whitehead, and E. Worcester, “Reconstruction performance studies for liquid argon time projection chambers with two and three readout planes,” <https://www.osti.gov/biblio/1826741>.
- [44] **DUNE Collaboration** Collaboration, B. Abi *et al.*, “Neutrino interaction classification with a convolutional neural network in the dune far detector,” *Phys. Rev. D* **102** (Nov, 2020) 092003. <https://link.aps.org/doi/10.1103/PhysRevD.102.092003>.
- [45] C. Rubbia, “The liquid argon time projection chamber: A new concept for neutrino detectors.” CERN-EP/77-08 (1977).
- [46] C. Cantini *et al.*, “Performance study of the effective gain of the double phase liquid Argon LEM Time Projection Chamber,” *JINST* **10** no. 03, (2015) P03017, arXiv:1412.4402 [physics.ins-det].
- [47] F. Sauli, “The gas electron multiplier (GEM): Operating principles and applications,” *Nucl. Instrum. Meth. A* **805** (2016) 2–24.
- [48] B. Baibussinov *et al.*, “Operation of a LAr-TPC equipped with a multilayer LEM charge readout,” *JINST* **13** no. 03, (2018) T03001, arXiv:1711.06781 [physics.ins-det].

- [49] DUNE Collaboration, “Anode PCB CAD Drawings.” <https://edms.cern.ch/document/2670965/1>, 2021.
- [50] DUNE Collaboration, “Tde adapter boards files,” 2022. <https://edms.cern.ch/document/2717223>.
- [51] DUNE Collaboration, “Bde adapter boards,” 2022. <https://edms.cern.ch/document/2765576>.
- [52] DUNE Collaboration, “Edge connector pcbs,” 2022. <https://edms.cern.ch/document/2785495>.
- [53] LBNF/DUNE, “Project Schedule Reports from P6, 24 Feb 2023.” Available upon request.
- [54] E. Voirin, “LAr Thermal Fluid and Impurity Simulations – Vertical Drift 3 View Detector,” 2021. <https://edms.cern.ch/document/2675694>.
- [55] “TDE Grounding Document.” <https://edms.cern.ch/document/2737071>, 2022.
- [56] DUNE Collaboration, “Tde to crp interface.” Online, March, 2022. <https://edms.cern.ch/document/2618998/1>.
- [57] DUNE Collaboration, “Fd2-vd daq and tde consortia interface document.” Online, March, 2022. <https://edms.cern.ch/document/2618999/2>.
- [58] DUNE Collaboration, “Tde to installation/integration interface.” Online, June, 2022. <https://edms.cern.ch/document/2648556>.
- [59] “MCH and 40Gbit/s connectivity.” <https://edms.cern.ch/document/2737105/1>, 2022.
- [60] D. Autiero, “TDE Data Format.” <https://edms.cern.ch/document/2737054/1>.
- [61] V. Radeka, “Shielding and grounding in large detectors,” in *4th Workshop on Electronics for LHC Experiments (LEB 98)*. 1998.
- [62] C. Hu, S. C. Tam, F.-C. Hsu, P.-K. Ko, T.-Y. Chan, and K. W. Terrill, “Hot-electron-induced mosfet degradation—model, monitor, and improvement,” *IEEE Transactions on Electron Devices* **32** no. 2, (Feb, 1985) 375–385.
- [63] G. D. Geronimo, A. D’Andragora, S. Li, N. Nambiar, S. Rescia, E. Vernon, H. Chen, F. Lanni, D. Makowiecki, V. Radeka, C. Thorn, and B. Yu, “Front-end ASIC for a liquid argon tpc,” *IEEE Transactions on Nuclear Science* **58** no. 3, (June, 2011) 1376–1385.
- [64] D. W. Cline and P. R. Gray, “A power optimized 13-b 5 msamples/s pipelined analog-to-digital converter in 1.2 micron CMOS,” *IEEE Journal of Solid-State Circuits* **31** no. 3, (Mar, 1996) 294–303.



- [65] E. G. Soenen and R. L. Geiger, “An architecture and an algorithm for fully digital correction of monolithic pipelined adcs,” *IEEE Transactions on Circuits and Systems II: Analog and Digital Signal Processing* **42** no. 3, (Mar, 1995) 143–153.
- [66] C. Grace *et al.*, “ColdADC\_P2: A 16-Channel Cryogenic ADC ASIC for the Deep Underground Neutrino Experiment,” *IEEE Trans. Nucl. Sci.* **69** no. 1, (2021) 105–112.
- [67] “I2c info - i2c bus, interface and protocol.” <https://www.i2c-bus.org/>.
- [68] Teverovsky, Alexander, “Reliability of electronics at cryogenic temperatures.” <https://nepp.nasa.gov/DocUploads/1BCC6326-46F7-4C5E-94D476A8B6176ED1/Approach%20to%20Reliability%20Testing%20at%20cryo%20NEPP.pdf>, 2005.
- [69] H. Chen *et al.*, “Lifetime Study of COTS ADC for SBND LAr TPC Readout Electronics,” in *21st IEEE Real Time Conference*. 6, 2018. arXiv:1806.09226 [physics.ins-det].
- [70] S. Li, J. Ma, G. D. Geronimo, H. Chen, and V. Radeka, “LAr TPC electronics CMOS lifetime at 300 K and 77 K,” *IEEE Trans. Nuclear Science* **60** (2013) 4737.
- [71] J. R. Hoff, G. W. Deptuch, G. Wu, and P. Gui, “Cryogenic lifetime studies of 130 nm and 65 nm nmos transistors for high-energy physics experiments,” *IEEE Transactions on Nuclear Science* **62** no. 3, (June, 2015) 1255–1261.
- [72] J. Ma, *Hot Carrier Study of MOSFET at 300K and 77K*. PhD thesis, Stony Brook University, 2015. <https://ir.stonybrook.edu/xmlui/handle/11401/77479;jsessionid=B48204706883E63FBFAD1431023EDAB0>.
- [73] Yu, B., “DP HVS Conceptual Design,” 2019. <https://edms.cern.ch/document/2084051/1>.
- [74] “High voltage feedthrough technical drawings.” <https://edms.cern.ch/document/2593486/1>.
- [75] A. Catinaccio, “LBNF Cryostat: Design and Structural Assessment.” Available upon request.
- [76] Asaadi *et al.*, “Testing of high voltage surge protection devices for use in liquid argon TPC detectors,” *JINST* **9** no. 09, (2014) P09002, arXiv:1406.5216 [physics.ins-det].
- [77] T. Doke, “Fundamental properties of liquid argon, krypton and xenon as radiation detector media,” *Portugal. Phys.* **12** (1981) 9–48.
- [78] A. Hitachi, T. Doke, and A. Mozumder, “Luminescence quenching in liquid argon under charged-particle impact: Relative scintillation yield at different linear energy transfers,” *Phys. Rev. B* **46** (Nov, 1992) 11463–11470.
- [79] C. Wahl, E. Bernard, W. Lippincott, J. Nikkel, Y. Shin, and D. Mckinsey, “Pulse-shape

- discrimination and energy resolution of a liquid-argon scintillator with xenon doping,” *JINST* **9** (2014) 06013, [arXiv:1403.0525](#) [[physics.ins-det](#)].
- [80] S. Kubota, M. Hishida, S. Himi, J. Suzuki, and J. Ruan, “The suppression of the slow component in xenon-doped liquid argon scintillation,” *Nucl. Instrum. Meth. A* **327** (1993) 71–74.
- [81] M. Babicz, S. Bordoni, A. Fava, U. Kose, M. Nessi, F. Pietropaolo, G. Raselli, F. Resnati, M. Rossella, P. Sala, F. Stocker, and A. Zani, “A measurement of the group velocity of scintillation light in liquid argon,” *JINST* **15** no. 09, (2020) P09009, [arXiv:2002.09346](#) [[physics.ins-det](#)].
- [82] **WArP** Collaboration, R. Acciarri *et al.*, “Effects of Nitrogen contamination in liquid Argon,” *JINST* **5** (2010) P06003, [arXiv:0804.1217](#) [[nucl-ex](#)].
- [83] Y.-J. Wu, C. Y. R. Wu, S.-L. Chou, M.-Y. Lin, H.-C. Lu, J.-I. Lo, and B.-M. Cheng, “Spectra and Photolysis of Pure Nitrogen and Methane Dispersed in Solid Nitrogen with Vacuum-Ultraviolet Light,” *ApJ* **746** no. 2, (2012) 175.
- [84] **DUNE** Collaboration, B. Abi *et al.*, “The Single-Phase ProtoDUNE Technical Design Report,” (2017) , [arXiv:1706.07081](#) [[physics.ins-det](#)].
- [85] B. J. P. Jones, C. S. Chiu, J. M. Conrad, C. M. Ignarra, T. Katori, and M. Toups, “A Measurement of the Absorption of Liquid Argon Scintillation Light by Dissolved Nitrogen at the Part-Per-Million Level,” *JINST* **8** (2013) P07011, [arXiv:1306.4605](#) [[physics.ins-det](#)]. Erratum: *JINST* **8** (2013) E09001.
- [86] H. V. Souza *et al.*, “Liquid argon characterization of the X-ARAPUCA with alpha particles, gamma rays and cosmic muons,” *JINST* **16** no. 11, (2021) P11002, [arXiv:2106.04505](#) [[physics.ins-det](#)].
- [87] **DUNE** Collaboration, C. Palomares, “Detection efficiency measurement and operational tests of the X-Arapuca for the first module of DUNE Far Detector,” in *Light Detection In Noble Elements*. 11, 2022. [arXiv:2211.15503](#) [[hep-ex](#)].
- [88] **DUNE** Collaboration, L. Paulucci, “The DUNE vertical drift photon detection system,” *JINST* **17** no. 01, (2022) C01067, [arXiv:2112.09520](#) [[physics.ins-det](#)].
- [89] M. Hofmann, T. Dandl, T. Heindl, A. Neumeier, L. Oberauer, W. Potzel, S. Roth, S. Schönert, J. Wieser, and A. Ulrich, “Ion-beam excitation of liquid argon.,” *The European Physics Journal* **C73** (Oct, 2013) 2618.
- [90] D. Akimov, V. Belov, A. Konovalov, A. Kumpan, O. Razuvaeva, D. Rudik, and G. Simakov, “Fast component re-emission in xe-doped liquid argon.,” *Journal of Instrumentation* **14** (Sep, 2019) P09022.
- [91] A. L. Fahrenbruch, L. Lopez-Otero, J. G. Werthern, and T.-C. Wu, “GaAs- and

- InAlGaAs-based concentrator-type cells for conversion of power transmitted by optical fibers,” *Conference Record of the Twenty Fifth IEEE Photovoltaic Specialists Conference - 1996*, (1996) 117–120.
- [92] B. Dinkespiler *et al.*, “Development of an analog optical link for the front end readout of the ATLAS electromagnetic calorimeter,” *Nucl. Instrum. Meth. A* **431** (1999) 531–547.
- [93] L. Consiglio, “The cryogenic electronics for Dark Side-20k SiPM readout,” *JINST* **15** no. 05, (2020) C05063.
- [94] **DUNE** Collaboration, “Fd1-hd tpc/fd2-vd bde and jt daq consortia interface document.” Online, January, 2022. <https://edms.cern.ch/ui/#!/master/navigator/document?P:100297753:100944889:subDocs>.
- [95] **DUNE** Collaboration, “Pds and jt daq consortia interface documents.” Online, January, 2022. <https://edms.cern.ch/ui/#!/master/navigator/document?P:100297753:100944098:subDocs>.
- [96] **DUNE** Collaboration, “Jt daq and jt cal/ci consortia interface document.” Online, December, 2021. <https://edms.cern.ch/ui/#!/master/navigator/document?P:100297753:100646719:subDocs>.
- [97] **DUNE** Collaboration, “Jt comp and jt daq consortium interface document.” Online, December, 2021. <https://edms.cern.ch/ui/#!/master/navigator/document?P:100297753:100646716:subDocs>.
- [98] **DUNE** Collaboration, “Dune network design draft.” Online, January, 2022. <https://edms.cern.ch/ui/#!/master/navigator/document?D:100973491:100973491:subDocs>.
- [99] “Kubernetes Documentation.” <https://kubernetes.io/docs/home/>.
- [100] **DUNE** Collaboration, “Jt daq installation interface.” Online, January, 2022. <https://edms.cern.ch/ui/#!/master/navigator/document?D:101007827:101007827:subDocs>.
- [101] “Cryostat and Cryogenics Infrastructure for the DUNE Far Detector, Design Report.” <https://edms.cern.ch/document/2810252>.
- [102] LBNF/DUNE, “LBNF/DUNE US FDC ES&H Installation Plan.” <https://edms.cern.ch/document/2858967>.
- [103] “LBNF-DUNE Project Management Plan.” <https://edms.cern.ch/document/2808700>.
- [104] “DUNE Governance.” <https://edms.cern.ch/document/2808699>.
- [105] “Draft LBNF-DUNE DOE Project Execution Plan for CD1RR.” <https://edms.cern.ch/document/2808695>.

- [106] LBNF/DUNE, “LBNF/DUNE Requirements.”  
<https://edms.cern.ch/project/CERN-0000214368>.
- [107] “LBNF-DUNE Risk Registry.” <https://edms.cern.ch/document/2808697>.
- [108] **DUNE** Collaboration, B. Abi *et al.*, “Deep Underground Neutrino Experiment (DUNE), Far Detector Technical Design Report, Volume III. DUNE Far Detector Technical Coordination,” *JINST* **15** no. 08, (2020) T08009, arXiv:2002.03008 [physics.ins-det].
- [109] “Far Site DUNE Mechanical Integration.”  
<https://edms.cern.ch/project/CERN-0000204070>.
- [110] “LBNF-DUNE Systems Engineering Management Plan.”  
<https://edms.cern.ch/document/2808693>.
- [111] “DUNE design review process.” <https://edms.cern.ch/document/2173197>.
- [112] Fermilab, “Fermilab ES&H Manual.”  
<https://publicdocs.fnal.gov/cgi-bin/ListBy?topicid=49>.
- [113] “DUNE subsystem and component design reviews.”  
<https://indico.fnal.gov/category/586>.
- [114] “DUNE subsystem and component design review reports.”  
<https://edms.cern.ch/project/CERN-0000211273>.
- [115] “DUNE subsystem and component design review recommendation tracking.”  
<https://edms.cern.ch/project/CERN-0000204073>.
- [116] “LBNF-DUNE Quality Assurance Plan.” <https://edms.cern.ch/document/2808696>.